

Lecture Notes in Production Engineering

Steffen Ihlenfeldt *Editor*

3rd International Conference on Thermal Issues in Machine Tools (ICTIMT2023)

OPEN ACCESS

 Springer

Lecture Notes in Production Engineering

Series Editors

Bernd-Arno Behrens, *Leibniz Universitaet Hannover, Garbsen, Niedersachsen, Germany*

Wit Grzesik , *Opole, Poland*

Steffen Ihlenfeldt, *Institute of Mechatronic Engineering, TU Dresden, Dresden, Germany*

Sami Kara, *Mechanical & Manufacturing Engg, University of New South Wales, Sydney, NSW, Australia*

Soh-Khim Ong, *Mechanical Engineering, National University of Singapore, Singapore, Singapore*

Tetsuo Tomiyama, *Tokyo, Japan*

David Williams, *Loughborough, UK*

Lecture Notes in Production Engineering (LNPE) is book series that reports the latest research and developments in Production Engineering, comprising:

- Biomanufacturing
- Control and Management of Processes
- Cutting and Forming
- Design
- Life Cycle Engineering
- Machines and Systems
- Optimization
- Precision Engineering and Metrology
- Surfaces

LNPE publishes authored conference proceedings, contributed volumes and authored monographs that present cutting-edge research information as well as new perspectives on classical fields, while maintaining Springer's high standards of excellence. Also considered for publication are lecture notes and other related material of exceptionally high quality and interest. The subject matter should be original and timely, reporting the latest research and developments in all areas of production engineering. The target audience of LNPE consists of advanced level students, researchers, as well as industry professionals working at the forefront of their fields. Much like Springer's other Lecture Notes series, LNPE will be distributed through Springer's print and electronic publishing channels.

Indexed in Scopus To submit a proposal or request further information please contact Anthony Doyle, Executive Editor, Springer (anthony.doyle@springer.com).

Steffen Ihlenfeldt
Editor

3rd International Conference on Thermal Issues in Machine Tools (ICTIMT2023)

 Springer

Editor
Steffen Ihlenfeldt
Institute of Mechatronic Engineering
TU Dresden
Dresden, Germany



ISSN 2194-0525 ISSN 2194-0533 (electronic)
Lecture Notes in Production Engineering
ISBN 978-3-031-34485-5 ISBN 978-3-031-34486-2 (eBook)
<https://doi.org/10.1007/978-3-031-34486-2>

© The Editor(s) (if applicable) and The Author(s) 2023. This book is an open access publication.

Open Access This book is licensed under the terms of the Creative Commons Attribution 4.0 International License (<http://creativecommons.org/licenses/by/4.0/>), which permits use, sharing, adaptation, distribution and reproduction in any medium or format, as long as you give appropriate credit to the original author(s) and the source, provide a link to the Creative Commons license and indicate if changes were made.

The images or other third party material in this book are included in the book's Creative Commons license, unless indicated otherwise in a credit line to the material. If material is not included in the book's Creative Commons license and your intended use is not permitted by statutory regulation or exceeds the permitted use, you will need to obtain permission directly from the copyright holder.

The use of general descriptive names, registered names, trademarks, service marks, etc. in this publication does not imply, even in the absence of a specific statement, that such names are exempt from the relevant protective laws and regulations and therefore free for general use.

The publisher, the authors, and the editors are safe to assume that the advice and information in this book are believed to be true and accurate at the date of publication. Neither the publisher nor the authors or the editors give a warranty, expressed or implied, with respect to the material contained herein or for any errors or omissions that may have been made. The publisher remains neutral with regard to jurisdictional claims in published maps and institutional affiliations.

This Springer imprint is published by the registered company Springer Nature Switzerland AG
The registered company address is: Gewerbestrasse 11, 6330 Cham, Switzerland

Presentation of CIRP

CIRP was founded in 1951 with the aim to address scientifically, through international co-operation, issues related to modern production science and technology. The International Academy for Production Engineering takes its abbreviated name from the French acronym of **C**ollege **I**nternational pour la **R**echerche en **P**roductique (CIRP) and includes some 500 members from 50 countries. The number of members is intentionally kept limited, so as to facilitate informal scientific information exchange and personal contacts.

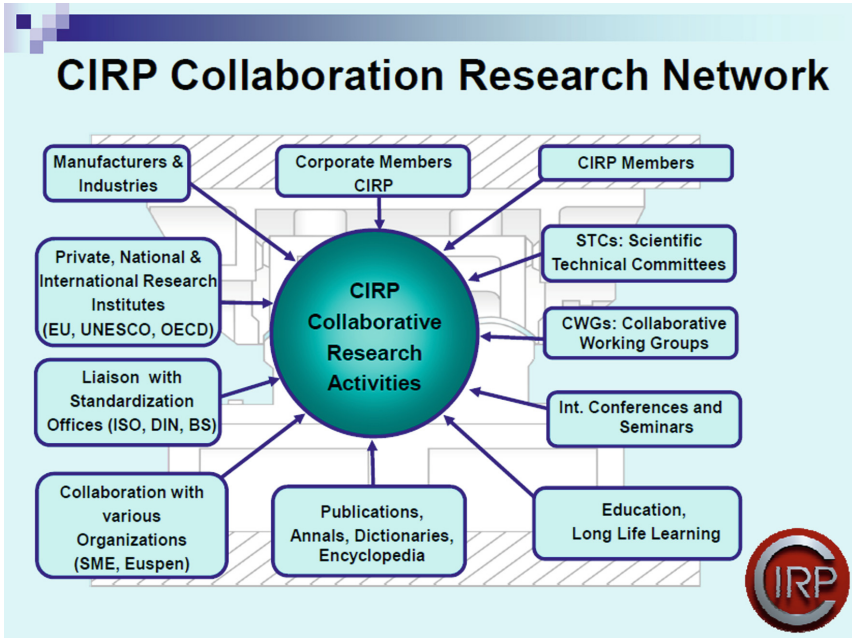
CIRP has some 180 fellows and honorary fellows who are internationally recognized scientists elected to be CIRP members for life. Due to the limited number of CIRP fellows, the election of a fellow is a lengthy, rigorous process ensuring the highest possible academic standards.

CIRP includes some 150 associate members and well-known scientists, with high potential, elected typically for a period of three years with the possibility of renewal. A number of associate members eventually become fellows. Some associate members may also belong to fields related to manufacturing.

CIRP, although an academic organization, encourages the participation of industry in its activities. There are some 150 corporate members who follow the research work of the academic members of CIRP and very often contribute to the information exchange within CIRP by presenting their views on industrial needs and perspectives.

Young research affiliates and some invited members, particularly from countries not yet involved in CIRP, are also included in the CIRP community.

In a recent development, there is work under way to establish a CIRP network of young scientists active in manufacturing research.



CIRP is organized along the lines of a number of Scientific Technical Committees (STCs) and Working Groups (WGs), covering many areas. CIRP organizes annually a General Assembly and the so-called Winter Meetings. In the General Assembly (GA), which lasts for a week, there is an intensive technical program with over 140 technical paper presentations from different fields of manufacturing, a number of keynote papers, at the opening of the conference, as well as technical work within the STCs.

In parallel, there is a social program, aiming at making the culture of the General Assembly site known to the members and also at creating an informal environment for information exchange among the members. The Winter Meetings are always organized in Paris and last three days. Moreover, CIRP organizes, through its membership, a number of conferences, notably the Manufacturing Systems Seminar and a number of other conferences with relevant topics. CIRP members also organize a variety of conferences, under the sponsorship of CIRP.

The main publications of CIRP are the CIRP Annals under ISI standards with two volumes; Volume I, with refereed papers presented in the GA by fellows, associate, corporate and invited members and Volume II with refereed keynote papers. Then there is the Journal of Manufacturing Science and Technology, with four volumes. There are also proceedings of CIRP conferences available online on Procedia-CIRP, tri-lingual dictionaries of production engineering and their Encyclopedia of Production Engineering, etc. A Newsletter is published twice a year. Currently, the CIRP Annals and the Journal of Manufacturing Science and Technology are published by Elsevier, while Springer Verlag publishes the Dictionaries of Production Engineering and the Encyclopedia of Production Engineering.

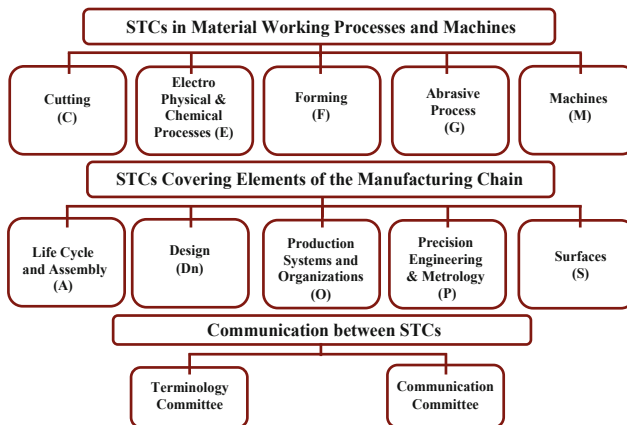
The CIRP organization includes besides the president, who is elected annually, the Council and a number of other committees ensuring a continuous improvement and reflecting the changing needs of manufacturing science and technology.

CIRP has its headquarters in Paris, staffed by permanent personnel and welcomes potential corporate members and interested parties in CIRP publication and activities in general.

CIRP Scientific Technical Committees

Ten Scientific and Technical Committees (STCs) are responsible for their subject areas of interest and for coordinating CIRP run collaborative research projects.

Additionally, working groups are created to investigate the special problems of education and training associated with new manufacturing technology.



Preface

The thermal behavior of machine tools is widely considered as one of the most important impacts on the machining accuracy. Classic strategies to cope with negative thermal influences comprise conditioning the air in the manufacturing facility, part production at thermal steady state of machine tools and the cooling of their heat generating components. These measures consume significant additional energy and require expensive production equipment, facilities and operational costs. This motivated researchers and engineers in academia and industry all over the world to explore new methods for minimizing thermal errors with no additional costs and minimal ecological footprint.

On this path, better and faster computer models became key factors for correcting thermally induced errors in production or for compensating them through design measures and mechatronic equipment based on much better predictions of the thermal machine behavior. The ICTIMT 2023 at the Technische Universität Dresden featured the current international state of the art on research and development in the field of thermal issues in milling machines and lathes with a special focus on model-based correction and compensation methods. I want to acknowledge and thank all researchers featured in these proceedings for their hard work and dedication.

As special the conference highlighted 12 years of development by the CRP/TR 96 research community from Dresden, Aachen and Chemnitz who created, investigated and advanced numerous approaches to compensate and correct deviations at the tool center point.

The proceedings addresses researchers as well as engineers in industrial companies who are looking for inspiration and new solutions to solve the thermal issues in their production equipment.

Enjoy a great read of this collection of innovative technologies. I am sure you will find the right approach, idea and contact for your specific needs.

Sincerely yours

Steffen Ihlenfeldt

Organization

Editorial Committee

T. Bergs	RWTH Aachen University, Germany Laboratory for Machine Tools and Production Engineering
C. Brecher	RWTH Aachen University, Germany Laboratory for Machine Tools and Production Engineering
E. Budak	Sabanci University, Türkiye Faculty of Engineering and Natural Sciences
B. Denkena	Leibniz Universität Hannover, Germany Institute of Production Engineering and Machine Tools
M. Dix	Fraunhofer Institute for Machine Tools and Forming Technology IWU, Germany
O. Horejš	Czech Technical University in Prague, Czechia Research Center of Manufacturing Technology
P. Kolar	Czech Technical University in Prague, Czechia Research Center of Manufacturing Technology
M. Mareš	Czech Technical University in Prague, Czechia Research Center of Manufacturing Technology
H.-C. Möhring	University of Stuttgart, Germany Institute for Machine Tools
L. Penter	TU Dresden, Germany Chair of Machine Tools Development and Adaptive Controls
M. Ritou	Université de Nantes, France Laboratoire des Sciences du Numérique de Nantes
M. Sulitka	Czech Technical University in Prague, Czechia Research Center of Manufacturing Technology
R. Wertheim	Braude College, Israel Faculty of Mechanical Engineering

Contents

Thermal Error Compensation and Correction

Development of Thermal Displacement Prediction Model and Thermal Deformation Measurement Methods	3
<i>Koji Ota, Masahiko Mori, and Naruhiro Irino</i>	
Thermal Compensation of Sudden Working Space Condition Changes in Swiss-Type Lathe Machining	15
<i>Petr Kaftan, Josef Mayr, and Konrad Wegener</i>	
Hybrid Thermal Error Compensation Combining Integrated Deformation Sensor and Regression Analysis Based Models for Complex Machine Tool Designs	28
<i>Christian Naumann, Andreas Naumann, Nico Bertaggia, Alexander Geist, Janine Glänzel, Roland Herzog, Daniel Zontar, Christian Brecher, and Martin Dix</i>	
Thermal Error Compensation Models Utilizing the Power Consumption of Machine Tools	41
<i>Sebastian Lang, Nico Zimmermann, Josef Mayr, Konrad Wegener, and Markus Bambach</i>	
An Indicative Model Considering Part of the Thermo-Mechanical Behaviour of a Large Grinding Machine	54
<i>Martin Mareš, Otakar Horejš, and Pravoslav Nykodým</i>	
Adaptive Thermal Model for Structure Model Based Correction	67
<i>Xaver Thiem, Holger Rudolph, Robert Krahn, Steffen Ihlenfeldt, Christof Fetzter, and Jens Müller</i>	
Adaptive Thermal Error Compensation Model of a Horizontal Machining Centre	83
<i>Otakar Horejš, Martin Mareš, Michal Straka, Jiří Švéda, and Tomáš Kozlok</i>	
Analysing the Impact of Process Dependent Thermal Loads on the Prediction Accuracy of Thermal Effects in Machine Tool Components	99
<i>Eric Wenkler, Christoph Steiert, Eugen Boos, and Steffen Ihlenfeldt</i>	

Process Parallel Models

A Data-Based Model of the Thermo-Elastic TCP Error Using the Encoder
Difference and Neural Networks 119
Christian Brecher, Mathias Dehn, and Stephan Neus

Model Order Reduction Strategies for the Computation of Compact
Machine Tool Models 132
Quirin Aumann, Peter Benner, Jens Saak, and Julia Vettermann

Simulation of Thermoelastic Behavior of Technical Systems
with Relatively Moving Parts - Modeling Process, Part Coupling
Approaches and Application to Machine Tools 146
Stefan Sauerzapf and Michael Beitelschmidt

Thermal Modal Analysis for Volumetric Error Characterization 159
*Natalia Colinas-Armijo, Beñat Iñigo, Luis Norberto López de Lacalle,
and Gorka Aguirre*

Development of a System for the Evaluation and Recommendation
of Solution Methods for Thermally Induced Errors on Machine Tools 168
Carola Gißke, Axel Fickert, and Hajo Wiemer

Sensor Integration

Smart Pressure Film Sensor for Machine Tool Optimization
and Characterization of the Dynamic Pressure Field on Machine Surfaces 179
*Andreas Erben, Alexander Geist, Immanuel Voigt, Björn Senf,
Thomas Mäder, Janine Glänzel, Steffen Ihlenfeldt,
and Welf-Guntram Drossel*

Thermally Induced Clamping Force Deviations in a Sensory Chuck
for Thin-Walled Workpieces 192
Berend Denkena, Heinrich Klemme, Eike Wnendt, and Matthias Meier

Components

Improving the Thermal Behavior of High-Speed Spindles Through the Use
of an Active Controlled Heat Pipe System 203
*Lucas Jonath, Jörg Luderich, Jonas Brezina,
Ana Maria Gonzalez Degetau, and Selim Karaoglu*

Thermal Growth of Motor Spindle Units 219
*Tassilo Heinze, Hans-Joachim Koriath,
and Alexander Pavlovich Kuznetsov*

Thermal Modeling Challenges of High-Speed Motorized Spindles 240
Lukas Koch, Felix Butz, Gordana Krüger, and Frank Döpfer

Design and Materials

Experimental Investigation of Passive Thermal Error Compensation
Approach for Machine Tools 265
Immanuel Voigt, Axel Fickert, Hajo Wiemer, and Welf-Guntram Drossel

Determination of the Thermal Properties of Pre-stressed Fiber-Reinforced
Polymer Concrete 278
Michelle Engert, Kim Torben Werkle, and Hans-Christian Möhring

Tools and Processes

Simulation of cBN Grain Wear During Single Grain Engagement
Considering Cleavage Planes 289
Marc Bredthauer, Sebastian Barth, Patrick Mattfeld, and Thomas Bergs

Development of a Tool Temperature Simulation During Side Milling 308
*Thorsten Helmig, Hui Liu, Simon Winter, Thomas Bergs,
and Reinhold Kneer*

Three-Dimensional Modeling of Thermomechanical Tool Loads During
Milling Using the Coupled Eulerian-Lagrangian Formulation 318
Hui Liu, Markus Meurer, and Thomas Bergs

Model Verification

Definition of a Non-contact Induction Heating of a Cutting Tool
as a Substitute for the Process Heat for the Verification of a Thermal
Simulation Model 333
Lukáš Topinka, Radomír Pruša, Rostislav Huzlík, and Joachim Regel

Measuring Thermally Induced Tool Center Point Displacements
on Milling Machines Using a Test Workpiece 345
Axel Fickert, Hajo Wiemer, Carola Gißke, and Lars Penter

Author Index 359

Thermal Error Compensation and Correction



Development of Thermal Displacement Prediction Model and Thermal Deformation Measurement Methods

Koji Ota^(✉), Masahiko Mori, and Naruhiro Irino

DMG MORI Co., Ltd., 2-3-23 Shiomi, Koto-ku, Tokyo 135-0052, Japan
ko-ota@dmgmori.co.jp

Abstract. In machine tools, it is important to maintain accuracy against heat in the entire machining space. The reduction of thermal displacement is achieved by measuring it accurately and then clarify the relationship between the temperature change and the thermal deformation and then creating the prediction and compensation model or applying the countermeasure to suppress the thermal deformation. To solve this issue, the authors have developed methods to measure thermal deformation in two-dimensional space using a laser tracker and cameras. A laser tracker method achieved higher accuracy and smaller measurement uncertainty. Vision-based methods achieved equivalent measurement accuracy to a laser tracker method at shorter measurement time and lower cost. To compensate thermal displacement, convolutional neural network model was developed. Thermal displacement was predicted from temperature sensors with higher accuracy than conventional models. These methods contribute to the development of higher precision machine tools.

Keywords: Thermal error · Metrology · Accuracy

1 Introduction

Thermal displacement is one of the most significant factors that degrade machine accuracy. With the progress of process integration and automation of machining process, it has become more important to maintain dimensional and geometric accuracy over the entire machining space of a machine during operation. The reduction of thermal displacement is achieved by measuring it and thermal deformation accurately and clarify the relationship between the temperature change and the thermal deformation and then creating the prediction and compensation model or applying the countermeasure to suppress the thermal deformation. Many studies have been conducted about reduction of thermal displacement [1]. The laser tracker was used to measure the thermal displacement of 5-axis machine tool [2]. About compensation for thermal displacement, the method using temperature sensors [3] and NC unit internal data [4] are developed and robust and accurate prediction models are developed for compensation [5, 6]. To reduce thermal deformation, isolation of heat sources, reduction of generated heat and equalization of temperature distribution are applied [7].

We have developed both measurement method and compensation method of tool trajectory. A laser tracker and vision cameras are used to measure the thermal displacement on a two-dimensional plane to visualize thermal deformation. Deep-learning is used for accurately predicting and compensating thermal displacement from temperature sensors. A measurement using a laser tracker achieved higher accuracy and smaller measurement uncertainty than the previous method. A measurement using vision cameras achieved shorter measurement time and lower cost than a laser tracker method. Deep-learning prediction model achieved higher accuracy than conventional models. In this paper, we present the detail of these methods.

2 Thermal Displacement Prediction by Deep-Learning

2.1 Convolutional Neural Network (CNN)

By using convolutional neural network (CNN), a type of deep learning, thermal displacement can be predicted with higher accuracy [8]. CNN is a commonly used method in the field of image recognition, which extracts image features by convolution and pooling process. Figure 1 shows a conceptual diagram of a CNN. In predicting thermal displacement, temperature data of machine structure is used as input and displacement as output.

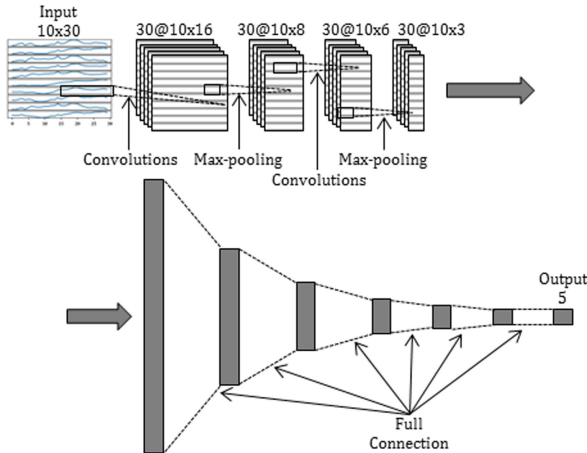


Fig. 1. A conceptual diagram of a CNN

2.2 Thermal Sensitivity

To predict thermal displacement from temperature data, it is necessary to know the contribution of temperature variation of the machine structure to thermal displacement and install temperature sensors at the large contribution. Therefore, we defined the

relationship between temperature and thermal displacement as thermal sensitivity as follows:

$$W = K^{-1}H \quad (1)$$

where W is the thermal sensitivity, K is the stiffness matrix of the structure, and H is the temperature-load transformation matrix expressed as:

$$p = H \Delta t \quad (2)$$

where p is the load applied to the machine structure by the temperature variation and Δt is the temperature variation.

The thermal sensitivity was calculated on a turning center. Figure 2 shows the thermal sensitivity in the X-axis direction. The red area shows the displacement of the turret and headstock away from each other as the temperature increases, and the blue area is in the opposite direction.

2.3 The Prediction Results

Figure 3 shows the performance of the CNN. By using temperature data from 10 locations, calculations were performed with ridge regression, non-convolutional NN and CNN. The CNN prediction error was 59.5% smaller than ridge regression and 71.6% smaller than non-convolutional NN.

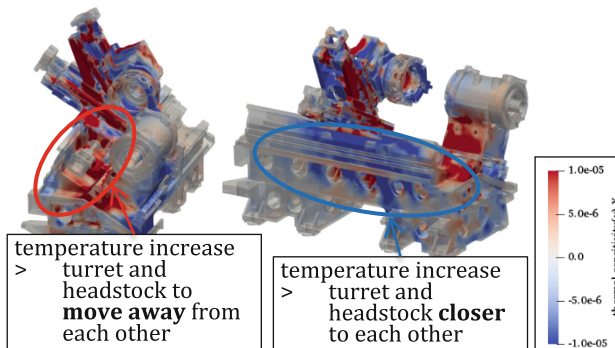


Fig. 2. Thermal sensitivity of X-axis of turning center

Figure 4 shows the learning results. The prediction result of the evaluation data shows small error. The results show that CNN compensations can reduce the thermal displacement by 81.2% and 88.5% than non-compensation results.

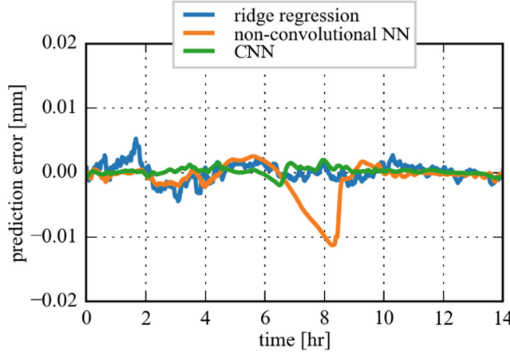


Fig. 3. Comparison between CNN and conventional methods

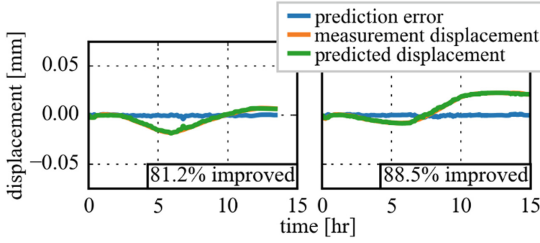


Fig. 4. Thermal displacement prediction result by evaluation data

3 Thermal Deformation Measurement on a Two-Dimensional Trajectory

3.1 Principle of Error Estimation

Table 1 shows the geometric error parameter to be identified as an example of the measurement on the YZ plane of a vertical machining center. The two-dimensional trajectory can be calculated by using them. The purpose of the algorithm is to identify them for every point of measurement range, $(y_1, \dots, y_{N_y}$ in Y-axis and z_1, \dots, z_{N_z} in Z-axis). (y_0, z_0) are the reference point where all geometric errors are defined zero [9]. $E_{YY}(y_j)$ are defined as the values measured at $z = z_0$.

The measurement is taken in YZ plane with the laser tracker. As shown in Fig. 5 a retroreflector attached to the spindle is positioned at every stop position $\mathbf{P}_n^* = [y_j, z_k]^T$ ($n = 1, \dots, N$) and the distance d_0 ($n = 1, \dots, N$) between the tracker and the retroreflector is measured. The 2D positioning error $\Delta \mathbf{P}_n$ for each command position can be expressed as follows by using the symbols in Table 1.

$$\Delta \mathbf{P}_n = \begin{bmatrix} E_{YY}(y_j) + E_{YZ}(z_k) - (E_{A0Y} + E_{AY}(y_j))(z_k - z_0) + \Delta y_0 \\ E_{ZY}(y_j) + E_{ZZ}(z_k) + \Delta z_0 \end{bmatrix} \quad (3)$$

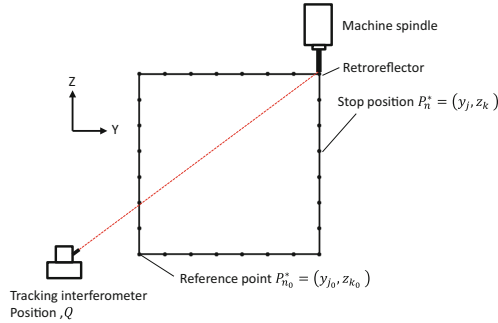
Table 1. Geometric error parameters on the YZ plane [10].

y_0, z_0	Reference point of geometric error
$E_{YY}(y_j)$	Linear positioning deviation of Y-axis at $y = y_j, z = z_0$
$E_{ZY}(y_j)$	Straightness deviation of Y-axis at $y = y_j$
$E_{AY}(y_j)$	Pitch error motion of Y-axis at $y = y_j$
$E_{YZ}(z_k)$	Straightness deviation of Z-axis at $z = z_k$
$E_{ZZ}(z_k)$	Linear positioning deviation of Z-axis at $z = z_k$
$E_{A(0Y)Z}$	Squareness error of Z-axis to Y-axis

With these definitions, the parameters in Table 1 can be identified by solving the following problem.

$$\min_e \sum_n (|\mathbf{P}_n^* + \Delta \mathbf{P}_n - \mathbf{Q}| - (d_n + d_0))^2 \quad (4)$$

where, $\mathbf{Q} = [y_q, z_q]^T$ is the tracker position and d_0 is the dead path length. \mathbf{e} is unknown values consisting of \mathbf{Q} , d_0 , and parameters in Table 1. $(\Delta y_0, \Delta z_0)$ is defined as the displacement of reference point. The assumption that the tracker position \mathbf{Q} is constant throughout the experiment leads to increased uncertainty [2]. By these additional parameters, the tracker position can be handled as a constant. $(\Delta y_0, \Delta z_0)$ is directly measured with a displacement sensor and then uncertainty is greatly reduced.

**Fig. 5.** Tracking measurement on YZ plane

3.2 Experimental Results

Thermal deformation in the YZ plane of vertical machining center was measured. Figure 6 shows the configuration of the machine. The following measurements are performed at each measurement cycle. The distance between the tracker and the retroreflector was measured at every stop position along the rectangular trajectory shown in Fig. 5.

E_{YY} is measured directly by the tracker at the tracker's Z position and E_{AY} is measured by a level simultaneously. E_{ZZ} is measured at the tracker's Y position. $(\Delta y_0, \Delta z_0)$ is measured directly by displacement sensors. The above measurements were taken twice at one-hour intervals while the Z-axis was moving back and forth at the maximum speed, and then twice again at one-hour intervals while the machine was stopped. Figure 7 shows the experimental result and calculated 2D trajectory. The estimated trajectory is shifted to Z + direction due to heat generated by Z-axis movement. At the same time, Z-axis is tilted to the Y- direction. This indicates that heat generated by Z-axis movement caused thermal deformation of the machine column.

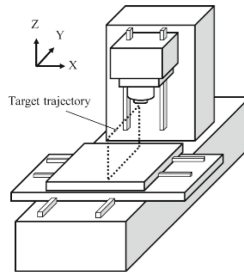


Fig. 6. Machine configuration

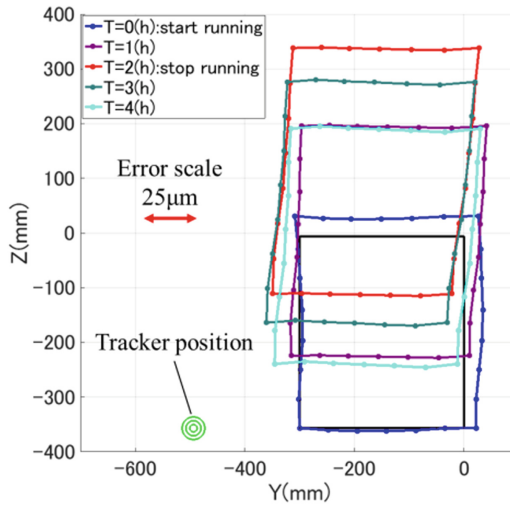


Fig. 7. Tool center point trajectory by Z-axis reciprocal motion

4 Vision-Based Machine Accuracy Measurement

4.1 Displacement Measurement Using Vision Camera

Figure 8 shows the principle of displacement measurement by camera. The deviation in the image due to camera movement is measured as a displacement. The grid intersection is defined as a target and the amount of movement is defined as the displacement. Figure 9 shows the process of detecting an intersection of the grid.

4.2 Accuracy Measurement Using Vision Camera

Figure 10 shows the setup to measure the displacement in the XY-plane. The camera is mounted on the spindle of the machine tool. Move the camera in the X-direction while overlapping the imaging range by 1mm and repeat capturing the image. The geometric accuracy is measured by identifying the displacement x , y and angle θ in the XY-plane and the displacement is calculated as follows [11]:

$$V_{i,j}^{(k,l)} = \begin{Bmatrix} x_{i,j}^{(k,l)} \\ y_{i,j}^{(k,l)} \end{Bmatrix} \quad (5)$$

$$\begin{bmatrix} E_{XX}^{(k,l+1)} \\ E_{YX}^{(k,l+1)} \\ E_{CX}^{(k,l+1)} \end{bmatrix} = \begin{bmatrix} V_{i,j+1}^{(k,l)} - V_{i,j}^{(k,l+1)} \\ E_{CX}^{(k,l)} - \theta_{i,j}^{(k,l+1)} \end{bmatrix} \quad (6)$$

$$\begin{bmatrix} E_{YY}^{(k+1,l)} \\ E_{XY}^{(k+1,l)} \\ E_{CY}^{(k+1,l)} \end{bmatrix} = \begin{bmatrix} V_{i+1,j}^{(k,l)} - V_{i,j}^{(k+1,l)} \\ E_{CY}^{(k,l)} - \theta_{i,j}^{(k+1,l)} \end{bmatrix} \quad (7)$$

Figure 11 shows the setup for multiple cameras to obtain a higher accuracy of angular deviation. The two-dimensional positional error Δp_E for each command can be described as follows:

$$\Delta p_E = \begin{bmatrix} E_{XX}(x_v) + E_{XY}(y_w) + (E_{CX}(x_v) + E_{C(0X)Y})y_v \\ E_{YX}(x_v) + E_{YY}(y_w) \end{bmatrix} \quad (8)$$

The relationship among the measurement result p_d , the position of each camera x_{cam} , the command position p_{cmd} , the positioning error of the machine Δp_E and the measurement target x_{tgt} can be described as follows:

$$p_d \cong x_{cam} + p_{cmd} + \Delta p_E - x_{tgt} \quad (9)$$

The geometric error parameters are obtained to solve the minimize problem.

$$\min_e \sum_{m=1, \dots, N} ((p_d - (x_{cam} + x_{cmd} + \Delta p_E - x_{tgt}))^2) \quad (10)$$

where e represents all the parameters obtained from Eq. 10 noted in Table 2. N represents the number of measurements. The squareness error $E_{C(0X)Y}$ can be estimated by pre-calibration of the camera position.

Table 2. Calculated parameters of X and Y-axis

$E_{CX}(x_v)$	Yaw error motion
$E_{XY}(y_w)$	Straightness deviation of Y-axis at $y = y_w$
$E_{XX}(x_v)$	Linear positioning deviation of X-axis at $x = x_v$
$E_{C(0X)Y}$	Squareness error of Y-axis to X-axis
E_{YX}	Straightness deviation of Y-axis at $y = y_w$
E_{YY}	Linear positioning deviation of Y-axis at $y = y_w$
x_{cam}	Each camera position (2-dimension)
x_{tgt}	Target point position (2-dimension)

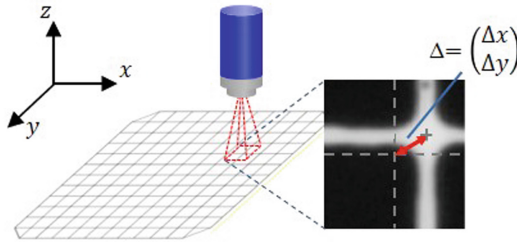


Fig. 8. Vision-based displacement measurement system

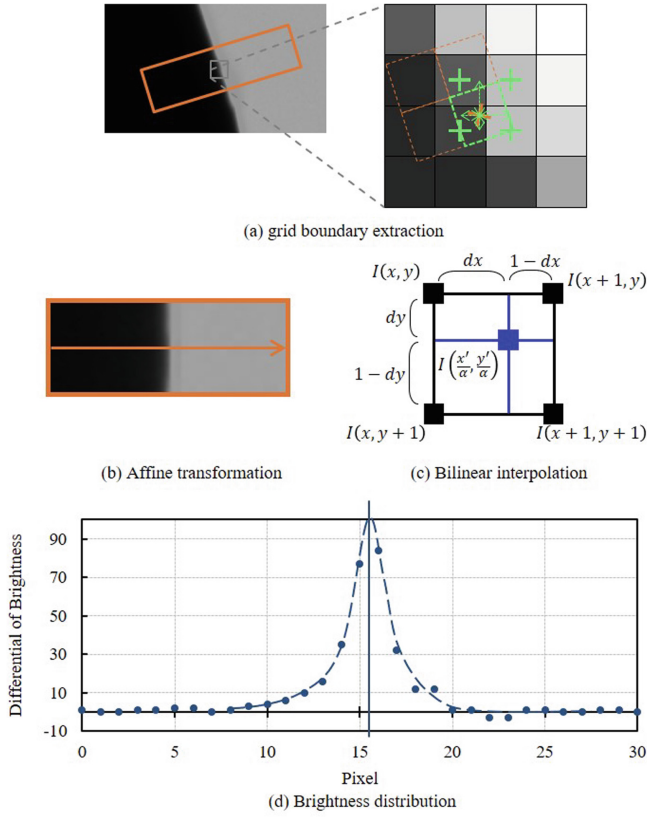


Fig. 9. Edge detection by using bilinear interpolation

4.3 Two-Dimensional Thermal Displacement Measurement Under the Ambient Temperature Change

The thermal displacement of a two-dimensional plane is measured under the ambient temperature change. Figure 12 shows the results and comparison to our previous method using a tracker [8]. The results tend to be in good agreement. The measurement time was about twice as fast as the previous method by a tracker.

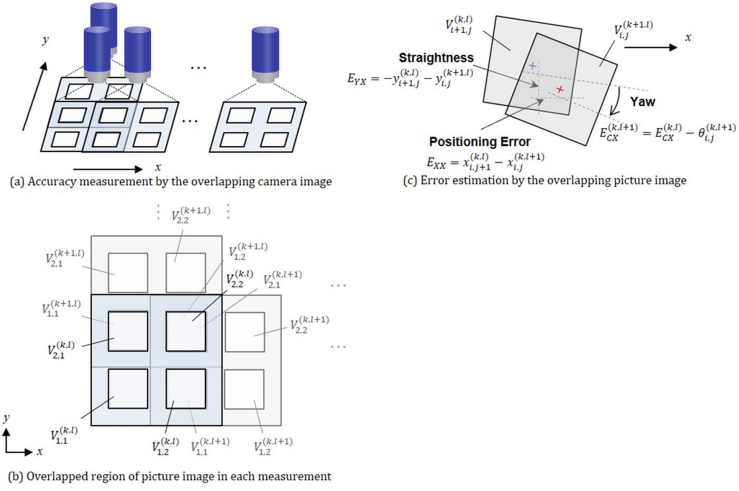


Fig. 10. The error measurement by vision camera

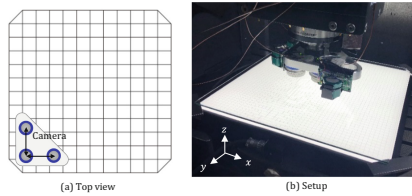


Fig. 11. Three vision cameras measurement

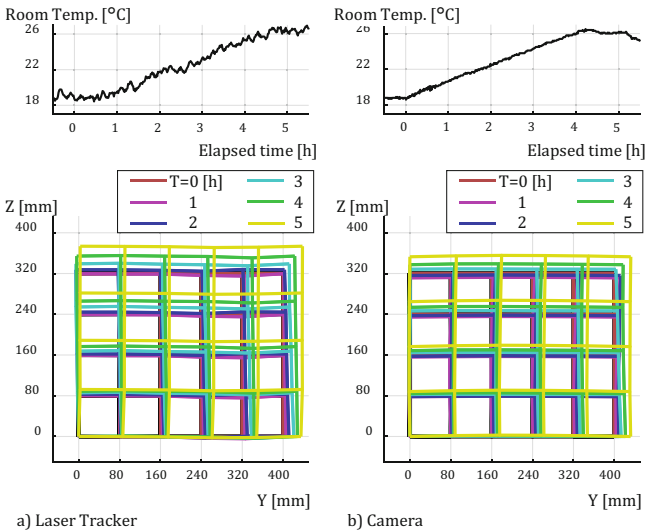


Fig. 12. Two-dimensional thermal deformation measurement results. (a) laser-based method [8], (b) vision-based method.

5 Conclusion

By using deep learning model, thermal displacement can be predicted with higher accuracy. The thermal displacement on a two-dimensional plane can be measured in a short time with high accuracy by using a laser tracker. Furthermore, vision cameras can measure thermal displacement in a shorter time and at a lower cost. Two-dimensional displacement can be used to see thermal deformation of the machine structure. Thermal displacement is caused by thermal deformation of machine structures by temperature variations. Therefore, these methods will clarify the root causes of thermal displacement and contribute to the development of machine tools with thermally robust and high accuracy.

Disclaimer. This article is a keynote contribution and as such non peer-reviewed.

References

1. Mayr, J., et al.: Thermal issues in machine tools. *CIRP Ann. Manuf. Technol.* **61**(2), 771–791 (2012)
2. Ibaraki, S., Blaser, P., Shimoike, M., Takayama, N., Nakaminami, M., Ido, Y.: Measurement of thermal influence on a two-dimensional motion trajectory using a tracking interferometer. *CIRP Ann. Manuf. Technol.* **65**(1), 483–486 (2016)
3. Moriwaki, T., Shamoto, E.: Analysis of thermal deformation of an ultraprecision air spindle system. *CIRP Ann. Manuf. Technol.* **47**(1), 315–319 (1998)
4. Brecher, C., Hirsch, P., Weck, M.: Compensation of thermo-elastic machine tool deformation based on control internal data. *CIRP Ann. Manuf. Technol.* **53**(1), 299–304 (2004)
5. Moriwaki, T., Shamoto, E., Kawano, M.: Estimation of thermal deformation of machine tool by applying neural network (improvement of estimation accuracy by utilizing time-series data of temperature on machine surfaces). *Trans. Japan Soc. Mech. Eng. Ser. C* **61**(584), 1691–1696 (1995). (in Japanese)
6. Mayr, J., Blaser, P., Ryser, A., Hernández-Becerro, P.: An adaptive self learning compensation approach for thermal errors on 5-axis machine tools handling an arbitrary set of sample rates. *CIRP Ann. Manuf. Technol.* **67**(1), 551–554 (2018)
7. Ito, Y.: *Thermal Deformation in Machine Tools*. McGraw-Hill books, New York. ISBN: 978-0-07-163517-2 (2010)
8. Fujishima, M., Narimatsu, K., Irino, N., Ido, Y.: Thermal displacement reduction and compensation of a turning center. *CIRP J. Manuf. Sci. Technol.* **22**, 111–115 (2018)
9. Mori, M., Irino, N., Shimoike, M.: A new measurement method for machine tool thermal deformation on a two-dimensional trajectory using interferometer. *CIRP Ann. Manuf. Technol.* **68**(1), 551–554 (2019)
10. Ibaraki, S., Knapp, W.: Indirect measurement of volumetric accuracy for three-axis and five-axis machine tools: a review. *Int. J. Autom. Technol.* **6**(2), 110–124 (2012)
11. Irino, N., Shimoike, M., Mori, K., Yamaji, I., Mori, M.: A vision-based machine accuracy measurement method. *CIRP Ann. Manuf. Technol.* **69**, 445–448 (2020)

Open Access This chapter is licensed under the terms of the Creative Commons Attribution 4.0 International License (<http://creativecommons.org/licenses/by/4.0/>), which permits use, sharing, adaptation, distribution and reproduction in any medium or format, as long as you give appropriate credit to the original author(s) and the source, provide a link to the Creative Commons license and indicate if changes were made.

The images or other third party material in this chapter are included in the chapter's Creative Commons license, unless indicated otherwise in a credit line to the material. If material is not included in the chapter's Creative Commons license and your intended use is not permitted by statutory regulation or exceeds the permitted use, you will need to obtain permission directly from the copyright holder.





Thermal Compensation of Sudden Working Space Condition Changes in Swiss-Type Lathe Machining

Petr Kaftan¹✉, Josef Mayr², and Konrad Wegener¹

¹ Institute of Machine Tools and Manufacturing (IWF), ETH Zürich, Zürich, Switzerland
kaftan@iwf.mavt.ethz.ch

² inspire AG, Technoparkstrasse 1, 8005 Zürich, Switzerland

Abstract. The Swiss-type lathe is a specialized turning machine of Swiss-origin with a wide range of applications across the precision machining industry. Its unique features enable it to mass produce parts at high speeds and with high precision. However, the complex non-symmetric structure of the machine tool makes it particularly susceptible to the adverse effects of thermal influences. These internal and external thermal influences cause an offset at the tool center point and degrade the accuracy of the produced part. It is a common practice in Swiss-type lathe machining for an operator to open the machine door during a production run to exchange tools or inspect the produced part. Consequently, thermal boundary conditions change rapidly when cooler ambient air enters the working space of the machine tool and when the air heats up after the machine tool is restarted. The machine tool exhibits short cool-down and warm-up cycles during which the thermal errors change abruptly and can be challenging to compensate, as it is well known in the machine tool industry. This work develops a novel methodology based on artificial intelligence that compensates thermal errors associated with sudden boundary condition changes. The results show that thermal error residual peaks associated with a machine tool door opening are significantly attenuated and the peak-to-peak thermal error of the Swiss-type lathe is reduced.

Keywords: Thermal Errors · Thermal Compensation · Swiss-type Lathe

1 Introduction

Customers of the machine tool industry demand increasingly precise machines to manufacture their products with tight tolerances in the micrometer range. To enable production of such demanding specifications, continual advances in precision of machine tools are required. Machine tools are susceptible to a range of error sources, of which up to 70% can be attributed to thermal influences, as reported by Mayr et al. [1]. Internal and external thermal influences act on machine tools, cause an offset of the tool center point (TCP) and degrade workpiece accuracy. Most common internal influences are due to heat generated in electrical components such as motors, due to mechanical friction in bearings, ballscrews and gearboxes, and due to the cutting process. External influences

are typically the environment and personal radiations. These are summarized in the thermal chain of causes from Wegener et al. [2]. To reduce the undesirable impact of thermal effects, options are to thermally stabilize machine tools via cooling and/or to compensate the machine tool via correcting the NC-axes or tool position. Due to the rising necessity to reduce energy consumption, thermal compensation is an increasingly sought-after solution, as reported by Wegener et al. [3]. As opposed to a *resource-based* approach, it is a *knowledge-based* approach, and a crucial step in the direction of increasing energy efficiency.

Two approaches to thermal compensation are generally distinguished: physics-based and data-based. The physics-based approach describes the deformation of the machine tool by differential equations. Physics-based models compute temperature dependent displacements at discrete points of the machine tool, typically via finite elements. To reduce the computational time, these models are coupled with model-order reduction techniques, such as in the work of Hernández Becerro [4]. Physical models can further be improved by parameter tuning based on on-machine measurements. Ihlenfeldt et al. [5] performed a parameter analysis to determine the parameters with the highest impact on the overall machine tool accuracy. The data-based approach is an alternative grey/black box methodology that correlates relevant input and output variables. A wide range of data-based models, from simple regression models to more advanced models such as long short-term memory neural networks, have been applied in the literature. Blaser et al. [6] used ARX (AutoRegressive with eXogenous inputs) to develop a thermal adaptive learning control approach for the compensation of rotary axes of a 5-axis machine tool. This methodology was further improved by Zimmermann et al. [7] who addressed the issue of adaptive input selection. The ARX model was also used by Horejš et al. [8] in their investigation of the effects of fluid cooling systems, underlining the model's suitability for thermal compensation. Mareš et al. [9] proposed an approach to modelling the thermal errors of a turning-milling centre based on ARX, tested three typical experimental setups (drilling, milling, and turning) under load free conditions and applied compensation offline. Fujishima et al. [10] proposed a deep learning approach to predict thermal errors of a turning center under severe situations such as unexpected temperature change or sensor failure. Ngoc et al. [11] applied LSTM to predict 10 geometric errors of a 5-axis machine tool using the rotational B- and C- axes power information as inputs to the model.

This work focuses on the thermal compensation of a Swiss-type lathe. A number of features distinguish it from a 5-axis machine tool: it incorporates multiple TCPs on tool holders and turrets, its headstock is moveable and facilitates workpiece movement in the z-axis direction, it contains a bar-feeder, a guide bush, and in general a higher number of axes. The lathe has a complex non-symmetric structure and is therefore especially susceptible to thermal influences. Works on thermal compensation of Swiss-type lathes are rare in literature. Ouerhani et al. [12] modelled the warm-up behavior of a Tornos SwissNano4 with four different machine-learning models. A reduction of 90% was reported, however, the thermal loads in the training and validation cases were very similar. Wang et al. [13] used rough-set theory in combination with a CNN to measure the spindle axial deformation but only on a very short time sample of one-hundred minutes. A further investigation is thus clearly mandated.

This publication is structured as follows: Sect. 2 explains the methodology applied for thermal compensation, Sect. 3 introduces the experimental setup on the Swiss-type lathe, Sect. 4 presents the results and Sect. 5 summarizes the work.

2 Methodology of Thermal Error Compensation

This work proposes the application of a novel stacked model for thermal error compensation based on ARX and RFR (Random Forest Regression). Input data (temperatures) are preprocessed via empirical mode decomposition to achieve a more stable model performance.

2.1 Empirical Model Decomposition

Empirical Mode Decomposition (EMD) was proposed by Huang et al. [14] for the analysis of non-stationary time series. The purpose of EMD is to find an intuitive representation of the frequency content of complex dynamic signals, for which Fourier-transform based methods are not suitable, due to their non-sinusoidal nature. EMD decomposes a signal in the time domain into a number of temporally adaptive basis functions called the Intrinsic Mode Functions (IMF) by using a ‘sift’ algorithm. As opposed to a Fourier decomposition, IMFs usually have a variable amplitude and frequency, and the number of IMF components is determined by a convergence to a stoppage criterion defined by a limit of the standard deviation of two consecutive sifting results. The EMD algorithm is used to remove noisy high-frequency components from data to improve the robustness of the thermal compensation model.

EMD considers an input $x(t)$, generates an upper envelope $U(t)$ and lower envelope $L(t)$ based on the local extrema of $x(t)$, and computes the mean value $m(t)$ as an average of the upper and lower envelopes. The first iteration for the first IMF component is given by:

$$x(t) - m_{10}(t) = h_{10}(t) \quad (1)$$

The next iteration, where $m_{11}(t)$ is determined from $h_{10}(t)$:

$$h_{10}(t) - m_{11}(t) = h_{11}(t) \quad (2)$$

The generalized equation for the IMF component h_{ik} , where i is the i^{th} IMF component and k is the k^{th} sifting operation is given by Eq. (3). The number of sifting operations is determined by convergence to a stoppage criterion, also defined by Huang et al. [14].

$$h_{i(k-1)} - m_{ik} = h_{ik} \quad (3)$$

2.2 Autoregressive Model with Exogenous Inputs (ARX)

The ARX model originates from the field of linear system identification; it is a linear representation of a dynamic system in discrete time steps. ARX considers past and present system inputs as well as past system outputs to compute the prediction for the current system output. The model structure is expressed by the following linear difference equation, adapted from the work of Ljung [15]:

$$y(t) + a_1y(t-1) + \dots + a_{n_a}y(t-n_a) = b_1u(t-1) + \dots + b_{n_b}u(t-n_b) \quad (4)$$

y represents the model output (thermal error) and u the model input (e.g. temperature). The model coefficients can be collected in the $\underline{\theta}$ matrix and the time series of past outputs and inputs in the matrix $\underline{\varphi}(t)$.

$$\underline{\theta} = [a_1 \ a_2 \ \dots \ a_{n_a} \ b_1 \ b_2 \ \dots \ b_{n_b}] \quad (5)$$

$$\underline{\varphi}(t) = [-y(t-1) \ \dots \ -y(t-n_a) \ u(t-1) \ \dots \ u(t-n_b)] \quad (6)$$

Model parameters n_a and n_b , i.e. orders of the autoregressive and exogenous parts respectively, can be determined e.g. via partial autocorrelation function analysis. The coefficient matrix $\underline{\theta}$ can be calculated via least squares and the thermal error \hat{y} predicted:

$$\hat{\underline{\theta}} = \left[\sum_{i=1}^N \underline{\varphi}(i)\underline{\varphi}^T(i) \right]^{-1} \sum_{i=1}^N \underline{\varphi}(i)y(i) \quad (7)$$

$$\hat{y} = \underline{\varphi}^T(t)\hat{\underline{\theta}} \quad (8)$$

2.3 Random Forest Regression (RFR)

Random Forest Regression (RFR) is a supervised learning algorithm based on decision trees that can be applied for both classification and regression tasks. RFR fits a multitude of decision trees in training time (ensemble learning) on variously subsampled data (bootstrapping) and returns the average prediction of individual trees. The original RFR algorithm was first proposed by Tin Kam Ho in 1995 [16]. RFR is a versatile regression algorithm with successful applications across various fields from medical diagnostics to financial fraud detection.

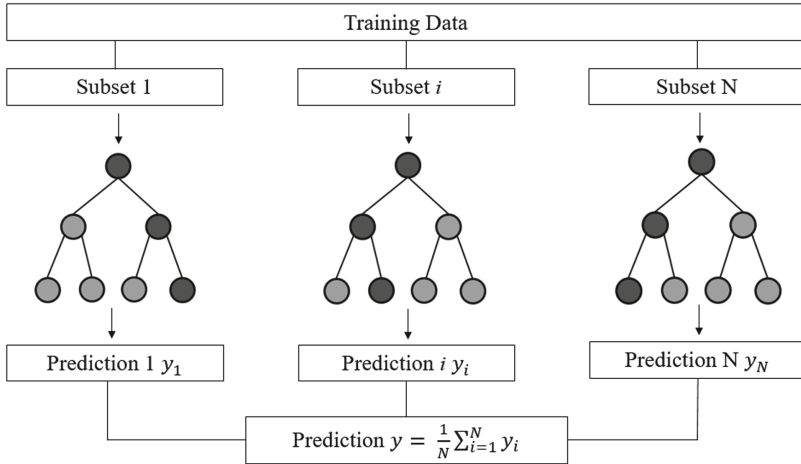


Fig. 1. Random Forest Regression model schematic.

The schematic of the RFR model is shown in Fig. 1. In the training process, each regression tree is assigned a bootstrapped subset of the training data, thus generating N new sets of training data, where N is the total number of trees in the model. $N = 100$ is applied in this work. Feature sampling is also commonly performed, although here only one feature, the smoothed door status signal, is used and therefore this feature is used at every internal node. In this sense, the RFR model is similar to a bag of trees model. The squared error is taken as the split criterion at every internal node. The output of the model is the average of the values predicted by the N trees.

2.4 Stacked ARX-RFR Model for Thermal Compensation

The ARX-RFR model consists of a calibration phase in which model parameters are calculated and a prediction phase in which the model is applied to compensate errors without in-process error measurement. The model structure is shown in Fig. 2.

Calibration Phase

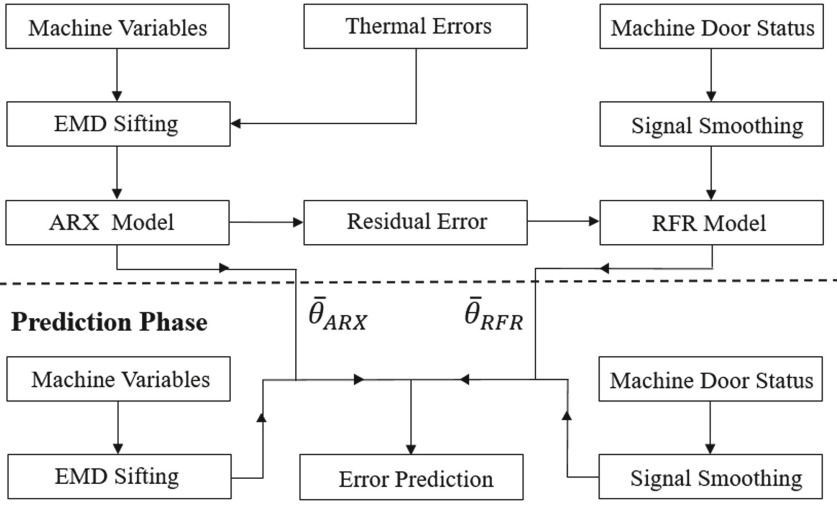


Fig. 2. ARX-RFR model schematic for thermal error compensation.

The ARX model is trained with sifted temperature and thermal error data with a time frequency of approximately five minutes. The list of all possible inputs of the ARX model is specified in Table 1 in the next section. Specific inputs are chosen based on knowledge of the machine tool behaviour. The output of the model is the thermal error, for each thermal error a differently parametrized ARX model is constructed.

The inputs of the RFR model are the thermal error residual of the ARX prediction and the smoothed machine door status signal with a time frequency of approximately one minute. The smoothing is performed with a smoothing function shown in Eq. (9).

$$y_{t,smoothed} = \frac{1}{1 + e^{-k(t_0-t)}} y_t \quad (9)$$

The machine door status signal y_t is a binary signal, 0 when the door is closed and 1 when the door is open. t_0 corresponds to the time at which a status change occurs, $k = 1$ when the door status changes from 0 to 1 and $k = -1$ when the door status changes from 1 to 0. In the prediction phase the models are applied in a stacked manner, i.e. the model predictions are added together.

3 Experimental Setup

3.1 Machine Tool and Measurement Equipment

The experimental machine tool is a Swiss-type lathe, whose kinematic chain can be described as H[w-[S1'-Z1' S2'-Y2'-Z2'-X2']-b-[t X1-Y1-[t (S11)-t]]] according to the notation outlined in ISO 10791-1:2015 [17]. Displacement probes are mounted on the tool holder to measure errors in the X - and Y - axes directions, as shown in Fig. 3.

Thermal errors are measured between the main spindle S1 and the tool holder. Twelve temperature measurements are monitored, of which seven are from externally mounted temperature sensors and five are from internal NC data, as summarized in Table 1. Temperature sensors are also mounted directly on the tool holder, as shown in Fig. 3.

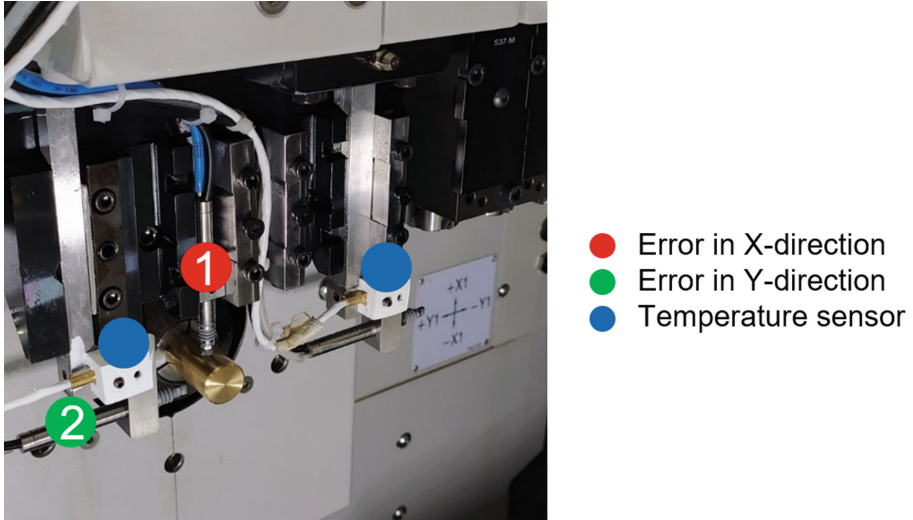


Fig. 3. Working space of the Swiss-type lathe. The tool holder can be equipped with turning, drilling, and boring tools. Displacement probes and temperature sensors mounted on the tool holder are shown.

For the X-axis compensation, sensors 1, 2, 6, 8, 11, 12 are chosen; for the Y-axis compensation, sensors 1, 2, 6, 10, 11, 12 are chosen.

3.2 Model Calibration Phase

The ARX-RFR model is calibrated with a thermal load cycle of varying spindle and driven tools motor speeds, rapid axes motions, and machine door openings. In this manner, different thermal states of the machine are excited while thermal errors are measured intermittently at a constant frequency of approximately five minutes. The training cycle is shown in Fig. 4.

3.3 Thermal Test Piece

The ARX-RFR model is validated on a thermal test-piece shown in Fig. 5. The test-piece has a varying diameter from 7 to 16 mm and a length of 28 mm. The cycle to produce this part runs on the machine tool virtually, i.e. without any material cutting. The influence of heat that would be released during the production of the real part, i.e. with material cutting, is not considered in this work. The cycle per part lasts approximately 60 s: this corresponds to a typical industrial production on a Swiss-type lathe, in which

Table 1. Temperature Sensors.

Sensor Number	Name	Type
1	Ambient	External
2	Cutting oil	External
3	Spindle cooling	External
4	Machining area	External
5	Tool holder 1	External
6	Tool holder 2	External
7	Tool holder 3	External
8	X-axis motor	Internal
9	Z-axis motor	Internal
10	Y-axis motor	Internal
11	Spindle motor	Internal
12	Driven tools motor	Internal

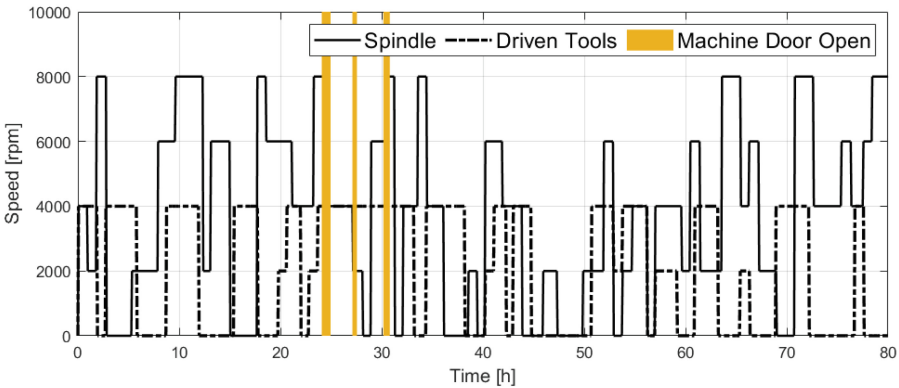


Fig. 4. Spindle and driven tool speed profiles for the calibration of the ARX-RFR model. The total duration of the data used for training is 80 h. The door of the machine tool is also opened several times during the model calibration phase.

a manufacturing cycle for a single part can last around a minute. The production is interrupted a number of times when the machine door is opened.

4 Results

EMD is applied to relevant temperature measurements with high frequency content to improve the robustness of the ARX-RFR model. As an example, EMD analysis is applied to the ambient temperature measurement. The machine tool is located in an

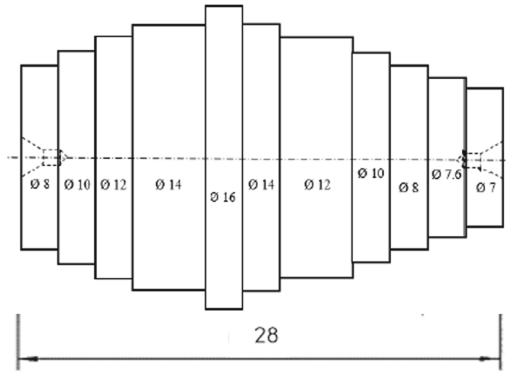


Fig. 5. Thermal test-piece. A cycle corresponding to the thermal test-piece runs on the machine but without any machining because tools are replaced by pneumatic probes.

air-conditioned hall with a set target temperature. However, the hall also has some non-negligible heat losses resulting in an on/off behavior of the air-conditioning and therefore a noisy ambient temperature measurement. This can be seen in the top graph in Fig. 6. The noisy part corresponds to daytime and the decrease in temperature to nighttime when the air-conditioning is turned off.

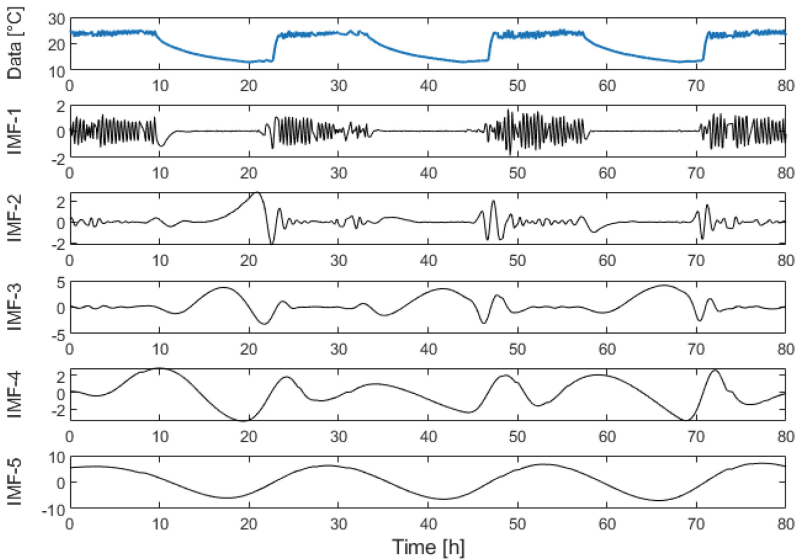


Fig. 6. Empirical mode decomposition of the ambient temperature into the first five intrinsic mode functions. The units of the y-axis are °C with the IMF components centered around zero.

The first IMF component has low magnitude and high frequency and can therefore be removed. The ambient temperature measurement with the IMF-1 component removed is shown in Fig. 7. Similar analysis is performed for other data where relevant.

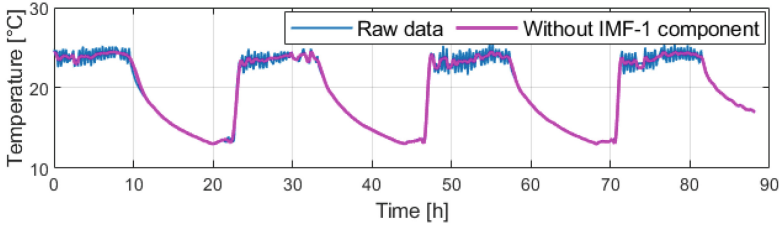


Fig. 7. Plot of raw ambient temperature measurement and with IMF-1 component removed.

Figures 8 and 9 show results of the ARX-RFR compensation model compared to only an ARX model, Fig. 8 the X-axis direction error and Fig. 9 the Y-axis direction. The cycles correspond to the production of the thermal test piece. The yellow stripes indicate the time during which the machine tool door is open and the black line the residual or remaining thermal error.

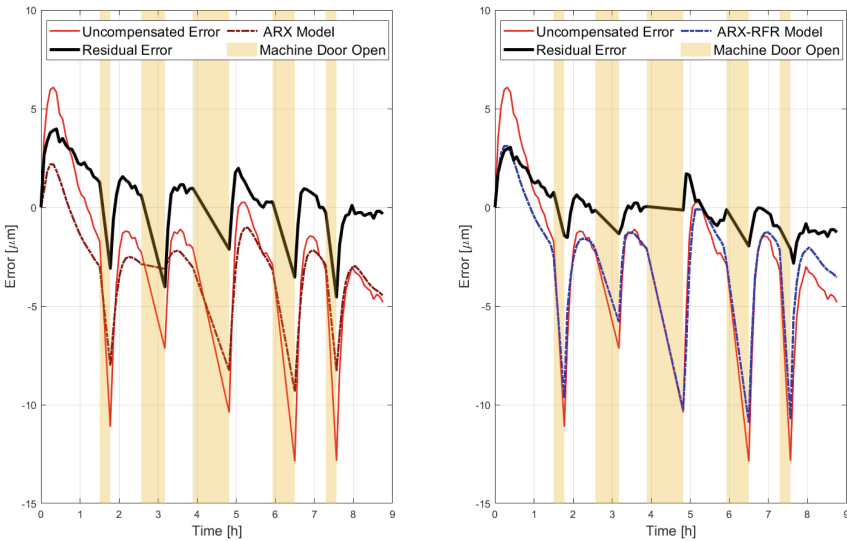


Fig. 8. Left: ARX compensation model for the virtual production of the thermal test piece for the X-axis direction. Right: ARX-RFR compensation model on the same data with a lower residual thermal error (black).

The plots visually indicate that the residual thermal error is reduced more during and after the machine tool door opening by the ARX-RFR model. The peak-to-peak

residual errors and error reductions of the ARX-RFR and ARX models are summarized in Tables 2 and 3. The peak-to-peak is defined as the absolute difference between the maximum and minimum value of the plot. The root mean square residual errors and error reductions are presented in Tables 4 and 5.

Table 2. Peak-to-peak residual errors of ARX and ARX-RFR models

Error	Uncompensated	ARX Residual	ARX-RFR Residual
X-axis	19.0 μm	8.5 μm	5.9 μm
Y-axis	21.7 μm	4.1 μm	3.3 μm

Table 3. Peak-to-peak error reductions of ARX and ARX-RFR models

Error	ARX reduction	ARX-RFR reduction	Improvement
X-axis	55%	69%	14%
Y-axis	81%	85%	4%

Table 4. Root-mean-square residual errors of ARX and ARX-RFR models

Error	Uncompensated	ARX Residual	ARX-RFR Residual
X-axis	4.2 μm	1.8 μm	1.2 μm
Y-axis	17.1 μm	1.4 μm	0.6 μm

Table 5. Root-mean-square error reductions of ARX and ARX-RFR models

Error	ARX reduction	ARX-RFR reduction	Improvement
X-axis	58%	70%	12%
Y-axis	92%	96%	4%

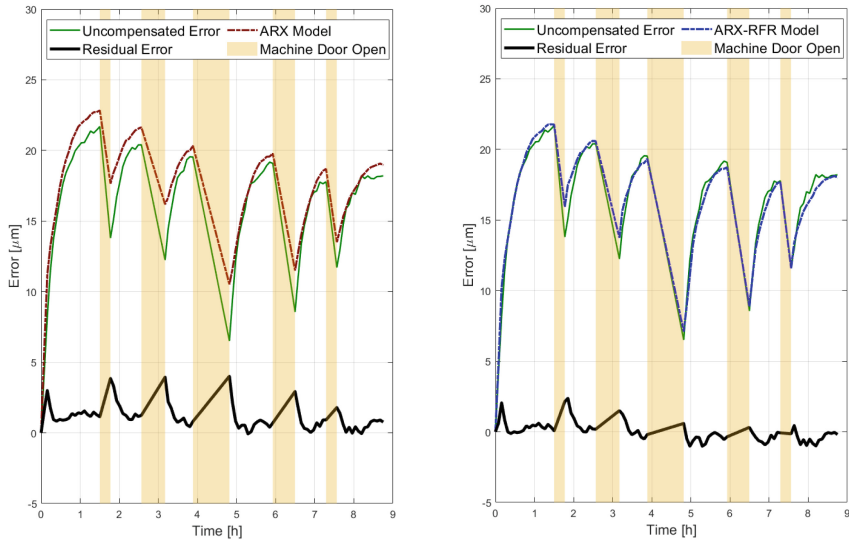


Fig. 9. Left: ARX compensation model for the virtual production of the thermal test piece for the Y-axis direction. Right: ARX-RFR compensation model on the same data with a lower residual thermal error (black).

5 Conclusion

This work applies a new ARX-RFR thermal compensation model to the virtual production of a thermal test piece interrupted by a number of door openings. Door openings can occur during a production run for example when the working space needs to be cleaned or when a part needs to be inspected. As a result, the working space conditions change as cooler air enters and the precision of the machine tool degrades due to thermal errors. The ARX-RFR model is compared to the well-known ARX model and it is demonstrated that it performs more favorably for the case of a door opening.

References

1. Mayr, J., et al.: Thermal issues in machine tools. *CIRP Ann.* **61**, 771–791 (2012)
2. Wegener, K., Weikert, S., Mayr, J.: Age of compensation – challenge and chance for machine tool industry. *Int. J. Autom. Technol.* **10**, 609–623 (2016)
3. Wegener, K., Gittler, T., Weiss, L.: Dawn of new machining concepts: compensated, intelligent, bioinspired. *Procedia CIRP* **77**, 1–17 (2018). 8th CIRP Conference on High Performance Cutting (2018)
4. Hernández-Becerro, P., Spescha, D., Wegener, K.: Model order reduction of thermo-mechanical models with parametric convective boundary conditions: focus on machine tools. *Comput. Mech.* **67**(1), 167–184 (2020). <https://doi.org/10.1007/s00466-020-01926-x>
5. Ihlenfeldt, S., Schroeder, S., Penter, L., Hellmich, A., Kauschinger, B.: Adjustment of uncertain model parameters to improve the prediction of the thermal behavior of machine tools. *CIRP Ann.* **69**(1), 329–332 (2020)

6. Blaser, P., Pavliček, F., Mori, K., Mayr, J., Weikert, S., Wegener, K.: Adaptive learning control for thermal error compensation of 5-axis machine tools. *J. Manuf. Syst.* **44**, 302–309 (2017). NAMRC45
7. Zimmermann, N., Lang, S., Blaser, P., Mayr, J.: Adaptive input selection for thermal error compensation models. *CIRP Ann.* **69**(1), 485–488 (2020)
8. Horejš, O., Mareš, M., Fiala, Š., Havlík, L., Stríteský, P.: Effects of cooling systems on the thermal behaviours of machine tools and thermal errors models. *J. Mach. Eng.* **20**(4), 5–27 (2020)
9. Mareš, M., Horejš, O., Havlík, L.: Thermal error compensation of a 5-axis machine tool using indigenous temperature sensors and CNC integrated Python code validated with a machined test piece. *Precis. Eng.* **66**, 21–30 (2020)
10. Fujishima, M., Narimatsu, K., Irino, N., Mori, M., Ibaraki, S.: Adaptive thermal displacement compensation method based on deep learning. *CIRP J. Manuf. Sci. Technol.* **25**, 22–25 (2019)
11. Ngoc, H.V., Mayer, J.R.R., Bitar-Nehme, E.: Deep learning LSTM for predicting thermally induced geometric errors using rotary axes' powers as input parameters. *CIRP J. Manuf. Sci. Technol.* **37**, 70–80 (2022)
12. Ouerhani, N., Loehr, B., Rizzotti-Kaddouri, A., Santos de Pinho, D., Limat, A., Schinderholz, P.: Data-driven thermal deviation prediction in turning machine-tool - a comparative analysis of machine learning algorithms. *Procedia Comput. Sci.* **200**, 185–193 (2022)
13. Wang, K.C., Shen, H.C., Yang, C.H., Chen, H.Y.: Temperature sensing and two-stage integrated modeling of the thermal error for a computer-numerical control swiss-type turning center. *Sens. Mater.* **31**(3), 1007 (2019)
14. Huang, N.E., et al.: The empirical mode decomposition and the Hilbert spectrum for nonlinear and non-stationary time series analysis. *Proc. Roy. Soc. Lond. Ser. A* **4**(54), 903–995 (1998)
15. Ljung, L.: *System Identification - Theory for the User*. Prentice Hall PTR (1999)
16. Ho, T.K.: The random subspace method for constructing decision forests. *IEEE Trans. Pattern Anal. Mach. Intell.* **20**(8), 832–844 (1998)
17. ISO 10791-1:2015, *Test Conditions for Machining Centres Part 1: Geometric tests for machines with horizontal spindle (horizontal Z-axis)*. International Organization for Standardization ISO, Geneva, Switzerland (2015)

Open Access This chapter is licensed under the terms of the Creative Commons Attribution 4.0 International License (<http://creativecommons.org/licenses/by/4.0/>), which permits use, sharing, adaptation, distribution and reproduction in any medium or format, as long as you give appropriate credit to the original author(s) and the source, provide a link to the Creative Commons license and indicate if changes were made.

The images or other third party material in this chapter are included in the chapter's Creative Commons license, unless indicated otherwise in a credit line to the material. If material is not included in the chapter's Creative Commons license and your intended use is not permitted by statutory regulation or exceeds the permitted use, you will need to obtain permission directly from the copyright holder.





Hybrid Thermal Error Compensation Combining Integrated Deformation Sensor and Regression Analysis Based Models for Complex Machine Tool Designs

Christian Naumann¹ (✉) , Andreas Naumann^{2,3} , Nico Bertaggia⁴ ,
Alexander Geist¹, Janine Glänzel¹, Roland Herzog^{2,3} , Daniel Zontar⁴ ,
Christian Brecher^{4,5} , and Martin Dix^{1,2}

¹ Fraunhofer IWU Chemnitz, 09126 Chemnitz, Germany
christian.naumann@iwu.fraunhofer.de

² Chemnitz University of Technology, 09126 Chemnitz, Germany

³ Heidelberg University, 69117 Heidelberg, Germany

⁴ Fraunhofer IPT Aachen, 52074 Aachen, Germany

⁵ WZL RWTH Aachen University, 52062 Aachen, Germany

Abstract. Thermal errors remain the dominant sources of positioning inaccuracies in machine tools. Various methods of reducing them have already been developed, ranging from cooling and air conditioning strategies, thermally optimized machine tool designs and component optimization to accurate model based thermal error estimation methods used for control-integrated compensation. Some reasons for the limited success of these strategies are the general complexity of the thermo-elastic and thermodynamic processes involved and the fact that many models' effectiveness is dependent on the machine tool type, workpiece, climatic conditions, tool, CAM strategy, condition of the machine tool and other factors. Depending on these circumstances, all model-based estimation and compensation methods have specific strengths and weaknesses, which make them more suitable in some aspects and less suitable in others. A possible way of circumventing this is via the combination of several methods to hybrid compensation. The goal of this investigation is to develop an effective hybrid compensation strategy for the 5-axis machine tool DMU 80 eVo by combining measurement-based compensation using integrated deformation sensors (IDS) with characteristic diagram based compensation. The former is used for the compensation of thermal errors in the vertical column containing the larger assemblies of the x, y, and z-axis and the latter is used for the table, which contains two rotational axes.

The IDS placement has been determined through expert knowledge and compared to placement, which minimizes the variance of the TCP displacement. The hybrid compensation is tested on the DMU 80 eVo.

Keywords: Machine tools · Thermal error compensation · Integrated deformation sensors · Multiple regression analysis · Optimal sensor placement

1 Introduction: Motivation and State of the Art

Thermal errors in machine tools, meaning positioning inaccuracies due to thermal influences, are the most significant factors in determining the machining precision. They outweigh geometric, static and dynamic error components and are generally assumed to account for around two thirds of the overall positioning inaccuracies [1].

There are numerous strategies for dealing with thermal errors in machine tools. They can generally be grouped into:

- methods for cooling or stabilizing the temperature field (e.g. by reducing the waste heat influx, cooling, air conditioning, controlling the heat flow, increasing the thermal inertia, etc.),
- methods for reducing the impact of temperature changes (e.g. thermo-symmetric design, materials with low thermal expansion, decoupling of heat sources, etc.),
- methods for directly measuring the thermal error with subsequent compensation,
- methods for estimating the thermal error indirectly using model and/or sensor based prediction algorithms with subsequent compensation.

The first two groups are typically combined into error avoidance and the latter two into error compensation [2]. The thermal error compensation based on measurements or predictions is performed in the machine tool control via position offsets. The optimal strategy typically depends on the machine tool (type, kinematics, workspace, heat sources and sinks, support systems, available sensors, etc.) and the use case (small/large batch size, wet/dry cutting, workpiece, CAM strategy, etc.). Other factors such as experienced personnel, cost of installation and model training, maintenance effort, achievable accuracy improvement, reliability, transferability to other machines, etc. also play an important role.

With this multitude of factors, it is inevitable that all methods have their individual strengths and weaknesses. While cooling and thermal machine tool design are a necessary and ubiquitous element of modern machine tools, by themselves they are rarely enough to guarantee high-precision machining. Therefore, error compensation is likewise an important part of thermal error management. Error compensation also has the advantage that it is usually energy-efficient and quite effective at dealing with thermal errors. Measurement based compensation, while effective and straightforward in its usage, is often disruptive to the machining process, as it requires, e.g. production halts for intermittent recalibration. Model based compensation is less intrusive and usually only requires software and sensor installation. Popular model types for thermal error compensation include multiple regression models, transfer functions, artificial neural networks, support vector machines, fuzzy models, finite element models, lumped capacitance models, geometric elasticity models and control oriented models.

While all of these compensation models have their uses, they each have weaknesses as well. Regression analysis, while simple and time-independent, is also highly dependent on both the training data selection and the temperature sensor placement. Simulation based approaches, such as using FEM, are generally quite accurate in a wide range of load cases but they require a large modelling and parametrization effort. Compensation based on transfer functions presents a good compromise between the aforementioned but has often trouble if too many heat sources and sinks affect the same components.

Compensation using integrated deformation sensors (IDS) is simple and effective but IDS cannot always be installed in all relevant components. To solve this dilemma, more and more researchers are turning to hybrid compensation schemes combining two or more methods to eliminate individual weaknesses and combine the strengths of each method [6].

One way to achieve this, is by combining sensor-based and sensorless methods. Jedrzejewski and Kwasny have used temperature sensors to approximate the error of the machine tool structure and combined this with a spindle shift compensation based on control-internal data [7]. In another work by Zhou and Harrison, a hybrid compensation model is constructed using a fuzzy controller enhanced by a supervised neural network to estimate the time-varying positioning error from in-cycle measurements via a touch trigger probe [8]. Xiang et al. combine a multivariable linear regression model, a natural exponential model and a finite element method model to a vector-angle-cosine prediction vector. The weights of the constituent models within the hybrid model are then optimized by maximizing the cosine between the prediction vector and the measured deformation vector [9]. Thiem et al. use an FEM simulation based compensation model and eliminate the problem of unknown initial conditions and thermal drift over time by temperature sensor based monitoring and recalibration of their thermal model [10]. Finally, a hybrid compensation model combining regression analysis and IDS based compensation has previously been suggested in [11] but had not been fully developed and tested, yet.

This contribution presents the combination of an IDS measurement based with a characteristic diagram based compensation method. Section 2 briefly describes the demonstrator and the FE model used to simulate the thermo-mechanical behavior of this machine tool. This model is the basis for the compensation methods in the upcoming sections. Section 3 describes the use of the FEM simulations to construct the characteristic diagrams. In Sect. 4, the IDS will be explained and an experience-based and a mathematical placement strategy will be described. The validation in Sect. 5 shows the efficiency of the compensation approach for a test load case. Finally, a summary and outlook will be given in Sect. 6.

2 FE Model of the Demonstrator DMU 80 eVo

For the investigation and later the validation of the individual as well as the hybrid compensation strategies, the DMU 80 eVo of DMG Mori was used. It is a five-axis machining center with a workspace of $850 \times 650 \times 550 \text{ mm}^3$. The DMU has eight temperature sensors installed, see Fig. 1. There are also various cooling systems, e.g. for the spindle, the axis bearings, the motors, the guides and the machining table.

For the training of the characteristic diagram based compensation, an FEM simulation model of the DMU was created in ANSYS. A detailed description of the modeling approach can be found in [3]. This model has been validated using measurements inside a climate chamber. This ensures, that the initial conditions of simulation and measurement match well and that the machine tool's behavior under known ambient temperature changes also matches the simulation model. In Sect. 4, this same FEM simulation model is used for both the manual and optimal sensor placement.

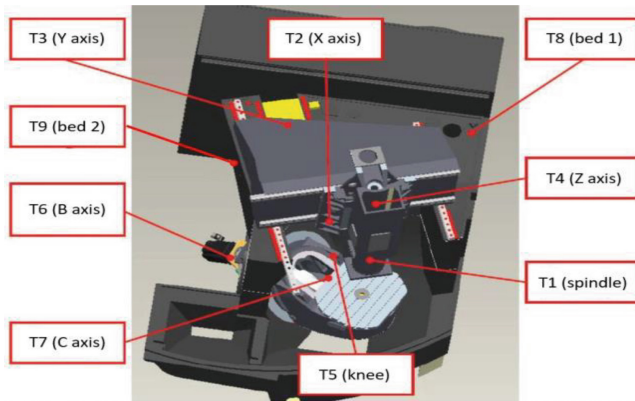


Fig. 1. Temperature sensors of the DMU 80 eVo

3 Characteristic Diagram Based Compensation

Characteristic diagram based compensation is a type of regression analysis using high-dimensional characteristic diagrams. Usually, a set of temperature sensors along with the axis positions of the machine tool are mapped directly onto the TCP displacement with a piecewise multilinear model. The details on how to construct these models and how to select suitable temperature sensor locations can be found in [12]. Some publications on the subject speak of “correction” instead of the more commonly used term “compensation” and may be viewed as synonymous in the context of thermal error reduction. Correction is in some ways a more clear description of this type of method since it implies the existence of the thermal error, which is to be estimated or measured, and thus clearly sets it apart from error avoidance methods.

In the context of the DMU 80 eVo, characteristic diagram based compensation is only partially suitable due to the predetermined temperature sensor placement. For the column, by which we refer to the assembly carrying the X, Y and Z axis, the single temperature sensor per assembly is not enough to accurately identify different thermal states. For the machine table, using characteristic diagrams based on the three temperature sensors installed there, is a good way to predict the thermal deformation. Moreover, installing IDS in the table is not possible and simulation based approaches have had difficulties in modelling and correctly parametrizing the table due to its complex design.

The initial compensation model proposed for the table in [13] used only five parameters to describe the thermal displacement of the table. These parameters are dx , dy , dz , rx and ry , referring to the displacement and tilting of the table as a whole. In this model, the table cannot expand in x or y direction and it cannot assume convex or concave shapes. These limitations were made because the limited reliability of the simulated table deformation made determining the exact deformed shape of the table nearly impossible and it is unclear just how much of the table expansion would even affect a workpiece fixed on that table. In order to determine how well characteristic diagram based compensation could theoretically predict the thermal error of the table, a more detailed model will now be presented using the assumption that the simulated table deformation correctly

matches that of the actual machine tool. The improved modelling technique will be useful for similarly designed machine tools as well as for the DMU 80 eVo once more accurate FEM models have been developed.

In order to provide full flexibility regarding the table deformation, the first step was to approximate the deformation using a 2D characteristic diagram of the table surface, where in the case of the DMU 80 eVo a 5-by-5 grid was sufficient for good results. For each grid vertex, the table deformation as calculated by FEM can be mapped in the second step using a thermal compensation model dependent on the temperature sensor readings. Since for many of the table nodes, the thermal deformation is highly non-linear and cannot be accurately predicted with regression analysis alone, a hybrid model using first order time delay functions (PT_1) and temperature sensors was used for the thermal models. For each table node, individual compensation models have to be created and parametrized depending on their nonlinear thermal behavior. This process was automated by providing a set of function types and parameter ranges followed by a brute-force trial-and-error model optimization, which simply tested all possible models and compared them by maximum and mean residual errors. In the future, a neural network or genetic algorithm could be used to speed up the training process by preselecting suitable model types or refining the parameter ranges. Figure 2 shows the old table model on the left and the new, improved model on the right.

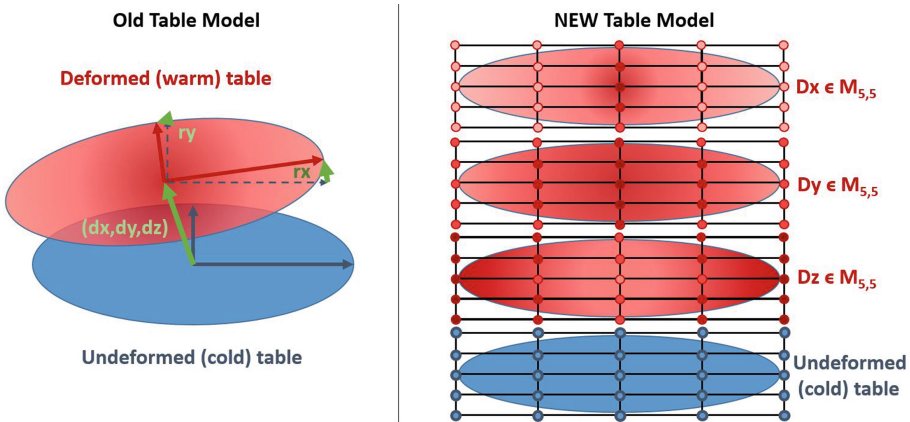


Fig. 2. New vs old table model for thermal error prediction

One last aspect, which proved to be important was that separate compensation models were needed for the dry heating, heating with coolant and cool-down phases of the machine tool operation. Due to the completely changing thermo-elastic behavior of most table vertices for these situations, separate modelling was the only way to obtain good approximations. More complex thermo-elastic models instead of the mostly regression based models could eliminate this need in the future, however.

4 Integrated Deformation Sensors

4.1 Description of the IDS

To compensate the thermal deviation of the TCP, the Fraunhofer IPT developed integrated deformation sensors, abbreviated as IDS [15]. These IDS consist of CFRP rods which, in theory, are perfectly thermally stable, though in reality, the thermal expansion coefficient (TEC) can fluctuate between -0.12 and $1.9 \frac{\mu\text{m}}{\text{m}\cdot\text{K}}$ [4]. Compared to materials that are often used in machine tools, like grey cast iron ($9 \frac{\mu\text{m}}{\text{m}\cdot\text{K}}$) or steel (ca. $11.5 \frac{\mu\text{m}}{\text{m}\cdot\text{K}}$) in a range of temperature that is suitable for production halls, this low value enables the CFRP rods to be used in thermal deformation sensors, as was shown in [5].

To measure the thermally induced length change of the machine's structural parts, the CFRP rod is mounted with a fixed bearing on the right-hand side and a loose bearing on the left-hand side. A displacement sensor is then added on the left and can measure the change in length via tactile measurement (Fig. 3).

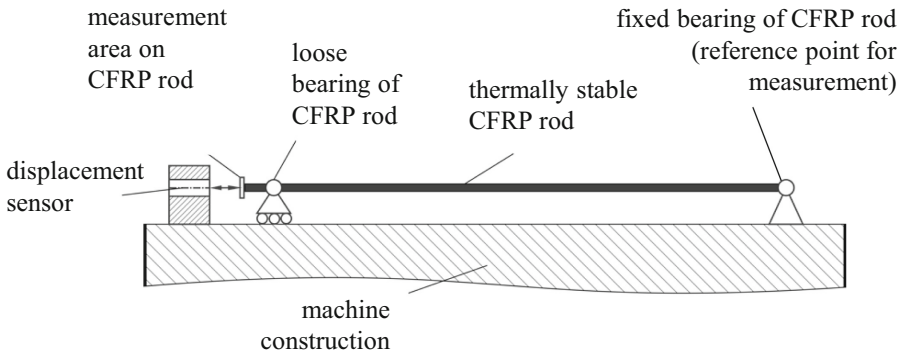


Fig. 3. Operating principle of the integrated deformation sensor

According to this principle, the thermo-elastic behavior of the large structural components of the machine can be measured. We apply the Euler-Bernoulli beam theory to obtain a model, which gives the relationship between the measured IDS values and the TCP displacement. Depending on the shape of the machine components, other theories might also be applied, for example shell theory for thin components. Expert placement of the IDS using this model was compared to mathematical approaches in [16].

4.2 Experience Based Sensor Placement

The placement of the IDS is the basis for a good prediction of the TCP deviation. In order to determine a suitable sensor placement, the machine's structural parts are investigated in an FEM simulation. Heat sources like motors, friction in axis guides or bearings are simulated as well as fluctuations in the ambient temperature. The simulations calculate the resulting temperature fields and based on this, the thermally induced deformation. An example result of such a simulation is shown in Fig. 4.

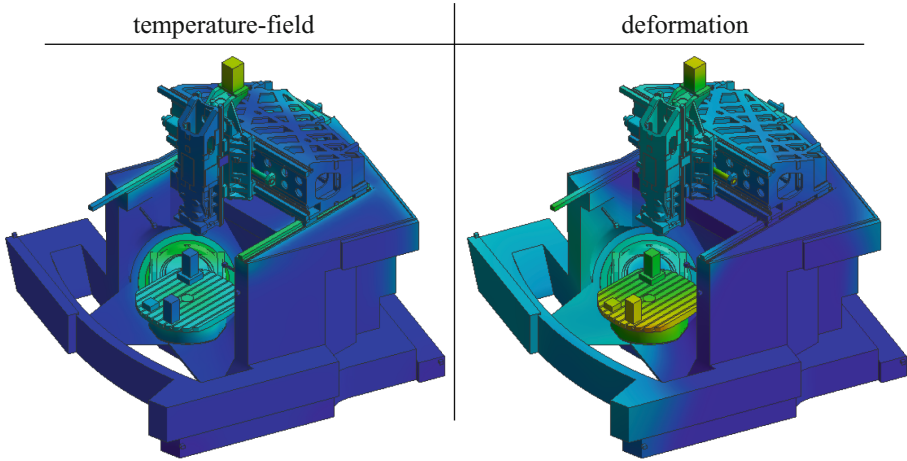


Fig. 4. Simulation results, left: temperature field, right: deformation field

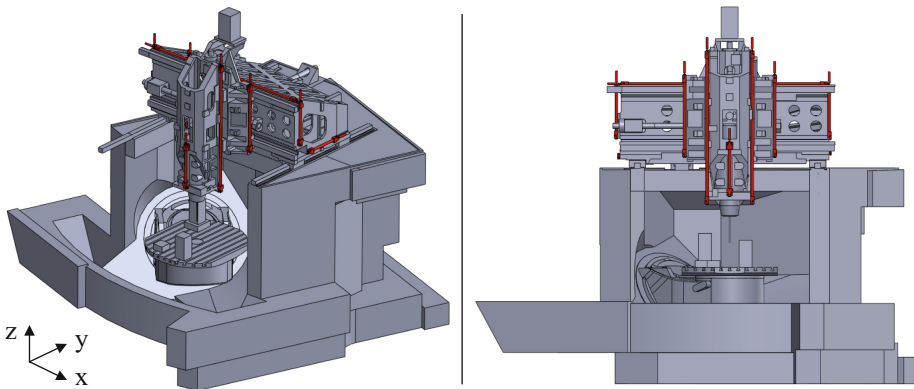


Fig. 5. Sensor placement in two views

Based on this displacement, the sensor placement shown in Fig. 5 was proposed.

Three sensors are placed at the headstock. Two additional sensors are placed at the cross slide and five sensors are placed at the moving column for the y -direction. Although the biggest deformation can be found at the table, no sensors are placed there. This is because the measuring unit itself is not suitable for the workspace due to its lack of resistance to cooling lubricants. Furthermore, there are no sensors placed at the machine bed. This can be justified by the fact that there is no main direction of deformation, which prevents a reasonable placement.

4.3 Mathematical Sensor Placement Using an FE Model

The basis for the mathematical sensor placement is the estimation of the uncertain model parameters using measurements. Given the estimation problem, one has to place

the sensors such that the uncertainty of the predicted TCP displacement is as small as possible. The FE model described above has the structure

$$\begin{aligned} E\dot{T}(t, p) &= A(t, p)T(t, p) + Bu(t, p) \\ y_{mech}(t, p) &= C_{mech}T(t, p) \\ d_{CFK}(t, p) &= H(y_{mech}(t, p)) \\ y_{TCP} &= C_{TCP}T(t, p) \end{aligned}$$

where the coefficient matrices E , $A(t, p)$ and B are the heat capacity matrix, the heat conduction (and heat exchange) matrix and the input matrix, respectively.

The uncertain heat exchange coefficients enter the matrix A , whereas the heat loads are part of the inputs u . The output matrix C contains the stationary equations of linear thermo-elasticity reduced to the desired displacements in the sensor locations.

The output operator H provides the distances between the mounting points from the displacements y_{mech} , which correspond to the measurements. The change in length is nonlinear in the displacement, but the relative change is very small. Therefore, it is customary to linearize the change in length in the undeformed state.

The parameter estimation corresponds to solving the least square problem

$$\min_p \sum_{i,m} \left| d_{CFK_m}(t_i, p) - \hat{d}_{CFK_m}(t_i) \right|_{\sigma_m^{-2}}^2 + \left| p - p^{bg} \right|_{\alpha^{-2}}$$

where $\hat{d}_{CFK}(t_i)$ are the measured rod lengths. All measurement errors are independent and normally-distributed with standard deviation σ_m^2 . Due to the length-dependent measurement errors, there are in general different standard deviations for every rod. The parameter α is a small regularization parameter, which penalizes too large deviations from the background parameters.

In the optimal sensor placement, the measurement carries the most information about the parameters. At the same time, the parameters are weighted according to their impact on the TCP displacement. One measure for the accuracy of the TCP displacement is the D-criterion [14], which is related to the volume of the covariance ellipsoid of the TCP displacement $y_{TCP}(t, p)$. The optimal sensor placement leads to a problem of the form

$$\begin{aligned} \min_w \log \det \text{Cov}_{TCP}(w) \\ \text{Cov}_{TCP}(w) &= J_{y_{mech}}(t_f) \text{Cov}^{-1}(w) J_{y_{mech}}^T(t_f) \\ \text{Cov}(w) &= \sum_{i,m} \frac{w_m}{\sigma_{d,m}^2} J_{CFK_m}^T(t_i) J_{CFK_m}(t_i) + \alpha^{-2} \mathbf{I} \end{aligned}$$

The symbols $J_{y_{mech}}$ and J_{CFK_m} denote the Jacobian of the displacement and the length with respect to the parameters p , respectively. The placement-dependent matrix Cov_{TCP} represents the covariance matrix of the TCP displacement at the final time step.

Thus, the optimal sensor placement depends on the derivative of the observation and of the quantity of interest (QOI, here the TCP location) with respect to the parameters. This observation is key for an efficient implementation as well as for the offline computation of optimal sensor positions during the machine design. Parameters which enter

only the sources u have temperature-independent sensitivities. Their sensitivity, however, might depend on other parameters. Examples for those are the amplitude of friction losses and ambient temperatures. In contrast, if a parameter influences the coefficients, the derivatives are temperature-dependent and thus the optimal placement also depends on the corresponding loads.

Figure 6 depicts both sensor placements. The mathematical placement adds two sensors next to the rails on the bed and one additional rod inside the x-sledge near the motor, which is not visible. The right image shows only the optimized sensor locations for a fixed number of five IDS (Table 1).

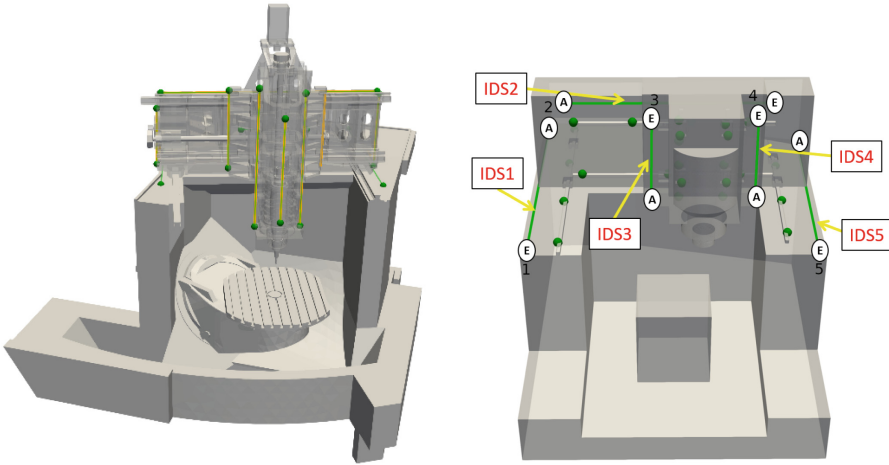


Fig. 6. Sensor placement manual and optimized (left) and optimized sensor placement for five IDS (right)

Table 1. Optimization criteria and highest uncertainty of the TCP relative to expert placement

N° Rods	$J(w_{math}) - J(w_{expert})$	$\max(\mu_{math}) / \max(\mu_{expert})$
2	8.69	1.90
3	6.12	1.87
4	5.73	1.77
5	1.64	0.89
6	1.22	0.88
7	0.87	0.85
8	-0.52	0.76
9	-0.14	0.80
10	-1.90	0.67

Table 1 compares the optimization criteria relative to the expert placement. The expert placement always consists of ten rods, whereas the optimized placement was computed for smaller numbers of rods, too. A difference of about -2.3 corresponds to approximately one tenth of the volume due to the natural logarithm. The second column relates the largest standard deviations μ of the different placements to each other. Thus, the optimal placement reduced the uncertainty to about 2/3. Furthermore, one can expect a reduction to about 3/4 of the uncertainty with eight sensors.

5 Validation

For the validation of the new hybrid compensation method, an independent test load case was simulated, which could then be compared to the estimated relative displacement. The estimate is calculated from the characteristic diagram based estimation of the table error minus the IDS based estimation of the column's thermal error.

The test load case consists of four parts: a short 2h heating phase with X 90%, Y 34%, Z 56% and B 38% of maximum axis speed; followed by a 1h cool-down phase (all 0%); followed by a longer 4h heating phase with X 45%, Y 60%, Z 30%, B 90% and C 45% of maximum axis speed; and finally another 4h cool-down. Since the simulation does not actually contain motion, the 90% in this example refers to 90% of the maximum waste heat, which is applied to the guides, bearings and motors. 0% is a predefined low standby waste heat.

The resulting temperatures at the sensor locations can be seen in Fig. 7.

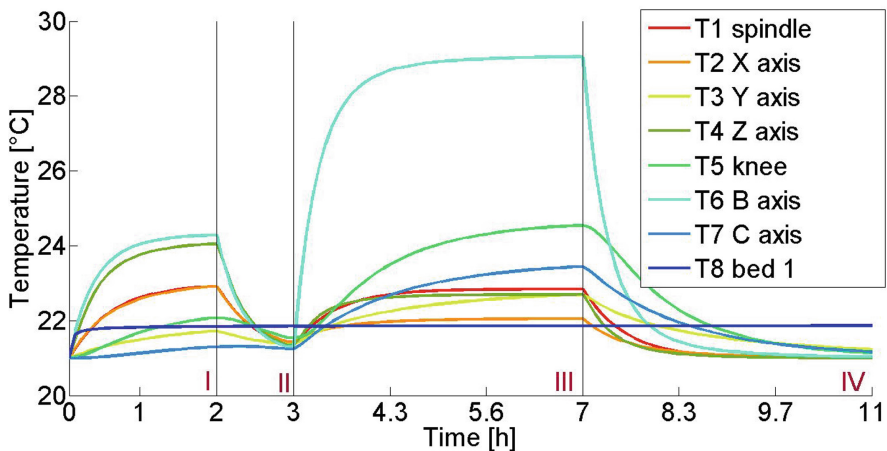


Fig. 7. Temperatures of the test load case containing four sections

Figure 8 shows the simulated error of the test load case as compared to the estimation. It shows a good agreement of the estimation with the simulated values, reducing the error by about 2/3. For the characteristic diagram based estimation of the table error, more training data would result in better approximations, as the test data was not part

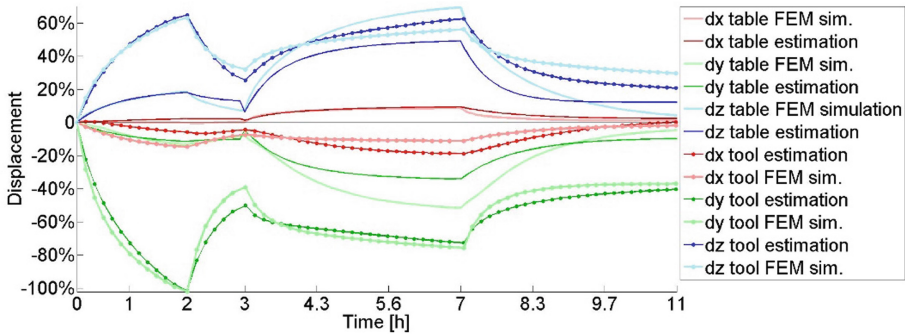


Fig. 8. Displacements of tool and table: simulated vs. estimation

of the limited set of training data. Since some other parts of the table have a very different thermo-elastic behavior, an additional validation for all table nodes would be recommended. The IDS based estimation of the tool error resulting from the thermal column deformation also shows a high achievable accuracy. This result is based on the optimized IDS placement in Fig. 6, right. The x-displacement is calculated from the elongation of IDS2 and the difference in elongation of IDS3 and IDS4, although IDS2 has little effect, since the x-axis position is in the middle. The y-displacement is calculated from IDS2 and the average of IDS1 and IDS5, where the latter again has little effect due to the position being the middle of the y-axis. The z-displacement is calculated from IDS2 and the average of IDS3 and IDS4. Thus the bending of the y-sledge as detected by IDS2 contributes strongly to the thermal error of the column. It is also clear, that along with the amplitude of the IDS elongation, a geometric understanding of the elongation and bending behavior of the components is required for good estimations using IDS. Testing further machine poses and different load cases will also be required to optimize and fully validate the approach.

6 Summary and Outlook

The thermal behavior of a machine tool is one of the most significant factors in determining its positioning accuracy. Various methods from thermal error avoidance (e.g. cooling or thermo-symmetric design) to thermal error compensation (e.g. model based error estimation) can be employed to improve this thermal behavior. Compensation strategies are especially important in this regard, since they are effective, energy-efficient and are often non-invasive and thus suitable for both new and existing machine tools. Since each thermal error compensation strategy has its own strengths and weaknesses depending on the situation, hybrid strategies combining several different methods can be used to eliminate the weaknesses of individual methods.

The DMU 80 eVo is a five-axis machining center which is popular in the industry due to its small space requirements compared to its workspace. Since it has, however, a complex thermal behavior, a hybrid compensation approach combining IDS based compensation for the machine tool column and characteristic diagram based compensation for the machining table was developed and described in this paper.

In a first step, the machine's thermal behavior was analyzed via FEM simulations. Based on the results of this analysis, the placement of the IDS on the main structural parts was determined. Based on the expected thermal behavior, a model of the machine was developed to be able to calculate the TCP deviation from the IDS measurement.

To show the functionality of the IDS and the model, a theoretical experiment was performed. As the simulation model was experimentally validated, it can be used as a substitute for an experiment actually carried out on the physical machine. This eliminates the need to physically install the IDS in the machine tool. An example load case for the DMU 80 eVo was simulated, which computed the length change of the IDS and the corresponding TCP deviation. The length change of the IDS could then be calculated into a predicted TCP deviation via the model. In order to be able to make a statement about the quality of the IDS as the basis of a compensation method, these TCP deviations can be compared.

The estimation of the table error was calculated from the three temperature sensors installed in the table using regression analysis combined with first order time delay elements (PT_1). This model has shown good agreement with the simulated displacement for the investigated test load case. One crucial part of this table model was the subdivision into dry milling, wet milling and cool-down (stand-by). To further validate this new table compensation model, more test load cases will be created with several sudden shifts between these three production phases in order to test the composite model under more realistic conditions. Additional tests will also be performed to evaluate the accuracy of the table model at different table locations within the workspace. Finally, the entire hybrid compensation model will be tested and compared to existing thermal compensation methods.

Acknowledgement. This research was funded by a German Research Foundation (DFG) grant within the Collaborative Research Centers (CRC) / Transregio (TR) 96, Project ID 174223256 – TRR96, subprojects B08, B09 and C03, which is gratefully acknowledged.

References

1. Ramesh, R., Mannan, M.A., Poo, A.N.: Error compensation in machine tools – a review: part II: thermal errors. *Int. J. Mach. Tools Manuf.* **40**, 1257–1284 (2000)
2. Ni, J.: CNC machine accuracy enhancement through real-time error compensation. *J. Manuf. Sci. Eng.* **119**, 717–725 (1997)
3. Geist, A., Naumann, C., Glänzel, J., Putz, M.: Methods for determining thermal errors in machine tools by thermo-elastic simulation in connection with thermal measurement in a climate chamber. In: *International. Conference on Thermal Issues in Machine Tools 2021*, Prague, CZ (2021)
4. Dong, C., et al.: Evaluation of thermal expansion coefficient of carbon fiber reinforced composites using electronic speckle interferometry. *Optics Express* **26**, 531–543 (2018)
5. Dietzel, F.: *Technische Wärmelehre*. Vogel Verlag, Würzburg (1990). ISBN 3-8023-0089-0, p. 159 ff.
6. Turek, P., Jedrzejewski, J., Modrzycki, W.: Methods of machine tool error compensation. *J. Mach. Eng.* **10**(4), 5–25 (2010)

7. Jedrzejewski, J., Kwasny, W.: Modelling of angular contact ball bearings and axial displacements for high-speed spindles. *CIRP Ann. Manuf. Tech.* **47**(2), 377–382 (2010)
8. Zhou, E.P., Harrison, D.K.: Improving error compensation via a fuzzy-neural hybrid model. *J. Manuf. Syst.* **18**(5), 335–344 (1999)
9. Xiang, S., Lu, H., Yang, J.: Thermal error prediction method for spindles in machine tools based on a hybrid model. *J. Eng. Manuf.* **229**(1), 130–140 (2015)
10. Thiem, X., Rudolph, H., Murali, S., Ihlenfeldt, S., Müller, J., Penter, L.: Vorgehensweise für die Umsetzung der strukturmodellbasierten Korrektur. *Industriekolloquium SFB/TR96, Chemnitz, 2022*
11. Naumann, C., Tzanetos, F., Baum, C., Brecher, C., Ihlenfeldt, S., Putz, M.: Hybrid correction of thermal errors using temperature and deformation sensors. In: *1st Conference on Thermal Issues in Machine Tools, Dresden (2018)*
12. Naumann, C., Riedel, I., Ihlenfeldt, S., Priber, U.: Characteristic diagram based correction algorithms for the thermo-elastic deformation of machine tools. *Procedia CIRP* **41**, 801–805 (2016)
13. Naumann, C., Naumann, A., Bertaggia, N., Glänzel, J., Brand, M.: Hybride Korrektur thermo-elastischer Fehler an komplexen Bearbeitungszentren. *Industriekolloquium SFB/TR96, Chemnitz, 2022*
14. Atkinson, A.C., Donev, A.N., Tobias, R.D.: *Optimum Experimental Designs, with SAS*, vol. 34, Oxford Statistical Science Series, Oxford University Press, Oxford (2007)
15. Brecher, C., Klätte, M., Wenzel, C.: Application of machine integrated deformation sensors. In: *Proceedings of the 11th International Lamdamap Conference, Huddersfield, Bedfordshire, United Kingdom, 2015*, pp. 8–17 (2015)
16. Brecher, C., et al.: Optimal positioning methods of integral deformation sensors – expert knowledge versus mathematical optimisation. *ICTIMT Spec. Issue MM Sci. J.* **2021**, 4628–4635(2nd ICTIMT, MM Publishing, 2021). https://doi.org/10.17973/MMSJ.2021_7_2021069




Open Access This chapter is licensed under the terms of the Creative Commons Attribution 4.0 International License (<http://creativecommons.org/licenses/by/4.0/>), which permits use, sharing, adaptation, distribution and reproduction in any medium or format, as long as you give appropriate credit to the original author(s) and the source, provide a link to the Creative Commons license and indicate if changes were made.

The images or other third party material in this chapter are included in the chapter’s Creative Commons license, unless indicated otherwise in a credit line to the material. If material is not included in the chapter’s Creative Commons license and your intended use is not permitted by statutory regulation or exceeds the permitted use, you will need to obtain permission directly from the copyright holder.





Thermal Error Compensation Models Utilizing the Power Consumption of Machine Tools

Sebastian Lang^{1,2} , Nico Zimmermann², Josef Mayr², Konrad Wegener³ ,
and Markus Bambach¹ 

¹ Advanced Manufacturing Laboratory, ETH Zürich, 8092 Zürich, Switzerland
selang@ethz.ch

² inspire AG, 8005 Zurich, Switzerland

³ Institute of Machine Tools and Manufacturing (IWF), ETH Zurich, 8092 Zurich, Switzerland

Abstract. Thermal errors are among the most significant contributors to deviations of products manufactured on modern machine tools (MTs). Reducing them is typically achieved through either design adaptation, active cooling of the MT and its environment, or compensation using measurements or model-based predictions. Model-based compensation strategies promise to have the lowest environmental footprint by far. In general, a compensation model needs to be accurate, robust to changing boundary conditions and must require only minimal experimental efforts as this reduces the productivity of the MT. Model inputs such as temperature measurements or the power consumption of various components, can be used to predict the thermal errors. The temperature inputs require additional sensors, effort and cost for the MT manufacturer to install and ensure up-time while the power consumption could be logged and are typically provided from the control system anyway. Adaptive compensation models are created using four different sets of inputs consisting of 13 temperature sensors and 7 power measurements. While the best results were obtained with all 20 inputs, the 7 energy recordings give similar results as the 13 temperature sensors if the environmental temperature is considered. The volumetric RMSE was reduced by 72% and the maximal error from 32.75 μm to 9.5 μm . ARX models proved to be suitable and even outperform more complex model structures such as LSTM and especially those without time dependency such as feed forward neural networks.

Keywords: Thermal errors · Machine tools · Compensation · Power Consumption · Temperature Measurement

1 Introduction

Thermal errors of machine tools (MTs) are among the most significant issues in precision manufacturing and can be responsible for up to 75% of the overall geometric errors on a produced workpiece [1]. Different mitigation strategies are employed by both MT manufacturers and users [2]. For example, thermo-symmetrical design introduces symmetry planes to reduce the effect of thermal errors. This is typically only possible in the design phase of MTs and does not remove all thermal errors [3]. Another approach

is improved cooling of the MT and its environment to prevent or reduce temperature gradients both spatially and temporally [4]. Geometrical on-machine measurements can also be used to recalibrate the MT while reducing productivity [5]. On top of this, companies typically utilize warm-up cycles and skilled operators who are able to reduce the effects of thermal errors based on their experience. However, these are all resource-intensive approaches. Another approach to mitigate the thermal errors is to predict and compensate them, which is seen as an intelligence-based approach. The modelling is typically carried out on an edge device that feeds the compensation values to the MT [6, 7]. Significant improvements of model-based thermal compensation were achieved with newly developed data-driven models and utilization of artificial intelligence [8]. The modelling approach can be classified into white, grey and black box models [9]. White box models allow the relationship between temperature and deformation to be fully understood and typically utilize FEM simulations or idealized geometries for this [10]. Grey Box models allow the partial reconstruction of the relationship of individual inputs on the thermal errors, while black box models prevent simple analysis of the model behavior. The field of thermal error compensation has seen all these modelling approaches applied.

Blaser et al. [11] and Mayr et al. [12] developed the thermal adaptive learning control (TALC), a closed-loop thermal error compensation which was implemented using an autoregressive model with exogeneous inputs (ARX). Zimmermann et al. [13, 14] expanded this work by using adaptive input selection in the closed loop, utilizing, among other methods, k-means clustering to prevent collinear inputs. These compensation approaches can also be validated using thermal test pieces in various production scenarios such as with metal working fluid (MWF), demonstrating the validity and necessity of robust data-driven models [15, 16]. Other model types that are often applied in thermal error compensation are artificial neural networks (ANNs) [17]. Recurrent neural networks (RNNs) are ANNs that can feed information from previous timesteps back in the model, similar to ARX models which makes them suitable for the time dependent nature of thermal errors and are therefore different compared to the purely feedforward nature of other ANNs. Long short-term memory networks (LSTMs) are one of the most popular types of RNNs that have been implemented for thermal error compensation [18]. Ngoc et al. [19] used such an LSTM with only the rotary axes power as model inputs to predict some axis-specific errors.

Temperature sensors can be used as model inputs, as pointed out by Kizaki et al. [20] to directly model the deformation analytically from the measured temperature field. Adding temperature sensors is a significant change on the MT and introduces an additional risk of failure, which has to be considered as demonstrated by Fujishima et al. [21]. In order to reduce the complexity and risk of failure already available measures might be preferable. However, the suitability of specific model inputs for thermal compensation is often not known and many different scenarios for both measurement and modelling are in theory feasible. Using control values can be an option to measure internal MT behavior without requiring additional sensor hardware.

In order to answer the question what type of model inputs are suitable for thermal compensation, especially considering the power uptake and model structure, this work applies both grey box models in the form of ARX models as well as black box models in

the form of two different neural network architectures, utilizing purely dense feedforward layers or two LSTM layers with hidden states with various sets of model inputs from power measurements to temperature measurements and combinations thereof. Section 2 describes the experimental set up while Sect. 3 describes the compensation approaches and the subsequent results of differing input sets consisting of either both temperature and power measurements or each of them individually or the environmental temperature and the power measurements in order to capture the external behavior of the MT.

2 Experimental Set up

The proposed compensation methods are exemplarily applied to compensate the thermal errors of a rotary axis of a 5-axis MT.

2.1 Analyzed Machine Tool

Basis for the experimental investigations is a Mori Seiki NMV 5000. The kinematic chain of the investigated MT can be described according to ISO 10791-2:2001 [22] as: V [w-C'-B'-b-[Y1, Y2] - X - [Z1, Z2] -(C)- t]. The MT is equipped with a turning option in the C-axis which allows a maximum speed of 1200 rpm. This high-powered drive requires a second coolant cycle, which is installed and dedicated only for the rotary table. Therefore, two dedicated heat pumps are used to temper the MT. In order to measure the thermal errors a discrete R-Test is carried out with a precision sphere mounted eccentrically on the table. This precision sphere is measured at varying C-positions using a Renishaw OMP 60 touch trigger probe. The first measurement is defined as the reference state. All deviations from the reference state are defined as thermal errors, allowing the time dependent motion of the tool center point (TCP) relative to the workpiece. The separated axis-specific thermal errors E_{XOC} , E_{YOC} , E_{ZOT} , E_{ROT} , E_{AOC} , E_{BOC} , E_{COC} can be observed with repeatabilities below $0.6 \mu\text{m}$ and $3 \mu\text{m/m}$ for $k = 2$ on this specific MT [11].

2.2 Power Intake Measurement

The power intake of the MT is significant for its thermal behavior and depicted in Fig. 1. All power taken in will be transformed into heat besides the process work, for example, in the form of electric losses in the motors or as friction in the guides. In the case of the analyzed air cuts all power is transformed into thermal loads.

The electrical power intake of the MT is measured in real-time by six Acuvim II sensors in order to avoid and validate the values from the control directly, as described by Zimmermann and Gontarz et al. [23, 24]. One measures the power uptake by the linear axes, B-axis as well as the spindle motor (E1). Another measures the power uptake of the C-motor that can perform turning operations (E2). The electrical power uptake of both coolant systems is measured (E3 & E4). Another component that is observed is the hydraulic pump which is used to clamp and release the tool in the spindle (E6). The total power consumption of the MT is also measured (E5). In turn, this allows the calculation of all other components lumped together by subtracting the five individual

measurements from the total power uptake of the MT. This “other” component (E7) contains, for example, the chip conveyor, the automatic tool changer or valves for cutting fluid which are negligible during the idling state.

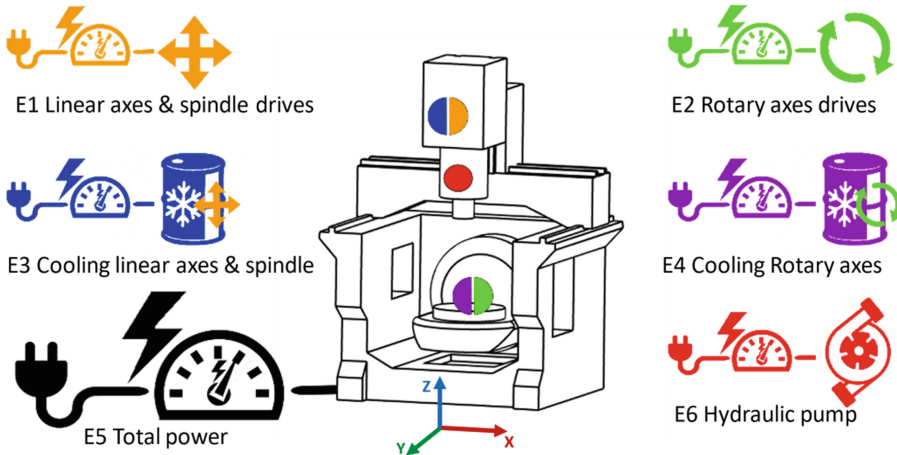


Fig. 1. Power measurement of the six main components of the 5-axis MT. The linear and rotary motors and their respective cooling systems as well as the hydraulic pump and total electrical power intake are measured.

2.3 Temperature Measurement

The temperature is measured at twelve positions located on and around the MT as depicted in Fig. 2.

Beside the structural sensors two air temperature sensors are located within the working space of the MT and one environmental temperature sensor is located outside the MT. A virtual sensor is generated by calculating the delta between the inlet and outlet temperature of the cooling system for the C-axis.

2.4 Experimental Load Case

In total, six experiments are carried out on the MT. The first experiment has a duration of 96 h followed by another 24-h load case of the same type. Here a random speed profile is applied to the C-axis in 300 rpm steps between 0–1200 rpm for random time durations between one and three hours. This is followed by two experiments (72 and 24 h) in which the B-axis is indexed at varying angles between 0 and 90°, in this mode the turning mode is not activated, so the C-axis rotates around ten times slower between 0–120 rpm (proportional to the B-angle). After this, additional 96- and 24-h experiments are carried out with the initial turning load case. In between the experiments the machine is in varying states and the interruptions are not of constant duration (between 15 min

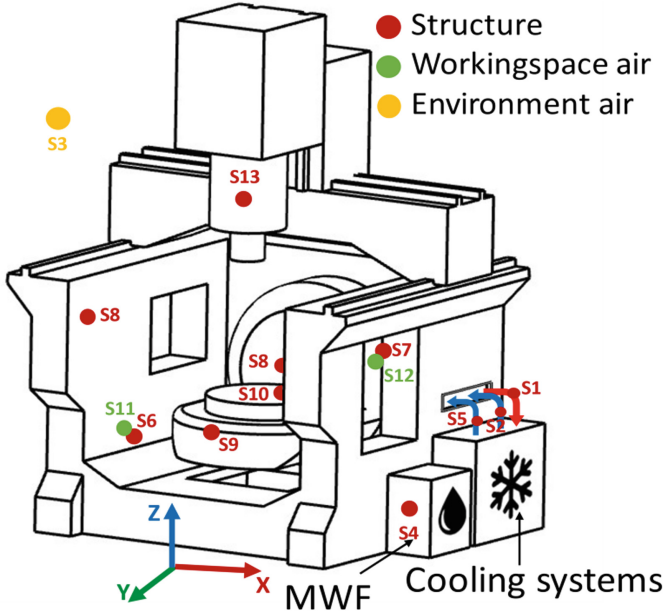


Fig. 2. Temperature sensors located on and around the investigated 5-axis MT.

and various days of other activity), thus no assumptions on the MTs initial state are possible.

Figure 3 shows the measurements of electrical power consumption of the main components. It is noted that the other components (E7) are almost always 0 and only becomes relevant when the metal working fluid is activated. During idling the MT consumes around 2.8 kW and during the turning load case around 4.2–4.5 kW at maximum speed. During the B-axis load case this is increased to approximately 4.75 kW in a much more stable distribution. This indicates that during the turning load case more thermally dynamic behavior is expected due to varying heat sources and sinks changing compared to the more stationary B-axis load case.

3 ARX Compensation Model

In order to predict thermal errors of MT, ARX models are used. As thermal errors can be described by a linear time-invariant dynamic system, they can be represented as a weighted sum

$$\begin{aligned}
 & y[k] + a_1 \cdot y[k - 1] + \dots + a_{n_a} \cdot y[k - n_a] \\
 & = b_{0,1} \cdot u_1[k] + b_{1,1} \cdot u_1[k - 1] + \dots + b_{n_b(1),1} \cdot u_1[k - n_b(1)] + \dots \quad (1) \\
 & + b_{0,M} \cdot u_M[k] + \dots + b_{n_b(M),M} \cdot u_M[k - n_b(M)]
 \end{aligned}$$

at the time step k , consisting current and past outputs y , the current and past values of an input u , of which M different ones can be used and the model parameter a_i and $b_{j,m}$. The order n_a defines the number of past system outputs that influence the current time step

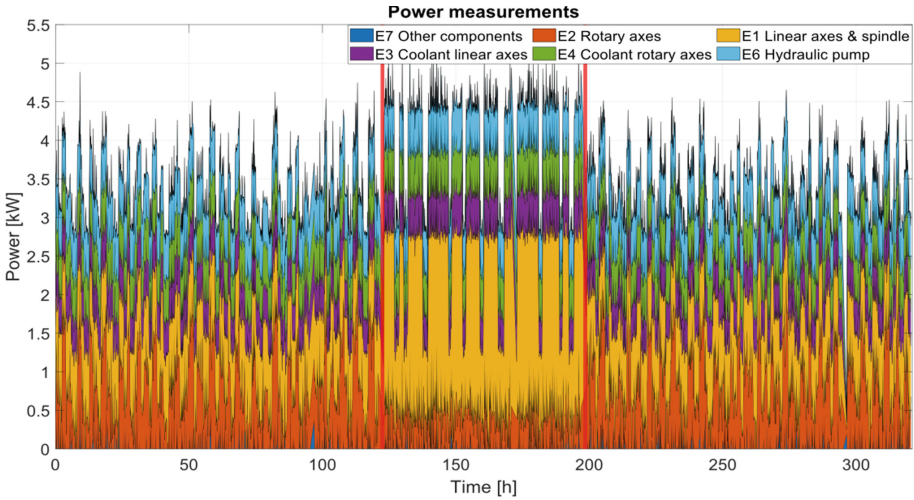


Fig. 3. Electrical power intake during the six experiments. The red lines indicate a change in the load case from the turning mode to positioning rotations of the C-axis at varying B-angles. (Color figure online)

and $n_{b,m}$ represents the considered time steps of the model input. As model inputs both temperature measurements and power measurements are used. The parameters of ARX models can be calculated using weighted least squares as shown by Mayr et al. [12] and the orders (n_a and n_b) are optimized following the Akaike Information Criterion (AIC). Model Inputs are selected by K-means clustering, where the number of clusters is defined by the Calinski-Harabasz Criterion [25] and subsequent cross correlation analysis. In TALC, which is shown in Fig. 4, periodical on-machine measurements are used to verify whether the residual is within the set action control limit (ACL) of 5 μm for position or 15 $\mu\text{m}/\text{m}$ for orientation errors deviation of the true measurement. In case a residual error exceeds the corresponding ACL a not-good (NG) mode is initialized in which 18 measurements are gathered and used to retrain the compensation model. Whenever experiments are joined together to one time series at the interconnection an NG mode is carried out to allow the previous memory to be filled, as otherwise no memory components are available at machine start.

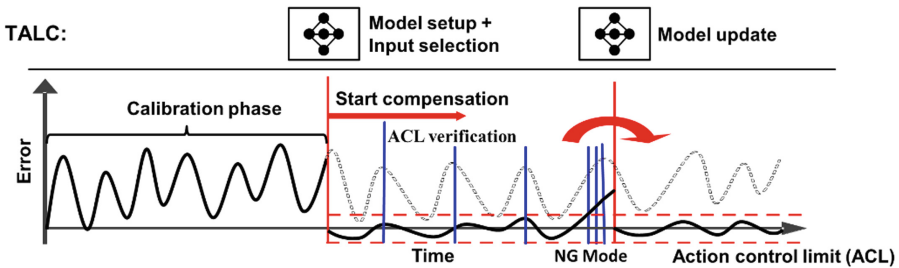


Fig. 4. TALC schematic adapted from Blaser et al. [11] and Zimmermann et al. [14].

3.1 Temperatures and Power Intake as Model Inputs

The thermal error E_{Z0T} is shown in Fig. 5 with and without thermal compensation during the 320-h experiment. All recorded model inputs were used during the input selection. During the turning load cycle, the measured error shown in Fig. 5(a) is highly fluctuating with an amplitude of up to 25 μm . In case of the B-axis load case, which is conducted in the middle of the test series, the error behavior appears significantly different, less dynamical changes and overall, a reduced amplitude of about 10 μm with more plateaus compared to the more transient behavior in the C-axis load case. This is also apparent in the model inputs, for example the table suspension temperature sensor (S8) shows similar changes in behavior as the thermal error. Both power measurements as well as temperatures are used as model inputs, in this case for example the total power consumption or the C-axis motor power consumption are used to predict the thermal error besides the temperature measurements. The first 160 h of measurement are used for parameter identification of the model described in Eq. (1). The residual error, shown in Fig. 5(b) during this training is very close to 0 with an average of 1.4 μm and appears to be only noise as there are no significant remaining patterns. Which indicates that the model inputs contain no additional information and can compensate well, if the situation is known exactly. The subsequent 160 h are used to validate this compensation to ensure a robust model even in slightly varying conditions. ACL verification measurements are carried out hourly and indicated by the light blue dashed line. They are not fed back to the model. Once the control measurement indicated that the ACL of any thermal error is exceeded a NG mode is triggered, which is indicated by the red vertical solid line. The maximal peak-to-peak error is reduced from 24.75 μm to 11.75 μm (53% reduction) and the root mean square error (RMSE) from 3.76 μm to 1.87 μm (50% reduction).

3.2 Temperatures as Model Inputs

Figure 6 depicts the compensation model for E_{Z0T} in the case where only temperature sensors are used as model inputs. E_{X0C} is the least significant of all observed thermal errors as it represents the symmetry plane of the MT which only observed symmetric load excitation. As in the case with only power + env. Temp 2 NG modes are triggered compared to the single NG mode of the input set with all possible sensors. Again, the compensation quality is high qualitatively and the reduction of the peak-to-peak error is -19%, 75% and 56% for E_{X0C} , E_{Y0C} and E_{Z0T} in line with the other shown results. To allow comparison to other errors.

3.3 Power Intake and the Environmental Temperature as Model Inputs

Figure 7 shows the compensated and uncompensated thermal error E_{Z0T} . As input set in this case only the power measurements and the environmental temperature sensor are used. All other modelling parameters are identical to the above model with all possible inputs, but a second NG mode was triggered in this case. The peak-to-peak error can be reduced from 32.75 μm to 9.5 μm which is a 70.1% reduction and the RMSE from 8.1 μm to 1.4 μm which is a 81.8% reduction indicating that the compensation fit is still good even if no structural temperature sensors are used.

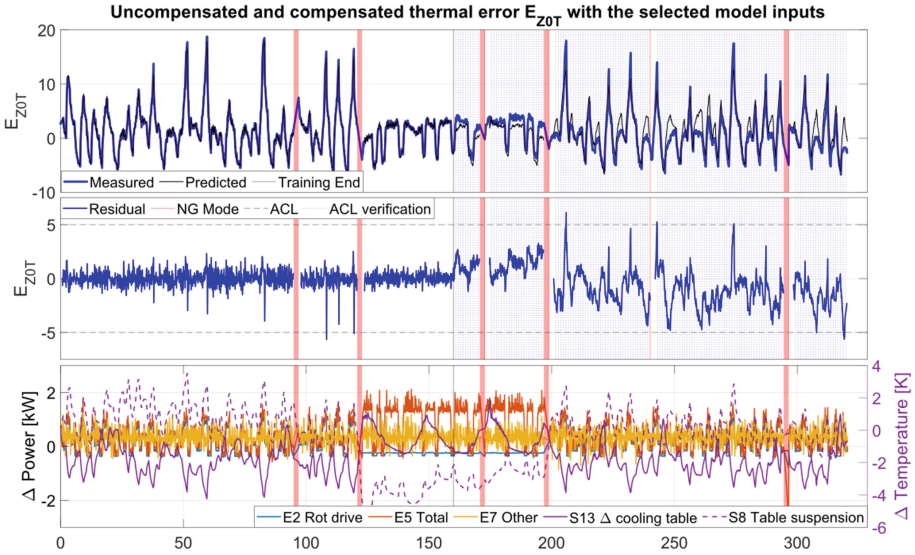


Fig. 5. Uncompensated and compensated thermal error E_{Z0T} measured during the 320 h of experiments. The model inputs are selected from all available temperature sensors and power intake measurements and therefore either in K or kW relative to the reference state of the first measurement. The red shaded areas with a duration of 2 h are a not-true-to-scale representation of the MT interruption between measurements which are followed by a NG mode (vertical red line) for model initialization after the training phase.

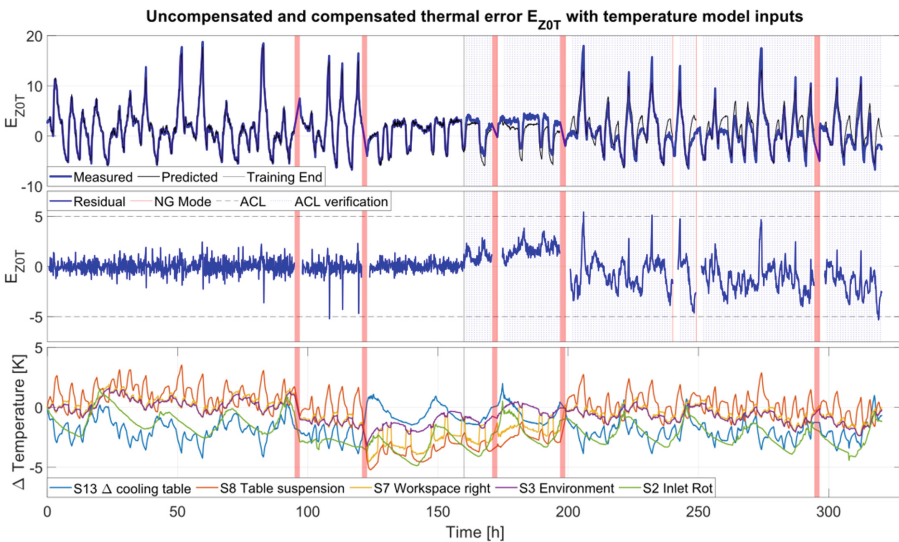


Fig. 6. The model inputs are selected only from all available temperature sensors.

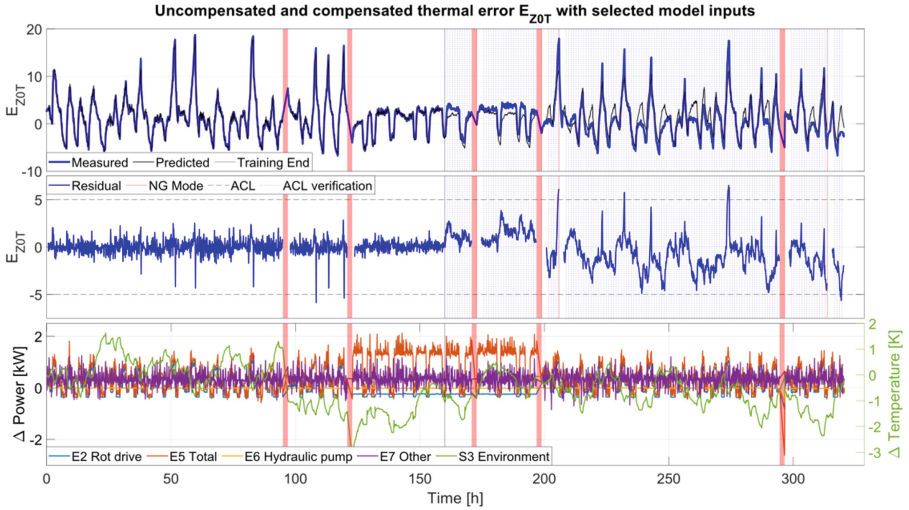


Fig. 7. Model inputs are selected only from the power intake measurements as well as the environmental temperature sensor and therefore either in K or kW.

3.4 Power Intake as Model Inputs

Another case considers only the power intake in the MT as potential inputs and therefore not the environmental temperature or direct source of information about the external heat sources of the MT. Figure 8 shows this, as the amount of six NG modes is clearly significantly higher than one in the case of all inputs or two in the case of solely temperatures it can be concluded that the temperature is a more flexible input compared to the power intake as it can contain both external and internal heat sources as it represents the actual temperature of the measured position. However, adding just one environmental temperature sensor to the power measurements reduces the number of NG modes from six to two despite both having five input variables and a similar performance as the temperature sensors.

3.5 Comparison of Input Sets Using the Volumetric Error

Table 1 shows the volumetric error reductions at the sphere position, which is uncompensated a RMSE of $9.7 \mu\text{m}$ or $29.9 \mu\text{m}$ in the peak. The volumetric error is defined as the Euclidean length of the error vector in space at the sphere position. Typically, the differences between the different input sets appear small but are rather significant. It is to be noted that the number of required NG modes differs between six for the case with only power inputs and one for the case with both power and temperature inputs. Therefore, also the case without TALC or by using all available data for model training is showcased. It is clear that using all inputs for selection is ideal, but the compensation quality can be satisfactorily achieved either with solely the temperature sensors or the environmental temperature and the power intakes. This quality cannot be achieved with the power as the sole input without any environmental measurements as no external effects are represented in the model inputs. Furthermore, a LSTM network and a

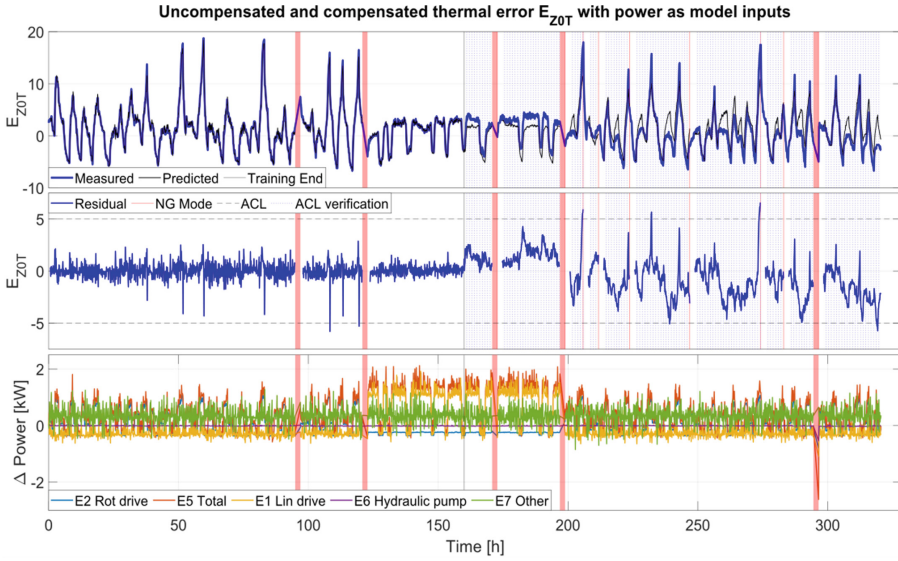


Fig. 8. The model inputs are selected only from the power intake measurements in kW.

Table 1. Reduction for the peak-to-peak value (P2P) the RMSE of the volumetric error due to the differences in input set and model training, between TALC, a version with no model updates or all data as training.

Model	Volumetric Error metric	Power + Temperatures	Temperature	Power + Env.	Power
ARX TALC	RMSE Reduction	72%	71.8%	70.7%	68.7%
	P2P reduction	77.7%	76.4%	74.3%	74.7%
	# NG modes	1	2	2	6
ARX no ST updates	RMSE Reduction	72%	70%	68.9%	64.2%
	P2P reduction	76.8%	74.9%	73.8%	74.3%
LSTM	RMSE Reduction	61.7%	66.9%	63.4%	58.9%
	P2P reduction	66.4%	72.5%	55.3%	50.8%
Feed forward ANN	RMSE Reduction	57.7%	59.6%	52.1%	50.6%
	P2P reduction	37.8%	37.6%	38.4%	38.3%

regular feedforward ANN are used to validate these results. For these models no input selection is carried out, so they are used end to end, and all potential model inputs are used. Therefore, the case with all possible inputs performs slightly worse compared to the input selection carried out, in the case of the ARX model. It can be noted that the significantly increased training effort $\sim 10,000$ trainable parameters compared to 20–50

parameters in the case of the ARX model is not beneficial, the time dependency of the model however clearly is beneficial as the feedforward ANN has none.

4 Conclusion and Outlook

Data-driven thermal error compensation can significantly reduce the thermally induced errors in MTs with a wide range of suitable input sets and models if they are set up well. Both power measurements and temperature measurements are suitable for this if the measurements of internal sources are extended for those of external sources such as the environment and achieve volumetric error reductions around 72%. This allowed the robust compensation of two significantly different types of load cases with varying forms of models or inputs. In general, the time dependency of the model is seen as highly beneficial. Simpler models such as ARX models are more suitable than LSTM models, which can also achieve acceptable accuracy requiring magnitudes more total parameters and therefore training effort. Inputs that do not consider any external effects such as the environmental temperature are not as suitable as a significant effect cannot be represented.

Future work should focus on increasing the training efficiency of these compensation models in order to learn even broader types of loads with reduced training time. Industrialization of the thermal compensation should be pursued in order to increase the energy efficiency of advanced manufacturing.

Acknowledgements. Co-financed by Innosuisse - Swiss Innovation Agency, Project no. 27835.1 IP-ENG as well as the Swiss Federal Office of Energy, Project no. SI/502305 for which the authors want to express their gratitude.

References

1. Mayr, J., et al.: Thermal issues in machine tools. *CIRP Ann.* **61**, 771–791 (2012)
2. Putz, M., Richter, C., Regel, J., Bräunig, M.: Industrial consideration of thermal issues in machine tools. *Prod. Eng. Res. Devel.* **12**(6), 723–736 (2018). <https://doi.org/10.1007/s11740-018-0848-6>
3. Großmann, K. (ed.): *Thermo-Energetic Design of Machine Tools*. LNPE, Springer, Cham (2015). <https://doi.org/10.1007/978-3-319-12625-8>
4. Hellmich, A., Glänzel, J., Pierer, A.: Analyzing and optimizing the fluidic tempering of machine tool frames. In: *Conference on Thermal Issues in Machine Tools, Proceedings, Dresden* (2018)
5. Zimmermann, N., Mayr, J., Wegener, K.: Extended discrete R-Test as on-machine measurement cycle to separate the thermal errors in Z-direction. In: *Proceedings of the euspen's Special Interest Group: Thermal Issues* (2020)
6. Mareš, M., Horejš, O., Havlík, L.: Thermal error compensation of a 5-axis machine tool using indigenous temperature sensors and CNC integrated Python code validated with a machined test piece. *Precis. Eng.* **66**, 21–30 (2020)

7. Mares, M., Horejs, O.: Enhancement of specialised vertical turning lathe accuracy through minimisation of thermal errors depending on turning and milling operations. *MM Sci. J.* **2021**, 4512–4518 (2021)
8. Czwartosz, R., Jedrzejewski, J.: Application of machine learning in the precise and cost-effective self-compensation of the thermal errors of CNC machine tools—a review. *J. Mach. Eng.* **22** (2022)
9. Gißke, C., Albrecht, T., Wiemer, H., Esswein, W., Ihlenfeldt, S.: A proposal for a systematization and taxonomy of methods to rectify thermally induced errors on existing machine tools. *Int. Conf. Therm. Issues Mach. Tools* **1269**, 4692–4697 (2021)
10. Li, J.W., Zhang, W.J., Yang, G.S., Tu, S.D., Chen, X.B.: Thermal-error modeling for complex physical systems: the-state-of-arts review. *Int. J. Adv. Manuf. Technol.* **42**, 168–179 (2009)
11. Blaser, P., Pavliček, F., Mori, K., Mayr, J., Weikert, S., Wegener, K.: Adaptive learning control for thermal error compensation of 5-axis machine tools. *J. Manuf. Syst.* **44**, 302–309 (2017)
12. Mayr, J., Blaser, P., Ryser, A., Hernandez-Becerro, P.: An adaptive self-learning compensation approach for thermal errors on 5-axis machine tools handling an arbitrary set of sample rates. *CIRP Ann.* **67**, 551–554 (2018)
13. Zimmermann, N., Büchi, T., Mayr, J., Wegener, K.: Self-optimizing thermal error compensation models with adaptive inputs using Group-LASSO for ARX-models. *J. Manuf. Syst.* **64**, 615–625 (2022)
14. Zimmermann, N., Lang, S., Blaser, P., Mayr, J.: Adaptive input selection for thermal error compensation models. *CIRP Ann.* **69**, 485–488 (2020)
15. Lang, S., Zimmermann, N., Mayr, J., Bambach, M., Wegener, K.: Influences of metalworking fluid on the thermal errors of a 4-axis thermal test piece. In: *Special Interest Group Meeting on Thermal Issues*, pp. 4–7 (2022)
16. Wiessner, M., Blaser, P., Böhl, S., Mayr, J., Knapp, W., Wegener, K.: Thermal test piece for 5-axis machine tools. *Precis. Eng.* **52**, 407–417 (2018)
17. Fines, J.M., Agah, A.: Machine tool positioning error compensation using artificial neural networks. *Eng. Appl. Artif. Intell.* **21**, 1013–1026 (2008)
18. Liu, J., Ma, C., Gui, H., Wang, S.: Thermally-induced error compensation of spindle system based on long short term memory neural networks. *Appl. Soft. Comput.* **102**, 107094 (2021)
19. Vu Ngoc, H., Mayer, J.R.R., Bitar-Nehme, E.: Deep learning LSTM for predicting thermally induced geometric errors using rotary axes' powers as input parameters. *CIRP J. Manuf. Sci. Technol.* **37**, 70–80 (2022)
20. Kizaki, T., Tsujimura, S., Marukawa, Y., Morimoto, S., Kobayashi, H.: Robust and accurate prediction of thermal error of machining centers under operations with cutting fluid supply. *CIRP Ann.* **70**, 1–4 (2021)
21. Fujishima, M., Narimatsu, K., Irino, N., Mori, M., Ibaraki, S.: Adaptive thermal displacement compensation method based on deep learning. *CIRP J. Manuf. Sci. Technol.* **25**, 22–25 (2019)
22. International Organization for Standardization (ISO) Geneva Switzerland: ISO 10791–2:2001 Test conditions for machining centres — Part 2: Geometric tests for machines with vertical spindle or universal heads with vertical primary rotary axis (vertical Z-axis) (2001)
23. Zimmermann, N., Mayr, J., Wegener, K.: An action-oriented teaching approach for intelligent and energy efficient precision manufacturing. *Manuf. Lett.* **33**, 961–969 (2022)
24. Gontarz, A., Weiss, L., Wegener, K.: Energy consumption measurement with a multichannel measurement system on a machine tool. In: *Proceedings of the International Conference on Innovative Technologies*, pp. 499–502 (2010)
25. Caliński, T., Harabasz, J.: A dendrite method for cluster analysis. *Commun. Stat.* **3**, 1–27 (1974)

Open Access This chapter is licensed under the terms of the Creative Commons Attribution 4.0 International License (<http://creativecommons.org/licenses/by/4.0/>), which permits use, sharing, adaptation, distribution and reproduction in any medium or format, as long as you give appropriate credit to the original author(s) and the source, provide a link to the Creative Commons license and indicate if changes were made.

The images or other third party material in this chapter are included in the chapter's Creative Commons license, unless indicated otherwise in a credit line to the material. If material is not included in the chapter's Creative Commons license and your intended use is not permitted by statutory regulation or exceeds the permitted use, you will need to obtain permission directly from the copyright holder.





An Indicative Model Considering Part of the Thermo-Mechanical Behaviour of a Large Grinding Machine

Martin Mareš¹(✉), Otakar Horejš¹, and Pravoslav Nykodym²

¹ Faculty of Mechanical Engineering, Department of Production Machines and Equipment, RCMT, Czech Technical University in Prague, Horská 3, 128 00 Prague, Czech Republic
m.mares@rcmt.cvut.cz

² TOS Hostivař s.r.o., Rádiová 1431/2a, 102 00 Praha 10, Czech Republic

Abstract. Machine tool (MT) thermal errors are an important element in machined workpiece inaccuracies. In the past few decades, thermal errors associated mainly with one particular source (e.g. spindle or environment), have been successfully reduced by SW compensation techniques such as multiple linear regression analysis, finite element method, neural network, transfer function (TF) within similar calibration and verification conditions. An approach based on TFs is used for thermal error modelling in this research. This method respects basic heat transfer mechanisms in the MT and requires a minimum of additional gauges. The approach provides insight into the share of each source in the total machine thermal error through a combination of linear parametric models. The aim of this research is to develop an indicative model for a large grinding machine with predictive functionality focused on part of the thermo-mechanical behaviour within different configurations of the headstock, tailstock and workpiece. Unlike a compensation model, an indicative model has no connection to the MT feed drives and can only provide the machine operator with information regarding the actual direction and relative magnitude along with prediction of the time constant and steady state of the non-stationary thermal error. The second aim is to compare the difficulty of measuring at the stator and rotating machine part levels, the thermal behaviour linearity at both levels and the possibility of upgrading the indicative model to a compensation model to extend industrial applicability.

Keywords: Grinding Machine · Thermal Errors · Control Limits

1 Introduction

The heat generated e.g. by moving axes and machining processes creates thermal gradients, resulting in the thermal elongation and bending of machine tool (MT) elements, which substantially deteriorate MT accuracy. Consequently, up to 75% of all geometrical errors of machined workpieces are caused by temperature effects [1]. Thermal errors may be sufficiently reduced by new MT design concepts which are less sensitive to thermal effects. This type of intervention in the MT structure leads to a pareto set of different

parameters, and designers have to concentrate on preserving other MT properties as well [2]. Redesigning the MT structure is usually possible in the prototype phase of new products. Adaptive or intelligent control of cooling systems [3], integrated additional sensors in the MT structure [4] or direct (in-process) measurement techniques [5] may also be very efficient in minimising thermo-mechanical impacts on MT accuracy. However, they do increase machine and operational costs and result in machining process interruptions and prolonged production time. A very promising contemporary approach is the use of finite element method (FEM) [6], especially coupled with model order reduction (MOR) techniques to reduce computing time [7]. The problem of boundary condition complexity at the machine or component level, however, is still present in this solution. In contrast, indirect (software) compensation of thermal errors at the tool centre point (TCP) is one of the most widely employed reduction techniques due to its cost-effectiveness and ease of application. Different types of software error compensation are becoming a crucial part of modern technological development in the context of Industry 4.0 and intelligent MT [8].

Ordinarily, approximation models are based on measured auxiliary variables [9] (temperature, spindle speed, etc.) used to calculate the resulting thermally induced displacements at the TCP. Many strategies have been investigated to establish these models, e.g. multiple linear regressions (MLR) [10], artificial neural networks (ANN) [11], transfer functions (TF) [9], etc. The majority of the compensation models introduced in the literature have the potential to significantly reduce MT thermal errors. The methods differ in the amount and type of input variables, and the training and modelling time required for composition and model architecture (white, black or grey-boxes [12]). Therefore, efforts should be focused on the applicability and verification of approaches in real industrial conditions to meet end-users' needs as well.

An approach to thermal error modelling of a large turning-milling centre in regard to various MT configurations was presented in [13], followed by a presentation of the limits of a similar linear parametric model in compensating efforts for the effect of different grinding wheels on the thermal behaviour of a large grinding machine [14]. In this research, the approach is further advanced and critically evaluated by application on the same large grinding machine but within the headstock and tailstock activity with varying axial and radial force. The implementation and application possibilities of the designed thermal error models on the stator and rotor MT part levels are discussed here.

The rest of the paper is arranged as follows: in Sect. 2, the experimental setups and conditions are described. In Sect. 3, the measured data and analysis are presented. The modelling approach is described in Sect. 3.3 in more detail along with an indicative model structure applied on the measured data. Based on the results the model is upgraded to compensate for thermal errors. All of the results are critically discussed in Sect. 4, followed by conclusions and the outlook for further research.

2 Experimental Setup and Conditions

The target machine for this article is a large grinding machine for round grinding operations. The machine consists of two separate beds. The front bed carries a headstock and a tailstock movable along the Z-axis. The linear movement of both components serves

for positioning the workpiece. The workpiece clamped in the headstock performs a rotational movement. The rear bed carries a wheel head movable in the X and Z directions as shown in Fig. 1. The maximum diameter of the grinding wheel is 915 mm with rotation of 1350 rpm. The maximum diameter of a clamped workpiece is 1000 mm, the length is 4000 mm and the weight is 9000 kg. The maximum speed of a headstock spindle is 50 rpm and the axial force exerted by the tailstock for workpiece clamping is 60 kN. The machine bodies are made of cast iron.

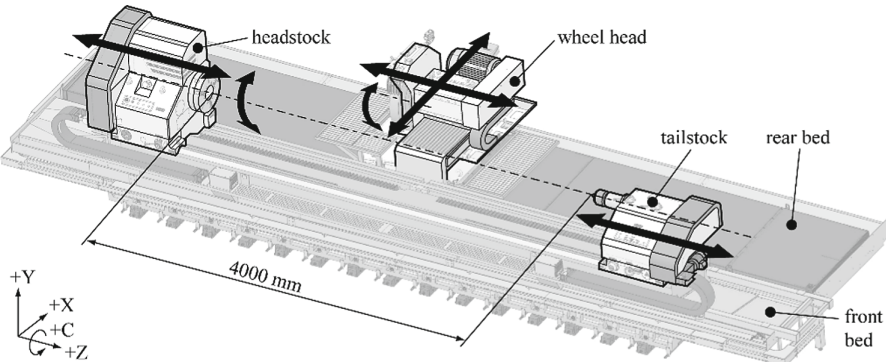


Fig. 1. Schema of the target machine with the indicated kinematics.

The target machine was placed in a MT manufacturer's assembly room. The room is a huge, unair-conditioned open space equipped with a row of production machines. Despite the character of the room, the environment is considered stable during the tests.

Basically, grinding machines for round grinding are capable of simultaneous rotation realised in three components: the wheel head (rotation of the grinding wheel), headstock and tailstock (rotation of the workpiece). This research is focused on the impact of workpiece rotation on MT thermal error. The MT is considered in three configurations. The schema of the machine in a configuration with the workpiece clamped with the 'loose end' in chuck is depicted on the left side of Fig. 2. The workpiece is represented by the testing mandrel. The schema of the machine in a configuration with a small workpiece clamped 'between the centres' of the headstock and tailstock is depicted on the right side of Fig. 2. The tailstock exerts a clamping force on the workpiece, causing an axial load on the headstock and tailstock bearings. The schemas contain the approximate positions of three temperature probes (Pt100, Class A, 3850 ppm/K; headstock bearings temperature $T_{hs\ bearings}$, tailstock bearings temperature $T_{ts\ bearings}$ and reference temperature $T_{reference}$ reflecting changes in the environment). These sensors are embedded in the MT control system. The schema of the machine in the third configuration with a large workpiece (1800 kg) clamped 'between the centres' is depicted on the left side of Fig. 3. The weight of the workpiece adds a radial load on the bearings. The location of the deformation sensors on the machine in the third configuration is indicated on the right side of the same figure. Displacements were measured between the stator parts of both components ($\delta_{X\ stat}$; indicating relative displacement of the entire headstock and wheel head bodies) and between their axes of rotation ($\delta_{X\ rot}$; displacement reflecting the direct impact on

workpiece accuracy, mostly subject to compensation). Eddy-current sensors (PR6423) clasped in magnetic holders were used for noncontact sensing of displacements between the rotating parts and contact probes (Peter Hirt T100) between the stators.

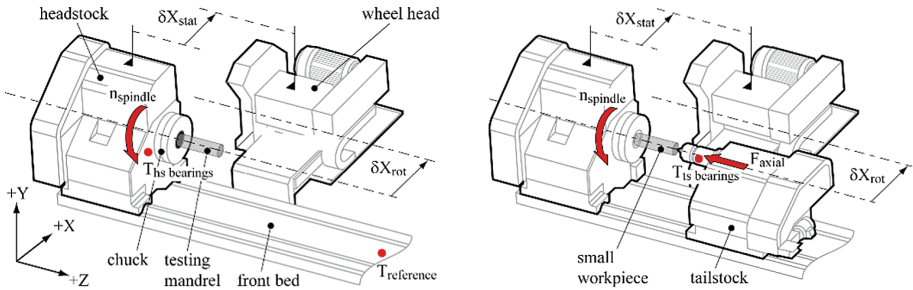


Fig. 2. Schema of the experimental setup with headstock activity during rotation of the clamped testing mandrel (left) and with clamped small workpiece (right).

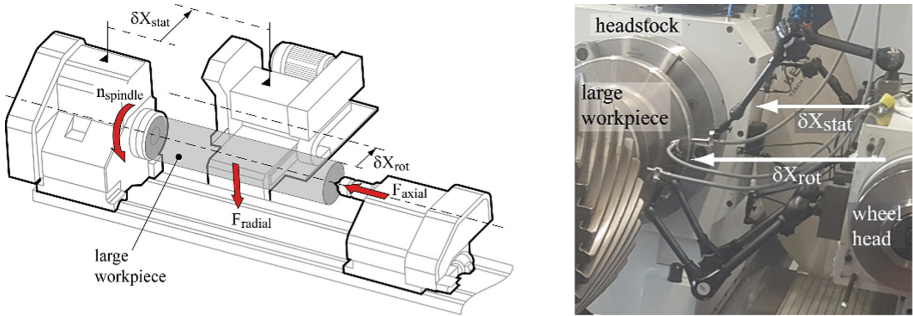


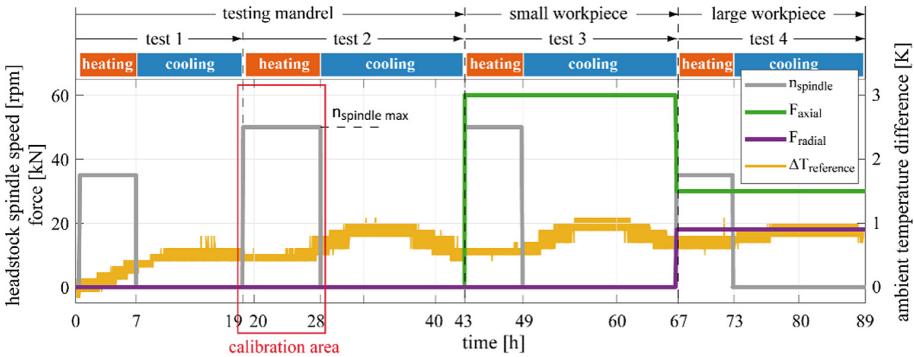
Fig. 3. Experimental setup with headstock and tailstock activity with clamped large workpiece: schema (left), on machine (right).

Four experiments were carried out within the three machine configurations. The experimental setups are summarised in Table 1.

Detailed setup and conditions of the realised tests are shown in Fig. 4, containing the headstock spindle speed and axial and radial forces applied over 4 days of testing. The highlighted area of the test 2 heating phase is intended for calibration of the models. Each test consists of a part of the transient behaviour between two thermodynamic equilibria (the MT in approximate balance with its surroundings and the MT steady state during heat source activity), concluded after one work shift (6 to 8 h) followed by a cooling phase (16 to 18 h). Test 3 extends tests 1 and 2 with the addition of axial force and test 4 extends the settings with the addition of radial force application. The rpm settings of test 1 and test 2 differ. The four tests are designed to evaluate the linearity of MT thermo-mechanical behaviour. Process cooling and the process itself were inactive during testing. The positions of the headstock and wheel head were similar in all of the setups. Further efforts are focused on the main direction X of the machine generally affecting the accuracy of the ground workpiece diameter.

Table 1. Setup of realised tests.

Test no.	Machine configurations	Active heat source	Rotation speed [rpm]	Axial force [kN]	Radial force [kN]
1	loose end (testing mandrel)	Headstock	35	–	–
2	loose end (testing mandrel)		50	–	–
3	between the centres (small workpiece)	Headstock and tailstock	50	60	–
4	between the centres (large workpiece)		35	30	18

**Fig. 4.** Spindle speed, axial and radial force profiles along with ambient temperature changes during tests 1 and 2 (testing mandrel), 3 (light workpiece) and 4 (large workpiece).

3 Thermal Error Analyses, Model Developments and Verification

3.1 Modeling Approach and Efficiency Evaluation Method

The concept behind the modelling approach lies in the usage of a minimum of additional gauges (only from the MT control system [9]), an open structure that is easy to extend and modify (advantageous for machine learning principles [16]), real time application and ease of implementation into MT control systems.

A compensation strategy based on TFs is a dynamic method with a physical basis. A discrete TF is used to describe the link between the excitation and its response:

$$y(t) = u(t) \cdot \varepsilon + e(t) \quad (1)$$

The vector $\mathbf{u}(t)$ in Eq. (1) is the TF input and $\mathbf{y}(t)$ is the output vector in the time domain, ε represents the general TF in the time domain, and $\mathbf{e}(t)$ is the disturbance value (further neglected). The TF form of polynomials' quotient is expressed by Eq. (2).

$$\frac{Z\{y(t)\}}{Z\{u(t)\}} = \frac{a_n \cdot z^{-n} + \dots + a_1 \cdot z^{-1} + a_0 \cdot z^0}{b_m \cdot z^{-m} + \dots + b_2 \cdot z^{-2} + b_1 \cdot z^{-1} + b_0 \cdot z^0}, \quad (2)$$

where Z is the Z-transform of the time discretized function, z is the complex variable, n is the order of the TF numerator, m is the order of the TF denominator and holds that $m > n$. Further, $a_{0:n}$ are the calibration coefficient of the TF input, and $b_{0:m}$ are the calibration coefficient of the TF output. The difference form of the discrete TF (a generally suitable form for modern MT control systems using their programming languages) in the time domain is introduced in Eq. (3).

$$y(k) = \frac{u(k-n) \cdot a_n + \dots + u(k-1) \cdot a_1 + u(k) \cdot a_0 - y(k-m) \cdot b_m - \dots - y(k-1) \cdot b_1}{b_0}, \quad (3)$$

where k represents the examined time instant and $k-n$ ($k-m$) is the n -multiple (m -multiple) delay in the sampling frequency 1 s^{-1} of the measured input vector (simulated output vector). A linear parametric model with an autoregressive with external input (ARX) identifying structure is used with the help of *Matlab Identification Toolbox* [15]. The ARX as an optimal model structure (with the best fit in quality and robustness) is also discussed in [16].

The approximation quality of the simulated behaviour is expressed by a global approach based on the least square method (*fit*; a percentage value where 100% would equal a perfect match of the measured and simulated behaviours):

$$fit = \left(1 - \frac{\|measured - simulated\|}{\|measured - mean(measured)\|} \right) \cdot 100. \quad (4)$$

The *measured* value in Eq. (4) is the measured output (here displacements in the X direction), *simulated* is the simulated model output, and *mean(measured)* expresses the arithmetic mean of the measured output over time.

3.2 Linearity Analyses of Thermo-Mechanical Behaviour

An analysis of the linearity between the input (measured temperature) and the outputs (measured deformations) of the thermal mechanical system during the heating phases of the 4 tests at the level of the stators and the axis of rotation is shown in Fig. 5.

The results demonstrate that changing the experimental setup does not affect the linearity of the whole system at the level of the stator parts of the components (due to its informative nature only, the expression is in relative values, however, the axis division of the two diagrams is equally selected) in contrast to the level of the rotation axes, where the change in the test settings affects the gain of thermo-mechanical transient behaviour while maintaining similar time constants. Thus, the modelling difficulty at the two levels differs considerably. This also confirms the assumption of a higher system linearity on the shorter links of the machine's kinematic chain.

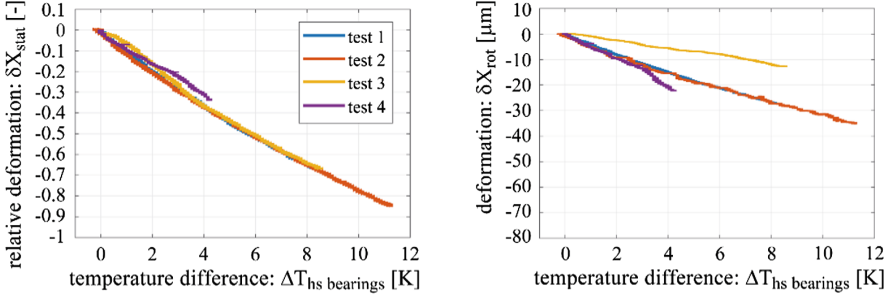


Fig. 5. Linearity analysis between the temperature of the headstock bearings and the deformations measured on the stators (left) and axes of rotation (right) during the heating phases of the tests.

3.3 Indicative Model of MT Thermal Behaviour with Predictive Functionality

Working on grinding machines generally requires high precision and reliability. Both producers and users are reluctant to fully rely on any built-in indirect compensation approaches in control systems. Frequent measurement of the workpiece geometric accuracy and considerable operator experience are required. The following section presents the functionality of the thermal error model within the expert system with predictive functions, providing the operator with informative data for better orientation, expectation and understanding of the machine's behaviour during the current process.

The expected functionalities of the expert system are as follows:

- A) Determination of the development and direction of the thermal error in accordance with the machine coordinate system;
- B) estimation of the time constants of transient phenomena;
- C) prediction of the time to reach a steady state during the activity of the described heat source, assuming that the power value of the source would not change.

This is possible based on a known power input quantity to the model. In this case, the input is the course of headstock spindle revolutions. The model for estimating the behaviour of headstock spindle bearings' temperature change is given in Eq. (5).

$$\Delta \mathbf{T}_{hs\ bearings}^{simulated} = \mathbf{n}_{spindle} \cdot \gamma_{test\ 2} \cdot k_{\vartheta}, \quad (5)$$

where $\Delta \mathbf{T}_{hs\ bearings}^{simulated}$ is the simulated vector of the temperature difference, $\gamma_{test\ 2}$ is the identified 2nd order discrete TF in the time domain with power excitation (calibration coefficients are summarised at the end of the section) and k_{ϑ} is the correction factor between the simulated and measured temperature unique for each test. Given the measured temperature values that are available, it is possible at any time t_j to adapt the simulated value to the measured reality according to Eq. (6).

$$k_{\vartheta} = \frac{\Delta \mathbf{T}_{hs\ bearings}^{measured}(t_j)}{\Delta \mathbf{T}_{hs\ bearings}^{simulated}(t_j)} \quad (6)$$

The model input during calibration test 2 and the measured and simulated behaviours of the temperature changes during the heating phases of all tests are depicted in Fig. 6.

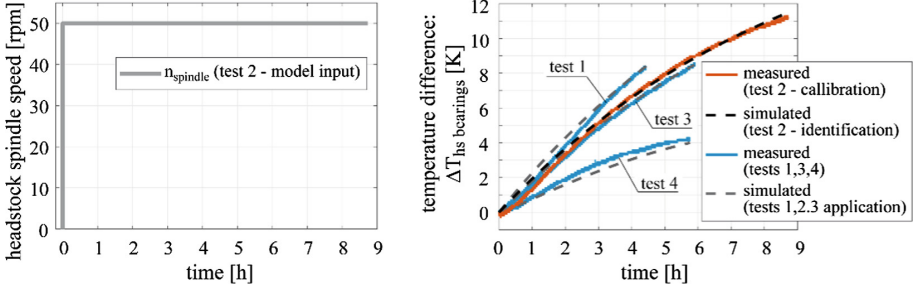


Fig. 6. Model input vector of the recorded headstock spindle speed during the heating phase of calibration test 2 (left) and the headstock bearing temperatures, measured and simulated according to Eq. (5) during the heating phases of all tests 1 to 4 (right).

Generally, indicative models have no link to the MT feed drives and can only provide the machine operator with data of an informational nature. The description of the indicative model of the temperature errors caused by the rotation of the workpiece, respecting the different settings of all tests, benefiting from the linear behavior of the deformations at the level of the stator parts of the components (see the left side of Fig. 5), and the predictive properties of the model from Eq. (5), follows in Eq. (7).

$$\delta X_{stat}^{simulated} = (\mathbf{n}_{spindle} \cdot \gamma_{test 2} \cdot k_{\vartheta}) \cdot \varepsilon_{test 2}, \quad (7)$$

where $\delta X_{stat}^{simulated}$ is the simulated vector of relative deformations at the stator parts of the MT components, $\varepsilon_{test 2}$ is the identified 3rd order discrete TF in the time domain with temperature excitation (calibration coefficients are summarised at the end of the section). The results of identification (test 2) and application (test 1, 3 and 4) of the indicative model for the heating phases are shown on the left side of Fig. 7. Predictive functionality, assuming the same technological parameters of the current process, estimating the time to reach the steady state and calculating the time constant τ of the transition phenomenon, is shown on the right side of Fig. 7 for the test 4.

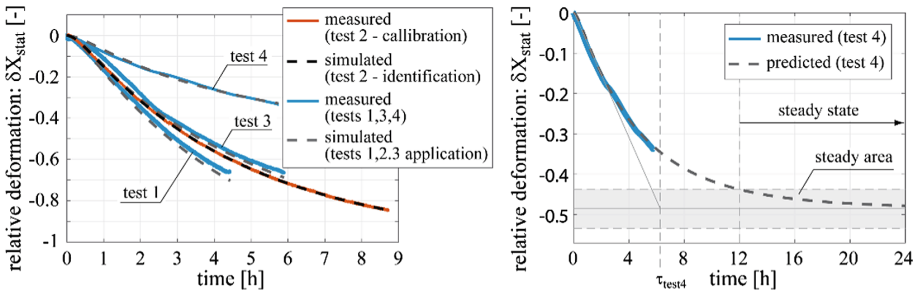


Fig. 7. Relative deformations, measured and simulated by the indicative model (Eq. (7)), on the stators of the headstock and wheel head during heating phases of all tests 1 to 4 (left) and demonstration of the model's predictive functionality during the heating phase of test 4 (right).

The figure shows that in the case of the test 4 setup, a stable area (10% envelope of the steady state point) will be reached after 12 h of heat source activity. The calculated time constant of the transient phenomenon from the predicted behaviour of test 4 is $\tau_{\text{test}4} = 6.5$ h. This information, data and the trends contained in the expert system can be provided to the operator both in terms of temperatures (Eq. (5)) and deformations (Eq. (7)) to help plan production progress on the machine.

3.4 Upgrade of Indicative Model to Compensate for Thermal Errors

The right side of Fig. 5 shows obvious differences in the linear dependence between the temperature near the heat source and the deformations measured at the axes of the rotation level. The model from Eq. (7) may be updated to the compensation level of Eq. (8) by finding the transfer between the deformations of the stator parts and the deformations at the rotation level axes and including a simple gain-scheduling problem [17] in the model structure.

$$\delta X_{\text{rot}}^{\text{simulated}} = \left[(\mathbf{n}_{\text{spindle}} \cdot \gamma_{\text{test}2} \cdot k_{\vartheta}) \cdot \varepsilon_{\text{test}2} \right] \cdot \delta_{\text{test}2} \cdot k_{\text{test}i}, \quad (8)$$

where i indicates the tests 1, 2, 3, 4. The $\delta X_{\text{rot}}^{\text{simulated}}$ in Eq. (8) is the simulated vector of deformations at the rotation level axes, $\delta_{\text{test}2}$ is the identified 1st order discrete TF in the time domain with deformational excitation (calibration coefficients are summarised at the end of the section) and $k_{\text{test}i}$ is the adaptive gain factor depending on time $t_{\text{test}i}$ and measured deformation and is unique to each machine configuration. Time $t_{\text{test}i}$ is determined for each test setting when the value of the adaptation factor according to Eq. (9) stabilizes and does not change any further.

$$k_{\text{test}i} = \frac{\delta X_{\text{rot}}^{\text{measured}}(t_{\text{test}i})}{\delta X_{\text{rot}}^{\text{simulated}}(k_{\text{test}1,2}, t_{\text{test}i})}, \quad \text{where } k_{\text{test}1,2} = 1 (\text{model calibration}). \quad (9)$$

The results of the compensation model from Eq. (8) application along with the highlighted values of the adaptation coefficients and the time required for their determination are shown on the left side of Fig. 8. The right side contains the theoretical values of the residual thermal errors after compensation model application.

The application of the model from Eq. (8) to test 4 (3.7 μm) shows the largest residual error, the smallest to test 1 (1.3 μm). The total residual deformation over all tests reaches a value of 4.5 μm . The determined uncertainty of deformation measurement is ± 0.92 μm .

The following table lists all the calibration coefficients of the identified TFs in Eqs. (5), (7) and (8) and the maximum approximation quality achieved during the identification process. The achieved approximation quality is one of the criteria for choosing a TF in the model structure. The second criterion is the TF stability check verified by linear time invariant (LTI) step response [15]. LTI expresses a clear dependency between an input (unit jump of TF excitation) and output (predicted TF response) of the thermo-mechanical system. LTI diagrams with the TF responses to unit excitations are shown in Fig. 9. The graphs enable a better understanding of the links in the investigated thermo-mechanical system.

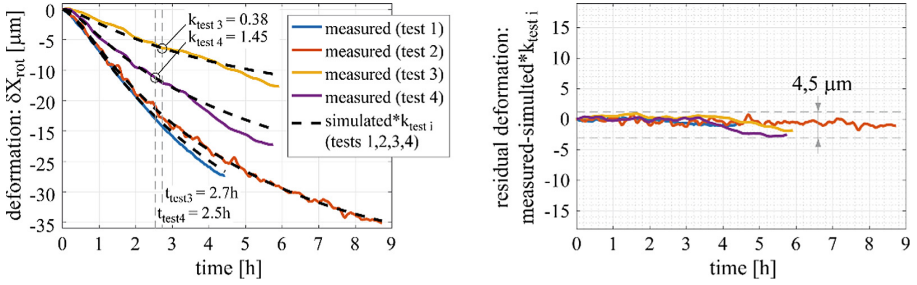


Fig. 8. Deformations on rotation level axes of the headstock and wheel head during heating phases of all tests 1 to 4, measured and simulated by compensation model (Eq. (8)) (left) and demonstration of residual errors after the model application (right).

Table 2. Identified parameters of thermal error model.

TF	a_0	a_1	b_0	b_1	b_2	b_3	fit
$\gamma_{test\ 2}$	$7.3665e - 07$	0	1	-1.93457	0.93457	0	92%
$\varepsilon_{test\ 2}$	-0.16306	0.16305	1	-0.71385	0.10325	-0.38936	95%
$\delta_{test\ 2}$	0.1063	0	1	-0.9975	0	0	94%

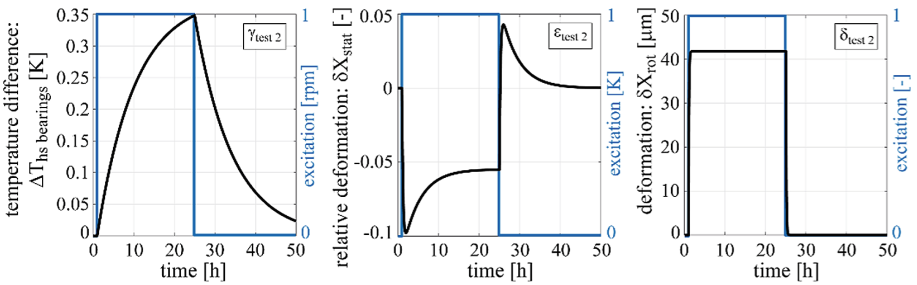


Fig. 9. LTI step responses of identified TFs in the compensation model (Eq. (8)) to headstock spindle speed (left), temperature difference of headstock spindle bearing (middle) and relative deformations on machine stator parts (left) unit excitation.

4 Discussion of Results and Conclusions

The axial and radial bearings load has no observable influence on the linearity of the thermo-mechanical behaviour (as can be seen from the dependence of temperatures and deformations on the level of the stators of the target machine; see right side of Fig. 5). The system is retuned by changing the clamping of the workpiece from ‘loose end’ to ‘between the centres’, manifested by a change in the linear dependence of temperatures and deformations at the rotation level axes. This fact is caused by another heat source engaged in the kinematic chain of the machine - the tailstock. The inclusion of the

tailstock results in a significant angular error of the Z-axis of the workpiece in the xz plane, thus emphasising the influence of clamped workpiece dimensions.

An accurate grinding process requires frequent in-process measurement of the ground surface accuracy. The indicative model (Eq. (7)) helps the operator when the measurement needs to be intensified, otherwise, when frequent measurement is redundant due to the thermal stability of the machine. The indicative model has been implemented into the control system of the machine as interactive diagnostic screens via a superstructure environment by mySCADA technology programmed in Javascript.

The compensation model (Eq. (8)) finds practical applications in the machining of long workpieces, which requires a long time for one operation without interruption by measuring the geometric accuracy of the workpiece. The effectiveness of the compensation model applied to a complete, uninterrupted experiment from Fig. 4 is demonstrated in Fig. 10. The approximation quality drops from an average of 87% to 63% compared to heating phase only compensation, as can be seen from the last row in Table 3. The residual deformation more than doubles, from $4.5 \mu\text{m}$ to $10.5 \mu\text{m}$. The model shows good long-term stability due to the small influence of the surrounding environment. The approximation of the entire progress may be refined by including the cooling phase in the calibration measurement. However, this approach will either negatively affect the approximation of the heating phase or complicate the structure of the model with another TF describing the cooling phase with the requirement to control the switching between approximations of both phases.

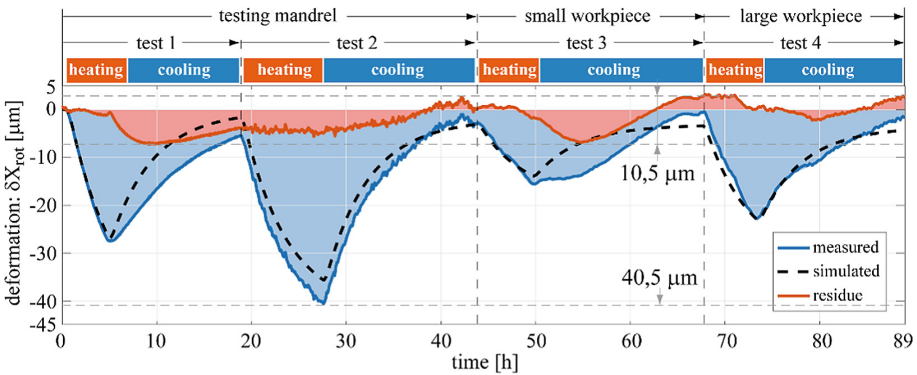


Fig. 10. Results of compensation model (Eq. (8)) application on the entire measurement.

A critical evaluation of the presented models follows. The indicative model does not need any correction factors. Its outputs are only informative (with predictive functionalities) and are expressed in relative values. The achieved average efficiency of the indicative model is 93% within this research. The informative indicative model can be upgraded to the compensation model with an action link to the machine's feed drives. The compensation model requires adaptive gain-scheduling elements obtained from direct measurements and its average efficiency is 5% lower (88%). The compensation has a direct positive link to the increase in the geometric accuracy of the workpiece and is

Table 3. Approximation quality of indicative and compensation models.

Test No.	1	2 (calibration)	3	4	Whole behaviour
Model	<i>fit</i>				
Indicative (Eq. (7))	91%	95%	91%	93%	–
Compensation (Eq. (8))	93%	94%	81%	81%	63%

carried out in the background of the process without the necessary intervention (or even awareness) of the operator.

Measuring the mutual displacement of the stator parts of the machine to further extend the validity of the indicative model is easier to implement, especially by using laser interferometry. Contrarily, it is convenient, but more difficult, to obtain data for the compensation model directly from accuracy measurements on the workpiece.

Future research will focus on the positional dependence of machine thermal errors, the influence of process fluid in the concept of an energy-efficient machine, hybrid compensation (using both direct and indirect compensation strategies) and extending the model applicability depending on the FEM outputs.

Acknowledgement. This research (Heavy Duty Grinder TOS Hostivař) received funding from the Ministry of Industry and Trade of Czech Republic (Project FV30223).

References

1. Mayr, J., et al.: Thermal issues in machine tools. *CIRP Ann. – Manuf. Technol.* **61**(2), 771–791 (2012)
2. Grossmann, K.: Thermo-Energetic Design of Machine Tools: A Systemic Approach to Solve the Conflict Between Power Efficiency, Accuracy and Productivity Demonstrated at the Example of Machining Production. *Lecture Notes in Production Engineering*, p. 260. Springer, Cham (2015). <https://doi.org/10.1007/978-3-319-12625-8>. ISBN 978-3-319-12624-1
3. Hellmich, A., Glänzel, J., Ihlenfeldt, S.: Methods for analyzing and optimizing the fluidic tempering of machine tool beds of high performance concrete. In: *CIRP-Sponsored 1st Conference on Thermal Issues in Machine Tools*, Dresden, Germany (2018)
4. Naumann, C., Brecher, C., Baum, C., Tzanetos, F., Ihlenfeldt, S., Putz, M.: Hybrid correction of thermal errors using temperature and deformation sensors. In: *CIRP-Sponsored 1st Conference on Thermal Issues in Machine Tools*, Dresden, Germany (2018)
5. Zimmermann, N., Mayr, J., Wegener, K.: Extended discrete R-test as on-machine measurement cycle to separate the thermal errors in Z-direction. In: *Proceedings of the Euspen's Special Interest Group: Thermal Issues*, Aachen, Germany, pp. 21–24 (2020)
6. Glänzel, J., Naumann, A., Kumart, T.S.: Parallel computing in automation of decoupled fluid-thermostructural simulation approach. *J. Mach. Eng.* **20**(2), 39–52 (2020)
7. Hernández-Becerro, P., Spescha, D., Wegener, K.: Model order reduction of thermal models of machine tools with varying boundary conditions. In: *CIRP-Sponsored 1st Conference on Thermal Issues in Machine Tools*, Dresden, Germany (2018)

8. Liu, K., Liu, H., Li, T., Liu, Y., Wang, Y.: Intelligentization of machine tools: comprehensive thermal error compensation of machine-workpiece system. *Int. J. Adv. Manuf. Technol.* **102**(9–12), 3865–3877 (2019). <https://doi.org/10.1007/s00170-019-03495-7>
9. Brecher, C., Hirsch, P.: Compensation of thermo-elastic machine tool deformation based on control internal data. *CIRP Ann. – Manuf. Tech.* **53**(1), 299–304 (2004)
10. Naumann, C., Glänzel, J., Putz, M.: Comparison of basis functions for thermal error compensation based on regression analysis – a simulation based case study. *J. Mach. Eng.* **20**(4), 28–40 (2020)
11. Mize, C.D., Ziegert, J.C.: Neural network thermal error compensation of a machining center. *Prec. Eng.* **24**(4), 338–346 (2000)
12. Li, J.W., Zhang, W.J., Yang, G.S., Tu, S.D., Chen, X.B.: Thermal-error modeling for complex physical systems: the-state-of-arts review. *Int. J. Adv. Manuf. Technol.* **42**, 168–179 (2008)
13. Mareš, M., Horejš, O., Hornych, J.: Thermal error minimization of a turning-milling center with respect to its multi-functionality. *Int. J. Autom. Technol.* **14**(3), 475–483 (2020)
14. Horejš, O., Mareš, M.: Limits of linear parametric models for thermal error compensation of a large grinding machine. In: *Proceedings of the Euspen's Special Interest Group: Thermal Issues*, 4 p. ETH, Zurich (2022)
15. Ljung, L.: *System identification toolbox™ user's guide*. The MathWorks (2015)
16. Blaser, P., Mayr, J., Wegener, K.: Long-term thermal compensation of 5-axis machine tools due to thermal adaptive learning control. *MM Sci. J.* **4**, 3164–3171 (2019)
17. Rugh, W.J., Shamma, J.S.: Research on gain scheduling. *Automatica* **36**(10), 1401–1425 (2000)





Open Access This chapter is licensed under the terms of the Creative Commons Attribution 4.0 International License (<http://creativecommons.org/licenses/by/4.0/>), which permits use, sharing, adaptation, distribution and reproduction in any medium or format, as long as you give appropriate credit to the original author(s) and the source, provide a link to the Creative Commons license and indicate if changes were made.

The images or other third party material in this chapter are included in the chapter's Creative Commons license, unless indicated otherwise in a credit line to the material. If material is not included in the chapter's Creative Commons license and your intended use is not permitted by statutory regulation or exceeds the permitted use, you will need to obtain permission directly from the copyright holder.





Adaptive Thermal Model for Structure Model Based Correction

Xaver Thiem¹ , Holger Rudolph¹, Robert Krahn² , Steffen Ihlenfeldt¹ ,
Christof Fetzer² , and Jens Müller¹

¹ TU Dresden, Chair of Machine Tools Development and Adaptive Controls, Helmholtzstraße
7a, 01062 Dresden, Germany

xaver.thiem1@tu-dresden.de

² TU Dresden, Chair of Systems Engineering, Nöthnitzer Straße 46, 01187 Dresden, Germany
{robert.krahn, christof.fetzer}@tu-dresden.de

Abstract. This paper discusses structure model based correction of thermal induced errors at machine tools. Using a machine model evaluated in thermal real-time, the thermal induced errors at the tool center point (TCP) are calculated based on information gotten from the machine control (e.g., axes velocities, positions, and motor currents) and ambient temperature. The machine model describes the physical relationships and considers the structure and structural variability resulting in traverse movements of the feed axes – the so-called structure model. To create this, finite elements are used as thermal and thermo-elastic models, and model order reduction (MOR) techniques are used to enable the calculation of high-resolution models in thermal real-time. Subsequent parameter updates can improve the accuracy of the initial parameter set of thermal models. A systematic procedure developed for this purpose and its application to a demonstrator machine are presented. For the update, parameters are selected which can change over the operating time, e.g., due to wear. Temperature sensor positions are chosen, sensitive to changes in these parameters. Simulations with parameters varied in a plausible range are used to determine whether parameter optimizations are reasonable. The parameter optimization runs in a trusted execution environment (TEE) on a server in parallel to the calculation of the correction model on the machine control. The confidential input data of the model and the model itself have to be protected from unauthorized access. The efficient model calculation and parameter optimization in a secure server environment leads to an adaptive thermal model (digital twin).

Keywords: Machine tool · Digital twin · Temperature · Optimization · Trusted execution environment (TEE)

1 Introduction

Conventional counter measures for the reduction of thermal errors of machine tools like machine cooling are energy consuming [1]. Alternative approaches without additional energy consumption are model based corrections of the errors [2]. One of these

approaches is the structure model based correction [3]. The structure model is a physical based model of the machine tool, e.g., a finite element model. Accessible data (e.g., axes velocities, axes positions, motor currents) in the control are utilized as input information for the model. Based on this information, the heat sources (e.g., friction) in the machine tool are calculated. Additionally, the heat conduction depending on this information is determined, e.g., heat conduction in bearings. For these calculations, empirical models are normally used. The temperature field of the machine tool is calculated based on the heat sources and thermal conductions by a physical based model. The thermal deformation of the machine tool is calculated with the help of the temperature field also by a physical based model. In this way, the error at the tool center point is determined and corrected. This paper focuses on the thermal model as part of the structure model.

The thermal behavior of machine tools change over the lifetime due to wear, changed preload and lubrication of machine components. For example, in [4] significant changes in the friction of linear axes are detected after four and seven years. The friction has reduced up to 70%. The reasons therefore are the run in process and the wear caused reduction of the diameter of rolling elements, which leads to a reduced preload. The temperature field is influenced by the reduced heat flow due to the reduced friction. Other examples are the reduced preload between ball screw nut and ball screw spindle of up to 75% over lifetime in [5] and the preload degradation for linear rolling guides of up to 82% in [6]. The preload degradation leads to a reduced friction in these machine components.

The parameters of the model should be updated over the lifetime to match these changes in order to maintain and improve the accuracy of the calculated temperature field and therefore the quality of the correction. In this paper, a systematic procedure is developed for this purpose. At first, a workflow for the creation of efficient calculating models is introduced. Afterwards, the approach for the parameter update is explained. Additionally, the trusted execution environment (TEE) is described, which is used to run the parameter optimization safely on a server in parallel to the calculation of the correction model on the machine control. Finally, the approach is applied to a demonstrator machine.

2 Thermo-Elastic Model

2.1 Fundamentals

The basis of all structural models consists in physically founded model formulations, which require the solution of partial differential equations. Using a discretization method, here by FEA (Finite Element Analysis), results in a system of coupled ordinary differential Eqs. (1), which allow the simulation by numerical time integration routines.

$$\begin{bmatrix} \mathbf{M}_{uu} & 0 \\ 0 & 0 \end{bmatrix} \cdot \begin{Bmatrix} \ddot{\mathbf{U}} \\ \ddot{\mathbf{T}} \end{Bmatrix} + \begin{bmatrix} \mathbf{D}_{uu} & 0 \\ \mathbf{C}_{Tu} & \mathbf{C}_{TT} \end{bmatrix} \cdot \begin{Bmatrix} \dot{\mathbf{U}} \\ \dot{\mathbf{T}} \end{Bmatrix} + \begin{bmatrix} \mathbf{K}_{uu} & \mathbf{K}_{uT} \\ 0 & \mathbf{L}_{TT} \end{bmatrix} \cdot \begin{Bmatrix} \mathbf{u} \\ \mathbf{T} \end{Bmatrix} = \begin{Bmatrix} \mathbf{F} \\ \mathbf{Q} \end{Bmatrix} \quad (1)$$

The coefficients are:

\mathbf{M}_{uu} – the matrix of inertia properties

\mathbf{D}_{uu} – the matrix of damping properties

\mathbf{K}_{uu} – the matrix of stiffness properties

\mathbf{K}_{uT} – the coupling matrix to consider the thermally induced strain

\mathbf{C}_{TT} – the matrix of heat capacities

\mathbf{L}_{TT} – the matrix of heat conduction and heat transfer within the system

\mathbf{C}_{Tu} – the coupling matrix to consider the heat generation by deformation

\mathbf{T} – the vector of temperatures

\mathbf{F} – the vector of external forces and moments

$\dot{\mathbf{Q}}$ – the vector of heat flows at the system boundaries

The elimination of sub-matrixes in Eq. (1), which are not required from a technical point of view and with respect to their characteristics, enables the separate solution of thermal and mechanical problem on different time steps:

$$\mathbf{C}_{TT} \cdot \dot{\mathbf{T}} + \mathbf{L}_{TT} \cdot \mathbf{T} = \dot{\mathbf{Q}} \quad (2)$$

$$\mathbf{K}_{uu} \cdot \mathbf{u} = \mathbf{F} - \mathbf{K}_{uT} \cdot \mathbf{T} \quad (3)$$

2.2 Modeling Conception

The modeling pursues the goal of integrating a state space model into a CNC in form of a process-parallel program code. This code calculates correction values based on current thermal state and their resulting thermally induced deformation of a machine in order to apply them to the axis set points of the machine control. For this purpose, a programming environment with its own model description language (here MATLAB® with its programming language “M”) constitutes the central working environment. The FEA software environment (here ANSYS®) is used exclusively for the creation of the state space model and the associated system matrixes.

From a programmer’s perspective, the modeling follows an object-oriented concept in form of a class library. The individual classes encapsulate various model information and provide methods for managing a structural model. The class library divides into four categories:

- Elements and parts represent the sub-models in the sense of an FEA environment and provide the import and conversion routines, among other things.
- Groups and axes allow parts and elements to be combined into assemblies that are stationary resp. Movable relative to each other.
- Configurations represent the physical domains in the model as well as the individual variants of a model’s pose dependencies in the workspace.
- Matrixes and additional information contain the mathematical representation of the sub-models and manage the assignments to the finite elements and nodes as well as their degree of freedom.

From the user’s perspective, the modeling follows an assembly-oriented concept. The instantiation of the mentioned classes allows the construction of a model hierarchy, which in turn follows the kinematic chain of a machine tool.

2.3 Modeling Procedure

The setup of a model, the computation of its temperature fields and resulting elastic deformations can be summarized in the following basic procedure, see Fig. 1:

1. Preparation of CAD geometry for all machine parts: This includes geometry defeaturing, segmentation of functional surfaces etc. and assembling.
2. Definition of all surfaces where thermal and/or mechanical boundary conditions or coupling conditions will be modeled later.
3. Discretization of the geometry into finite elements, parametrization of the time-invariant quantities (e.g. material parameters) and creation of the system matrices in a FEA software.
4. Export of the required data from the FEM environment.
5. Import of these data into the already mentioned programming environment with structured data storage as well as the separation of the thermal (according to Eq. (2)) and mechanic (according to Eq. (3)) model equations.
6. Supplementing the parameterization functions for the time-dependent parameters and boundary conditions: This includes motion profiles of the machine axes, power loss models, free and forced convection, etc.
7. Simulation of the temperature field in time domain,
8. Computation of the deformation field from the temperature field at discrete points in time and
9. Calculation resp. Application of the axis correction values and/or visualization and evaluation of the results, either in the programming environment or after re-transmission in the FEA environment.

Especially for steps 7 and 8 in order to limit the computation times, it is recommended to reduce the system degree of freedom (DoF) by applying model order reduction (MOR) procedures. These generate the projection matrixes \mathbf{V} and \mathbf{W} for the subspaces (with index R). In this case, the state space model has a control matrix $\mathbf{B}_R = \mathbf{W}^T$ and observer matrixes $\mathbf{C}_{Rth} = \mathbf{V}$ resp. $\mathbf{C}_{Rel} = -\mathbf{K}_{uu}^{-1} \cdot \mathbf{K}_{uT} \cdot \mathbf{V}$.

3 Parameter Update

In this section, the approach for the parameter update is explained. In Fig. 2 the flowchart for the parameter update is shown. On the left, the results of the thermal simulation are compared cyclical at specific points (marked in the picture with red dots) with the measured temperatures. If the difference between simulated and measured temperatures exceeds the required limits for the model accuracy, measures have to be taken to increase the accuracy of the model. These limits depend on the requirements of the specific model application. In order to correct the thermal-based errors, the goal is to maintain the model accuracy throughout the lifetime of the machine. The next step is to check if a parameter optimization is reasonable. Therefore, the parameters in question are varied in a plausible range to determine minimum and maximum reachable temperature with the simulation model. This calculation can be done on a server. If the measured temperature exceeds these extrema, a parameter optimization is not reasonable because there are no plausible parameters, which allow the model to reach the measured value. Possible reasons for this

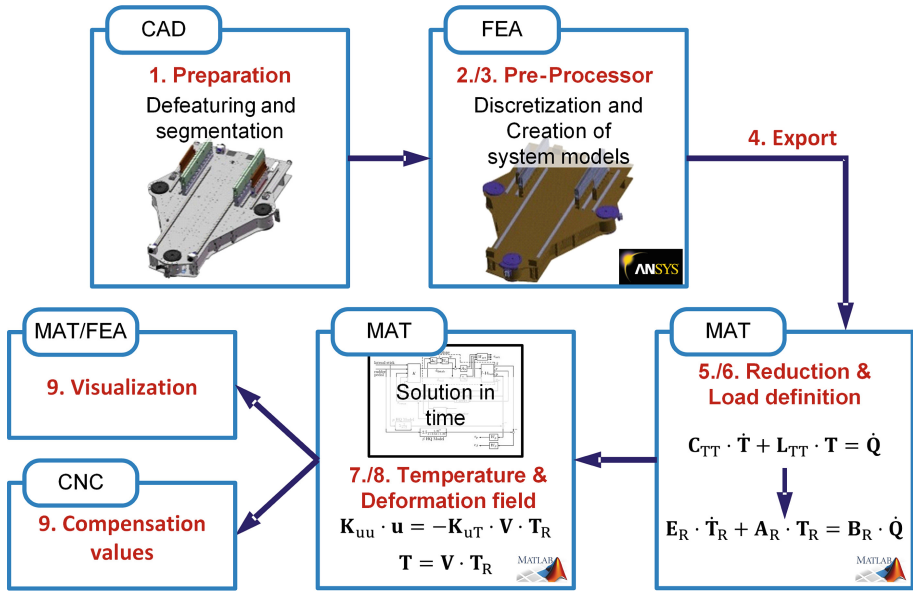


Fig. 1. Modelling workflow for thermo-elastic model

are a defect sensor, a defect machine component or an insufficient model. Either way, the user is getting a warning ((6) in Fig. 2) and no parameter optimization and update is conducted. If the measured value is within range, a parameter optimization is done. The results are fed back to the cyclical running thermal model at the machine control.

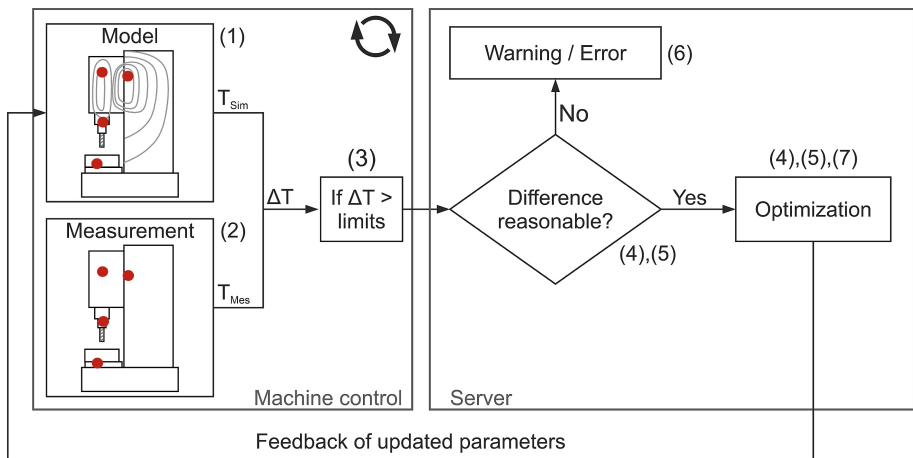


Fig. 2. Flowchart for parameter update

To perform the described procedure, certain information is required:

At first the parameters in the model ((1) in Fig. 2) are determined, which are uncertain over the lifetime of the machine tool and have a significant influence on the temperature field of the machine tool. Heat sources and heat sinks have a dominant influence and are model by empirical functions. The parameters of these functions are usually uncertain [7]. Components at which friction occurs are able to change their behavior during the life time due to wear (e.g., pitting, micro pitting, cracks), changes in lubrication (e.g., aging, regreasing, other lubricant, filling quantity), changed preload, fouling with dust and dirt particles.

In the second step, sensor positions have to be selected for the temperature measurement ((2) in Fig. 2). A sensitivity analysis has to be conducted to find the positions at which the temperature is dominantly influenced by a heat source or heat sinks. In addition, the influence of the heat sources and sinks should be separable at the positions. The necessary datasets for the analysis can be gathered by simulation or experiments. For the analysis, the temperature field during thermal steady state is used. Because at this state the heat capacity, which is a certain model parameter, has no effect and the heat conduction (partially uncertain) and heat sources and sinks (uncertain) determine the temperature field. As load cases, combined and separated loads at heat sources and sinks in different heights should be used. One possible method for the sensitivity analysis is “pearson partial correlation coefficients adjusted for internal variables” [8, 9]. The temperature sensor positions with highest pearson partial correlation coefficient to the heat source or sink is selected. In addition, the p-value have to be checked. If it is above the significance level of 5%, the influence of the heat sources or sinks cannot be separated.

The maximum permissible difference (limits) between measurement and simulation at these positions has to be defined ((3) in Fig. 2) after the selection of the sensor positions. These values determine the accuracy of the correction over the whole lifetime of the machine tool. The first parameterization of the model based on literature values is usual uncertain. Therefore, experiments are conducted to adjust the model parameters before the correction is activated. The maximum absolute difference between simulation and measurement after the adjustment is the model accuracy, which should be obtained. Whenever the simulated temperatures exceed these limits the variant calculations should be conducted and if reasonable the parameter optimization.

A reasonable range of the model parameters ((4) in Fig. 2) have to be estimated for the calculation of the maximum and minimum reachable temperatures at the measurement positions. The range have to be obtained from literature, which investigates the behavior of machine components over lifetime. It defines also the lower and upper boundaries for the optimization of the model parameters.

The time window ((5) in Fig. 2) for which the variant calculation and the parameter optimization has to be conducted depends on the thermal time behavior of the components of the machine tool. Therefore, the thermal time behavior has to be characterized. This behavior can be approximated by lag elements of first order. This property is also used by correction approaches that use transfer functions as a model [10–12]. The time behavior of a lag element of first order depends on the time constant τ . The time constant is determined by fitting a lag element to a simulated step response for a load step. Since

the thermal time behavior can be load depended, different load steps are applied to the machine component models, e.g. 10%, 50% and 100% of the maximum load. The loads are distinguished into internal and external influences on the machine component [13]. Typical internal heat sources and sinks are the power losses in the drives, friction and machine cooling. The environment of the machine tool is the external influence via heat conduction to the machine foundation, convection to the surrounding air and radiation to the background. The largest time constant τ_{\max} determines how large the time window for the variant calculation and the parameter optimization has to be. The permissible error resulting from only using this time window for the calculation of the temperature field should be an order of magnitude smaller than the reasonable parameter range. The temperature error (ΔT_E) is quantified in relation to the thermal steady-state temperature after a load step (ΔT_S) (e.g. $\Delta T_E / \Delta T_S = 1\%$). With the permissible error and the Eq. (4) the time window t_{Window} for the variant calculation and parameter optimization can be determined.

$$t_{\text{Window}} = -\tau_{\max} \cdot \ln\left(\frac{\Delta T_E}{\Delta T_S}\right) \quad (4)$$

In the optimization ((7) in Fig. 2) the error squares between measured and simulated temperature values are minimized. An optimization method is needed for nonlinear multivariable problems with constrained variables. In this paper, the interior point method [14] is chosen. In previous studies [3, 15] this method has to been shown to be suitable for parameter optimization of thermal models. All parameters of the machine component are optimized at the same time, which belong to the sensor that exceeds the permitted difference to the simulated value. The optimization is computationally expensive, which is why it should be performed in a trusted execution environment on a server.

4 Trusted Execution Environment

Servers located at datacenters provide a cost-efficient yet powerful option to execute parameter optimizations at machine runtime and during simulations. To address security concerns, e.g., data theft or manipulation by collocated potentially malicious software or personnel, modern technologies offer protection beyond data encryption on a hard drive. Nowadays, software can be shielded against privileged software, e.g., the operating system, that could use its elevated permissions for attacks. During execution, when code and data have been loaded into memory, other (malicious) software could try to read, steal or corrupt data. This includes machine models or parameter settings, which in turn could have disastrous effects in production.

Among other technology providers, Intel has developed dedicated hardware instructions called Software Guard Extensions (Intel-SGX) [16] that allow for the creation of a trusted execution environment (TEE). TEEs execute software in an enclave, with encryption facilitated only by the processor. Both the executed code and data loaded to main memory is encrypted directly by the processor, effectively shielding it from access by any other application. Combined with encrypted communication, parameter optimizations can be executed on a server distant to the in-production machines without sacrificing security.

While encryption increases security, it also implies additional operations to be executed. Given that all accessed data and code in memory needs to be decrypted and encrypted by the processor during execution of the application, a potentially non-negligible performance reduction can be observed. Reducing the performance penalty imposed by Intel-SGX has been the focus of many researchers, allowing optimized code to be executed with a 10% to 20% slowdown, while non-optimized code could face a 100% slowdown (calculations take twice as long).

5 Application at Demonstrator Machine

The approach for the parameter update is demonstrated on the model of a Cartesian 3-axis machine. The machine is shown in Fig. 3. The slides of the machine are built with braced aluminum plates in order to get a lightweight structure. Three ball screw axes drive the Z-slide. Two linear direct drives drive the Y-slide and one linear direct drive drives the X-slide. The components are connected via profile rail guides and bearings. Except for the main spindle, the machine has no build in cooling. Due to the aluminum plate construction and the uncooled heat sources in the machine structure, it is susceptible to thermally induced errors. This makes the machine an interesting demonstration object.

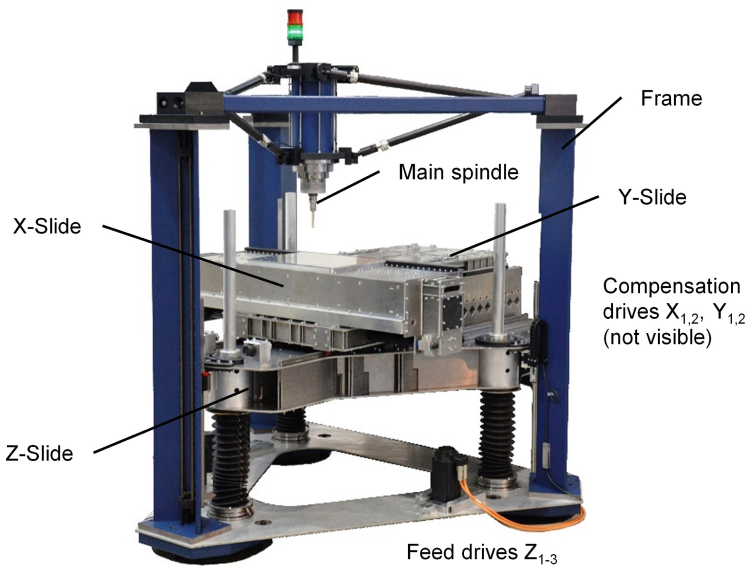


Fig. 3. Demonstrator machine

5.1 Model of the Demonstrator Machine

The entire structural model is divided into main assemblies named above. The creation and preparation of the geometry model of the main assemblies follows the original CAD, but with these simplifications for the subsequent FE model:

- the removal of all screw holes,
- the removal of all tension rods, because no suitable multi-physics elements exist for them within used FEA system,
- the reduction of the cross-sections of the profiled rail guides to a rectangular profile and of the ball screw spindles to a circular profile, and
- the segmentation of the functional surfaces, especially on the guiding elements, so that they correspond to the actual movement length of the axes.

The submodels for the main assemblies each have their own FE model. These define the solid bodies of the components, all surfaces of the boundary and transition conditions (for convection, thermal transition, contact stiffness etc.), the mesh of the finite elements as well as the resulting system matrices according to Eq. (1). In this state, the FE model of the complete machine including test arbor has a degree of freedom of 345,256 in the thermal and of 1,035,768 in the elastic partial model.

Importing the model data into MATLAB, instantiating the model objects and grouping them to match the kinematic chain results in a model structure as shown in Fig. 4. The tension rods, the contacts in bearings and guides, and the machine grounding are supplemented by additional finite elements from the library. In the figure, these and all interface objects for the boundary conditions are neglected to maintain clarity. The latter are assigned to the configurations.

In respect to the time-consuming calculation of the thermally induced displacements in an elastic model at each time step, the working space is divided into $3 \times 3 \times 3$ discrete grid points and the solution will be performed only for these points. Figure 5 shows three of the 27 configurations under MATLAB.

Figure 6 shows as an example two simulated temperature fields of the demonstrator machine. The left temperature field results from a continuous movement of the Y-axis over 15 min. The right temperature field shows the temperature field after 120 min of movement. The temperature at the linear direct drives and the profile rail guides increases significantly, which results in a temperature rise in the Y- and Z-slide. Therefore, the model parameters of the power loss in profile rail guides and linear direct drives have a big impact on the temperature field.

5.2 Parameter Update of Friction Model of Profile Rail Guides

Uncertain parameters over the lifetime of the demonstrator machine model refer to components with friction, wear and changed lubrication. These components are profile rail guides, bearings, contacts between ball screw spindles and ball screw nuts. The profile rail guides in Y-direction are chosen as example in this paper.

47 Pt100 resistance temperature sensors are applied within the demonstrator machine. 26 sensors are in the Y- and the Z-slide. For these sensors, a sensitivity analysis is conducted with “pearson partial correlation coefficients adjusted for internal variables”

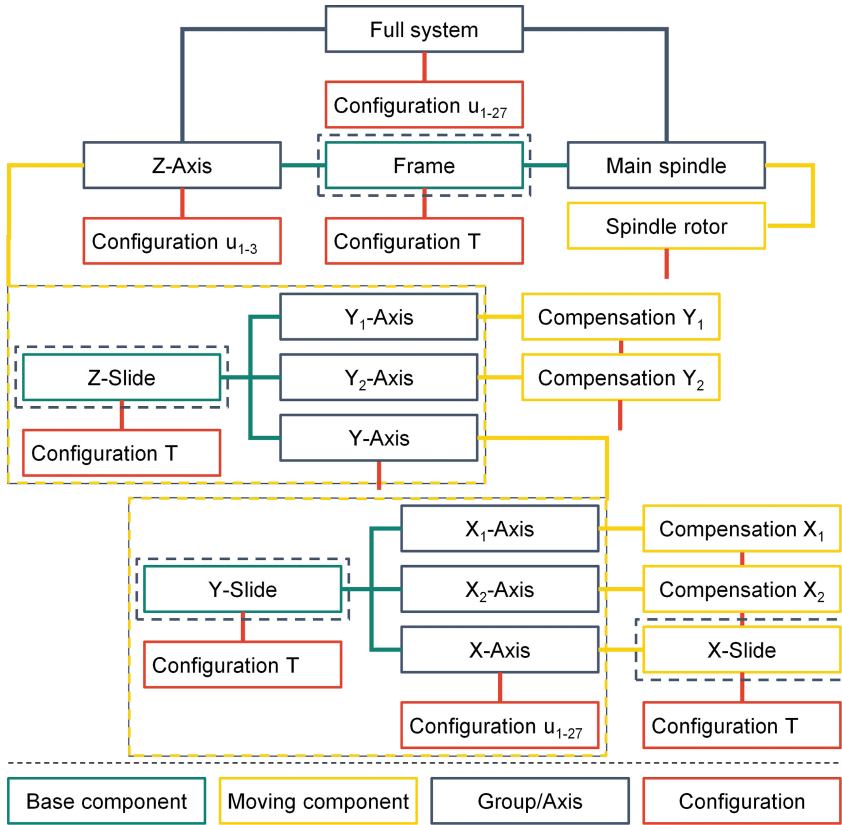


Fig. 4. Model structure of demonstrator machine

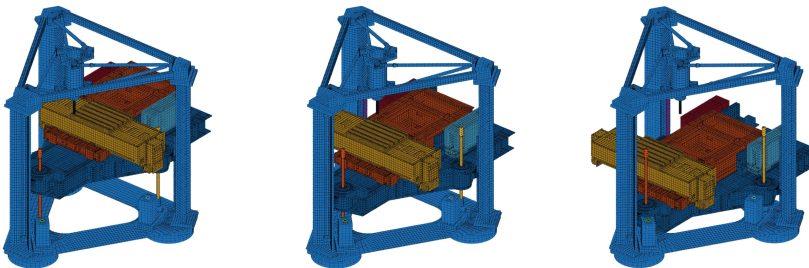


Fig. 5. Configurations

and a wide range of simulated load cases. Two sensors (see Y1 and Y2 in Fig. 7) under the profile rail guides in Y-direction are selected. The correlation coefficients to the heat source friction in the guides are 0.9978 for both sensor positions. The p-values are 1.5E-21 (sensor Y1) and 1.8E-21 (sensor Y2). This is far below the significance level

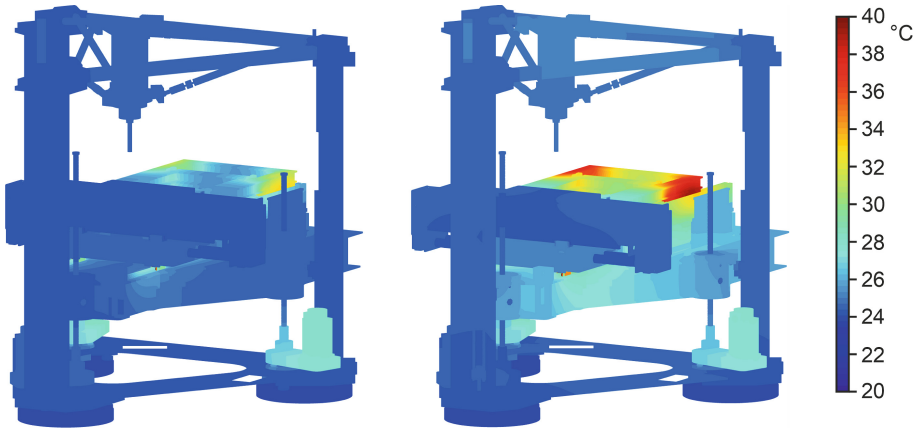


Fig. 6. Temperature field after 15 min (left) and 120 min (right) of Y-axis movement

of 5%. Therefore, the two sensors are suitable for monitoring the friction in the profile rail guides.

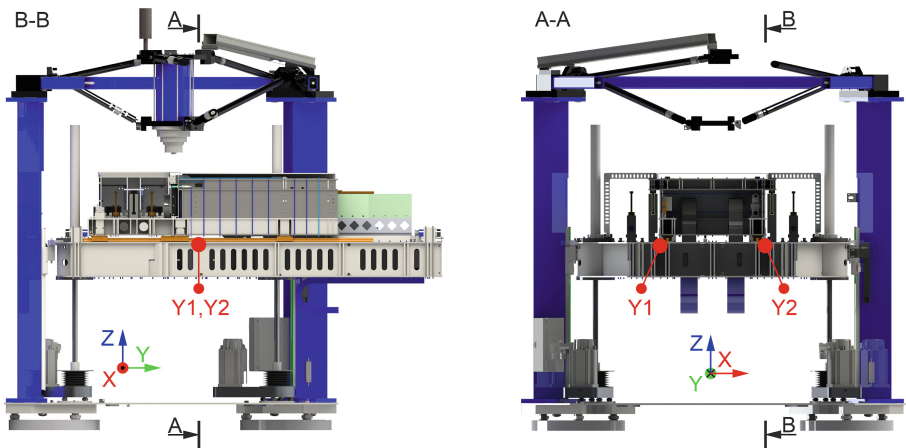


Fig. 7. Sectional views of the demonstrator machine with sensor positions Y1 and Y2

An initial parameter adjustment was carried out based on experiments with different movement speed of the Y-axis. The maximum error between measurement and simulation after the parameter adjustment was ± 0.82 K for Y1 and ± 0.76 K for Y2. These errors are selected as the limit value for the deviation between simulation and measurement in further operation of the machine. Therefore, a parameter update will be initiated after exceeding these limits. The friction is described qualitative well by an empirical function [17] but have to be adjusted to meet the quantitative real behavior. Therefore, scaling factors are introduced as parameters for the calculation of the friction for both

guides. The plausible range for these scaling factors is defined based on literature references and assumptions. In [18] the friction of the investigated profile rail guides is reduced by up to 90% over the lifetime. This includes run-in effects at the beginning of the lifetime. The lower limit of the scaling factor is 0.1. Regreasing of the guides can lead to an increased friction. It is assumed that the increase is in guides similar to bearings. Newly greased bearings can have an up to 45% increased friction [19]. Therefore, the upper limit of the scaling factor is estimated with 1.45.

The thermal time behavior of the Y-slide and the Z-slide is investigated as described in Sect. 3. The maximum time constant for the Y-slide is 75 min and for the Z-slide is 116 min. The larger time constant is selected for the calculation of the time window (see Eq. (4)) for the variant calculation and parameter optimization. The maximum error for the calculation is defined with $\Delta T_E / \Delta T_S = 1\%$. The resulting time window is $t_{Window} = 534$ min.

The initial parameter adjustment was conducted in 2017. In the following, an experiment is evaluated, which was conducted three years later in 2020. During the experiment, the Y-slide is moved over nearly the whole axis length from axis position -190 mm to 190 mm. The movement parameters are: maximum velocity of 0.75 m/s, maximum acceleration of 1.8 m/s² and maximum jerk of 400 m/s³. The duration of the movement is 25 min and followed by a measurement cycle. The displacement of the tool center point (TCP) is measured during the measurement cycle. Only slow movements and therefore a small load is applied to the guides. The measurement cycle takes 6 min. Movement and measurement cycle are repeated cyclically until the thermal steady state is nearly reached.

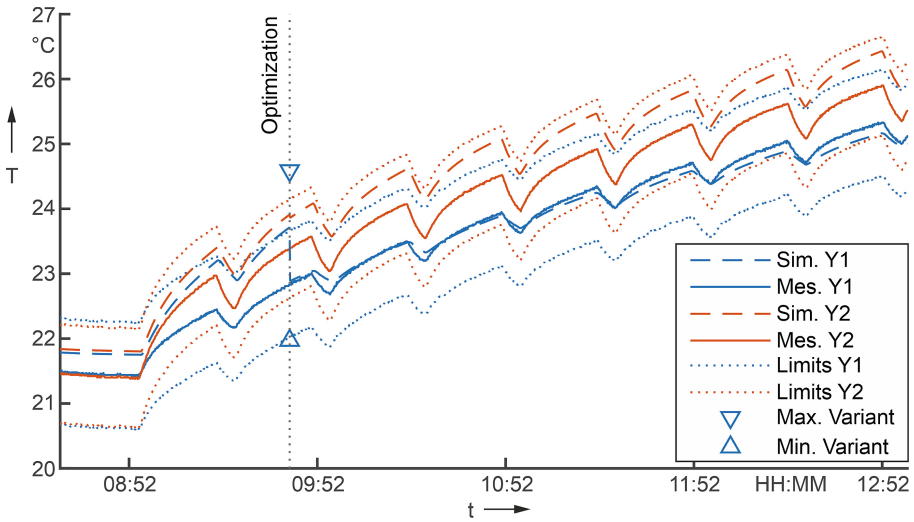


Fig. 8. Temperatures at profile rail guides in Y-direction (Color figure online)

The temperature curves at the sensor positions for both profile rail guides are pictured in Fig. 8. The limit values (blue dotted line) is exceeded at sensor Y1 after about 49 min of movement (marked with a vertical dotted line). The simulated values (dashed

line) at sensor position Y2 stay below the upper limit. After the limit is exceeded, different variants of parameters are calculated to determine the minimum and maximum temperature (marked with blue triangles) with plausible parameters. The measured value at Y1 is 22.83 °C. The minimum temperature is 21.98 °C and the maximum temperature is 24.58 °C. Therefore, the parameter adjustment is reasonable. The optimization leads to a decreased friction in the model by 46%. The simulated values fit the measured value (solid line) well after the optimization. Three hours after the optimization, the simulated values are slightly lower than the measured value.

The accuracy improvement is shown in Fig. 9 based on the residual temperature error. The maximum and mean residual error is compared for the simulation model without parameter update (solid line) and with parameter update (dashed line). Therefore, the 26 temperature sensors within the Y- and the Z-slide are evaluated. After the optimization and the parameter update (dotted vertical line) the maximum residual error as well as the mean residual error are reduced at these sensor positions. The mean residual error is reduced from 0.457 K to 0.342 K for the time period shown. In conclusion, the parameter update leads to a significant improvement of the model accuracy for the changes in thermal behavior three years after initial parameter adjustment.

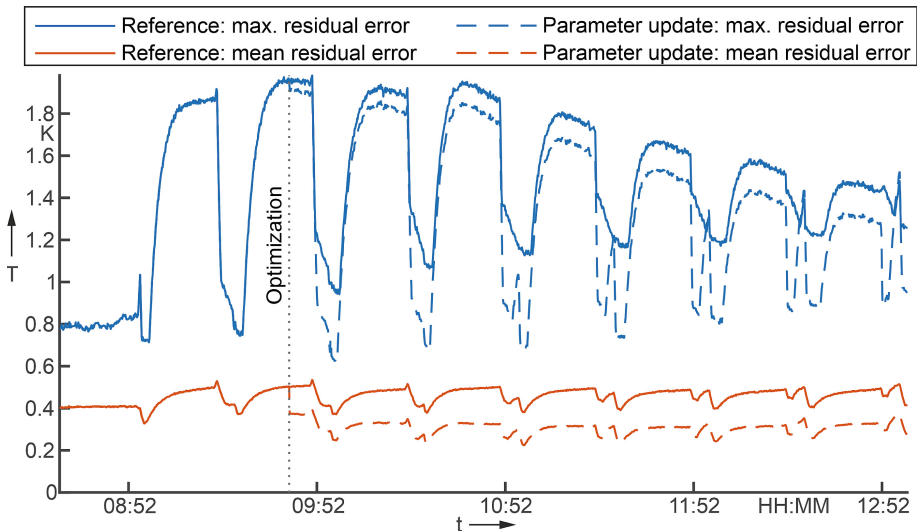


Fig. 9. Residual error of simulation at 26 sensor positions in Y- and Z-slide

5.3 Performance in Trusted Execution Environment

In addition to the evaluation depicted beforehand, we evaluated the calculation of the temperature model with regard to performing a computationally intensive tasks within trusted execution environments (TEEs), (see Sect. 4). To make use of the dedicated hardware instructions that create the encrypted enclave, we incorporated the SCONE framework [20]. SCONE allows for the execution of applications within a TEE on Intel

CPUs without code manipulations or recompilation. Unfortunately, some limitations apply as SCONE is only available for Linux and currently doesn't support Matlab. Therefore, the Matlab code to perform calculations for the temperature model was ported to Python. The Python code is then executed on a server running Ubuntu-Linux 20.04 in different variants. As it is common practice to execute applications on servers in virtualized environments, we additionally used Docker to run the application and evaluate the increase in execution runtime for the different variants.

Docker is a lightweight alternative and performant alternative to a virtual machine. Similar to virtual machines, Docker containers include an operating system that runs the desired application. Figure 10 depicts different variants for executing the Python application in different Docker containers and without Docker. Additionally, the evaluation shows the performance impact of the trusted execution environment (SCONE). The bars in Fig. 10 are split into the main calculation of the temperature model with order reduction (MOR) and the retransformation from the reduced model to a full model. The fastest execution is achieved by the calculation without Docker virtualization and without added security by the SCONE framework (TEE). It takes $53.4 + 6.2$ s to calculate the machine temperature fields for a full hour with a step size of 10 s. By executing the calculation in a Docker container with Ubuntu Linux as operating system, the execution time is increased by 17% to 70.2 s. Executing the Python application inside a TEE in a Docker container further increases the duration by 10% to 77.8 s (or by 30% in total).

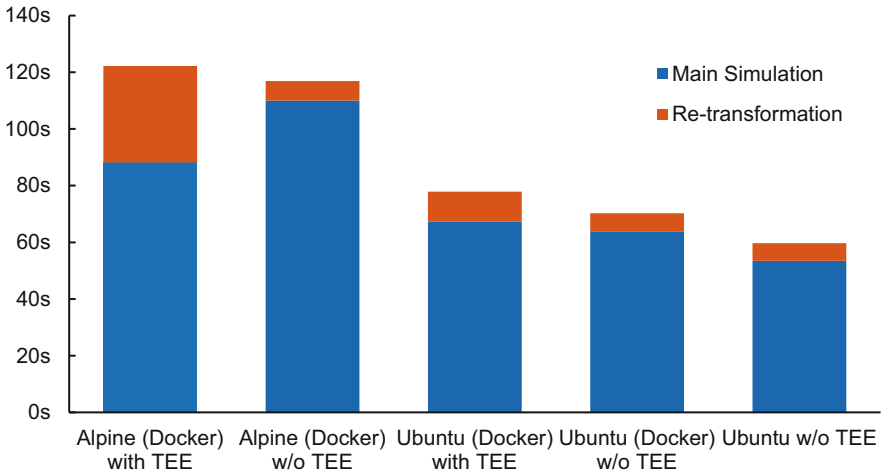


Fig. 10. Comparison of calculation times for the simulation of the temperature model

6 Summary and Outlook

In this paper, a modelling workflow for the efficient creation and calculation of thermal models is introduced. Based on this kind of model, a workflow for the parameter update of the machine model over machine lifetime is presented. The approach is

demonstrated using the example of a 3-axis machine in lightweight design. It is shown that the presented approach can be beneficial to maintain the accuracy of the thermal model even over long operating time of the machine tool. The parameter optimization can be conducted safely in a trusted execution environment on a server with acceptable additional computation time. Further performance improvements for calculations within trusted execution environments are anticipated by using Matlab, as it provides higher efficiency compared to Python. The current execution overhead of about 30% for the trusted execution environment can additionally be further reduced by code optimization.

In future works, the parameters of the empirical models for friction should be updated separately (e.g., the lubrication viscosity). Furthermore, the model needs an improvement of the convection description in order to increase the overall accuracy of the model.

Acknowledgements. Funded by the German Research Foundation – Project-ID 174223256 – TRR 96.

References

1. Denkena, B., Abele, E., Brecher, C., Dittrich, M.-A., Kara, S., Mori, M.: Energy efficient machine tools. *CIRP Ann.* **69**, 646–667 (2020). <https://doi.org/10.1016/j.cirp.2020.05.008>
2. Großmann, K. (ed.): *Thermo-Energetic Design of Machine Tools*. LNPE, Springer, Cham (2015). <https://doi.org/10.1007/978-3-319-12625-8>
3. Thiem, X., Kauschinger, B., Ihlenfeldt, S.: Online correction of thermal errors based on a structure model. *Int. J. Mechatron. Manuf. Syst.* **12**, 49–62 (2019). <https://doi.org/10.1504/IJMMS.2019.097852>
4. Reuss, M., Dadalau, A., Verl, A.: Friction variances of linear machine tool axes. *Procedia CIRP* **4**, 115–119 (2012). <https://doi.org/10.1016/j.procir.2012.10.021>
5. Zhou, H.-X., Zhou, C.-G., Wang, X.-Y., Feng, H.-T., Xie, J.-L.: Degradation reliability modeling for two-stage degradation ball screws. *Precis. Eng.* **73**, 347–362 (2022). <https://doi.org/10.1016/j.precisioneng.2021.09.018>
6. Zhou, C.-G., Ren, S.-H., Feng, H.-T., Shen, J.-W., Zhang, Y.-S., Chen, Z.-T.: A new model for the preload degradation of linear rolling guide. *Wear* **482–483**, 203963 (2021). <https://doi.org/10.1016/j.wear.2021.203963>
7. Schroeder, S., Kauschinger, B., Hellmich, A., Ihlenfeldt, S., Phetsinorath, D.: Identification of relevant parameters for the metrological adjustment of thermal machine models. *Int. J. Interact. Des. Manuf.* **13**(3), 873–883 (2019). <https://doi.org/10.1007/s12008-019-00529-y>
8. Stuart, A., Ord, J.K., Arnold, S., Kendall, M.G.: *Classical Inference and the Linear Model*. 6th edn., Wiley, Chichester (2008)
9. Fisher, R.A.: The distribution of the partial correlation coefficient. *Metron*, pp. 329–332 (1924)
10. Mareš, M., Horejš, O., Havlík, L.: Thermal error compensation of a 5-axis machine tool using indigenous temperature sensors and CNC integrated Python code validated with a machined test piece. *Precis. Eng.* **66**, 21–30 (2020). <https://doi.org/10.1016/j.precisioneng.2020.06.010>
11. Bitar-Nehme, E., Mayer, J.R.R.: Modelling and compensation of dominant thermally induced geometric errors using rotary axes' power consumption. *CIRP Ann.* **67**, 547–550 (2018). <https://doi.org/10.1016/j.cirp.2018.04.080>

12. Wennemer, M.: Methode zur messtechnischen Analyse und Charakterisierung volumetrischer thermo-elastischer Verlagerungen von Werkzeugmaschinen. Apprimus Wissenschaftsverlag, Aachen (2018)
13. Weck, M., McKeown, P., Bonse, R., Herbst, U.: Reduction and compensation of thermal errors in machine tools. *CIRP Ann. Manuf. Technol.* **44**, 589–598 (1995). [https://doi.org/10.1016/S0007-8506\(07\)60506-X](https://doi.org/10.1016/S0007-8506(07)60506-X)
14. Waltz, R.A., Morales, J.L., Nocedal, J., Orban, D.: An interior algorithm for nonlinear optimization that combines line search and trust region steps. *Math. Program.* **107**, 391–408 (2006). <https://doi.org/10.1007/s10107-004-0560-5>
15. Thiem, X., Kauschinger, B., Ihlenfeldt, S.: Structure model based correction of machine tools. In: *Conference on Thermal Issues in Machine Tools*. Verlag Wissenschaftliche Scripten, Auerbach/Vogtl, pp. 309–3018 (2018)
16. Costan, V., Devadas, S.: Intel SGX explained. *IACR Cryptol. ePrint Arch.* (2016)
17. Jungnickel, G.: Simulation des thermischen Verhaltens von Werkzeugmaschinen. Modellierung und Parametrierung. Schriftenreihe des Lehrstuhls für Werkzeugmaschinen, Dresden (2010)
18. Wang, X.-Y., Zhou, C., Ou, Y.: Experimental analysis of the wear coefficient for the rolling linear guide. *Adv. Mech. Eng.* **11** (2019). <https://doi.org/10.1177/1687814018821744>
19. Reibung und Erwärmung | Schaeffler medias. <https://medias.schaeffler.de/de/friction-and-inc-reases-in-temperature>. Accessed 2 Sep 2022
20. Arnautov, S., et al.: SCONE: secure Linux containers with Intel SGX. In: *OSDI*, vol. 16, pp. 689–703 (2016)

Open Access This chapter is licensed under the terms of the Creative Commons Attribution 4.0 International License (<http://creativecommons.org/licenses/by/4.0/>), which permits use, sharing, adaptation, distribution and reproduction in any medium or format, as long as you give appropriate credit to the original author(s) and the source, provide a link to the Creative Commons license and indicate if changes were made.

The images or other third party material in this chapter are included in the chapter's Creative Commons license, unless indicated otherwise in a credit line to the material. If material is not included in the chapter's Creative Commons license and your intended use is not permitted by statutory regulation or exceeds the permitted use, you will need to obtain permission directly from the copyright holder.





Adaptive Thermal Error Compensation Model of a Horizontal Machining Centre

Otakar Horejš¹ (✉), Martin Mareš¹, Michal Straka¹, Jiří Švéda¹, and Tomáš Kozlok²

¹ Faculty of Mechanical Engineering, Department of Production Machines and Equipment, RCMT, Czech Technical University in Prague, Horská 3, 128 00 Prague, Czech Republic
o.horejs@rcmt.cvut.cz

² TOS VARNSDORF a. s., Říční 1774, 407 47 Varnsdorf, Czech Republic

Abstract. The state-of-the-art method to reduce CNC machine tool thermal errors is real-time error compensation based on the thermal error estimation models. However, it is difficult to establish a thermal error compensation model with good versatility, high accuracy, and strong robustness due to various manufacturing conditions and a thermally varying surrounding environment. It causes that thermal behaviour of the machine tools is nonlinear and varying in real time. Consequently, the pre-trained and non-adaptive model may not be accurate and robust enough for long-term application. The presented research shows a systematic adaptation technique to update the thermal error compensation model of a horizontal machining centre under varying conditions, which differ from the calibration test. System identification theory is applied to build a dynamic thermal error model for a horizontal machining centre based on calibration test. Linear parametric models of autoregressive with external input (ARX) present an established dynamic method, and its modelling and calculation speed are suitable for real-time applications. Additionally, process-intermittent probing and thermal error model are integrated into the machine management software of the horizontal machining centre to monitor and compensate for thermal errors at the tool centre point (TCP) in real time using C#/C++ programming language. The results show that the prediction accuracy measured as peak-to-peak values and the normalized root mean squared error of the thermal error compensation models are improved by up to 33% and 51%, respectively, when adaptive compensation model is applied.

Keywords: Compensation · Thermal Errors · Probing · Adaptive Model

1 Introduction

One of the most challenging issues in the manufacturing industry is continuous part quality maintenance by reducing machine tool thermal errors. The state-of-the-art method for minimizing thermal errors in CNC machine tools is real-time error compensation based on thermal error estimation models [1].

Numerous error compensation models have been proven to be effective of mitigating thermally induced errors using temperature sensor measurements. A thorough review

of the thermal error modelling methods that have been investigated and applied is presented in [2]. The predicted accuracy and robustness of the thermal error model is a key factor here. Robustness reflects the holding capacity of predicted accuracy under various external conditions. It is an important indicator of the thermal error compensation effect on machine tools [3].

However, the low prediction accuracy and poor robustness of these models under varying manufacturing conditions and the thermally varying surrounding environment have also been recognised [4, 5]. The cause is that thermal error compensation models strongly depend on the characteristics of the training data. However, model training conditions cannot typically cover all of the machine working conditions that are necessary to derive an accurate and robust model due to limited resources and limited availability of machine time for testing. Furthermore, potential users of thermal error compensation technique (typically machine tool manufacturers) shy away because of the lengthy period of time required to characterize the thermal behavior of a machine tool. It takes many hours for a machine structure to reach its thermal steady state and then to cool to its original state. As a result, thermal error compensation models represent physics incompletely and the robustness in the prediction performance of thermal behaviour that differs from training phase may be poor. Therefore, various model adaptations have been developed to refine the prediction accuracy and robustness of the model according to continuous changes in machine operation status. This is especially essential in small-batch production, where the manufacturing processes change frequently and the pre-trained thermal error model is typically not robust enough.

A feasible strategy for improving robustness has been updating the model parameters periodically using process-intermittent probing to identify any changes in thermal errors at the tool centre point (TCP). Numerous on-machine measurement methods can be applied to provide thermally induced displacements as feedbacks for compensation model. Gao et al. [6] present state-of-the-art in-process and on-machine measurement systems and sensor technologies. As touch probe systems have become common accessories in a wide variety of precision machine tools, their application seems a promising solution for the adaptation of thermal error models. On-machine measurement (typically by touch probe) represents the common practice of using a machine tool to measure the workpiece while it is still on the machine rather than moving the workpiece to the metrology room. It significantly corrects geometric errors on the part before the part is removed from the machine tool. Consequently, it decreases the scrap parts. In principle, on-machine probing can be used for direct compensation of thermal error at the TCP thanks to intermittently measured resulting displacements at the machine tool TCP (e.g., a test mandrel clamped in the spindle with noncontact displacement sensors placed on the working table as shown in Sect. 2 or a touch probe in combination with a datum sphere mounted on the working table). Subsequently, the measured displacements can be superposed to the desired position of the particular axis. The significant benefit of the on-machine probing approach is that the thermal displacements that have to be compensated are directly available. Nevertheless, a sufficient sampling rate of the on-machine measurement has to be selected, as interruptions to the process lead to lower machine tool productivity.

An issue related to the updating the compensation model parameters periodically using on-machine measurements is the reduction in machine productivity, since the machining cycle may be unnecessarily interrupted during probing. Early methods used process-intermittent probing to constantly update the model. Mou [7] presented an adaptive error correction method using feature-based analysis techniques for machine tool error correction. Process-intermittent gauging and state observation techniques were integrated to track the thermal effect in real time and fine tune the error model coefficients as the cutting process proceeds. A multiple linear regression model was derived to identify the time-varying thermally induced errors and form the state observer model. However, these techniques were based on the conventional static thermal error model. As a result, the thermal error model thus developed may not accurately reveal the dynamic nature of the thermoelastic system.

Yang and Ni [8] proposed an adaptive model estimation of thermal errors based on a recursive dynamic modeling strategy. This approach significantly improved the accuracy and robustness of the thermal error model by considering the dynamic effects of machine thermo-elastic systems. Intermittent probing was carried out periodically using a sampling time of 3.5 min. Thus, the probing may occur when not required. Consequently, it decreases the machine productivity. Blaser et al. [9] developed a thermal error compensation of 5-axis machine tools that is extended by on-machine measurements. The compensation model predicts the thermally induced errors caused by the rotary axis C, environmental temperature change and cutting fluid. The information gained by the process intermittent probing is used to adaptively update the model parameters. During the compensation phase, periodic measurements are essential to control the required precision of the compensation model. Measurement interval times only from 5 to 60 min were tested in 5 min steps. It was proposed that the measurement cycle should be performed every 25 min or less to ensure stable compensation by the model. However, such periodic on-machine measurements significantly reduce the obtainable productivity of the machine tools. Furthermore, Zimmermann et al. [10] replaced periodically performed on-machine measurements with adaptive on-machine measurements which are triggered based on temperature measurements when unknown thermal conditions occur to optimize the trade-off between the precision and productivity of the proposed compensation model.

This paper presents a new insight into the adaptation of thermal error compensation models using on-machine measurements to improve the prediction performance of the compensation algorithm. In contrast to the previous research, this study is focused on wider range of the on-machine sampling interval from 30 to 180 min. The goal is to increase the sampling interval to minimize interruption of the machining process by intermittent probing. The relationship between compensation model accuracy, the sampling interval length, the size of the tolerance band and required number of model updates is investigated in detail. The rest of this paper is organized as follows. In Sect. 2, the machine tool and experimental setup are described. Section 3 deals with the modelling approach, thermal error model structure, and approximation quality expression. Furthermore, Sect. 3 involves the calibration of the model parameters and identification procedures. In Sect. 4, the adaptive compensation model is derived using process-intermittent probing. A brief summary is discussed in Sect. 5.

2 Thermal Error Experiments

The tested machine tool is a large horizontal machining centre with table dimensions of 1250×1250 mm, and a retractable spindle with a diameter of 112 mm was used to demonstrate the method. The machine tool has a spindle with 31 kW power and the maximal spindle speed is 6000 rpm. Basic heavy machine parts (table, palettes, longitudinal and transverse beds) are casted from grey iron, see [11]. The machine column is designed as a twin shell casting also made of grey iron with an optimized structure. The tested machining centre is placed in a machine tool producer's shop floor, which is a non-air-conditioned room. The machining centre is equipped with a standard Siemens SINUMERIK 840D sl CNC controller and a unique programming environment (TOS Control management software). The thermal error model (see Sect. 3) is implemented in the TOS Control programming environment as an independent application developed in C#/C++ programming language.

The large horizontal machining centre is equipped with temperature sensors (Pt100, Class A, 3850 ppm/K) placed close to the main heat sources by the machine tool manufacturer. Today, almost every spindle is equipped with sensors to monitor the bearing temperature, including the tested machine centre. Of all heat sources that lead to thermal distortion, the spindle is a dominant contributor to total thermal errors due to the large amount of heat generated by its high-speed revolutions and quick response inducing thermal errors at the TCP. Therefore, the thermal error compensation model will focus on the heat source represented by the spindle. The key input of the model is the temperature measured close to the spindle front bearing (ΔT_{in}). Tests for thermal distortion caused by rotating spindles were carried out according to the ISO 230-3 international standard [12]. To measure relative displacements in the X, Y and Z directions between the TCP represented by a test mandrel (length, 125 mm; diameter, 40 mm) and the working table of the horizontal machining centre, non-contact eddy current displacement sensors with a resolution ratio of $0.1 \mu\text{m}$ were installed (sensor type PR6423, produced by Emerson [13]). Eddy current sensors are supported by a magnetic stand and the measurement point is placed at the side of the table to sense thermally induced displacements at the zero position of the retractable spindle position ($W = 0$ mm). The experimental setup on the horizontal machining centre per ISO 230-3 including the machine tool structure with the indicated kinematics is shown in Fig. 1.

Data were acquired using a cRIO 9024 programmable automation controller (PAC) [14] with LabVIEW software (the sampling rate was 1 s). Temperature sensors installed by the machine tool manufacturer and other NC data such as effective power, electric current, torque, feed rate, and motor temperatures were logged using OPC UA (Open Platform Communications United Architecture) communication between the machine controller and the PAC cRIO 9024.

A one-dimensional network of spindle excitation points was proposed for the Y-axis (the vertical position of the spindle stock on the column) with a constant W-axis position (retractable spindle position $W = 0$ mm). Spindle excitation was performed in 3 different linear Y-axis positions in total (Fig. 1). Tests with a constant spindle speed, along with a spindle speed spectrum test, were designed to validate the thermal error model and the adaptive compensation model using on-machine measurement (Table 1).

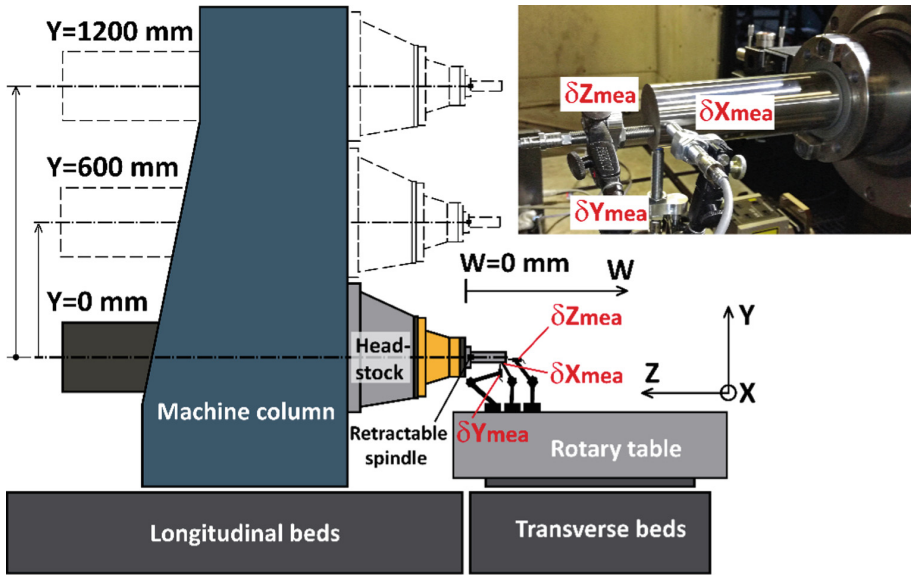


Fig. 1. Experimental setup.

Table 1. Spindle speed and vertical Y-axis position of the spindle stock on the column during tests.

Test no.	Rotation speed [rpm]	Vertical Y-axis position [mm]
1	4000	0
2	2000	600
3	4000	1200
4	4000	600
5	4000	0–1200

Each test in Table 1 was followed by a cooling phase until the machine tool was close to a steady state with the surrounding environment, which took several hours. As a result, one test was conducted per day. Data acquisition was only realized during the heating phase (working cycles according to Table 1). It is supposed that the compensation model is always updated by the first on-machine measurement at the beginning of each work shift when the machine tool is cooled down (in the morning). Thus, the initial error is removed and it is not necessary to measure during the cooling phase.

The heating phase of test no. 1 was chosen to identify a thermal error compensation model (see Sect. 3). Verification tests (tests no. 2 to no. 5) were carried out under different conditions than the calibration test. The spindle speed and the position of the heat source (the vertical position of the spindle stock on the column) varied during the verification tests; see Table 1.

3 Thermal Error Model for a Horizontal Machining Centre

A discrete transfer function (TF) is used to describe the link between the excitation and its response

$$\mathbf{y}(t) = \mathbf{u}(t) \cdot \varepsilon + \mathbf{e}(t). \quad (1)$$

The vector $\mathbf{u}(t)$ in Eq. (1) is the TF input vector in the time domain, $\mathbf{y}(t)$ is the output vector in the time domain, ε represents general TF in the time domain, $\mathbf{e}(t)$ is the disturbance value (further neglected). The difference form of a discrete TF (generally suitable for programming languages like Python or C#/C++) in the time domain is introduced in Eq. (2)

$$y(k) = \frac{u(k-n) \cdot a_n + \dots + u(k-1) \cdot a_1 + u(k) \cdot a_0 - y(k-m) \cdot b_m - \dots - y(k-1) \cdot b_1}{b_0}, \quad (2)$$

where n is the order of the TF numerator, m is the order of the TF denominator, $m > n$, k represents the examined time instant, $k-n$ ($k-m$) is the n -multiple (m -multiple) delay in sampling frequency of the measured input vector (simulated output vector), a_n is the calibration coefficient of the TF input and b_m is the calibration coefficient of the TF output.

Linear parametric models of autoregressive with external input (ARX) or outputs error (OE) identifying structures are used with the help of Matlab Identification Toolbox [15]. The linear parametric model ARX as an optimal model structure (with the best fitting quality and robustness) is discussed in [16] where MISO (multiple input single output) models handling with arbitrary TCP measurements are introduced. Excitations in the case of the applied TFs mean temperatures measured close to heat sinks or sources, and the responses stand for the linear deflections in the examined directions.

The approximation quality of the simulated behaviour is expressed by a local peak-to-peak approach

$$p2p = |\max(\delta\mathbf{Z}_{mea} - \delta\mathbf{Z}_{sim})| + |\min(\delta\mathbf{Z}_{mea} - \delta\mathbf{Z}_{sim})|, \quad (3)$$

where $p2p$ is the abbreviation for a peak-to-peak evaluation method, $\delta\mathbf{Z}_{mea}$ in Eq. (3) represents the measured output (thermal displacement at the TCP in the Z direction) and $\delta\mathbf{Z}_{sim}$ is the simulated (predicted) thermal displacement obtained by applying the thermal error compensation model. In this paper, the approximation quality of the identified compensation models is also expressed by the *fit* value, the normalized root mean squared error expressed as a percentage, see [15], defined as follows

$$fit = \left(1 - \frac{\|\delta\mathbf{Z}_{mea} - \delta\mathbf{Z}_{sim}\|}{\|\delta\mathbf{Z}_{mea} - \overline{\delta\mathbf{Z}_{mea}}\|} \right) \cdot 100. \quad (4)$$

The $\overline{\delta\mathbf{Z}_{mea}}$ stands for the arithmetic mean of the measured output (thermal displacement) over time. The *fit* represents a global approach to express the approximation quality of the compensation model, it is a percentage value where 100% would equal a perfect match of measured and simulated behaviours.

3.1 Identification of the Compensation Model

A thermal error compensation model is developed for large horizontal machining centre (see Sect. 2). As the spindle is a dominant contributor to total thermal errors, model predicts thermally induced displacements at the TCP caused by the spindle. It is a simple compensation model, other influences (linear axis etc.) on thermally induced errors at the TPC are not taken into account. To reduce the major thermal error of the horizontal machining centre (in the Z-axis direction), a compensation ARX model was calibrated on test no. 1 (see Table 1). The input is the temperature measured on the spindle front bearing (ΔT_{in}) and the output is the displacement measured in the Z-axis direction (δZ_{mea}). The TF-based model of thermal displacement in the Z-axis direction is expressed by Eq. (5) as

$$\delta Z_{sim} = \Delta T_{in} \cdot \varepsilon, \quad (5)$$

where δZ_{sim} is the simulated thermal displacement in the Z-axis direction) and ε is the TF identified in the time domain.

The measured input (ΔT_{in}), measured output (δZ_{mea}) and simulated output (δZ_{sim}) used in the identification process of the TF model are shown in Fig. 2 (all quantities are expressed in relative coordinates). Temperature fluctuations (see ΔT_{in} in Fig. 2) are caused by the control of the cooling fluid circuit. The approximation quality is $fit = 89\%$ and $p2p = 16.6 \mu\text{m}$.

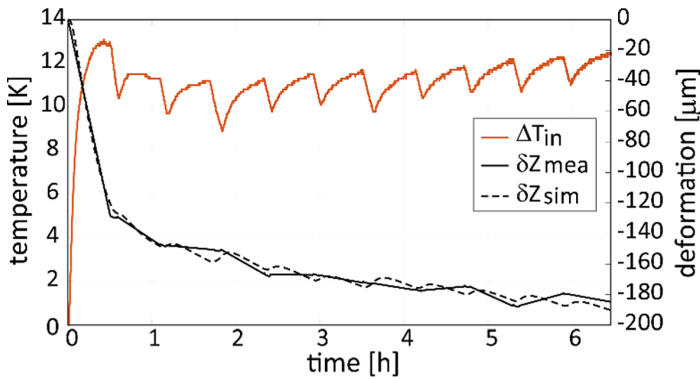


Fig. 2. Model identification process - measured input temperature, measured and simulated thermal errors at the TCP in the Z-axis direction of the large horizontal machining centre (test no. 1 at the position $Y = 0 \text{ mm}$).

The stability of the identified TF model is expressed by the Linear Time Invariant (LTI) step response test shown in Fig. 3. System excitation represents the sudden change of the key temperature equal to 1 K (red curve in the graph in Fig. 3), and system response is the predicted displacement at the TCP in the Z-axis direction given by Eq. (5), see black curve in Fig. 3.

The established calibration coefficients a_n and b_m of the identified 2nd order discrete TF are summarised in Table 2. The order of the TF was selected based on the best fit value, see Eq. (4).

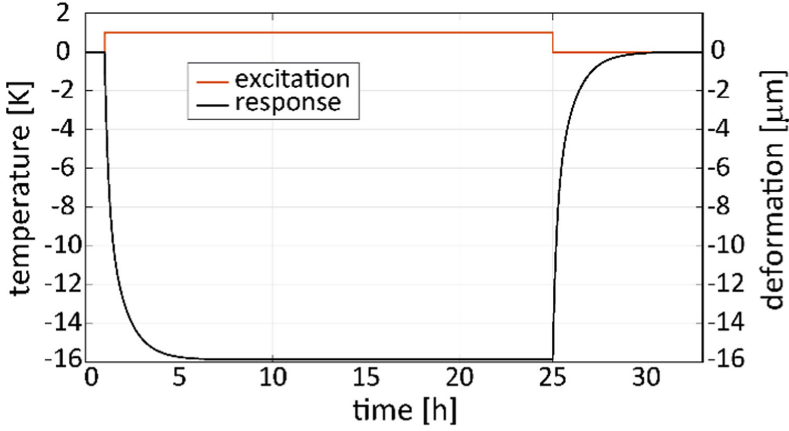


Fig. 3. LTI step response of the identified TF.

Table 2. Identified parameters of the thermal error model describing the influence of spindle rotation on thermal error at the TCP in the Z-axis direction.

TF	method	a_0 ($\mu\text{m}\cdot\text{K}^{-1}$)	a_1 ($\mu\text{m}\cdot\text{s}^{-1}\cdot\text{K}^{-1}$)	b_0 (-)	b_1 (s^{-1})	b_2 (s^{-2})	fit (%)
ε	ARX	-0.0130427	0.0130361	1	-1.9982716	0.998272	89

3.2 Verification Tests Results

The model identified in Sect. 3.1 was applied to the heating phase of tests no. 2 to no. 5 (see Table 1). Figure 4 depicts the behaviour of the front bearing temperature ΔT_{in} , ambient temperature ΔT_{amb} behaviour over time, the position of the TCP in the Y-axis direction and the spindle speed during verification tests on the large horizontal machining centre. The data measured during the heating phases (active heat source represented by spindle rotation) of tests no. 2, 3, 4, 5 according to Table 1 are presented in Fig. 4. The cooling phases of each measurement are omitted, as the data acquisition was not realized during the cooling phases. Moreover, the heating phases of tests no. 2 to no. 5 are linked together in order to present the measured data in a single graph in Fig. 4. This data representation is in accordance with the intended adaptation of the compensation model using on-machine measurement presented in Sect. 4.

The resulting displacements at the TCP obtained by on-machine measurement can be employed as feedbacks for the compensation model to refine its prediction accuracy. Consequently, this leads to a lower sampling rate for the on-machine measurement. Since a manufacturing process begins basically from an initial alignment of the workpiece, the on-machine measurement is often the first task that must be performed. Subsequently, the compensation model is supposed to always be updated at the beginning of each work shift (see Sect. 4). Figure 5 depicts the thermal displacement measured at the TCP in the Z-direction (solid blue curve) and the predicted thermal displacement (solid red curve) of the large horizontal machining centre obtained from the TF model calculated by Eq. (5)

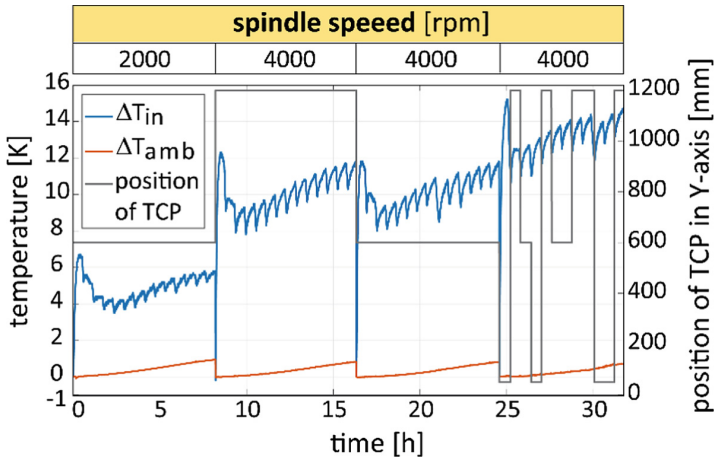


Fig. 4. Temperature measured at the spindle front bearing, ambient temperature, spindle speed, and position on the Y-axis during verification tests no. 2 to 5.

for the verification tests no. 2 to no. 5. The data in Fig. 5 are presented analogously to Fig. 4 (linked heating phases of the verification tests without the cooling phases).

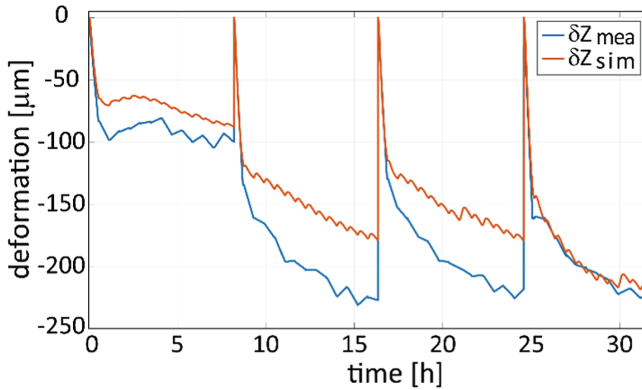


Fig. 5. Thermal displacement measured and simulated in the Z-direction during verification tests no. 2 to 5.

Approximation quality expressed by the *fit* value given by Eq. (4) is only 41.5%. The approximation quality expressed by the *p2p* value of the thermal error compensation model according to Eq. (3) is $64 \mu\text{m}$ for the verification tests. Identification of the TF-based model is derived from test no. 1 which was set at the zero position of the linear Y-axis (the lowest vertical position of the spindle stock on the column, $Y = 0 \text{ mm}$). The model training conditions applied in Sect. 3.1 evidently differ from the machine tool working conditions during the verification tests no. 2 to no. 5, see Table 1.

Firstly, the position of the heat sources (the vertical position of the spindle stock on the column) varied during the verification tests. Secondly, the spindle speed also varied

during the tests. Previous studies (e.g., [17, 18]) showed that a TF-based compensation model is capable of sustaining the high approximation quality (stability in prediction performance) in the event of a changeable spindle speed that differs from the training phase. However, in the previous studies mentioned above, the compensation model of a medium-sized CNC machining centre was investigated only in one spindle excitation position. On the contrary, the verification tests on a large horizontal machining were intended to excite the heat source, represented by the spindle, in various machining centre positions. It results in low compensation model prediction accuracy of thermal errors at the TCP in the Z direction, as shown in Fig. 5.

4 Adaptive Compensation Model

Due to the complexities of manufacturing processes, real machining conditions may not be identical to the experimental conditions used for the compensation model derivations shown in Sect. 3. Therefore, to increase the robustness of the prediction performance of thermal error Z-direction displacement, a process intermittent probing is used to adaptively update the model parameters (on-machine measurement with eddy current type displacement sensors and the test mandrel, see Sect. 2).

4.1 Principle of Model Adaptation

Adaptation of the compensation model is realised using the gain. The gain is defined as follows

$$gain_{tol}^{\tau} = \frac{\delta Z_{mea}(t_u)}{\delta Z_{sim}(t_u)}, \quad (6)$$

where $\delta Z_{mea}(t_U)$ represents the measured thermal displacement in the Z-axis direction at times t_U , $\delta Z_{sim}(t_U)$ is the simulated thermal displacement obtained by the thermal error compensation model according to Eq. (5), see Sect. 3, τ is the on-machine measurement sampling interval, and parameter tol is the size of the tolerance band of the residual error res (residuum res is given by Eq. (8), see below) at times t_U .

The initial value of the gain in Eq. (6) is equal to 1. The simulated displacement calculated by the adaptive compensation model is defined as

$$\delta Z_{sim-adap}^{\tau, tol} = \delta Z_{sim} \cdot gain_{tol}^{\tau}, \quad (7)$$

where δZ_{sim} is the original compensation model of thermal errors at the TCP in Z-axis direction calculated according to Eq. (5).

The residual error of the original compensation model (see Eq. (5)) is expressed as

$$res = \delta Z_{mea} - \delta Z_{sim}. \quad (8)$$

Thus, the adaptive compensation model is only updated if

$$|res(t_u)| > tol. \quad (9)$$

There are two adjustable parameters of the adaptive model. First, it is the sampling interval τ . The second is the selected tolerance band tol of the residual error res . This approach enables rapid updating of the original thermal error compensation models with minimal additional modelling effort, since only one quotient needs to be calculated ($gain_{tol}^{\tau}$). Primarily, no special software (e.g., System Identification Toolbox™ for Matlab software [15]) is required to continually update the compensation model as it is needed for the adaptive model, which has to identify completely new set of transfer function parameters (see [9]). Consequently, the proposed method of model updating using a gain factor can be quickly and easily implemented into the standard CNC controller of the machining centre without additional costs (e.g., no industrial PC with software is required for the identification process of the transfer function parameters).

Moreover, the substantial advantage of the proposed solution is that the original compensation model parameters can remain unaffected, thus preserving model transparency. Instead, the gain is modified to multiply the original compensation model. Furthermore, the method also provides information on the required sampling frequency of the on-machine measurement and its effect on the resulting approximation quality of the updated model, which is discussed in Sect. 4.2.

4.2 Adaptive Compensation Results

The adaptive compensation model was tested for various values of the sampling interval τ . Specifically, the parameter τ was set as $\tau = \{30, 60, 90, 120, 150, 180\}$ minutes and for different values of the parameter tol (specifically for $tol = \{1, 3, 5, 10, 15, 20, 25\}$ μm).

Figure 6 depicts the measured, simulated displacement in the Z-axis direction (identified in Sect. 3.1) and the predicted displacements by adaptive model with sampling interval values $\tau = 30$ min and tolerance band $tol = 10$ μm . The black dashed line shows the value of the set tolerance band and the purple curve shows the absolute value of the residual displacement res ; see Eq. (8). The red dotted lines indicate the sampling intervals when the condition in Eq. (9) is evaluated. The green dotted lines indicate moments when the compensation model was adapted according to Eq. (7). In this example, a significant reduction in the required number of the model updates (NoU) depending on the selected value of the parameter tol can be observed (red dotted lines vs. green dotted lines).

The results of the adaptive compensation model for the other tolerance band tol are shown in Fig. 7.

Figure 7 depicts the approximation quality of the simulated displacement in the Z-axis direction (dashed lines) and the approximation quality of the displacement calculated by the adaptive model depending on the selected value of the parameter tol at $\tau = 30$ min. The yellow curve represents the required number of model updates (NoU) depending on the selected value of the parameter tol for the adaptive compensation model. As mentioned in Sect. 3.2, the approximation quality of the thermal behaviour during verification tests is expressed by the $p2p$ value of the thermal error compensation model according to Eq. (6) is 64 μm (see black dashed line in Fig. 7) and the fit value is only 42% (see red dashed line in Fig. 7). The fit value for the adaptive model according to Eq. (7) increases from 78% to 92% (solid red line in Fig. 7) depending on the tolerance

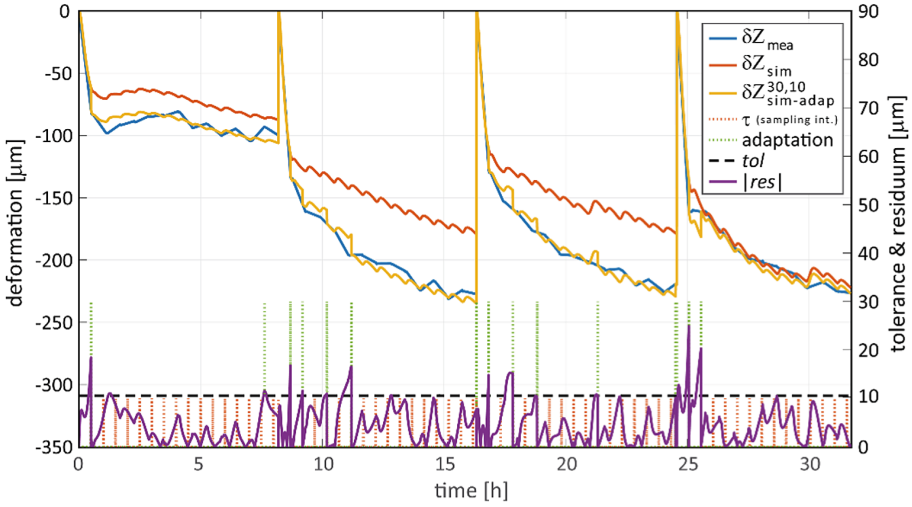


Fig. 6. Comparison of adaptive model results with (for $\tau = 30$ min and $tol = 10 \mu\text{m}$) with measured data.

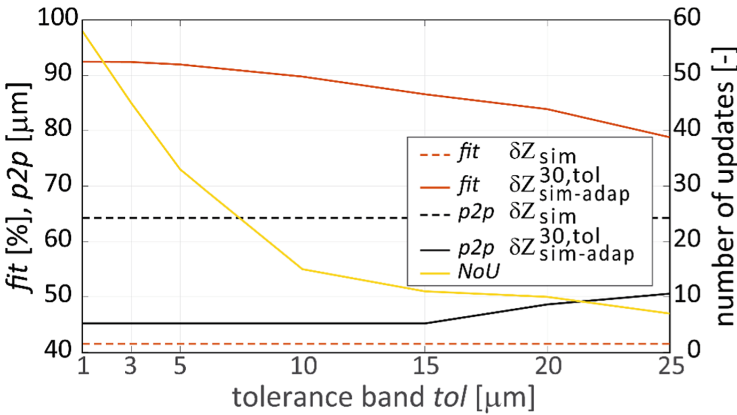


Fig. 7. Approximation quality and the required number of model updates NoU of the adaptive compensation model for $\tau = 30$ min and different values of the parameter tol .

band tol (from $25 \mu\text{m}$ to $1 \mu\text{m}$). The $p2p$ value for the adaptive model is reduced from $51 \mu\text{m}$ to $45 \mu\text{m}$ on the tolerance band tol (from $25 \mu\text{m}$ to $1 \mu\text{m}$). The application of the adaptive model has a positive effect on the resulting fit value and the $p2p$ value, as expected.

The dependence of the required number of model updates NoU on the sampling interval values τ and the tolerance band tol is shown in Fig. 8. The dependence of the number of the model updates NoU on the values of the τ and tol in Fig. 8 reveals that the maximum model updates NoU is 58 for the shortest (tested) sampling interval $\tau = 30$ min and the strictest (tested) tolerance band $tol = 1 \mu\text{m}$ as expected. The minimum

number of model updates NoU is 5 for the longest sampling interval $\tau = 240$ min and the most benevolent tolerance band $tol = 25$ μm , also as expected. The number of model updates NoU increases significantly for the strict tolerance band (especially 5 μm and smaller).

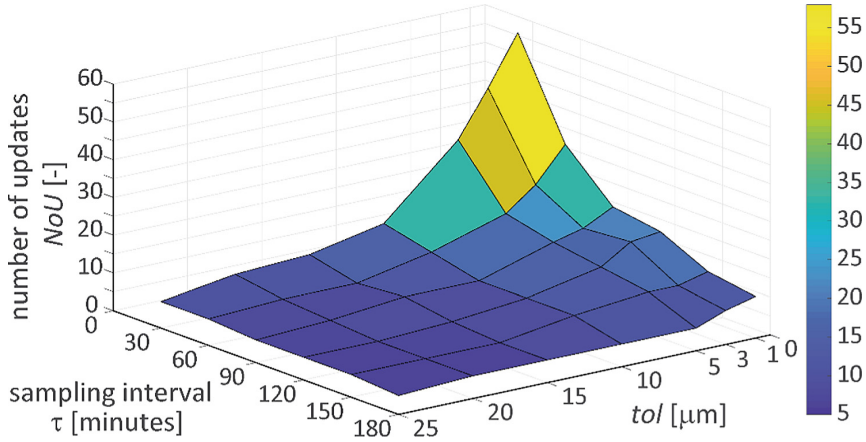


Fig. 8. Dependence of the required number of model updates NoU value on the values of the τ and tol .

Similar graphs for the approximation quality expressed by fit and $p2p$ are shown in Fig. 9 and Fig. 10. The dependence of the approximation quality on the sampling interval values τ and the tolerance band tol is not unambiguous. For the global approximation quality expressed by fit , the results are always better with a smaller sampling interval (the smaller the sampling interval, the higher the fit value). However, the local approximation quality expressed by the peak-to-peak ($p2p$) method can be worse in some cases, as shown in Fig. 10. Taken together, these findings suggest that the length of the sampling interval has to be selected carefully and the shorter sampling interval is not always beneficial. The relationships between length of the sampling interval, number of model updates, tolerance band and achievable accuracy were detailedly explored for particular adaptive compensation model of the horizontal machining centre. This analysis enables to select proper on-machine sampling interval and tolerance band tol to achieve required accuracy of the machine tool (compensation model) and to ensure high productivity of the machining process without excessive interruption by on-machine probing.

Generally, specific thermal error compensation model has to be developed for particular machine tools depending on the machine tool structure, its size, heat sources and heat sinks etc. However, the proposed updating of the compensation model using a gain factor can be universally applied as extension for this particular (original) compensation model of thermally induced errors for particular machine tool. Thus, the adaptive compensation model using a gain factor will be always based on this 'original' compensation model for a particular machine tool. However, the method of updating the model using a gain factor is fully transferable. Furthermore, it can be assumed that the length of the sampling interval, number of model updates and the resulting precision of the adaptive

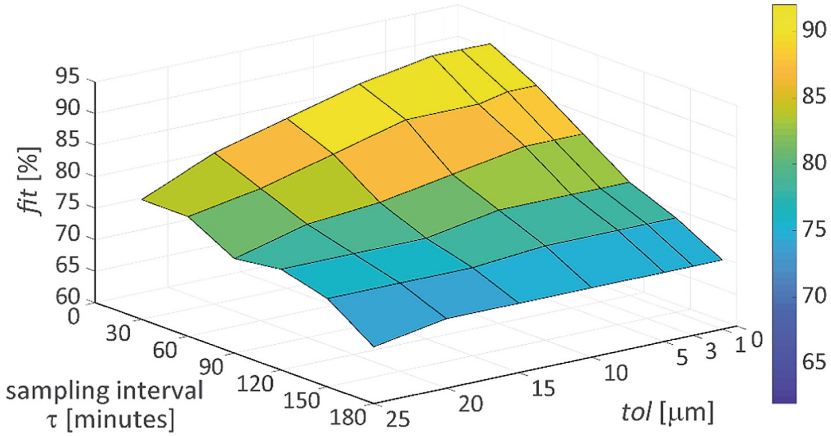


Fig. 9. Dependence of the *fit* value on the values of the τ and *tol* parameters.

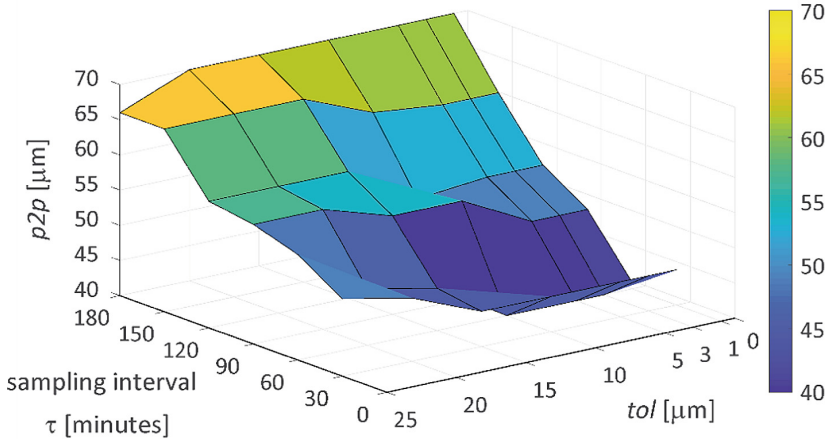


Fig. 10. Dependence of the *p2p* value on the values of the τ and *tol* parameters.

model will be significantly influenced by the prediction accuracy and the robustness of the ‘original’ compensation model.

5 Conclusions

This paper investigates the adaptation of thermal error compensation models using on-machine measurements to improve prediction performance. Specifically, the relationships between compensation model accuracy, the sampling interval length, the size of the tolerance band and required number of model updates are discussed in detail. The study is focused on wider range of the on-machine sampling interval from 30 to 180 min. The goal is to increase the sampling interval to minimize interruption of the machining process by intermittent probing.

First, a TF-based model was built to compensate for the thermal errors of the large horizontal machining centre caused by the spindle. Tests with spindle excitation were performed in 3 different linear Y-axis positions in total. TF-based model identification is derived from measurement at the lowest linear Y-axis position. Furthermore, the developed model was applied in verification tests with the spindle excitation in different Y-axis positions. This resulted in a low prediction accuracy of thermal errors at the TCP in the Z-axis direction. Consequently, an adaptive model was proposed using on-machine measurements and gain factor technique. The presented findings confirm that the prediction accuracy measured as peak-to-peak values and the normalized root mean squared error of the thermal error compensation models are significantly improved by up to 33% (from 64 μm to 43 μm) and 51% (from 78% to 92%) respectively when adaptive compensation model is applied using on-machine measurement. Future studies should concentrate on experimental verification of the proposed compensation model updating using a gain factor for different machine tools (thermal error compensation models) to show if the results are transferable. Additional data collection would help to determine if the relationship between the length of the sampling interval, number of model updates, tolerance band and achievable accuracy shows similar trends.

Acknowledgement. This work was supported by the Grant Agency of the Czech Technical University in Prague, grant no. SGS22/159/OHK2/3T/12. The results are also obtained thanks to previous funding support from the Czech Ministry of Education, Youth and Sports under the project CZ.02.1.01/0.0/0.0/16_026/0008404 “Machine Tools and Precision Engineering” financed by the OP RDE (ERDF), co-financed by the European Union.

References

1. Mayr, J., et al.: Thermal issues in machine tools. *CIRP Ann. Manuf. Technol.* **61**(2), 771–791 (2012)
2. Li, Y., Yu, M., Bai, Y., Hou, Z., Wu, W.: A review of thermal error modeling methods for machine tools. *Appl. Sci.* **11**(11), 5216 (2021)
3. Liu, H., Miao, E.M., Wei, X.Y., Zhuang, X.D.: Robust modeling method for thermal error of CNC machine tools based on ridge regression algorithm. *Int. J. Mach. Tools Manuf.* **113**(2017), 35–48 (2017)
4. Mareš, M., Horejš, O., Hornych, J., Smolík, J.: Robustness and portability of machine tool thermal error compensation model based on control of participating thermal sources. *J. Mach. Eng.* **13**(1), 4–36 (2013)
5. Miao, E.-M., Gong, Y.-Y., Niu, P.-C., Ji, C.-Z., Chen, H.-D.: Robustness of thermal error compensation modeling models of CNC machine tools. *Int. J. Adv. Manuf. Technol.* **69**(9–12), 2593–2603 (2013). <https://doi.org/10.1007/s00170-013-5229-x>
6. Gao, W., et al.: On-machine and in-process surface metrology for precision manufacturing. *CIRP Ann.* **68**(2), 843–866 (2019)
7. Mou, J.: A method of using neural networks and inverse kinematics for machine tools error estimation and correction. *ASME J. Manuf. Sci. Eng.* **119**(2), 247–254 (1997)
8. Yang, H., Ni, J.: Adaptive model estimation of machine-tool thermal errors based on recursive dynamic modeling strategy. *Int. J. Mach. Tools Manuf.* **45**(1), 1–11 (2005). <https://doi.org/10.1016/j.ijmactools.2004.06.023>

9. Blaser, F., Pavliček, F., Mori, K., Mayr, J., Weikert, S., Wegener, K.: Adaptive learning control for thermal error compensation of 5-axis machine tools. *J. Manuf. Syst.* **44**(2), 302–309 (2017)
10. Zimmermann, N., Breu, M., Mayr, J., Wegener, K.: Autonomously triggered model updates for self-learning thermal error compensation. *CIRP Ann.* **70**(1), 431–434 (2021)
11. WHT 110 (C). <https://www.tosvarnsdorf.cz/files/machines/tos-katalog-wht-2017-aj.pdf>. TOS VARNSDORF a. s., Accessed 21 Sept 2022
12. ISO 230-3 - Test Code for Machine Tools - Part 3: Determination of Thermal Effects, Geneva (2020)
13. Eddy Current Displacement Transducer Specifications. <https://www.emerson.com/documents/automation/specifications-sheet-eddy-current-displacement-transducer-specifications-pr-6423-003-0d1-asset-optimization-en-39116.pdf>. Emerson, Accessed 19 Oct 2022
14. NI cRIO-9024 User manual and specifications. <https://www.ni.com/pdf/manuals/375233f.pdf>. National Instruments. Accessed 25 Oct 2022
15. Ljung, L.: System Identification Toolbox™ User's Guide. The MathWorks, Inc. (2021)
16. Mayr, J., et al.: An adaptive self-learning compensation approach for thermal errors on 5-axis machine tools handling an arbitrary set of sample rates. *CIRP Ann.* **67**(1), 551–554 (2018). ISSN 0007-8506
17. Mares, M., et al.: Thermal error compensation of a 5-axis machine tool using indigenous temperature sensors and CNC integrated Python code validated with a machined test piece. *Precis. Eng.* **66**(1) (2022). ISSN 0141-6359. <https://doi.org/10.1016/j.precisioneng.2020.06.010>
18. Horejš, O., et al.: Compensation of thermally induced errors in five-axis computer numerical control machining centers equipped with different spindles. *J. Manuf. Sci. Eng.* **144**(10), 101009-1–101009-10 (2022). ISSN 1087-1357. <https://doi.org/10.1115/1.4055047>

Open Access This chapter is licensed under the terms of the Creative Commons Attribution 4.0 International License (<http://creativecommons.org/licenses/by/4.0/>), which permits use, sharing, adaptation, distribution and reproduction in any medium or format, as long as you give appropriate credit to the original author(s) and the source, provide a link to the Creative Commons license and indicate if changes were made.

The images or other third party material in this chapter are included in the chapter's Creative Commons license, unless indicated otherwise in a credit line to the material. If material is not included in the chapter's Creative Commons license and your intended use is not permitted by statutory regulation or exceeds the permitted use, you will need to obtain permission directly from the copyright holder.





Analysing the Impact of Process Dependent Thermal Loads on the Prediction Accuracy of Thermal Effects in Machine Tool Components

Eric Wenkler^{1,2}(✉), Christoph Steiert¹, Eugen Boos¹, and Steffen Ihlenfeldt^{1,2}

¹ TU Dresden, Institute of Mechatronic Engineering, 01062 Dresden, Germany
eric.wenkler@tu-dresden.de

² Fraunhofer Institute for Machine Tools and Forming Technology IWU, 01069 Dresden, Germany

Abstract. Thermal changes are one major reason for machining errors. The simulation of thermal compensation processes is therefore of extraordinary importance for the correction and compensation of thermal errors. Most models assume static power losses in machine components and neglect the influence of the machining task on the resulting power losses. Previous research showed that the machine tool activity has a significant effect on occurring power losses. Coupled to a FE model, thermal errors can be predicted more accurately. To investigate the advantages and disadvantages of this approach, the procedure was applied and examined on a machine basis, which is one of the most complex components of a machine tool from a thermal point of view. Therefore, this work describes the concept, application and evaluation of the task-specific thermal prediction. The paper showed that this strategy allows the extrapolation to an unknown and complex load scenario with only 30% prediction error.

Keywords: Machine Tool · Temperature · FEM · Automation

1 Introduction

Machine tools are the core manufacturing system for an efficient machining of high-quality parts. Their accuracy and performance drastically increased within the last decades, and with that the major problem domain shifted from limited positioning accuracy and stiffness to thermally caused positioning errors. It is assumed that more than half of all machining errors is caused by thermal effects [1]. Because of this reason, high effort is put on the compensation and correction of thermal errors. Compensational approaches try to minimize the thermal sensitivity of the machine tool by integrating passive or active elements, while correctional approaches attempt to estimate thermal errors and minimize them by considering the thermal error within the machine tool control as dynamic position offset. First, compensational approaches are discussed, which can further be divided in passive and active.

Passive compensational approaches are mainly achieved by the integration of thermally resistant materials, which are chosen for example by their conductivity, heat capacity or expansion coefficient. Möhring et al. gave a broad overview of developments in machine tool relevant materials [2]. A typical example is the use of stone and ceramic composites for machine bases. Such thermally and mechanically resistant materials are mainly used as carrier material for unmoved parts in the machine tool. Another recent example for a passive compensation approach is examined by Voigt et al., who attached phase changing materials to the nut of a ball screw drive [3]. If the phase change temperature is reached, the material changes its structure and with that increases its heat capacity significantly. This raises the heat capacity of the whole assembly and reduces further thermal changes.

On the other side are active compensational approaches, which characterize by a requirement for additional energy. Typical solutions for this group are fluid based cooling systems, which are state of the art for modern machine tools. Basic fluid cooling systems start with the machine tool and continuously pump fluid through lossy assemblies to remove the heat and prevent the assembly from excessive heating. Since the convective heat transfer raises in efficiency with increasing temperature difference, most cooling systems are fully active or 2-point controlled, which means that they start when a predefined temperature is reached in the assembly. This prevents the cooling system of consuming energy in case of minor temperature differences, where no significant heat removal can be achieved. Mori et al. applied this approach to a spindle cooling system and showed that energy savings from 15% to 75% can be achieved, depending on the operational state of the spindle [4]. Recent research shows a great potential in volume flow controlled cooling systems [5, 6]. If a thermal difference between assembly and coolant tank is given, the volume flow of the cooling system can be changed to maintain the machine tool temperature at a specified value. Such a thermal difference can be achieved by using a compressor or allowing higher temperatures in the machine tool.

The second major group are correctional approaches, which characterize by accepting the thermo-elastic error and correct it together with the machine tool control. Therefore, the precise measurement or prediction of thermo-elastic displacements is of high priority. Finite element (FE) based simulations are most common in this field, since they are able to consider nearly all physical effects, relevant for thermal changes. The greatest disadvantage in FE based simulations is the high effort, required to obtain an accurate simulation [7]. Especially for machine tools, such simulations require major effort, since a machine tool includes multiple assemblies, which additional may have losses and change their position with time (e.g. X-Axis position). This requires a dynamically connected model to consider positional changes and additional a great experimental effort to determine losses, which may also change depending on the assembly's operational state. Further heat transfer properties at the joints between assemblies must be determined, which is practically only possible by disassembling the whole machine tool with major experimental setups.

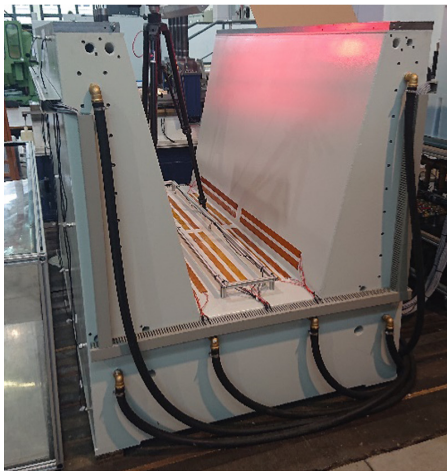
Because of the great effort required for a machine tool FE model, alternative approaches are researched, to predict thermo-elastic effects. A typical alternative is the determination of characteristic maps and their use for thermal predictions [8]. Such

approaches are mostly data driven and do not consider physical mechanisms of heat transfer. Therefore, their ability for inter- and extrapolation is strongly limited.

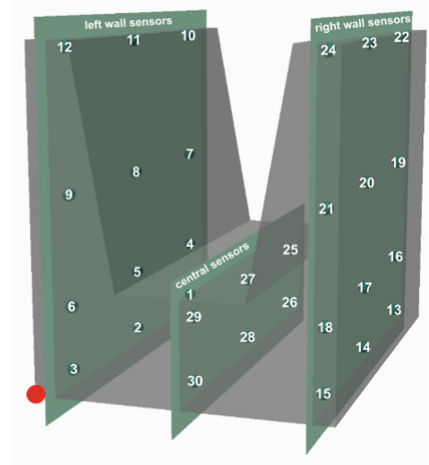
In nearly all forecast strategies, the task caused change in power loss of lossy machine tool assemblies is not considered. Instead, average losses are measured and used. Previous research showed that the manufacturing task (G-code) greatly effects losses and with that the resulting temperature [9, 10]. According to this finding, this paper describes the creation of a FE model, capable to consider the varying and task specific heat introduction.

2 Research Overview

The focus of this research is the consideration of task dependent losses in machine tools to increase the accuracy of FE predictions. Since complete machine tool models require great effort in finite element model (FEM) creation and adjustment of model parameters, a machine basis was used as research object. This reduces the effort for the FEM creation, which is not in focus of this paper. The chosen machine basis is a unique basis build for research of tempering strategies and does not belong to a real machine tool. Since no lossy assemblies are mounted, heating pads were attached, to simulate such lossy assemblies. Figure 1 shows a picture of the machine basis, that is equipped with 20 heating pads, 7 cooling circuits and 30 temperature sensors. Its core material is made up of Hydropol [11], with steel casing and reinforcement. It has a width of 1.4 m, a depth of 2 m and a height of 1.6 m.



a) Photo of the machine basis



b) Integrated sensor locations

Fig. 1. Research object: machine basis

The abstract procedure for creating a FE Simulation, that considers task specific varying thermal loads is illustrated in Fig. 2. It implies the creation of a model, the optimization of parameters to improve model accuracy and the accurate prediction of thermal

loads, used as bounding conditions for the FEM. The paper describes the application and analysis of this approach for the machine basis as demonstrator.

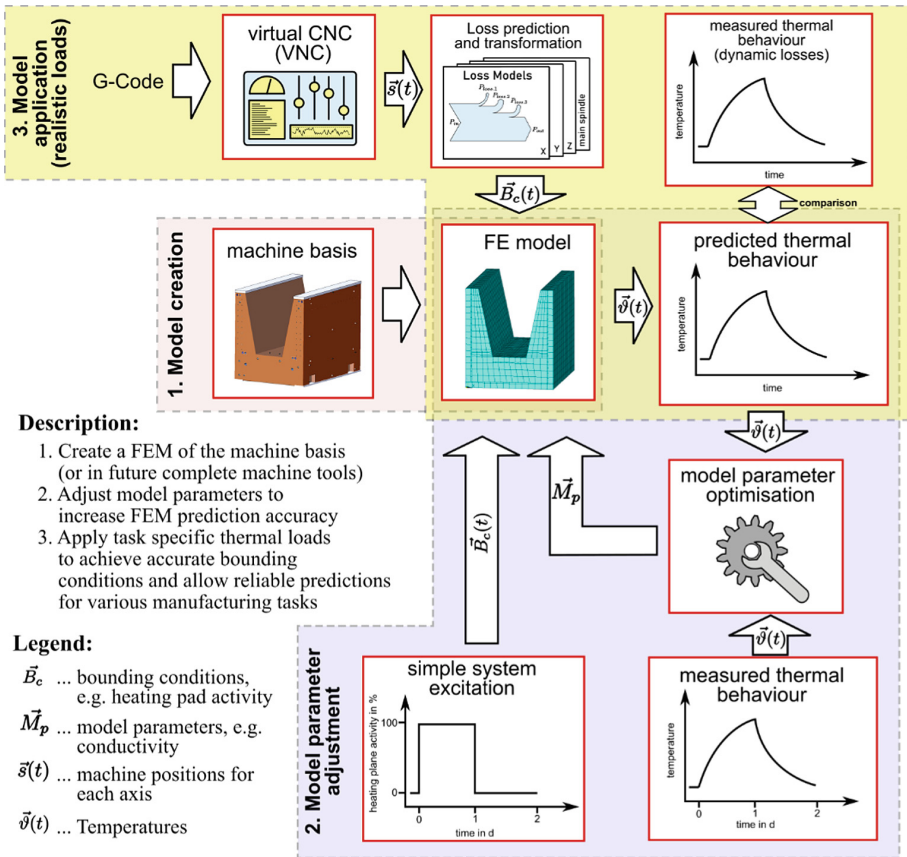


Fig. 2. Abstract overview to the application of task dependent loads in FEM

3 Finite Element Model

3.1 General Procedure of Thermal Error Estimation

Accurate thermal and thermo-elastic predictions are of major importance in the field of machine tools. Deviations between expected and real temperatures lead to positional deviations and therefore directly affect the manufacturing quality. Common approaches for thermal predictions focus on the physical simulation of heat transfer processes, which is mostly achieved with the use of finite element models (FEM) or finite difference models (FDM). These models discretize the body of the simulation object and calculate the heat transfer mechanisms for small and easy shaped elements with the use of basic heat transfer equations.

The accuracy of such approaches depend on two major points:

- **Model quality:** The simulation is always abstracted and cannot be as accurate as the real object. For example, the model discretization strongly effects the simulation accuracy and the computing effort, which is why a trade-off between simulation speed and accuracy is necessary. Further it is common to ignore small geometrical features, that are assumed to have no impact, but consequently they lead to slight deviations and the sum of such simplifications can lead to major deviations. Therefore, the simulation model contains a base error that cannot be overcome.
- **Boundary condition quality:** The boundary conditions define the excitation of the system. The simulation model takes them and computes heat transfer processes. Incomplete or inaccurate boundary conditions lead to wrong excitations of the system and therefore to wrong simulation results. According to this, it is from major importance to achieve as realistic boundary conditions as possible.

Especially boundary conditions for internal heat sources are often abstracted in thermal simulations of machine tools and their correlation to the machining task is not considered. It is a common procedure to create a thermal simulation, define boundary conditions at areas where heat is expected, like motors or bearings, and perform measures to calibrate the power loss for the specific boundary condition. Such tests are mostly done by performing trivial machine movements, like repetitive linear movements of the machine axes, as done in thermal stability measures normed in ISO 230-3. This strongly deviates from the machine movement under production conditions, which is very task dependent. Since the emitted power losses in active machine assemblies strongly depend on their operational state (e.g., the rotational speed of a feed axis bearing), a static power loss, as assumed in most models, leads to major simulation deviations. This reasons the following investigation on the consideration of task dependent loads within FEM.

The following sections describe the creation (Sect. 3.2) and optimization (Sect. 3.3) of the FEM, for a later application of task dependent loads.

3.2 FE Model Creation

The model for the machine basis was created with Ansys APDL (Ansys Parametric Design Language), which is the original Ansys application. The script support allows a graphicly guided development and debug of the model, but also the automated execution in background. The capability for automated execution will be used for an optimization of model parameters within the next Sect. 3.3. Figure 3 gives a general introduction to the created model. The major geometrical features of the machine basis were considered during the recreation within Ansys. To force the creation of Nodes at positions with bounding conditions, the initial body was cut multiple times (see Fig. 3a). The resulting volumes were roughly meshed with an edge size of 100 mm. This in fact leads to a rough model with limited accuracy, but significantly decreases the computation time, which will already be big according to the transient simulation.

The model considers three bounding conditions, which are:

1. **Fluid circuits:** The machine basis has 7 separate cooling circuits, which are individually controlled. These circuits were modelled with 1D-Fluid-Elements as illustrated

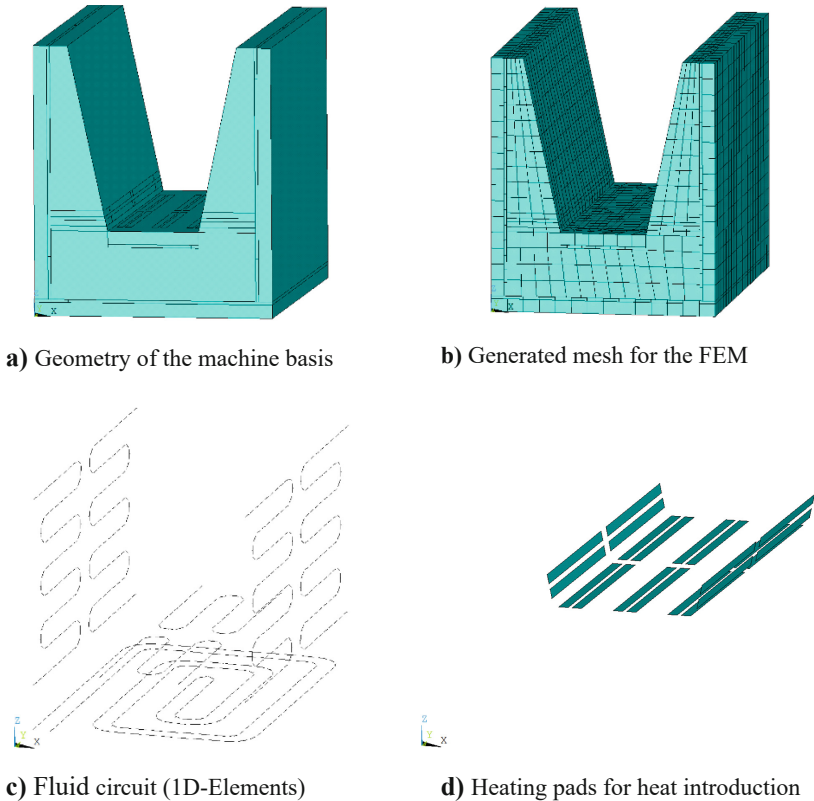


Fig. 3. Created FE-Model

in Fig. 3c. The elements can be controlled by defining volume flow and fluid inlet temperature.

2. **Heating pads:** In the central area of the machine basis are 20 heating pads mounted. Each wall is attached with 4 pads, while 12 pads are mounted in the central (horizontally oriented) surface (see Fig. 1 or 13). Therefore 20 bounding conditions were added to the model, with a controllable heat flow through each of the 20 surfaces.
3. **Convection:** Since the heat exchange to the environment is an important heat sink for the model, convection was defined at all outer surfaces of the model. For simplification the heat transfer coefficient α was assumed to be equal at each surface.

The activity of a bounding condition can be set from outside over an CSV file, which is passed to the model and read during simulation start. With this setup, the model can efficiently be applied to various load scenarios, which is important for further practical applications.

It is to mention that the presented model is a rough model, only considering major thermal impacts. The geometry is simplified and inner steel inlets for reinforcement are not modelled. Effects like the varying heat transfer coefficient over the surface, or the radiation with the environment could have increased the model accuracy, but also

require a huge experimental effort. Since the goal is to generally show the possibility for predicting the thermal behaviour in machine components, with consideration of the task, such high-effort-low-gain effects were neglected.

3.3 Automated Optimization of FEM Parameters

The created model was initialized with default material properties obtained from common material tables. Together with the geometrical simplification of the model, simulation errors are unavoidable. Since all models are a simplification of the real object, it is a common approach to adjust model parameters to increase the model accuracy [7]. Therefore, simple load cases were prepared and applied to the machine basis, to measure the real thermal behaviour and use it for a model parameter optimization, as illustrated in Fig. 2. One reference measure was taken for the heating with heating pads and one for the cooling with the cooling system. Within these test cases, all heating pads/cooling-circuits were fully active for one day, and then turned off to measure the harmonization behaviour for one additional day. For simplification, the focus is put on the heating pads while the cooling system is not considered. For consistency it is to mention, that the following parameter adjustment procedure is identical for heating pads and cooling circuits.

The adjustment of model parameters based on thermal measures is an iterative task since discrete models as FEM do not allow a direct quantification of the thermal impact of a specific parameter. In fact, if a parameter is changed, the whole simulation must be repeated, to compare results and quantify the impact of the model parameter and decide how to adjust a parameter. Since this is the core intention of mathematical optimization approaches, an optimizer was implemented for the model parameter adjustment.

The optimizer takes a set of parameters with bindings, that he is allowed to adjust, and repetitively executes the FE model with different parameters, to quantify the impact on the model and decide how to adjust parameters to minimize the model error. Since optimizers try to minimize a scalar error value, the computation of an error value was required, that represents the error between the measured and simulated temperature curves over each 30 sensors. Therefore, Eq. 1 was used as cost function, which represents the mean square error (MSE). Parameters are: number of sensors s , number of simulated/measured time steps l (must be equal), simulated temperatures S and measured temperatures M .

$$E = \frac{\sum_{n=1}^s \sum_{m=1}^l (S_{m,n} - M_{m,n})^2}{s \cdot l} \quad (1)$$

MSE is a common cost function that aims to globally fit the curves. According to the square of the difference, great differences have a huge impact on the overall error, while minor differences have a small one. Therefore, MSE will always lead to slight deviations since local error maxima have the main influence on the total error, that are reduced on cost of places with small errors.

The used optimizer was COBYLA (Constrained Optimization By Linear Approximation), which showed the best performance and a fast convergence under 10 tested gradient free optimizers. The test was performed by comparing the simulation

time and final MSE, achieved after 50 optimization steps by providing the simple system excitation together with the measured behaviour (see Fig. 4 block 1). Figure 4 shows a more detailed overview of the implemented optimization procedure.

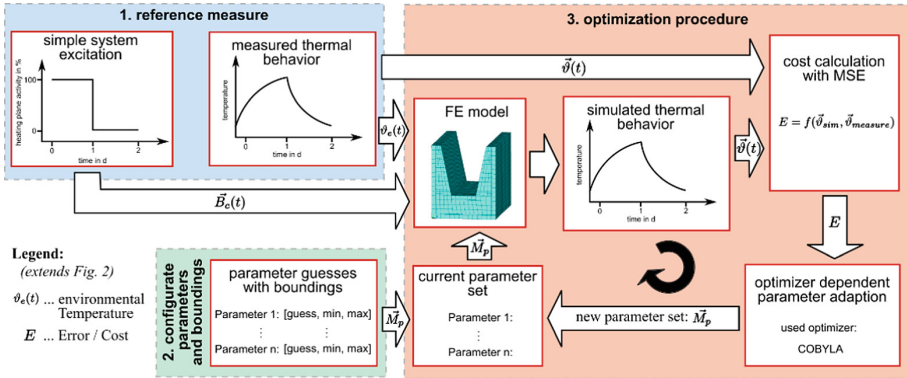


Fig. 4. Block diagram showing the procedure for parameter optimization

Table 1. Optimization configuration and result

Parameter	Unit	Start value	Minimum	Maximum	Optimum
Power of heating pad	W	45	0	50	49.3
Air conv. Coefficient	$W m^{-2} K^{-1}$	10	8	100	12.1
Hydropol conductivity	$W m^{-1} K^{-1}$	6.2	6.2	50	6.2
Hydropol density	$kg m^{-3}$	2450	2450	7850	4588.4
Hydropol heat capacity	$J kg^{-1} K^{-1}$	980	470	980	979.2

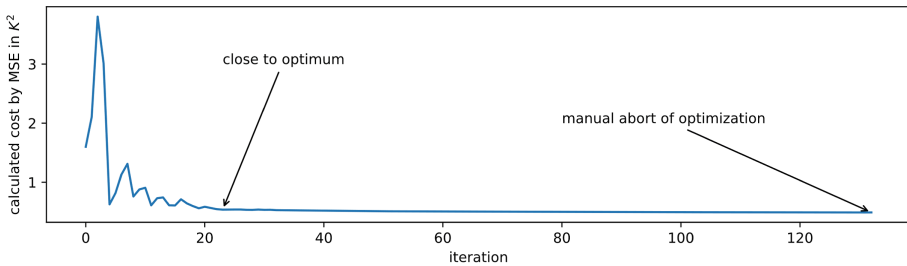


Fig. 5. Cost (MSE) development during optimization procedure

The optimization was started with default parameters (see Table 1). The bindings were set, so that the parameters remain within the range between Hydropol and steal, since the steel inlets were not modelled, and optimal parameters may move in between. According to Fig. 5, the MSE dropped from $1.60 K^2$ to $0.53 K^2$ after already 20 iterations.

The optimization was manually aborted with a final MSE of 0.48 K^2 , which describes an average prediction error reduction from 1.26 K to 0.69 K . Even if this reduced the range of absolute errors from $[-1.54 \text{ K}, 3.2 \text{ K}]$ to $[-1.5 \text{ K}, 2 \text{ K}]$, some local errors increased (compare Fig. 6 and 7). This normally occurs when the model capacity is reached, forcing the optimizer to start with the error distribution, to minimize the cost criteria. Therefore, a further error reduction could be achieved with a more detailed model.

At this point the model is created and parameters are improved to achieve maximum correlation between reality and simulation, allowing the application of process dependent loads.

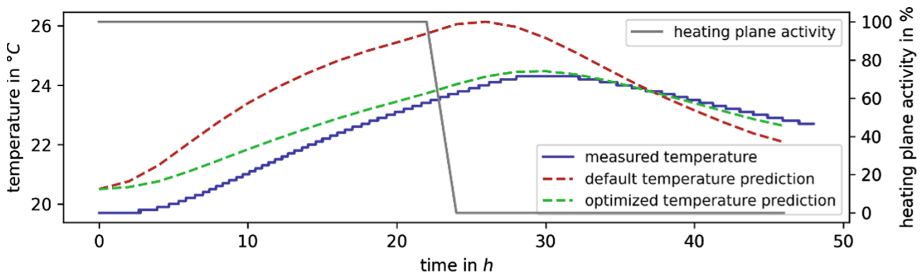


Fig. 6. Exemplary local accuracy increase by global parameter adjustment (Sensor 26)

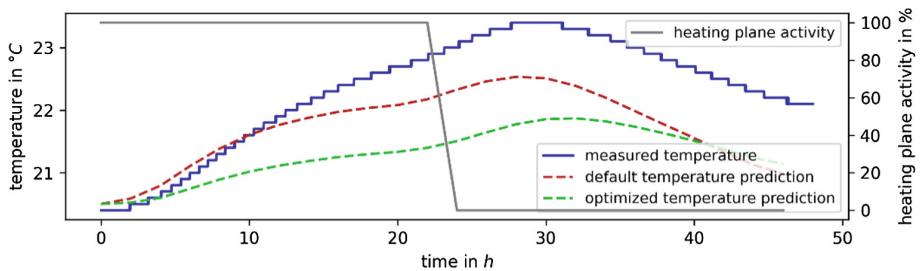


Fig. 7. Exemplary local accuracy decrease by global parameter adjustment (Sensor 19)

4 Obtain Manufacturing Task Characteristic Thermal Loads

The determination of thermal loads that come with a manufacturing task (G-code) requires the interpretation of the G-code, to determine resulting movements and apply axis specific loss models. This procedure was analysed in [9, 10] and its application, to estimate realistic thermal loads for the FEM, is described in this section.

4.1 Reference Task for Realistic Load Scenario

Realistic thermal loads can be achieved by the usage of a typical industrial manufacturing task. Therefore, a part was constructed that is characteristic for the field of aerospace,

which mainly requires the parts to be light and stable. Since sheet metal constructions do not achieve the required stability, the parts are mostly manufactured from the solid and have great volume reduction rates above 80%.

Figure 8 shows the constructed part that is typical for support structures as used in pads, rockets or satellites. Its main dimensions are $504 \times 291 \times 140$ mm and the corresponding raw part dimensions are $514 \times 310 \times 150$ mm. Only 6% of the initial material remain in the final part. The planned technology includes only the first clamping, which is for the upper half of the part and contains a roughing and two finishing operations. A third and final finishing operation is assumed to be performed at the end of the second clamping, which is therefore not considered here. The many finishing operations are essential, since residual stress is released during the material removal, leading to a part deformation, and therefore requiring a slow iteration down to the final part geometry. Figure 8 summarizes the technological steps used for the considered first clamping process.

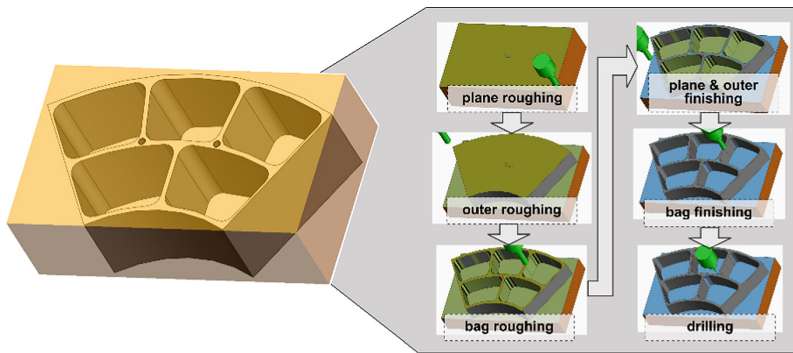


Fig. 8. Reference task and prepared technology (process steps)

4.2 Task Characteristic Power Loss Estimation

The estimation of task characteristic power losses was already developed for a hexapod in previous research [9, 10], which will be reused for this approach. The solution interprets the G-Code with the use of a virtual numerical control (VNC) that mimics the real control of the machine tool. Consequently, the machine movement can be predicted, which further allows the application of power loss models to estimate power losses within the machine tools lossy assemblies (see Fig. 9).

Most machine tools have a serial kinematic, since the general accuracy and complexity of the machine tool is lower, compared to a parallel kinematic machine. Because of this, a serial setup was assumed to be mounted at the machine basis. Since the reused solution was created for a hexapod that has a parallel kinematic, the predicted losses would not be characteristic for an axis with a serial machine kinematic, not allowing a transfer of estimated losses. Therefore, the power loss prediction with the hexapod was performed without the hexapods kinematic transformation (on axis level). This forces

the VNC to ignore the axis setup of the hexapod and directly transfers positions to the physical axis, only considering the first 3 axes of the hexapod as it would be the X, Y and Z axis of a serial machine setup. With this adaption of the solution, the predictions become comparable to the assumed serial axis setup at the machine basis, which allows a transfer to the research object.

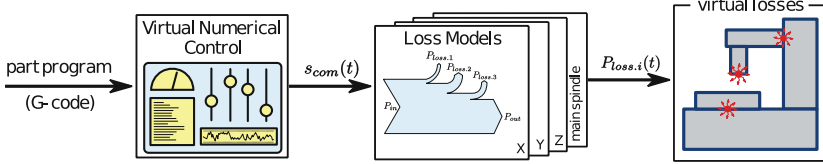


Fig. 9. Procedure for the prediction of task specific losses

4.3 Transformation of Thermal Loads

The machine basis has no lossy assemblies mounted that could introduce process dependent heat. Instead, 20 heating pads are mounted to mimic such losses (see Fig. 1 and 13). Therefore, an X-axis was assumed to be mounted in the centre of the machine basis, as illustrated at the bottom of Fig. 10. The loss prediction in the previews section was created for a hexapod without kinematic transformation (see top of Fig. 10 for axis setup). The predicted power losses for the hexapod are therefore comparable to a serial machine axis as assumed at the demonstrator. To transfer the losses from the hexapod axis to the demonstrator, the assembly characteristic losses are mirrored and scaled to the corresponding position of the assumed demonstrator axis (see Fig. 10). In the following is described how this transfer was achieved.

The loss simulation for the task of the previews section led to characteristic losses in the hexapods motor, bearing and ball screw drive (spindle nut contact). These losses will further be used for the assumed X-axis at the machine basis. The ball screw drive loss was not considered, since it leads to a heat introduction in the spindle and nut, which are not modelled and additional have no direct contact to the machine basis. Figure 11 shows the unmodified power loss predictions for the hexapod. Since the hexapod contains no profile rail guide power loss, this loss was separately modelled with the use of an empirical model [12]. Parameters are: power loss P , frictional force F , axis speed v , width of the rail guide b , preload force F_v and dynamic load rating C .

$$P(t) = F(t) \cdot v(t) = b \cdot 10^3 \cdot \left(0.46 + 66 \cdot \left(\frac{F_v}{C} \right)^{2.5} + \left(0.46 + 5.2 \cdot \left(\frac{F_v}{C} \right) \right) \cdot v(t) \right) \cdot v(t) \quad (2)$$

The axis speed $v(t)$ was obtained from the loss prediction and losses were computed for a rail guide with of $b = 40$ mm and a preload of $F_v/C = 0.075$. Figure 12 shows the resulting power loss for a single rail guide.

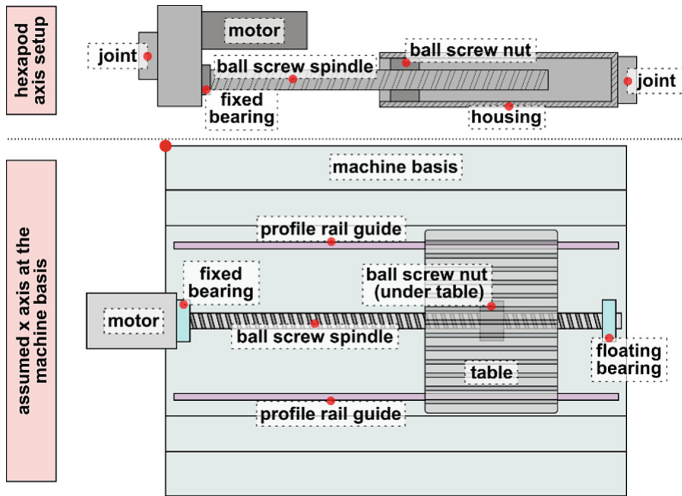


Fig. 10. Assumed constructive setup for thermal load transformation

A correlation between all curves can be seen, caused by the following general loss equation. Parameters are: power loss P , loss moment M , angular speed ω , loss force F , axis speed v and time t .

$$P(t) = M(t, \omega) \cdot \omega(t) = F(t, v) \cdot v(t) \tag{3}$$

Since $M \sim \omega$ and $F \sim v$, the power loss mainly depends on the activity (rotational speed ω or axis speed v) of the assembly, which can be expressed as $P \sim \omega^2 \sim v^2$ and reasons the obvious correlations of the curves.

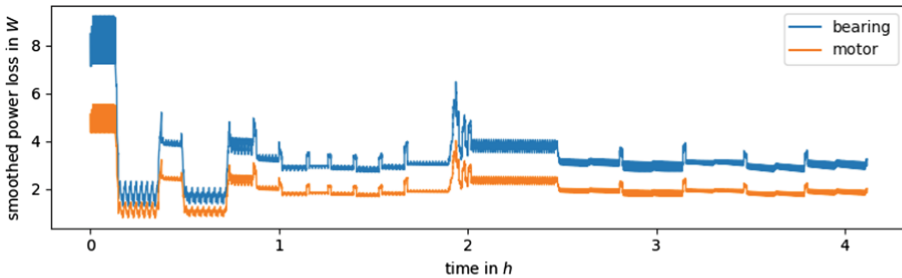


Fig. 11. Predicted power losses at the hexapod

At this point, all required characteristic power loss curves for lossy assemblies are defined. To mimic this relational behaviour with the heating pads, the curves need to be attached to the closest heating pads and a final normalisation over all curves is required, to obtain activity values within the range $[0, 1]$ for direct application in the machine tool PLC (**P**rogrammable **L**ogical **C**ontroller) and the FEM. The attachment and resulting normalized curves are shown in Fig. 13b.

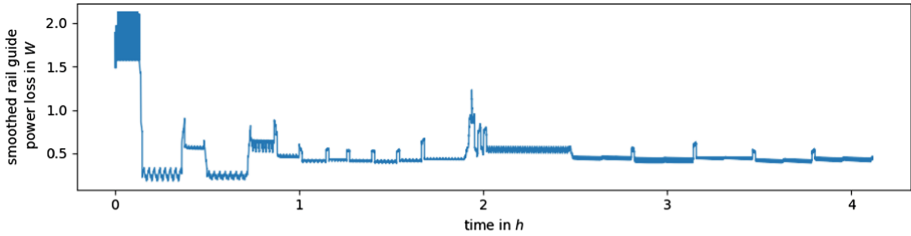
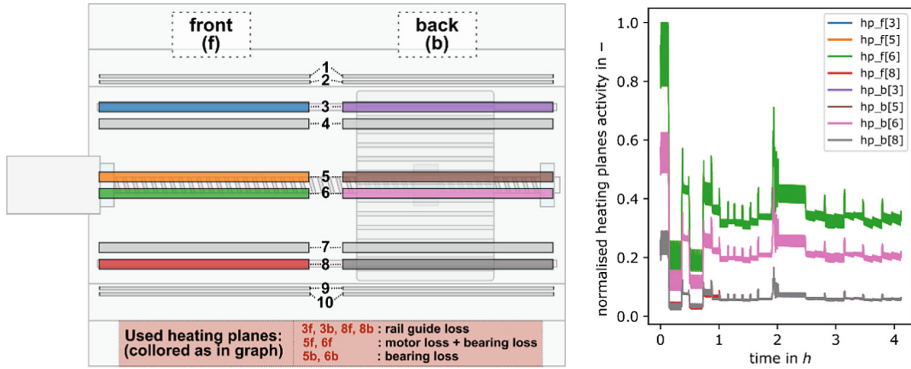


Fig. 12. Modelled power loss for a single profile rail guide



a) Heating pad positions with underplayed axis setup used for power loss assignment to specific pads

b) Derived heating pad activities

Fig. 13. Definition of realistic heating pad activities to mimic a real X-axis (Color figure online)

The attachment was performed manually by putting the assembly specific losses to the closest heating pad. Heating pad 5f and 6f are the closest to the fixed bearing and the motor. Therefore, both loss curves were added and equally divided to both heating pads. The floating bearing loss was attached to heating pads 5b and 6b. Profile rail guide losses were attached twice, once to heating pads 3f and 3b, and once to 8f and 8b. The position dependency was considered during loss assignment of the rail guide loss, by computing the absolute position of the front and back table edge, where a contact between table and rail guide was assumed. The loss got then attached to the closest heating pad, resulting in slight differences at the roughing operation, where it occurred that both contacts are closer to the front or back pad (see red curve under grey curve in Fig. 13).

5 Application and Evaluation of Dynamic Thermal Loads in FEM

The determined dynamic loads of the previous section are now applied to the machine basis and the FEM, to evaluate the forecast accuracy under dynamic thermal loads. First the application to the machine basis is described, followed by the application to the FEM. Finally, both results are compared and evaluated.

5.1 Dynamic Thermal Load Application to Machine Basis

Since Hydropol has a high heat capacity and a low conductivity, slow thermal changes arise as visible in Fig. 6 and 7, where even after 1 day no static temperature was reached. Therefore, the machine basis PLC was prepared to repetitively execute the thermal load scenario to get into the static state. This repetition mimics the conditions for manufacturing a batch of parts in a three-shift operation. Since a completion of one task requires a workpiece change and therefore a pause between two applications of the load scenario, a 10-min pause was added after each execution.

The measure was taken for one week, resulting in 40 measurements, one for each repetition. These measure represents the reference where the FEM will be compared to in Sect. 5.3. The measure includes the environmental temperature, which was measured by one sensor that was provided with fresh air by a fan. Inhomogeneity effects in environmental temperature could therefore not be detected, which for example could be caused by hall gates.

5.2 Dynamic Thermal Load Application in FEM

The load scenario was repetitively executed with a 10-min pause in between, for 40 times at the real machine basis. To simulate the same time with the FEM, a concatenation of the load scenario was performed, considering the 40 repetitions with 10-min pauses in between. The resulting CSV was passed to the FEM together with the optimized parameters and the simulation was started with a time step of 2 h. The simulation was completed after approximately half a day and will be compared with the measured behaviour in Sect. 5.3.

5.3 Comparison and Evaluation of Measured and Simulated Behaviour

The measured and simulated machine basis behaviour contains 30 temperature curves over one-week repetitive task application. Figure 14 shows an exemplary sensor and its measured and simulated temperature. Since a single discussion of all 30 temperature deviations would exceed the limits of this paper, some specific evaluations were performed to identify extremes and discuss them in detail. The equations are listed in the following. Parameters are: measured temperature series for a specific sensor T_{mea} , simulated temperature series for a specific sensor T_{sim} .

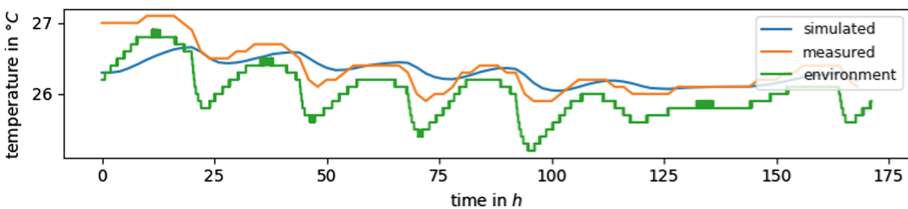


Fig. 14. Comparison of simulated and measured temperatures at sensor 3 (best correlation)

- Range of thermal change in measured behaviour ΔT_{mea} , which is further used as reference for relative error computation.

$$\Delta T_{mea} = \max(T_{mea}(t)) - \min(T_{mea}(t)) \quad (4)$$

- Mean error between measured and simulated sensor temperature E_m .

$$E_m = \overline{|\Delta T(t)|} = \overline{|T_{mea}(t) - T_{sim}(t)|} \quad (5)$$

- Relative error between measured and simulated behaviour E_r .

$$E_r = \frac{\overline{|\Delta T(t)|}}{\Delta T_{mea}} = \frac{\overline{|T_{mea}(t) - T_{sim}(t)|}}{\Delta T_{mea}} \quad (6)$$

Figure 15 shows these three quantities over the 30 sensors to give a general impression of the model accuracy (see Fig. 1b for sensor locations). Sensors 1 to 22 show a small relative error with about 20% deviation on average (see Fig. 14, which is representative for these sensors). Great relative errors with approximately 60% occurred at sensors 23 to 30. Globally this results in a mean relative error of 30% with a mean absolute error of 0.55 K. The biggest deviations occurred in the bottom of the basis, with a maximum relative error of 104% at sensor 26. Figure 16 shows the measurement and simulation for this sensor. A quite stable offset is visible, which may be caused by a thermal offset in the sensor. Additionally, the overall temperature change at this sensor is relatively small with 0.7 K, reasoning the great relative error at this sensor.

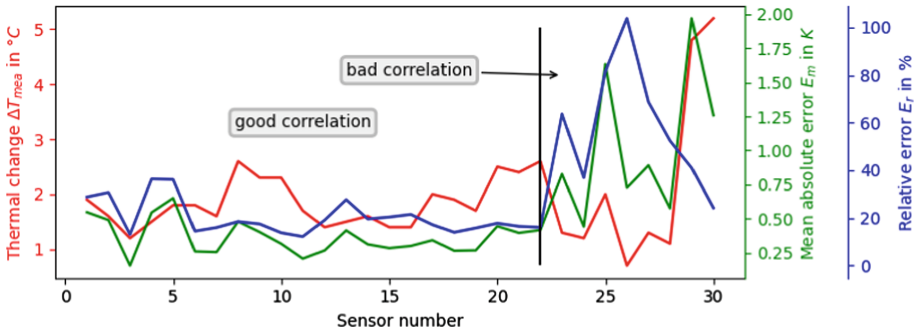


Fig. 15. Statistics of FEM

Overall can be said that the general accuracy of the model is quite accurate with a relative error of 30% and an absolute error of 0.55 K. The remaining error is assumed to be caused by the limited model capacity. A further error reduction should be possible by using a more detailed model. It is important to consider, that the model was only trained with one simple load scenario and can predict an untrained dynamic load scenario with no significant accuracy decrease. This shows that the consideration of task dependent loads, could improve thermal predictions in the field of machine tools.

The measures show one additional characteristic in the machine basis, that was already mentioned in Sect. 5.1: the slow thermal change. Figures 14 and 16 show the

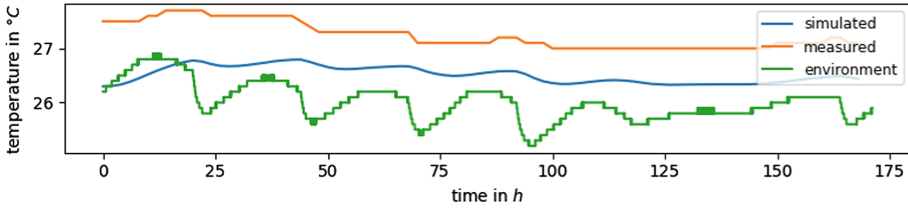


Fig. 16. Comparison of measured and simulated temperatures at sensor 26 (worst correlation)

thermal behaviour at specific positions in the machine basis, which is mainly dominated by the thermal change of the environment. The measures even show that the dynamics in environmental boundary conditions decrease at the weekend (hours 120 to 170 in Fig. 14 and 16), where no one is working.

The process itself is not directly visible, and mainly causing an offset between sensor temperature and environment. This makes short timed thermal simulations difficult, since past thermal loads influence the thermal starting condition. Such approaches are therefore difficult for small batch sizes, but can be valuable for large batch sizes, where quite static machine behaviour is achieved because of repetitive task execution.

6 Conclusion and Outlook

The paper issued the application of task dependent thermal loads in FEM simulations on the example of a machine basis. Section 3 showed the creation and parameter optimization for the FEM. With the use of APDL, the whole model could be tuned and optimized by command line, which allows automation and could be valuable for the goals of digitalization, industry 4.0 or digital twins of machine tools [13]. Further the determination of task dependent thermal loads were presented in Sect. 4, which allows a more accurate consideration of thermal loads in FEM and with that increases the prediction accuracy. The whole procedure was applied and analysed in Sect. 5, where a good correlation between measure and simulation could be achieved.

It is important to consider that only one simple static load scenario was provided to optimize the FEM parameters. With this the model was capable to extrapolate from static loads to dynamic task dependent loads without an increase of the prediction error.

The overall model error is with 30% relatively high, but mainly caused by the simplified FEM, used in this research. Most limiting is the assumed homogeneous convection over all surfaces, not considered steel inlets and the rough model discretization. Further analyses will therefore focus on the increase of model detail, to validate the expected increase in simulation accuracy.

Acknowledgements. The authors want to thank Framag Industrieanlagenbau GmbH [11] for providing the machine basis with integrated sensors and cooling circuits, the Hydac Cooling GmbH for providing the cooling aggregate as well as the German Research Foundation for funding the Project with Project-ID 174223256 – TRR 96.

References

1. Ramesh, R., Mannan, M.A., Poo, A.N.: Error compensation in machine tools – a review. Part I: geometric, cutting-force induced and fixture-dependent errors. *Int. J. Mach. Tools Manuf.* **40**(9), 1235–1256 (2000)
2. Möhring, H.C., Brecher, C., Abele, E., Fleischer, J.: Materials in machine tool structures. *CIRP Ann.* **64**(2), 725–748 (2015)
3. Voigt, I., Navarro de Sosa, I., Wermke, B., Bucht, A.: Increased thermal inertia of ball screws by using phase change materials. *Appl. Therm. Eng.* **155**, 297–304 (2019)
4. Mori, K., Bergmann, B., Kono, D., Denkena, B., Matsubara, A.: Energy efficiency improvement of machine tool spindle cooling system with on-off control. *CIRP J. Manuf. Sci. Technol.* **25**, 14–21 (2019)
5. Shabi, L.: Thermo-Energetic Optimized Fluid Systems for Machine Tools. Dr.-Ing. Dissertation, Institute of Mechatronic Engineering, TU Dresden (2019)
6. Weber, J., Steiert, C., Weber, J., Shabi, L.: Investigation of the thermal and energetic behavior and optimization towards smart fluid systems in machine tools. *Procedia CIRP* **99**, 80–85 (2021)
7. Schroeder, S., Kauschinger, B., Hellmich, A., Ihlenfeldt, S., Phetsinorath, D.: Identification of relevant parameters for the metrological adjustment of thermal machine models. *Int. J. Interact. Des. Manuf.* **13**(3), 873–883 (2019). <https://doi.org/10.1007/s12008-019-00529-y>
8. Naumann, C., et al.: Hybrid correction of thermal errors using temperature and deformation sensors. In: 1st Conference on Thermal Issues in Machine Tools, Dresden, Germany (2018)
9. Wenkler, E., Hellmich, A., Schröder, S., Ihlenfeldt, S.: Part program dependent loss forecast for estimating the thermal impact on machine tools. *MM Sci. J.* **3**, 4519–4525 (2021)
10. Wenkler, E., Selch, M., Hellmich, A., Ihlenfeldt, S.: Process concatenation to reduce thermal changes in machine tools. *Int. J. Mechatron. Manuf. Syst.* **15**(2–3), 167–184 (2022)
11. Hydropol® machine frames/machine beds. <https://www.framag.com/en/products/hydropol-machine-frames-4621.html>. Accessed 26 Sep 2022
12. Jungnickel, G.: Simulation des thermischen Verhaltens von Werkzeugmaschinen, Modellierung und Parametrierung, published by Großmann, K., TU Dresden, Dresden (2010)
13. Hänel, A., et al.: Digital twins for high-tech machining applications – a model-based analytics-ready approach. *J. Manuf. Mater. Process.* **5**(3), 80 (2021)

Open Access This chapter is licensed under the terms of the Creative Commons Attribution 4.0 International License (<http://creativecommons.org/licenses/by/4.0/>), which permits use, sharing, adaptation, distribution and reproduction in any medium or format, as long as you give appropriate credit to the original author(s) and the source, provide a link to the Creative Commons license and indicate if changes were made.

The images or other third party material in this chapter are included in the chapter's Creative Commons license, unless indicated otherwise in a credit line to the material. If material is not included in the chapter's Creative Commons license and your intended use is not permitted by statutory regulation or exceeds the permitted use, you will need to obtain permission directly from the copyright holder.



Process Parallel Models



A Data-Based Model of the Thermo-Elastic TCP Error Using the Encoder Difference and Neural Networks

Christian Brecher, Mathias Dehn^(✉), and Stephan Neus

Laboratory for Machine Tools and Production Engineering (WZL) of RWTH Aachen University,
Aachen, Germany

{c.brecher,m.dehn}@wzl.rwth-aachen.de

Abstract. The thermo-elastic tool center point (TCP) error has been an ongoing research focus, due to its large effect on the workpiece quality. Existing models to compute the thermo-elastic TCP error already perform quite well regarding the accuracy and speed of computation. However, the models are often time consuming in their parameterization, expensive to apply or are error-prone due to the used model inputs. The work presented in this paper addresses these issues by introducing the encoder difference as model input. Since the encoder difference is easy and inexpensive to measure, it yields a high potential for industrial use. Therefore, in this paper, the correlation between the encoder difference and the thermo-elastic TCP error is investigated. Since the physical relationship between the encoder difference and the thermo-elastic TCP error is complex, it is necessary to use an artificial neural network to compute the resulting TCP error. Due to the variety of artificial neural network (ANN) types, with different capabilities, a range of different networks is tested regarding their capability to compute the thermo-elastic TCP error. To conclude the paper, a method to parametrize such models is derived from the gathered results.

Keywords: thermo-elastic TCP error · ANN · encoder difference

1 Introduction

There is an ongoing trend in the machine tool industry for more productive machine tools and higher workpiece quality, while reducing the environmental machine footprint. This trend is initiated by industry branches like the aerospace industry or the automotive industry which need to cut costs to be competitive, but also need to meet requirements for energy efficiency and reliability.

To keep up with the demand for more accurate machine tools, manufacturers need to reduce error influences impacting the machining quality. One of the most dominant errors when machining is the thermo-elastic error. During operation, external and internal heat sources warm up the machine structure, which leads to a deformation of the structure resulting in a displacement of the TCP. This effect is even more dominant when the

machine tool operates with higher productivity, since this implies higher axis speeds, which result in an increased heat generation causing a higher TCP displacement.

Current research approaches are seeking to reduce the resulting thermo-elastic TCP displacement. The approaches can be clustered into error compensation methods, which focus on reducing heat introduced into the machine structure and error correction approaches, which focus on modeling the TCP displacement to correct it using the machine tool control. The error compensation methods center around the machine coolant system. DONMEZ ET AL. were able to reduce the spindle axial spindle drift by up to 36% using a novel approach to control the machine structure temperature using compressed air and silicon tubing [1]. The error compensation approaches show a reliable performance in machine tools. However, cooling the structure components leads to an additional energy usage [2]. This is not compatible with the effort to reduce machine energy consumption to lower the CO₂ footprint of the industrial sector triggered by economic, social and governance stakeholders.

A less energy-consuming way to reduce the thermo-elastic TCP error is the error correction using the machine control. Hence, the majority of ongoing research focusses on modeling the thermo-elastic error. WENNEMER models the thermo-elastic error using low-order delay elements [3]. To parametrize the elements, four laserTRACERs are installed in a machine tool. Correcting the TCP position using this method delivers good results. However, the parametrization is time-consuming and the measurement equipment is expensive.

Another commonly used method to model the thermo-elastic TCP error focuses on finite element (FE) methods. GALANT ET AL. use an FE model in combination with model order reduction (MOR) techniques to compute the thermo-elastic deformation of a machine structure component with high accuracy and a low computation time [4]. The same technique is used by BRECHER ET AL. when simulating the machine spindle [5], reaching similar results.

While the computation of thermo-elastic displacement of machine components is already well progressed, the computation of the whole machine structure still shows drawbacks. Here, either the computation time is high or the accuracy is low [6, 7]. The low computation accuracy of FEM models arises from the complexity of the calculation and the large number of unknown boundary conditions. Heat convection parameters can vary notably depending on the surface conditions. To address these issues, new approaches focus on modeling the thermo-elastic TCP error using machine learning techniques. An advantage of using machine learning is the lack of the need for a profound knowledge of the complex physical heat transfer and deformation processes. Most research done in this area relies on temperature as input data to the neural network [8–12]. The results achieved using this method are promising. The machine learning techniques determine the thermo-elastic TCP error accurately. GUO ET AL. were able to reduce the TCP error of an inclined bed turning machine from 33 μm to 8 μm using an ant colony algorithm-based back propagation neural network [8]. The downside of the neural networks in the literature is their dependence on error-prone temperature sensors. The sensors need to be installed, maintained and in case of failure, they can influence the TCP correction resulting in machining errors on the workpiece. To address this issue, a model is presented in this paper, that only relies on machine internal data as input by using interaction of the

encoder difference and the thermo-elastic machine error. This correlation is described in the following chapter.

2 Encoder Difference

Most linear machine tool axes are equipped with two position measurement systems. A standard setup of the measurement systems in a machine tool axis is shown in Fig. 1.

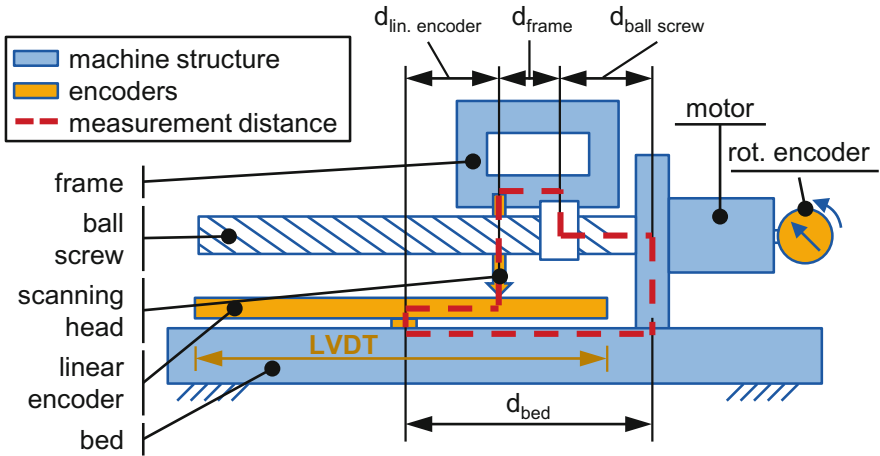


Fig. 1. Schematic view of a linear machine tool axis

Machine tools with rotary motors use a ball screw to drive the axis. The motor that turns the ball screw has a rotary encoder mounted onto the end, which measures the rotary position of the Motor and thus the ball screw. This measurement is used in the position control loop. By counting the rotations of the ball screw, the rotary encoder indirectly measures the axis position. To increase the positioning accuracy of the machine tool, most machine tools also have a linear encoder, which is mounted on the machine bed to measure the axis position directly.

Without error influences the position information of the two measurement systems is redundant. However, due to geometric errors of the ball screw, the measured position from the rotary encoder always deviates from the position measured using the linear encoder. Another influence leading to a deviation between the two position measurements is a thermal expansion of the components close to the axis. If any components marked in Fig. 1 (measurement distance) deform due to thermal influences, this affects the difference between the two encoder values. Thus, the encoder difference measures the thermo-elastic deformation close to the machine axis. Since the deformation directly influences the thermo-elastic TCP error, the encoder difference serves as a promising data point to model the thermo-elastic TCP error. However, no research has been conducted, which investigates the correlation between the encoder difference and the thermo-elastic TCP error. Therefore, in this paper, a model is created that computes the thermo-elastic

TCP error based on the encoder difference. Since it is assumed that the relationship between the two values is complex and difficult to describe analytically, artificial neural networks will be used to model the TCP error.

3 Methods

This paper analyses a model of the thermo-elastic TCP error using the encoder difference as input data. The models are based on data gathered from a five axes double spindle machining center. The following chapter introduces the measurement setup and the load cases used to generate the data. It concludes by presenting the model architectures of the models presented, to model the thermo-elastic TCP error.

3.1 Measurement of Model Inputs and Model Outputs

The previous chapter has shown, that the encoder difference can be used to model the TCP error. However, apart from the encoder difference, there are also other machine internal data, that correlate with the thermo-elastic TCP error. Some of the main heat sources in a machine tool are the motors. The heat generated during operation flows into the machine tool structure. The amount of heat generated is dependent on the motor current. Therefore, there is a dependency between the motor current and the thermo-elastic TCP error. The motor current is available as a machine internal data point and will be used as model input.

The moving axis components are connected by guide rails. Heat is transferred through the guide rails into the adjacent machine components. The position of the TCP defines the position on the guide rail, where the heat flows. Therefore, the machine tool position will also be used as model input.

The environmental temperature also affects the thermo-elastic TCP error. To evaluate the model's ability to compute the environmental influences on the TCP error only based on the encoder difference, two models will be created in this paper. The first network uses the environmental temperature as input data and the second only uses the encoder difference and other machine internal data. The environmental temperature is measured by a single thermal sensor.

A key question of the work is whether the encoder difference can model the TCP error, by giving an indication of the machine structure deformation close to the machine axis. To validate whether the model can compute the deformation of the machine structure, this deformation is measured using LVDT sensors and a rod made from Invar. Invar is a nickel-iron alloy with a low thermal expansion. The location of the measurement is marked as "LVDT" in Fig. 1. By fixing the rod on one end to the machine structure and measuring on the other end with the LVDT sensor, the thermal deformation underneath the rod is measured (compare Fig. 2) [13].

The right side of Fig. 2 shows an ETVE test following ISO 230-3 [14]. The ETVE test is used to measure the thermo-elastic TCP error in x, y, z, a and b direction which are the model outputs. The ETVE test is mounted in the left working area. The thermo-elastic TCP error is therefore measured in this central machine pose.

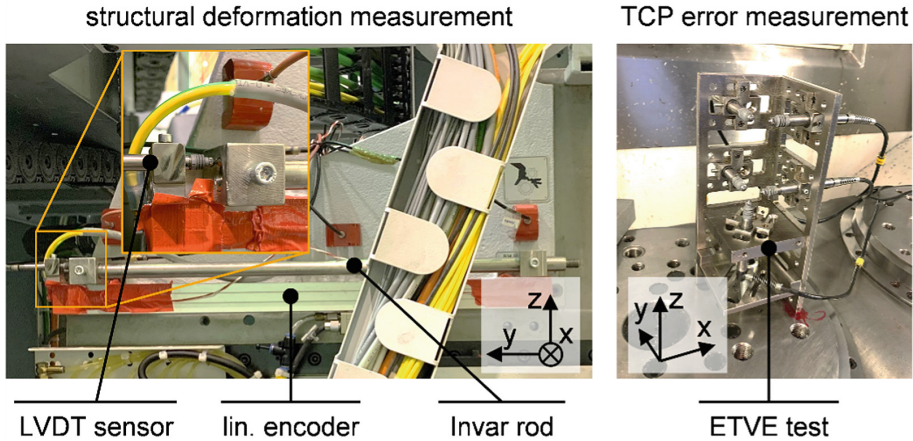


Fig. 2. Measurement setup the measurement of the structural deformation and the TCP error

3.2 Artificial Neural Networks

Since the relationship between the input data and the thermo-elastic TCP error is complex and hard to describe analytically, an artificial neural network is used. For modeling the TCP error, the time dimension is of great importance since a heat flow into the machine structure does not have an immediate effect on the TCP error. However, it influences the TCP error within the next couple of hours. To model this delay between the input and output variables, HOCHREITER ET AL. present a long short-term memory (LSTM) network [15]. This type of network can “memorize” information over time, thus being able to model the aforementioned behavior. In the work of LIU ET AL., a LSTM network has shown good results in modeling the thermo-elastic TCP error [16]. A special form of LSTM networks are bidirectional LSTM networks (BiLSTM). Here, the input data is fed into the network forwards and backwards, which has shown to improve the accuracy of the network on big data sets [17] as well as the computation of the thermo-elastic TCP error [18]. The model architecture, as it is implemented for an LSTM and a BiLSTM network, is shown in Fig. 3.

Since the encoder difference has proven to be an indicator of the current thermo-elastic machine state, it may not be necessary to use the more computation-intensive LSTM architecture. Therefore, a less computation intense backpropagation (BP) network is used as well. The architecture of the utilized BP network is shown in Fig. 4.

For all models the same input data set was used consisting of the encoder difference, the axis speed and axis position and the axis motor current of all three linear axis, resulting in twelve variables. The data is sampled in five minute intervals during the whole experiment resulting in 2,532 for the first and 3,936 data points for the second load case. The number of hidden neurons was optimized for each network using a bayesian optimizer with boundaries of 25 to 250 hidden neurons. The number of hidden neurons as optimized by the bayesian optimizer was typically between 100 and 140 hidden neurons.

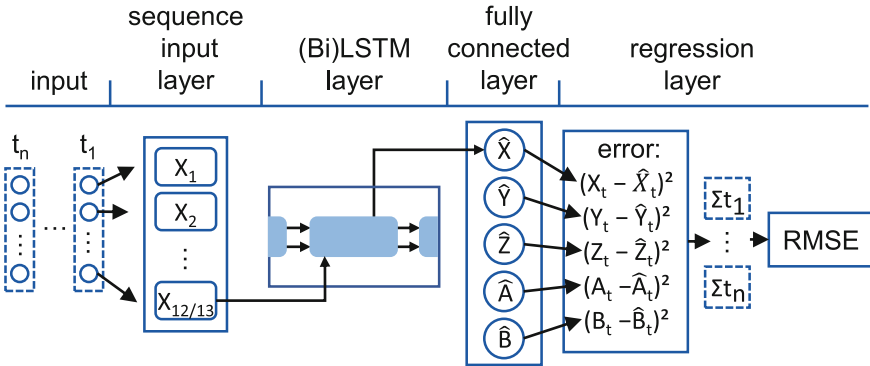


Fig. 3. LSTM and BiLSTM architecture

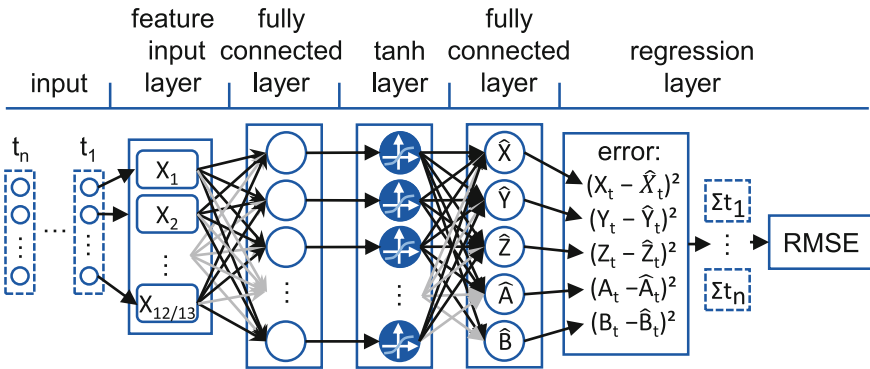


Fig. 4. BP network architecture

3.3 Machine Loads

The models are tested for two different load cases. The first load case consists of straight axes movements. The machine moves on a linear path between two random positions in the working volume at a random speed for a random duration of up to 2 h. After approximately 6 h the machine stops for up to 5 h, thus simulating a cool-down phase due to workpiece setup or machine operator break times. During the whole test, the machine error is measured approximately every 5 min using the ETVE test. All translatory errors $\Delta X, \Delta Y$ and ΔZ as well as the derived rotary errors ΔA and ΔB were evaluated and used as output data for the networks. The test duration was 211 h, where the first 80% were used as training data and the last 20% at the end of each experiment as validation data.

The second load case is supposed to simulate a real production. For this load case, various geometry elements are implemented, representing real geometries that are often used when machining components, like pockets or holes. The timing for the measurement of the TCP error and the cool-down phases, as well as the ratio for training and validation

data, are chosen equal to the ones of the first load case. The total test duration for the second load case was 328 h.

4 Results

In the following chapter, the results of the models are shown for the load cases listed in Sect. 3.3. First, the performance of the proposed neural networks in regards to computing the structural deformation close to the machine axes is evaluated. Then the models will be transferred to model the TCP error. Finally, the benefit of the environmental temperature as model input will be analyzed.

4.1 Structural Deformation Close to the Machine Axes

The basis of the proposed model is the dependency between the encoder difference and the structural deformation close to the machine axis. To validate this dependency, a LSTM, a BiLSTM and a BP network are used to compute the structural deformation based on the machine internal data. Figure 5 shows the result of the computation of the measured structural deformation ΔX_s close to the x axis for the proposed models.

All three models can compute the measured structural deformation accurately. However, the BP network shows the largest deviation from the measurement. This is expected, since the BP network cannot memorize the historic data. The fact that the BP network can compute the deformation fairly accurately shows, that the encoder difference, which is the only input that indicates the current machine state, is a powerful value to compute the structural deformation. This can be derived from the results, since the other input data are not expected to be valuable in a BP network, which is not able to memorize information. Therefore, the results provide a proof of concept, that the encoder difference can be used as input data to derive the thermo-elastic structural deformation and thus the thermo-elastic machine error.

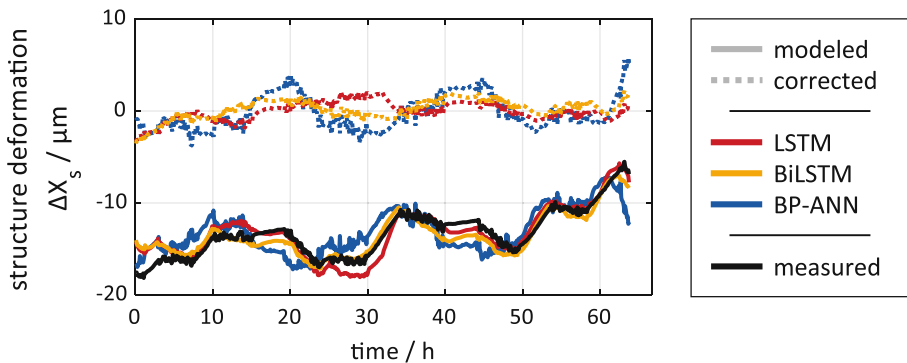


Fig. 5. Measured, modeled, and residual structural deformation close to the x axis for the validation data set

4.2 First Load Case

The correlation between the encoder difference and the TCP displacement in x direction is shown in Fig. 6. For a more comprehensive overview, Table 1 shows the correlation coefficient between the encoder differences of all axes and the TCP displacement and tilt errors. The correlation coefficients are calculated using Eq. 1.

$$\rho(A, B) = \frac{1}{N-1} \sum_{i=1}^N \left(\frac{A_i - \mu_A}{\sigma_A} \right) \left(\frac{B_i - \mu_B}{\sigma_B} \right) \quad (1)$$

where μ_A and σ_A (μ_B and σ_B) are the mean and standard deviation of A (B).

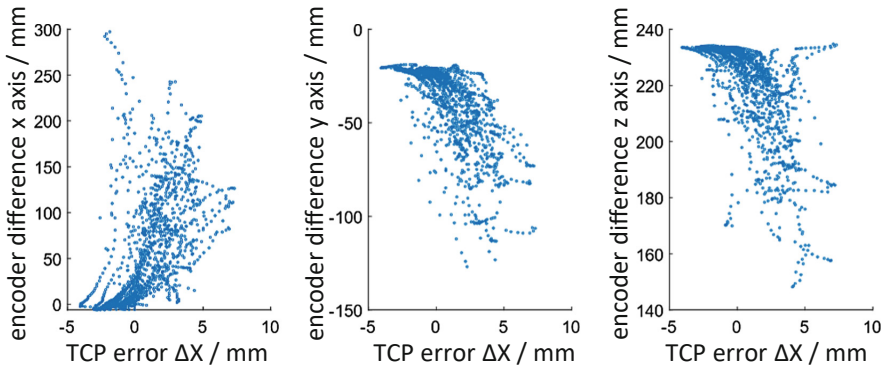


Fig. 6. Correlation between the encoder difference and the TCP displacement in x direction for the first load case

Table 1. Absolute value of the correlation between the encoder difference and the TCP displacement

correlation coefficient		TCP displacement μm			TCP tilt	
		ΔX	ΔY	ΔZ	ΔA	ΔB
encoder difference	X	0.57	0.5	0.42	0.63	0.36
	Y	0.71	0.76	0.51	0.76	0.64
	Z	0.64	0.6	0.23	0.64	0.46

The correlation coefficients range from 0.23, indicating a bad correlation, to up to 0.76, indicating a good correlation. This shows, that there is a relationship between the values, that can be used, to compute the TCP error. However, it can not be modeled with a linear model. Therefore, it was assumed correctly, that a more complex model, such as an artificial neural network is required.

The three neural networks are used to compute the TCP error of the first load case. Figure 7 shows the result using the TCP error in y direction for the validation data.

The figure shows, that all three models can reflect the measured TCP error. However, the BP neural network overshoots the measured displacement in many cases at the peaks.

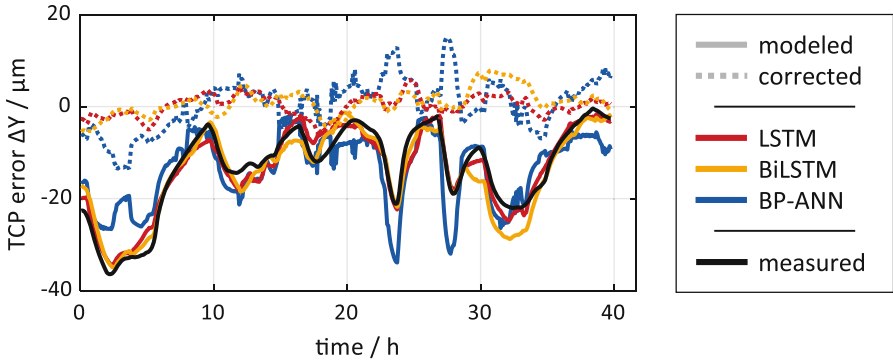


Fig. 7. Measured, modeled and residual TCP error in y direction for the first load case

Furthermore, the BP neural network shows small erratic jumps at some positions. The LSTM and BiLSTM networks show a smooth course, following the TCP displacement. Table 2 summarizes the results by comparing the RMSE and the peak to valley (PV) error which is initially measured with the corresponding model error after correcting the TCP error mathematically, for the individual TCP errors. While an improvement of the RMSE shows that the correction generally improves the TCP error, an improvement in the PV error shows that the largest occurring errors are improved as well.

Table 2. RSME and peak to valley after correction with the corresponding model using only machine internal data input

		RMSE / μm (μrad)					peak to valley error / μm (μrad)				
		X	Y	Z	A	B	X	Y	Z	A	B
measurement		6	266	159	127	429	10	36	16	41	58
w/o env. temp.	LSTM	1	8	15	27	12	5	12	9	23	18
	BiLSTM	3	29	10	63	15	5	17	11	28	20
	BP-ANN	2	32	13	105	31	6	26	17	39	23

The results show, that all models were able to improve the thermo-elastic TCP error. However, the LSTM network shows the best improvement in the average displacement and the error range. The BP network was able to improve the TCP error on average, however, the mentioned overshooting led to a minimal worsening of the TCP error in the z axis, thus making the model invaluable for practical use.

4.3 Second Load Case

The second load case represents a production scenario, as it would occur in standard industrial applications. Since ANN models are in general only valid for the type of load cases that it is trained with, a different correction ability is expected. The model results

for the validation data set are shown in Fig. 8. The model was trained exclusively on the data set of the second load case.

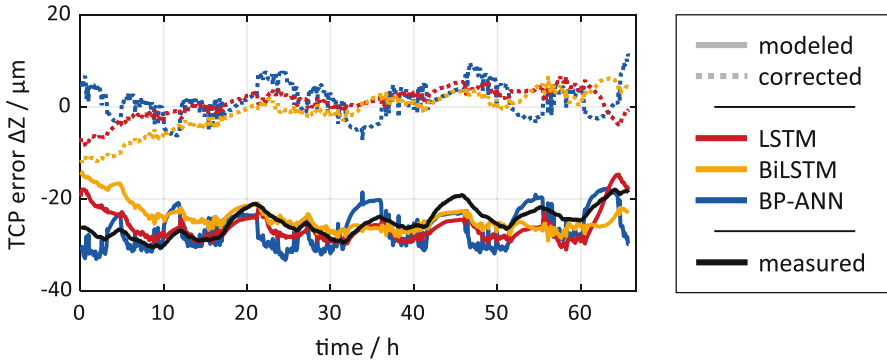


Fig. 8. Measured, modeled and residual TCP error in Y direction for the second load case

The models show similar behavior for the second load case, as they do for the first load case. While the LSTM and BiLSTM networks compute the measured TCP error quite accurately, the BP network on the other hand shows erratic jumps and overshoots for the TCP error peaks. Table 3 summarizes the results by comparing the RMSE and the PV error, which is initially measured with the corresponding model error after correcting the TCP error mathematically.

Table 3. Residual error of the second load case after correction with the corresponding model using only machine internal data or adding the environmental temperature as an input

		RMSE / μm (μrad)					peak to valley error / μm (μrad)				
		X	Y	Z	A	B	X	Y	Z	A	B
measurement		23	5	639	140	72	3	9	13	17	14
w/o env. temp.	LSTM	0	3	55	10	21	3	6	16	16	16
	BiLSTM	2	7	28	44	7	3	5	12	12	16
	BP-ANN	0	5	20	7	8	3	6	15	14	17
with env. temp.	LSTM	0	1	20	9	20	3	5	19	14	12
	BiLSTM	1	3	10	8	13	3	5	15	12	14
	BP-ANN	0	2	14	9	6	3	6	19	14	17

For the second load case, the networks were able to improve the RMSE of the thermo-elastic TCP error as well. An exception is the BiLSTM network for the TCP error in y direction. The reason for this may be the low initial RMSE. The observed RMSE is significantly lower for the models using the environmental temperature as an input parameter. The LSTM network, that does not use the environmental temperature reduces the RMSE on average by 79.8%. By adding the environmental temperature, this

can be improved to 88.1%. This is an indication, that the encoder difference may not be sufficient as input data to model the environmental influence of the thermo-elastic TCP error completely. A solution for this problem may be the usage of the encoder difference at multiple machine poses. The encoder difference at different machine poses is mostly influenced by the thermal elongation of the ball screw. Since the ball screw has a large surface-to-volume ratio, its elongation is heavily influenced by environmental temperature. Therefore, this could improve the network performance regarding external thermal influences.

The second difference between the two load scenarios is the lower improvement of the peak to valley error. For all types of networks at least one error is higher than the initially measured error. The reason for this is the low initial peak to valley error in this load case. The peak to valley errors that are worse after correction only increase the corresponding error by a few micrometers.

5 Conclusion and Further Work

The work presented in the paper shows an approach of modeling the thermo-elastic TCP error using the encoder difference and artificial neural networks. Using two different load scenarios, it is shown, that the encoder difference can be used to model the thermo-elastic structural deformation close to the machine axes, as well as the thermo-elastic TCP error. While the used BP-ANN was able to show good results, the LSTM and BiLSTM networks can compute the TCP error more accurately. Using the LSTM network for the second load case, the RSME of the TCP error was reduced on average by 79.8%.

An even higher improvement of the thermo-elastic TCP error was achieved by adding the environmental temperature gathered by a single thermal sensor. Using this additional input data, the RSME was reduced on average by 88.1% using the LSTM network. This shows that the encoder difference is not able to fully compute the environmental influence on the thermo-elastic error accurately.

To improve the computation of the environmental influence on the machine tool, further work should focus on adding the encoder difference of different machine poses to the machine model. The ball screw is heavily influenced by the environmental temperature due to its large surface area and low volume. Adding the encoder difference at multiple positions along the ball screw could therefore improve the model accuracy under changing environmental conditions.

The presented model can compute the TCP error at a specific machine pose. In order to be more usable in industry applications, it is necessary to extend the model to be able to compute the volumetric machine error. To do this, the measurement system should be adapted to measure the volumetric error.

Funding. The presented findings are funded by the Deutsche Forschungsgemeinschaft (DFG, German Research Foundation) – Project number 174223256.

References

1. Donmez, M.A., Hahn, M.H., Soons, J.A.: A novel cooling system to reduce thermally-induced errors of machine tools. *CIRP Ann.* **56**(1), 521–524 (2007)

2. Gontarz, A., Weiss, L., Wegener, K.: Energy consumption measurement with a multichannel measurement system on a machine tool. In: *Proceedings of International Conference on Innovative Technologies*, pp. 499–502 (2010)
3. Wennemer, M.: *Methode zur messtechnischen Analyse und Charakterisierung volumetrischer thermo-elastischer Verlagerungen von Werkzeugmaschinen*. Apprimus Verlag, Aachen (2018)
4. Galant, A., Beitelschmidt, M., Großmann, K.: Fast high-resolution FE-based simulation of thermo-elastic behaviour of machine tool structures. *Proc. CIRP* **46**, 627–630 (2016)
5. Brecher, C., Ihlenfeldt, S., Neus, S., Steinert, A., Galant, A.: Thermal condition monitoring of a motorized milling spindle. *Prod. Eng. Res. Devel.* **13**(5), 539–546 (2019)
6. Turek, P., Jedrzejewski, J., Modrzycki, W.: Methods of machine tool error compensation. *J. Mach. Eng.* (10) (2010)
7. Brecher, C., Neus, S., Dehn, M.: Efficient FE-modelling of the transient thermo-elastic machine behaviour of 5-axes machine tools thermal issues. In: *Proceedings Cover 2020. Special Interest Group Meeting: Thermal Issues: Laboratory for Machine Tools and Production Engineering (WZL) of RWTH Aachen, and Fraunhofer Institute for Production Technology IPT, DE, 26th–27th February 2020, Aachen, Germany*, pp. 148–149 (2020)
8. Guo, Q., Yang, J., Wu, H.: Application of ACO-BPN to thermal error modeling of NC machine tool. *Int. J. Adv. Manuf. Technol.* **50**(5–8), 667–675 (2010)
9. Ramesh, R., Mannan, M.A., Poo, A.N., Keerthi, S.S.: Thermal error measurement and modelling in machine tools. Part II. Hybrid Bayesian network—support vector machine model. *Int. J. Mach. Tools Manuf.* **43**(4), 405–419 (2003)
10. Srinivasa, N., Ziegert, J.C.: Automated measurement and compensation of thermally induced error maps in machine tools. *Precis. Eng.* (19), 112–132 (1996)
11. Wissmann, A.: *Steuerungsinterne Korrektur thermisch bedingter Strukturverformungen von Bearbeitungszentren*. Apprimus Verlag, Aachen (2014)
12. Yang, H., Ni, J.: Adaptive model estimation of machine-tool thermal errors based on recursive dynamic modeling strategy. *Int. J. Mach. Tools Manuf.* **45**(1), 1–11 (2005)
13. Baum, C., Brecher, C., Klatte, M., Lee, T.H., Tzanetos, F.: Thermally induced volumetric error compensation by means of integral deformation sensors. *Proc. CIRP* **72**, 1148–1153 (2018)
14. ISO: Test code for machine tools: Part 3: Determination of thermal effects (230-3). Schweiz (2007). Accessed 8 July 2020
15. Hochreiter, S., Schmidhuber, J.: Long short-term memory. *Neural Comput.* **9**(8), 1735–1780 (1997)
16. Liu, J., Ma, C., Gui, H., Wang, S.: Thermally-induced error compensation of spindle system based on long short term memory neural networks. *Appl. Soft Comput.* **102**, 107094 (2021)
17. Siami-Namini, S., Tavakoli, N., Namin, A.S.: The performance of LSTM and BiLSTM in forecasting time series. In: *2019 IEEE International Conference on Big Data (Big Data) (Editor: IEEE International Conference on Computing, Control and Industrial Engineering)*, 09–12 December 2019, pp. 3285–3292. IEEE (2019)
18. Liu, P.-L., Du, Z.-C., Li, H.-M., Deng, M., Feng, X.-B., Yang, J.-G.: Thermal error modeling based on BiLSTM deep learning for CNC machine tool. *Adv. Manuf.* **9**(2), 235–249 (2021). <https://doi.org/10.1007/s40436-020-00342-x>

Open Access This chapter is licensed under the terms of the Creative Commons Attribution 4.0 International License (<http://creativecommons.org/licenses/by/4.0/>), which permits use, sharing, adaptation, distribution and reproduction in any medium or format, as long as you give appropriate credit to the original author(s) and the source, provide a link to the Creative Commons license and indicate if changes were made.

The images or other third party material in this chapter are included in the chapter's Creative Commons license, unless indicated otherwise in a credit line to the material. If material is not included in the chapter's Creative Commons license and your intended use is not permitted by statutory regulation or exceeds the permitted use, you will need to obtain permission directly from the copyright holder.





Model Order Reduction Strategies for the Computation of Compact Machine Tool Models

Quirin Aumann¹, Peter Benner^{1,2}, Jens Saak^{1,2}, and Julia Vettermann¹(✉)

¹ Chemnitz University of Technology,
Reichenhainer Str. 41, 09126 Chemnitz, Germany
julia.vettermann@mathematik.tu-chemnitz.de

² Max Planck Institute for Dynamics of Complex Technical Systems,
Sandtorstr. 1, 39106 Magdeburg, Germany

Abstract. The deviation of the tool center point (TCP) of a machine tool from its desired location needs to be assessed correctly to ensure an accurate and safe operation of the machine. A major source of TCP deviation are thermal loads, which are constantly changing during operation. Numerical simulation models help predicting these loads, but are typically large and expensive to solve. Especially in (real-time feedback) control settings, but also to ensure an efficient design phase of machine tools, it is inevitable to use compact reduced-order surrogate models which approximate the behavior of the original system but are much less computationally expensive to evaluate. Model order reduction (MOR) methods generate computationally efficient surrogates. Classic intrusive methods require explicit access to the assembled system matrices. However, commercial software packages, which are typically used for the design of machine tools, do not always allow an unrestricted access to the required matrices. Non-intrusive data-driven methods compute surrogates requiring only input and output data of a dynamical system and are therefore independent of the discretization method. We evaluate the performance of such data-driven approaches to compute cheap-to-evaluate surrogate models of machine tools and compare their efficacy to intrusive MOR strategies. A focus is put on modeling the machine tool via individual substructures, which can be reduced independently of each other.

Keywords: Model order reduction · Loewner framework · Balanced truncation · Rational interpolation · Machine tools

1 Introduction

Model order reduction (MOR) plays an important role in the energy efficient correction of thermally induced errors of machine tools during the production process [10, 18]. Therefore, compact simulation models for fast computations are required for the efficient operation of machine tools enabling, e.g., online correction of the thermally induced displacement of the tool center point (TCP), predictive maintenance, or online parameter estimation. Such models are also an enabler-technology for digital twins of machine tools [12].

Machine tools are complex technical systems consisting of a number of interconnected machine components, which can move relative to each other. In the following, these components will be referred to as subassemblies. The thermal behavior of the machine and its subassemblies is often modeled using the finite element method (FEM). Due to the need to resolve also small geometrical features of the machine tool, the number of degrees of freedom in such numerical models is typically high, and methods to reduce the computational complexity of solving the associated systems of equations are required. System-theoretic MOR methods have proven to be able to reduce these computational costs by computing surrogate models approximating the input/output behavior of the original model but having a much smaller size [2]. These methods have also been successfully applied to machine tool models [11, 14, 18]. They often show a better performance compared to modal methods [5, 16], which are not recommended for the reduction of thermal problems [4, 8].

An alternative to system-theoretic or modal methods are data-driven procedures. They construct surrogate models approximating the input/output behavior of the original model using snapshot data, e.g., evaluations of its transfer function. Data-driven methods can also be referred to as non-intrusive methods, because unlike intrusive system-theoretic or modal MOR methods, they do not require access to the matrices describing the numerical model. Especially when closed-source or proprietary finite element software solutions are employed, as it is often the case in industrial applications, these matrices are difficult or inconvenient to obtain and intrusive MOR methods might not always fit the design workflow of machine tools. However, the snapshot data required for data-driven MOR methods can be obtained from standard finite element software by performing, e.g., a frequency sweep analysis.

An efficient modeling of the time-varying coupling conditions between subassemblies is crucial for a successful simulation of different work processes. Using an approach originally presented by Hernández-Becerro et al. [11], it is possible to precompute parts of the coupling terms required to model the thermal flow between subassemblies. Depending on the position of the coupling at the current simulation time, the coupling condition can be assembled by a linear combination of the precomputed values. As no further modifications of the numerical model are required, the same numerical model can be used to model any relative movements between subassemblies. The precomputed coupling terms can be added as additional inputs and outputs to the original system description, such that the coupling can also be realized in the reduced space.

In this contribution, we show how a data-driven MOR strategy based on the Loewner framework [15] can be used to obtain reduced-order models of machine tool systems consisting of multiple subassemblies. Surrogate models computed by the Loewner framework can be expressed as state space systems. Therefore they can easily be integrated into existing modeling workflows. We also evaluate the impact of the high number of system inputs and outputs added by the coupling conditions on the approximation quality and reduction efficacy. The performance of the resulting surrogate models is compared to reduced-order models computed

using balanced truncation, an intrusive MOR method. Balanced truncation is especially suited for the reduction of thermal problems as it shows a global error behavior and an a priori error bound can be computed efficiently [1].

This contribution is structured as follows: In Sect. 2 we show some modeling aspects of machine tools. In Sect. 3 we discuss suitable intrusive and non-intrusive MOR techniques. Numerical investigations including a comparison of different reduction methods for a simplified 3-axis machine tool model are described in Sect. 4. A summary of our findings in Sect. 5 concludes the contribution.

2 Modeling of Machine Tools

The thermal behavior of a body of homogeneous and temporally constant material can be expressed by a partial differential equation (PDE) for the temperature field $T(t, \delta)$ at time t and location δ as

$$\rho c_p \frac{\partial}{\partial t} T(t, \delta) - \Delta \lambda T(t, \delta) = \dot{q}(t, \delta). \quad (1)$$

The external thermal load is given by \dot{q} and the material is characterized by its density ρ , heat capacity c_p , and conductivity λ . The dot defines a derivative in time and $\Delta = \nabla \cdot \nabla$ is the Laplace operator.

2.1 System-Theoretic Approach

Discretizing this PDE in space with, e.g., the finite element method allows to formulate the system in a state-space representation

$$\Sigma: \begin{cases} \mathbf{E}\dot{\mathbf{x}}(t) = \mathbf{A}\mathbf{x} + \mathbf{B}\mathbf{u}(t), \\ \mathbf{y}(t) = \mathbf{C}\mathbf{x}, \end{cases} \quad (2)$$

with capacity and conductivity matrices $\mathbf{E}, \mathbf{A} \in \mathbb{R}^{n \times n}$, input and output mappings $\mathbf{B} \in \mathbb{R}^{n \times m}$, $\mathbf{C} \in \mathbb{R}^{p \times n}$, states $\mathbf{x} \in \mathbb{R}^n$, inputs $\mathbf{u} \in \mathbb{R}^m$, and outputs $\mathbf{y} \in \mathbb{R}^p$. Many MOR methods require the original system to be described in frequency domain. This transformation is performed using the Laplace transform and setting the Laplace constant to $s = i\omega$, where ω is the excitation frequency. An important analysis tool of frequency domain systems is the transfer function, which depicts the input to output mapping of the system. For a thermal system in state-space form (2), the transfer function is given by

$$\mathbf{H}(s) = \mathbf{C}(s\mathbf{E} - \mathbf{A})^{-1}\mathbf{B}. \quad (3)$$

2.2 Efficient Modeling of Time-Varying Thermal Couplings

Machine tools are composed of different subassemblies which can move relative to each other. This results in time-varying coupling conditions between the subassemblies, which have to be represented efficiently in the modeling process,

as a re-meshing of the complete model after each relative movement is not feasible. Another benefit of modeling the subassemblies independent of each other is that individual parts can be exchanged during the design process without affecting the other parts of the machine.

In the following, the heat transfer between machine subassemblies is modeled with bushing interface conditions, a type of multi point constraint. Here, the heat flux \dot{q} between two coupled boundaries is defined by relating the average temperature at the boundaries $\bar{\theta}_1, \bar{\theta}_2$ and scaling it with the heat transfer coefficient h :

$$\dot{q} = h (\bar{\theta}_1 - \bar{\theta}_2). \quad (4)$$

The benefit of this approach is that it is independent of the discretization of the boundaries and that no matching grids are required. It should be noted that bushing interface conditions are not accurate for interfaces with high temperature gradients due to the averaging performed in (4). Many coupling interfaces in machine tool models, for example the interaction between a rail and a carriage, are relatively small and have a rather uniform temperature distribution, so bushing conditions can be applied efficiently in this setting [10].

In order to realize an efficient time-varying thermal coupling of the subassemblies, we use an approach by Hernández-Becerro et al. [11]. This strategy precomputes general boundary terms, which are valid for any relative position of the two subassemblies, and makes a re-evaluation of the coupling terms for changing positions unnecessary. The moving interface is defined by a weighting function $w(d, d_c)$ on the boundaries with the location of the respective mesh node on the boundary d and the center position of the interface d_c . An interaction between the boundaries only happens for $w(d, d_c) \neq 0$. The gist of the approach is to separate the variables d and d_c , such that all contributions depending on d can be precomputed. This is done by approximating the weighting function by a Fourier series

$$w(d, d_c) = a_0 + \sum_{k=1}^{n_h} a_k(d_c) \cos(2\pi kd) + \sum_{k=1}^{n_h} b_k(d_c) \sin(2\pi kd),$$

and precomputing the terms which are not depending on d_c for all nodes on the boundary. In practice, this can be achieved by applying corresponding loads on the boundary. A vector \mathbf{b} defining the weighted average over the corresponding boundary, given the location of the coupling d_c , can then be formed by a linear combination of the precomputed vector quantities and some scalar factors:

$$\mathbf{b}(d_c) = \mathbf{b}_0 + \sum_{k=1}^{n_h} a_k(d_c) \mathbf{b}_{k,\cos} + \sum_{k=1}^{n_h} b_k(d_c) \mathbf{b}_{k,\sin}.$$

This vector \mathbf{b} acts as input and output in the system-theoretic formulation of the thermal system (2), as, on the one hand, it averages the temperature on the boundary according to the weighting function, on the other hand, it maps the resulting heat flux from (4) back onto the boundary.

3 Model Order Reduction for Machine Tools

The computational cost for evaluating numerical models of machine tools (2) and (3) is often very high and thus may hinder an efficient design phase and prohibit their direct use for online control. A large part of the computational complexity roots in the need for (repeated) decompositions of matrices of order n , which is the number of degrees of freedom of the model. In practical applications, n can be very large, as also complex geometric features need to be resolved by a fine mesh. MOR methods find a surrogate model

$$\widehat{\Sigma}: \begin{cases} \widehat{\mathbf{E}}\dot{\widehat{\mathbf{x}}}(t) = \widehat{\mathbf{A}}\widehat{\mathbf{x}} + \widehat{\mathbf{B}}\mathbf{u}(t), \\ \widehat{\mathbf{y}}(t) = \widehat{\mathbf{C}}\widehat{\mathbf{x}}, \end{cases} \quad (5)$$

with the reduced matrices $\widehat{\mathbf{E}}, \widehat{\mathbf{A}} \in \mathbb{R}^{r \times r}$, $\widehat{\mathbf{B}} \in \mathbb{R}^{r \times m}$, $\widehat{\mathbf{C}} \in \mathbb{R}^{p \times r}$ and the states in reduced space $\widehat{\mathbf{x}} \in \mathbb{R}^r$. The model (5) can serve as a surrogate for the original model (2), if the reduced-order model's output is up to a specific tolerance ε similar to the original output, i.e.

$$\|\mathbf{y} - \widehat{\mathbf{y}}\| \leq \varepsilon \|\mathbf{u}\|,$$

under an appropriate norm $\|\cdot\|$ and for all feasible inputs \mathbf{u} . The transfer function of the reduced-order model is given by

$$\widehat{\mathbf{H}}(s) = \widehat{\mathbf{C}} \left(s\widehat{\mathbf{E}} - \widehat{\mathbf{A}} \right)^{-1} \widehat{\mathbf{B}}. \quad (6)$$

The underlying reduced-order model is an appropriate surrogate, if

$$\left\| \mathbf{H} - \widehat{\mathbf{H}} \right\| \leq \varepsilon,$$

as for appropriately chosen norms,

$$\|\mathbf{y} - \widehat{\mathbf{y}}\| \leq \left\| \mathbf{H} - \widehat{\mathbf{H}} \right\| \cdot \|\mathbf{u}\|.$$

Among other methods, the reduced quantities in (5) and (6) can be obtained from projecting the original system matrices onto a lower dimensional subspace, which contains the sought after solution [2]. This subspace $\mathcal{V} \subset \mathbb{C}^n$ and the corresponding test space $\mathcal{W} \subset \mathbb{C}^n$ are spanned by two truncation matrices $\mathbf{V}, \mathbf{W} \in \mathbb{C}^{n \times r}$, respectively. The reduced-order quantities can then be computed by

$$\widehat{\mathbf{E}} = \mathbf{W}^H \mathbf{E} \mathbf{V}, \quad \widehat{\mathbf{A}} = \mathbf{W}^H \mathbf{A} \mathbf{V}, \quad \widehat{\mathbf{B}} = \mathbf{W}^H \mathbf{B}, \quad \widehat{\mathbf{C}} = \mathbf{C} \mathbf{V}. \quad (7)$$

Note, that it is often convenient to choose real-valued truncation matrices \mathbf{V}, \mathbf{W} to preserve the realness of the original model also in reduced space.

3.1 Intrusive MOR with Balanced Truncation

Balanced truncation (BT) is a widely used projection-based MOR method. Balancing in this context means to transform the system to a form where reachability and observability of the system states are equivalent concepts. This transformation does not influence the input/output behavior, as it leads to a different realization of the same system. States which are at the same time hard to reach and yield little observation energy can be identified given such representation. Truncating these states reduces the size of the system while the input/output behavior is not greatly influenced. Balanced truncation also offers a computable a priori error bound relating the energy of the truncated states to the approximation error of the surrogate model [1]. The truncation matrices \mathbf{V} , \mathbf{W} for (7) are computed by performing a singular value decomposition (SVD) of the system Gramians and truncating all singular vectors whose corresponding singular values do not contribute considerably to the truncation error. Solving the dual Lyapunov equations

$$\begin{aligned} \mathbf{A}\mathbf{P}\mathbf{E}^\top + \mathbf{E}\mathbf{P}\mathbf{A}^\top + \mathbf{B}\mathbf{B}^\top &= 0 \\ \mathbf{A}^\top\mathbf{Q}\mathbf{E} + \mathbf{E}^\top\mathbf{Q}\mathbf{A} + \mathbf{C}^\top\mathbf{C} &= 0 \end{aligned} \quad (8)$$

yields the required reachability Gramian \mathbf{P} and observability Gramian $\mathbf{E}^\top\mathbf{Q}\mathbf{E}$. The system matrices in (8) are often large and sparse. In this case, there is a variety of established and efficient solution algorithms, which compute low-rank approximations of the Gramians, such that $\mathbf{P} \approx \mathbf{Z}_P\mathbf{Z}_P^\top$ and $\mathbf{E}^\top\mathbf{Q}\mathbf{E} \approx \mathbf{Z}_Q\mathbf{Z}_Q^\top$; see, e.g., [6]. If the states corresponding to the r largest singular values $\Sigma_1 = \text{diag}(\sigma_1, \dots, \sigma_r)$ of the SVD

$$\mathbf{S}\Sigma\mathbf{T} = [\mathbf{S}_1\mathbf{S}_2] \begin{bmatrix} \Sigma_1 \\ \Sigma_2 \end{bmatrix} [\mathbf{T}_1\mathbf{T}_2]^\top = \mathbf{Z}_Q^\top\mathbf{Z}_P$$

should be preserved in the reduced-order model, the corresponding truncation matrices are formed from the left and right singular vectors as

$$\mathbf{V} = \mathbf{Z}_P\mathbf{T}_1\Sigma_1^{-\frac{1}{2}}, \quad \mathbf{W} = \mathbf{Z}_Q\mathbf{S}_1\Sigma_1^{-\frac{1}{2}}.$$

Balanced truncation preserves the stability of the original system automatically.

3.2 Non-intrusive MOR with the Loewner Framework

The computation of system Gramians or their low-rank factors requires direct access to the original system matrices. However, these matrices are often not readily available or inconvenient to obtain explicitly. The Loewner framework [15] uses solely transfer function measurements or evaluations to find a surrogate model, which interpolates the transfer function of the original system (3), and provides a realization of this interpolant as a state-space system. The general procedure is shortly summarized in the following.

Given N measurements $\mathbf{H}_k \in \mathbb{C}^{p \times m}$, $k = 1, \dots, N$ of the transfer function at some locations $s_k \in \mathbb{C}$, the data is partitioned into two disjoint sets

$$\begin{cases} (\lambda_i, \mathbf{r}_i, \mathbf{w}_i), \text{ where } \lambda_i = s_i, \mathbf{w}_i = \mathbf{H}_i \mathbf{r}_i, i = \{1, \dots, \rho\}, \\ (\mu_j, \mathbf{l}_j, \mathbf{v}_j), \text{ where } \mu_j = s_{\rho+j}, \mathbf{v}_j^H = \mathbf{l}_j^H \mathbf{H}_{\rho+j}, j = \{1, \dots, \nu\}, \end{cases}$$

with $N = \rho + \nu$ and right and left tangential directions $\mathbf{r}_i, \mathbf{l}_j$. For numerical reasons it is often beneficial to partition the data in an alternating way. The partitioned data is now arranged in the Loewner and shifted Loewner matrices \mathbb{L} and \mathbb{L}_σ given by

$$\mathbb{L} = \begin{bmatrix} \frac{\mathbf{v}_1 \mathbf{r}_1 - \mathbf{l}_1 \mathbf{w}_1}{\mu_1 - \lambda_1} & \dots & \frac{\mathbf{v}_1 \mathbf{r}_\rho - \mathbf{l}_1 \mathbf{w}_\rho}{\mu_1 - \lambda_\rho} \\ \vdots & \ddots & \vdots \\ \frac{\mathbf{v}_\nu \mathbf{r}_1 - \mathbf{l}_\nu \mathbf{w}_1}{\mu_\nu - \lambda_1} & \dots & \frac{\mathbf{v}_\nu \mathbf{r}_\rho - \mathbf{l}_\nu \mathbf{w}_\rho}{\mu_\nu - \lambda_\rho} \end{bmatrix},$$

$$\mathbb{L}_\sigma = \begin{bmatrix} \frac{\mu_1 \mathbf{v}_1 \mathbf{r}_1 - \lambda_1 \mathbf{l}_1 \mathbf{w}_1}{\mu_1 - \lambda_1} & \dots & \frac{\mu_1 \mathbf{v}_1 \mathbf{r}_\rho - \lambda_\rho \mathbf{l}_1 \mathbf{w}_\rho}{\mu_1 - \lambda_\rho} \\ \vdots & \ddots & \vdots \\ \frac{\mu_\nu \mathbf{v}_\nu \mathbf{r}_1 - \lambda_1 \mathbf{l}_\nu \mathbf{w}_1}{\mu_\nu - \lambda_1} & \dots & \frac{\mu_\nu \mathbf{v}_\nu \mathbf{r}_\rho - \lambda_\rho \mathbf{l}_\nu \mathbf{w}_\rho}{\mu_\nu - \lambda_\rho} \end{bmatrix}.$$

If the matrix pencil $(\mathbb{L}_\sigma, \mathbb{L})$ is regular, $\mathbf{H}_r(z) = \mathbf{Y} (\mathbb{L}_\sigma - z\mathbb{L})^{-1} \mathbf{X}$ tangentially interpolates the given data, such that $\mathbf{H}_r(\lambda_i) \mathbf{r}_i = \mathbf{w}_i$, $\mathbf{l}_j^H \mathbf{H}_r(\mu_j) = \mathbf{v}_j^H$. A state space realization of the surrogate is thus given by

$$\begin{aligned} \mathbf{E}_\mathbb{L} &= -\mathbb{L}, \quad \mathbf{A}_\mathbb{L} = -\mathbb{L}_\sigma, \\ \mathbf{B}_\mathbb{L} &= \mathbf{X} = [\mathbf{v}_1^H, \dots, \mathbf{v}_\nu^H]^H, \quad \mathbf{C}_\mathbb{L} = \mathbf{Y} = [\mathbf{w}_1, \dots, \mathbf{w}_\rho]. \end{aligned} \tag{9}$$

The dimension of this system can further be reduced by projection. The required truncation matrices \mathbf{V}, \mathbf{W} are concatenations of the right and left singular vectors obtained from an SVD of \mathbb{L} . Truncating the matrices of singular vectors after r columns and projecting the Loewner realization (9) using (7) yields a reduced-order model of order r . Note, that it is also possible to use uncompressed transfer function data, i.e. omitting the tangential directions. This results in Loewner matrices with a block structure, as every transfer function evaluation has dimension $p \times m$. However, if the system that shall be approximated has a high number of inputs and outputs, the Loewner matrices grow fast. In such cases the resulting surrogate may be either too large for an efficient use or the SVD may be not computationally feasible anymore. Therefore, the compression of the original via tangential directions is often a more efficient approach, although it involves a loss of information for the reduced-order model. Other interpolation-based MOR methods employ similar strategies [1].

As the resulting surrogates should be used in time domain, they have to preserve the realness and stability of the original model. Realness can be enforced

in the Loewner framework by adding also the complex conjugates of the transfer function measurements to the database. In practice, this is performed by pre- and post-multiplying the Loewner and shifted Loewner matrices by block-diagonal matrices

$$\mathbf{J} = \mathbf{I} \otimes \left(\frac{1}{\sqrt{2}} \begin{bmatrix} 1 & -i \\ 1 & i \end{bmatrix} \right),$$

where \mathbf{I} is an identity matrix of appropriate size. \mathbf{X} , \mathbf{Y} in (9) have to be modified accordingly [3].

Realizations computed with the Loewner framework do not automatically preserve the stability of the original model, so the surrogate computed with the Loewner framework has to be post-processed. Different strategies for ensuring the stability of the Loewner surrogate can be identified: (i) truncating the unstable part of the model, (ii) flipping the unstable part, or (iii) computing a stable approximation to the original interpolant that is optimal regarding an appropriate norm [9,13]. In the following, we will use the first strategy and truncate all states of the identified system (9) which correspond to unstable eigenvalues, i.e. eigenvalues with a positive real part. For this, the unstable and infinite parts of the system need to be identified. This can be achieved by finding transformation matrices \mathbf{T}_L , \mathbf{T}_R , such that

$$\mathbf{T}_L (\lambda \mathbf{E}_L - \mathbf{A}_L) \mathbf{T}_R = \lambda \begin{bmatrix} \mathbf{E}_s & & \\ & \mathbf{E}_u & \\ & & \mathbf{E}_\infty \end{bmatrix} - \begin{bmatrix} \mathbf{A}_s & & \\ & \mathbf{A}_u & \\ & & \mathbf{A}_\infty \end{bmatrix}.$$

Here, subscript \cdot_s stands for the stable, \cdot_u for the unstable, and \cdot_∞ for the infinite part of the system. In practice, such transformation can be achieved with the help of the matrix disk and sign functions; see, e.g., [7]. Using the ingredients summarized above, it is possible to compute real and stable realizations of systems, from which only transfer function data are available.

4 Numerical Experiments

For the following numerical experiments, we consider a model of a general 3-axis machine tool. The machine consists of four subassemblies: the machine bed and three sliders for independent movements in x , y , and z -direction. The geometry has been described in [17]; a sketch of the geometry is given in Fig. 1. The differential equation for the temperature field acting on the machine (1) is discretized with a finite element method using the MATLAB Partial Differential Equation Toolbox. As only a movement in y -direction is modeled in the following experiments, two subassemblies are formed: one consisting of the machine bed and the x -slider, referred to as **A1** in the following, and **A2** consisting of the sliders for the y and z -directions. The guide rail along which **A2** is moving measures 1400 mm. The resulting numerical models have orders of $n_{A1} = 22\,799$ and $n_{A2} = 18\,685$, respectively. The system is subject to two external heat fluxes, one at the TCP location and one at the top of the workpiece. Additionally, we apply

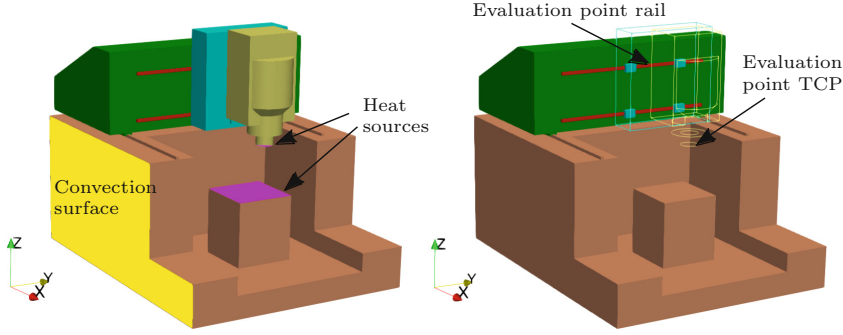


Fig. 1. Left: Sketch of the 3-axis machine tool model consisting of machine bed (brown) and three sliders (x -direction: dark green; y -direction: cyan; z -direction: yellow). The guide rail for the y -slider is marked in red. Right: Subassembly A2 is visualized as wire frame. The guide cars attached to A2 and moving along the guide rail are drawn solid and marked in cyan.

heat fluxes at the guide cars of A2 to model heat resulting from friction (cf. Fig. 1). Exchange of heat between the subassemblies due to radiation is neglected. Energy is dissipated by convection boundary conditions applied to the outer walls of the machine bed.

The subassemblies are coupled via four guide cars, two moving along the upper and lower rail of A1 each. This coupling is realized with the method described in Sect. 2.2 and adds 44 inputs and outputs to A1, respectively 4 inputs and outputs to A2. Only one input/output per location is required for A2, as the coupling location only moves along the rail and is stationary at the coupling points on the y -slider. These additional inputs and outputs are equivalent in original space. However, this is not the case in reduced space, as often $\mathbf{V} \neq \mathbf{W}$. Therefore it is important to use the reduced outputs $\hat{\mathbf{C}} = \mathbf{C}\mathbf{V}$ to obtain the average temperatures θ_1, θ_2 in (4) and the reduced inputs $\hat{\mathbf{B}} = \mathbf{W}^H\mathbf{B}$ to apply the resulting load \dot{q} to the interface. The slider moves for 600 s with constant velocity along the guide in y -direction and changes direction when one end of the rail is reached. After this time, the machine stops and enters a cooling phase. Here, the external heat flux is set to zero. The movement profile of subassembly A2 is given in Fig. 2. We evaluate the temperature at the TCP and at a point located in the middle of the upper rail of A1 during the complete work process.

Surrogate models for an efficient time simulation of the work process are computed using balanced truncation and the Loewner framework as described in Sect. 3. For the Loewner framework, we first compute samples of the transfer function at 200 logarithmically distributed frequencies between $\omega = [1 \cdot 10^{-6}, 1 \cdot 10^{-2}] \text{ rad s}^{-1}$ for both subassemblies. The main dynamics of both systems can be observed in this frequency range and the sampling rate ensures a sufficiently high resolution to capture all important features of the transfer functions. The samples are post-processed to obtain real-valued Loewner and shifted Loewner matrices as described in Sect. 3.2. Their normalized singular

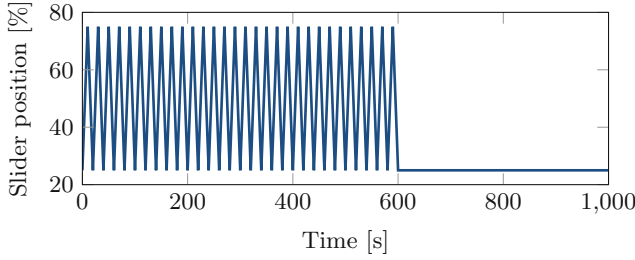


Fig. 2. Movement of subassembly A2 along the rails on A1. The position of the midpoint of A2 is plotted in relation to the total length of the rail.

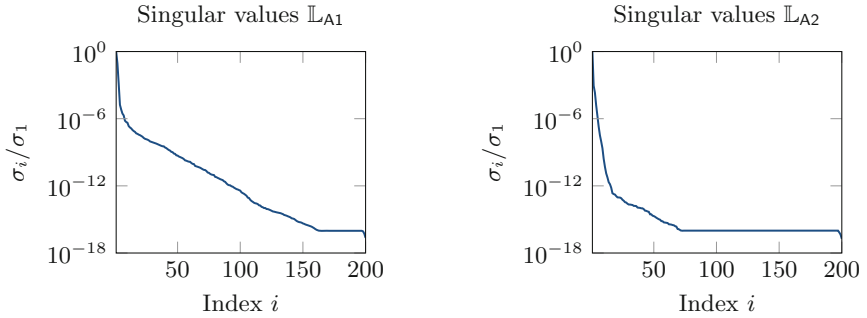


Fig. 3. Singular values of the Loewner matrices \mathbb{L} for A1 (left) and A2 (right).

values are given in Fig. 3 and show a rapid decay for A2, but a slower decay for A1. This means that a larger reduced-order model is required to approximate A1 accurately. The reason for this is the higher number of inputs and outputs of A1 compared to A2.

We truncate all states of the surrogate model which correspond to singular values $\sigma_i < 1 \cdot 10^{-12}$ and remove unstable poles. This leads to stable and real-valued surrogates with order $r_{A1} = 92$ and $r_{A2} = 14$, respectively. The sizes of the reduced-order models computed from balanced truncation are set to the same values to allow a fair comparison. The time simulation results for both surrogate models as well as the reference solution obtained from the full-order model and the corresponding errors relative to the solution of the full-order model are given in Figs. 4 and 5. At the TCP the temperature rises smoothly, as a constant heat flux is applied here until $t = 600$ s. After this, the machine cools slowly. The effect of the moving interface is clearly visible in Fig. 5, where the temperature at the midpoint of the upper rail in the subassembly A1 is evaluated. As the heat sources are located on the guide cars on A2, which are constantly moving along the rail, the increase in temperature is oscillating, depending on where the cars are located. Both surrogates approximate the full order model with acceptable errors. It should be noted that also the dynamic behavior of the moving interface can be approximated well by the reduced-order models.

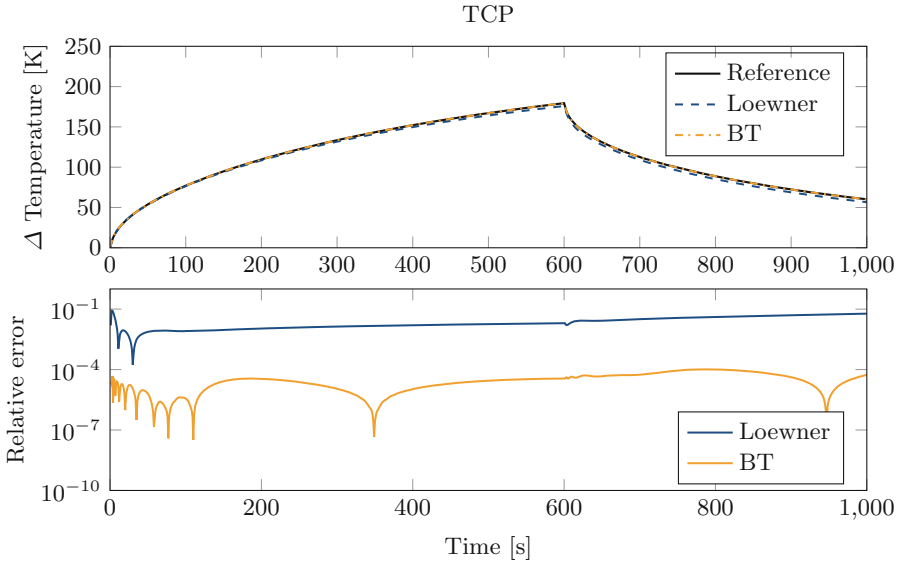


Fig. 4. Temperature change at TCP during the simulated work process. Time responses of the reference full order model and the surrogate models computed by the Loewner framework and balanced truncation as well as the corresponding relative errors.

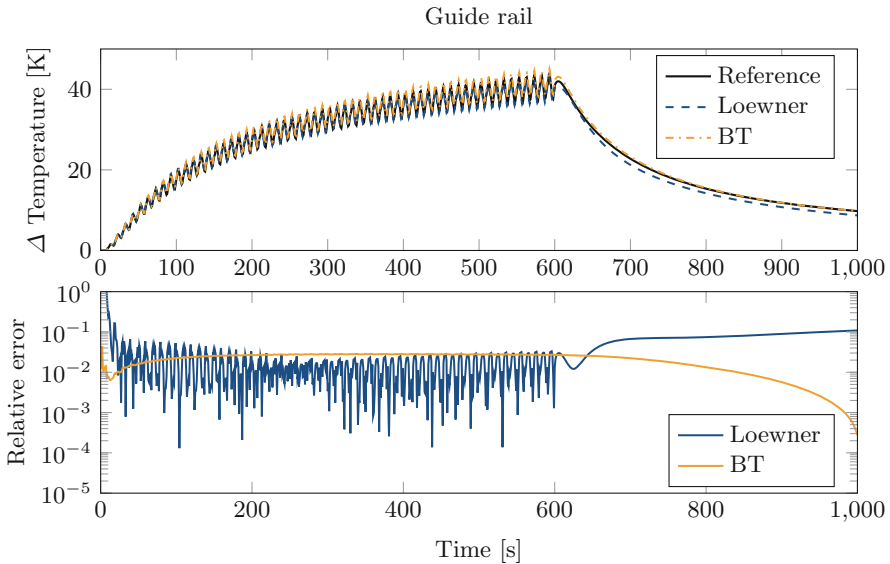


Fig. 5. Temperature change at the midpoint of the upper rail in A1 during the simulated work process. Time responses of the reference full order model and the surrogate models computed by the Loewner framework and balanced truncation as well as the corresponding relative errors.

As expected, the accuracy of the reduced-order model computed with balanced truncation is better over nearly the complete time range for both evaluation points.

5 Conclusion

In this contribution, we showed and compared two methods to compute compact surrogate models describing the thermal behavior of machine tools. The time-varying heat flows between subassemblies resulting from relative movements of the machine were modeled using a weighted average on the interaction surfaces. The coupling was preserved in the reduced space and the reduction processes of different subassemblies were therefore independent of each other. This theoretically also allows the reduction of the subassemblies using different reduction methods, e.g., based on model properties like local nonlinearities [19]. The relatively high number of inputs and outputs did not pose problems to the reduction algorithms.

We compared reduced-order models computed with balanced truncation, an intrusive MOR method, to surrogates obtained from the non-intrusive Loewner framework. While the reduced-order models computed with balanced truncation were more accurate, the Loewner framework does not require access to the assembled system matrices of the full order model and is, therefore, especially suited for an industrial setting.

Acknowledgment. Funded by the German Research Foundation – Project-ID 174223256 – TRR 96.

References

1. Antoulas, A.C.: Approximation of Large-Scale Dynamical Systems. Adv. Des. Control, vol. 6. SIAM Publications, Philadelphia (2005). <https://doi.org/10.1137/1.9780898718713>
2. Antoulas, A.C., Beattie, C., Gugercin, S.: Interpolatory Methods for Model Reduction. Computational Science and Engineering, vol. 21. SIAM Publications, Philadelphia (2020). <https://doi.org/10.1137/1.9781611976083>
3. Antoulas, A.C., Lefteriu, S., Ionita, A.C.: A tutorial introduction to the Loewner framework for model reduction. In: Benner, P., Ohlberger, M., Cohen, A., Willcox, K. (eds.) Model Reduction and Approximation, pp. 335–376. SIAM, Philadelphia (2017). <https://doi.org/10.1137/1.9781611974829.ch8>
4. Benner, P.: Numerical linear algebra for model reduction in control and simulation. GAMM-Mitt. **29**(2), 275–296 (2006). <https://doi.org/10.1002/gamm.201490034>
5. Benner, P., Bonin, T., Faßbender, H., Saak, J., Soppa, A., Zaeh, M.: Novel model reduction techniques for control of machine tools. In: Proceedings of ANSYS Conference & 27. CADFEM Users’ Meeting 2009, 18–20 November 2009, Congress Center Leipzig. CADFEM GmbH, Grafing (2009). ISBN/ISSN 3-937523-06-5
6. Benner, P., Saak, J.: Numerical solution of large and sparse continuous time algebraic matrix Riccati and Lyapunov equations: a state of the art survey. GAMM-Mitt. **36**(1), 32–52 (2013). <https://doi.org/10.1002/gamm.201310003>

7. Benner, P., Werner, S.W.R.: MORLAB—the Model Order Reduction LABORatory. In: Benner, P., Breiten, T., Faßbender, H., Hinze, M., Stykel, T., Zimmermann, R. (eds.) *Model Reduction of Complex Dynamical Systems*. ISNM, vol. 171, pp. 393–415. Springer, Cham (2021). https://doi.org/10.1007/978-3-030-72983-7_19
8. Bonin, T., Soppa, A., Saak, J., Zäh, M., Faßbender, H., Benner, P.: Moderne Modellordnungsreduktionsverfahren für Finite-Elemente-Modelle zur Simulation von Werkzeugmaschinen. In: *Fachtagung MECHATRONIK 2011*, Dresden, pp. 333–338 (2011)
9. Gosea, I.V., Poussot-Vassal, C., Antoulas, A.C.: On enforcing stability for data-driven reduced-order models. In: *2021 29th Mediterranean Conference on Control and Automation (MED)*. IEEE (2021). <https://doi.org/10.1109/med51440.2021.9480216>
10. Hernández-Becerro, P.: Efficient thermal error models of machine tools. Ph.D. thesis, ETH Zurich (2020). <https://doi.org/10.3929/ETHZ-B-000449279>
11. Hernández-Becerro, P., Spescha, D., Wegener, K.: Model order reduction of thermo-mechanical models with parametric convective boundary conditions: focus on machine tools. *Comput. Mech.* **67**(1), 167–184 (2020). <https://doi.org/10.1007/s00466-020-01926-x>
12. Jones, D., Snider, C., Nassehi, A., Yon, J., Hicks, B.: Characterising the digital twin: a systematic literature review. *CIRP J. Manuf. Sci. Technol.* **29**, 36–52 (2020). <https://doi.org/10.1016/j.cirpj.2020.02.002>
13. Köhler, M.: On the closest stable descriptor system in the respective spaces RH_2 and RH_∞ . *Linear Algebra Appl.* **443**, 34–49 (2014). <https://doi.org/10.1016/j.laa.2013.11.012>
14. Lang, N., Saak, J., Benner, P.: Model order reduction for systems with moving loads. *at-Automatisierungstechnik* **62**(7), 512–522 (2014). <https://doi.org/10.1515/auto-2014-1095>
15. Mayo, A.J., Antoulas, A.C.: A framework for the solution of the generalized realization problem. *Linear Algebra Appl.* **425**(2–3), 634–662 (2007). <https://doi.org/10.1016/j.laa.2007.03.008>
16. Saak, J., Siebelts, D., Werner, S.W.R.: A comparison of second-order model order reduction methods for an artificial fishtail. *at-Automatisierungstechnik* **67**(8), 648–667 (2019). <https://doi.org/10.1515/auto-2019-0027>
17. Sauerzapf, S., Vettermann, J., Naumann, A., Saak, J., Beiteltschmidt, M., Benner, P.: Simulation of the thermal behavior of machine tools for efficient machine development and online correction of the tool center point (TCP)-displacement. In: *Special Interest Group Meeting on Thermal Issues Laboratory for Machine Tools and Production Engineering (WZL) of RWTH Aachen, Germany, February 2020*. EUSPEN (2020)
18. Vettermann, J., et al.: Model order reduction methods for coupled machine tool models. *MM Sci. J.* **2021**(3), 4652–4659 (2021). <https://doi.org/10.17973/mmsj.2021.7.2021072>
19. Vettermann, J., Steinert, A., Brecher, C., Benner, P., Saak, J.: Compact thermo-mechanical models for the fast simulation of machine tools with nonlinear component behavior. *at-Automatisierungstechnik* **70**(8), 692–704 (2022). <https://doi.org/10.1515/auto-2022-0029>

Open Access This chapter is licensed under the terms of the Creative Commons Attribution 4.0 International License (<http://creativecommons.org/licenses/by/4.0/>), which permits use, sharing, adaptation, distribution and reproduction in any medium or format, as long as you give appropriate credit to the original author(s) and the source, provide a link to the Creative Commons license and indicate if changes were made.

The images or other third party material in this chapter are included in the chapter's Creative Commons license, unless indicated otherwise in a credit line to the material. If material is not included in the chapter's Creative Commons license and your intended use is not permitted by statutory regulation or exceeds the permitted use, you will need to obtain permission directly from the copyright holder.





Simulation of Thermoelastic Behavior of Technical Systems with Relatively Moving Parts - Modeling Process, Part Coupling Approaches and Application to Machine Tools

Stefan Sauerzapf^(✉) and Michael Beitelschmidt

Faculty of Mechanical Science and Engineering, Institute of Solid Mechanics,
TU Dresden, Marschnerstraße 30, 01307 Dresden, Germany

`stefan.sauerzapf@tu-dresden.de`

Abstract. Models of technical systems play an essential role from the conceptual phase to the end of life of the system, as they allow the prediction of the behavior of the real world instance by simulation. Time and money spent on building prototypes can be saved, and the development process can be significantly accelerated. Furthermore, simulations allow the optimization of systems in advance.

A major problem in modeling modern systems is complexity, as machines increasingly include components from different areas such as cooling systems, active bearings, etc., along with the control units that govern the interaction. The model must incorporate all these systems and reflect their behavior with sufficient accuracy. This results in the need to modularize the modeling process and create a model from all these sub-modules.

Within the framework of the Collaborative Research Center/TR96 (CRC/TR96), a methodology has been developed to solve the above problems. It enables the coupling of several sub-models to a complex system model. The methodology is described together with the open-source and proprietary tools used to facilitate all necessary modeling and simulation steps.

As an example of the application of the described methodology, the modeling and simulation of a complete machine tool is presented. Special attention is given to the modeling of the moving part contacts, since they have a significant influence on the simulation result. Different approaches for contact modeling are compared.

Finally, the next steps for transferring the developed methodology to practical applications are outlined.

Keywords: Model Exchange · Finite Element Method · Thermoelastic Simulation · Contact Modeling · Simulation Tools

1 Introduction

In recent years, the simulation of technical systems has an increasing role from the concept phase up to the systems end of life. So called “digital twins” of real

world systems allow the prediction of the machine behavior through simulations, allowing optimizations of the system during development and operation, model predictive control or predicting service intervals. Furthermore, time and money can be saved due to a significant acceleration of the development process. Different system concepts can be studied for the best suiting solution. Components can be investigated and optimized before building prototypes.

Unfortunately, using all available tools to develop modern systems, results in an steadily rising machine complexity. Systems from different areas like fluid components for temperature management, active bearings, sensors, actors and gears, etc., along with lots of control components that govern the interaction are incorporated into one machine.

To model the behavior of those complex systems, it is necessary to apply the principle of “divide and conquer” by modularizing the system model. Each individual module must represent its respective component with the application sufficient accuracy and finally, all those sub-modules have to be incorporated into the full system model.

The process of assembling the whole system model requires a standardized way to bring all the sub-models together and allow the simulation of the whole system. This is, unfortunately, a very difficult task, as there exist numerous proprietary and open source tools to facilitate different modeling techniques and approaches, which are best suitable in their respective field. A nowadays widely used tool to exchange models, even across software packages, is the standardized Functional Mockup Interface (FMI) [5]. It allows the easy combination of multiple system models through standardized interfaces for model inputs and outputs. As every tool, FMI has limitations, which will be addressed next.

To calculate the distribution of field quantities like the temperature or the displacement vector, partial differential equations (PDE) have to be solved. In most cases, no closed solution for those PDEs can be given for real world problems, since the systems geometries and governing equations are too complex. Therefore mathematical discretisation methods like the Finite Element Method (FEM), Finite Difference Method (FDM) or Finite Volume Method (FVM) have been developed to calculate approximate solutions to those field equations [6, 7]. Typically, the FEM is used to solve the here discussed thermoelastic problems.

Section 2 gives a short theoretical overview of the system equations resulting from the application of FEM to the governing PDEs. Model Order Reduction (MOR) as a tool to increase the simulation efficiency will be introduced. The system equations for thermoelastic problems are given.

Widely used proprietary CAE tools like Ansys[®] or Abaqus[®] cannot fulfill all modeling and simulation demands of the CRC/TR96, like model predictive control of machine tools by process parallel simulation or parameter optimization. An exchange format for PDEs with geometry information, similar to FMI, which also incorporates moving contact surfaces and loads, was necessary to facilitate the exchange and cooperation between the multiple specialized groups in the CRC/TR96. Efforts, mentioned in [9, 13] did not suffice the needs of the modeling goals.

Section 3 therefore will propose a toolchain developed in the CRC/TR96 to tackle the before mentioned model exchange and combination issues, using multiple developed data formats as interfaces between different software modules used to solve the modeling and simulation tasks.

After introducing all the tools, a comprehensive example for the usage of the toolchain is given by describing the modeling process for an in production machine tool. Different coupling approaches for the moving part contacts are discussed and exemplary simulation results are given.

The final section discusses the next steps necessary to facilitate the usage of the tools and proposed model in practical applications.

2 Theoretical Background

The derivation of equations to model physical phenomena on an infinitesimal small representative volume element, along with constitutive equations for the material behavior, typically results in a time and position dependent PDE. Those PDEs cannot be solved in a closed manner on the simulation domain in most cases, since the investigated problem is too complex. Approximation methods, become necessary to calculate an approximate field quantity distribution. One such method is the FEM, which will be introduced next.

FEM. The first step to apply the FEM consists of splitting the simulation domain into multiple small geometric segments, the finite elements. Each of those elements has edges and nodes on those edges. The entirety of nodes and elements of the domain is called the FE-mesh.

The real physical field, for example the temperature or the deformation, in each element is approximated by shape functions whose coefficients are the approximated field values at the nodes. Further mathematical transformations result in element matrices for every single finite element. Those element matrices can then be assembled together into the system matrices resulting in the following system of equations.

$$\mathbf{M}\ddot{\boldsymbol{\phi}}(t) + \mathbf{D}\dot{\boldsymbol{\phi}}(t) + \mathbf{K}\boldsymbol{\phi}(t) = \mathbf{r}(t) \quad (1)$$

For demonstration purposes, it is assumed that all system matrices are time independent. The symbols $\mathbf{M} \in \mathbb{R}^{n \times n}$, $\mathbf{D} \in \mathbb{R}^{n \times n}$ and $\mathbf{K} \in \mathbb{R}^{n \times n}$ represent the mass, damping and stiffness matrix of the system, $\boldsymbol{\phi} \in \mathbb{R}^n$ is the system degree of freedom vector and $\mathbf{r} \in \mathbb{R}^n$ denotes the right hand side vector.

Typically, those system matrices are sparse but have a very high dimension, which results in large simulation times, making those systems not applicable to the use as models for model predictive control. Furthermore, parameter studies and optimization runs can be very time consuming.

MOR can be a helpful tool in those circumstances, as it allows the reduction of the system degrees of freedom while preserving, the correct method provided, the chosen model outputs up to a certain accuracy.

MOR. The Eq. (1) generally can be rewritten into the state space form, further called input-output (IO)-Model.

$$\mathbf{E}\dot{\mathbf{x}}(t) = \mathbf{A}\mathbf{x}(t) + \mathbf{B}\mathbf{u}(t) \quad (2a)$$

$$\mathbf{y}(t) = \mathbf{C}\mathbf{x}(t), \quad (2b)$$

with the matrices $\mathbf{E} \in \mathbb{R}^{n \times n}$, $\mathbf{A} \in \mathbb{R}^{n \times n}$ and $\mathbf{B} \in \mathbb{R}^{n \times p}$ $\mathbf{C} \in \mathbb{R}^{m \times n}$, the system states $\mathbf{x} \in \mathbb{R}^n$, the inputs $\mathbf{u} \in \mathbb{R}^p$ and the model outputs $\mathbf{y} \in \mathbb{R}^m$. The fact that every second order system can be rewritten as a first order system of double size is used.

By means of MOR it is possible to reduce the high-order IO-Model to a reduced order model (ROM). Typical methods to reduce the model order with projection based techniques are balanced truncation, moment matching and the iterative rational Krylov algorithm (IRKA) [3].

All those methods produce so called truncation matrices $\mathbf{V}, \mathbf{W} \in \mathbb{R}^{n \times r}$ where the dimension r is much smaller than n . The matrices can then be used to generate a lower dimension state space model of the form

$$\mathbf{W}^T \mathbf{E} \mathbf{V} \dot{\mathbf{x}}_r(t) = \mathbf{W}^T \mathbf{A} \mathbf{V} \mathbf{x}_r(t) + \mathbf{W}^T \mathbf{B} \mathbf{u}(t) \quad (3a)$$

$$\mathbf{y}_r(t) = \mathbf{C} \mathbf{V} \mathbf{x}_r(t), \quad (3b)$$

the further called reduced IO-Model. The symbols $\mathbf{x}_r \in \mathbb{R}^r$ and $\mathbf{y}_r \in \mathbb{R}^m$ denote the reduced state and output vector.

It must be noted that the MOR techniques aim to get good approximations of the outputs \mathbf{y} , therefore it can be stated that $\mathbf{y}_r \approx \mathbf{y}$. Approximating the full state vector \mathbf{x} by $\hat{\mathbf{x}}$ obtained from

$$\hat{\mathbf{x}} = \mathbf{V} \mathbf{x}_r \quad (4)$$

is not necessarily accurate and should be handled with care.

Thermoelastic System Equation. Applying the FEM on the thermoelastic coupled PDE results in the following ODE-system. Note that for demonstration purposes, constant material properties are assumed.

$$\begin{bmatrix} \mathbf{M}_{uu} & 0 \\ 0 & 0 \end{bmatrix} \begin{bmatrix} \ddot{\mathbf{u}} \\ \ddot{\mathbf{T}} \end{bmatrix} (t) + \begin{bmatrix} \mathbf{D}_{uu} & 0 \\ \mathbf{D}_{Tu} & \mathbf{D}_{TT} \end{bmatrix} \begin{bmatrix} \dot{\mathbf{u}} \\ \dot{\mathbf{T}} \end{bmatrix} (t) + \begin{bmatrix} \mathbf{K}_{uu} & \mathbf{K}_{uT} \\ 0 & \mathbf{K}_{TT} \end{bmatrix} \begin{bmatrix} \mathbf{u} \\ \mathbf{T} \end{bmatrix} (t) = \begin{bmatrix} \mathbf{r}_u \\ \mathbf{r}_T \end{bmatrix} (t) \quad (5)$$

The vectors $\mathbf{u} \in \mathbb{R}^{du}$ and $\mathbf{T} \in \mathbb{R}^{dT}$ denote the deformation and temperature degrees of freedom. The matrices $\mathbf{M}_{uu}, \mathbf{D}_{uu}, \mathbf{K}_{uu} \in \mathbb{R}^{du \times du}$ denote the mass, damping and stiffness matrices of the elastic system. The symbols $\mathbf{D}_{TT}, \mathbf{K}_{TT} \in \mathbb{R}^{dT \times dT}$ are the capacity and conductivity matrices of the thermal system. The load vector \mathbf{r} is split into its elastic part $\mathbf{r}_u \in \mathbb{R}^{du}$ and thermal part $\mathbf{r}_T \in \mathbb{R}^{dT}$. Furthermore, two field coupling matrices, $\mathbf{D}_{Tu} \in \mathbb{R}^{dT \times du}$ and $\mathbf{K}_{uT} \in \mathbb{R}^{du \times dT}$ exist. For lots of thermoelastic problems, another simplification is possible. By assuming that the deformation damping effects generate few heat, the matrix

D_{Tu} can be neglected and both physical domains can be evaluated sequentially. First, the temperature field is calculated. Then, the resulting temperatures are used as input vector to calculate the right hand side of the deformation equation. The resulting systems of equations are

$$D_{TT}\dot{\mathbf{T}} + \mathbf{K}_{TT}\mathbf{T} = \mathbf{r}_T \quad (6a)$$

$$\mathbf{M}_{uu}\ddot{\mathbf{u}} + \mathbf{D}_{uu}\dot{\mathbf{u}} + \mathbf{K}_{uu}\mathbf{u} = \mathbf{r}_u - \mathbf{K}_{uT}\mathbf{T}. \quad (6b)$$

This approach allows the calculation of the time accurate deformation field by sequential integration of the Eqs. (6a) and (6b).

Neglecting all dynamic effects results in the equations,

$$\mathbf{K}_{TT}\mathbf{T} = \mathbf{r}_T \quad (7a)$$

$$\mathbf{K}_{uu}\mathbf{u} = \mathbf{r}_u - \mathbf{K}_{uT}\mathbf{T}. \quad (7b)$$

By calculating the temperature field at a given point in time and then applying (7b), it is possible to calculate the quasi static deformation field.

3 Modeling and Simulation Framework

After introducing the main model usages and giving a short overview of the theoretical background to simulate the time propagation of systems describable with PDEs and discretized with FEM, an overview of the tools and methods developed and used in the CRC/TR96 to model and simulate the machine tool behavior will be given next.

3.1 Concept

The modeling and simulation process typically consists of multiple steps which demand different software components. CAE-Tools like Ansys[®] integrate all the necessary components into one software solution to carry out most of the engineering demands but do not offer much flexibility. The various research questions and model applications of the CRC/TR96 projects demand a modular approach that allows a simple model exchange and cooperation, even between experts from different fields like mathematicians, physicists and engineers.

To solve this task, a new modeling approach using json files with custom schemes was developed. These files serve as the interfaces between different software components and allow the independent development of those by different contributors.

The most important building block is the coupled problem description file which is used to exchange system PDE-problems. It contains all information describing the model geometry like coordinate systems, FE-meshes and parts along with materials, loads, constraints, part couplings, movements etc. A detailed overview of the format, along with its application is given in [10, 14] and [15].

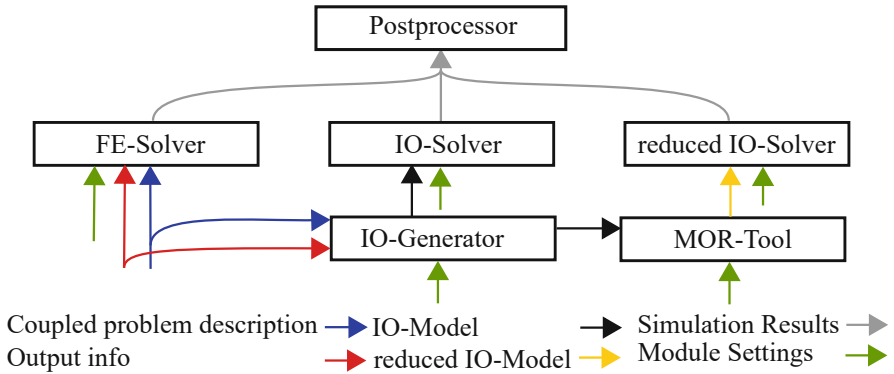


Fig. 1. Software components along with file formats as interfaces

The different modules, along with all files that are used as interfaces are shown in Fig. 1. Each module takes the relevant model data and produces inputs for the next one. Along with all necessary model and task specific data, module dependent settings files can be provided to customize the module behavior. Since each individual module can operate and be developed independently, flexible, problem specific toolchains can be created very efficiently. The knowledge of experts can be encapsulated and made accessible for third party users.

The FE-Solver takes the coupled problem description, the output description and settings and produces the simulation result file for postprocessing tasks. The IO-Generator is used to create IO-problems according to 2 from the coupled problem description and output information. A description of the IO-format is given in [10]. MOR is performed by the MOR-Tool. It produces another form of the IO-format, additionally containing the truncation matrices. Three different solvers for the FE-Problem and the two IO-configurations produce result files which can then be processed by the postprocessing module.

Those before mentioned basic modules can be put together for more complex tasks. For the application in model predictive control scenarios, a fast model execution is needed. Therefore the simulation of the full order FE-model is not applicable. By using the IO-Generator, the MOR-Tool and a special form of the reduced model IO-Solver, it is possible to realize such a fast, controller integrable, model. A second example for the tool combination are parameter optimizations. Since a ROM has much smaller simulation times, an optimization tool incorporating IO-Generator, MOR-Tool and IO-solver can reduce the time for parameter studies significantly.

3.2 Coupled Problem Combiner

For complex systems or to speed up the development process, the possibility to split the model into smaller sub-system models is necessary. Those submodels must then be assembled efficiently to the complete system model.

The presented modeling approach using interface files allows exactly that. For each sub-system, a coupled problem description can be developed. In the next step, a combination tool takes all the sub-models and builds the assembled model description, along with a combination of the output info file.

In the CRC/TR96 such a model combiner was realized and its application could already be demonstrated for an experimental machine tool.

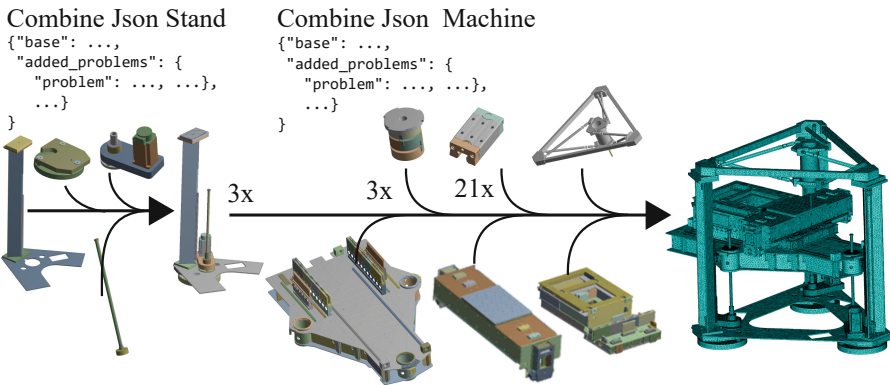


Fig. 2. Assembly process of machine tool using combination tool

Figure 2 illustrates the described process of the model assembly. Each step needs the sub-system models along with an assembly describing json file. It contains links to the models combined, optional geometric transformations and the additional functions needed to realize the part couplings in the full model. Simulation results and comparisons of the full model and the ROM simulations for the machine shown in Fig. 2 can be found in [16].

With this approach, it is easily possible to compare models of different detail levels, reuse or swap models for different configurations.

3.3 CRC/TR96 - Realized Simulation Framework

The modeling and simulation framework developed in the CRC/TR96 to realize and demonstrate the concept described in Sect. 3.1 is shown in Fig. 3. The interoperability between open-source and proprietary tools illustrates the high flexibility of the proposed concept.

DUNE, an open source FE-Toolbox written in C++ [2], is used to realize the FE-solver and IO-Generator. MOR is done using a custom MOR-Tool, a collection of functions built on top of the Matrix Equation Sparse Solver (M.E.S.S.)

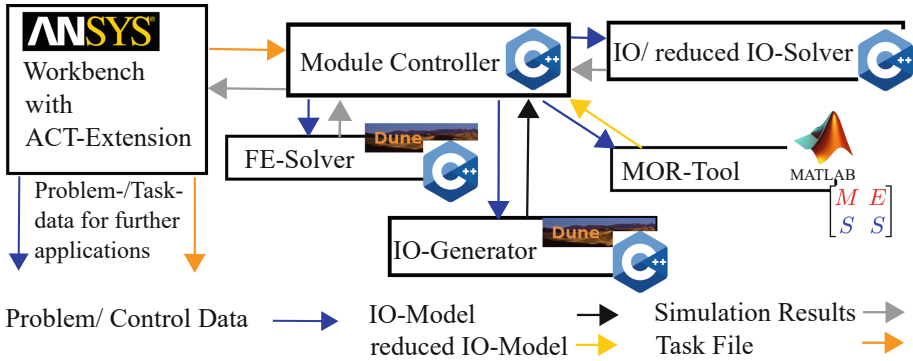


Fig. 3. Modeling and simulation framework of the CRC/TR96

[4]. It allows the semiautomatic calculation of reduced IO-Models from the full IO-model format. Time step integration of the IO- and reduced IO-System is done using a custom solver specifically tailored for the needs of the CRC/TR96 problems. The same mathematical structure of the IO- and reduced IO-Models results in a reduction of maintenance and implementation overhead because the same solver algorithms can be used for both model types.

Since most of the FE-modeling and -simulation realized in the CRC/TR96 is done using Ansys[®] Workbench (WB), a tool to make the file interface driven toolchain available for as many projects as possible was developed and shall be described next. The basis is a custom extension to WB using the Ansys[®] Application Customization Toolkit (ACT). By introducing new buttons and objects into the GUI of WB, it is possible to simply generate coupled problem descriptions from the modeled system. Furthermore, the definition of movements, coupling functions or integration of specialized CRC/TR96 parameterization functions is possible. After defining the model, the user has different options. Either, generate the problem description for model exchange or create a task file along with the description and call a custom module controller. This controller allows the chained call of the complete CRC/TR96 toolchain to do tasks like IO-Generation, MOR and time step simulations. The generated simulation results can be imported with another part of the ACT-Extension, allowing comparisons of Ansys[®] Mechanical APDL and open-source toolchain results. An example of the usage of this approach for a simple thermal model was already presented in [15]. Using the extension allowed project contributors the easy usage of the developed toolchain, even without knowledge of module internals.

4 Example Machine Tool Model

To demonstrate the developed methods and tools of the CRC/TR96 a model of the in production used machine tool DMG MORI DMU 80 eVo (DMU80eVo) was developed, which will be introduced next.

4.1 Base Model

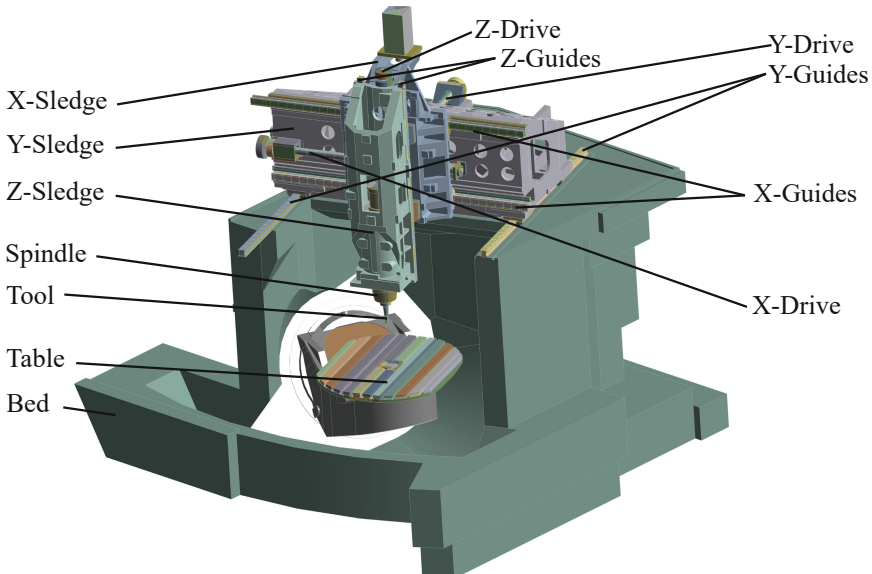


Fig. 4. Overview of the DMU80eVo-Model with main components

Figure 4 shows the geometry of the machine model, along with the relevant contacts between the moving sledges. For simplification reasons the table rotation axes are fixed, resulting in a model representing a 3-axes machine tool.

Each sledge is guided by two linear guide rails with two wagons respectively driven by a ball screw drive, resulting in 15 moving contacts. The ball screw drive spindles are supported using roller bearings, which also need special modeling efforts. Furthermore, seventeen interfaces between machine tool and fluid system exist, which for now are modeled as simple convection boundaries. Currently, the FE-model is discretized using ca. 700k elements and 1.4 million nodes, resulting in 1.4 million thermal and 4.2 million elastic degrees of freedom.

Those stats already show the high complexity of the model, resulting in a time consuming parametrization and simulation process. Especially the usage in process parallel simulations demands MOR to speed up the simulation.

4.2 Moving Contacts

Machine tools consist of multiple axis assemblies that execute large relative movements. The correct modeling of guides, drives and their internal moving contacts, providing the ability to execute those movements, is essential for a high simulation accuracy.

Linear guide wagons or ball screw drive nut assemblies and their inner parts are too complex to be modeled in a high geometrical resolution for the application in complete machine tools. The system degree of freedom would rise in a non reasonable manner. Furthermore, numerical stability issues, especially for the simulation of larger time steps, arise. The nonlinear behavior of the Hertzian deformation of the contact partners results in further overhead. The complexity of those detailed component models can be seen in publications, like [11] or [8], where the derivation of surrogate models is presented.

The common used approach for more complex systems is to replace the detailed contact geometry with a simplified, problem adapted one. The rolling parts and their respective contact behavior for thermal and elastic contacts can be replaced with surrogate models of different complexity. Ansys[®] Mechanical APDL allows the realization of such a surrogate model for the elastic contact by using MPC184 bushing elements. The thermal coupling can be modeled using face-face-contacts [1]. A similar approach, along with the possibility to use non-linear coupling behavior in the contact region and showing the application of MOR techniques to speed up the simulation, is given in [17].

Using finite element couplings can significantly slow down the simulation, as contact searching is expensive and large time steps result in errors due to large relative movements per time step, which was shown and tackled using an averaging technique in [12]. By reducing the system order with MOR techniques, smaller time increments are usable, reducing the position induced errors. The application of MOR requires the definition of inputs and outputs in the zones of moving contacts, which is realized by segmenting the contact zones. The coupling model acts at the segments which are currently in contact. Figure 5 shows one such possible master-slave pair. A conflict of goals arises, as a high segment count is beneficial for the model accuracy, but as shown in [16], more segments result in a larger ROM, directly impacting the solution time per step.

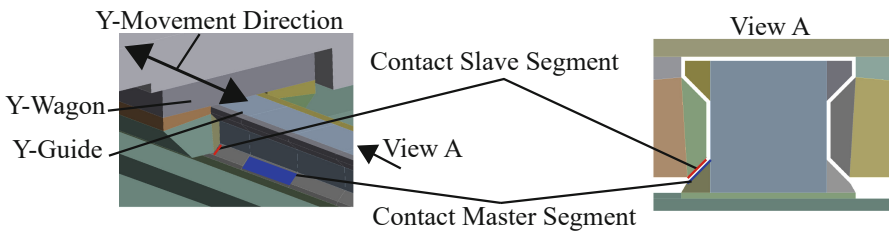


Fig. 5. Illustration of the segmentation approach for moving contacts on the y-guide of the DMU80eVo

Similar considerations apply for the roller bearings used in the presented model, which uses simplified models for the inner and outer bearing rings and coupling models between them.

4.3 Simulation Results

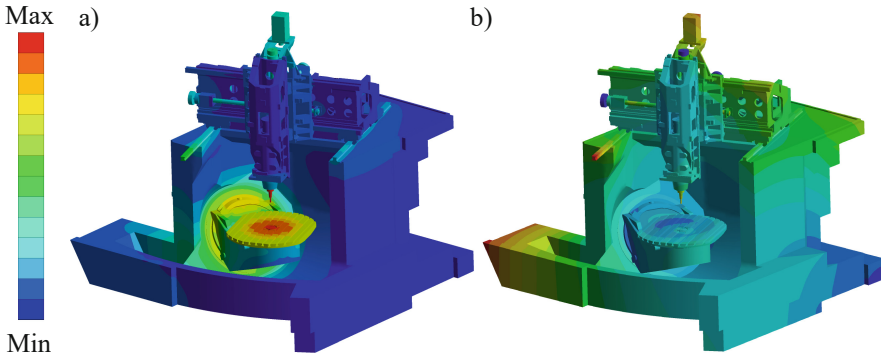


Fig. 6. Calculated fields after 10000 s operation a) temperature, b) deformation

The results of a system simulation of the DMU80eVo using Ansys[®] Mechanical APDL are shown in Fig. 6. For confidentiality reasons, no absolute values are shown. The temperature was calculated by integrating Eq. (6a) and used as input to compute the deformations using Eq. (7b). The thermal coupling of the moving contacts was realized using face-face-contact elements [1], the elastic model uses linear MPC bushings. The friction heat in the guide is modeled by time dependent heat fluxes while heat convection to the environment is realized by using models with time dependent external temperatures and heat transfer coefficients. Heat fluxes in the table center and on the tool tip model the process heat. As can be seen, the highest temperatures result at the tool tip. The impact of the guide and drive friction is small. Further detailed discussions of the modeling approaches and results are omitted, since the optimization and validation of the model using measurements is still in progress. The application of MOR techniques with a quantitative comparison of the optimized, full order model with the ROM using the presented toolchain along with detailed modeling aspects and simulation results will be presented in a future publication.

5 Conclusion and Outlook

This contribution introduced a framework to model complex technical systems using an interface file based, modular modeling approach, allowing simple model exchange and independent development of different, task specific tools.

MOR and its usage as an important tool to increase the simulation efficiency preserving a given model accuracy were shown.

After that, a toolchain realizing the described modular approach, which was developed and used in the CRC/TR96, was presented. References to multiple

usage examples, showing applications and proving the flexibility of the approach, were given.

Finally, a model and simulation results of the thermoelastic behavior of an in production machine tool, which is one of the main demonstration objects of the tools and methods developed in the CRC/TR96, were shown. Different coupling approaches, especially for moving contacts of linear guides and ball screw drives, were discussed.

Further development steps to facilitate the process parallel simulation of production processes using the presented machine tool model will be executed. This includes model validation with measurements and parameter optimization, integrating a sophisticated model of the fluid system and applying MOR techniques to speed up the simulations. Furthermore, different coupling techniques, like the one given in [17], shall be implemented and compared with the here presented approach to further enhance the model accuracy.

Acknowledgment. Funded by the German Research Foundation - Project-ID 174223256 - TRR 96.

References

1. ANSYS Inc., Canonsburg, PA: Ansys[®] Mechanical APDL, Release 2022 R2, Help System, Contact Technology Reference, release 2022 r2 edn. (2022)
2. Bastian, P., et al.: The dune framework: basic concepts and recent developments. *Comput. Math. Appl.* **81**, 75–112 (2021). <https://doi.org/10.1016/j.camwa.2020.06.007>. <https://www.sciencedirect.com/science/article/pii/S089812212030256X>. Development and Application of Open-source Software for Problems with Numerical PDEs
3. Benner, P., Grivet-Talocia, S., Quarteroni, A., Rozza, G., Schilders, W.H.A., Silveira, L.M. (eds.): *Model Order Reduction. Volume 1: System- and Data-Driven Methods and Algorithms*. De Gruyter, Berlin (2021). <https://doi.org/10.1515/9783110498967>
4. Benner, P., Köhler, M., Saak, J.: Matrix equations, sparse solvers: M-M.E.S.S.-2.0.1—philosophy, features, and application for (parametric) model order reduction. In: Benner, P., Breiten, T., Faßbender, H., Hinze, M., Stykel, T., Zimmermann, R. (eds.) *Model Reduction of Complex Dynamical Systems*. ISNM, vol. 171, pp. 369–392. Springer, Cham (2021). https://doi.org/10.1007/978-3-030-72983-7_18
5. Blochwitz, T., et al.: The functional mockup interface for tool independent exchange of simulation models, pp. 105–114 (2011). <https://doi.org/10.3384/ecp11063105>
6. LeVeque, R.J.: *Finite Volume Methods for Hyperbolic Problems*. Cambridge Texts in Applied Mathematics. Cambridge University Press (2002). <https://doi.org/10.1017/CBO9780511791253>
7. Lui, S.H.: *Numerical Analysis of Partial Differential Equations*. Pure and Applied Mathematics: A Wiley Series of Texts, Monographs and Tracts. Wiley, Hoboken (2011). <https://doi.org/10.1002/9781118111130>
8. Maier, W.: Erwärmung von kugelgewindetrieben. *wt Werkstattstechnik Online* **105**(7/8), 475–481 (2015)

9. Michopoulos, J., Mast, P., Chwastyk, T., Gause, L., Badaliance, R.: FemML for data exchange between FEA codes. In: ANSYS Users' Group Conference
10. Naumann, A., Saak, J., Sauerzapf, S., Vettermann, J., Beitelschmidt, M., Herzog, R.: Advanced open source data formats for geometrically and physically coupled systems. In: Proceedings Asian Modelica Conference 2022. Modelica Association and Linköping University Electronic Press, Tokyo, Japan (2022)
11. Ohta, H., Tanaka, K.: Vertical stiffnesses of preloaded linear guideway type ball bearings incorporating the flexibility of the carriage and rail. *J. Tribol.-Trans. ASME* **132** (2010). <https://doi.org/10.1115/1.4000277>
12. Partzsch, M., Beitelschmidt, M., Khonsari, M.M.: A method for correcting a moving heat source in analyses with coarse temporal discretization. *Proc. Inst. Mech. Eng. Part C: J. Mech. Eng. Sci.* **232**(15), 2736–2750 (2018). <https://doi.org/10.1177/0954406217722807>
13. Pinheiro, M.C., Moita, G.F.: Usando xml para criação de um padrão para o intercâmbio de dados entre programas de elementos finitos **9**(1)
14. Sauerzapf, S., Naumann, A., Beitelschmidt, M.: Building models for coupled thermo elastic problems in different software architectures using a new model exchange format. In: PAMM, vol. 21 (2021). <https://doi.org/10.1002/pamm.202100035>. <https://onlinelibrary.wiley.com/doi/full/10.1002/pamm.202100035>
15. Sauerzapf, S., Vettermann, J., Naumann, A., Saak, J., Beitelschmidt, M., Benner, P.: Simulation of the thermal behavior of machine tools for efficient machine development and online correction of the tool center point (TCP)-displacement. In: Conference Proceedings on Thermal Issues, pp. 135–138. Euspen, Bedford (2020)
16. Vettermann, J., et al.: Model order reduction methods for coupled machine tool models. In: Proceedings of the 2nd International Conference on Thermal Issues in Machine Tools, pp. 199–206. CTU, Prague (2021)
17. Vettermann, J., Steinert, A., Brecher, C., Benner, P., Saak, J.: Compact thermo-mechanical models for the fast simulation of machine tools with nonlinear component behavior. *at - Automatisierungstechnik* **70**(8), 692–704 (2022). <https://doi.org/10.1515/auto-2022-0029>

Open Access This chapter is licensed under the terms of the Creative Commons Attribution 4.0 International License (<http://creativecommons.org/licenses/by/4.0/>), which permits use, sharing, adaptation, distribution and reproduction in any medium or format, as long as you give appropriate credit to the original author(s) and the source, provide a link to the Creative Commons license and indicate if changes were made.

The images or other third party material in this chapter are included in the chapter's Creative Commons license, unless indicated otherwise in a credit line to the material. If material is not included in the chapter's Creative Commons license and your intended use is not permitted by statutory regulation or exceeds the permitted use, you will need to obtain permission directly from the copyright holder.





Thermal Modal Analysis for Volumetric Error Characterization

Natalia Colinas-Armijo¹  , Beñat Iñigo¹ , Luis Norberto López de Lacalle² ,
and Gorka Aguirre¹ 

¹ IDEKO, Elgoibar, Spain
ncolinas@ideko.es

² University of the Basque Country (UPV/EHU), Bilbao, Spain

Abstract. The volumetric accuracy of machine tools is significantly impacted by thermal errors, making the evaluation of volumetric accuracy a significant challenge for the manufacturing industry. Several technical solutions have been implemented, both at the industrial and research level, to address this issue. However, considering thermal errors in the volumetric error characterization adds complexity to the process and remains an open topic of research in the field.

In this study, a novel volumetric error characterization technique based on simulated Thermal Modal Analysis is proposed for a three-axis machine tool. This approach involves analyzing the impact of thermal modes of the machine tool's structural elements on the volumetric error, providing a characterization that incorporates the physical meaning of the structure. This simulated characterization will serve as a foundation for future experiments that combine it with other techniques to achieve a comprehensive understanding of volumetric errors.

Keywords: Thermal Modal Analysis · Volumetric Error · Thermal Error

1 Introduction

Controlling the volumetric error caused by thermal effects remains a major challenge in the field of machine tools. This is due to the increasing demand for more accurate products, which require tighter tolerances and higher quality, while maintaining high productivity [1].

Thermal distortions, caused by various heat sources, are among the primary contributors to the accuracy degradation of machine tools. These heat sources can arise from various elements of the machine, such as motors, spindles, and ball screws, as well as from the machining process itself, such as tool/workpiece heating, heat/cooling from lubrication, and external sources such as ambient temperature and radiation. Despite the efforts to control these heat sources, some may remain unknown or difficult to regulate.

Another important factor is the transient thermal state of the machine during the machining process, as the time constants of the machine elements involved are of the order of hours, which are longer than the typical operation times. This makes it challenging to reach a thermal steady-state for the machine.

Analytical approaches, such as Thermal Modal Analysis, have been employed to study the thermal behavior of machine tools [2, 3], model thermal errors [4, 5], and determine optimal sensor placement for machine error estimation [6, 7]. However, since machine operations occur within the machine volume, it is necessary to accurately characterize the volumetric error of the machine [8], which is impacted by the thermal distortions.

With these considerations in mind, this work proposes a methodology for analyzing the volumetric error due to thermal effects, induced by the thermal modes of the machine tool bodies. The methodology includes an in-depth explanation of thermo-elastic modeling and Thermal Modal Analysis, followed by the presentation of a Volumetric Thermo-Elastic Modal Analysis method for a multi-axis milling machine. The most relevant volumetric errors caused by thermal modes are then analyzed and discussed. Finally, the conclusions of this work and future steps are outlined.

2 Modelling

In this section, a comprehensive explanation of the thermo-elastic modeling and Thermal Modal Analysis (TMA) formulation is provided. The formulation outlined here applies to the finite element model of a single body, but can easily be extended to cover multiple interconnected bodies.

2.1 Thermo-Elastic Model

The equation for the calculation of the thermal field can be expressed in matrix form as follows.

$$\mathbf{C}^t \dot{\boldsymbol{\theta}}(t) + \mathbf{K}^t \boldsymbol{\theta}(t) = \mathbf{q}(t) \quad (1)$$

where \mathbf{C}^t represents the specific heat or thermal inertia matrix, \mathbf{K}^t represents the conductivity matrix, $\mathbf{q}(t)$ denotes the thermal load vector, and $\boldsymbol{\theta}(t)$ denotes the temperature vector. The equation that couples the thermal and elastic behavior, in the absence of mechanical loads, can be represented as follows.

$$\mathbf{K}^u \mathbf{u}(t) + \mathbf{K}^{ut} (\boldsymbol{\theta}(t) - \boldsymbol{\theta}_{ref}) = 0 \quad (2)$$

where \mathbf{K}^u represents the stiffness matrix, \mathbf{K}^{ut} represents the thermo-elastic stiffness matrix, $\mathbf{u}(t)$ denotes the displacement vector, $\boldsymbol{\theta}(t)$ denotes the temperature vector, and $\boldsymbol{\theta}_{ref}$ represents the initial temperature vector.

The equation for a coupled thermo-elastic analysis, which results from the combination of Eqs. (1) and (2), can be expressed in matrix form as follows:

$$\begin{bmatrix} \mathbf{0} & \mathbf{0} \\ \mathbf{0} & \mathbf{C}^t \end{bmatrix} \begin{bmatrix} \dot{\mathbf{u}}(t) \\ \dot{\boldsymbol{\theta}}(t) \end{bmatrix} + \begin{bmatrix} \mathbf{K}^u & \mathbf{K}^{ut} \\ \mathbf{0} & \mathbf{K}^t \end{bmatrix} \begin{bmatrix} \mathbf{u}(t) \\ \boldsymbol{\theta}(t) \end{bmatrix} = \begin{bmatrix} \mathbf{K}^{ut} \boldsymbol{\theta}_{ref} \\ \mathbf{q}(t) \end{bmatrix} \quad (3)$$

where \mathbf{C}^t is the specific heat or thermal inertia matrix, \mathbf{K}^t is the conductivity matrix, \mathbf{K}^u is the stiffness matrix, \mathbf{K}^{ut} is the thermo-elastic stiffness matrix, $\mathbf{q}(t)$ is the thermal load vector, $\mathbf{u}(t)$ is the displacement vector, and $\boldsymbol{\theta}(t)$ is the temperature vector. It is important to note that in Eq. (3), only thermal loads are considered and structural loads are not taken into account.

2.2 Thermal Modal Analysis

The discrete heat equation derived from Eq. (1) can be written as follows:

$$\mathbf{C}^t \frac{d\boldsymbol{\theta}(t)}{dt} + \mathbf{K}^t \boldsymbol{\theta}(t) = \mathbf{q}(t). \quad (4)$$

Equation (4) represents a system of n first-order linear differential equations with constant coefficients. Hence, the general solution of this system is the sum of the general solution of the homogeneous system plus a particular solution of the entire system.

The homogeneous system can be expressed as:

$$\mathbf{C}^t \frac{d\boldsymbol{\theta}(t)}{dt} + \mathbf{K}^t \boldsymbol{\theta}(t) = 0 \quad (5)$$

Its solution is given by:

$$\boldsymbol{\theta}(t) = \boldsymbol{\Phi} e^{-\lambda t}, \quad (6)$$

By substituting this solution into the homogeneous system, the following result is obtained:

$$(\mathbf{K}^t - \lambda \mathbf{C}^t) \boldsymbol{\Phi} = 0 \quad (7)$$

This system constitutes a general problem of eigenvalues and eigenvectors. The characteristic equation of this system is given by $|\mathbf{K}^t - \lambda \mathbf{C}^t| = 0$. Solving this equation results in n eigenvalues, $\lambda_1, \lambda_2, \dots, \lambda_n$. These eigenvalues represent the inverse of the time constants of each mode, $\tau_1, \tau_2, \dots, \tau_n$. By replacing the eigenvalues in the system and solving it, a series of eigenvectors, $\boldsymbol{\Phi}_i$, associated with them is obtained. As a result, the general equation of the homogeneous system is derived.

$$\boldsymbol{\theta}(t) = \sum_{i=1}^n \mathbf{D}_i \boldsymbol{\Phi}_i e^{-\lambda_i t} \quad (8)$$

where \mathbf{D}_i represents a vector of coefficients.

The eigenvectors $\boldsymbol{\Phi}_i$ form a set of n linearly independent vectors that make up a basis. The temperature vector $\boldsymbol{\theta}(t)$ can be represented in relation to this basis with new coordinates $\boldsymbol{\xi}(t)$, as follows:

$$\boldsymbol{\theta}(t) = \sum_{i=1}^n \boldsymbol{\Phi}_i \xi_i(t) = \boldsymbol{\Phi} \boldsymbol{\xi}(t). \quad (9)$$

Replacing Eq. (9) in the original system of Eq. (4) and multiplying by $\boldsymbol{\Phi}^T$

$$\boldsymbol{\Phi}^T \mathbf{C}^t \boldsymbol{\Phi} \dot{\boldsymbol{\xi}}(t) + \boldsymbol{\Phi}^T \mathbf{K}^t \boldsymbol{\Phi} \boldsymbol{\xi}(t) = \boldsymbol{\Phi}^T \mathbf{q}(t). \quad (10)$$

then, if $\boldsymbol{\Phi}^T \mathbf{q}(t) = \boldsymbol{\psi}(t)$, Eq. (10) may be re-written as

$$\dot{\boldsymbol{\xi}}(t) + \boldsymbol{\lambda} \boldsymbol{\xi}(t) = \boldsymbol{\psi}(t), \quad (11)$$

since $\Phi^T C^t \Phi = 0$ and $\Phi^T K^t \Phi = \lambda$, which are due to the orthogonality of the eigenvectors with respect to the matrices K^t and C^t , and λ is a diagonal matrix, it is immediately evident that Eq. (11) represents a system of n uncoupled equations in the form:

$$\dot{\xi}(t) + \lambda_i \xi(t) = \psi_i(t). \quad (12)$$

Therefore, by introducing the natural coordinates $\xi(t)$, the system of n linear differential equations with constant coefficients is reduced to n uncoupled equations of a single variable. The eigenvectors Φ_i are known as natural thermal modes, and the process of decoupling the thermal balance equations is referred to as Thermal Modal Analysis (TMA). Each natural thermal mode has a time constant defined as $\tau_i = 1/\lambda_i$.

3 Volumetric Thermo-Elastic Modal Analysis

In this section, a methodology is presented to assess the impact of thermal modes on the volumetric error of a multi-axis machine tool. Volumetric error refers to the deviation in the volume of the machine tool resulting from structural effects, thermal effects, and errors caused by positioning and acting elements. The contribution of thermal effects to volumetric error is significant and difficult to identify.

As volumetric error significantly affects the accuracy of machine tools, this study focuses on evaluating its possible thermal sources, through the examination of thermal modes as heating patterns of the machine bodies.

3.1 Machine Finite Element Model

A case study of a cantilever-style traveling column milling machine with three linear axes is presented to illustrate the proposed methodology (as depicted in Fig. 1). The machine consists of moving parts such as the column (X), console (Z), and ram (Y), which are supported by a bedtable that is fixed to the ground. The kinematic chain of the milling machine is Tool-Y-Z-X-Bedtable and the working volume of the machine is defined as X: 0–4000 mm, Y: 0–1200 mm, and Z: 0–1500 mm.

The model was developed using an in-house software implemented in MATLAB. This software allows for the input of body matrices (exported from ANSYS), followed by the definition of links (such as linear guideways, ballscrews, linear scales, etc.), application of structural and/or thermal boundaries and loads, and ultimately, the solution of the model.

The structural part of the machine model consists of four bodies (bedtable, column, console, and ram) that are connected by appropriate links such as linear guideways, ballscrews, and linear scales. The linear guideway links were simplified and modelled as ensembles of springs with equivalent stiffness, while the ballscrews were simplified and modelled as linear springs with position-dependent stiffness. The linear scales were included in the model as constraint equations.

The developed finite element model allows for easy evaluation of the volumetric error by changing the machine position. This is achieved by moving the bodies to the desired position, linking the body matrices considering simplifications of the mechanical connections, and generating the structural model matrices (K^u and K^{ut}) for each position for use in Eq. (3).

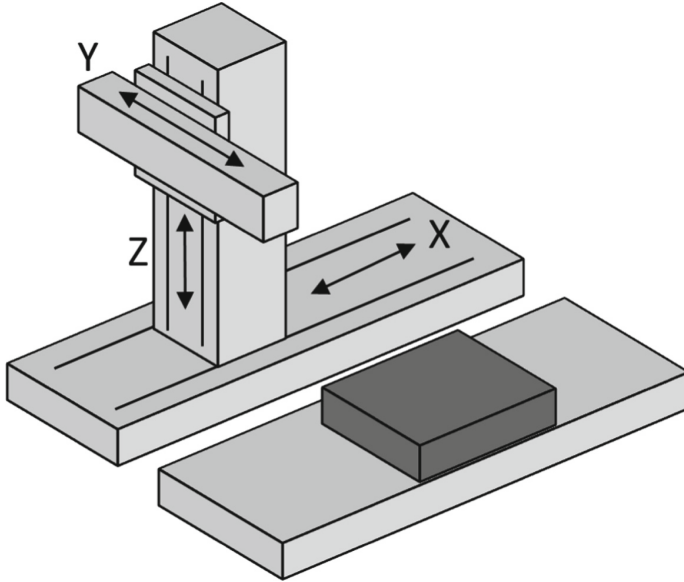


Fig. 1. Machine model.

3.2 Volumetric Thermo-Elastic Modal Analysis

The purpose of this paper is to examine the impact of thermal variations on machine tools on their accuracy. To achieve this goal, the methodology presented in this paper uses normalized thermal modes and assesses their effect on the volumetric error. The normalized thermal modal loads have been selected as they are unique to the bodies and independent of the loads.

This research did not consider the thermal connections between the various structural components of the machine tool, as recalculating the thermal modes at each evaluated position within the workspace would be required in this case. It is assumed that the thermal connections between these components are weak, and as such, this assumption was made to simplify the simulation process.

To implement the proposed methodology, the first 50 modes of each body of the machine tool are calculated according to the procedure described in Sect. 2.2. It should be noted that the thermal modes of the machine bodies are only affected by the convection thermal boundary, as the thermal modes are only dependent on the bodies' thermal matrices (C^t and K^t). The convection boundary affects the conductivity matrix K^t , so it is important to mention that for the analysis conducted in this work, a convection boundary load (with $h = 10 \text{ W}/(\text{m}^2\text{K})$) was added to the external faces of the bodies.

To evaluate the volumetric error caused by the thermal modes of the bodies, the thermal modes are introduced as a thermal field in each body separately. The thermal modes are normalized with zero mean and in the range $[-1, 1]$, and then introduced as the body temperature (θ_{ref} in $^\circ\text{C}$) in Eq. (3), as shown in Fig. 2, with only the structural equation considered.

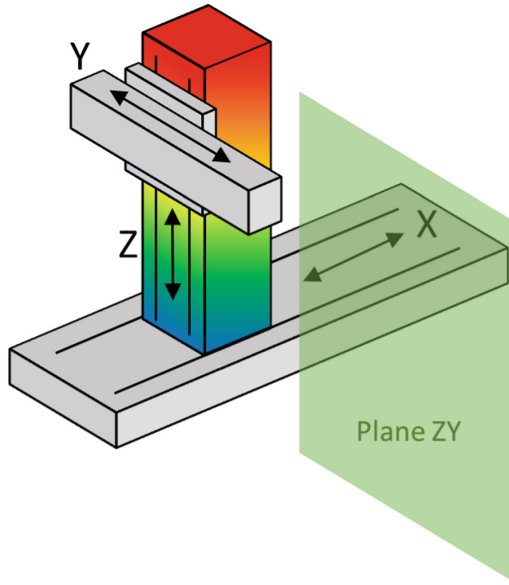


Fig. 2. Machine model and error analysis plane (Plane ZY).

The aim is to observe how the body thermal modes affect the volumetric error (in this case study only in the ZY plane). Equation (3) is then solved in a mesh of positions in the ZY plane with 100 mm steps in each direction and the volumetric error for each body mode is calculated.

4 Results and Analysis

In this section, an analysis of the most significant results obtained from the methodology described in the previous section is presented. As previously explained, the volumetric error on the ZY plane (discretized with 100mm mesh intervals) was evaluated for the first 50 modes of each body, resulting in 200 evaluations of the error on the ZY plane.

To evaluate the effect of the body modes on the volumetric error, only the modes with the largest magnitude or most significant shape are analyzed. In this work, two such modes are discussed.

The most significant volumetric error found in the analysis was due to mode 9 of the ram, which has a time constant of 0.9 h and is depicted in Fig. 3. In the first image of Fig. 3, the shape and magnitude of the thermal mode is represented, while in the second image, the error components (X, Y, Z translations, A, B, C rotations) for the ZY plane are shown. It is observed that the volumetric error changes significantly with Y axis movement, while Z axis movement also only has a relevant effect on EY.

Another mode that has a significant volumetric error is mode 9 of the column, which has a time constant of 2 h and is depicted in Fig. 4. In the first image, the shape of mode 9 of the column body is shown, while in the second image, the volumetric error for the ZY plane under study is shown, with magnitudes that are smaller than those caused by

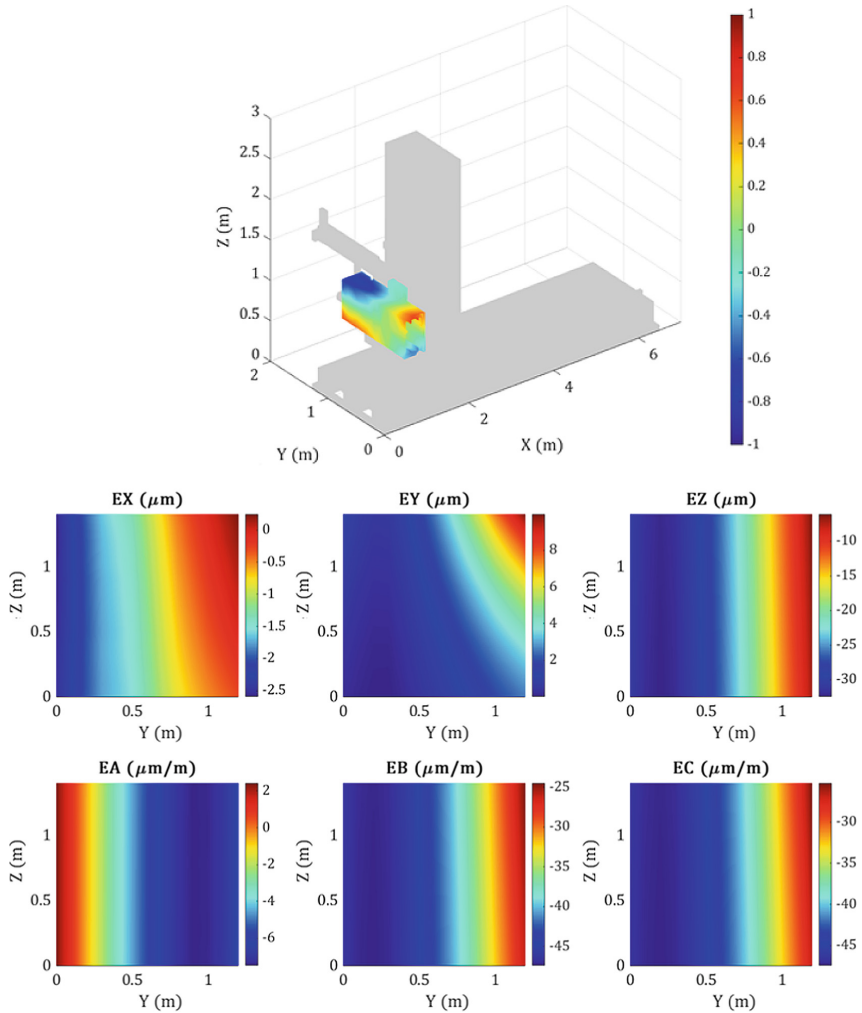


Fig. 3. Mode 8 – Ram.

mode 8 of the ram, but still significant. In this case, it can be observed that the Z axis movement has a significant impact on the volumetric error due to the thermal mode shape, and the Y axis movement also has an impact on error EZ.

From these results, it is evident that certain thermal loads on the bodies may have a significant impact on the volumetric error of a machine tool. This information is relevant in identifying the errors that can be caused by specific thermal shapes. In this work, thermal modes were used due to their physical significance, but the presented methodology can be used to identify thermal errors due to any thermal basis.

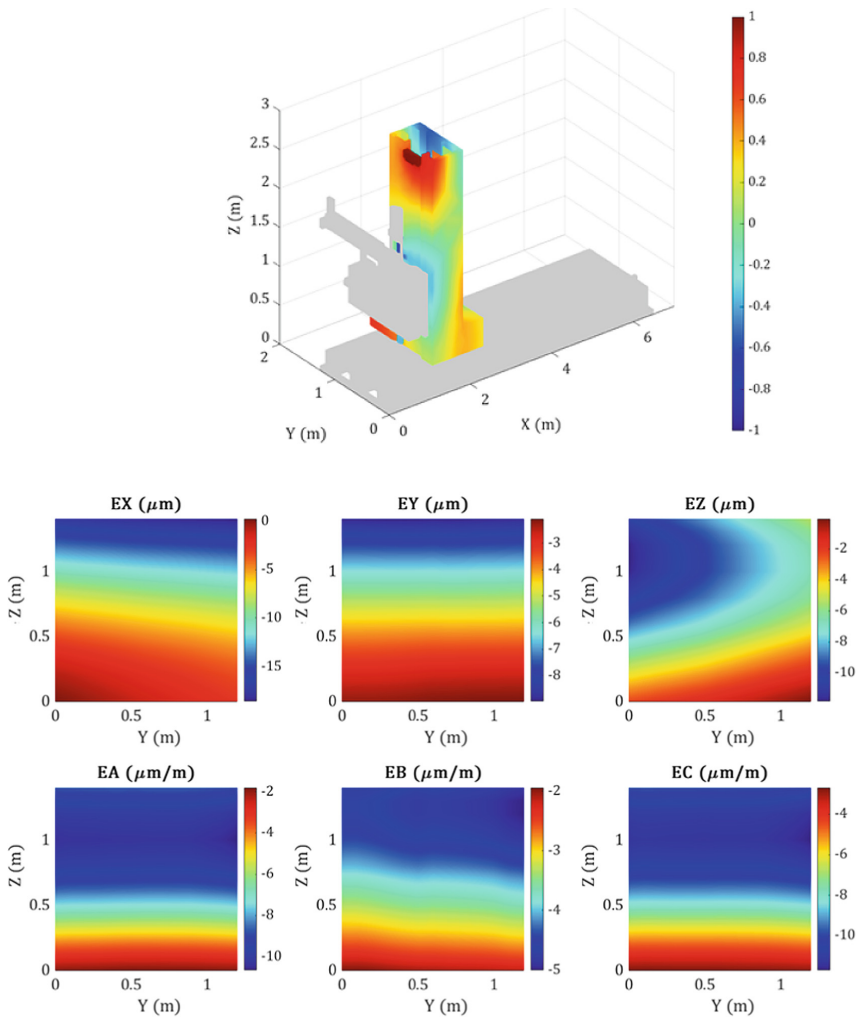


Fig. 4. Mode 9 - Column.

5 Conclusions and Future Steps

The study introduced a novel thermal modal volumetric error analysis for multi-axis machine tools. The purpose of this methodology is to gain a deeper understanding of the thermal behavior of the structural components of machine tools and to develop tools that can help improve machine tool accuracy.

The results obtained from this type of analysis can have several practical applications. Firstly, the results can be used to identify the most relevant positions to monitor the thermal field of the machine, which can help optimize sensor placement for thermal error compensation models, for example.

Lastly, this analysis can be used to identify avoidable temperature fields in machine tools and take mitigating measures at design stage. Reducing the thermal modal volumetric error, the machine tool can be designed to perform more accurately.

Overall, this research highlights the importance of understanding the thermal behavior of machine tools and the potential benefits that can be derived from a thermal modal volumetric error analysis. This information can be used to improve machine tool accuracy, which is critical for many industrial applications.

References

1. Mayr, J., et al.: Thermal issues in machine tools. *CIRP Ann. Manuf. Technol.* **91**, 61–771 (2012)
2. Bueno, R., et al.: Thermal modal analysis and modelling of machine-tools. In: Chedmail, P., Bocquet, J.C., Dornfeld, D. (eds.) *Integrated Design and Manufacturing in Mechanical Engineering*, pp. 307–315. Springer, Dordrecht (1997). https://doi.org/10.1007/978-94-011-5588-5_31
3. Colinas-Armijo, N., et al.: Comparison of thermal modal analysis and proper orthogonal decomposition methods for thermal error estimation. In: *Euspen Thermal Issues (2020)*
4. Zhu, et al.: Robust machine tool thermal error modelling through thermal mode concept. *J. Manuf. Sci. Eng.* **130**(6), 061006 (2008)
5. Morishima, et al.: Thermal displacement error compensation in temperature domain. *Precis. Eng.* **42**, 66–72 (2015)
6. Koevoets, A.H., et al.: Optimal sensor configuring techniques for the compensation of thermo-elastic deformations in high-precision systems. In: *13th International Workshop on Thermal Investigation of ICs and Systems (THERMINIC)*, pp. 208–213 (2007)
7. Colinas-Armijo, N., et al.: Optimal temperature sensor placement for error compensation of distributed thermal effects. In: *CIRP - International Conference on Thermal Issues in Machine Tools (2021)*
8. Digital twin-based analysis of volumetric error mapping procedures. *Precis. Eng.* **72**, 823–836 (2021)



Open Access This chapter is licensed under the terms of the Creative Commons Attribution 4.0 International License (<http://creativecommons.org/licenses/by/4.0/>), which permits use, sharing, adaptation, distribution and reproduction in any medium or format, as long as you give appropriate credit to the original author(s) and the source, provide a link to the Creative Commons license and indicate if changes were made.

The images or other third party material in this chapter are included in the chapter's Creative Commons license, unless indicated otherwise in a credit line to the material. If material is not included in the chapter's Creative Commons license and your intended use is not permitted by statutory regulation or exceeds the permitted use, you will need to obtain permission directly from the copyright holder.





Development of a System for the Evaluation and Recommendation of Solution Methods for Thermally Induced Errors on Machine Tools

Carola Gißke¹, Axel Fickert²(✉) , and Hajo Wiemer² 

¹ Technische Universität Dresden, Digital Health, Münchner Platz 3, 01087 Dresden, Germany

² Technische Universität Dresden, LWM, Helmholtzstr. 7a, 01067 Dresden, Germany

axel.fickert1@tu-dresden.de

Abstract. Thermally-induced displacements cause large parts of residual machining errors on modern machine tools. Their transient behavior makes it difficult to manufacture with high accuracy. To still increase machining accuracy and to meet the demands of the industry, research offers various solution methods to minimize this error.

Within the Collaborative Research Centre Transregio 96 (CRC/TR96), various solutions have been developed that either try to compensate the heat flow in the machine so that large temperature gradients and resulting displacements are avoided or aim to predict the amount and direction of the thermally induced deviation at the TCP.

In order to make these solutions comparable, they were first consistently classified and analyzed in terms of their implementation effort and risks. Potential benefits were proved by measurements. The benefits and efforts identified in this way were evaluated with the help of a multi-criteria decision analysis method so that the feasibility and implementation effort of the various solutions can be estimated for manufacturers and users of machine tools.

A software-based tool was developed to help interested industrial users to select a suitable process for their individual production scenario from the available processes via an input mask. The tool thus fulfills two aspects. On the one hand, it facilitates the transfer of the developed solutions into industrial applications. On the other hand, it documents the research status of the various solutions, shows potential for improvement, and new methods can be uniformly documented in the future and thus, made comparable.

Keywords: Thermally-induced errors · Solutions · Machine tool · Recommender system · Multi-criteria decision analysis

1 Introduction

Thermally-induced displacements have been known for a long time as a relevant cause of the reduced machining accuracy of machine tools. In the course of the last decades, thermal problems have been extensively investigated in the research. As a result, measurement methods and simulation methods are now available for recording temperature

gradients and the resulting displacements in the entire machine structure [1]. With the help of these methods, it was possible to develop a large number of correction and compensation solutions to minimize thermally induced displacements [2].

However, these solutions differ greatly in their approaches and have been explored in research under different conditions, for example on different machine tools or with different working conditions. This makes direct comparability difficult in terms of effort and benefit in the application, since a possible advantage by applying a method on one machine tool can become obsolete on another tool [3]. Moreover, due to production-related different boundary conditions and requirements of each manufacturer as well as different development statuses of the methods from research, it is difficult to estimate the advantages and disadvantages of one method compared to other alternatives for a potential user interested in applying such a solution.

Due to the increasing research in this field, more literature focusses on the comparison of different compensation or correction methods [3, 4]. However, the methods in these works are considered and compared from the perspective of their technical functioning. A comparative consideration of the economic effects in terms of resource consumption as well as implications for manufacturing are lacking in the literature.

For this reason, an evaluation metric has been developed in the course of the research project Collaborative Research Centre Transregio 96 (CRC/TR96), which allows a statement about the estimated effort and benefit of correction and compensation solutions developed in this research project from an economical process-oriented as well as technical point of view with respect to application-specific use cases. This metric is the baseline for a software-based application that offers a potential industrial user the possibility of a user-specific evaluation by comparing the different solutions based on personal preferences, suggesting suitable solution methods which meet the user's requirements. The approach presented in this paper to make a comparative evaluation based on economical as well as technical aspects from a process perspective and the development of a software-based evaluation tool is, best to the authors knowledge, new to research.

In the following, the development of this recommender tool and the underlying evaluation metric are presented.

2 Methodology

In order to be able to evaluate the solutions developed in the project holistically concerning technological as well as economic aspects, an evaluation metric was developed that should assess these aspects on a case-by-case basis, meaning that the gathered criteria are to be assessed based on an application scenario, taking into account machine tool configuration possibilities, operational boundaries and technological use cases. The overall assessment of the solution methods will thereby, be application-specific. The evaluation metric is depicted in Fig. 1.

In order to derive the assessment criteria needed, two approaches were pursued.

To evaluate the effort involved, expert interviews were conducted with the researchers responsible for the respective solutions [5]. To be able to comprehensibly map the required resources and risks during implementation and application, the implementation process of the solution was modeled from the interviews using the semi-formal modeling language Business Process Model and Notation (BPMN), and the required resources

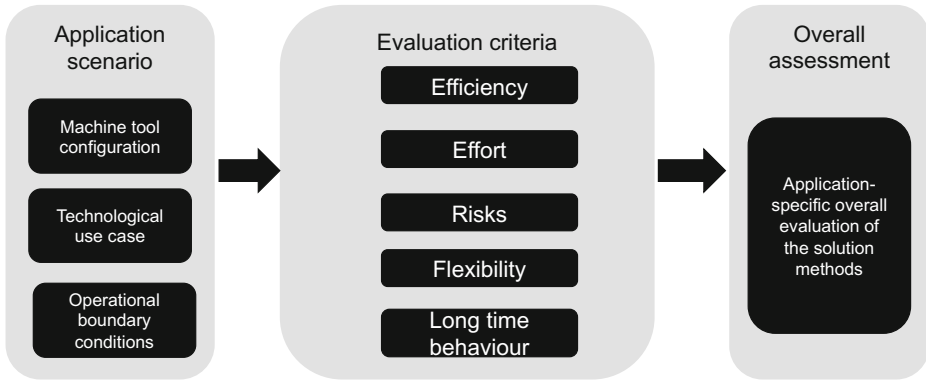


Fig. 1. Evaluation metric.

were directly applied to the respective work steps. On the one hand, it was possible to derive properties for the solutions from the evaluation of the interviews according to which the various processes can be uniformly classified, which enables comparability. On the other hand, quantifiable criteria could be identified for which an estimation of the expected amount of effort was made by the experts interviewed [5]. The identified criteria are demonstrated in Table 1.

Table 1. Quantifiable criteria and properties of correction and compensation methods following [5].

Quantifiable criteria	Solution properties
Material requirements	Application use case
Engineering hours	Flexibility
Technician hours	Degree of invasiveness
Machine downtime	Maintenance interval
Software license requirements	Access to machine control
Machine control license requirements	Necessity of machine downtime
Maintenance effort	Air conditioning required
Machine model adjustment effort	

To prove the effectiveness of the developed methods, a test workpiece developed within the CRC/TR 96 is used to quantify thermal defects [6]. For this purpose, load regimes were defined that represent the technological use cases of single-unit production and series production. For all solutions, the load regimes are run on different machine tools, each with and without implementation of the method, and an improvement of the thermal error at the tool center point is demonstrated by test measurements on the test workpiece.

Since both of the aforementioned aspects of cost-effectiveness and technology are to be part of the evaluation basis for comparing the solutions with each other, a suitable analysis method must be found as the basis for evaluation. The evaluation of the identified efforts and benefits for each solution, however, bears some challenges. First, the identified criteria are of both, qualitative and quantitative nature. Second, a user-specific assessment must be made possible that considers the user's preferences and initial operational situation. For this purpose, the collected effort must be differentiated to enable the user to compare the criteria with each other. For these reasons, the use of a multi-criteria decision analysis (MCDA) method will be used since it enables a display of evaluation results in ranking order, incorporates the user's preferences into the analysis, and allows for a sensitivity analysis of the criteria used [7–9]. Available MCDA methods were analyzed regarding their feasibility. The analysis resulted in the use of the Preference Ranking Organization Method for Enrichment of Evaluations (PROMETHEE I) as a basis for the implementation of the evaluation metric.

The documentation of the technological and economic aspects as well as the implementation of the evaluation metric serve as a basis for the development of the web-based decision support tool. This is explained in the following.

3 Development of a Documentation and Evaluation System

To document the developed compensation and correction solutions and their assessments and to implement an application-specific effort-benefit assessment from them, a web-based software solution was developed. In this documentation and assistance system, the various solutions are both uniformly documented and analyzed, and evaluated on a case-by-case basis.

The documentation is based on the identified criteria and is uniform for all solutions. In addition to the criteria and the mapping of the implementation process as BPMN, a detailed description of the individual process steps and the resources required in each case is presented. This makes the collection of the effort comprehensible and transparent for the user. Furthermore, the measurements carried out to prove the effectiveness of the solutions are documented in detail so that the user receives an overview of the test setup, the test protocol, and an evaluation of the measurement results. This documentation can be accessed independently from the evaluation process and therefore, serves as an information and overview function of the solutions developed in the project.

Regarding the recommendation function of the system, the quantifiable criteria as explained in Table 1 are being used as a baseline for the evaluation. As already mentioned, the interpretation of efforts can vary between users. For example, a high amount of material costs needed for the implementation of a solution can be an exclusion criterion for one user, whereas another user, due to staff shortages, would prefer a solution that requires few engineering hours and does not place so much emphasis on the use of materials. In order to be able to take these personal preferences into account, the MCDA method used for the calculation of the ranking provides for a weighting of the criteria. Since it is difficult for users to determine individual weightings, the Simple Multi-Attribute Rating Technique (SMART) method for weighting the criteria was implemented as an auxiliary tool. With this technique, 100 points are assigned to the

most important attribute in the eyes of the user of the system. All other attributes are assigned points in the range between 0 and 100 depending on their relative importance concerning this criterion (e.g. 50 = half as important, 100 = equally important). The sum of all points is then used to determine the percentage of each characteristic, which ultimately represents its weighting. Figure 2 exemplarily shows the implementation of criteria weighting for material and immaterial resource requirements. Depending on the weighting of the criteria, the calculated ranking of the solutions changes accordingly.

Criteria	Points	Weighting
Material resource requirements		
Materials required	70	0,32
Engineer hours	100	0,45
Technician hours	50	0,23
Immaterial resource requirements		
Machine tool downtime	100	0,43
Software	30	0,14
Machine control license	100	0,43

Fig. 2. Excerpt of weighting options for quantitative criteria based on the SMART method.

The identified properties as shown in Table 1 are implemented as filtering criteria. This allows the user to further limit the selection of solutions and adapt more to his individual situation, for example by only displaying solutions in the result ranking that do not require permanent intervention in the machine structure and hall air conditioning during operation time.

The MCDA method underlying the calculation uses a calculation of input and output flows for each alternative based on the defined weights of the criteria to determine the ranking. The output flow describes how strongly the procedure dominates all others, i.e. how strongly the procedure fulfills the criteria weighting compared to the other procedures and is the better the larger the value.

The input flow describes the opposite, i.e. how strongly the procedure is dominated by all others and is better the smaller it is. The input flow thus indicates how unsuitable the procedure is in relation to the criteria weighting compared to the other procedures. According to this logic, an alternative is preferred over another if its output flow is greater and its input flow is smaller, its output flow is greater and its input flow is equal, or its output flow is equal and its input flow is smaller than that of the others. This means that the favored alternative is characterized by more strengths and at the same time fewer weaknesses. The result of this difference is expressed in net flow. The best net flow indicates the most suitable solution. The resulting ranking accordingly shows the user which solutions correspond most to the weighting of the criteria, i.e. his preferences.

In the software tool, the calculated flows are displayed as a bar chart for traceability as shown in Fig. 3, where the alternative methods are arranged in descending order from left to right according to their ability to fit the user's preferences. By changing the weightings (see Fig. 2), the user can independently perform a sensitivity analysis to see to what extent the ranking would change or remain the same if the weightings were shifted.

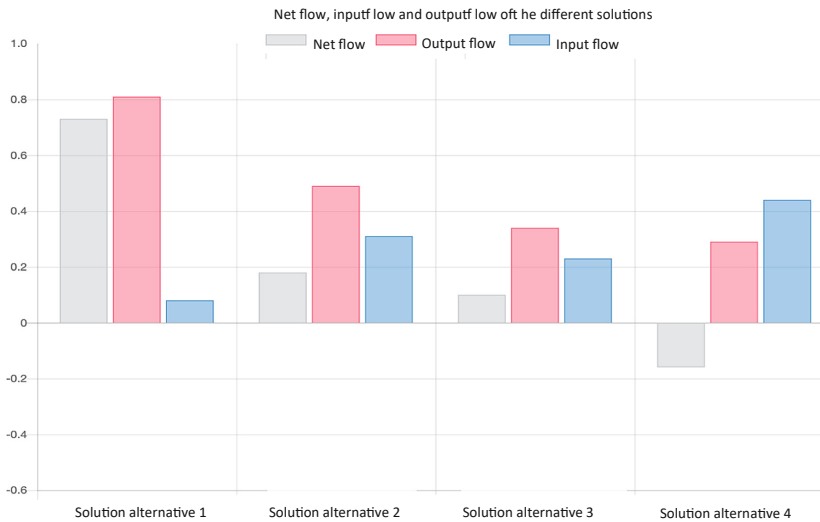


Fig. 3. Display of the calculated ranking order based on input and output flows

The user can then view the documentation of the corresponding solutions to get a detailed overview of the implementation steps and general properties, as well as the determined resource input and functional measurements carried out.

4 Discussion

It has to be emphasized that the effort of the solutions surveyed in the interviews with the experts is only an abstract survey, as the solutions are basic research and have not yet reached a final stage. The mapping of the effort, as well as the measurements, is thus not static and can change as the development of the solution progresses. Accordingly, the system can only be seen as a representation of an intermediate state and must be continuously adapted. A further step could be an extended development of the evaluation metric, in which improvement potentials of the solutions can be taken into account and assumed when a higher research state is reached, which could lead to a reduction of the effort and thus improve the evaluation of the solutions. Compensation and correction methods could, therefore, be classified according to the Technology Readiness Level.

Furthermore, it must be noted that the documentation of the measurements carried out is currently not included in the evaluation, as a direct comparison of the measurement

results cannot be carried out. This is because, within the CRC/TR 96, different machine tools are being used as demonstrator machines for the test measurements. A direct comparison of measurements can, therefore, not be carried out since the baseline situation of the tests is not the same. The documentation of the measurements allows an interested user to get a rough orientation of the effectiveness of the process and a detailed description and test data.

In the current state, only solutions from the CRC/TR 96 research project are documented in the system. To evaluate the applicability of the documentation method and the evaluation metrics, further solutions from the research could be integrated into the system in a further step. Moreover, the evaluation of solutions is based on abstract estimations of effort and properties of the methods. However, no concrete problems from industrial practice can be queried in the recommender system; the solutions are not yet developed far enough for this.

5 Conclusion

The development of methods that correct the thermal error on machine tools is a current field of research that produces diverse possibilities for correcting the thermal error. These procedures are very different in character and method.

On the one hand, the development of the system presented in this thesis enables the structured and uniform documentation of the solution methods developed in the CRC/TR 96.

Thus, the state of research is recorded and the many different solutions, which vary in character, are clearly presented. This can also serve as a link to structured documentation for further procedures developed outside the underlying research project, which can facilitate the overview for researchers. Furthermore, starting points for future research fields can be revealed by showing development potentials in the system.

On the other hand, the recommendation system is a step toward facilitating the transfer of the developed methods to industry.

Future research steps should focus on integrating other solutions outside the CRC/TR 96 into the system and depicting concrete use cases from the industry to test the system for transferability and suitability and develop it further based on this.

Acknowledgment. This research was funded by the German Research Foundation – Project-ID 174223256- TRR 96, which is gratefully acknowledged.

References

1. Mayr, J., et al.: Thermal issues in machine tools. *CIRP Ann.* **61**(2), 771779 (2012). ISSN 0007-8506
2. Wegener, K., Welkert, S., Mayr, J.: Age of compensation – challenge and chance for machine tool industry. *Int. J. Autom. Technol.* **10**(4), 609–623 (2016)

3. Li, Y., et al.: A review of thermal error modeling methods for machine tools. *Appl. Sci.* **11**(11), 5216 (2021)
4. Li, Y., et al.: A review on spindle thermal error compensation in machine tools. *Int. J. Mach. Tools Manuf.* **95**, 20–38 (2015)
5. Gißke, C., et al.: A proposal for a systematization and taxonomy of methods to rectify thermally induced errors on existing machine tools. *MM Sci. J.* (3), 4692–4697 (2021)
6. Höfer, H., Wiemer, H.: Measurement of test pieces for thermal induced displacements on milling machines. In: *Conference on Thermal Issues in Machine Tools, Proceedings*. Dresden (2018)
7. Diakoulaki, D., Grafakos, S.: *Externalities of Energy: Extension of Accounting Framework and Policy Applications - Multicriteria Analysis*/National Technical University Athens, Greece (2004)
8. Geldermann, J., Lerche, N.: *Leitfaden zur Anwendung von Methoden der multikriteriellen Entscheidungsunterstützung*. Georg-August- Universität Göttingen (2014)
9. Zopounidis, C., Doumpos, M.: PREFDIS: a multicriteria decision support system for sorting decision problems. *Comput. Oper. Res.* **27**(7–8), 779–797 (2000)

Open Access This chapter is licensed under the terms of the Creative Commons Attribution 4.0 International License (<http://creativecommons.org/licenses/by/4.0/>), which permits use, sharing, adaptation, distribution and reproduction in any medium or format, as long as you give appropriate credit to the original author(s) and the source, provide a link to the Creative Commons license and indicate if changes were made.

The images or other third party material in this chapter are included in the chapter's Creative Commons license, unless indicated otherwise in a credit line to the material. If material is not included in the chapter's Creative Commons license and your intended use is not permitted by statutory regulation or exceeds the permitted use, you will need to obtain permission directly from the copyright holder.



Sensor Integration



Smart Pressure Film Sensor for Machine Tool Optimization and Characterization of the Dynamic Pressure Field on Machine Surfaces

Andreas Erben¹(✉), Alexander Geist¹, Immanuel Voigt², Björn Senf¹, Thomas Mäder¹, Janine Glänzel¹, Steffen Ihlenfeldt^{1,3}, and Welf-Guntram Drossel^{1,2}

¹ Fraunhofer IWU, Nöthnitzer Straße 44, 01187 Dresden, Germany

Andreas.Erben@iwu.fraunhofer.de

² TU Chemnitz, Straße der Nationen 62, 09111 Chemnitz, Germany

³ TU Dresden, Helmholtzstraße 7a, 01069 Dresden, Germany

Abstract. Knowledge of thermal interactions with the environment is essential for improving the performance of machine tools. Therefore, it is necessary to detect and quantify the convective heat flows at machine tool surfaces, that occur in the workspace as a result of cutting fluid use or outside the machine due to active air flow. Thin-film sensors made of shape memory alloys with integrated small temperature sensors are suitable for detecting very fine pressure differences and can be used to estimate convective heat transfer. By measuring the pressure differences, the dynamic pressure field at the surface can be determined. Since the pressure field correlates with the flow field, conclusions can be drawn about the flow velocity. This leads to more profound and extended possibilities to match flow fields from CFD simulations with measured data. At the same time, the surface temperature is also recorded by this sensor. Reference measurements of the temperature in the free flow are used to characterize the heat transfer. By knowing the pressures, temperatures and the correlating flow velocity near the wall, the heat transfer coefficient can be determined. Against this background, this paper demonstrates the behavior of shape memory alloys as fluid pressure sensors and addresses the development of such sensors for machine tools. For this purpose, sensor units are to be developed that can be placed as a sensor network (composite of several sensors on one surface) inside and outside the workspace.

Keywords: Memory shape alloy · sensor development · fluid flow measurement · machine tool

1 Introduction

For the qualitative determination of the heat transfer in the working space and on the outer surface of machine tools, the exact recording of the flow conditions is necessary. For this purpose, it is inadequate when temperatures or heat flows are estimated using a limited number of measuring points in order to determine the thermal behavior of

the object under investigation with sufficient accuracy. The convective heat transfer and thus the energy exchange of the machine with its environment depend strongly on the flow velocity and type of fluid medium. It is known from the literature that in forced convection with air, the heat transfer coefficient can increase by a factor of 10 to 50 compared to natural convection, depending on the flow velocity. With water, on the other hand, factors >100 are possible, which is why this aspect plays a major role, especially when cooling lubricants are used in the workspace. It is therefore very important to know not only the surface temperature and flow direction but also the flow velocity outside the fluid boundary layer in order to determine or estimate the heat transfer coefficient. Conventional flow velocity measuring devices (pitot tubes, Prandl probes, anemometers) are not applicable in most cases due to their design and size or cannot be placed sensibly. In addition, such devices influence the flow field and distort the measurement result due to their construction space. Furthermore, it is known from fluid mechanics that in the momentum equation (Navier-Stokes equation) the flow velocity is related to the dynamic pressure or pressure changes. By means of a metrological detection of the fine changes in the total pressure in the total pressure as well as the direction, the variations in velocity and flow conditions can be determined. Preliminary investigations at Fraunhofer IWU have shown that the use of shape memory alloys (SMA) as piezoresistive sensor material can detect particularly small pressure differences in the single-digit Pascal range.

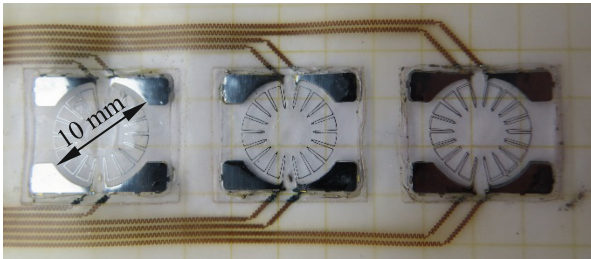


Fig. 1. Preliminary sensor design based on a stretchable printed circuit board.

The small size of these sensors allows for the integration in confined spaces. With a thickness of only a few micrometers, the sensors can be embedded in special foils and placed directly on smooth surfaces. Due to the flat structure, there is no influence on the flow along the surface. The prototype design is shown in Fig. 1.

Due to a further development of this sensor technology, the reproducibility of the measurement accuracy could be further improved and additional measured variables for the detection of relevant process parameters (e.g. temperature) could be recorded by the sensor structure. The sensor behavior was investigated in detail under laboratory conditions in order to achieve, on the one hand, a measuring instrument for the improved simulation of heat transfer in machine tools and, on the other hand, to obtain a qualitative and quantitative data basis in comparison with conventional measuring technology and thus for the utilization of the novel sensor technology.

2 State of the Art

2.1 Pressure, Temperature and Flow Sensors

The motivation for the research and development activities is the more precise detection of flows on the machine tool surfaces by means of sensors made of shape memory alloy. In order to be able to consider the flow field coupled with the energy equation, the three variables “pressure, temperature and flow velocity” must be known, whereby the total pressure can be correlated to the flow velocity. Most sensors on the market are designed to measure a single physical quantity and are developed for a specific application. The main characteristics here are low-cost production and high volumes to qualify a sensor in a broad application. The most important quality criteria are resolution and linearity over the measuring range.

Temperature Sensors

The two most important groups of temperature sensors are resistance thermometers (Pt100 and Pt1000) and thermocouples based on the thermoelectric effect. Both have advantages and disadvantages in terms of sensor size and cable routing. A thermocouple always consists of a wire pair of different metals (e.g. nickel - chrome-nickel), which are connected at the measuring point. The size depends on the wire diameter. The disadvantage is that the entire sensor cable must consist of the same metal pairing as the sensor. With the resistance sensor, conventional copper material can be used as the wire. The cables are not only less expensive, but can also be extended more easily.

With modern manufacturing processes, miniature resistance thermosensors with a size of a fraction of a millimeter can be produced at low cost. These are optimally suited for embedding in small systems or foils and are therefore used in the developed measuring system. As a variant, the Pt1000 (resistance 1000 Ω at 0 °C) is preferable due to the higher resolution and the 4-wire technology. With the 4-wire technique, the line resistance can be fully compensated and the line length has no negative influence on the measurement result. Temperature sensors are often offered together with a humidity sensor (dual sensors). There are even extensions with a pressure sensor for measuring the absolute air pressure (triple sensor). However, this type is a special case and is used rather rarely. A wide variety of designs exist, to name a few here:

- Pipe contact sensor with curved surface
- Flat contact sensor with or without magnetic head
- Free wire end sensors
- Screw-in sensors with standardized thread
- Metal bars or flat bed versions.

Flow Sensors and Pressure Sensors

There are many different sensor designs for pressure sensors with regard to the pressure range to be measured. Due to technical requirements (e.g. hydraulic and process engineering), the most common sensors are designed for higher pressures of a few mbar to > 1000 bar and are therefore unsuitable for very small pressure differences. The higher the pressure range, the lower the resolution. The consequence is that small changes in

measured variables, e.g. due to flow at low air velocities, cannot be detected by the sensor at all.

Electrical pressure measurement technology includes different types of sensors that measure different physical effects. However, all of them often have the characteristic that the resolution is very coarse or the measuring range is too small. Other aspects that make miniaturization difficult are the size, the materials used and the necessary electrical circuits.

The limitations are similar for speed sensors. Many have too coarse resolution or require a minimal velocity. Other disadvantages are that they must be oriented normal to the flow direction and affect the flow field. The two most important groups include the anemometers and dynamic pressure measurement devices (Prantl probes).

2.2 Shape Memory Alloy Thin Film Sensors

SMA like nickel-titanium are commonly used in medical applications like stents because of their high elasticity and fatigue resistance [1]. These material properties of superelastic SMA are due to the reversible stress induced phase transformation between austenite and martensite. This phase transformation leads to a change in the specific electrical resistance in addition to the geometric influence because of an applied load (see Fig. 2).

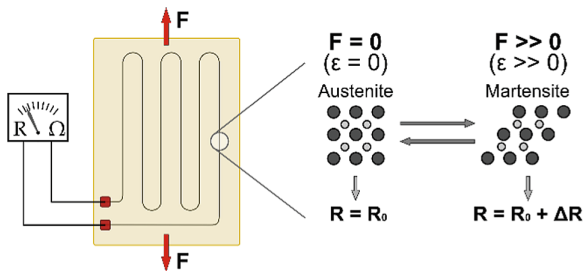


Fig. 2. Schematic of the phase transformation and correlating electrical resistance change of a superelastic SMA sensor because of an applied load.

The correlation of the change in electrical resistance of a superelastic SMA to an applied load or strain is almost linear (see Fig. 3). SMA is capable to be used as a highly elastic and sensitive strain sensor [2, 3]. Figure 3 shows an influence of the temperature on the electrical resistance-strain-characteristic, that needs to be considered.

There exist several ways for temperature compensation that can be applied to SMA strain sensors. A Wheatstone bridge offers the possibility for temperature compensation if the sensors can be arranged in a way, where the thermal effects have an equal influence, but the mechanical load is applied with opposite sign on the sensors. This compensation method can be supplemented or replaced by computational approaches among others, which will be focused in future research.

Hunek et al. showed a design of a pressure sensor based on a NiTi wire [4]. Another approach is to implement pressure sensors based on SMA thin films. If a pressure load is applied to a membrane, compressive and tensile strain regions can be observed (see

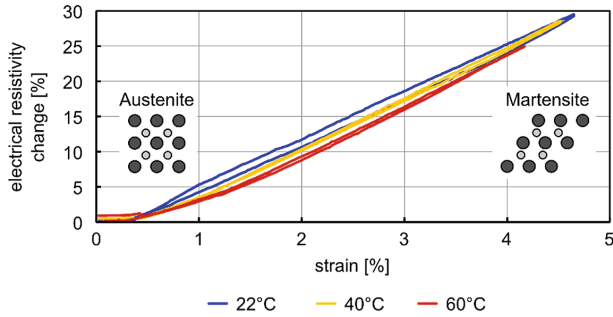


Fig. 3. Change in resistance depending on the strain of a superelastic shape memory alloy sensor at different temperatures.

Fig. 4). If strain sensors are applied to these regions, the measurement signal correlates with the pressure.

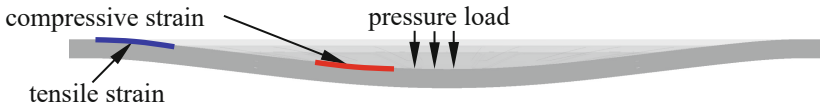


Fig. 4. Principle of a pressure sensor based on different strain loads of a membrane with applied load.

This paper presents an approach to use SMA thin films as strain sensors for this purpose. These so called SMA thin film pressure sensors (SMATFiPS) are designed to use the unique properties of SMA to improve the characterization of the heat flow on machine tools.

3 Methods

In the following, potential application cases of SMATFiPS in machine tools are discussed. The sensor design and manufacture are explained. Finally, the set-up used for the sensor characterization is presented.

3.1 Use in Machine Tools

Modern machine tools are characterized by a wide field of application, high precision as well as high productivity and availability and are used in almost all branches of the manufacturing industry. By means of optimized CNC control technology and several machine axes, complex 3D geometries can be manufactured with the help of 5-axis machining. The trend in industry is towards higher accuracy with shorter cycle times (= higher productivity). This is achieved by faster feed rates and more powerful machine components [12]. These components (especially drive motors, bearings and motor spindles) do not only require more energy, but also generate greater heat loss. In the industry,

it has been demonstrated that 40–80% of workpiece dimensional errors are caused by thermal effects in the machine tool [11]. The largest thermal influence on machine accuracy is exerted by the ambient temperature and the flow in the working space as well as the type of process (dry or wet machining). Convective heat transfer as a result of free or forced flow is the dominant factor. From the point of view of industry and machine tool manufacturers, the following scenarios have the greatest thermal effects and thus errors on the workpiece:

- a) Major daily air temperature fluctuations (day-night cycle)
- b) Change of the flow velocity at the external structure due to open hall doors or neighboring installations (ventilators)
- c) One-sided solar radiation
- d) Opening of the work space door (change of the flow in the work space)
- e) Change from dry to wet processing, switching on the cooling lubricant system
- f) Work area flushing and use of an aspiration system (flow amplification)
- g) Breaks in cooling lubricant supply.

The global factors in a) and c) can only be minimized by hall air-conditioning or darkening, which, however, requires an energetic and expensive hall air-conditioning system. The other factors are often random and subject to statistical fluctuations. These cannot be prevented but lead to most scrap due to thermal errors in practice [13]. These effects occur at very short notice and cannot be planned, therefore, thermal correction methods used in machine control do not take these into account. However, in most cases, these effects are not even measured by the machines and therefore cannot be corrected. The effect only becomes apparent during the subsequent quality control of the workpiece. Thus, it is not unusual that most rejects occur after longer break times and machine changeover times.

With the help of the newly developed sensors, new fields of application can be opened up and measured variables can be recorded in places that are not accessible by conventional methods. A possible application would be the use of several sensors in an interconnected network to monitor the flow condition in the machine, as well as in the external structure and in the working space (see Fig. 5).

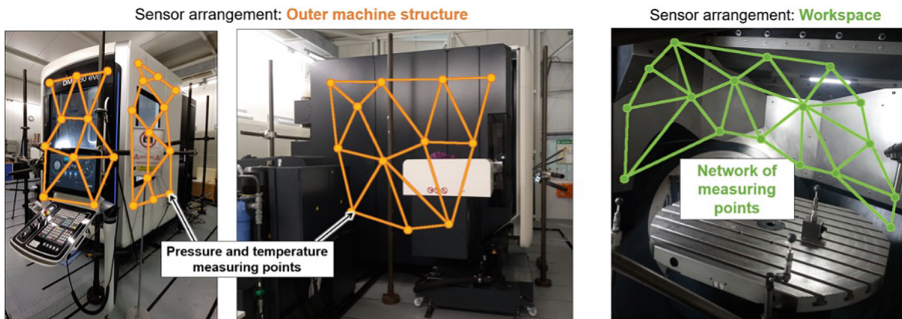


Fig. 5. Sensor arrangement concept.

Several sensors can be placed on suitable surfaces and combined to form a network, with each individual network node representing an independent measured value. The greater the number of sensors and the finer the network density, the finer the resolution of the pressure and temperature field on the surface. The nodes can be related to simulation model positions of the CFD and FEM analysis in the spatial coordinates in order to verify the simulation models with experimental data. From the simulations, the optimal positions for the real sensors can be determined on the basis of the pressure and temperature gradients.

In practical applications, just a few measuring points are sufficient to register flow changes outside and inside the machine's working space. A possible field of application would be the condition monitoring of the production. For example, if a threshold value is exceeded, a message could be sent to the machine operator warning that more waste parts are to be expected. The operator can then take appropriate measures and, if necessary, change the conditions. Correction algorithms can also be trained and expanded with the new additional input variables to increase their reliability in the event of stochastic environmental fluctuations.

3.2 Design and Manufacture of the Flow Sensors

SMA thin films from ACQUANDAS GmbH are used as the sensor structure for measuring the change in air pressure. The SMA thin films are produced by UV lithography and subsequent deposition of the nickel titanium layer. A subsequent wet etching process removes the unwanted parts. The films have a thickness between 15 μm and 30 μm . The outer diameter of the sensors is approximately 10 mm. For better utilization of the SMA films, the sensors are manufactured as a composite and must be separated before use. Figure 6 shows two sensors, for better understanding, one sensor is threaded in green. The remaining structure serves as a support structure that prevents destruction during transport and handling.

The contacting of the SMA sensors is done by soldering. The low-temperature solder from Chip Quik SMD 291 and the silver solder Stannol HS10 were considered as soldering tins. Both soldering tins enable the soldering of the enameled copper wires on the SMA foils. Considering the downstream process of hot pressing and the resulting temperatures of 180 °C, the low-temperature solder was rejected as it would melt causing separation of the NiTi and copper wire. Furthermore, the liquid solder spreads between the two TPU foils and can lead to a short circuit in the sensor structure. Hence, the silver solder was chosen.

To record the temperature in combination with the air pressure, a temperature sensor must be integrated close to the effective point. To select the appropriate sensor, the size of the sensor, in particular the height of the sensor including cables, the complexity of the downstream evaluation electronics and the price should be evaluated. Based on the requirements, the following six temperature sensors were compared with each other (see Fig. 7):

- PT 100 sensor, [5]
- Thermistor in SMD design (0201, 0402, 0603), [6]
- Non-contact temperature measurement infra-red sensor, [7]

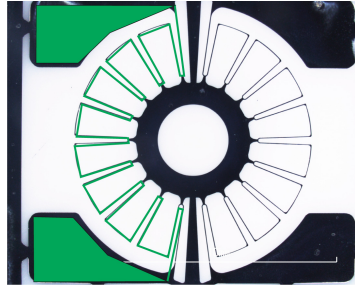


Fig. 6. Two SMA sensors with additional support structure.

- Printed electronic, [8]
- Thermistor in thin film design, Alpha-therm TTF series, [9]
- Seebeck thermocouples. [10]

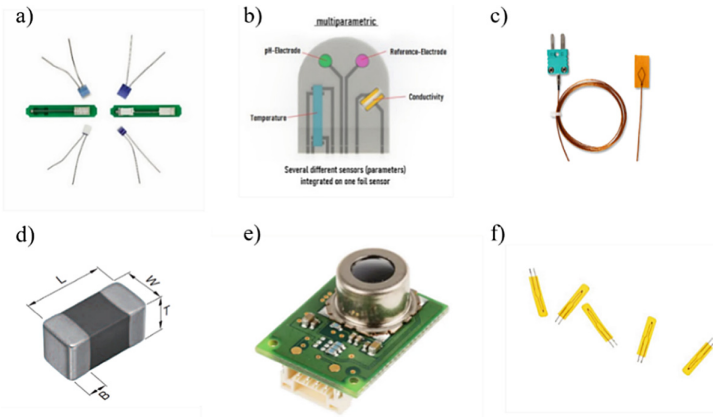


Fig. 7. Temperature sensor types – a) PT 100 b) Printed Electronic c) Seebeck thermocouple d) Thermistor SMD e) Infra-red sensor f) Thermistor thin film.

The comparison of the different sensors (Table 1) shows that SMD sensors are the most suitable. The size 0402 (0,4 mm × 0,2 mm) was selected because these sensors can still be soldered by hand and can therefore be contacted with cables. The contact is made by means of enameled copper wires similar to the SMA sensors. 100 μm enameled copper wires prove to be suitable since these do not negatively influence the stiffness of the composite. The influence on the stiffness is also the reason for thermocouples and thin-film sensors being unsuitable, as these are supplied in Kapton laminate, which is too stiff. In the future, the use of printed temperature sensors on TPU foils may also be an alternative. At present, this technology is not commercially available and was therefore not further considered. The use of PT100 sensors is not possible, since these are significantly thicker than the SMD components as the smallest versions are around

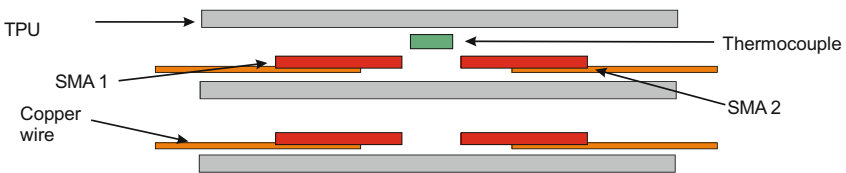
Table 1. Comparison of temperature sensor types.

Criterion	PT 100	Printed electronic	Thermistor SMD	Thermistor thin film	Non-contact	Thermocouple
Element size	0	0	+1	-1	+1	0
Use in machine tools	+1	+1	+1	+1	-1	+1
Flexibility	-1	-1	+1	-1	-1	0
Evaluation electronics	0	0	+1	+1	0	0
Cost	-1	-1	+1	0	-1	+1

800 μm thick and are pre-contacted. Non-contact temperature sensors turn out to be unsuitable, as they can be disturbed by the coolant droplets in the machine tool.

The sensor structures are manufactured as layered structures, which are then thermally pressed. A TPU foil with a thickness of approx. 100 μm serves as the carrier material. The sensor can be fabricated with one or two layers. Depending on the structure, the corresponding evaluation circuit is a full, half or quarter bridge (see Fig. 8).

In the case of the single-layer structure, the sensor layer is the intermediate layer of the assembled sensor and consists of the two SMA sensors with contacts which are led out within the intermediate position and are not led through the TPU foil and the selected temperature sensor.

**Fig. 8.** Sensor assembly for three-layer configuration.

For the development of the complete sensor structure, the focus is on the right process window for producing the TPU composite, in particular the temperature, the time, and the appropriate mold.

Since the issues of contacting and thermal buildup mutually influence each other, both were investigated simultaneously and developed iteratively. Optical criteria are used as evaluation criteria for thermal pressing. On the one hand, the composite should be completely bonded, i.e. no structure of the actual TPU is visible. On the other hand, the TPU film must not become too hot, otherwise bubbles will form in the intermediate layer. The function of the sensors is evaluated based on: (i) its electrical properties (ii)

after pressing the sensors must still be in contact, (iii) no cracks in the copper cable or unraveling the contact point again, (iiii) the thermocouple is not damaged.

The tests show that a press mold is necessary to produce the structures, because if the sensors are only pressed between two plates, on the one hand, the temperature sensor is destroyed by flattening the SMD component and on the other hand, the solder joints do not allow the layers to be pressed evenly. The set-up used for pressing is shown in Fig. 9.

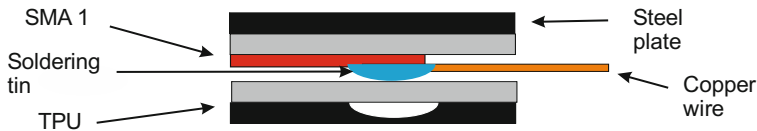


Fig. 9. Set-up for joining the sensor parts using a pressing mold.

The sensor structures realized so far exhibit the two-layered configuration. The overall composite has a resulting thickness of 180–190 μm around the sensor matrix and is shown in Fig. 10.

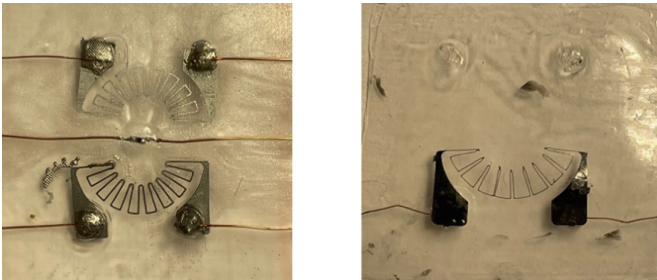


Fig. 10. a) SMATFiPS with two SMA sensors and centered temperature sensor (left) b) SMATFiPS with one SMA sensor and without temperature sensor (right)

3.3 Experimental Set-Up

To examine the sensors and evaluate the characteristic curve, the sensors were tested in a pressure chamber as shown in Fig. 11. For this purpose, the sensor was glued to a plate with a FR-4 spacer. This allowed the sensor to be deflected in both directions and to react to a change in air pressure. The change of the air pressure in the chamber is realized by means of a Festo pressure piston, which is controlled by a linear actuator and measured with the pressure difference sensor TYPE DS 2-010 from Kalinsky Sensor Elektronik. A Quantum MX410B from HBK is used to record the measured values.

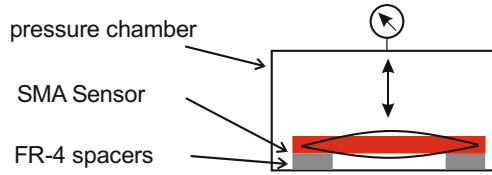


Fig. 11. Experimental set-up for sensor characterization.

4 Results and Discussion

Figure 12 shows the measured values from the pressure chamber with a single sensor, which is connected to a half bridge with a second passive resistor. The measurement shows a good agreement of the measured values with the applied air pressure change. In parallel, the measured values show a still strong drift of the measured values. This can result from the temperature change in the pressure chamber since the pressure piston constantly introduces heat into the system by compressing the air.

The experimentally obtained data demonstrate a strong correlation between the recorded resistance of the fabricated sensor and the varying pressure within the pressure chamber. At the same time, the results indicate a significant influence of the measured resistance on the thermal conditions. As the current sensor design is based on a quarter-bridge structure, it is sensitive to temperature changes. In order to compensate for the thermally induced resistance change, the quarter-bridge arrangement must be replaced by a half-bridge or full-bridge arrangement. The target design considers a full bridge as it not only enables temperature compensation but also exhibits the highest sensitivity to occurring strains. Accordingly, a further improvement of the sensor resolution is expected.

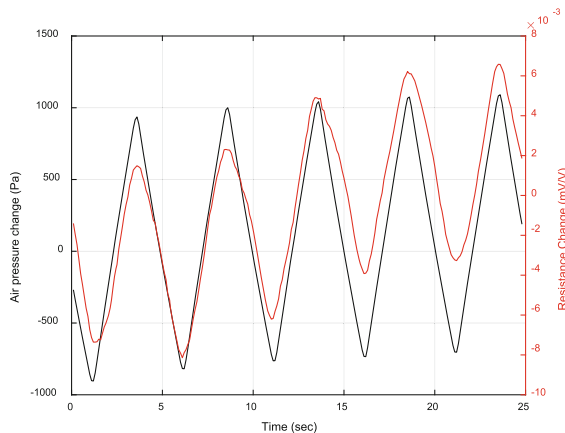


Fig. 12. Sensor response to varying pressure.

5 Summary

A novel pressure sensor design based on the piezoresistive properties of SMA was introduced. The development of SMATFiPS aims for recording pressure changes within fluids at high measurement resolution. Based on SMA thin films different sensors were fabricated by thermal pressing of various SMA and TPU layers. The experimental characterization of a fabricated sensor under varying air pressure proved that the sensor is capable of detecting the pressure rate. However, the results also point out the need of temperature compensation of the sensor signal and further improvement of the sensor sensitivity. To achieve this, the quarter-bridge design of the realized sensors has to be replaced by a half or full bridge.

The ongoing investigations aim for the application of the developed sensor to machine tool structures. In terms of sensor applicability and precision, an enhanced performance compared to conventional pressure sensors is expected. This leads to a high potential of SMATFiPS for precise detection of the flow conditions on outer machine surfaces and within the workspace. To examine the sensor performance under realistic machine tool conditions, the sensors need to be complemented by further supplementary such as wireless data transmission and energy storage.

References

1. Bechtold, C., Lima de Miranda, R., Quandt, E.: Capability of sputtered micro-patterned NiTi thick films. *Shape Mem. Superelasticity* **1**(3), 286–293 (2015)
2. Mäder, T., et al.: Highly elastic strain gauges based on shape memory alloys for monitoring of fibre reinforced plastics. *Key Eng. Mater.* **742**, 778–785 (2017)
3. Mäder, T., et al. (Hrsg.): D4.1 - Shape memory strain gauges. AMA Service GmbH, Von-Münchhausen-Str. 49, 31515 Wunstorf, Germany (2017)
4. Hunek, M., Pliva, Z.: Design and optimisation of NiTi pressure gauge. In: 2017 IEEE International Workshop of Electronics, Control, Measurement, Signals and their Application to Mechatronics (ECMSM), pp. 1–4. IEEE (2017)
5. Kamet. <https://de.kamet-trading.com/pt100-sensoren/>. Accessed 10 Oct 2022
6. Datasheet Chip NTC Thermistor, TDK, December 2017
7. Datasheet MEMS Thermal Sensors D6T
8. Accensors. <https://www.accensors.com/foleysensor-technology/>. Accessed 10 Oct 2022
9. Alpha therm. <https://www.alpha-therm.de/ntc.html>. Accessed 10 Oct 2022
10. THERMA Thermofühler GmbH. <https://www.thermagmbh.de/shop/>. Accessed 10 Oct 2022
11. Putz, M., Richter, C., Regel, J., Bräunig, M.: Industrial consideration of thermal issues in machine tools. *Prod. Eng. Res. Devel.* **12**(6), 723–736 (2018). <https://doi.org/10.1007/s11740-018-0848-6>
12. Wegener, K.: Innovative machine tool – precision, productivity, efficiency. In: Conference Transcript Industry 4.0 – The Intelligent Factory of the Future, pp. 259–269 (2014)
13. Bryan, J.: International status of thermal error research. *CIRP Ann.* **39**(2), 645–656 (1990)

Open Access This chapter is licensed under the terms of the Creative Commons Attribution 4.0 International License (<http://creativecommons.org/licenses/by/4.0/>), which permits use, sharing, adaptation, distribution and reproduction in any medium or format, as long as you give appropriate credit to the original author(s) and the source, provide a link to the Creative Commons license and indicate if changes were made.

The images or other third party material in this chapter are included in the chapter's Creative Commons license, unless indicated otherwise in a credit line to the material. If material is not included in the chapter's Creative Commons license and your intended use is not permitted by statutory regulation or exceeds the permitted use, you will need to obtain permission directly from the copyright holder.





Thermally Induced Clamping Force Deviations in a Sensory Chuck for Thin-Walled Workpieces

Berend Denkena¹, Heinrich Klemme¹, Eike Wnendt¹ (✉), and Matthias Meier²

¹ Institute of Production Engineering and Machine Tools (IFW), Leibniz Universität Hannover, An der Universität 2, 30823 Garbsen, Germany
wnendt@ifw.uni-hannover.de

² HWR Spanntechnik GmbH, Luxemburg-Straße 5, 28876 Oyten, Germany

Abstract. Deviations between nominal and actual tolerances are a challenging problem during turning processes of thin-walled workpieces. One main cause of these deviations is the clamping force applied by the turning chuck to hold the workpiece. Due to the low stiffness of thin-walled workpieces, large workpiece deformations can occur even when clamping forces are low. For this reason, the clamping force needs to be precisely adjusted. A possible approach are chucks with integrated actuators. As a result of the more direct power transmission, these chucks have a potentially higher clamping force accuracy compared to conventional external actuation. However, integrated actuators are additional heat sources resulting in thermal loads and thermally induced deformations of the chuck components. Due to the resulting mechanical distortion of the chuck system, the precise adjustment of clamping forces is not possible. Thus, this paper evaluates the thermally induced clamping force deviations on a novel turning chuck with four integrated electric drives. A test bench is used to analyse both a single drive and the combination of all four drives regarding the temperature effect on the clamping force adjustability. A clamping force deviation of up to 26% is observed. Based on the measured chuck temperature, a compensation method is introduced leading to a clamping force accuracy of 96.9%.

Keywords: Power chucks · Sensory machine components · Clamping force

1 Introduction

Precision turning of thin-walled workpieces such as bearings, thin rings or turbines is of key importance in aerospace, automotive and medical applications [1]. One main cause of shape deviations is the clamping force applied by the turning chuck to hold the workpiece [2]. Due to the low stiffness of thin-walled workpieces, large workpiece deformations can occur even when clamping forces are low. For this reason, the appropriate clamping force has to be applied. To estimate the appropriate clamping force and thus to reduce shape deviations, FE-simulations or analytical calculations are used [3]. In this context, Sergeev et al. proposed an algorithm to adjust the appropriate clamping force by an external clamping cylinder leading to clamping force errors of 12–15% [4]. Since

clamping force error and shape deviation are related linear proportional, shape deviations can occur in the same amount. Therefore, an external actuated chuck is insufficient to ensure tight tolerances. To avoid shape deviations, chucks with integrated actuators were developed [5, 6]. However, these chucks are only suitable for certain workpiece diameters or manufacturing processes. In contrast, the most commonly used clamping device in turning are chucks with three or four jaws [7]. Jaw-chucks allow a flexible clamping of different workpiece diameters. As a result, jaw-chucks are universally used for turning. For these reasons, a novel jaw-chuck for universal workpiece clamping is presented in this paper. Due to its integrated electric drives, higher clamping force accuracy and sensitivity are expected compared to a conventional external actuation. The design of the sensory chuck is explained in Sect. 2. In addition, the actuating concept is proofed using a test bench. In Sect. 3, the compensation method of thermally induced clamping force deviations is presented and the achievable clamping force accuracy is analysed.

2 Sensory Chuck for Thin-Walled Workpieces

2.1 Sensory Chuck Design

The design of the sensory chuck is shown in Fig. 1. It is composed of two different modules: A standard four-jaw-chuck HWR VT-S031 and a module with four actuator units. Each of the four actuator units consists of a Harmonic Drive SE FHA-14C gear motor and a leadscrew. The leadscrew allows the transmission of rotational movement of the motor into a linear positioning movement required to actuate the 4-jaw-chuck. The leadscrews are mechanically connected in parallel via a coupling element to transmit the actuation force F_{act} . In addition, the leadscrew is designed for self-locking to maintain the clamping force F_{cl} even when power failures of the motor occur.

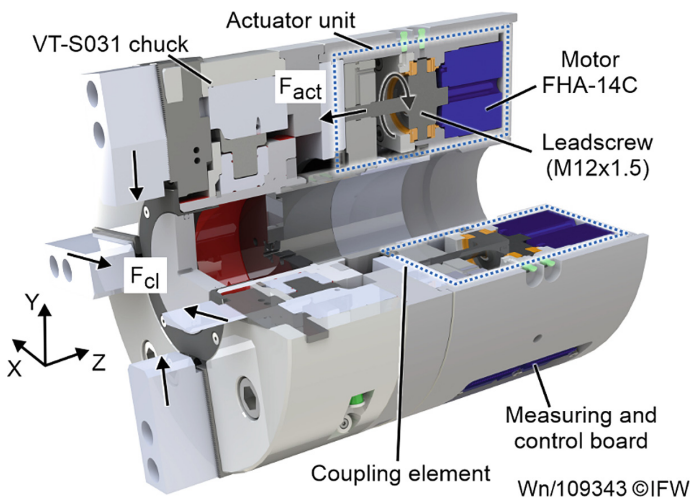


Fig. 1. Sensory chuck design

A total of four EJ7411 measuring and control boards from Beckhoff Automation GmbH & Co. KG are integrated into the chuck. Each EJ7411-module can measure and control the drive signals (motor torque M_m , angular position p) in a closed feedback loop. Based on the drive signals, the clamping force F_{cl} is calculated and adjusted considering a previously experimentally identified lookup table (see Sect. 3). Due to the self-locking leadscrew, clamping force adjustments are only possible by a feedforward control. For this reason, instationary variations of the clamping force (e.g. as a result of the cutting force) can not be considered.

The four-jaw-chuck HWR VT-S031 is designed to apply a maximum clamping force of $F_{cl,max} = 150$ kN. To achieve this force, each of the four actuator units has to provide an actuation force $F_{act} = 15$ kN. To proof the actuation concept, the test bench shown in Fig. 2a) is used. The test bench represents one of the four actuator units including one FHA-14C gear motor and the leadscrew. A force sensor based on strain gauges (Hottinger Brül & Kjaer U9C-50KN) measures the actuation force F_{act} . This sensor can measure forces in both +Z- and -Z- direction. During the experiments, different motor torques M_m are applied on the leadscrew and the resulting actuation force F_{act} is measured. As friction condition variations can lead to a significant deviation in axial forces for screws [8], two leadscrew lubricants (OKS265 and HLP32) are used to evaluate these correlations. The measurement is carried out at five different torques up to the limit for continuous loads of the motor ($M_m = 50\%$). The motor torque can be measured and adjusted by the EJ7411-module in percent of the peak motor torque.

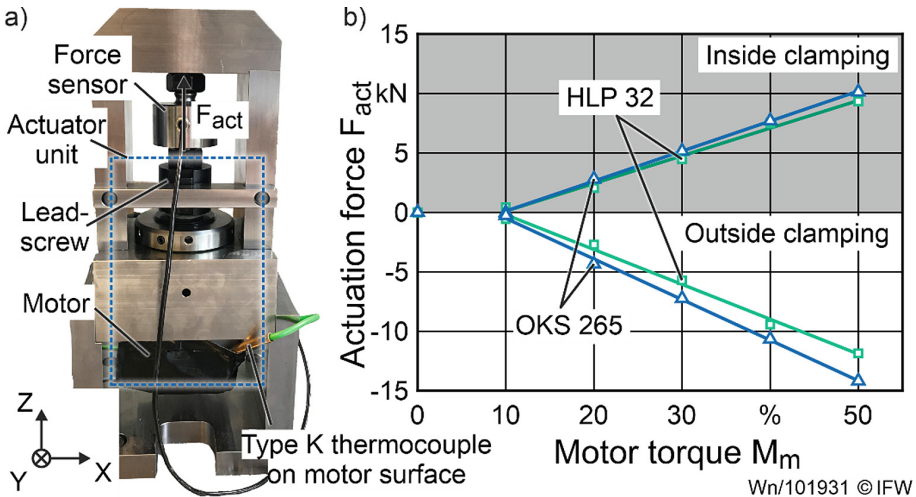


Fig. 2. Experimental setup to proof the actuation concept

The resulting correlations between the motor torque M_m and the actuation force F_{act} are presented in Fig. 2b). A linear proportional relationship between M_m and F_{act} can be observed. The highest force is $F_{act} = 14.5$ kN and occurs at the torque $M_m = 50\%$. For short-time ($t < 1$ s) peak torques, a maximal actuation force of $F_{act,max} = 18.3$ kN could be achieved (not shown in Fig. 2). Thus, the used actuation concept

provides sufficient high actuation forces to achieve a maximal clamping force of $F_{cl,max} = 150 \text{ kN}$. However, it can be seen that the actuation force also depends on the force direction due to the bearing friction moment between force sensor and leadscrew. Lower actuation forces can be achieved in + Z-direction which are used for inside clamping of workpieces. For inside clamping, the clamping force is increased by centrifugal forces during turning and thus lower actuation forces are sufficient for safe clamping. However, the results show higher actuation forces using OKS 265 lubricant. For outside clamping, the actuation force can be increased by up to 18.8% (8.5% for inside clamping) compared to HLP 30. Therefore, the OKS 265 lubricant is used for the prototype (see Sect. 3) to ensure high clamping forces.

2.2 Thermal Influences on the Actuation Force

For leadscrews, the actuation force highly depends on the friction coefficient μ in the thread [8]. In addition, high temperatures result in a generally high viscosity of the lubricant leading to a lower friction coefficient [9]. A lower friction coefficient increases the actuation force and thus the clamping force. Power losses of the motor are a heat source and could therefore affect the actuation force. To evaluate the influence of thermal losses on the actuation force, a reversing sequence of the motor was carried out with the test bench. A cycle of the sequence represents the clamping and machining of a typical ring-shaped workpiece. One cycle consists of a stepwise increase of the motor torque to $M_m = 50\%$ with subsequent constant torque for the time $t_{cl} = 10 \text{ s}$ (workpiece clamping and machining). For a complete cycle, the procedure is repeated in the opposite direction (workpiece removal and reloading). A total of $n = 1.000$ cycles are carried out while measuring the motor temperature with a type K thermocouple (Fig. 2a). In Fig. 3, the resulting correlation between the motor temperature ϑ and the actuation force

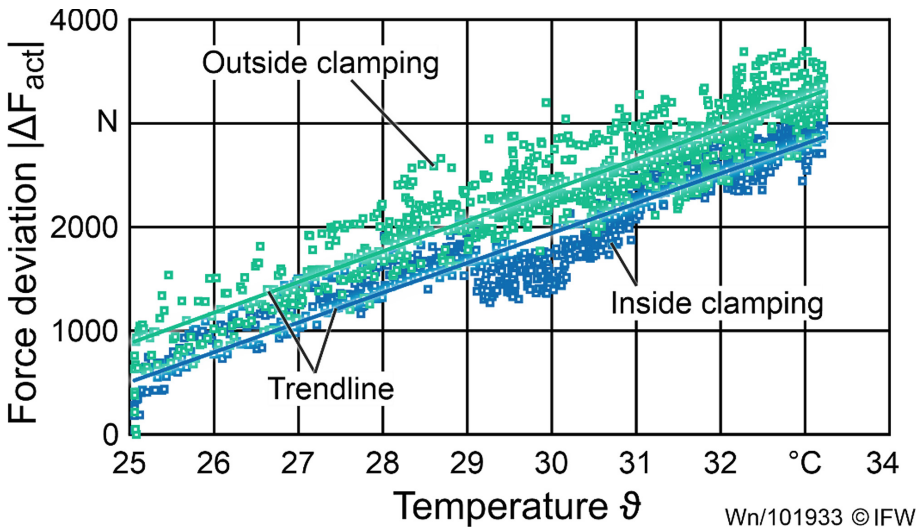


Fig. 3. Correlation between motor temperature and actuation force deviation

deviation $|\Delta F_{act}|$ is presented. This deviation is the difference between the measured force and the initial actuation force at a room temperature $\vartheta_0 = 25\text{ }^\circ\text{C}$. A linear proportional relationship between ϑ and $|\Delta F_{act}|$ can be observed. The highest actuation force deviation $|\Delta F_{act,max}| = 3.8\text{ kN}$ occurs for outside clamping at a temperature $\vartheta = 32.3\text{ }^\circ\text{C}$. This corresponds to a 26.2% increase in force compared to the initial actuation force $F_{act,0} = 14.5\text{ kN}$. Since the actuation force is proportional to the clamping force, thermally induced force deviations have a potentially significant influence on the clamping force. Therefore, this influence is evaluated in Sect. 3 using the assembled prototype.

3 Compensation of Thermally Induced Clamping Force Deviations

3.1 Clamping Force Adjustments with the Sensing Chuck Prototype

As shown in Sect. 2, thermal power losses of the actuation unit have a potentially significant influence on the clamping force. To evaluate this influence, the previously described experiments were repeated using the assembled prototype. First results showed, that the motor torque is not suitable to ensure a reliable clamping force adjustment. It is expected that highly non-linear friction between moving components of the chuck is the main cause of this issue. However, the measuring and control board of the chuck (see Fig. 1) provides an additional signal to adjust the clamping force: the angular position p . In order to verify whether the angular position allows a sufficiently high clamping force accuracy, the setup shown in Fig. 4a) was used. During the experiments, a reversing sequence of the motor was carried out. One cycle consists of a stepwise increase of the angular position up to the maximum achievable clamping force of the drives. A total of $n = 1.000$ cycles are carried out while measuring the motor temperature. During the experiments, the chuck temperature increased from $\vartheta_{chuck} = 23\text{ }^\circ\text{C}$ (room temperature) to a value of $\vartheta_{chuck} = 33\text{ }^\circ\text{C}$.

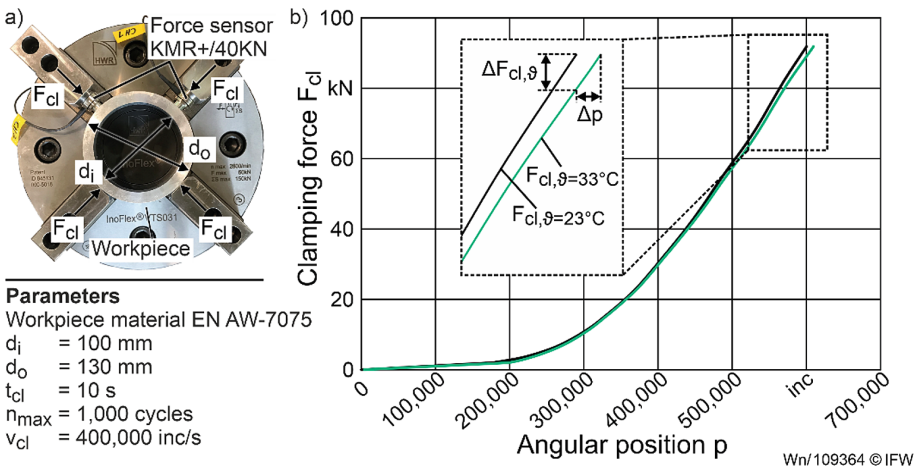


Fig. 4. Experimental setup and correlation between p and both F_{cl} and ϑ

In Fig. 4b), the resulting correlation between the angular position p and the clamping force F_{cl} is presented. In the diagram, the angular position is represented in increments. One increment (inc) represents the smallest detectable change in position. In addition, only the curve at the beginning ($\vartheta_{chuck} = 23\text{ }^{\circ}\text{C}$) and at the end ($\vartheta_{chuck} = 33\text{ }^{\circ}\text{C}$) of the measurements are shown. It can be seen that the clamping force also depends on the chuck temperature ϑ_{chuck} , resulting in small clamping force differences. The highest difference is $\Delta F_{cl,\vartheta} = 2.8\text{ kN}$ ($F_{cl,\vartheta=23\text{ }^{\circ}\text{C}} - F_{cl,\vartheta=33\text{ }^{\circ}\text{C}}$) and occurs at the position $p = 600,800\text{ inc}$. This corresponds to a relative clamping force error of $\Delta F_{rel} = 3.04\%$. In comparison, available clamping force measurement devices have a typical clamping force error of 3%. Therefore, the presented method of using the angular position for clamping force adjustments has a similar accuracy compared to specialized measuring devices on the market. To evaluate whether the error can be reduced further, a compensation method is proposed in Sect. 3.2.

3.2 Compensation of Clamping Force Errors

To evaluate whether the error can be reduced further, the identified correlation between angular position p , clamping force F_{cl} and chuck temperature ϑ are combined into a multidimensional lookup table. The lookup table was implemented into the EJ7411-modules and additional PT 100-sensors were integrated on the drives surface to monitor the chuck temperatures. Thereafter, the previous experiments were repeated. Based on five repetitions, the relative clamping force error ΔF_{rel} is calculated for each clamping force F_{cl} .

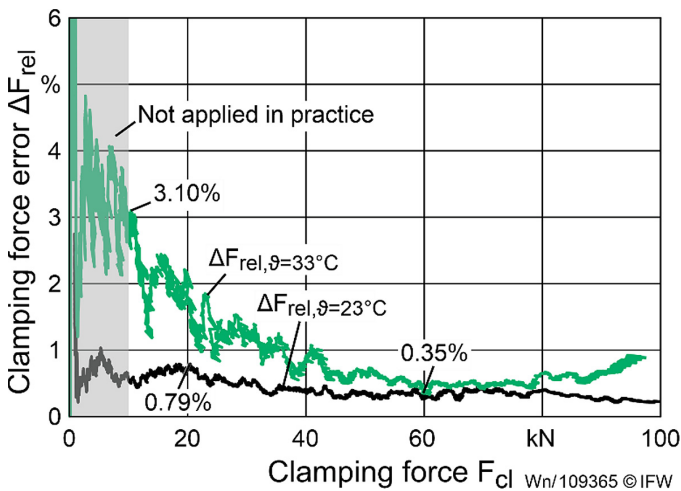


Fig. 5. Correlation between F_{cl} and both ΔF_{rel} and ϑ

In Fig. 5, the resulting correlation between the clamping force F_{cl} and the clamping force error ΔF_{rel} is shown. High errors ($\Delta F_{rel} > 3\%$) can be observed for clamping forces $F_{cl} \leq 10\text{ kN}$. According to [10], a minimum clamping force of $F_{cl,min} \approx 10\text{ kN}$

is required for safe clamping with the present chuck size. Below this clamping force, an uncontrollable workpiece release can occur. For this reason, clamping forces $F_{cl} \leq 10$ kN are not applied in practice. However, as the clamping force increases, smaller clamping force errors are achieved. The highest relative errors occur for $\vartheta_{chuck} = 33$ °C ranging from 0.35% to 3.10%. In addition, the highest absolute clamping force error is $\Delta F_{cl,max} = 862$ N at $F_{cl} = 97$ kN (not shown in Fig. 5). Compared to using only the angular position for clamping force adjustments (see Fig. 4, $\Delta F_{cl,\vartheta} = 2,800$ N), applying the lookup table reduces the clamping force errors by 69.3%. Especially for room temperature, the error is reduced to at least 0.79% respectively $\Delta F_{cl,max} = 325$ N ($F_{cl} = 80$ kN). Consequently, applying a lookup table allows a precise measurement and adjustment of the clamping force based on position and temperature signals of the drive.

4 Conclusion

This paper presents the design of a novel sensing chuck for clamping force measurement and adjustment. Thermal influences on the measurement accuracy are described and a compensation method is shown. With the compensation method, clamping force errors are reduced by 69.3%. Compared to common chucks ($\Delta F_{rel} \approx 10\%$), a lower clamping force error of 3.1% is achieved. Since the resulting shape deviation of thin-walled workpieces is proportional to clamping force [11], it is assumed that geometry deviations can be reduced to the same extent. Thus, future work aims to evaluate the machining tolerance achieved in cutting processes. In addition, further possible influences on the chuck accuracy (e.g. workpiece diameter, clamping position) will be investigated.

Acknowledgements. The results presented were obtained within research project “CyberChuck” (02P18K601). The authors thank the Federal Ministry of Education and Research for funding this project.

References

1. Brinksmeier, E., Sölter, J., Grote, C.: Distortion engineering – identification of causes for dimensional and form deviations of bearing rings. *CIRP Ann.* **56**(1), 109–112 (2007)
2. Heisel, U., Kang, C.: Model-based form error compensation in the turning of thin-walled cylindrical parts. *Prod. Eng.* **5**, 151–158 (2011)
3. Manikandan, H., Chandra Bera, T.: Modelling of dimensional and geometric error prediction in turning of thin-walled components. *Prec. Eng.* **72**, 382–396 (2021)
4. Sergeev, A.S., Tikhonova, Z.S., Krainev, D.V.: Automated thrust force calculation of machine tool actuators in fastening and turning steels. *Proc. Eng.* **206**, 1148–1154 (2017)
5. Denkena, B., Hülsemeyer, L.: Investigation of a Fine Positioning Method in Lathes Using an Active Clamping Chuck, pp. 245–246. *euspen* (2015)
6. Khaghani, A., Cheng, K.: Investigation on an innovative approach for clamping contact lens mould inserts in ultraprecision machining using an adaptive precision chuck and its application perspectives. *Int. J. Adv. Manuf. Tech.* **111**, 839–850 (2020)

7. Fleischer, J., Denkena, B., Winfough, B., Mori, M.: Workpiece and tool handling in metal cutting machines. *CIRP Ann.* **55**(2), 817–839 (2006)
8. Lambert, T.H.: Effects of variations in the screw thread coefficient of friction on the clamping force of bolted connections. *J. Mech. Eng. Science* **4**(4), 401–406 (1962)
9. Bair, S., Jarzynski, J., Winer, W.O.: The temperature, pressure and time dependence of lubricant viscosity. *Tribol. Int.* **37**(7), 461–468 (2001)
10. DIN German Institute for Standardization: Lathe Chucks, without Through-hole; Technical Conditions of Delivery for Power Operated Lathe Chucks (1983)
11. Estrems, M., Carrero-Blanco, J., Cumbicus, W.E., de Francisco, O., Sánchez, H.T.: Contact mechanics applied to the machining of thin rings. *Proc. Manuf.* **13**, 655–662 (2017)

Open Access This chapter is licensed under the terms of the Creative Commons Attribution 4.0 International License (<http://creativecommons.org/licenses/by/4.0/>), which permits use, sharing, adaptation, distribution and reproduction in any medium or format, as long as you give appropriate credit to the original author(s) and the source, provide a link to the Creative Commons license and indicate if changes were made.

The images or other third party material in this chapter are included in the chapter's Creative Commons license, unless indicated otherwise in a credit line to the material. If material is not included in the chapter's Creative Commons license and your intended use is not permitted by statutory regulation or exceeds the permitted use, you will need to obtain permission directly from the copyright holder.



Components



Improving the Thermal Behavior of High-Speed Spindles Through the Use of an Active Controlled Heat Pipe System

Lucas Jonath, Jörg Luderich[✉], Jonas Brezina, Ana Maria Gonzalez Degetau, and Selim Karaoglu

Technische Hochschule Köln, Cologne, Germany
joerg.luderich@th-koeln.de

Abstract. The thermo-elastic behavior of high-speed spindles has a significant influence on the machine accuracy. The Tool Center Point (TCP) changes continuously, not only due to the different temperature levels and energy inputs during warm-up, full-load and part-load operation, but also during interruptions for workpiece or tool changes. In this paper a heat pipe based tempering system is presented to control the spindle temperature and thus to keep the TCP displacement at a constant level, regardless of speed and load. As effective passive heat transfer components, heat pipes can be used not only to cool the system but also to insert heat into it. This capability of reversing the heat flow enables a high controllability of the temperature field in a bidirectional way and allows innovative capabilities of using advanced control algorithms. This paper describes the overall heat pipe concept and focuses on its potential as a key element for dynamic temperature control systems. Experimental results prove the feasibility of the concept with a simple on-off controller, achieving the reduction of the TCP displacement variation of a 2.2 kW spindle by 62% of its original value. The potential of the tempering concept forms the base for the deployment of various advanced control systems, such as Model-based Predictive Control (MPC), Fuzzy or Reinforcement Learning.

Keywords: high-speed motor spindle · heat pipes · thermal control

1 Introduction

Variations in the temperature of high-speed spindles in machining centers lead to thermo-elastic deformations of the spindle and thus to a displacement of the Tool Center Point (TCP). These deformations have a direct influence on the achievable workpiece accuracy, so it is desirable to make these distortions controllable in one way or another [1].

In practice, there are two basic approaches for solving this problem. The first possibility for compensating the changes of the TCP is through corrective measures. Based on spindle data, such as displacement, temperature, speed or power, the position of the TCP is estimated and adjusted in the machine control [2, 3]. Beside the required direct

intervention in the machine control system, an accurate thermal model of the spindle is required to estimate the thermal errors [4].

As second possibility, the temperature in the system can be stabilized. This approach often aims towards removing as much heat from the system as efficiently as possible, effectively by cooling the spindle or by isolating relevant machine components from the undesired heat input. Denkena distinguishes between motor, bearing and spindle shaft cooling, whereby in this work the focus is on motor cooling, more specifically, on stator cooling [5].

Regarding the cooling operation principle, a distinction can be made between passive and active methods. Passive measures usually describe the condition that no additional energy or periphery is required to dissipate the heat out of the system and they mostly consist in the optimal design of the spindle components, such as lamellar structures in the housing. While this approach generally results in low operation costs, the cooling capacity is insufficient in most of the cases for spindles with higher performance [5].

Active methods aim for a more efficient temperature management. The use of fluids, such as water, air or oil, enables the absorption of the generated heat close to the heat source, dissipating it rapidly and efficiently into the environment. Through the incorporation of cooling channels into the spindle design, the solely cooling of the motor presents the most widespread method of temperature control [5]. The solely cooling reduces the temperature level of the spindle, however cannot compensate completely the different energy in- and outputs that the spindle is exposed to during warm-up, full- and part load operations and pauses for workpiece or tool changes. This results in inhomogeneous temperature fluctuations in the spindle components and thus in an uncontrolled TCP displacement variation.

To address this issue, methods of temperature control with cooling and heating were researched by several scholars. One approach consists in the control of the temperature and volume flow of the cooling fluid. Steiert [6], for instance, achieves temperature fluctuations within a range of 0.5 °C using a cooling sleeve structure with decentralized coolant supply and feed forward control. Liu [7] developed a cooling system with multi-coolant channels, controlling independently the temperature of the bearings and motor and dissipating efficiently the internal generated heat of the spindle.

Another approach is the use of peltier elements or thermoelectric converters to regulate the temperature of the spindle components through targeted cooling and heating. Uhlmann [8] presented experimental evidence for the reduction of the TCP displacement using tubular peltier elements in combination with a fluid cooling sleeve. Ngo [9] developed a thermoelectric air-cooling module with different control mechanisms. The use of a PD controller for fast heating purpose and a PID controller for further temperature control provides a method to reduce the warm-up time and the TCP displacement. Fan [10] also presented a thermoelectric-based cooling system equipped with a water-based solution. With a PID controller, the temperature fluctuation can be kept within a range of 0.2 °C and the TCP displacement variation within a range of 12 µm during an experiment with different spindle speeds.

Summarizing the possible solutions for the displacement of the TCP, an overview of the existing methods is shown in Fig. 1.

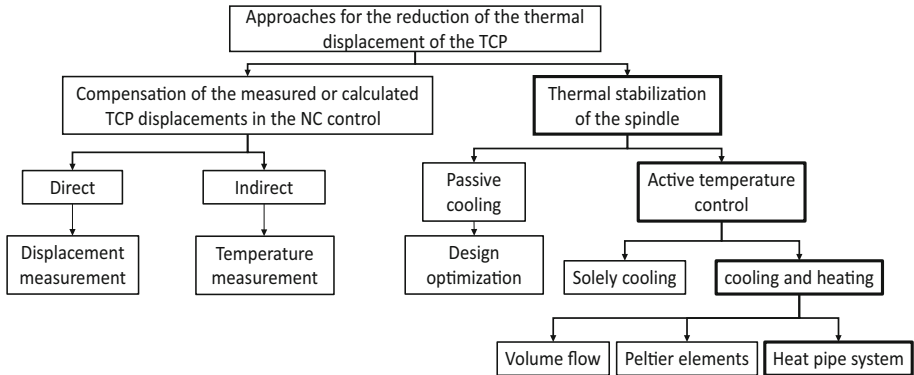


Fig. 1. Approaches for the reduction of the thermal displacement of the TCP

While the work of the other previous discussed scholars mainly focuses on the optimization of cooling strategies or on the controlling with peltier elements or volume flow, a different approach is presented in this paper. A heat pipe tempering system for the spindle stator is presented with the aim of effectively controlling the thermal field of high-speed spindles. The high thermal conductivity of heat pipes in combination with the reversibility of the heat flow provides the basis for a highly dynamic, function-oriented control of the spindle temperature, and thus of the TCP displacement.

Based on this, the following section focuses on the design of the heat pipe tempering concept. Subsequently, the specific design of the developed system for experimental purposes is described in Sect. 3. Furthermore, the test rig to validate the controllability of the spindle tempering system is introduced in Sect. 4. In Sect. 5, the results of selected experiments are presented and discussed. Section 6 finally draws a conclusion and presents next steps and future challenges in the development of a controllable spindle shaft displacement.

2 Concept Design

The foundation of the proposed spindle tempering concept is, as previously stated, the development of a heat pipe-based temperature control system. The usage of heat pipes for motor cooling has been reviewed in [11]. More specific, the advantages of heat pipes for cooling spindle shafts have been presented in [12].

The main focus in this project lays on the efficient integration of the heat pipes into a system that is capable of not just cooling, but also introducing heat into the spindle, thus reversing the heat transport. This will allow the development of an intelligent spindle temperature control system and, based on this, the control of the TCP displacement. Figure 2 shows the concept to integrate this bidirectional spindle tempering system into an existing machine tool.

The principal components of the concept are the spindle and the heat exchanger, the integrated heat pipes, the NC machine control, the frequency converter and a stand-alone microcontroller, the latter being responsible for the manipulation of the heat source and

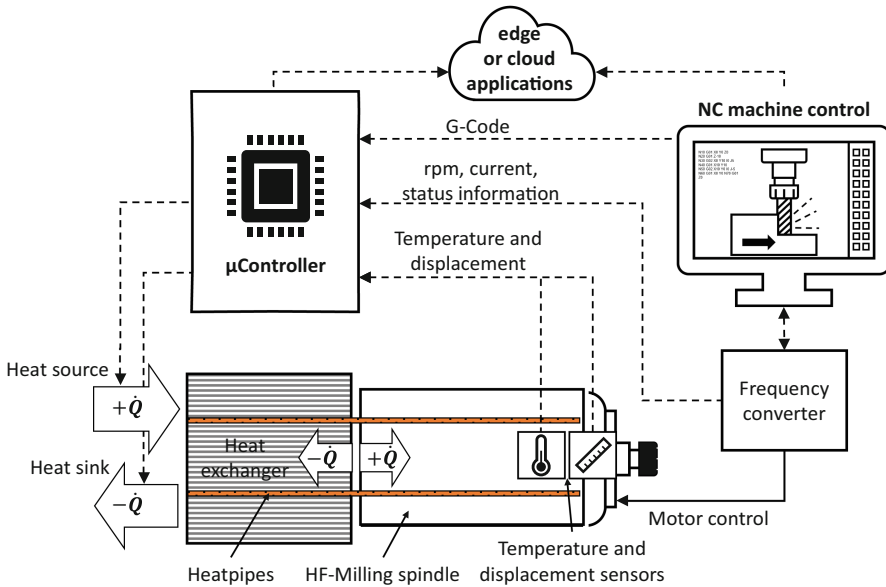


Fig. 2. Concept design for the heat pipe tempering system

heat sink. Different specific designs for these actuators are possible, like water- or air-cooled systems or various heat elements. The integration of an edge or cloud application for further implementations, like condition monitoring, is also possible.

Depending on the control task, various information can be acquired and passed to the controller. Temperature and displacement data are measured on the spindle. Electric current, spindle speed and status information can be taken from the frequency converter. Access to the G-code from the machine control, which describes the current or following machining task, offers potential, as it allows the expected thermal behavior of the machine to be anticipated.

In order to make the best use of this diverse information, intensive research is currently underway on various control approaches: on-off, PID control, fuzzy control, MPC, and a control system with a machine learning algorithm based on G-code data. All of these approaches are based on the performance of the bidirectional heat-pipe system described in this paper.

Controllability is assured by a high dynamic response of the heat pipes, enabling an effective heat transfer. This is achieved by evaporation of the working fluid at the heat input zone, followed by transport of the gaseous working fluid to the condensation zone, where it releases heat, condenses and then flows back through the capillary layer [13]. Hereby the condensation and evaporation zones depend on the external heating in-and outputs, so that the heat flow can occur in a bidirectional way.

3 Design of the Experimental Spindle

Based on the previously discussed design requirements, a 2.2 kW high-speed test spindle is developed and tested. The spindle design is based on a water-cooled reference spindle with the same technical parameters, which are summarized in Table 1. The only differences between these two is that the housing of the water-cooled spindle is made out of stainless steel, while the newly developed test spindle has a housing made out of aluminum with no water-cooling ducts inside. This freed-up space is used for mounting the sintered heat pipes.

Due to the good heat conduction properties, copper is used as the material for the heat pipes. A sintered structure has good gravity-independent properties, allowing a position-independent installation of the spindle. The working fluid is water, since it has a high specific power density between the operating temperature range of 20 °C and 80 °C [14]. A total of 12 heat pipes with a capacity of each 40 W, resulting in a total capacity of 480 W, are used, with one half of its length mounted in the spindle housing. The close positioning to the stator of the drive is advantageous, since the highest heat output is generated here and directly transferred into the heat pipes.

The other half of the heat pipes' length is mounted in the heat sink that serves the purpose of a heat exchanger, because both actuators for cooling and heating are integrated into it. In the inner surface of the heat sink, heat foils are mounted, allowing introduction of an additional heat of 180 W into the system. An axial fan for air cooling is placed on the opposite side from the spindle, pushing air through the heat sink. The exhaust air from the heat sink also flows along the spindle housing, thus ensuring further cooling due to forced convection. The slim design of the heat sink allows the practical integration of the tempering system into machine tool applications.

Table 1. Technical parameters of the spindle [15]

Parameter	Value
Max. Spindle speed	24000 rpm
Outer diameter	80 mm
Nominal power	2.2 kW
Torque	0.88 Nm
Frequency	400 Hz
Number of poles	2
Fixed bearing (front)	2x angular contact ball bearings
Loose bearing (back)	1x ball bearing
Max. Runout at the taper	5.0 μm
Tool holder	Manual ER 20 collets

Figure 3 shows the experimental spindle with the complete assembly unit of the heat pipe tempering system for high-speed spindles. With this setup, the temperatures of the

spindle system can be influenced bidirectionally. On one hand, the usual case would be heat flowing from the spindle to the heat sink. With the heat sink being in the condenser zone of the heat pipes and the spindle in the evaporator zone, the positioning ensures an effective cooling of the spindle. On the other hand, during warm-up or tool changes, the heat from the heating foils is directed into the spindle, reducing the heat up time of the machine or keeping the temperature at a constant level. With reversed roles - the heat sink in the evaporator zone and the spindle in the condenser zone - the spindle is effectively heated.

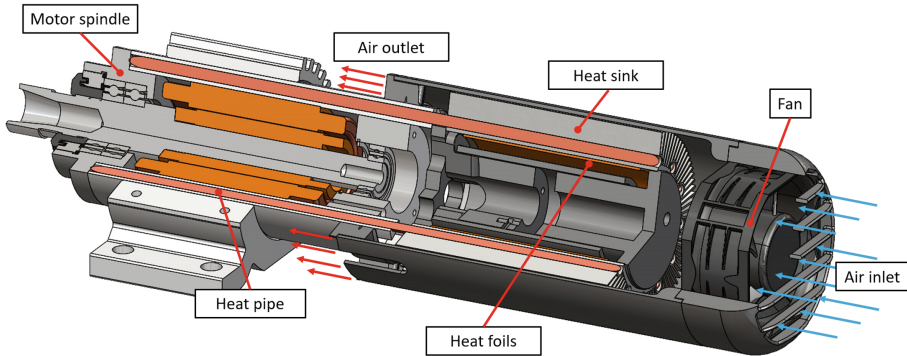


Fig. 3. Experimental spindle

Based on this construction, a network-based thermal model such as in [16] is implemented. It considers nine components of the spindle (fixed and non-fixed bearings, bearing seat, housing, holder, heat sink, drive, spindle nose and spindle shaft), which are the most relevant thermal masses of the system. Each mass is designed as a node with its respective thermal capacity and each node is connected to the adjacent ones through a thermal resistance, modelling this way the thermal conduction. The influence of the heat pipes is modelled through a dynamic thermal resistance depending on current temperatures. The forced convection due to the rotation parts which are in direct contact with the environment is calculated based on known formulas outlined in [17]. The heat transfer coefficients at the heat sink are determined based on NuBelt's similarity theory [18] and the air flow velocity in the channels is measured and implemented experimentally on the test bench as a function of the fan voltage and the corresponding speed. According to Liu [19], the heat generation at the heat sources is modelled. Finally, the TCP displacement is calculated via linear thermal expansion depending on the temperature of the spindle shaft.

Because of the focus on the experimental feasibility of the concept, a comprehensive analysis of the thermal model would go beyond of the scope of this publication. Nevertheless, the thermal model allows the conception and simulation of control strategies that can build on the results of the present work.

4 Experimental Setup

A corresponding spindle test rig is used for experimental investigations and to validate simulation results. The test rig shown in Fig. 4 has two different configurations: firstly, the heat pipe-based test spindle (a) as described in detail in the previous chapter is mounted on the right side. On the left side the load spindle generates the required torque loads on the test spindle.

Secondly, to be able to compare the test spindle with conventional cooling methods, a water-cooled spindle can be mounted on the test rig as shown in (b). The heat dissipation is realized by a compressor assisted cooling unit with 1 kW nominal power. The flow rate of the fluid is 4 l/min and the inlet temperature of the fluid at the spindle is set to 20 °C.

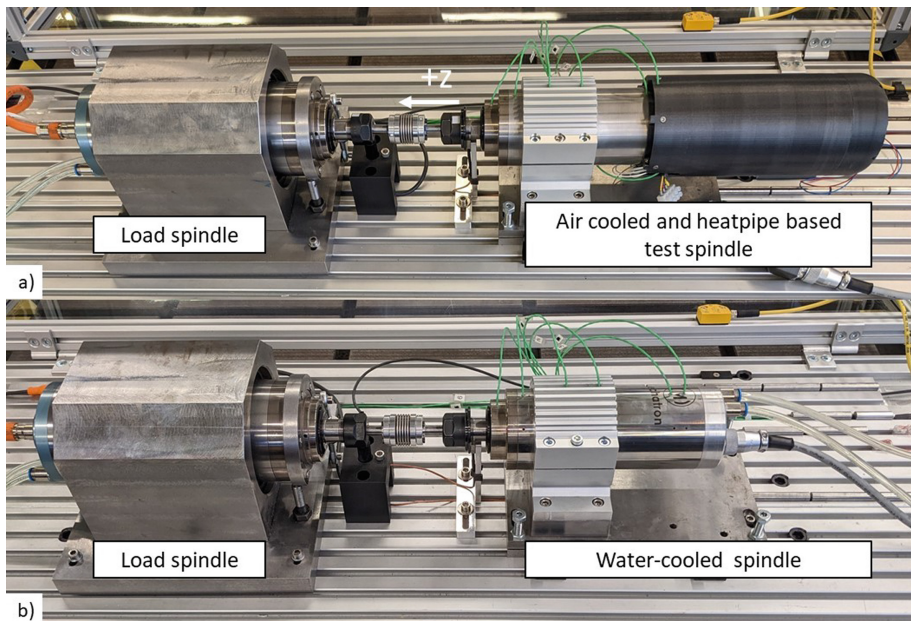


Fig. 4. Test rig: a) Test Spindle (air-cooled and heat pipe-based). b) Water-cooled spindle

The machine control (not shown in the figure) is required for controlling the test rig and recording the measurement data. To serve this purpose, the test spindle is equipped with a series of sensors. In total, seven type-k thermocouple sensors measure the temperature at different parts of the test spindle, while two additional sensors measure the ambient temperature. The temperatures recorded are those of the fixed and non-fixed bearing, as well as the temperature of the labyrinth seal, the stator, the housing, the non-fixed bearing seat, and the heat sink. To record the real spindle shaft elongation in the z-direction, an eddy current sensor with a resolution of 0.5 μm and a maximal linearity of $\pm 2 \mu\text{m}$ is used [20]. The target of this sensor is a ferromagnetic ring which is screwed onto the spindle shaft and locked with the collet nut. Afterwards, the displacement sensor

is adjusted so that the target is located within its measuring range of $500\ \mu\text{m}$. The sensor is calibrated to the target ring. The sensor is positioned so that the thermal expansion of the shaft increases its distance to the target. Furthermore, the actual spindle speed is measured by a hall effect sensor.

The test and load spindles are coaxially aligned and connected with a metal bellows coupling that can compensate for potential misalignment. The 4 kW load spindle is water-cooled and rotatably mounted in order to enable the detection of the applied torque, which is measured by a load cell by means of a corresponding lever arm on the load spindle. To generate a torque load, the load spindle is controlled at a lower speed than the test spindle. The resulting difference in speed causes a torque load to be applied and thus higher power usage results in a higher heat output than during idle. Both spindles are controlled by frequency inverters to generate the necessary speeds and torque loads. The energy drawn from the load spindle is converted into heat at an external braking resistor. The acquisition of the temperature data is done with a sampling rate of 1 Hz and the displacement and torque load with a sample rate of 250 Hz. The sensors for the torque, speed and displacement measurements are shown in Fig. 5.

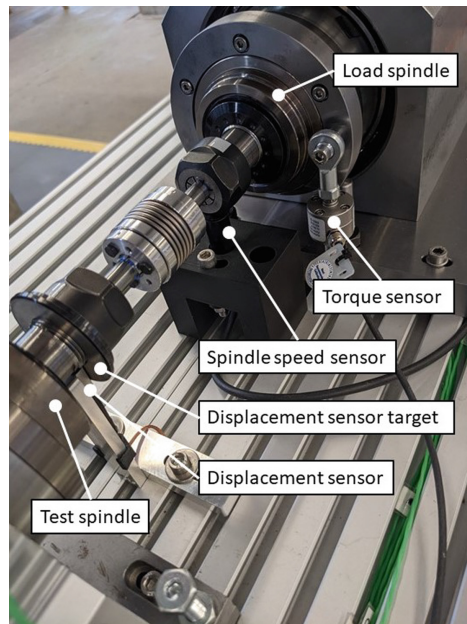


Fig. 5. Sensor positions on the test rig

5 Results and Discussion

The aim of the following experiments is to prove whether the temperature of the heat pipe system can be controlled with sufficient dynamics to reliably control the TCP displacement. In all experiments, the spindle speed is set to 24000 rpm while a torque

load of 0.58 Nm is applied to the spindle shaft. All tests are performed with a run-up time of 2 min for a better visualization. The cooling fan can operate within between an air velocity range of 8.5 m/s and 20 m/s, when active, while the heating elements operate within a range of 0 W and 180 W. The temperatures shown are measured at the fixed bearing, as this is the closest component to the spindle shaft, where the temperature can be measured during operation.

The results of the following tests are shown:

- Responsiveness of the spindle system to changes in heating and cooling capacity.
- Control of temperature and displacement with on-off controllers.

5.1 Responsiveness of the Spindle System to Changes in Heating and Cooling Capacity

The first of the following experiments as shown in Fig. 6 is designed to provide evidence of the high responsiveness of the heat pipe system to variable air velocity through the fan. This experiment is divided into three phases in which the cooling flow rate of the fan is varied. As the flow rate decreases, the temperature increases in each phase and stabilizes after a certain time. In the first phase, with a maximum air flow velocity of 20 m/s, the temperature of the spindle stabilizes at 44 °C; in the second, with an air flow velocity of 15 m/s, it stabilizes at 46.8 °C; and in the third phase, with 8.5 m/s, the spindle reaches a temperature of nearly 50.5 °C.

The displacement reacts to the changes of the cooling flow with a lesser and delayed intensity. This can be explained by the high thermal resistances between the spindle shaft and the spindle housing.

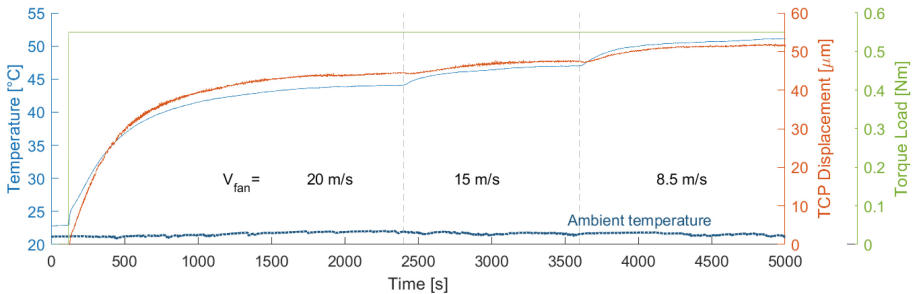


Fig. 6. Responsiveness to cooling flow variation

In the second experiment the effects of the heating elements are investigated. For this purpose, the thermal behavior of the spindle is investigated during the warm-up process with and without active heating elements. To describe at what point the system is thermal stable, the settling time t_s is used as the time where the temperature has entered the tolerance range of 1 °C around the steady value and doesn't leave it again [5].

Without heating elements (see Fig. 7), the spindle reaches its steady temperature of approx. 40.8 °C after a settling time of $t_s = 26.6$ min under load, similar to the displacement that reaches a steady value of 44.5 μm at the same point.

With forced heating (see Fig. 8), additional heat of 180 W is supplied into the system while the fan is turned off. Once a temperature of 43 °C is reached, the heating elements are shut off and the fan is turned on at its maximal air flow velocity of 20 m/s. The switch temperature was chosen based on previous measurements to ensure the shortest possible settling time.

During warm-up, temperature and displacement increase faster than without forced heating. After the heating is turned off and the fan on, a small overshoot on the temperature is registered and, after $t_s = 9.2$ min, the steady temperature of 40.8 °C is reached, effectively reducing the settling time of the temperature by 65%. The maximal displacement of 43 μm is reached after 15 min.

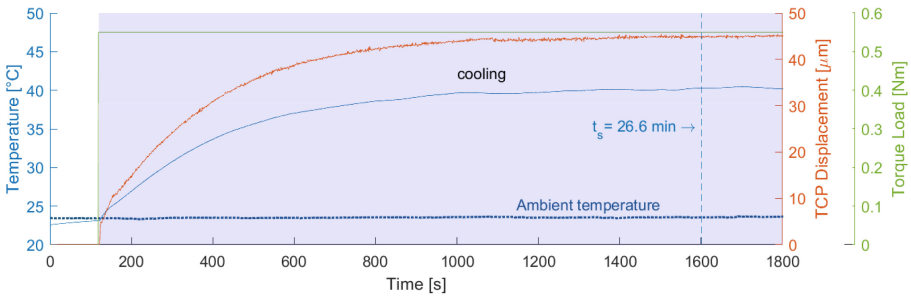


Fig. 7. Warm-up process without heating

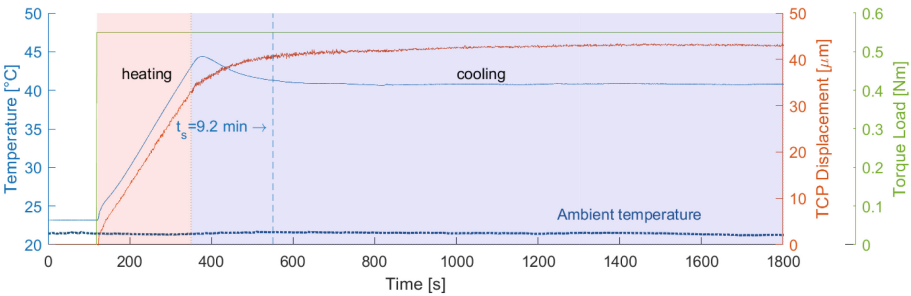


Fig. 8. Warm-up process with forced heating

Both experiments provide evidence for the responsiveness of the heat pipe system regarding temperature and displacement. The different slopes of the temperature during heating and cooling indicate that, with the heat foils, the heat can be introduced into the system faster than it can be removed through the cooling fan. While designing the controllers and its parameters, this has to be taken into consideration.

5.2 Control of Temperature and Displacement with On-Off Controllers

To be able to make a first prediction about the feasibility to reduce the TCP displacement variation by advanced control techniques two simple on-off controllers are implemented and tested. Primary goal is that, after the warm-up period, the displacement reached is kept as constant as possible, disregarding its maximal absolute value.

First, an indirect controller with the temperature as auxiliary variable is implemented and secondly the displacement is used as direct control variable. For reference, two measurements are made: the first one with the water-cooled spindle and the second one with the heat pipe-based spindle, showing its thermal behavior by constant cooling, i.e. without control. The underlying process inputs that also produce the heat generation are set as follows: the spindle speed remains constant at 24000 rpm, while the load is switched on and off periodically with a period duration of 15 min and a pulse width of 10 min, where the torque is set to 0.55 Nm.

Reference Measurement with the Water-Cooled Spindle

As described in Sect. 4 a similar spindle with a water-cooling system is used for comparison. With a compressor assisted cooling unit and a fluid inlet temperature of 20 °C the spindle temperature remains nearly constant at 26 °C with a slight variation of $\Delta T = 2.1$ °C, as shown in Fig. 9. The TCP displacement reaches a maximum of 31 μm and fluctuates around $\Delta\delta = 16$ μm in the z-direction. The displacement shows a nearly identical behavior at each torque period. The measurement shows that the temperature at the fixed bearing does not correlate to the TCP displacement. Regardless the nearly constant temperature, the displacement changes with a behavior of a first order lag.

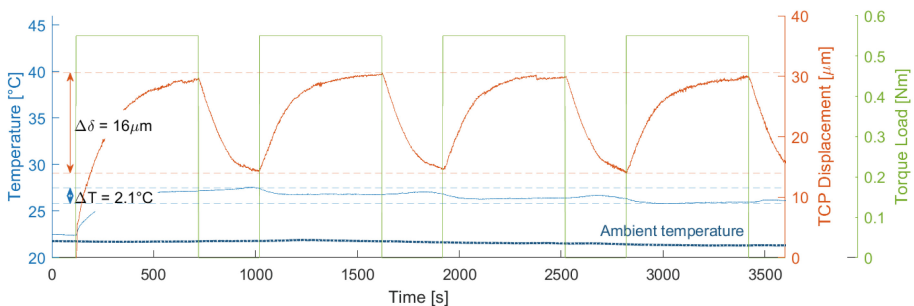


Fig. 9. Reference measurement with the water-cooled spindle

Reference Measurement with the Heat Pipe-based Spindle

In this reference measurement (see Fig. 10), the temperature fluctuates between 37.2 °C and 42.9 °C at an average ambient air temperature of 22.3 °C. This operating temperature is higher than the water-cooled one, but lies well in the operating range of the spindle.

The displacement fluctuates between 24 μm and 40.5 μm . The TCP position, thus, changes by $\Delta\delta = 16.5$ μm in z-direction during this test. The correlation between spindle temperature and TCP displacement is definitely higher with this heat pipe-based

spindle than with the water-cooled one. Nevertheless a few observations can be made: while the displacement reacts immediately to load changes, it can also be seen, that the temperature lags behind the displacement for about 50 s. Also, temperature and displacement behaviors do not show such high repeatability as with the water-cooled spindle.

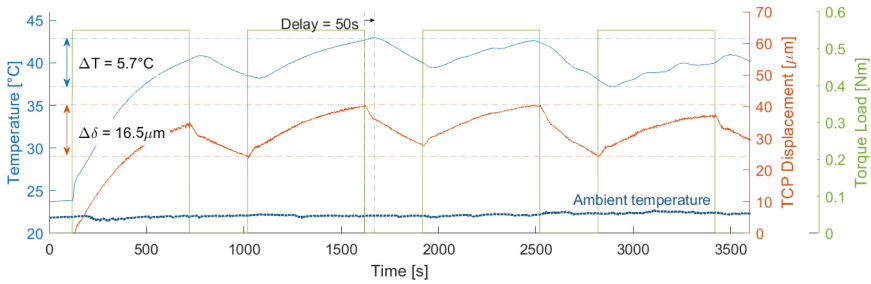


Fig. 10. Reference measurement with heat pipe-based spindle: uncontrolled process (only cooling)

Temperature Control

In the scenario shown in Fig. 11. The on-off controller uses the temperature of the fixed bearing as the control variable. The target temperature is set to 45 °C. Thus:

- Below 45 °C the heating is active with 180 W.
- Above 45 °C the cooling is active.
- Both actuators run at full power but never at the same time.

The heating elements can provide 180 W of extra heat and the fan is active at its maximum speed with an air velocity of 20 m/s. As displayed in the blue curve, the resulting temperature fluctuates at an ambient air temperature of 21.8 °C within a range of $\Delta T = 1.9$ °C and reaches a maximum of 46.7 °C. As soon as the target temperature is reached, the displacement fluctuates within a range of $\Delta \delta = 12$ μm.

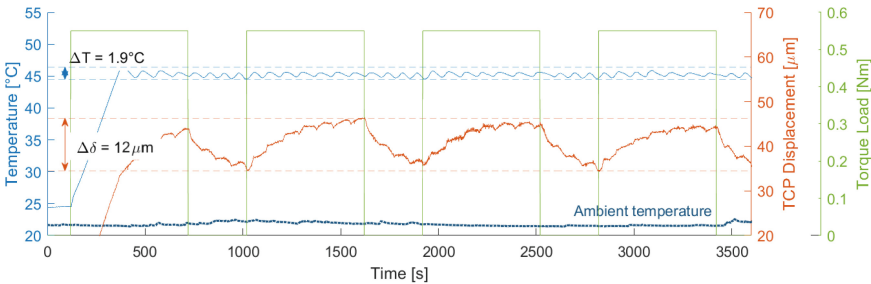


Fig. 11. Results of the on-off controller with the temperature as control variable

Even though the temperature control is acceptable, major variation in the displacement cannot be avoided. Due to the torque changes, additional heat is being introduced periodically, affecting directly the TCP displacement, pointing at the influence of another factor, depending on the torque load, that still has to be investigated. A similar behavior is observed on the water-cooled spindle: the temperature fluctuation remains on both systems nearly constant, though the variation of the TCP displacement of the heat pipe-based spindle is lower than of the water-cooled spindle.

Displacement Control

Because of the varying deformation, a second on-off controller as shown in Fig. 12 is implemented, now choosing the displacement as the direct control variable. Considering the temperature lag behind the displacement and need to compensate the inertias of the temperature, the switch rules are defined as follows:

- The heating remains active until a displacement of $43 \mu\text{m}$ is reached.
- Above a displacement of $45 \mu\text{m}$ the fan is active.
- Between these two thresholds neither of the two actuators is active, allowing the system to settle in.

This results in a stabilized displacement between $42 \mu\text{m}$ and $48.5 \mu\text{m}$ and an actual maximal displacement variation of $\Delta\delta = 6.5 \mu\text{m}$. The temperature fluctuates within a range of $\Delta T = 10^\circ\text{C}$ and reaches a maximum value of 52.6°C at an air temperature of 22.2°C .

A drop in the torque load causes a decreasing displacement, activating the heat introduction. Subsequently, the spindle temperature increases rapidly stopping the further displacement of the TCP. It can be clearly seen that the spindle shaft growth can be influenced and controlled by the thermal control of the spindle housing. In order to exploit this interaction to control the TCP displacement, the correlation between temperature distribution in the spindle and the TCP displacement should be considered in the control task.

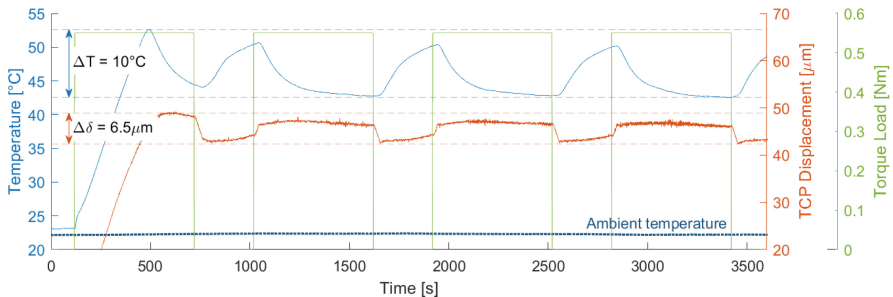


Fig. 12. Results of the on-off controller with the TCP displacement as control variable

Comparison of Displacement Variation

In Fig. 13 the curves of the TCP displacement with the four different approaches are

shown. With the water-cooled spindle, the displacement reaches a maximum value of $31 \mu\text{m}$ and a variation of $\Delta\delta = 16 \mu\text{m}$. In the reference measurement with the heat pipe-based spindle, i.e. solely air-cooling, the displacement fluctuates between $24 \mu\text{m}$ and $40.5 \mu\text{m}$, resulting in a variation of $\Delta\delta = 16.5 \mu\text{m}$ during operation, showing similar results to the water-cooled spindle. With an on-off control using the temperature as the control variable, this fluctuation is reduced by approx. 30% of the original value. Finally, with the displacement as the control variable, the on-off controller achieves a reduction by 62% of the displacement variation.

Using displacement as the control variable, instead of temperature, shows a better overall performance for the control task and can, therefore, be considered advantageous. However, an installation of a displacement sensor may not be desirable for all use cases, thus, model-based control approaches that operate solely with temperatures as input variables should be investigated.

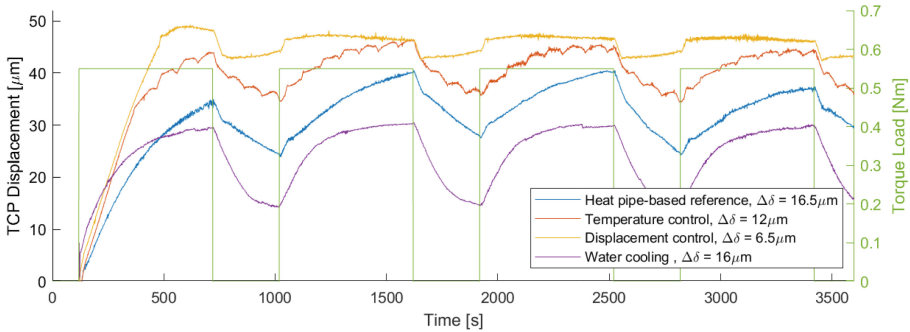


Fig. 13. Comparison of the TCP displacement variation

6 Conclusions and Ongoing Research

In this paper, a bidirectional tempering system based on heat pipes was introduced with the aim of stabilizing the TCP displacement. Integrated in an overall concept, the system's feasibility was proven and following conclusions can be drawn:

1. The dynamics of the heat pipes in combination with the actuators provide a good thermal responsiveness of the spindle system. This enables the controllability of the spindle temperature leading to wide possibilities for the control of the TCP displacement.
2. In comparison to a water-cooled spindle with constant inlet temperature, the controlled heat pipe-based spindle achieves a reduction of the TCP displacement variation. For this, two simple on-off controllers were implemented: with the temperature and with the actual displacement as control variables. While the first one only realizes a reduction of the displacement variation by approx. 30%, the latter achieves a reduction by 62% compared to the reference values ($\Delta\delta = 16 \mu\text{m}$ on the water-cooled spindle and $\Delta\delta = 16.5 \mu\text{m}$ on the uncontrolled heat pipe-based one).

3. Since a control by temperature is desirable, model-based control approaches should be also investigated.

To address this last issue and achieve a better control performance, more complex controllers are under development. Beside classical approaches such as PID, strategies like MPC and Fuzzy control are under investigation. Also, the anticipation of the thermal behavior using G-Code information and machine learning is ongoing research.

Furthermore, design-based approaches are in development. Since the currently used air-based cooling system is limited in its performance, heat sink solutions with a higher effectivity are tested in combination with the heat pipes. Likewise, the integration of more performant heating elements is considered.

Acknowledgements. The authors would like to thank the ZIM-Program (German Central Innovation Program) for funding and mechatron GmbH for their constant support during the project.

References

1. Mayr, J., et al.: Thermal issues in machine tools. *CIRP Ann. Manuf. Technol.* **61**(2), 771–791 (2012)
2. Brecher, C., Wissmann, A.: Compensation of thermo-dependent machine tool deformations due to spindle load: investigation of the optimal transfer function in consideration of rough machining. *Prod. Eng. Res. Dev.* **5**, 565–574 (2011)
3. Naumann, C., et al.: Hybrid correction of thermal errors using temperature and deformation sensors. In: Ihlenfeldt, S., et al. (eds.) *Conference on Thermal Issues in Machine Tools*, pp. 349–365, Dresden (2018)
4. Li, Y., et al.: A review of thermal error modeling methods for machine tools. *Appl. Sci.* **11**(11), 5216 (2021)
5. Denkena, B., Bergmann, B., Klemme, H.: Cooling of motor spindles – a review. *Int. J. Adv. Manuf. Technol.* **110**(11–12), 3273–3294 (2020)
6. Steiert, C., Weber, J., Weber, J.: Examination of cooling systems in machine tools regarding system structure and control systems. In: Ihlenfeldt, S., et al. (eds.) *2nd International Conference on Thermal Issues in Machine Tools*, MM Science Journal, Prague (2021)
7. Liu, T., Gao, W.: Power matching based dissipation strategy onto spindle heat generations. *Appl. Therm. Eng.* **113**, 499–507 (2017)
8. Uhlmann, E., et al.: Entwicklung einer thermoelektrisch temperierten Motorspindel. *wt Werkstattstechnik* **110**(5), 299–305 (2020)
9. Ngo, T., et al.: Developing a thermoelectric cooling module for control temperature and thermal displacement of small built-in spindle. *Therm. Sci. Eng. Process.* **25** (2021)
10. Fan, K., et al.: Thermoelectric-based cooling system for high-speed motorized spindle II: op-timization and validation strategy. *Int. J. Adv. Manuf. Technol.* **119**, 6521–6533 (2022)
11. Chen, Z., et al.: Study of heat pipe in motor cooling: a review. In: *E3S Web of Conferences*, p. 261 (2021)
12. Denkena, B., et al.: Cooling potential of heat pipes and heat exchangers within a machine tool spindle. In: Ihlenfeldt, S., et al. (eds.) *Conference on Thermal Issues in Machine Tools*, pp. 305–318, Dresden (2018)

13. Zouhri, B.: Heat Pipe Design and Technology, 2nd edn. Springer, Switzerland (2016). <https://doi.org/10.1007/978-3-319-29841-2>
14. deutscher Ingenieure, V.: VDI Wärmemaschinen, 11th edn. Springer, Heidelberg (2013). <https://doi.org/10.1007/978-3-642-19981-3>
15. Mechatron GmbH HFS-8022–24-ER20. https://www.mechatron-gmbh.de/fileadmin/user_upload/datenblaetter_2019/HFS-8022-24-ER20.pdf. Accessed 30 Sep 2022
16. Weber, J., Weber, J.: Thermo-energetic analysis and simulation of the fluidic cooling system of motorized high-speed spindles. In: The 13th Scandinavian International Conference on Fluid Power, Sweden (2013)
17. Koch, L., et al.: Coupled thermal and fluid mechanical modeling of a high speed motor spindle. *Appl. Mech. Mater.* **871**, 161–168 (2017)
18. Qian, H., et al.: Numerical simulation and experimental study of the air-cooled motorized spindle. *Proc. Inst. Mech. Eng. Sci.* **231**(12), 2357–2369 (2017)
19. Liu, Y., Ma, Y.-X., Meng, Q.-Y., Xin, X.-C., Ming, S.-S.: Improved thermal resistance network model of motorized spindle system considering temperature variation of cooling system. *Adv. Manuf.* **6**(4), 384–400 (2018). <https://doi.org/10.1007/s40436-018-0239-4>
20. Micro epsilon USA, eddyNCDT: Inductive sensors based on eddy currents. <https://www.micro-epsilon.com/download/products/cat-eddy/dax--eddyNCDT-SGS4701--en-us.html#page=2&zoom=Fit>. Accessed 30 Sep 2022

Open Access This chapter is licensed under the terms of the Creative Commons Attribution 4.0 International License (<http://creativecommons.org/licenses/by/4.0/>), which permits use, sharing, adaptation, distribution and reproduction in any medium or format, as long as you give appropriate credit to the original author(s) and the source, provide a link to the Creative Commons license and indicate if changes were made.

The images or other third party material in this chapter are included in the chapter's Creative Commons license, unless indicated otherwise in a credit line to the material. If material is not included in the chapter's Creative Commons license and your intended use is not permitted by statutory regulation or exceeds the permitted use, you will need to obtain permission directly from the copyright holder.





Thermal Growth of Motor Spindle Units

Tassilo Heinze¹ , Hans-Joachim Koriath¹  ,
and Alexander Pavlovich Kuznetsov² 

¹ SPL Spindel und Praezisionslager GmbH, 04720 Doebeln, Germany
dkoriath@t-online.de

² Moscow State University of Technology STANKIN, 127055 Moscow, Russia

Abstract. The paper deals with strategies for numerical compensation of thermo-mechanical deformation of machine tool spindles and the TCP, respectively. Methods for digital modelling and simulating the temperatures and thermo-elastic deformation are presented. This is done by considering the geometry, material data, drive signals and temperature values. The topic of compensating thermo-elastic effects in spindle units is an important topic in manufacturing. Analytical equation and function block methods for measuring and predicting thermal spindle growth are compared. The heat flow model converts variable spindle load, speed, coolant and ambient temperature into local temperatures followed by elastic deformations of the spindle unit. The simulation results were verified for different types of motor spindles by experiments on a spindle test rig at SPL GmbH. A thermal stiffness value [W/ μm] is characterized by the energy losses of the spindle, which result in thermal growth. Different strategies for digital reduction of a thermal spindle growth were developed.

Keywords: Motor spindle · thermal load · elastic body · simulation · test bench

1 Causes for Thermal Growth

The linear theory of thermoelasticity of materials was established by Cauchy and Timoshenko before 1914 and relates a heat flow to the local temperature gradient, a relationship known as Fourier's law. Under mechanical and thermal loading, an elastic spindle unit undergoes stresses, strains, and deformations that continue in spindle growth. Thermal growth of motor spindle units leads to significant manufacturing errors and risks due to lack of predictive applications and essential energy consumption until a thermostable state is reached.

The motor spindle units of SPL GmbH [1] are customized for machining processes (turning, milling, grinding, dressing, test bench) based on technical requirements including thermal spindle growth. Customized motor spindles require an approved design concept for mechanical and thermal stiffness, resource efficiency, service life reserve, precision and quality assessment at the test bench. A motor spindle unit, see Fig. 1, integrates the electric motor, shaft with bearing, tool holder, clamping, encoder and the housing with the stator, water cooling.

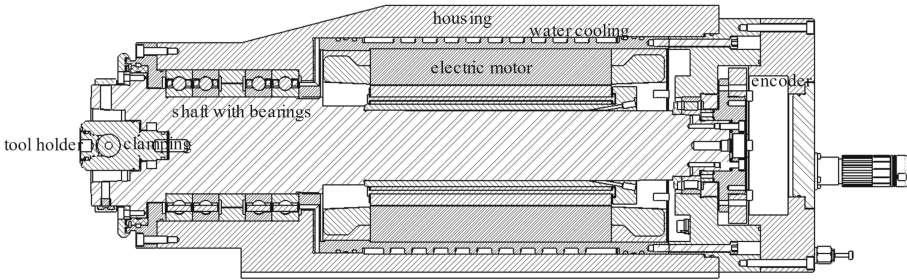


Fig. 1. Motor spindle unit SPL2782.1

The heat generation bases on the energy consumption of the spindle unit, the losses of electrical energy and the mechanical-fluidic friction losses under mechanical load. The causes for thermal growth are heat generation in the motor spindle unit by the electric motor, cooling water, process and ambient temperature, and thermal stiffness of the tool adapter, shaft, bearings, and housing.

In [2], a method for analytical calculation of heat transfer on spindle bearings was developed with the objective of axial and angular misalignment compensation.

[3] gives an overview of research activities in the field of thermal errors in machine tools, e.g., advances in the measurement of thermal errors and temperatures, methods for calculating thermal errors in machine tools, and reduction of thermal errors.

In [4–6], the state of the art on methods for controlled thermal deformations in machine tools is analyzed and compared, and mathematical methods for thermoenergetic-thermoelastic models and thermal stiffness are advanced.

Previous thermostable measurements, require lengthy investigations and have been extended by non-stationary thermal analytical methods [7].

Paper [8] gives an overview of various thermal failure modeling methods, including least squares method, multivariable regression analysis, Grey system, neural network, support vector machine, and hybrid model. One can measure a number of local temperatures and compare them with the component displacements, but the compilation of rigid bodies does not lead to correct thermal growth values.

There are two basic thermal deformation shapes, thermal elongation and thermal bending, shown in [9: Fig. 3.1] ... There are nine candidate temperature sensor locations for the thermal elongation, whereas there are eighteen, nine each in the upper and lower surfaces, for the thermal bending [9].

The International Organization for Standardization (ISO) has developed several standards for test methods for geometric accuracy under static or unloaded conditions: ISO 230-3 (Determination of thermal effects [10]); ISO 16907-2015 (Numerical compensation of geometric errors [11]).

The model-based prediction of thermoenergetic power transformations and heat flows, the influence of spindle thermoelasticity under process loads and the influence of the environment are not yet solved in the State of the Art. Compared to the research efforts on measurement, simulation and compensation strategies related to thermal growth of

motor spindles, this paper proposes a digital prediction and numerical compensation under real-time process load.

2 Prediction Methods

A quality assessment of the geometric accuracy and kinematic errors in a real tool, part or machine tool is usually defined by a series of standards (see Fig. 2 right) [10, 11]. Quality assessment of a thermal spindle growth is necessary for real and digital systems, where digital prediction methods are required. Digital models base on 1-deterministic relations (temperature, position sensors), 2-input-output relationships and 3-data correlations. Therefore, digital quality assessment methods of a thermal spindle growth will apply analytical equations, or parameterized function block models, or black boxes (see Fig. 2 left). The digital models require new virtual validation and verification methods (structural parametric method), like IEEE Standard for System, Software, and Hardware Verification and Validation [12].

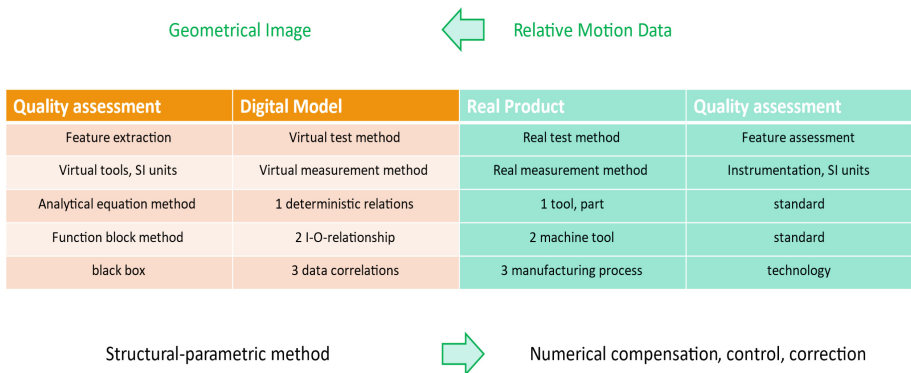


Fig. 2. Prediction and quality assessment methods

Digital prediction and numerical compensation methods are necessary for the thermal spindle growth, because of missing real temperature and position sensors on the shaft at high spindle speed and process load. This paper targets methods for a digital prediction and numerical compensation of thermal spindle growth by both methods for analytical equations and functional blocks.

2.1 Analytical Equation Method

The initial scientific and methodological assumptions for creating a thermal and thermoelastic model of a motor spindle is the idea of the thermal system of a machine tool [13]. A thermal system is a set of interconnected thermoactive elements (parts and assemblies) with quasi-stable thermal and thermoelastic relationships between them. In this work, the same systematic approach is applied to motor spindle units. A spindle

assembly (motor spindle) has inherent elements (see Fig. 1 and Fig. 3). Heat-active elements (parts and assemblies) are structurally interconnected with quasi-stable thermal and thermoelastic links. Heat carriers and heat sources are the main elements of the thermal system of the spindle unit. The heat released in the sources is partly transferred and redistributed between the heat-generating elements of the spindle unit. Partly it goes into heating the heat-generating sources themselves, and partly it is dissipated to the environment. Thus, there are thermal interactions or thermal connections between the main elements of the thermal system of the spindle unit and between the main elements of the thermal system and the environment.

Thermal interaction between two elements or between an element and the environment is understood to be such an interaction where a change in the thermal state of one element or the environment leads to a change in the thermal state of the other element. The thermal interaction between the main elements of the thermal system of the spindle assembly forms an internal thermal link. The thermal interaction between the main elements of the thermal system and the environment forms an external thermal connection. Thermal relations between the main elements in spindle units are realized by conduction (1), convection (2), radiation (3) and heat exchange (4). The heat flows between the thermal masses lead to physical phenomena of heat conduction, heat convection, heat radiation, heat exchange and lead to local spindle temperatures compared to environmental and coolant temperatures.

$$\dot{Q} = \frac{\lambda A t \Delta T}{L}; \quad (1)$$

$$\dot{Q} = \alpha A t \Delta T; \quad (2)$$

$$\Phi = \alpha \Phi_s; \quad (3)$$

$$c_1 m_1 \cdot (T_1 - T_m) = c_2 m_2 \cdot (T_m - T_2). \quad (4)$$

The set of internal thermal relations between the main elements of the thermal system forms the thermal structure of the spindle unit (or assembly or part) [4–6]. A thermal model (structure) of a spindle assembly is created by idealizing the structure of the heat-active elements of the spindle assembly, the connections between them and the heat transfer processes taking place within it. A mathematical model of the thermal structure of the spindle unit is created based on the concept of the thermal system and the cause-effect relationship diagram. To create a mathematical model, it is necessary to schematize the determining factors and proceed to their quantitative description.

The heat flow brought to the heat-active element from the sources is withdrawn into the environment and other heat-active elements of the spindle unit, as well as goes to the heating of the element itself. On the basis of the law of conservation of energy, the equation of heat balance of the thermoactive element i of the system will be written in the form of

$$Q_i + Q_{ienv} + \sum_{i=1, i \neq j}^n Q_{ij} = \sum_{i=1}^n Q_{iall}; \quad (5)$$

where Q_i – power losses, going for heating the thermoactive element i (accumulation of heat energy); Q_{ienv} – power losses transferred to the environment; Q_{ij} – power losses transferred to the thermoactive element i ; $\sum_{i=1}^n Q_{i\text{all}}$ – total power losses brought to this element from heat sources; n – number of thermoactive elements of the system.

According to the first law of thermodynamics, heat energy accumulation in the element i is described by the equation

$$\dot{Q}_i = c_i \cdot m_i \cdot \frac{d\tilde{T}_i}{dt}; \quad (6)$$

where c_i – specific heat capacity of the thermoactive element; m_i – mass of the thermoactive element; \tilde{T}_i – average temperature.

Similar equations can be written for other thermoactive elements of the system, then we get a system of thermal balance equations:

$$c_i \cdot m_i \cdot \frac{d\tilde{T}_i}{dt} + \alpha_i \cdot A_i \cdot (\tilde{T}_i - T_{ienv}) + \sum_{i=2, i \neq j}^n \alpha_{ij\text{cont}} \cdot A_{ij} \cdot (\tilde{T}_i - \tilde{T}_j) = \sum_{i=1}^n Q_{i\text{all}}; \quad (7)$$

where α_i – heat convection or radiation coefficient, A_i - heat transfer surface area, $\alpha_{ij\text{cont}}$ - heat conductivity coefficient of the junction between the contacting i and j elements (if the intermediate medium between the elements is air, oil, strips, inserts, wedges $\alpha_{ij\text{cont}} = (\alpha_{i\text{cont}}^{-1} + h/\lambda + \alpha_{j\text{cont}}^{-1})^{-1}$; A_{ij} - contact area of mating element surfaces, T_{ienv} – ambient temperature (air).

Then a system of equations can be written for the spindle unit (part, unit) in matrix form:

$$[C] \cdot \frac{d[T]}{dt} + [K] \cdot [T] = [\dot{Q}]; \quad (8)$$

where $[T]$ is the matrix column of average element temperatures,

$$[C] = \begin{pmatrix} c_{11} \cdot m_{11} & \dots & 0 \\ \vdots & \ddots & \vdots \\ 0 & \dots & c_{nn} \cdot m_{nn} \end{pmatrix}; \quad (9)$$

$$[\dot{Q}] = \begin{pmatrix} \sum_{i=1}^n Q_{i\text{all}} + \alpha_1 \cdot A_1 \cdot T_{1env} & \dots & 0 \\ \vdots & \ddots & \vdots \\ \sum_{i=1}^n Q_{i\text{all}} + \alpha_n \cdot A_n \cdot T_{nenv} & \dots & 0 \end{pmatrix}; \quad (10)$$

$$[K] = \begin{pmatrix} \alpha_1 \cdot A_1 + \sum_{i=2, i \neq j}^n \alpha_{1j\text{cont}} \cdot A_{1j} & \dots & \alpha_{1n\text{cont}} \cdot A_{1n} \\ \vdots & \ddots & \vdots \\ \alpha_{n1} \cdot A_{n1} & \dots & \alpha_n \cdot A_n + \sum_{i=2, i \neq j}^n \alpha_{nj\text{cont}} \cdot A_{nj} \end{pmatrix}; \quad (11)$$

Solving the obtained system (8) or (7), we obtain the average temperatures of heat-active elements of the spindle unit (unit, part). Using the calculated average temperatures of thermoactive elements, we also obtain the distribution of heat flows in the thermal

structure. A thermo-energetic model can substitute the installed temperature sensors by virtual ones.

The thermoelastic model subsystem is implemented based on the representation of the thermoelastic structure of the motor-spindle (by analogy with a spindle unit [13]) as an interconnected set of homogeneous thermoactive elements that form and determine their spatial and temporal relative position. Over time and due to thermal influence, the thermoactive elements change their thermoelastic properties, and the relations between the two thermoactive elements of the system are also subject to the conditions of reciprocity and jointness of linear and angular motions, that is, each thermoactive element performs only those displacements that are allowed by their mutual link. In order to construct the thermoelastic structure of a motor-spindle, it is necessary to define in more detail the types of typical quasi-thermostable links, interacting thermoactive elements and thermal behavior functions. As the simplest thermoactive element, it is reasonable to choose [5] a rod of arbitrary cross-section, the movement of the ends of which is limited by the links imposed on them. The connection of the thermoactive elements by quasi-thermally stable links can be serial, parallel, or a combination thereof. If a thermoactive element transmits a thermoelastic action through an intermediate link, then such a thermoelastic structure consists of three links and functions of thermal behavior. Then a thermoelastic model of one thermoactive element with two quasi-thermostable links will describe its thermal behavior, the general solution of which will be defined by an expression of the following form:

$$\delta_{fr} = \int_0^x \beta \cdot T_1(x) \cdot dx + C_1 \cdot x + C_2; 0 < x < L_{fr}; \quad (12)$$

$$\delta_L = \int_{L-L_{fr}}^x \beta \cdot T_2(x) \cdot dx + C_3 \cdot x + C_4; L - L_{fr} < x < L; \quad (13)$$

where C_1, C_2, C_3, C_4 are determined from the conditions of reciprocity $\delta_T - \delta_P = \delta_0^* + \delta_{fr}^*$ and jointness of linear and angular motions in the places of quasi-thermostable links of the motor-spindle elements, $\delta_0^*, \delta_{fr}^*$ - displacements in the links, L - length of the motor-spindle shaft, L_{fr} - length between the front and rear supports, $(L - L_{fr})$ - length of the free part of the spindle shaft, $T_1(x), T_2(x)$ - temperature distribution between the supports and the free part of the spindle.

A TCP is located at the tool tip. If a tool is not clamped, the spindle front is the target. Then the axial displacement of the front end of the spindle will be defined as the vector sum of the elements of the thermoelastic structure of the motor-spindle.

2.2 Function Block Method

Analytical equation method for a shaft temperature over length in (14) uses closed-form solutions and offers a clear view into how variables and interactions between variables affect the result.

$$T(x) = \frac{Q_1}{A \cdot \lambda \cdot m} \cdot \frac{\cosh[m \cdot (l - x)]}{\sinh(m \cdot l)} + \frac{Q_2}{A \cdot \lambda \cdot m} \cdot \frac{\cosh(m \cdot x)]}{\sinh(m \cdot l)}; \quad (14)$$

A function block (see Fig. 3) graphically defines a physical function with input-output variables and parameter sets. The function block method uses lumped thermal masses linked to virtual temperature sensors by conductive, convective blocks. The function block model in Fig. 3 [14] applies the shaft model, parameters and equations of [6]. The friction heat generation was set to $Q_1 = 15 \text{ W}$ for the rear bearing A and $Q_2 = 45 \text{ W}$ for the front bearing B, spaced by the shaft length 0,5 m. The temperature sensor T represents one of 11 virtual sensors, spaced by 1/10 over the shaft length.

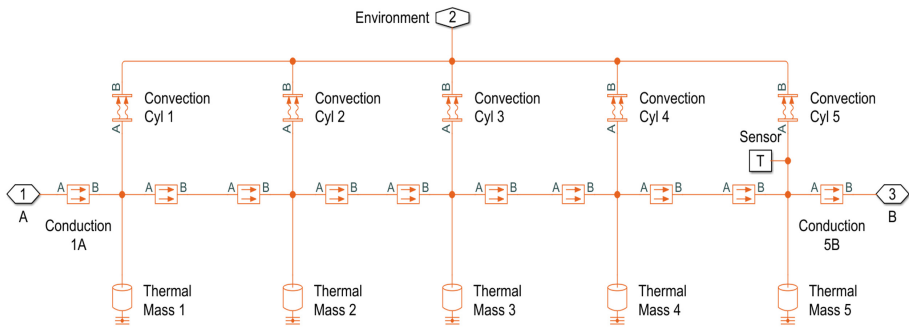


Fig. 3. Function block method for a spindle shaft (1-Rear bearing A, 2-Environment temperature, 3-Front bearing B, T-Temperature sensor)

Figure 4 shows a temperature comparison between the analytical equation $T(x)$ (14) and function block simulations T_{sim} of Fig. 3 aiming at a thermostable state.

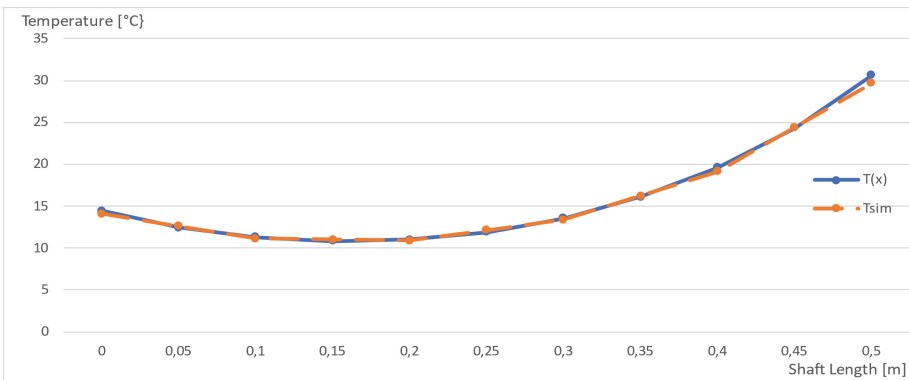


Fig. 4. Shaft temperature over length ($T(x)$ -analytical Eq. 5; T_{sim} -Function block)

Analytical equation method has a continuous high accuracy, when the function block method is using Fourier’s law for linear approximations by 5 sections in Fig. 4. The application of one of both methods depends on the spindle design and thermo-physical boundary conditions.

A thermal model of the spindle unit growth bases on linked physical phenomena of thermoenergetics and thermoelasticity, see Fig. 5. Parametrized function blocks reflect the motor spindle design and working conditions. Because of the model complexity, this paper describes a general structure following Fig. 3 and Fig. 5. Parametrized function blocks of the motor spindle unit SPL2782.1 were approved by MATLAB/Simulink, SimulationX and OpenModelica projects. The number of Simulink elements is 526, and 128 parameters define the element properties.

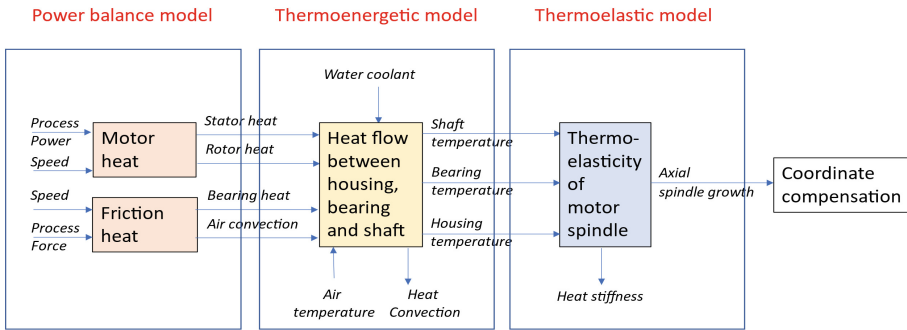


Fig. 5. Thermoenergetic and thermoelastic models

Power balance model (see Fig. 5): Process loads, motor power consumption P , spindle speed n , environmental and coolant temperatures are the variable input values. Motor spindle drive units provide digital values of the power consumption, speed.

Analytical equations calculate the motor heat power and bearing heat power from these variables and electric motor parameters. This deterministic model is parametrized for a special type out of a wide range of spindle modifications. Elements for asynchronous and permanent magnet synchronous motors are included. Motor heat power is available by analytical equations or from the SIEMENS calculation tool SIMOTICS M-1FE1 “Total power loss” [15]. Friction heat of different spindle bearing types and configurations is calculated under pre- and process loads. Friction and power loss calculation is available by analytical equations from the SKF product catalogue rolling bearings or an SKF application tool [16]. The mechanical spindle power minus heat power at the output in relation to the electrical power consumption at the input defines the actual energy efficiency of the motor spindle.

The **thermoenergetic model** (see Fig. 5) applies a lumped mass method, consisting of each five thermal masses along the shaft and housing axis. Heat flows between thermal masses are linked by conductive, convective elements. Variable environmental and water-cooling temperatures are reference temperatures for heat flows. Therefore, thermo-physical and thermomechanical parameters support the parametrized model elements. Following Fig. 1, the motor spindle CAD geometry provides geometrical parameters for the rotor, shaft, bearing shields, and stator housing. Referring to [6] the obligatory number of temperature elements was found at 11. Respectively 11 virtual temperature sensors elements monitor the shaft and housing temperature over the spindle length, extended

by 2 bearing temperatures. A thermo-energetic model can substitute the installed temperature sensors. Two alternative methods are included: whether the thermo-energetic model calculates virtual housing, bearing, shaft temperatures, or real sensors measure them.

The **thermoelastic model** (see Fig. 5) also bases on lumped masses linked by elastic Hook (spring) and Newton (damper) elements. The thermoelastic parameters define mechanical stiffness, damping and thermoelastic elongation values. The model output value generates the axial spindle growth at the shaft front end relative to the housing fixation below the front bearing. Simulated thermo-energetic temperatures and thermoelastic displacements were verified by installed sensor values, in order to monitor failure states of the spindle unit and/or assess the simulation. The simulation hardware was an Intel Core i5-7200U processor with 16 MB RAM and SSD under OS Windows 10. The input variables and output axial spindle growth of the simulation model build digital time series for monitoring and reporting issues. A typical simulation in variable step mode continues 12 s for a real 16 h spindle test cycle.

3 Verification of the Simulation by Test Bench Results

The simulated axial spindle growth bases on Fig. 5 and was verified by test results of motor spindle units. Main geometrical dimensions of the motor spindle unit base on CAD data in Fig. 6: shaft length 0.5295 m with HSK80C; tool dummy length 0.2 m; together with a mass of 36.7 kg, additional rotor 1FE1084-4WN31 with a mass of 6.2 kg. The dynamic load torque M_L is known from the motor torque M following (15)

$$M - M_L = J \cdot \frac{d\omega}{dt}, \quad (15)$$

where J is the moment of inertia, ω – the angular velocity (see Fig. 6). A motor spindle test at different speeds is required during 16 h under no load conditions for a bearing lubrication run and a quality assessment and actual spindle power [kW], see Fig. 7.

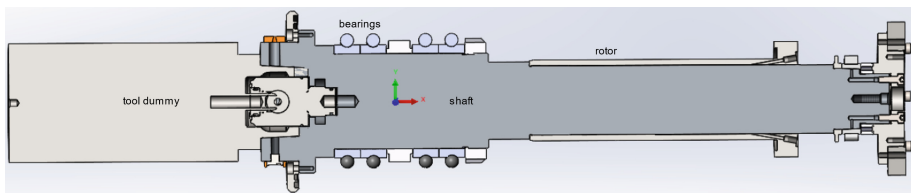


Fig. 6. Shaft of the motor spindle SPL2782.1

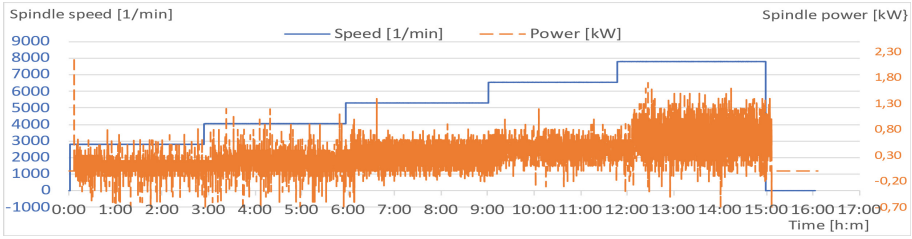


Fig. 7. Speed and actual spindle power during test cycle

Table 1. Internal sensor types

Assembly	Sensor type
stator	PT1000, PTC
bearing	PT100

Several temperature sensors (Table 1) were installed inside the spindle unit for data sampling. Installed sensors can monitor temperatures causing a thermal spindle growth. PT1000 with a resistance of 1000 Ω measures the stator temperature, caused by heat power loss (16)

$$P_{cu} = I^2 R(T); \quad (16)$$

where the resistance $R(T)$ depends on the winding temperature in (17) and thermal elongation coefficient of copper is $\beta_{20^\circ\text{C}} = 0.00393 \frac{1}{\text{K}}$ [17]

$$R(T) = R_{20^\circ\text{C}}(1 + \beta_{20^\circ\text{C}}(T - 20^\circ\text{C})). \quad (17)$$

A PTC-thermistor compares the winding temperature to a temperature limit relating to an electrical overload, before a switch-off by the power unit occurs. PT100 measures the bearing ring temperature from friction heat, caused by lubrication or bearing overloads. Magnetizing loss in the stator Q_h is determined by hysteresis coefficient k_h , frequency f , and magnetic induction Ψ (18):

$$Q_h = k_h \cdot f \cdot \Psi^2; \quad (18)$$

and eddy current loss Q_e [14] by eddy current coefficient k_e , frequency f , and magnetic induction Ψ (19):

$$Q_e = k_e \cdot f^2 \cdot \Psi^2. \quad (19)$$

Methods for the measurement of thermal spindle growth ΔL base on thermal elongation coefficient β , temperature difference ΔT , and length L (20):

$$\Delta L = \beta \cdot \Delta T \cdot L; \quad (20)$$

Table 2. Additional sensors

Assembly	Physical unit	Monitor
stator	temperature	water coolant
bearing	temperature	lubricant flow
rotor	temperature	magnetizing, eddy current
shaft	position	displacement

Additional measurements are necessary for temperatures of the water coolant, air-oil lubricant flow, rotor temperature and for the shaft displacement. While the stator sensors are measured by the drive control, the water coolant, lubrication flow and shaft position ask for a programmable logic controller function. A rotor temperature sensor at a rotating shaft with spindle speed is commonly not available. A digital eddy current measuring system for tool spindles type eddyNCDT SGS 4701 tests a spindle front position against the bearing shield.

Figure 8 presents the test scheme of the motor spindle SPL2782.1, including temperature T and position P sensors. Both front and rear bearings have a grease lubrication by the manufacturer. The motor spindle housing at the front end has a labyrinth ring with compressed air for sealing and bearing protection.

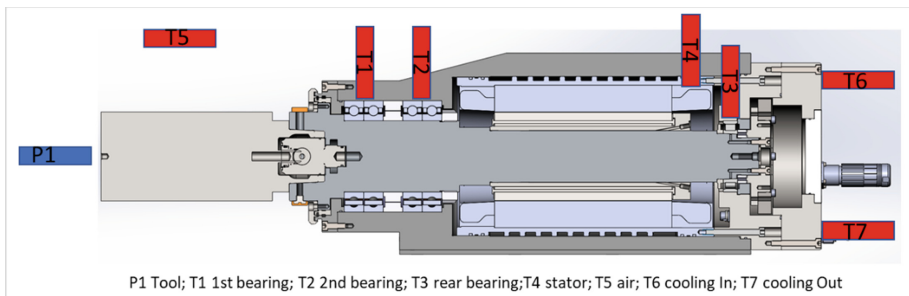
**Fig. 8.** Test scheme of the motor spindle SPL2782.1

Figure 9 shows a photo of the motor spindle 2782.1 with tool dummy at test bench. The SPL test bench is equipped with Sinamics® spindle power unit, PLC control of the water cooler, compressed air supply and PC measurement systems. Multichannel test data were measured in time periods of milliseconds and stored by the PC as raw data files. Without any thermostable climate in the test bench room, the environmental temperature changes. Following the test cycle in Fig. 7, a spindle unit is heating up to thermostable states and cooling down at the end.

Measured water coolant T_w and environment temperatures T_{env} are shown in Fig. 10 and build variables for the function block simulation.

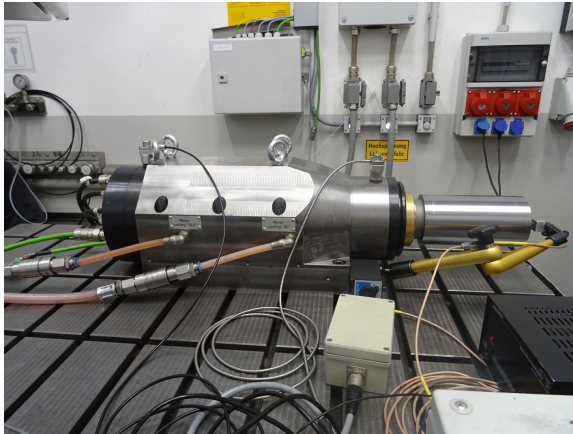


Fig. 9. Motor spindle 2782.1 with tool dummy at test bench

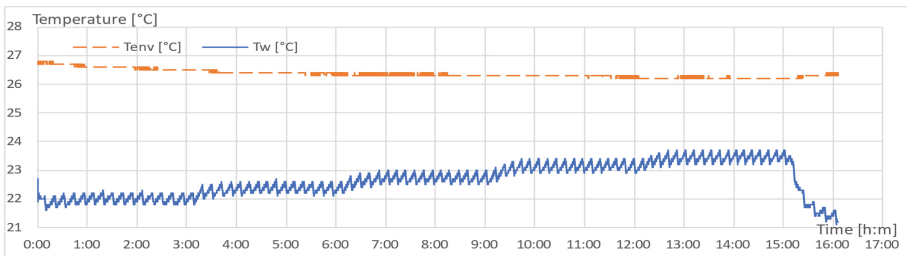


Fig. 10. Test of the water coolant T_w and environment temperatures T_{env}

Figure 11 presents T1 simulation and test temperatures of the front bearing pairs (see Fig. 8). The peak values are 32.1 °C for T1 temperature simulation drawn up as dash line, and 32.4 °C for the T1 Test temperature as continuous lines at sensor T1.

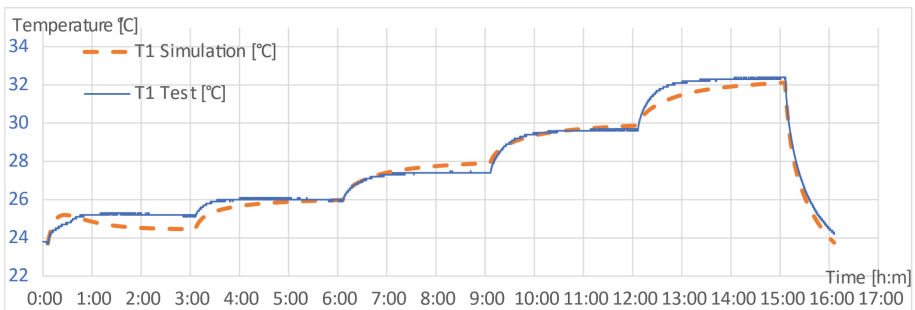


Fig. 11. T1 Simulation and T1 Test temperature of the front bearings

Figure 12 presents P1 simulation (dashed line) and P1 test results of the thermal spindle growth (see Fig. 8; continuous line). The peak values are $8\ \mu\text{m}$ for simulation, and $6.5\ \mu\text{m}$ for the measurement.

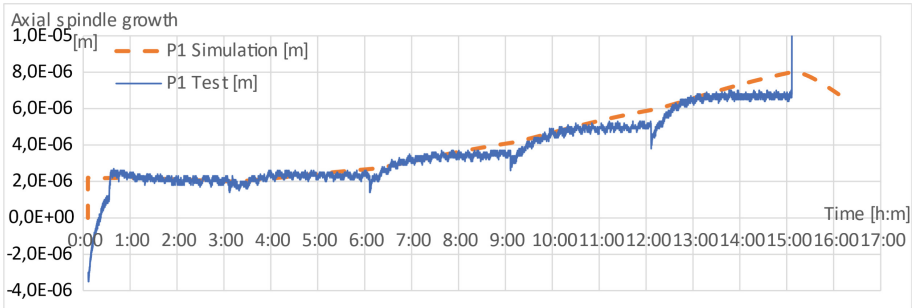


Fig. 12. P1 simulation and P1 test of the thermal spindle growth

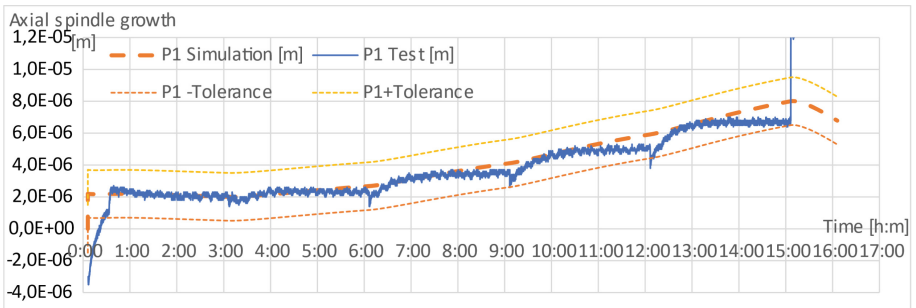


Fig. 13. P1 simulation $\pm 1.5\ \mu\text{m}$ tolerance and P1 test for thermal spindle growth assessment

Figure 13 bases on Fig. 11 and comprises a $\pm 1.5\ \mu\text{m}$ tolerance range to P1 simulation. Following Fig. 13, this digital assessment of a thermal spindle growth bases on the method of a function block simulation and a quality assessment of P1 test compared to P1 simulated values. Deviations between virtual and real sensor values between the tolerance limits indicate a good quality assessment, see Fig. 2. Otherwise, deviations outside the range are quality issues and may be assigned following the thermoenergetic and thermoelastic model in Fig. 5.

Another simulation run of the motor spindle 2782.1 was completed for spindle tests under nominal load power 38 kW/4300 rpm with 5146 W motor heat power losses and shaft temperature 41.6 K, housing temperature 46.1 K above the environmental temperature. Therefore, the axial spindle growth increases to $79.7\ \mu\text{m}$.

In addition, SPL checked the front-end position of the shaft of another 2176.0 spindle unit relative to the bearing shield with an internal eddyNCDT SGS 4701 digital eddy current measurement system. Figure 14 shows this internal position measurement “P1 intern” in the range (0.265:0.275) mm compared to an external position sensor “SPL extern” in the inverse range (0.275:0.265) mm. The internal readings do monitor a

thermal spindle growth and dynamic shaft position relative to the bearings, visible as axial vibration amplitudes $\pm 1 \mu\text{m}$ in the time domain (26:37) min, caused by switching on a speed of 1000 rpm. However, the thermal growth sensor produces stable submicron values at a speed of 8000 rpm for up to 3 h. Therefore, the internal sensor measures the thermal spindle growth including dynamic errors for digital compensation.

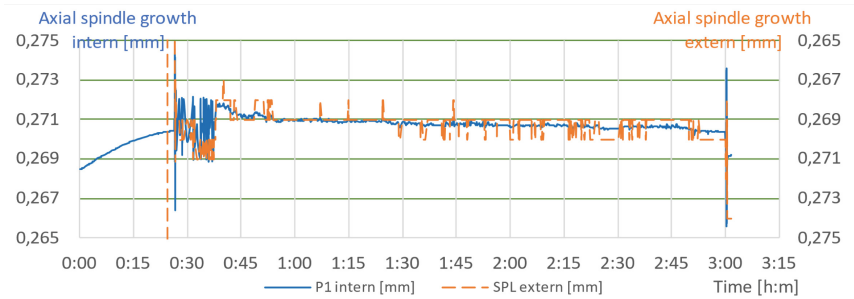


Fig. 14. Test of the thermal spindle growth with internal and external position sensor

Methods for predicting the thermal growth of motor spindle units based on virtual or real sensors, function block models and parameters were verified by test bench experiments. The function block models with parameter sets were verified for different SPL spindle unit types with asynchronous and synchronous motors and different bearing types. Small temperature deviations of 1 K and position deviations of $\pm 1.5 \mu\text{m}$ are acceptable for a wide range of precision spindle units at no load and under process load, even when the axial spindle growth increases to $79.7 \mu\text{m}$ under nominal load. A simulation-based reduction of the thermal spindle growth under nominal load from $79.7 \mu\text{m}$ to $1.5 \mu\text{m}$ is equivalent to 1.9%.

Digital prediction and numerical compensation of thermal growth in motor spindle units under process loads and environmental influences becomes a reality in a digital system such as the digital twin through a predictive model or through internal temperature and position sensors.

4 Thermal Stiffness Strategy

Thermal stiffness [W/ μm] is a key accuracy indicator, characterized by the power losses of the spindle, which result in thermal growth [5]. An innovative quality target is set by a minimal thermal growth or minimal power losses per thermal stiffness. Therefore, this chapter investigates methods for a maximal thermal stiffness and the impact potential from a reduced thermal growth by those methods.

Thermal spindle performance indicators for SPL 2782.1 spindle unit were calculated based on the methodology in [5] and simulation results under nominal load in Sect. 3:

- heat stiffness $K_{\alpha j} = 0.00019 \text{ K/W}$,
- temperature stiffness $K_{Tj} = 0.52 \text{ K}/\mu\text{m}$,
- thermal stiffness $K_{Qj} = 64.53 \text{ W}/\mu\text{m}$.

The definition of heat stiffness $K_{\alpha j}$ is given by Eq. (21) [5]:

$$K_{\alpha j} = \frac{\left[\theta_Q + \left(1 + \frac{\psi_{eq\alpha}}{\psi_{jeq}} \right) \right]}{\left[\psi_{\alpha j} + \psi_{eq\alpha} \cdot \left(1 + \frac{\psi_{\alpha j}}{\psi_{jeq}} \right) \right]}; \quad (21)$$

where $\theta_Q = \frac{Q_{eq}}{Q_j}$ - the ratio of the machine's internal heat sources to the source of the first heat-active element; $\psi_{eq\alpha} = \sum_{\substack{k=1 \\ k \neq j}}^n \psi_{ak}$ - thermal convection at the border between the body of the j - component and liquid (gas), [W/K]; $\psi_{jeq} = \sum_{\substack{k=1 \\ k \neq j}}^n \psi_{jk}$ - thermal conductance at the borders of the j and k - component, [W/K]; $\psi_{\alpha j}$ - thermal convection at the border between the body of the k - component and liquid (gas), [W/K].

The ability of a spindle unit to resist its heating under the action of internal and external sources is characterized and can be determined by the heat stiffness $K_{\alpha j}$ [K/W] as a special case of the heat stiffness of a machine tool, when the machine tool consists of one element – the spindle unit. The maximum and average spindle temperature can be determined as the products of this coefficient on the input power (heat loss in the bearings, stator, etc.). For this reason, there are two fundamentally different ways of ensuring the required or minimum heating of the spindle in both design and operation by controlling the heating. In both cases, a tool is needed to effectively evaluate these solutions. In particular, as tests have shown, the proposed model and its hardware-software solution (see Fig. 3) not only make it possible to determine, but according to the proposed method, it also makes it possible to evaluate solution options under various changing design and thermophysical parameters. A similar method also applies to the evaluation of axial thermoelastic deformations of the spindle, but in this case the inverse thermal stiffness $1/K_{Qj}$ [$\mu\text{m}/\text{W}$] of the spindle will be applied. Therefore, when designing a spindle, various design options and their thermal-physical characteristics can be considered, including heat transfer conditions both between the parts and the external environment.

For spindles that have a high coefficient of heat stiffness $K_{\alpha j}$, it is necessary to carry out measures aimed at reducing their average and maximum heating temperature. Assessing the effectiveness of these measures allows to choose the most rational way to

reduce the spindle temperature. Evaluating the effectiveness of these measures allows to choose the most rational way to reduce the spindle temperature. It was shown that the coefficients of heat and thermal stiffness are universal thermal characteristics of both the machine and the spindle. Therefore, the effectiveness of measures can be assessed by changing the value of heat stiffness coefficients before and after the measure to increase it. To evaluate this, we introduce a heat stiffness ratio λ_{tr} for the spindle (22):

$$\lambda_{tr} = \frac{K_{\alpha 1}}{K_{\alpha 2}}; \quad (22)$$

where $K_{\alpha 1}, K_{\alpha 2}$, - heat stiffness before and after the measure.

This heat stiffness ratio λ_{tr} characterizes the relative increase of the spindle's heat stiffness after the measure. Let's estimate the limits of change in the coefficient of increase of heat stiffness of the spindle λ_{tr} . To do this, we need to establish a functional relationship between the entered coefficient and the value of the spindle temperature decrease as a result of the measure with the heat stiffness ratio λ_{tr} .

Let's set the required value of the spindle temperature drop ΔT (23):

$$\Delta T = T_1 - T_2; \quad (23)$$

where T_1, T_2 , is the average spindle temperature respectively before and after the event.

Considering expressions (22), (23), and taking the temperature T_1 out of brackets, we obtain ΔT (24):

$$\Delta T = T_1 \left(1 - \frac{T_2}{T_1} \right) = T_1 \left(1 - \frac{1}{\lambda_{tr}} \right) = T_1 \left(\frac{\lambda_{tr} - 1}{\lambda_{tr}} \right) = T_1 \left(\frac{K_{\alpha 1} - K_{\alpha 2}}{K_{\alpha 1}} \right); \quad (24)$$

The graph of dependence $\Delta T = f(\lambda_{tr})$ is shown in Fig. 15. The curve of the spindle temperature decrease has an asymptotic character, and the decreasing rate of the spindle temperature reduces with the increase of the heat stiffness ratio λ_{tr} .

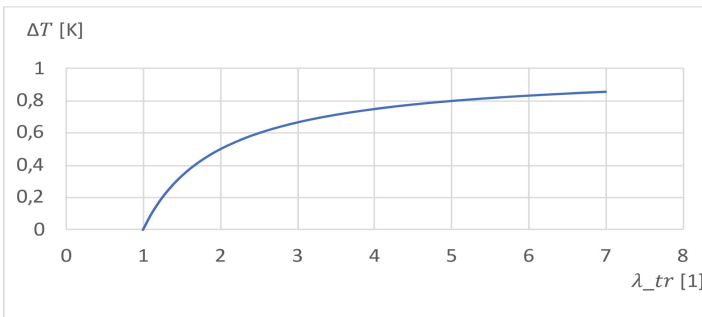


Fig. 15. Spindle temperature reduction ΔT as a function of the heat stiffness ratio λ_{tr}

This must be taken into account, because change is always associated with additional costs, and the effect of temperature reduction is not always proportional or effective to

the measures taken. Therefore, for practical purposes, the following limits of change can be recommended $1, 1 < \lambda_{tr} \leq 5 \dots 6$.

The spindle heating temperature is mostly influenced by the size and shape of the spindle structure parts and heat transfer conditions and thermophysical parameters.

The following **strategies for a reduction of the thermal spindle growth** can be distinguished by a heat stiffness $K_{\alpha 1}$ improvement (24):

1. changing the size and shape of the spindle assembly design parts, for example, increasing the area of the **heat dissipating surface**;
2. Change of spindle **material thermal-physical properties** (for instance, application of carbon fiber composite as in the paper [18] with thermal conductivity coefficient equal to $1,1 \text{ W/m}^2\text{K}$ – transversal, $186 \text{ W/m}^2\text{K}$ – longitudinal elements, a heat capacity coefficient of 850 J/kg K), and conditions of heat emission and heat transfer;
3. change in the structural size and shape of the spindle assembly design parts and thermophysical parameters to improve the conditions of **heat transfer and heat dissipation**.

In all of the following conclusions, the heat stiffness of the machine tool will be expressed in a simplified form with respect to the spindle as one of the heat-active elements of the thermal system.

The **first direction**, as an illustration of the method and principle, includes measures that improve the thermal characteristics of the spindle by introducing additional heat dissipating surfaces. In this case, let us give a notation of the heat stiffness ratio λ_{tr} aiming at a heat stiffness improvement of the spindle in a rather simplified form will be equal to (25):

$$\lambda_{tr}^I = \frac{\sum_{i=1}^n \alpha_i \cdot A_i}{\sum_{i=1}^n \alpha_i \cdot A_i + \alpha_{M1} \cdot A_{M1}}; \quad (25)$$

where α_i is the coefficient of heat transfer on the i surface of a spindle; A_i - area of the i surface; α_M - heat transfer coefficient on the additional surface; A_M - area of the additional surface.

The denominator of expression (25) characterizes the thermal stiffness of the spindle after the measure $K_{\alpha 2}$, and the numerator is equal to the initial value of the spindle heat stiffness $K_{\alpha 1}$. In the particular case where the heat transfer coefficients are the same and equal to α , expression (25) will take the form (26):

$$\lambda_{tr}^I = 1 + \frac{A_{M1}}{\sum_{i=1}^n A_i}; \quad (26)$$

It follows from expression (26) that the additional surface area must be larger or at least commensurate with the heat dissipating surface area of the spindle. Otherwise, the value λ_{tr} will be small and the efficiency of the measure is negligible. So, for example, with an area ratio of 1:1 the heat stiffness ratio λ_{tr} will be 2 and hence the heating temperature reduction will be twofold.

The **second direction** includes measures that increase the thermal characteristics of the spindle by improving the heat dissipation conditions on the spindle surface while its

structural shape and dimensions remain unchanged. In this case, the spindle's λ_{rt}^{II} will be equal (27):

$$\lambda_{rt}^{II} = \frac{\sum_{i=1}^{n-k} \alpha_i \cdot A_i + \sum_{j=1}^k \alpha_{M2} \cdot A_j}{\sum_{i=1}^n \alpha_i \cdot A_i} = 1 + \frac{\sum_{j=1}^k (\alpha_{M2} - \alpha_j) \cdot A_j}{\sum_{i=1}^n \alpha_i \cdot A_i}; \quad (27)$$

where k is the number of surfaces on which the heat transfer conditions are improved; α_{M2} - is the heat transfer coefficient after the heat transfer conditions are improved.

If the heat transfer coefficients are equal to α on the surfaces where the heat exchange conditions do not change, then

$$\lambda_{rt}^{II} = 1 + \left(\frac{\alpha_{M2}}{\alpha} - 1 \right) \frac{\sum_{j=1}^k F_j}{\sum_{i=1}^n F_i}; \quad (28)$$

where α is the heat transfer coefficient on those surfaces where the heat exchange conditions have not changed. It follows from expressions (27) and (28) that the effectiveness of measures of the second group depends on the surface area, on which the heat transfer conditions are improved, and on the ratio of values of the heat transfer coefficient on this surface before and after the measures.

The **third direction** includes measures that improve the thermal characteristics of the spindle by introducing additional heat transfer surfaces and increasing the heat transfer coefficient. In this case, λ_{rt}^{III} of the spindle is determined by the following dependence:

$$\lambda_{rt}^{III} = 1 + \frac{\alpha_{M1} \cdot A_{M1}}{\sum_{i=1}^n \alpha_i \cdot A_i} + \frac{\sum_{j=1}^k (\alpha_{M2} - \alpha_j) \cdot A_j}{\sum_{i=1}^n \alpha_i \cdot A_i} = \lambda_{rt}^I + \lambda_{rt}^{II} - 1; \quad (29)$$

If the heat transfer coefficients on all spindle surfaces are equal (except those where the heat transfer coefficient is increased), then expression (28) will be written in the form:

$$\lambda_{rt}^{III} = 1 + \frac{A_{M1}}{\sum_{i=1}^n A_i} + \left(\frac{\alpha_{M2}}{\alpha} - 1 \right) \cdot \frac{\sum_{j=1}^k A_j}{\sum_{i=1}^n A_i}; \quad (30)$$

Comparison of expressions (29) and (30) allows us to draw an obvious conclusion that the measures of the third group will be much more effective, if additional surfaces improve the conditions of heat transfer.

An evaluation of influence of geometrical parameters is given for a spindle unit (d - diameter, L - length, q_1 - front heat flow density, q_2 - rear heat flow density, A - square area), and shown in Fig. 16, assuming invariable thermophysical parameters.

Similarly, based on the complete description of the components for the values of $K_{\alpha 1}$, indicators are formed both in their full form by (21), which take into account all structural and thermophysical components, and in a simplified form (neglecting some parameters due to their low influence on the temperature change), as given for all three strategies for a reduction of the spindle heating temperature. To estimate the influence of the spindle thermal mode on its thermoelastic displacements, in particular axial displacements, the expression for λ_{tr} will have the form (31):

$$\lambda_{tr} = \frac{K_{Q2}}{K_{Q1}}; \quad (31)$$

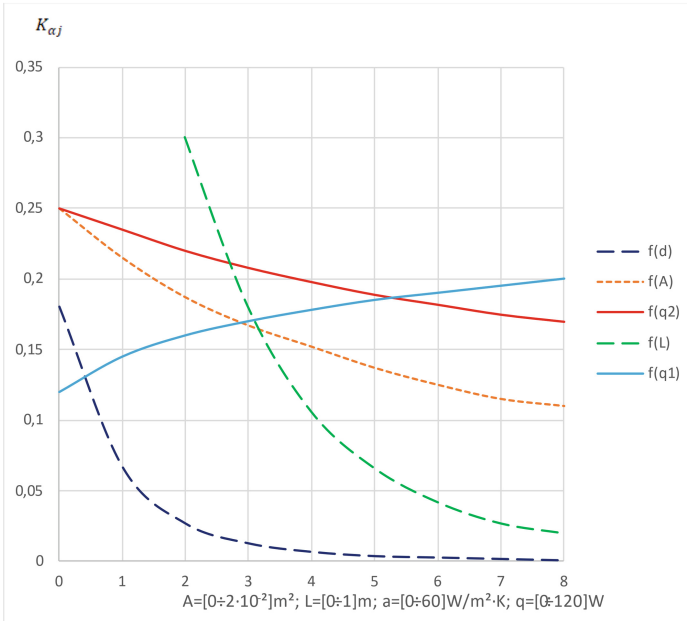


Fig. 16. Influence of geometrical parameters on the heat stiffness K_{α_j} of the spindle (where the abscise range $A = [0 \div 2 \cdot 10^{-2}] \text{ m}^2$; $L = [0 \div 1] \text{ m}$; $a = [0 \div 60] \text{ W/m}^2 \cdot \text{K}$; $q = [0 \div 120] \text{ W}$)

and the number of measures to manage the thermal deformation of the spindle will be supplemented (with respect to temperature reduction only) by redistributing the effects on the thermoelastic system of the spindle.

Considering the above, let us also introduce the reduction coefficient of excess spindle temperature ξ in (32)

$$\xi = \left(\frac{\lambda_{tr} - 1}{\lambda_{tr}} \right) 100\%; \quad (32)$$

which shows by how many percent the spindle temperature will be reduced as a result of the measure. In addition, an inverse problem can also be solved, in which the value of ξ is given and the value of λ_{tr} , is determined, and the effective and most rational option to improve the thermal resistance of the spindle is found.

5 Summary and Outlook

This paper presents and verifies digital methods for modeling and simulating a thermal growth of motor spindle units for digital prediction and numerical compensation of a thermal growth of motor spindle units. The digital model requires new virtual test and measurement methods, therefore models, parameters and variables are defined by data structures and simulated for test cycles. The State of the Art in thermal caused geometrical and kinematic errors is limited to quasi-static states and under no-load conditions. The

realized model simulation and experiments conclude in a verification of thermal growth and innovative prediction under load. The best location of temperature and position sensors is not sufficient for a correct prediction of thermal spindle growth. So far, the rotating shaft temperature was not measured, but this paper did simulate multiple virtual sensors at the shaft and housing.

A system analysis for transfer functions requires thermal sources, sinks and knowledge of thermoelasticity in components. Correlations between multiple input and output values depend on system and environmental conditions. The Analytical Equation Method investigates deterministic cause-effect-relationships. Parametrized function block models of the motor spindle unit types SPL2782.1 were approved by MATLAB/Simulink, SimulationX and OpenModelica projects and verified by similar SPL test bench measurements. The parametrized Function Block Models provides a temperature and thermal spindle growth prediction for different motor spindle types. The model flexibility is given by modular blocks, as for asynchronous or synchronous motors and water cooling.

Compared to longtime FEM simulations, the Function Block simulation allows real-time applications and closed-loop control for a CNC compensation. The short simulation time enables real-time digital compensation applications in order to reduce thermal growth of spindle units and machine tools under load. Simulated bearing temperature values are comparable to integrated sensor values and predict thermal properties (temperature, position growth) of the spindle unit design SPL2782.1 for different load conditions. Temperature deviations of 1 K and position deviations of $\pm 1.5 \mu\text{m}$ are acceptable for a wide range of precision spindle units under no load and process loads, reducing the thermal growth of spindle units. Simulation extends the test stand measurements for spindle tests under load power without a second load motor and power unit. Simulated thermal spindle growth is comparable to internal and external position sensor values, even when external sensors are not applicable for machining processes.

The spindle thermal stiffness strategies present three methods for a heat stiffness improvement for further spindle design variants. Different methods for a digital reduction of a thermal spindle growth were developed and ask further work on a real-time controller in a digital twin for a TCP coordinate shift. Further investigations are needed on model parameter optimization and on digital targets for a quality assessment regarding the thermal growth of motor spindle units.

Acknowledgements. The authors thank SPL GmbH for their important support of this collaborative work without any project funding during the year 2021 and the CIRP sponsored 3rd International Conference on Thermal Issues in Machine Tools 2023 for publishing support.

References

1. SPL. <http://www.spl-spindel.de>. Accessed 28 Aug 2022
2. Spur, G., et al.: Thermal behaviour optimization of machine tools. *Ann. CIRP* **37**(1), 401–405 (1988)
3. Mayr, J., Jedrzejewski, J.: Thermal issues in machine tools. *CIRP Ann.* **61**(2) <https://doi.org/10.1016/j.cirp.2012.05.008>

4. Kuznetsov, A.P., Koriath, H.-J.: The Methods for Controlled Thermal Deformations in Machine Tools. ICTIMT, Verlag Wissenschaftliche Scripten, Dresden, pp. 47–60 (2018)
5. Kuznetsov, A.P., Koriath, H.-J.: Thermal stiffness – a key accuracy indicator of machine tools. *MM Sci. J.* (2021). https://doi.org/10.17973/MMSJ.2021_07_2021058
6. Kuznetsov, A.P., Koriath, H.-J.: Comparison of methods for controlled thermal deformations in machine tools. *MM Sci. J.* (2021). https://doi.org/10.17973/MMSJ.2021_07_2021065
7. Kuznetsov, A.P.: Non-stationary temperature behavior of spindle assemblies and ball screw gears for high precision metal cutting machines. In: *EPJ Web of Conferences*, vol. 248, p. 04020 (2021). <https://doi.org/10.1051/epjconf/202124804020>
8. Li, Y., Yu, M.: A review of thermal error modeling methods for machine tools. *Appl. Sci.* **11**, 5216 (2021). <https://doi.org/10.3390/app11115216>
9. Jie, Z.: Robust thermal error modeling and compensation for CNC machine tools. Ph.D. thesis, The University of Michigan (2008)
10. ISO 230-3:2020-11 Test code for machine tools - Part 3. Determination of thermal effects. <https://www.iso.org/standard/73291.html>
11. ISO/TR 16907:2015-04 Machine tools - Numerical compensation of geometric errors. <https://www.iso.org/standard/57912.html>
12. IEEE Standard for System, Software, and Hardware Verification and Validation. IEEE 1012-2016, IEEE Computer Society, New York (2016)
13. Kuznetsov, A.P.: Thermal processes in machine tools. *Technosphere*, 488 p. (2019). (in Russian)
14. <https://de.mathworks.com/help/simscape/ug/heat-conduction-through-iron-rod.html>. Internet Accessed 20 Dec 2022
15. SIMOTICS M-1FE1 Tool to calculate the total power loss. <https://support.industry.siemens.com/cs/document/109771175/simotics-m-1fe1-tool-to-calculate-the-total-power-loss?dti=0&lc=en-MK>. Accessed 29 Aug 2022
16. BearingSelect. <https://www.skf.com/group/support/engineering-tools/bearing-select>
17. Nemeth-Csoka, M.: *Thermisches Management elektrischer Maschinen*. Springer Vieweg (2018). <https://doi.org/10.1007/978-3-658-20133-3>
18. Kondo, R., Kono, D., Matsubara, A.: Evaluation of machine tool spindle using carbon fiber composite. *Int. J. Autom. Technol.* **14**(2), 294–303 (2020). <https://doi.org/10.20965/ijat.2020.p0294>

Open Access This chapter is licensed under the terms of the Creative Commons Attribution 4.0 International License (<http://creativecommons.org/licenses/by/4.0/>), which permits use, sharing, adaptation, distribution and reproduction in any medium or format, as long as you give appropriate credit to the original author(s) and the source, provide a link to the Creative Commons license and indicate if changes were made.

The images or other third party material in this chapter are included in the chapter's Creative Commons license, unless indicated otherwise in a credit line to the material. If material is not included in the chapter's Creative Commons license and your intended use is not permitted by statutory regulation or exceeds the permitted use, you will need to obtain permission directly from the copyright holder.





Thermal Modeling Challenges of High-Speed Motorized Spindles

Lukas Koch¹ , Felix Butz², Gordana Krüger¹, and Frank Döpfer³ 

¹ Technical University of Applied Sciences Würzburg-Schweinfurt, Ignaz-Schön-Straße 11,
97421 Schweinfurt, Germany

lukas.koch@thws.de

² Weiss Spindeltechnologie GmbH, Birkenfelder Weg 14, 96126 Maroldsweisach, Germany

³ University of Bayreuth, Lehrstuhl für Umweltgerechte Produktionstechnik, Universitätsstraße
9, 95447 Bayreuth, Germany

Abstract. This paper investigates the thermal modeling challenges of high-speed motorized spindles up to 40,000 rpm. The thermal expansion and deflection of motorized spindles are critical determinants for the resulting tool center point displacement and the achievable machining accuracy of machine tools. In order to compensate, finite element and reduced physical models (digital twins) therefore require an accurate understanding of the thermal boundary conditions. In motorized spindles, heat sources are of great significance to the resulting temperature field. However, it is very difficult to accurately quantify the heat sources in motorized spindles. This is a particular challenge for high-speed applications exceeding 20,000 rpm, where commonly used boundary conditions are not validated. While the power loss of the electric motor could be quantified with reasonable accuracy, the calculation approaches for air and bearing friction proved to be inadequate. This paper introduces approaches to quantify the air and bearing friction of motorized spindles with improved accuracy for applications up to 40,000 rpm. The method was verified based on a coupled thermal/fluid-mechanical spindle simulation model. The mean absolute temperature difference between the model and the test bench was 1.5 K.

Keywords: Motorized Spindle · Thermal Modeling · Bearing Heat · Air Friction · Machine Tools

1 Introduction

The precision of metal-cutting machine tools is reduced by non-reproducible displacements of the tool center point. This displacement has geometrical, static, dynamic and thermal causes [1]. The thermal shift accounts for up to 75% [2] of the total displacement and is therefore the center of many recent research activities.

The reproducibility of the thermal displacement is challenging because of the complexity of the underlying thermo-mechanical problem. As outlined in our previous article [3], the investigated compensation approaches can be divided into data-based and physical model-based approaches. Data-based approaches are problematic due to extensive

calibration measurements. Physical model-based compensation strategies are challenging because the boundary conditions often lack the required accuracy. This is especially true for high-speed applications, where many of the earlier published quantification approaches for the boundary conditions are not validated.

Depending on the application, motorized spindles are regularly operated in speed ranges up to 60,000 rpm [4]. Spindles for internal grinding or drilling printed circuit boards operate even beyond 100,000 rpm. However, most of the previously published models are not considering high-speed applications. Figure 1 visualizes available models and their speed. Most publications [5–18] do not consider motorized spindles with more than 18,000 rpm. The recent addition of Denkana [19] showed modeling efforts for a spindle with 20,000 rpm. Denkana used manufacturer data for the problematic bearing friction loss and ignored air friction. That approach might lead to reasonable results in this speed range, but due to the nonlinear increase of air friction, it quickly becomes unsustainable beyond 20,000 rpm. Bossmanns [20] analyzed a motorized spindle with 25,000 rpm, including both bearing friction and air friction [22]. He derived an empirically-based bearing friction model through a curve fitting approach, circumventing the inaccuracy of the currently available bearing friction models. Furthermore, he recognizes the increasing issue of air friction, yet only quantifies the air friction directly in the air gap between stator and rotor. Gebert [21] simulated a motorized spindle with 36,000 rpm, modeling air and bearing friction. Solely Gebert sophisticatedly analyzed the air friction issue of the entire rotating shaft. However, he acknowledged the issue of the incalculability of air and bearing friction, suggesting an alternative empirically-based approach.

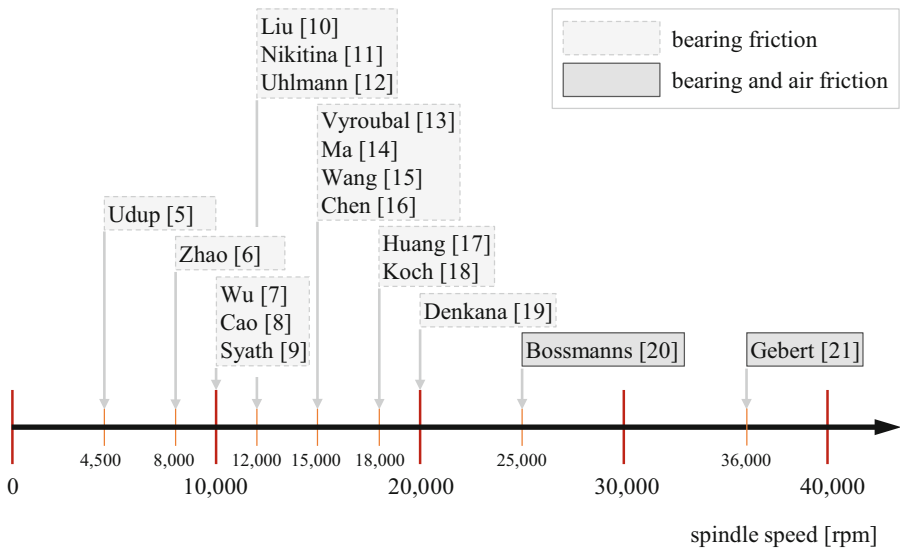


Fig. 1. Speed range of motor spindle models with the observed friction phenomena.

Unfortunately, Bossmann's and Gebert's approaches to quantify the bearing friction cannot be transferred to different spindles without extensive measuring effort. This paper presents a newly developed set of boundary conditions for high-speed motorized spindles, which was validated at 40,000 rpm. As outlined by the authors cited above, the greatest modeling challenge is an accurate quantification of the heat sources at high speeds. We suggest an improved analytical calculation of air friction with a more comprehensive set of friction coefficients, including the effects of Taylor vortices. The calculation of bearing friction at high speed remains problematic and requires further research. However, the total bearing friction can be estimated with reasonable accuracy based on energy conversion observations of the spindle. Unlike the previous high-speed modeling approaches, the presented modeling guideline should be transferable to other high-speed motor spindles with minimal measuring effort.

2 General Approach

The development of a reasonable set of boundary conditions for high-speed motor spindles was established through extensive empirical observations of a synchronous motor driven spindle with 40,000 rpm and 10 kW (Fig. 2, left). The spindle had a total length of 585 mm and an outer rotor diameter of 66 mm. The test bench was equipped with temperature sensors, which were attached to the surface and in boreholes of the spindle (see Sect. 4.2). The simulation model (Fig. 2, right) was a Finite-Element-Model (FEM) with an additionally coupled Computational-Fluid-Dynamics (CFD) simulation for the fluid cooling systems inside the spindle housing.

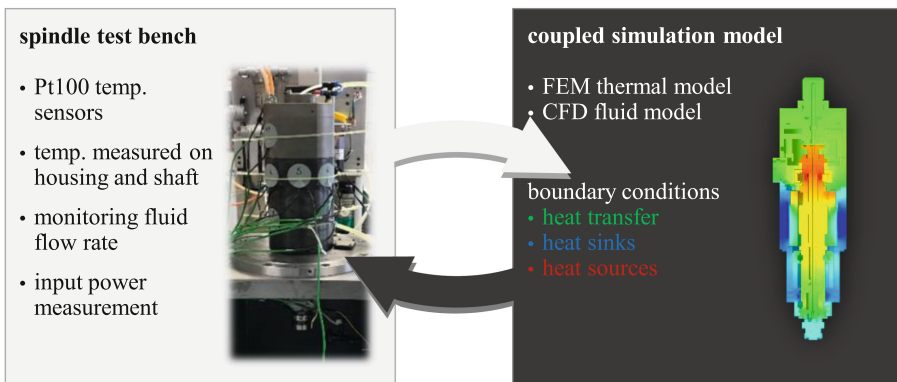


Fig. 2. Spindle test bench and simulation model.

The first version of the spindle simulation model was based on a set of boundary conditions published in our previous works on a spindle with 18,000 rpm [3, 18]. However, the empirical observation showed that this set of boundary conditions could not be conveyed to the test specimen of the analysis with 40,000 rpm. The comprehensive empirical observation allowed us to scrutinize the different boundary conditions separately. Temperature deviations were traced back to inaccuracies of individual boundary

conditions, allowing additional research on each specific physical problem. The boundary conditions of the simulation model were refined until the temperature deviation was reduced to 1.5 K in thermal equilibrium at 40,000 rpm.

3 Boundary Conditions for High-Speed Motorized Spindles

The boundary conditions required to reach that goal are visualized in Table 1 and the corresponding Fig. 3 below. The table visualizes the required heat transfer, heat sink and heat sources with recommended quantification approaches. The following Sects. 3.1–3.4 will discuss each quantification approach separately.

Table 1. Quantification approaches for thermal boundary conditions of high-speed motorized spindle models up to 40,000 rpm.

group	boundary condition	quantification approach / source
heat transfers (Sect. 3.1)	bearing geometry	[23]
	gap between shaft and housing	[24, 25]
	fixed solid body contact	[26–28]
	bushing housing contact	[26–28]
heat sinks (Sect. 3.2)	fluid cooling	CFD-simulation
	ambient air (free convection)	[30]
	ambient air (forced convection)	[31, 32]
	machine interface	[26–28]
	drill hole systems	[33, 34] or CFD-simulation
heat sources (Sect. 3.3)	asynchronous motor	[35] or [36]
	synchronous motor	[37, 38]
	air friction	page 7 et seq. (Table 2)
	bearing friction	page 11 et seq
solid motion effect (Sect. 3.4)	shaft rotation	[52]

3.1 Heat Transfer

The bearings of the spindle (Fig. 3) need to be described as heat sources and heat transfer systems. The heat transfer through a roller bearing is mostly limited by the contacts between rolling element and ball raceway. There are different approaches available in literature, but most of them are based on the Hertzian contact theory. For our investigations, the approach of Weidemann [23] gave accurate results.

We know from the observations of Gebert [21] that the heat transfer between the rotating shaft and the stationary housing is highly relevant for the generated temperature field of high-speed motorized spindles. The approach of Tachibana [24] worked

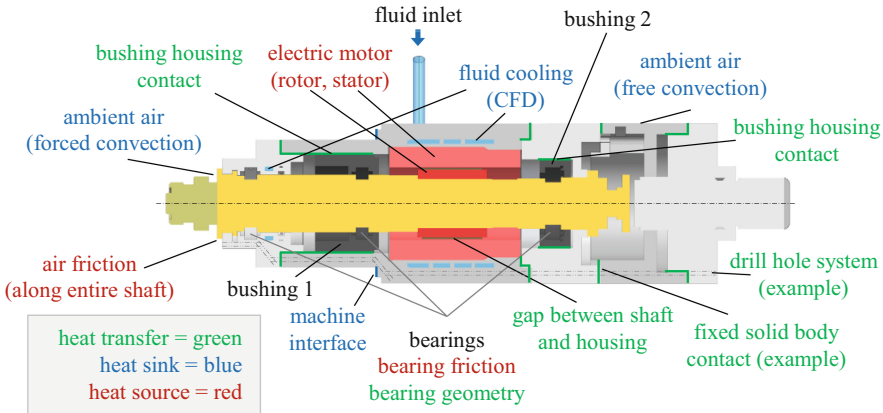


Fig. 3. Visualization of the boundary conditions of the observed motor spindle.

for the geometrical dimensions and spindle speed relevant to our observation. If the spindle specimen does not meet the limitations of Tachibana, the review article of Fénot [25] is recommended. Fénot gives an overview of the available Nusselt correlations for concentric rotating cylinders with different dimensions and speeds.

The gap conductance of solid body contacts is quantified based on the works of Jovanovich [26, 27]. However, the suggested equations are often times not solvable, as they require specific knowledge of the contact parameters like pressure, roughness and air properties.

This is especially problematic for the bushings inside of the spindle. The floating bearings of motorized spindles are often times mounted in bushings (see Fig. 3) which allow an axial displacement to prevent thermally induced stresses. The parameters of these loose contacts are not quantifiable. However, the work of Negus and Yovanovich [28] gives tabular data for different load cases.

3.2 Heat Sinks

The most significant heat sink of motorized spindles is usually the fluid cooling. The fluid cooling primarily cools the electric motor, but often times the bearings are cooled through additional cooling rings. The coolant heats up over the course of the fluid flow, creating an asymmetric temperature field in the solid bodies of the spindle [3, 29]. In order to simulate accurate temperature fields and thermal deformations, this effect has to be considered. Therefore, the fluid cooling system has to be realized via a coupled CFD-simulation. The mesh of the fluid system should be created with boundary layer refinement to meet the Y^+ value requirement.

Motorized spindles generally have a cylindrical shape. Accordingly, the free convection of a spindle toward the ambient air can be modeled based on the findings of Churchill [30].

Free convection generally leads to much lower heat transfer coefficients than forced convection. Forced convection only appears on the rotating shaft of the spindle, usually near the tool. The parts of the shaft, which can be modeled as a rotating cylinder, can

be quantified based on the work of Dropkin [31]. The remaining parts of the shaft are usually modeled as a rotating plate [32].

The connection of the spindle toward the machine or test bench can be modeled as a solid body contact based on the work of Jovanovich [26–28]. As explained in Sect. 3.1, an accurate quantification of these heat transfer coefficients is difficult. In order to apply the heat transfer coefficient to a surface, the temperature of the opposite surface (test bench or machine part) must be considered. This temperature is not quantifiable without measurements. One alternative approach to circumvent that problem is modeling parts of the machine structure with their free convection boundary conditions. As displayed in Sect. 4.1, this boundary condition is not necessarily required for motorized spindles with fluid cooling.

The thermal influence of the drill hole systems, which are generally ignored by other authors, was also reviewed. Motorized spindles have a set of drill hole systems as exemplarily visualized in Fig. 3. These drill hole systems are required for the bearing lubrication, vacuum return, leakage, air sealing etc. They can be described by heat transfer coefficients based on tube flow observations. Often times the flow inside the boreholes is in transition between laminar and turbulent flow. The heat transfer coefficients can then be quantified based on Gnielinski [33]. Nusselt correlations for other flow conditions in tubes are discussed by Stephan [34]. However, the temperature of the flow inside of the boreholes rises quickly in some parts of the spindle, implying that the quantification based on fixed heat transfer coefficient and fluid temperature is not a sufficient method. If a drill hole system really is of significance for the spindle temperature, it should be modeled as separate CFD simulations, just as the fluid cooling system itself.

3.3 Heat Sources

Heat sources form the most significant boundary conditions for the resulting temperature field of motorized spindles. At the same time, they are the most difficult boundary conditions to quantify. Unlike the purely analytical approach on heat transfer systems (Sect. 3.1) and heat sinks (Sect. 3.2), the accurate quantification of the heat sources requires additional empirical observation of the input power of the spindle.

The electric motor is usually the most significant heat source in motorized spindles. The use of an asynchronous motor can be thermally quantified based on Richter [35]. Richter quantifies copper losses, iron losses and additional losses separately. Alternatively, asynchronous motors can be quantified based on motor slip [36], requiring less input parameters than Richter's approach [35] but the aforementioned measurement of the input power.

The thermal description of a synchronous motor can be established based on the works of Rothenbücher [37] and Gieras [38]. While the results of an analytical copper loss quantification are usually accurate, it is more difficult to quantify the iron loss accurately. This is due to influences of the processing procedure, alternating the parameters of the metal sheets through shape and stress variations. For this reason, the analytically quantified iron loss value is multiplied by an empirical factor. In any case, it is advisable

to directly contact the motor manufacturer. Only the manufacturers themselves know the empirical data of their motors.

Air Friction

Air friction becomes increasingly relevant with higher speed. It raises to nearly the power of three of the rotational speed. An accurate understanding of the problem is indispensable for a spindle with 40,000 rpm. However, the published approaches on air friction in motorized spindles [20, 21] were not suitable for quantifying the air friction accurately. The measurements suggest higher air friction losses than determined, especially in spindle areas with large cavities between shaft and housing.

Therefore, a new set of quantification approaches was developed and validated. The analytical determination of air friction is not a trivial problem, especially for high-speed applications. While exact solutions based on the Navier-Stokes equations are available for problems with low rotational speed and laminar flow, solving the equation is usually impossible for problems with high speed and turbulent flow [21]. The friction between two concentric cylinders can be expressed as the air's shear stress τ [45]:

$$\tau = \rho(\nu + \varepsilon_M) \cdot r \frac{\partial}{\partial r} \cdot \left(\frac{u}{r} \right) \quad (1)$$

where ρ is the air density, ν is the kinematic viscosity, ε_M is the eddy diffusivity of momentum, r is the radius and u is the tangential fluid velocity ($u = r \cdot \omega$). Equation (1) is not solvable, as the eddy diffusivity and the velocity distribution are not determinable for turbulent flows. Therefore, a dimensionless friction coefficient C_f is used instead for these problems, which is defined for rotating parts as follows:

$$C_f = \frac{\tau_r}{\frac{1}{2} \cdot \rho \cdot u_r^2} \quad (2)$$

τ_r is the shear stress on the surface A of the rotating body and u_r is the tangential velocity on the rotor's surface. Based on the shear stress τ_r (Eq. (2)) the resisting force F can be quantified with Eq. (3). The air friction torque M_{air} in Eq. (4) is then quantified by multiplying with the rotor's radius r_r .

$$F = \tau_r \cdot A \quad (3)$$

$$M_{air} = F \cdot r_r = C_f \cdot \frac{1}{2} \cdot \rho \cdot u_r^2 \cdot A \cdot r_r = C_f \cdot \frac{1}{2} \cdot \rho \cdot r_r^3 \cdot \omega^2 \cdot A \quad (4)$$

Equation (4) is generally valid. The shaft of motorized spindles is geometrically complex. In order to make the air friction of the shaft quantifiable, it has to be observed as a number of rotating cylinders and disks. The air friction torque of rotating cylinders in Eq. (5) is determined with its lateral surface. Where l is the length of the observed cylinder. The frictional torque of the disks in Eq. (6) is quantified through observing the disk surface as annulus with outer and inner radii (r_o , r_i).

$$M_{air,cylinder} = C_f \cdot \rho \cdot r_r^4 \cdot \omega^2 \cdot \pi \cdot l \quad (5)$$

$$M_{air,disk} = C_f \cdot \frac{1}{2} \cdot \rho \cdot \omega^2 \cdot (r_o^5 - r_i^5) \quad (6)$$

The remaining unknown C_f is then described as the empirically determined function of Reynolds number Re . There is a large number of foundational research on the empirical quantification of these functions. Table 2 visualizes our set of quantification approaches for C_f which was developed for high-speed applications based on the empirical observation (Sect. 2). The calculation of the friction coefficients in Table 2 requires the tip Reynolds number Re_r (Eq. (7)), the Couette Reynolds number Re_δ (Eq. (8)) and the axial Reynolds number Re_a for observations with an additional axial flow (Eq. (9)).

$$Re_r = \frac{\rho \cdot u_o \cdot r_o}{\mu} \quad (7)$$

$$Re_\delta = \frac{\rho \cdot u_o \cdot \delta}{\mu} \quad (8)$$

$$Re_a = \frac{\rho \cdot v_m \cdot 2\delta}{\mu} \quad (9)$$

where u_o is the peripheral speed of the rotor, δ the air gap in radial direction, μ the dynamic viscosity of the fluid and v_m the mean axial fluid velocity, which is calculated based on the axial flow rate and the cross section of the air gap. Table 2 is explained based on the corresponding Fig. 4, which displays a part of the spindle with all relevant physical phenomena. The parts of the shaft, which can be observed as disks rotating in free space ((1) in Fig. 4 and Table 2), are quantified based on the approaches of Kreith [39].

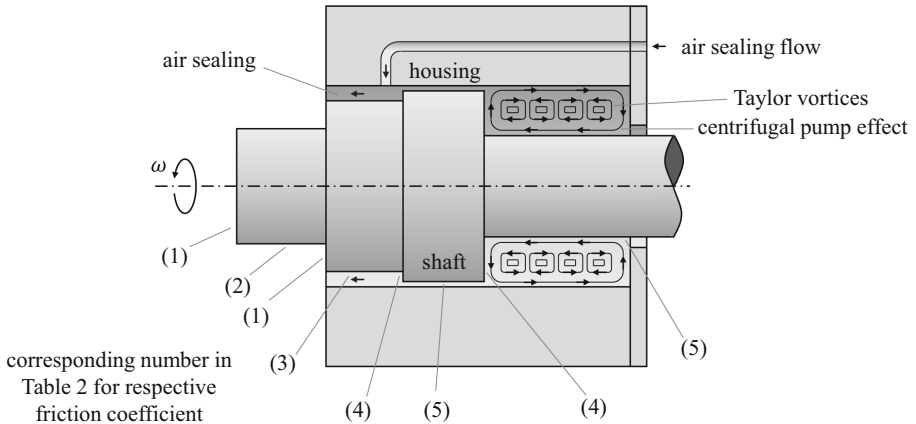


Fig. 4. Exemplary observation of the air friction phenomena in high-speed motorized spindles.

Parts of cylindrical shape rotating in free air ((2) in Fig. 4 and Table 2) are described with Theodorson's [40] approaches. A motorized spindle commonly features at least one air sealing. These sealings work through an additional axial airflow (3). The flow

in the air gap between shaft and housing thus has tangential and axial components. In this case, the friction coefficient can be calculated based on the works of Yamada [41]. Radial surfaces in the enclosure of the housing (4) are quantified based on Schulz-Grunow's work [42]. There is no known quantification approach for radial disks with an additional radial flow for areas with an air sealing. Therefore, they have to be described with Schulz-Grunow's approach, which gave fitting results for these areas.

Table 2. Quantification approaches of air friction coefficients for high-speed motorized spindle models up to 40,000 rpm.

#	physical problem	friction coefficient	eq.	applicability	source
(1)	rotating disk in free space	$C_f = \frac{3.87}{Re_r^{0.5}}$	(10)	$Re_r < 3 \cdot 10^5$	[39]
		$C_f = \frac{0.146}{Re_r^{0.2}}$	(11)	$Re_r > 3 \cdot 10^5$	
(2)	rotating cylinder in free space	$C_f = \frac{4}{Re_r}$	(12)	$Re_r < 80$	[40]
		$\frac{1}{\sqrt{C_f}} = 4.07 \cdot \log_{10}(Re \cdot \sqrt{C_f}) - 0.6$	(13)	$Re_r > 80$	
(3)	concentric cylinder with axial flow	$C_f = \frac{0.0152}{Re_\delta^{0.24}} \cdot \left[1 + \left(\frac{\delta}{7}\right)^2 \left(\frac{4 \cdot Re_a}{Re_\delta}\right)^2 \right]^{0.38}$	(14)	–	[41]
(4)	rotating disk in enclosure	$C_f = 2 \cdot \pi \cdot \frac{r_\delta}{\delta} \cdot \frac{1}{Re_r}$	(15)	$Re_r < 5.54 \cdot \left(\frac{r_\delta}{\delta}\right)^2$	[42]
		$C_f = \frac{2.67}{\sqrt{Re_r}}$	(16)	$5.54 \cdot \left(\frac{r_\delta}{\delta}\right)^2 < Re_r < 2.8 \cdot 10^5$	
		$C_f = 0.0622 \cdot Re_r^{-0.2}$	(17)	$2.8 \cdot 10^5 < Re_r$	
(5)	rotating cylinder in enclosure (with axial flow)	Stuart's approaches for low rpm / Re_δ	(18)	refer to Taylor number	[43]
		$C_f = 0.515 \cdot \frac{\left(\frac{\delta}{ra}\right)^{0.3}}{Re_\delta^{0.5}}$	(19)	$500 < Re_\delta < 10^4$	[44, 45]
		$C_f = 0.0325 \cdot \frac{\left(\frac{\delta}{ra}\right)^{0.3}}{Re_\delta^{0.2}}$	(20)	$10^4 < Re_\delta$	[44, 45]

Parts of the shaft, which represent a cylinder rotating in an enclosure (5), are most difficult to quantify for high-speed motorized spindles. The results obtained from the previously suggested approach from Stuart [43] proposed by Gebert [21] were too low. The reason for this deviation is probably the occurrence of Taylor vortices, even though the rotational speed and Reynolds number are very high. This problem should be clarified based on Fig. 5. In order to make the graphs comparable, the Taylor number definition

given by Saari [45] is applied to both illustrations. Figure 5 a) shows the conventional understanding of airflows in concentric cylinders. Up to a certain Taylor number ($1.7 \cdot 10^3$ [46]) the flow between the rotating shaft and the housing is laminar. The flow then changes into Taylor vortices, which are circular velocity fluctuations (see Fig. 4 and [43]).

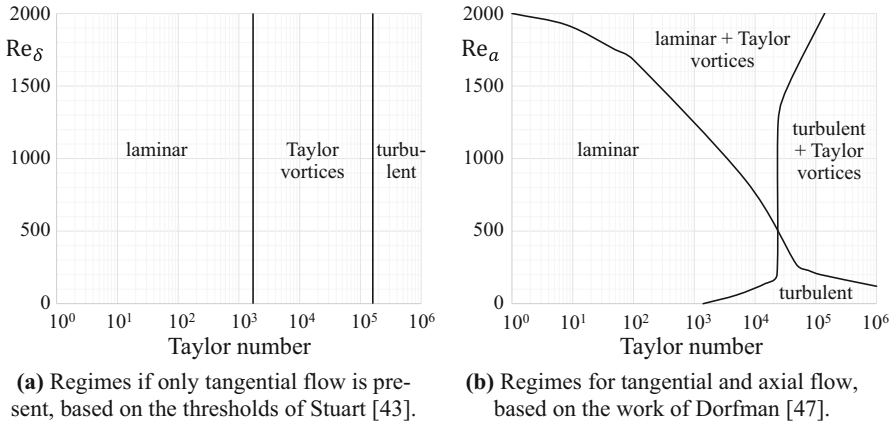


Fig. 5. Contradicting understandings of the flow regimes in concentric cylinders. The strictly separated regimes in (a) are conventionally used to describe the flow in motorized spindles or electric motors while the regimes outlined in (b), featuring an additional axial flow, are a better fit for our measurements.

After the second threshold in Fig. 5 a), the flow changes to an entirely turbulent flow. This regime is of greatest significance for high-speed applications, as the high speed should lead to a consistently turbulent flow. Comparing the results of an accordingly configured simulation model and the temperatures recorded in our experiments (see Sect. 4.2), we concluded that this understanding derived from idealized experimental assemblies of concentric cylinders, cannot be transferred to high-speed motorized spindles. Assuming an additional axial flow, leading to Taylor vortices, which increase the air friction, results in higher, more realistic temperatures with minor deviations.

According to Dorfman [47] (Fig. 5 b)), an additional axial flow leads to four instead of three flow regimes. The thresholds change with increasing axial Reynolds number. Interestingly, the Taylor vortices do not disappear with increasing rotational speed. These effects are not modeled in Stuart's equations [43]. The approaches of Saari [45] (Eq. (19) and (20) in Table 2) based on the work of Bilgen [44] incorporate them. Previously, the measurements deviated most significantly in areas with large cavities between rotor and stator. The simulation results with the equations considering the occurrence of Taylor vortices [44, 45] are two to four times higher in these areas and the resulting temperatures

are comparable to the measurements. The additional axial flow itself could be caused by two different reasons:

- The air sealings create an axial flow in motorized spindles. However, it appears to be unlikely that these additional devices have a significant impact on the airflow inside of the spindle housing.
- Motorized spindle shafts are geometries with varying radii. Different diameters lead to different tangential fluid velocities, creating pressure deviations in axial direction of the air gap, which might lead to an axial flow. This effect was actually observed by Daily [48] based on observations of rotating disks. Disks within an enclosure work like a centrifugal pump (visualized in Fig. 4). The air flows outwards near the rotating disk (4), then axially through the cavity and radially inward on the opposing static wall. The rotational direction of Taylor vortices next to each other is opposed. This phenomena together with the centrifugal pump issue, creates different opposed fluid flows, potentially causing the observed increase in air friction. This issue is only present with enough clearance between rotor and housing [48], directly explaining our previous measurement deviations in areas with large cavities. When the gap decreases, the boundary layers of the shaft and the wall merge. Under these circumstances, the axial flow component disappears, leading to a solely tangential flow.

In general, we strongly advice to make as few geometrical simplifications as possible for the calculation of air friction. Averaging radii quickly leads to significantly lower results as the air friction increases with the fourth or even fifth power of the radius (see Eq. (5) and (6)).

Bearing Friction

While the quantification of air friction appears to be possible with a more sophisticated understanding of the issue, the accurate analytical determination of bearing friction is not possible for high-speed applications. Although there is still research on the topic, the underlying issue of the empirical basis is not addressed. Instead of novel quantification strategies, the published approaches build on each other:

- Palmgren [49] quantifies the bearing friction moment $M_{b,1}$ based on separate determinations of a load-independent (viscous) moment M_0 and load-dependent moment M_1 (Eq. (21)). These quantification approaches are based on empirical observations carried out in the 1940s and 1950s.

$$M_{b,1} = M_0 + M_1 \quad (21)$$

- Harris [50] quantifies the load-independent M_0 and load-dependent moments M_1 based on Palmgren and adds an additional gyroscopic or spinning moment M_{Spin} (Eq. (22)).

$$M_{b,2} = M_0 + M_1 + M_{Spin} \quad (22)$$

- Kosmol [51] incorporates these works and adds additional friction torques due to rolling movement $M_{T(r)}$ and sliding movement $M_{T(s)}$ (Eq. (23)).

$$M_{b,3} = M_0 + M_1 + M_{Spin} + M_{T(r)} + M_{T(s)} \quad (23)$$

According to the comparison with our experiments (Sect. 4.2), the calculation of the viscous load-independent moment M_0 and load-dependent moment M_1 is highly inaccurate for high-speed applications of hybrid bearings in motorized spindles. Abele reported the same issue [4]. The calculated friction torque $M_{b,1}$ from Eq. (21) is already too high by two to five times in the examined speed range, making the more recently formulated additional terms of Harris [50] and Kosmol [51] ineffectual. The calculation is furthermore problematic, as the kinematic viscosity of the lubricant is highly temperature dependent. The lubricant temperature is not determinable without additional temperature sensors inside of the bearings. However, even conservatively estimated temperatures generate too high results. Therefore, the empirical basis itself [49] appears to be unsuitable for high-speed applications. Until the very basis of these quantification approaches is reworked, an analytical calculation of bearing friction probably stays impossible.

Our study on a motorized spindle with 18,000 rpm [3] already pointed toward a practical alternative solution for this problem. Instead of calculating bearing heat analytically, it can be quantified based on the energy conversion of the spindle. In idle mode, the input power P_{in} is equal to the power loss of the spindle. The input power P_{in} can be measured and the power loss can be split into motor P_{motor} , air P_{air} and total bearing friction $P_{b,tot}$. Using the aforementioned approaches to quantify motor and air friction, they can be subtracted from the input power P_{in} to determine the total bearing heat $P_{b,tot}$ (Eq. (24)).

$$P_{b,tot} = P_{in} - P_{motor} - P_{air} \quad (24)$$

The total bearing heat can then be distributed to each bearing based on the aforementioned quantification approaches [49, 50]. While the absolute values of the results of these equations are unusable, their relation to each other appears to be reasonable.

3.4 Solid Motion Effects

The aim of the thermal modeling of machine tool components is usually a better understanding of the thermo-mechanical cause-effect relationships. This is achieved through an accurate representation of the temperature fields, which is primarily accomplished through an accurate set of thermal boundary conditions. However, our thermo-mechanical research pointed toward a kinematic problem, which has to be considered during the thermal modeling phase already. This issue is ignored by other thermal modeling approaches on motorized spindles, nevertheless appears to be essential if the temperature field and thermo-mechanical displacement should be quantified accurately.

The rotation of the shaft has a significant influence on its temperature field, which is explained based on Fig. 6. Usually the temperature field is determined without considering the shaft's rotation. As displayed in Fig. 6 a), the temperature distribution looks in this case similar to the asymmetric [3] housings temperature field. Spindles only have these temperature fields if the shaft is not rotating. A temperature distribution as displayed in Fig. 6 b) is much more common. The shaft's rotation leads to a homogenization in tangential direction. This difference is also relevant for the thermo-mechanical displacement.

While the shaft's temperature field in Fig. 6 a) leads to an axial and radial displacement at the tool center point, the shaft's displacement with the temperature field in Fig. 6 b) is purely axial. The radial displacement of the shaft of a temperature field as displayed in Fig. 6 a) is often times counteractive to the radial tool center point displacement induced by the housing. This creates misleading results, making the consideration of the problem essential for accurate simulation results. The thermo-mechanical cause-effect relationships are explained in greater detail in Sect. 3.2 of our previous article [3].

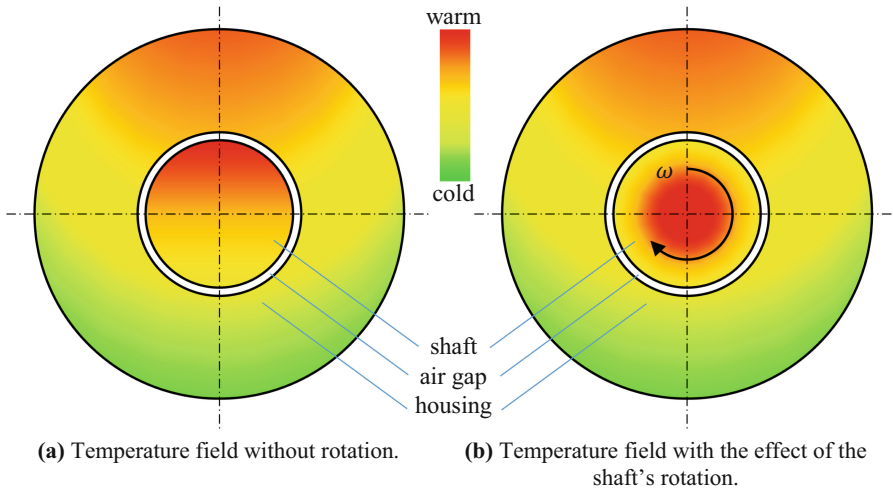


Fig. 6. Qualitative observation of the solid motion effect on the temperature field of motorized spindles. The shaft's rotation leads to a homogenization of its temperature field.

Modern simulation programs have suitable boundary conditions to implement this homogenization-phenomenon. We suggest to realize it with a solid motion effect [52], which has to be applied to the rotating body parts. The thermal solver then calculates the problem in a number of rotational steps. Subsequently, the solver averages the thermal boundary conditions of the shaft, creating a tangentially homogenous temperature field as displayed in Fig. 6 b).

4 Spindle Model and Validation

In the next step, the boundary conditions given in the previous chapter are transferred to the test specimen with 40,000 rpm. The way the boundary conditions are applied to the coupled simulation model is outlined in Sect. 4.1. Finally, the validation of the model is presented in Sect. 4.2.

4.1 Boundary Condition Application to the Simulation Model

All heat transfer systems shown in Table 1 are applied to the spindle simulation model in Fig. 8. The three bearing geometry's heat transition coefficients are applied to the housing's and the shaft's contact surfaces of each respective bearing. Tachibana's approach

[24] was used to quantify the heat transfer coefficients between the shaft and housing. The coefficients are separately calculated and applied to each respective combination of shaft and housing diameters. The spindle housing consisted of several solid bodies. Based on [28], the contacts in-between were modelled with a heat transfer coefficient of $3000 \text{ W/m}^2\text{K}$. The contacts between the bushings and the housing are even harder to quantify, as the respective contact situation is not known (see Sect. 3.1). Based on [28] and our empirical observation we suggest a heat transfer coefficient of $1,500 \text{ W/m}^2\text{K}$ for the radial bushing contacts.

The fluid cooling is realized as heat sink through the definition of its inlet and outlet surface. The inlet surface's flow rate is 10 l/min. The fluid domain's material is water with 43% ethylene glycol. The heat transfer coefficients to the ambient air are applied to each respective surface of the housing (free convection) and the shaft (forced convection). Based on temperature measurements on the rig and additional thermal test bench simulation models, we concluded that the total heat transferred to the test rig is only about 40 W at 40,000 rpm. The nearby fluid cooling transfers about 1423 W out of the spindle, easily replacing the heat transfer to the test bench. Our validation suggests that this boundary condition, which always requires additional measurements, is not necessarily required for fluid cooled motorized spindle models. This perception greatly increases the transferability of the presented modeling approach. Therefore, the model iteration presented for the validation in Fig. 9 does intentionally not include this boundary condition, depicting the validity of the simplification. The drill hole systems were also modelled in earlier iterations of the model. Modeling them with constant heat transfer coefficients and fluid temperatures, increases the model accuracy locally, but decreases it at other positions. This is due to the continuous fluid temperature increase in reality, which cannot be modelled without CFD simulations. In order to get the mean absolute temperature deviation below 1.5 K (Fig. 9) such additional CFD simulations were not necessary. Nonetheless, the borehole systems are geometrically still part of the final model iteration (see Fig. 8).

The power loss of the synchronous motor was assigned to the stator and the rotor geometry. Each bearing's heat generation is applied to its contact surfaces towards the housing and the shaft. In order to quantify the air friction, the spindle's shaft shown in Fig. 3 was divided in 43 combinations of shaft and housing geometries to get accurate results with the approaches given in Table 2. Following the required mathematical simplification introduced with Eq. (2), the air friction is usually [45] applied solely to the surface of the shaft. Our validation (see Sect. 4.2) showed that this approach might be problematic, as the shaft becomes up to 7 K too warm, while the housing stays too cold. The mean absolute difference of the model (shaft and housing) then deviates by 3.12 K. While the physically accurate Eq. (1) quantifies the (entire) air's shear stress between shaft and housing, Eq. (2) reduces this issue to a surface layer problem of the shaft. The simplification issue can be visualized based on a quantification of the air's velocity inside of a spindle cavity. Air speed directly determines the present air friction (see Eq. (1)). The velocity field can be quantified with a mechanical/fluid-mechanical model of the spindle, which is visualized in Fig. 7.

The spindle model in Fig. 7 is reduced to the area with the largest cavity on the right side of Fig. 3. In the first step (Fig. 7), the air's domain is added to the model as

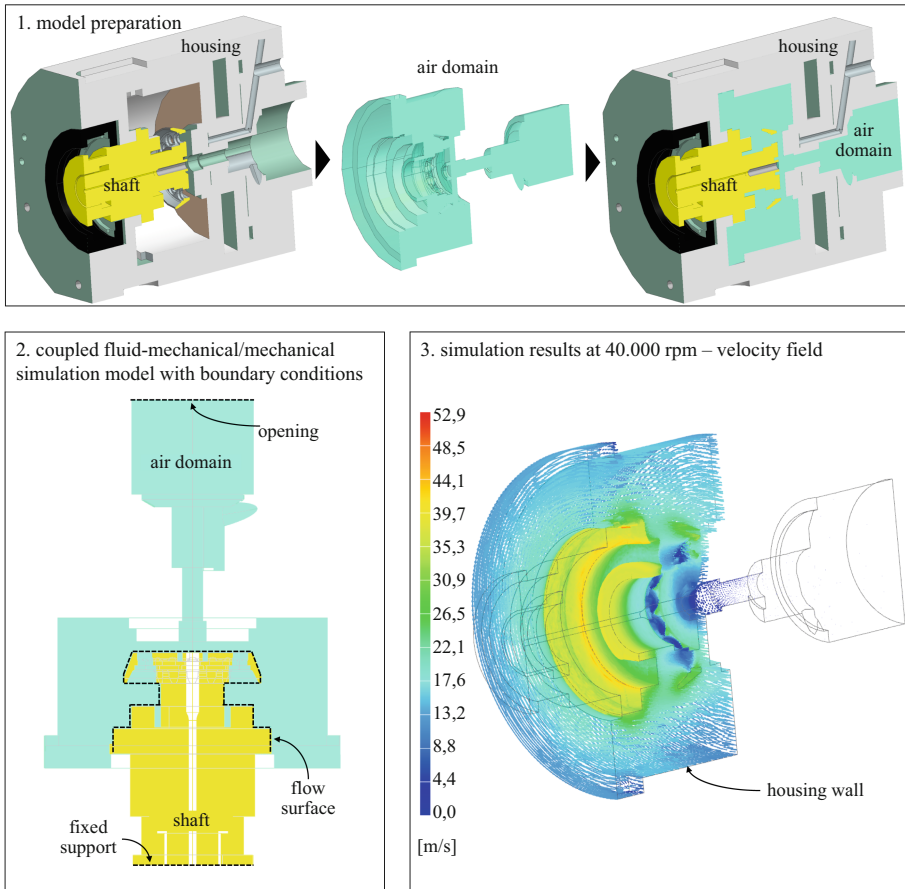


Fig. 7. Coupled mechanical/fluid-mechanical observation of a cavity inside of the spindle. The air's velocity at the housing is still about half of the velocity near the shaft, suggesting a different application method for the air friction boundary condition.

geometry. The model (second step) is then reduced to the air domain and the solid shaft. As boundary conditions an opening and a fixed support is necessary. Furthermore, the model has a flow surface boundary condition, which is required to assign the spindle's speed of 40,000 rpm to the shaft. The resulting velocity field is visualized in the third step of Fig. 7. The air speed near the shaft is about 35 m/s. Interestingly, the air speed near the housing's wall is still about 17.5 m/s.

With the knowledge of the velocity distribution, applying the air friction to both the shaft and the housing seems more reasonable. The exact distribution is not quantifiable. The shaft's surface area is about half of the opposing housing's surface area. However, the air velocity near the shaft is about twice the velocity near the housing. Based on that, we suggest that the heat generation of each of the 43 air friction subranges is halved and equally assigned to both the shaft and the housing. This approach significantly increases

the model's accuracy, lowering the shaft temperature (see Fig. 9) and increasing the housing temperature. Therefore, the mean absolute temperature difference was reduced to 1.48 K, which is derived in the following chapter. Alternatively, the air domain geometry itself could be added to the thermal/fluid-mechanical model. The air friction could then be directly assigned to its origin. This idea should be further researched with additional simulation models in the future.

Finally, the rotation boundary condition is applied to the shaft of the spindle's simulation model visualized in Fig. 8. The figure also visualizes the in- and outlet surfaces of the fluid domain. It also shows the individual geometries of the housing and the bushings, allowing the application of the contact boundary conditions.

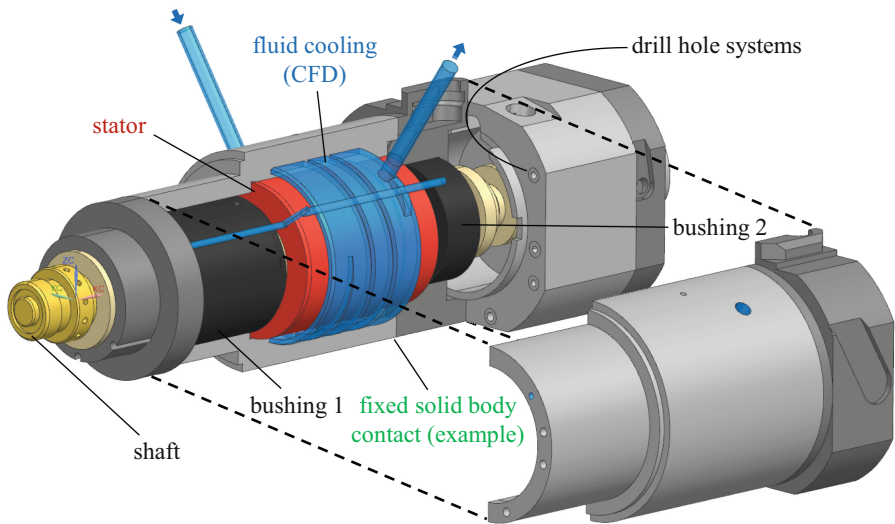


Fig. 8. Coupled thermal/fluid-mechanical simulation model of the motorized spindle.

4.2 Test Bench and Model Validation

The test bench visualized on the left of Fig. 9 measures input power, fluid flow rate and the temperature. Measuring the input power allows the calculation of the bearing friction (Sect. 3.3). The measurement of the flow rate and fluid's in- and output temperature is required to monitor the cooling rate.

The temperature measurement in Fig. 9 and the developed validation method should be outlined in detail. The housing's temperature is measured with 21 Pt100 sensors. The spindle was observed in different speed stages, the most challenging stage at 40,000 rpm is visualized in Fig. 9. The test bench temperatures are given after four hours at 40,000 rpm, which is directly comparable to the thermal equilibrium observation of the simulation model. In order to increase the reliability of the validation, the empirical observation was repeated five times. The sensor values shown in Fig. 9 are based on arithmetic averages of these measurements.

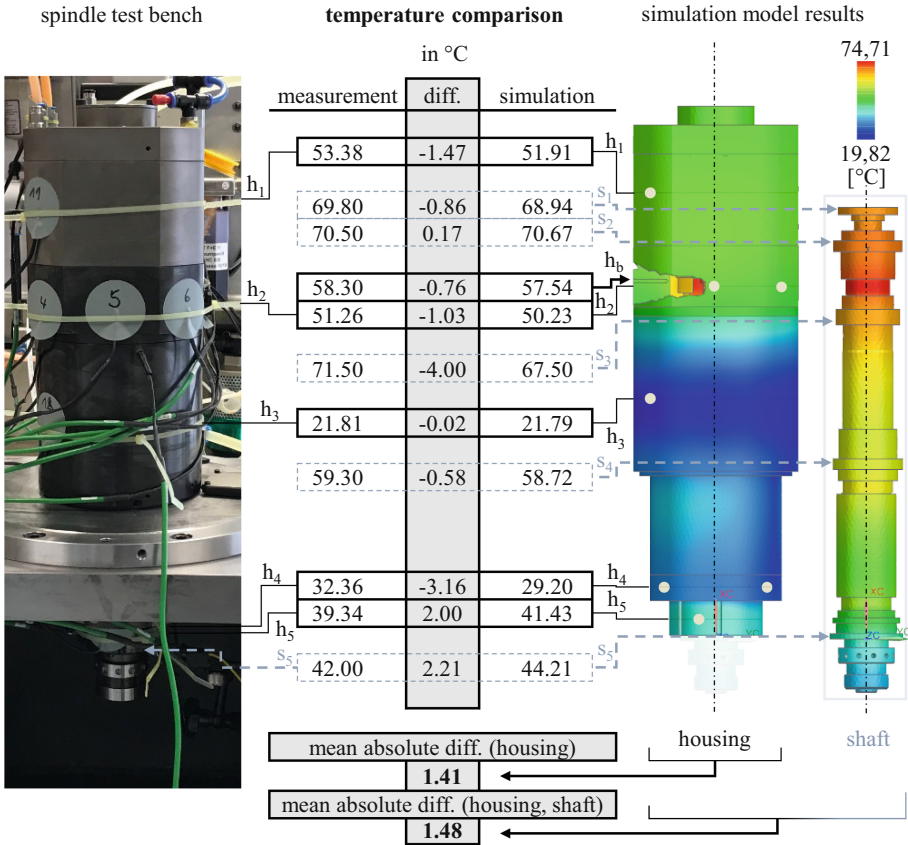


Fig. 9. The spindle test bench (left) and the results of the simulation model (right) at 40,000 rpm. The model temperatures are picked at the same spots as the test bench’s temperatures. The temperatures are averaged at each spot and the difference between the test bench and the model is calculated. Finally, the mean absolute temperature differences are calculated for the validation.

The individual sensors were mainly applied to the housing’s surface on five different locations (h₁, h₂, h₃, h₄ and h₅). Based on the complexity of each location’s temperature field, a different number of sensors was attached to each position along the circumference. For example, h₁ required only two sensors, of which one is visible and the other arranged in an 180° angle. The sensor values of each position were averaged. The averaged values are visualized in the table in the figure (left column). The simulation model’s temperatures are taken at the same positions (see Fig. 9, right) and averaged in the same way (right column), creating comparable values.

Additionally, one sensor was positioned inside of the spindle. This sensor at h_b is located in a borehole near the rear bearing of the spindle, visualized based on the simulation model to the right. Furthermore, the shaft’s temperature was measured on five different locations, which are depicted based on the simulation model (s₁, s₂, s₃, s₄ and s₅) in Fig. 9. The shaft’s temperature field is symmetrical (Sect. 3.4), making the

angular position of the shaft irrelevant for the measurement. However, while the housing temperature can be measured while the spindle is running, the rotating shaft's temperature could only be measured after the spindle was stopped. This issue makes these values less reliable, but the additional information regarding the shaft's temperature should nonetheless increase the validity.

The difference between the temperatures of the test bench and the simulation model is displayed in the center column of Fig. 9. Larger temperature differences can be observed at s_3 , h_4 and in the frontal area at h_5 and s_5 . The deviation at s_3 could be due to the geometrical complexity of the housing behind the electric motor (see Fig. 3), making an accurate calculation of the heat transfer coefficient based on correlation equations impossible. The difference at h_4 could be due to the missing CFD-simulation of the borehole systems (see Sect. 4.1) which are numerous in this area. The inaccuracies at h_5 and s_5 probably have the same reason: There is currently no model available to consider the transition between the forced convection on the shaft to the free convection on the surrounding spindle housing. The heat transfer coefficient to the ambient air abruptly drops from $312.37 \text{ W/m}^2\text{K}$ (shaft) to $4.87 \text{ W/m}^2\text{K}$ (housing), creating too high temperatures in the housing.

Finally, the mean absolute differences of the temperatures are calculated below the center column in Fig. 9. We generally suggest using absolute values for thermal validation procedures. As outlined above, the mean absolute difference of the housing's temperatures (1.41 K) is the more reliable value. However, the mean absolute difference of the housing's and the shaft's temperatures (1.48 K) includes more information. Apart from the described outliers, the simulation model seems to represent the reality accurately with temperature differences of 1 K or less.

5 Spindle Power Loss Observation

This paper concludes with an observation of the spindle's power loss in idle mode, depicting the loss distribution in different operating points (Fig. 10). The input power in the graphs (159 W, 412 W, 807 W and 1,507 W) are measured values from the test bench (Sect. 4.2), while the output values are calculated based on the approaches given in Sect. 3.3.

Figure 10 a) displays the power loss at 10,000 rpm. The motor loss is clearly most significant at that point, while the bearing friction is much smaller. The air friction plays an insignificant role in this speed range. However, at 20,000 rpm the torque due to bearing and air friction is substantially larger (Fig. 10 b). Above 20,000 rpm, the electric motor's field-weakening sets in. Even in the relative observation in Fig. 10 c), the air friction becomes more significant at 30,000 rpm. Interestingly, the relative share of the bearings stays almost identical at that point. At 40,000 rpm (Fig. 10 d)) more than one third of the frictional loss is caused by air friction. The percentage will increase even further above 40,000 rpm, underlining the increasing importance of air friction observations for high-speed applications.

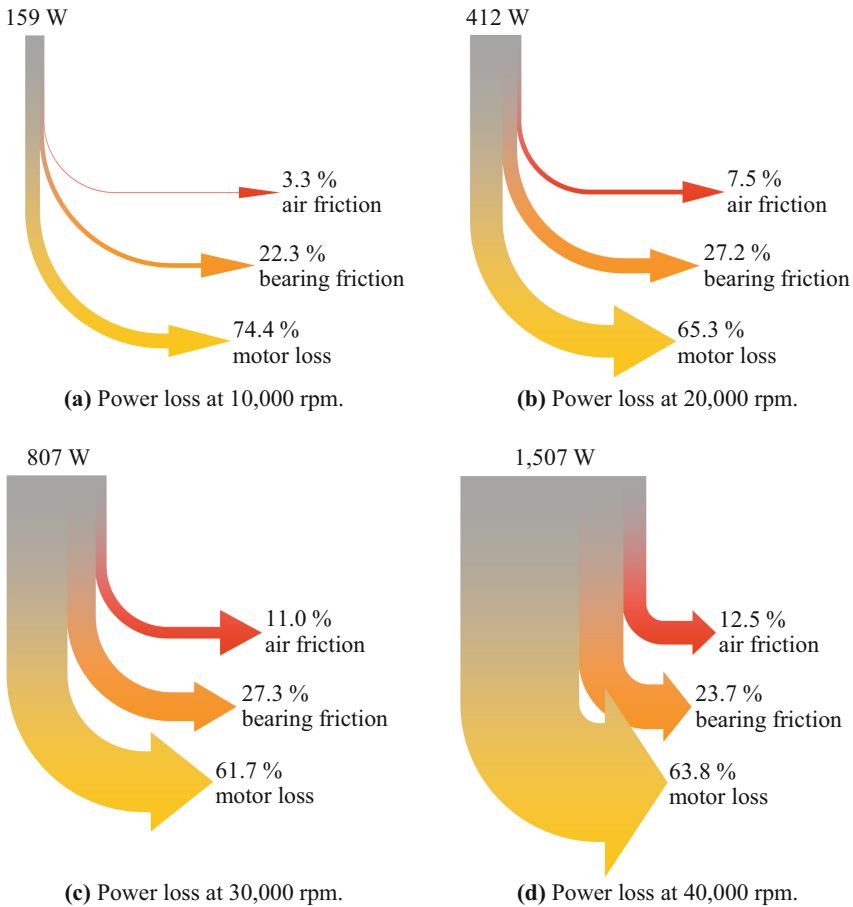


Fig. 10. Observation of the motor spindle's energy conversion in idle mode at 10,000 rpm (a), 20,000 rpm (b), 30,000 rpm (c) and 40,000 rpm (d).

6 Conclusion and Outlook

The thermally induced displacement of the tool center point most significantly decreases the manufacturing precision of metal cutting machine tools. In order to compensate the displacement, the cause-effect relationship has to be reproduced through thermal and mechanical modeling. Section 1 outlines that thermal modeling is especially challenging for high-speed motorized spindles, as over 20,000 rpm only two modeling attempts exist (25,000 rpm [20] and 36,000 rpm [21]), which rely on extensive empirical observations.

This paper introduces for the first time a thermal modelling approach for motorized spindles at 40,000 rpm with minimal measuring effort. The declared objective of the parallel simulative and empirical observation was the identification of inaccuracies of individual boundary conditions, allowing further research for additional or alternative quantification approaches. The investigated boundary conditions are subsequently presented in Sect. 3. They are split into heat transfer systems, heat sinks and heat sources.

While quantification approaches for the heat transfer through the bearings and the gap between shaft and housing generated reliable results, the quantification of solid body contacts proved to be more challenging. Apart from the ambient air and the machine interface, the heat sinks should preferably be quantified as additional coupled CFD-simulations. The heat sources have the greatest influence on the resulting temperature field of motorized spindles. While the electric motor can be quantified with reasonable accuracy, the precise calculation of air and bearing friction is really challenging for high-speed applications. In Table 2 of this paper, a new set of quantification approaches for air friction coefficients in motorized spindles is introduced. This set incorporates for the first time the appearance of Taylor vortices in the air gap, significantly increasing the air friction torque. While such development was possible for the air friction, a comparable improvement could not be found for the bearing friction torque. All existing quantification approaches are based on the work of Palmgren [49], whose empirically determined equations are not compatible with high-speed applications of modern hybrid bearings. Instead, we suggest the calculation of the bearing friction torque based on a measurement of the input power. Additionally, a solid motion effect is introduced for the first time in thermal models of motorized spindles to consider the temperature homogenization-effect of rotation.

In order to show the validity of the introduced set of boundary conditions, they are applied to a motorized spindle with 40,000 rpm in Sect. 4. The conceptualized set of boundary conditions is applied to the developed thermal/fluid-mechanical simulation model. Further research on the distribution of air friction with an additional mechanical/fluid-mechanical simulation model allowed us to reduce the mean absolute difference between the thermal/fluid-mechanical simulation model and measurement to 1.5 K.

Conclusively, Sect. 5 shows the spindle's energy conversion at 10,000 rpm, 20,000 rpm, 30,000 and 40,000 rpm in idle mode. The analysis shows that air friction becomes more significant with higher rotational speed. At 40,000 rpm the air friction causes already one third of the frictional losses, underlining the increasing importance of its accurate estimation for high-speed applications.

In the next steps, the inaccuracies of the current model iteration should be addressed further. The application of the air friction inside the spindle is still problematic, as it does not accurately represent the physical nature of the problem. Air friction occurs in the entire three dimensional air gap of the spindle. Therefore, its simplified application to the surrounding solid body surfaces (shaft, housing) is problematic. The problem could possibly be solved by adding the air inside the spindle as an additional geometric element. The air friction could then be assigned to the air element itself. The heat would then flow to the surrounding elements according to the second law of thermodynamics, representing the physical nature of the problem more accurately. Furthermore, the inaccuracy at the tip of the spindle near the tool (Fig. 9) should be investigated. Currently, there is no model for the transition area between the forced convection on the shaft and the free convection on the housing. A new boundary condition based on interpolation would further increase the validity of the presented modeling approach.

Acknowledgment. This research was supported by the Bayerisches Staatsministerium für Wirtschaft, Landesentwicklung und Energie.

References

1. Putz, M., et al.: Thermal errors in milling: comparison of displacements of the machine tool, tool and workpiece. *Procedia CIRP* **82**, 389–394 (2019)
2. Mayr, J., et al.: Thermal issues in machine tools. *CIRP Ann.* **61**(2), 771–791 (2012)
3. Koch, L., et al.: Thermal asymmetry analysis of motorized spindles. *MM Sci. J. Special Issue ICTIMT2021* 4612–4619 (2021)
4. Abele, E., et al.: Machine tool spindle units, *CIRP Ann. Manuf. Technol.* **59**, 781–802 (2010)
5. Udup, E., et al.: Numerical Model for the Thermo-Mechanical Spindle Behavior, *Advances in Production, Automation and Transportation Systems*, pp. 259–264 (2010)
6. Zhao, C., Guan, X.: Thermal analysis and experimental study on the spindle of the high-speed machining center. *AASRI Procedia* **1**, 207–212 (2012)
7. Wu, C.-H., Kung, Y.-T.: A parametric study on oil/air lubrication of high-speed spindle. *Precis. Eng.* **29**, 162–167 (2005)
8. Cao, Y.: *Modelling of high-speed machine-tool spindle-systems*, University of British Columbia, Vancouver (2006).
9. Syath, A., et al.: Dynamic and thermal analysis of high speed motorized spindle. *Int. J. Appl. Eng. Res.* **1**(4), 864–882 (2010)
10. Liu, D., et al.: Finite element analysis of high-speed motorized spindle based on ANSYS. *Open Mech. Eng. J.* **5**, 1–10 (2011)
11. Nikitina, L.: Modeling of motor-spindel thermal values. *Procedia Eng.* **206**, 1316–1320 (2017)
12. Uhlmann, E., Hu, J.: Thermal modelling of a high speed motor spindle. *Procedia CIRP* **1**, 313–318 (2012)
13. Vyroubal, J.: Compensation of machine tool thermal deformation in spindle axis direction based on decomposition method. *Precis. Eng.* **36**, 121–127 (2012)
14. Ma, C., et al.: Simulation and experimental study on the thermally induced deformations of high-speed spindle system. *Appl. Therm. Eng.* **86**, 251–268 (2015)
15. Wang, Z., Zhang, K., Wang, Z., Bai, X., Wang, Q.: Research on vibration of ceramic motorized spindle influenced by interference and thermal displacement. *J. Mech. Sci. Technol.* **35**(6), 2325–2335 (2021). <https://doi.org/10.1007/s12206-021-0505-4>
16. Chen, B., et al.: Simulation on thermal characteristics of high speed motorized spindle. *Case Stud. Therm. Eng.* **35**, 1–12 (2022)
17. Huang, Y.-H., et al.: An experimental and numerical study of the thermal issues of a high-speed built-in motor spindle. *Smart Sci.* **4**(3), 1–13 (2016)
18. Koch, L., et al.: Coupled thermal and fluid mechanical modeling of a high speed motor spindle. *Appl. Mech. Mater.* **871**, 161–169 (2017)
19. Denkana, B., et al.: Methodology for thermal optimization of motor spindles. In: *Special Interest Group Meeting on Machine Tools and Production Engineering (WZL) of RWTH Aachen, Germany* (2020)
20. Bossmanns, B., Tu, J.F.: A thermal model for high speed motorized spindles. *Int. J. Mach. Tools Manuf.* **39**, 1345–1366 (1999)
21. Gebert, K.: *Ein Beitrag zur thermischen Modellbildung von schnelldrehenden Motorspindeln*, Technische Hochschule Darmstadt, Shaker Verlag, Aachen (1997)
22. Bossmanns, B., Tu, J.F.: A power flow model for high speed motorized spindles – heat generation characterization. *J. Manuf. Sci. Eng. Trans. ASME* **123**, 494–505 (2001)
23. Weidemann, F.: *Praxisnahe thermische Simulation von Lagern und Führungen in Werkzeugmaschinen*. In: *19th CAD-FEM Users Meeting, Potsdam* (2001)

24. Tachibana, F., et al.: Heat transfer in an annulus with inner rotating cylinder. *Bull. JSME* **3**, 119–123 (1960)
25. Fénot, M., et al.: A review of heat transfer between concentric rotating cylinders with or without axial flow. *Int. J. Therm. Sci.* **50**, 1138–1155 (2011)
26. Yovanovich, M.M.: Four decades of research on thermal contact, gap, and joint resistance in microelectronics. *IEEE Trans. Compon. Package. Technol.* **28**(2), 182–206 (2005)
27. Yovanovich, M.M.: New contact and gap conductance correlations for conform rough surfaces. In: *AIAA 16th Thermophysics Conference*, Palo Alto, California (1981)
28. Negus, K.J., Yovanovich, M.M.: Correlation of the gap conductance integral for conforming rough surfaces. *J. Thermophys. Heat Transf.* **2**, 279–281 (1988)
29. Koch, L., et al.: Comparative analysis of the fluid cooling systems in motorized spindles. *MM Sci. J. Special Issue ICTIMT2021* 4620–4627 (2021)
30. Churchill, S.W., Chu, H.H.: Correlating equations for laminar and turbulent free convection from a vertical plate. *Int. J. Heat Mass Transf.* **18**, 1323–1329 (1975)
31. Dropkin, D., Carmi, A.: Natural-convection heat transfer from a horizontal cylinder rotating in air. *Trans. ASME* **5**, 741–749 (1957)
32. Hartnett, J.P.: Heat transfer from a nonisothermal disk rotating in still air. *J. Appl. Mech.* **12**, 672–673 (1959)
33. Gnielinski, V.: Neue Gleichungen für den Wärme- und Stoffübergang inturbulent durchströmten Rohren und Kanälen. *Forsch. Ing-wes* **41**(1), 8–16 (1975)
34. Stephan, P., et al.: *VDI-Wärmeatlas*. Springer Vieweg, Wiesbaden (2011). <https://doi.org/10.1007/978-3-642-19981-3>
35. Richter, R.: *Elektrische Maschinen - Band 1: Allgemeine Berechnungselemente*, 3rd edn. Birkhäuser-Verlag, Basel (1967)
36. Hering, E., et al.: *Elektrotechnik und Elektronik für Maschinenbauer*, 3rd edn. Springer, Berlin, Heidelberg (2018). <https://doi.org/10.1007/978-3-662-54296-5>
37. Rothenbücher, S., et al.: *Die Speisung macht's*. WB Werkstatt und Betrieb **142**(7–8), 62–65 (2009)
38. Gieras, J., Wing, M.: *Permanent Magnet Motor Technology*, 2nd edn. Marcel Dekker, New York (2002)
39. Kreith, F.: Convection heat transfer in rotating systems. *Adv. Heat Transf.* **5**, 129–251 (1968)
40. Theodorsen, T., Regier, A. A.: *Experiments on Drag of Rotating Disks, Cylinders and Rods at High Speeds*. Naca Report 793 (1944)
41. Yamada, Y.: Torque resistance of a flow between rotating co-axial cylinders having axial flow. *Bull. JSME* **5**(20), 634–642
42. Schulz-Grunow, F.: Der Reibungswiderstand rotierender Scheiben in Gehäusen. *Zeitschrift für angewandte Mathematik und Mechanik* **15**(4), 191–204 (1935)
43. Stuart, J.T.: On the non-linear mechanics of hydrodynamic stability. *J. Fluid Mech.* **4**, 1–21 (1958)
44. Bilgen, E., Boulos, R.: Functional dependence of torque coefficient of coaxial cylinders on gap width and Reynolds number. *Trans. ASME J. Fluid Eng.* **95**(1), 122–126 (1973)
45. Saari, J.: *Thermal analysis of high-speed induction machines*. Acta Polytechnica Scandinavia Electrical Engineering Series, p. 90, Helsinki (1998)
46. Gazley Jr, C.: Heat transfer characteristics of the rotational and axial flow between concentric cylinders. *Trans. ASME* **80**, 79–90 (1958)
47. Dorfman, L.A.: *Hydrodynamic resistance and the heat loss of rotating solids*, p. 244, Oliver & Boyd, Edinburgh and London (1963)
48. Daily, J.W., Nece, R.E.: Chamber dimensions effects on induced flow and frictional resistance of enclosed rotating disks. *Trans. ASME J. Basic Eng.* **82**(1), 217–232 (1960)
49. Palmgren, A.: *Grundlagen der Wälzlagertechnik*. Franckh'sche Verlagshandlung, Stuttgart (1964)

50. Harris, T.A., Michael, N.K.: Rolling Bearing Analysis: Advanced Concepts of Bearing Technology, 5th edn. Taylor & Francis Group LLC, Boca Raton (2007)
51. Kosmol, J.: Analytical and FEM simulation studies on friction resistances in angular ball bearings. *Int. J. Mod. Manuf. Technol.* **13**(1), 73–83 (2021)
52. Siemens NX Documentation Homepage, Solid Motion-Effekte – Drehoptionen. https://docs.plm.automation.siemens.com/tdoc/nx/1899/nx_help#uid:xid1128419:index_advanced:id1121662:xid390781:xid390784. Accessed 18 Aug 2022

Open Access This chapter is licensed under the terms of the Creative Commons Attribution 4.0 International License (<http://creativecommons.org/licenses/by/4.0/>), which permits use, sharing, adaptation, distribution and reproduction in any medium or format, as long as you give appropriate credit to the original author(s) and the source, provide a link to the Creative Commons license and indicate if changes were made.

The images or other third party material in this chapter are included in the chapter's Creative Commons license, unless indicated otherwise in a credit line to the material. If material is not included in the chapter's Creative Commons license and your intended use is not permitted by statutory regulation or exceeds the permitted use, you will need to obtain permission directly from the copyright holder.



Design and Materials



Experimental Investigation of Passive Thermal Error Compensation Approach for Machine Tools

Immanuel Voigt¹(✉), Axel Fickert², Hajo Wiemer², and Welf-Guntram Drossel^{1,3}

¹ Technische Universität Chemnitz, Reichenhainer Straße 70, 0126 Chemnitz, Germany
immanuel.voigt@mb.tu-chemnitz.de

² Technische Universität Dresden, Helmholtzstraße 7a, 01069 Dresden, Germany

³ Fraunhofer Institute for Machine Tools and Forming Technology, Reichenhainer Straße 88, 09126 Chemnitz, Germany

Abstract. Conventional approaches to counteract thermal issues in machine tools often require a significant amount of electrical energy input, such as in active cooling systems. An energy-efficient way for reducing thermal errors is to use passive components that redistribute heat introduced by feed drives and other internal heat sources. On the one hand, latent heat storage units can be integrated into the machine to enhance the thermal stability within the phase transition temperature range of the underlying phase change material. By using latent heat storage units, the impact of highly time-varying heat flows on the thermal displacement of the tool center point can be reduced. On the other hand, passive heat-transfer devices such as heat pipes allow for an increased heat exchange within the machine tool or between the machine tool and the environment. Heat pipes exhibit a very high effective thermal heat conductivity and can be used to transfer heat from machine-internal heat sources to additionally integrated heat sinks. A compensation system is presented combining latent heat storage units and heat pipe systems. To evaluate the effect of the corresponding components on thermally induced displacements, experimental investigations of the system within a machine tool are conducted. By means of temperature and displacement measurements it is demonstrated that the proposed compensation approach allows for partial compensation of the thermal error of the machine tool.

Keywords: Machine tool · thermal error · phase change material · heat pipe

1 Introduction

A significant share of geometrical machine tool errors is induced by thermal effects. Numerous solution strategies have been reported in literature that aim for reducing thermally induced errors [1]. One of the most common strategies is using active cooling systems to avoid high temperature fields within the machine tool components such as the main spindle and the feed drives. However, active cooling systems are one of the main energy consumers in machine tools [2].

In order to reduce the electric energy input into the machine tool while maintaining the demanded machine accuracy, passively operating thermal error compensation systems have been proposed in multiple studies [3–6]. The corresponding solutions are based on two basic approaches: On the one hand side it is proposed to use phase change materials (PCM) within machine tools. PCM are characterized by a high amount of energy that is absorbed to perform a phase change between liquid and solid state. The high energy density within the phase change temperature range of the corresponding material can be used to provide a higher thermal stability to the machine tool.

On the other hand, heat transfer devices based on two-phase fluid flow are a suitable tool. By means of heat pipes, heat can be transported at low thermal resistance and without the need to provide electric input. The convenient use of such devices within moving assemblies has been validated by recent experimental investigations [7].

This paper proposes a passive method for reducing thermal errors in machine tools based on the combination of PCM and heat pipes. The main purpose of the presented investigations was to determine the impact of corresponding components on the thermally induced displacements of a machine tool. To this end, the design of latent heat storage (LHS) units and heat pipe based heat sink assemblies is presented. The main content focusses on experimental investigations on an experimental machine tool applied with the fabricated compensation components. Temperature and displacement measurements demonstrate the effect of the components on the machine tool behavior in comparison to the reference state.

2 Compensation Method and Scenario

As numerous studies demonstrated, thermal issues need to be addressed during the design of machine tools. In this context, great importance is attached to the material selection [8]. For example, materials of high heat capacity can be used to obtain slow temperature responses to a certain thermal load. Besides storing heat sensibly, heat can be stored by means of the phase change of materials. This latent heat approach offers the advantages of high energy density and small temperature change within the phase change temperature range of the phase change material (PCM). The application of LHS units to increase the thermal stability of feed drive systems has been addressed in recent studies [4, 5].

Another requirement concerning the physical parameters of machine tool structures is high thermal conductivity. While few solid materials reach thermal conductivity values in the order of 10^3 W/(m K), fluid flow allows for heat transfer at even higher effective thermal conductivity. The present study considers the use of heat pipes that offer an effective thermal conductivity of up to the order of 10^5 W/(m K). Through the application of heat pipes within the machine tool structures, heat can be transferred within the machine tool or between the machine tool and the environment at low thermal resistance and without the need of electric energy input.

Both approaches form a passive compensation method that aims for reducing thermal errors by altering the heat flows within machine tools. With regards to the numerical description of corresponding components within machine tools, complexity arises due to the highly nonlinear relationship between temperature field and displacement

values. Therefore, the effect of LHS units and heat pipe based systems on thermally induced deformations was experimentally investigated using an experimental machine tool described in the following.

2.1 Experimental Machine MAX

The experimental lightweight machine tool MAX was developed as a test rig for fundamental investigations of novel structural concepts [10].

The machine tool realizes a 3-axis Cartesian kinematic with a fixed spindle and three movable slides, which are stacked on top of each other. The slides are composed of waterjet cut aluminum plates, which are prestressed with tie rods.

The slide-structure is shown in Fig. 1. The bottom slide (Z-slide) is driven by three parallel ball screw drives. The X- and Y-slides on top are driven by two ironless linear drives each. The two parallel drives for the Y-direction and the three parallel drives in the Z-direction enable for small corrections in all three rotational degrees of freedom [11, 12].

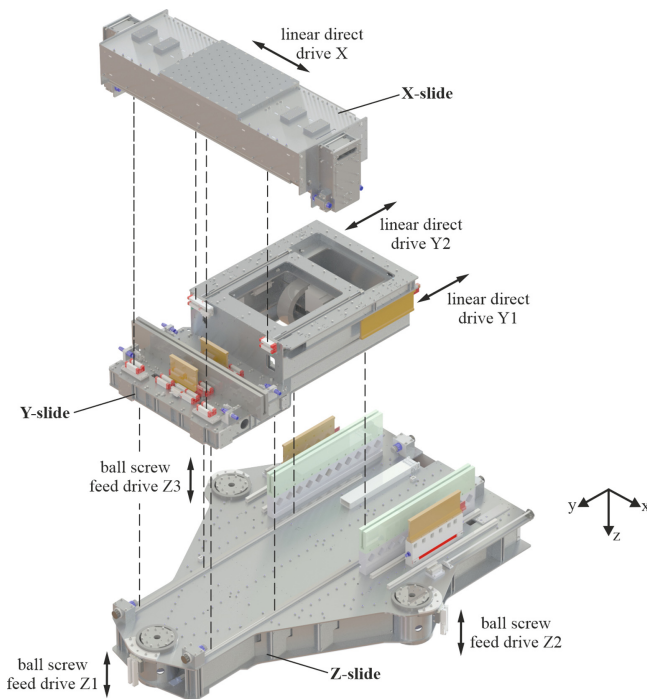


Fig. 1. Slide structure of experimental machine MAX, adapted from [12]. The compensation-slides used for reducing dynamic excitations are not illustrated.

2.2 Compensation Approach

The linear direct drives Y1 and Y2 are two of the main heat sources of the machine. The main heat losses of a linear direct drive occur in the primary part. Hence, the interface between the primary parts of Y1 and Y2 and the adjacent structure of the Y-slide was chosen as the integration location for the compensation components.

The proposed compensation approach aims for a thermal error reduction through redistribution of the heat losses caused by the primary parts of the Y-slide. Figure 2 illustrates the intended heat flow manipulation. Under load, the reference configuration is characterized by direct heat flow of the primary part into the Y-slide structure. In the compensation configuration, the heat losses flow into the LHS unit where the initially solid PCM starts melting upon reaching the phase transition start temperature. During the phase change, the heat input into the Y-slide structure is reduced by the amount of latent heat stored within the PCM.

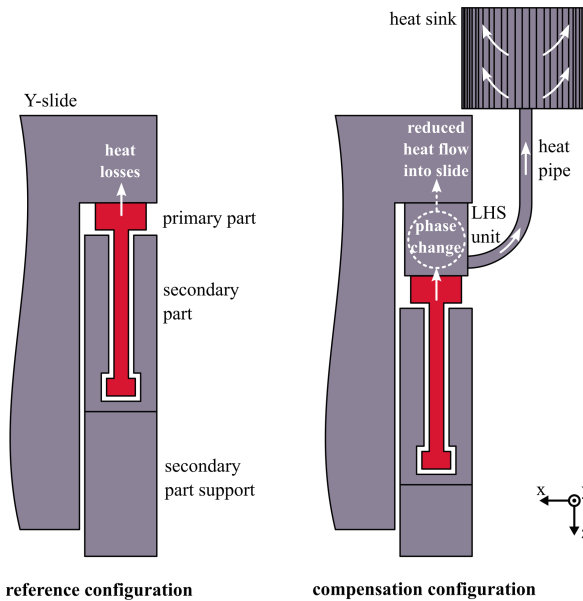


Fig. 2. Manipulating heat flow within Y-slide.

At the same time, heat pipes mounted between the primary part and the LHS unit transfer parts of the heat losses to additionally integrated heat sinks. As observed in previous studies, conventional heat pipes exhibit optimal performance in gravity-assisted orientation [7]. For this reason, the heat sinks were designed to be placed upon the Y-slide structure. The motion of the heat pipe heat sink assembly along with the Y-slide leads to increased convective heat transfer coefficients.

Both effects, the phase change within the LHS and the increased heat dissipation by means of the heat pipe heat sink assembly, were expected to contribute to a reduction of temperatures and thermally induced displacements within the Y-slide under load.

While the effect of LHS units on the slide temperature has been recorded in previous investigations, the heat pipes and heat sinks are added to the compensation system to further remove heat of the Y-slide after the melting of the PCM [4]. It was expected to thereby maintain compensation beyond the phase transition temperature range. The compensation approach considers a phase change temperature range less than 10 K above ambient temperature. Consequently, the temperature rise upon thermal loading is firstly countered by the increased energy density of the LHS units. With increasing temperature above phase transition end temperature, the LHS effect decreases while the dissipation through heat pipe and heat sink increases due to reduced thermal resistance at higher temperature gradients, as demonstrated in [7].

In the following, the design, fabrication, and properties of the compensation components are described.

2.3 Design of Compensation Components

The compensation components are shown in Fig. 3. One LHS unit for each of the two Y-drives was fabricated. Due to its high phase change enthalpy and compatibility with metals, the paraffin-based PCM RT28HC was chosen as storage material for the LHS units. It stores latent heat of around 220 kJ/kg within a phase transition temperature range between 24 °C and 29 °C. The PCM was filled in liquid state into a milled steel container. 225 g PCM was filled into each container. To counter the low thermal conductivity of the paraffin (0.2 W/(m K)), nano-graphite was added at 10% volume fraction. According to prior investigations, the thermal conductivity of the paraffin-nano-graphite-compound exhibits a thermal conductivity of around 1 W/(m K) [5]. The LHS unit was sealed using a top cover made of steel glued to the container using thermal adhesive.

The heat sinks were fabricated by electrical discharge wire cutting. One heat sink consists of two parts. In total, four heat sinks were fabricated. The free surface of one heat sink amounts to 1616 cm².

Conventional heat pipes with sintered capillary structure were used for the tests. The heat pipe heat sink assembly design required bending of the heat pipes with a bending radius of 4 cm.

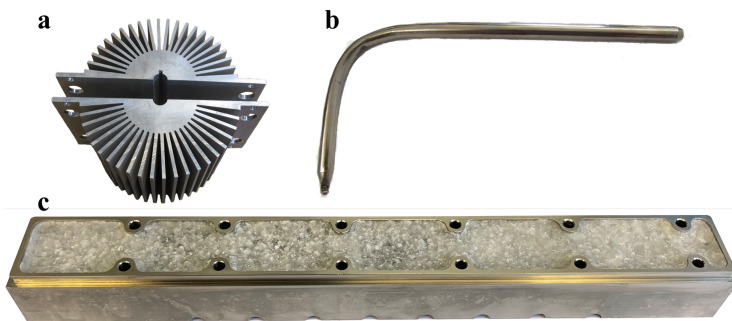


Fig. 3. Heat sink (a), heat pipe (b) and LHS unit (c, without top cover) used within the thermal error compensation system.

3 Experimental Investigations

3.1 Experimental Set-Up

The compensation components were integrated into the experimental machine MAX. To provide installation space for the LHS units, the secondary part supports were replaced by supports of reduced height. The LHS units were then mounted between each primary part and the adjacent slide structure. The heat sinks were mounted onto the Y-slide using 3D-printed PLA supports. The machine was equipped with a measurement arbor mounted into the main spindle nose and six precision probes attached to the X-slide. By means of the precision probes the relative displacements between X-slide and measurement arbor were recorded. Within the global coordinate system (s. Fig. 1), the precision probes were aligned along positive X-axis, negative Y-axis, and negative Z-axis. Figure 4 shows the experimental set-up. The machine is enclosed by walls to avoid exposure to air flow within the machine shop. However, no temperature control was installed within the machine enclosure itself.

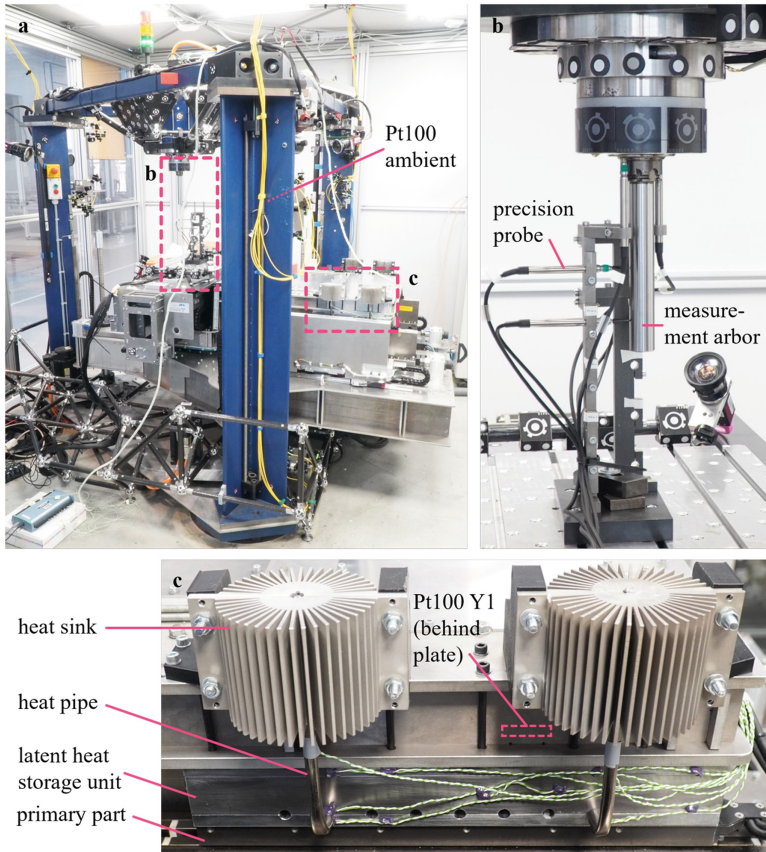


Fig. 4. Experimental set-up.

In addition to the displacement sensors, Pt100 temperature sensors were used to record the temperatures of the Y-slide and the environment. One sensor was placed above the Y1 drive (Pt100 Y1, see Fig. 4) and another one at the same Y and Z location above the Y2 drive. Furthermore, thermocouples of type K were attached to the LHS units, heat pipes and heat sinks.

3.2 Experimental Procedure

The machine was thermally loaded by means of the heat losses of the ball screw and linear direct drives under motion. Two different motion sequences were considered to evaluate the impact of the different drives on the occurring displacements. *Motion sequence A* was defined by cyclic motion of axis Y within the range $[-190 \text{ mm}; 190 \text{ mm}]$ and axis Z within the range $[-80 \text{ mm}; 220 \text{ mm}]$. One motion cycle of the machine is composed of three axis cycles in y and one axis cycle in z direction (see Fig. 5). The maximum feed rates along the y-axis and z-axis amount to 0.69 m/s and 0.18 m/s, respectively. *Motion sequence B* exhibits the identical motion profile in the y-direction with no motion in the z-direction. The z-position was set at 220 mm.

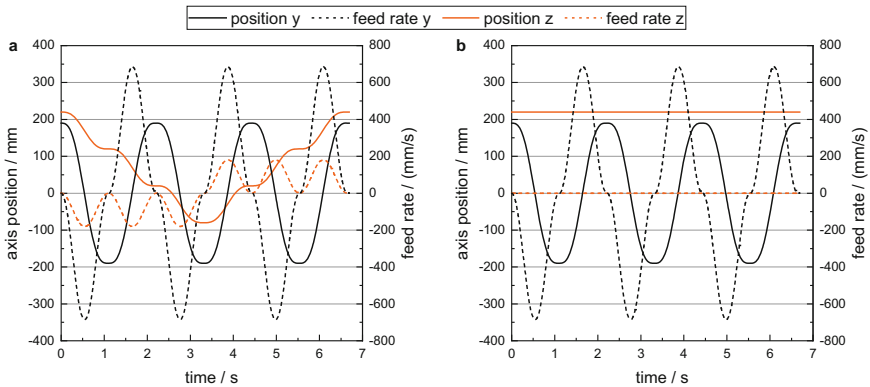


Fig. 5. Position and feed rate during one motion cycle of motion sequence A (a) and motion sequence B (b).

Prior to each experiment, the machine was turned off for at least 15 h to provide isothermal conditions of the machine at environmental temperature. At the beginning of each experiment and after each motion sequence, the displacements were measured. This was realized by moving the axes to the measurement position to contact the precision probes with the measurement arbor.

Two different test procedures were applied. *Test procedure A* was defined by measurement periods of 900 s, while the measurement periods during *test procedure B* lasted only 30 s. The initial displacements were recorded for 30 s. The averages of the initial displacements were used to scale the subsequent displacement measurements. Between two measurement sequences the axes were moved according to the corresponding motion sequence. Each motion sequence lasted for 2700 s.

The first test series were conducted after mounting the compensation components into the machine. Afterwards, the components were removed to repeat the test series in reference configuration. For each configuration three test cases were considered:

- motion sequence A with measurement sequences of 900 s,
- motion sequence B with measurement sequences of 900 s, and
- motion sequence A with measurement sequences of 30 s.

4 Experimental Results

The effect of the compensation components on the temperature field of the Y-slide was evaluated by comparing the temperature values of Y1 and Y2 measured in reference ($Y1_{\text{ref}}$, $Y2_{\text{ref}}$) and compensation configuration ($Y1_{\text{comp}}$, $Y2_{\text{comp}}$) as shown in Fig. 6. As expected, a temperature rise during the motion sequences and a temperature drop during the measurement sequences was observed. In all three test cases a significant reduction of the Y-slide temperature due to the compensation components was recorded.

No significant differences were observed between the slide temperatures under motion sequence A and B. The similar temperature profiles indicate that the ball screw drives (Z1, Z2, Z3) did not exhibit a significant influence on the Y-slide temperature. This was to be expected as few contact areas exist between the Z-slide and the Y-slide. The Y-slide excess temperatures in compensation configuration were found to be reduced between 36% and 74% at the end of each motion sequence for the first two test cases. During the measurement with shorter measurement cycles (test case 3, Fig. 6c), the slide excess temperatures were reduced by at least 38% and at most 82% in the compensation configuration. At around 5000 s a slight increase of the slide temperature rate can be seen. This indicates the end of the phase change process and, as a consequence, the abrupt change of the effective heat capacity.

The environment temperature exhibited an increase during all conducted experiments of approximately 2 °C. This is due to the limited heat transfer between the air within the machine enclosure and the air outside of the enclosure. Hence, the heat dissipation at the machine surfaces led to the observed temperature rise.

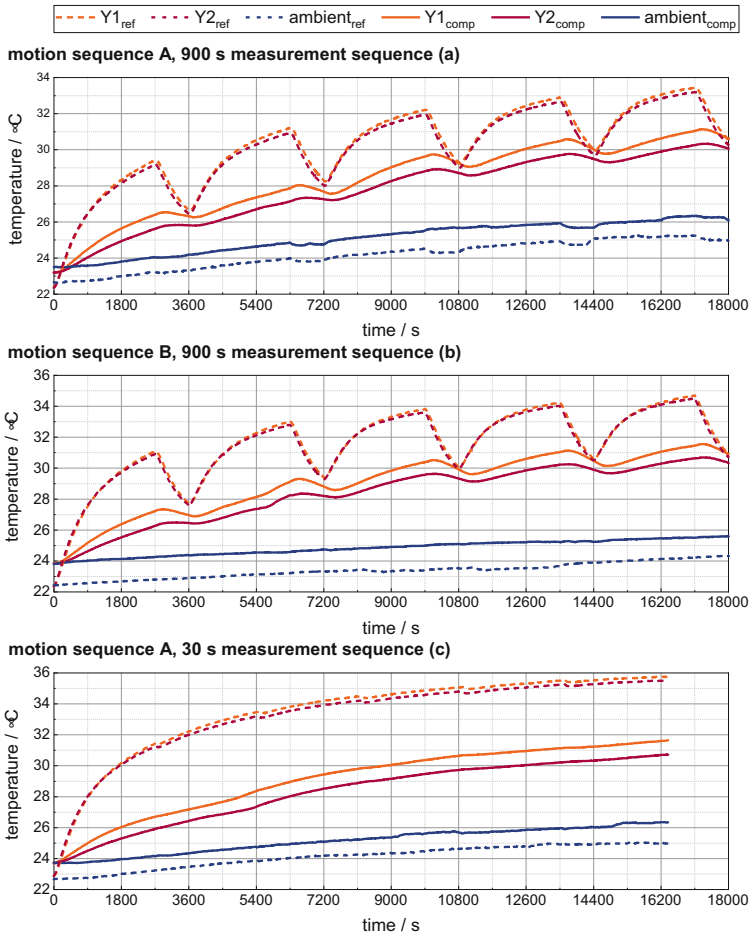


Fig. 6. Measured temperatures on Y-slide and ambient temperature in reference and compensation configuration for the three test cases.

The results of the displacement measurements shown in Fig. 7 demonstrate a significant difference of the Y-displacements in reference (Δy_{ref}) and compensation configuration (Δy_{comp}). By means of the compensation components the Y-error was reduced by around 20%. This reduction is caused by the lower temperatures of the Y-slide in the compensation configuration leading to decreased thermal expansion. In X-direction (Δx_{ref} , Δx_{comp}) and Z-direction (Δz_{ref} , Δz_{comp}) however, no favorable effect of the compensation components could be observed. On the contrary, the X-displacements were found to be slightly larger in the compensation configuration. A possible reason for this observation are the increased temperature differences between Y1 and Y2 that occurred in the compensation configuration. Unexpectedly, the Z-displacements were found to be in the same order for both motion profiles. Hence, the motion of the Z-drives

did not significantly contribute to the thermal error in Z-direction. The effect of the compensation components appeared to be unaltered between both motion scenarios.

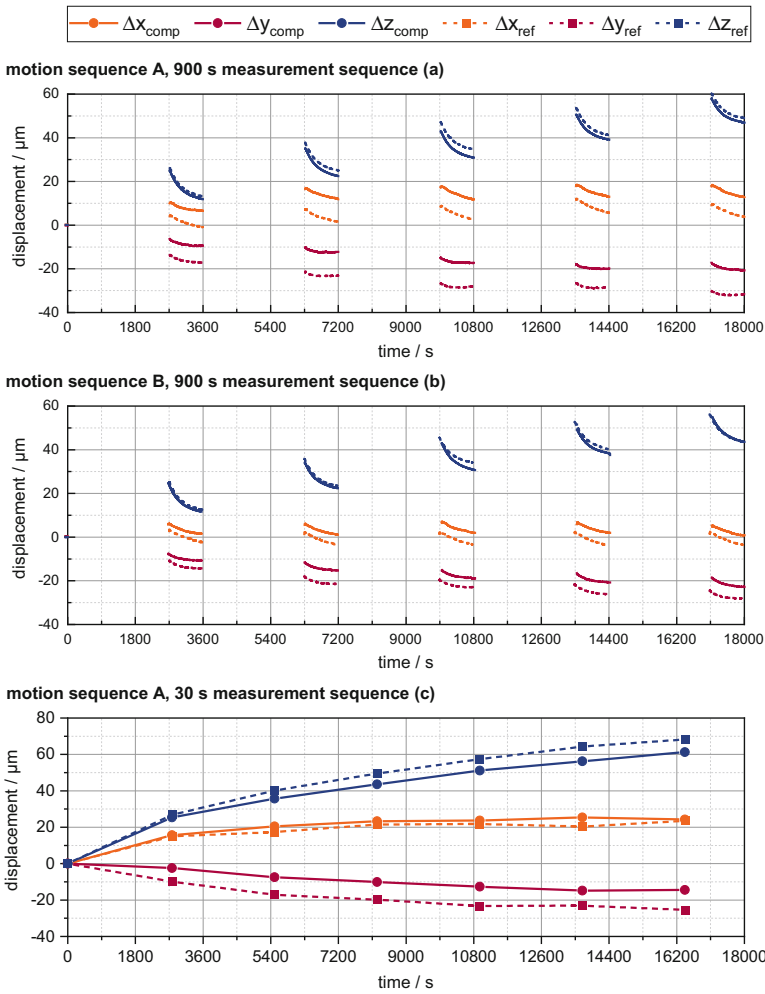


Fig. 7. Measured displacements in reference and compensation configuration for the three test cases.

5 Discussion

The results indicate a partial compensation of the thermally induced deformations due to the integrated compensation components. However, to evaluate the results, the accuracy of the used sensors must be considered. The Pt100 temperature sensors exhibit a measurement uncertainty of $\pm 0,1$ $^{\circ}\text{C}$. The measurement uncertainty of the precision probes

amounts to $\pm 0.7 \mu\text{m}$ [13]. The comparison of temperature and displacement between reference and compensation configuration demonstrates differences clearly exceeding these uncertainties. The measurement uncertainty is hence found to have neglectable influence on the main findings stated above.

In addition to the measurement uncertainties of the sensors, the influence of the ambient temperature needs to be evaluated. In absence of active cooling systems, the ambient temperature is highly relevant to the thermal behavior of the machine due to the convective heat transfer on the numerous machine surfaces. As the ambient temperature could not kept constant during the experiment, a direct influence on the temperature and displacement fields is assumed. Especially the high displacement values in Z-direction can be partially caused by changing environmental conditions as the machine columns exhibit higher absolute thermal displacements than the slides due to its greater spatial extent. However, the ambient temperature rise in each experiment amounted to values between 2.5 K and 3.0 K for motion sequence A and between 1.6 K and 1.9 K for motion sequence B. The uncertainties of the environmental conditions were hence found to be in a comparable order that does not affect the interpretation of the temperature and displacement comparison. Future investigations should further examine the effect of altering environmental conditions on the thermally induced displacement fields of the machine.

6 Summary

A passive compensation method based on the use of LHS and heat pipes was presented. The underlying approach aims for an increased thermal stability during the phase change of the corresponding PCM and an enhanced convective heat transport between the machine and the ambient air through heat pipe heat sink assemblies. To evaluate the impact of such components on the thermally induced displacements of a machine tool, investigations were conducted on an experimental machine. Compensation components were fabricated and attached to the machine to alter the heat flow between two linear motors and the adjacent slide structure. The machine was exposed to motion in two directions and thermally loaded by means of the linear direct and ball screw drives heat losses. Temperature and displacement measurements were conducted in the reference configuration of the machine as well as in compensation configuration with integrated compensation components.

The measured temperatures indicate a reduced heat input into the slide structure under load. The slide temperature rise was decreased by the order of 50%. The displacements in compensation configuration were found to be around 20% lower in Y-direction. It can be concluded that it is possible to partially compensate for thermal errors in machine tools using the proposed compensation approach. The passive compensation method hence can contribute to an improved overall thermal machine behavior and energy efficiency as the presented compensation components operate without additional power input. The experimentally obtained data can further be used to improve the thermoelastic simulation of the examined machine tool.

References

1. Mayr, J., et al.: Thermal issues in machine tools. *CIRP Ann. Manuf. Technol.* **61**, 771–791 (2012)
2. Brecher, C., Bäumlner, S., Jasper, D., Triebs, J.: Energy efficient cooling systems for machine tools. In: Dornfeld, D., Linke, B. (eds.) *Leveraging Technology for a Sustainable World*, pp. 239–244. Springer, Berlin, Heidelberg (2012). https://doi.org/10.1007/978-3-642-29069-5_41
3. Ohsenbrügge, C., Marth, W., y de Sosa, I.N., Drossel, W.-G., Voigt, A.: Reduced material model for closed cell metal foam infiltrated with phase change material based on high resolution numerical studies. *Appl. Therm. Eng.* **94**, 505–512 (2016)
4. Voigt, I., Winkler, S., Werner, R., Bucht, A., Drossel, W.-G.: Thermal error compensation on linear direct drive based on latent heat storage. In: *Proceedings of the Conference on Thermal Issues in Machine Tools, Dresden (2018)*
5. Voigt, I., de Sosa, I.N., Wermke, B., Bucht, A., Drossel, W.-G.: Increased thermal inertia of ball screws by using phase change materials. *Appl. Therm. Eng.* **155**, 297–304 (2019)
6. Voigt, I., Lütke, N., Thüsing, K., Winkler, M., Drossel, W.-G.: Development and examination of an internally switchable thermosiphon. *Energies* **15**(11), 3891 (2022)
7. Voigt, I., Drossel, W.-G.: Experimental investigation of heat pipe performance under translational acceleration. *Heat Mass Transf.* **58**(2), 209–219 (2021). <https://doi.org/10.1007/s00231-021-03106-w>
8. Möhring, H.-C., Brecher, C., Abele, E., Fleischer, J., Bleicher, F.: Materials in machine tool structures. *CIRP Ann. Manuf. Technol.* **64**, 725–748 (2015)
9. El-Nasr, A., El-Haggar, S.: Effective thermal conductivity of heat pipes. *Heat Mass Transf.* **32**, 97–101 (1996)
10. Peukert, C., et al.: Efficient FE-modelling of the thermo-elastic behaviour of a machine tool slide in lightweight design. In: *Proceedings of the Conference on Thermal Issues in Machine Tools*, pp. 61–71. Dresden (2018)
11. Ihlenfeldt, S., Müller, J., Merx, M., Peukert, C.: A novel concept for highly dynamic over-actuated lightweight machine tools. In: Yan, X., Bradley, D., Moore, P. (eds.) *Reinventing Mechatronics: Proceedings of Mechatronics 2018*, pp. 210–216. University of Strathclyde, Glasgow (2018)
12. Ihlenfeldt, S., Müller, J., Merx, M., Kraft, M., Peukert, C.: Simplified manufacturing of machine tools utilising mechatronic solutions on the example of the experimental machine MAX. In: Yan, X.-T., Bradley, D., Russell, D., Moore, P. (eds.) *Reinventing Mechatronics*, pp. 145–162. Springer, Cham (2020). https://doi.org/10.1007/978-3-030-29131-0_10
13. HAHN+KOLB Homepage. https://media.witglobal.net/stmedia/hahnkolb/documents/LANG_de/HK-39662321.pdf. Accessed 08 Sept 2022. Testo Homepage, <https://static-int.testo.com/media/1b/02/51ccb8bd5f9c/saveris-PROF-Bedienungsanleitung.pdf>. Accessed 08 Sept 2022

Open Access This chapter is licensed under the terms of the Creative Commons Attribution 4.0 International License (<http://creativecommons.org/licenses/by/4.0/>), which permits use, sharing, adaptation, distribution and reproduction in any medium or format, as long as you give appropriate credit to the original author(s) and the source, provide a link to the Creative Commons license and indicate if changes were made.

The images or other third party material in this chapter are included in the chapter's Creative Commons license, unless indicated otherwise in a credit line to the material. If material is not included in the chapter's Creative Commons license and your intended use is not permitted by statutory regulation or exceeds the permitted use, you will need to obtain permission directly from the copyright holder.





Determination of the Thermal Properties of Pre-stressed Fiber-Reinforced Polymer Concrete

Michelle Engert^(✉), Kim Torben Werkle, and Hans-Christian Möhring

Institute for Machine Tools, University of Stuttgart, Holzgartenstr. 17, 70174 Stuttgart, Germany
michelle.engert@ifw.uni-stuttgart.com

Abstract. With its low thermal conductivity and high thermal capacity, polymer concrete has excellent thermal properties that when used in machine tools ensure increased accuracy of the manufactured parts. Polymer concrete has been used successfully in machine tool construction for many years in the form of machine beds. The aforementioned thermal properties in combination with a low density, high damping and a lower primary energy requirement also make polymer concrete interesting for use as a structural component. However, the comparatively low tensile strength and creep tendency of the material pose a challenge here. One approach to increase the tensile strength of the material is the integration of prestressed carbon fibres into the material. In order to clarify the suitability of this hybrid material, its temperature behaviour is investigated in this paper. The focus is on the investigation of residual stresses that arise during heating, which result from the combination of the positive thermal expansion coefficient of polymer concrete with the negative thermal expansion coefficient of the carbon fibres. In addition, the flexural properties of pure polymer concrete and of pre-stressed fibre-reinforced polymer concrete are determined at different test temperatures within the scope of this paper. It is shown that the prestressing of fiber-reinforced polymer concrete leads to an improvement of the flexural strength and the stiffness of polymer concrete.

Keywords: Composite · Residual stress · Thermal effect

1 Introduction

Fluctuating ambient temperatures in production halls represent an obstacle to achieving the goal of capable and controlled manufacturing processes. Due to its low thermal conductivity and high thermal capacity, polymer concrete is a suitable material for machine tools to minimize the influence of these fluctuations. Polymer concrete, also known as mineral casting or reactive resin concrete, is a composite material consisting of inorganic mineral materials embedded in a matrix of resin (usually epoxy resin). The resin content is around 10–13%. In addition to its excellent thermal properties, the high damping properties of the material also contribute to the increased accuracy of the manufactured work pieces [1]. Other positive properties of the material include its low density [2] and its low carbon footprint, which is mainly due to the low primary energy requirement in the manufacturing process [1].

Polymer concrete has been used in machine beds since 1944 [1], but its high creep tendency and low tensile strength made it unsuitable for use in structural components until now. One approach to meet these challenges is the integration of fibers. In the past, the effect of the integration of different natural fibers [4, 5], recycled textile [6], as well as tire fibers [7], glass fibers, and carbon fibers has already been investigated. In particular, the integration of carbon fibers was found to have a positive effect, since they increase the compressive strength and better the failure behavior [8]. In order to further increase the positive influence of the integrated carbon fibers, a prestressing of the carbon fibers is tested. The principle of prestressing cement concrete by means of steel fibers or fiber-reinforced plastic tie rods is well known in the construction industry [3]. It is assumed that the prestressing of fibers cast into polymer concrete - as with cement concrete - introduces residual compressive stresses into the material and thus improves its mechanical properties. The determination of the flexural properties of the innovative prestressed fiber-reinforced polymer concrete at room temperature, as well as at an increased core temperature, is the subject of this paper. In addition, a comparison is made with pure polymer concrete and fiber-reinforced polymer concrete.

2 Material-Specific Structure of the Samples

The polymer concrete EPUMENT 130/3 manufactured by RAMPF Machine Systems is used for the investigation. This high-tech material is currently used for the production of machine frames in order to optimally withstand the geometrical position of the individual machine elements as well as the absorption of forces and moments under static, dynamic, thermal and acoustic loads. The manufactured test samples have the dimensions $50 \times 50 \times 500 \text{ mm}^3$. For statistical validation, three samples of each material are prepared and examined. For the fiber-reinforced samples, GRAFIL 34–700 carbon fibers from Mitsubishi Chemical Carbon Fiber and Composites were integrated. The fiber-reinforced samples are provided with the 24k fiber at 5 points on the sample (Fig. 1c). The prestressing force of the prestressed samples is $F_c = 1,800 \text{ N}$. The force is applied by means of specially developed prestressing mechanisms [9]. The determination of this force was done on the basis of the compressive strength f_v of the polymer concrete. The fibers are pre-impregnated with the epoxy resin, which is also the matrix component of the polymer concrete. In this way, complete infusion of the fibers can be ensured. Strain gauges (type: 6/120ZE LY41, manufacturer: HBM) are integrated into the test setup to monitor the internal stresses. To monitor the core temperature of the samples and to compensate the temperature of the strain gauges, additional encapsulated PT100 temperature sensors are integrated at the level of the strain gauges (see Fig. 1b). One strain gauge and one temperature sensor are placed on the lowest and one on the highest fiber level. The strain gauges are placed on the carbon fibers, the temperature sensors next to them (see Fig. 1b). The cables are led out at about half length of the sample.

All test samples are casted in aluminum molds, in which they cure for a period of 22 h according to the manufacturer's specifications before being stored for a period of four to six days. The curing process was recorded for all test samples and is shown as an example for a fiber-reinforced sample in Fig. 2. For a better overview, only the measured values of one strain gauge are shown. The average temperature difference was calculated

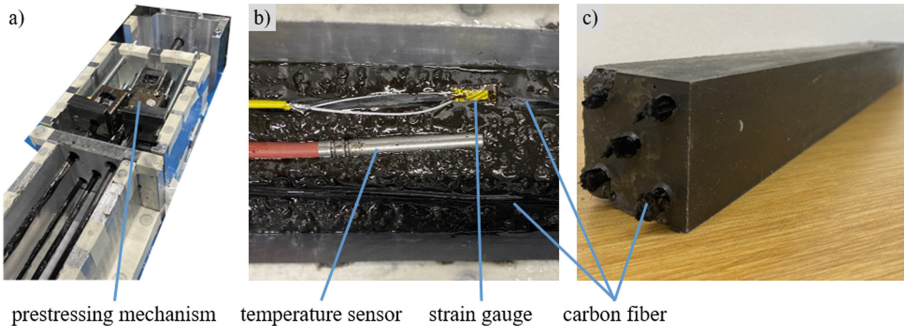


Fig. 1. a) Pretension of the carbon fibers; b) strain gauge and temperature sensor on and next to the carbon fibers; c) sample made out of prestressed fiber-reinforced polymer concrete.

from the measured values of the inserted temperature sensors and refers to the time $t = 0$ h.

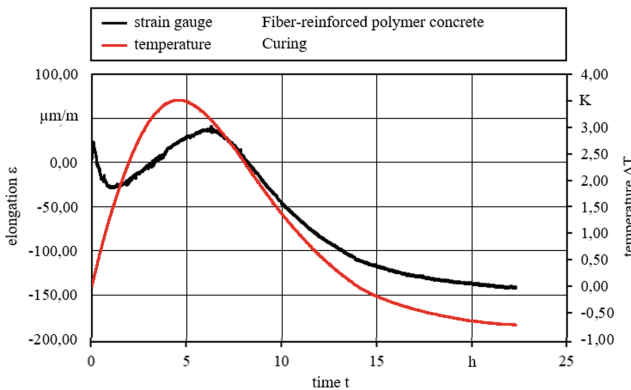


Fig. 2. Elongation and temperature during the curing process of fiber-reinforced polymer concrete

As shown in Fig. 2, the polymer concrete heats up by about $3.5\text{ }^{\circ}\text{C}$ in the first 5 h due to an exothermic reaction. This chemical process is well known and can be found in all polymer concrete samples without prestressing. In contrast, only a minimal increase of the core temperature by $0.1\text{ }^{\circ}\text{C}$ takes place in the prestressed samples (Fig. 3). This is due to the necessity to fix the molds on a machine table during the production of pre-stressed samples. During the production of the samples without prestressing, the molds were placed on a wooden base during curing.

During curing of the pre-stressed fiber-reinforced test samples, a significant increase in stress development occurs after a period of about 18.8 h. The exact cause of this increase in stress is currently the subject of further investigations. It is assumed that there might be a connection with the reaching of the gel point of the epoxy resin.

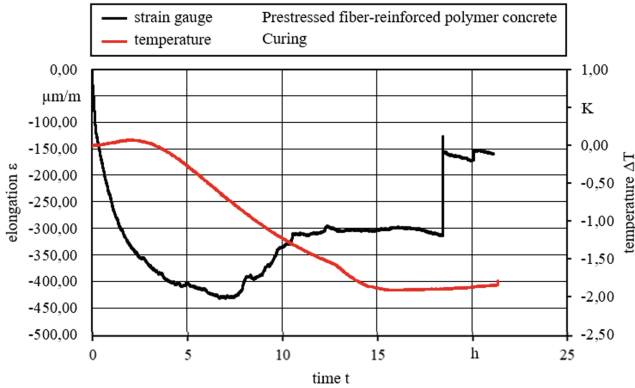


Fig. 3. Elongation and temperature during the curing process of prestressed fiber-reinforced polymer concrete

3 Behaviour Under Load at Different Sample Temperatures

The experimental setup is shown in Fig. 4. The sample is clamped between two 60 mm wide metal plates. The bending force is applied by a hydraulic cylinder and transmitted to the sample at a distance of 405 mm from the clamping via a load cell. The load cell is a KM26-10kN product from the manufacturer ME-Systeme. The deflection of the sample is measured by a dial gauge placed above the load cell. Two more dial gauges are used to monitor the position of the hydraulic cylinder and the clamping. The aim of the experimental setup is to imitate the static load condition of a machine arm in a single direction while milling. The fiber orientation of the sample was deliberately not modeled on the load paths of the applied force.

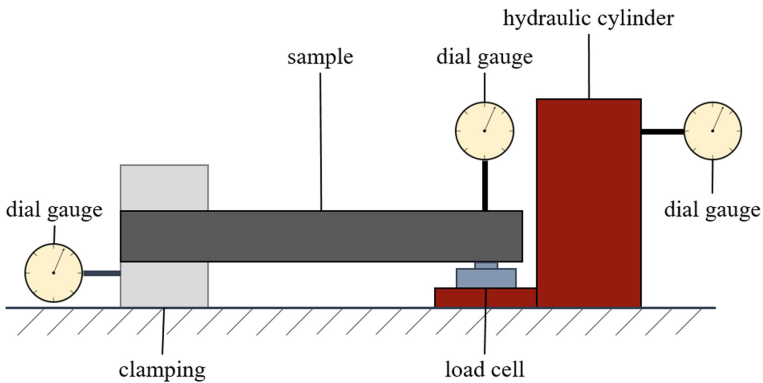


Fig. 4. Experimental setup

The samples are warmed up to a core temperature of 50 °C heat chamber. Further heating is not expedient for the given application of a machine arm. The development of temperature and stress during heating are shown, for example, for one sample per

material in Fig. 5. For a better overview, only the measured values of one strain gauge are shown. The average temperature was calculated from the two measured values of the inserted temperature sensors. In addition to the actual strains of the strain gauges, the theoretical strain ϵ of the pure polymer concrete is shown to validate the measurement methodology (cf. Formula 1).

$$\epsilon = \alpha \cdot \Delta T \tag{1}$$

The manufacturer specifies the coefficient of thermal expansion α of the polymer concrete used as $20 \cdot 10^{-6} \text{ K}^{-1}$ [10]. The temperature difference ΔT refers to the core temperature prevailing in the sample at time $t = 0 \text{ s}$.

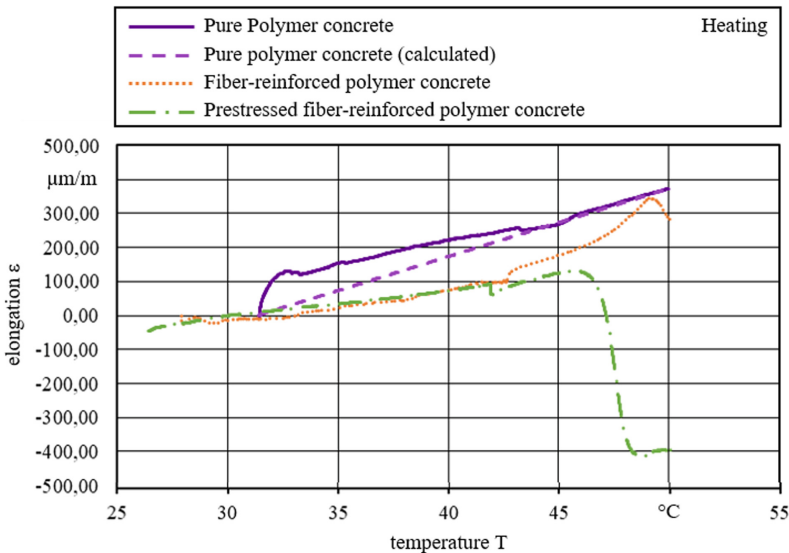


Fig. 5. Measured elongation during the heating of pure polymer concrete, fiber-reinforced polymer concrete and prestressed fiber-reinforced polymer concrete up to a core temperature of 50 °C, theoretically calculated thermal expansion of pure polymer concrete at the measured core temperature

The behavior of the strain gauges integrated in the pure polymer concrete during the heating of the sample is well in line with the current state of research [11]. As a result of the positive coefficient of thermal expansion of the material, strain occurs which, moreover, is close to the theoretically calculated values, especially in the range of higher temperatures.

The strain gauges integrated in the fiber-reinforced polymer concrete experience a lower strain. Here, too, the results can be reconciled with the statements of the current state of research [12] and justified by the negative coefficient of thermal expansion of the carbon fibers. However, since this is lower than that of the polymer concrete, expansion of the sample still occurs.

The prestressed samples initially experience expansion of similar value than the fiber-reinforced ones, but when the temperature reaches 46 °C, there is a sudden drop in strain. The reasons for this are as yet unknown and are currently the subject of further investigation.

The samples are subjected to the bending tests immediately after heating. Before the bending test the core temperature decreases insignificantly by around 1.5 °C. The test results of the bending tests are shown in Fig. 6.

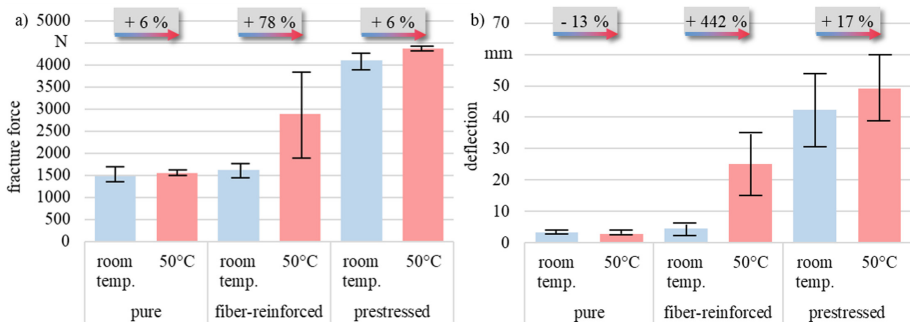


Fig. 6. Fracture force (a) and total deflection at breaking point (b) of the samples made out of pure polymer concrete, fiber-reinforced polymer concrete and prestressed fiber-reinforced polymer concrete at room temperature and after heating up to a core temperature of 50 °C

The prestressing of the polymer concrete by means of the carbon fibers leads to a significant increase in the breaking strength as well as to a significant increase in the deflection. Compared to the samples made of pure polymer concrete, the breaking load is increased by almost 180%.

For all materials considered, heating of the samples leads to an increase in the average breaking load. However, due to the high scatter of the results, this appears negligible for pure polymer concrete. The largest increase in the mean breaking load is found in the samples made of fiber-reinforced polymer concrete. There is a clear approximation to the mean breaking load of the prestressed samples, which is also reflected in the deflection. The results indicate the formation of residual compressive stresses in the sample during heating due to the unsigned coefficients of thermal expansion of the polymer concrete and the carbon fibers.

In order to assess the suitability of the materials for use in machine tool design, the stiffness of the materials is determined. For a better comparison of the materials, this is determined at the working point $F = 1320$ N (Fig. 7). The selected working point is based on 90% of the average breaking force of pure polymer concrete at room temperature.

Among the samples tested at room temperature, the prestressed fiber-reinforced polymer concrete exhibits the highest stiffness at the selected working point this is due to the applied residual compressive stresses. This suggests a possible use of the material for structural components in machine tool manufacturing. However, it is important to protect the components from strong heating due to thermal radiation in order to avoid a reduction of the stiffness as shown in Fig. 7.

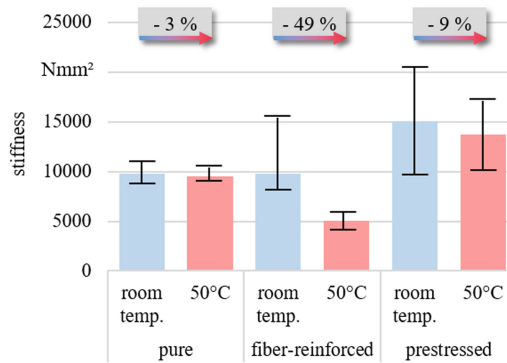


Fig. 7. Bending stiffness of pure polymer concrete, fiber-reinforced polymer concrete and prestressed fiber-reinforced polymer concrete at room temperature and after heating up to a core temperature of 50 °C at a force of $F = 1320$ N

4 Conclusion

In this research project, the flexural properties of polymer concrete, fiber-reinforced polymer concrete and prestressed fiber-reinforced polymer concrete were compared at room temperature and after heating up to 50 °C core temperature. In addition, integrated measurement technology was used to determine the strain during curing and during heating.

The flexural tests showed that the principle of prestressing, familiar from prestressed concrete, also leads to an improvement in the mechanical properties of polymer concrete. Heating prior to the bending tests led to at least a slight increase in the average breaking strength for all materials. The greatest increase in breaking strength was achieved by the fiber-reinforced polymer concrete. This indicates the development of residual compressive stresses in the sample during heating. This assumption is supported by the lower elongation during heating of the samples compared to the pure polymer concrete. Apart from that it was shown that the integration of measurement technology in polymer concrete delivers reliable results.

It can be concluded that the innovative material prestressed fiber-reinforced polymer concrete seems to have a great future for usage in machine tools as it was shown that the mechanical properties have significantly increased in comparison to pure polymer concrete.

Acknowledgement. The authors would like to thank the German Research Foundation (DFG) for funding this work as part of the project “Prestressed fiber-reinforced mineral cast” (MO2091/11–1).

References

1. Möhring, H.-C., Brecher, C., Abele, E., Fleischer, J., Bleicher, F.: Materials in machine tool structures. In: CIRP Annals – Manufacturing Technology, vol. 64, pp. 725–748 (2015)

2. Möhring, H.-C., Gessler, W., König, A., Nguyen, L.T., Nguyen, Q.P.: Modular intelligent fixture system for flexible clamping of large parts. *J. Mach. Eng.* **4**, 29–39 (2017)
3. Heo, S., Shin, S., Lee, C.: Flexural behaviour of concrete beams internally prestressed with unbonded carbon-fiber-reinforced polymer tendons. *J. Compos. Constr.* **17**, 167–175 (2013)
4. Barbuta, M., Harja, M.: Properties of fiber reinforced polymer concrete. *Bull. Polytech. Inst. Jassy, Construct. Archit. Sect.* **54**, 13 (2008)
5. Reis, J.M.L.: Fracture and flexural characterization of natural fiber-reinforced polymer concrete. *Constr. Build. Mater.* **20**, 673–678 (2006)
6. Reis, J.M.L.: Effect of textile waste on the mechanical properties of polymer concrete. *Mater. Res.* **12**, 63–67 (2009)
7. Martínez-Cruz, E., Martínez-Barrera, G., Martínez-López, M.: Polymer concrete reinforced with recycled-tire fibers: mechanical properties. *Mater. Sci. Eng.* **45**, 1–4 (2013)
8. Reis, J.M.L.: Mechanical characterization of fiber reinforced polymer concrete. *Mater. Res.* **8**, 357–360 (2005)
9. Engert, M., Werkle, K., Wegner, R., Möhring, H.-C.: Mechanisms for the production of prestressed fiber-reinforced mineral cast. In: *Production at the Leading Edge of Technology - Proceedings of the 12th Congress of the German Academic Association for Production Technology (WGP)*, Stuttgart (2022)
10. RAMPF Machine Systems GmbH & Co. KG: EPUMENT130/3 A3 technical data sheet (2017)
11. Möhring, H.-C., Wiederkehr, P., Baumann, J., König, A., Spieker, C., Müller, M.: Intelligent hybrid material slide component for machine tools. *J. Mach. Eng.* **17**(1), 17–30 (2017)
12. Ribeiro, M.C.S., Reis, J.M.L., Ferreira, A.J.M., Marques, A.T.: Thermal expansion of epoxy and polyester polymer mortars – plain mortars and fiber-reinforced mortars. *Polym. Testing* **22**, 849–857 (2003)

Open Access This chapter is licensed under the terms of the Creative Commons Attribution 4.0 International License (<http://creativecommons.org/licenses/by/4.0/>), which permits use, sharing, adaptation, distribution and reproduction in any medium or format, as long as you give appropriate credit to the original author(s) and the source, provide a link to the Creative Commons license and indicate if changes were made.

The images or other third party material in this chapter are included in the chapter's Creative Commons license, unless indicated otherwise in a credit line to the material. If material is not included in the chapter's Creative Commons license and your intended use is not permitted by statutory regulation or exceeds the permitted use, you will need to obtain permission directly from the copyright holder.



Tools and Processes



Simulation of cBN Grain Wear During Single Grain Engagement Considering Cleavage Planes

Marc Bredthauer^(✉), Sebastian Barth, Patrick Mattfeld, and Thomas Bergs

Laboratory for Machine Tools and Production Engineering (WZL) of RWTH Aachen University,
Aachen, Germany

M.bredthauer@wzl.rwth-aachen.de

Abstract. A large part of the energy introduced during grinding is converted into heat. As not all the heat can be dissipated by the cooling lubricant, thermally induced displacements in machine components occur. These displacements have a negative influence on the component quality. Since the grinding wheel topography changes during the grinding process due to wear, the wear mechanisms of grain splintering, grain breakage as well as abrasion were identified and quantified. In addition, their effect on heat generation was investigated. To predict the wear mechanisms, a Finite Element (FE) simulation model was developed that determines the grain shape change considering the cleavage planes in the grain. Three-dimensional real cBN grain geometries were used for the simulation of a single grain engagement in the workpiece of the 100Cr6 steel. In the presented model, the orientation of the cleavage planes is varied and their influence on the wear mechanisms as well as the resulting forces is investigated. In addition, empirical tests were conducted in order to adjust the model. The simulation showed that a cleavage plane variation resulted in stronger crack propagation when the cleavage plane was oriented away from the workpiece and when the distance of the cleavage plane from the point of application of the load was smaller.

Keywords: cBN wear mechanisms · Grinding · FE simulation

1 Introduction

During grinding process a large part of the introduced energy is converted into heat [1]. Since not all the heat can dissipate into the cooling lubricant, a high thermal load on the surface area of the workpiece can thermally damage the material structure [2] and therefore reduce component functionality. However, the topography of grinding wheels changes over the tool life due to wear. This leads to increasing heat fluxes due to higher friction [3]. Additionally, contact and cooling lubricant conditions in the contact zone between the grinding wheel and the workpiece are changed [4]. In order to analyze the wear behavior of grinding wheel topographies it requires to quantitatively describe grinding wheel wear. As yet, it is unknown whether the wear mechanisms change depending on the cleavage plane in the crystal lattice of the cBN grain. To develop a prediction method for cBN grinding wheel wear it is necessary to first develop

a wear prediction method for an isolated cBN grain, in order to ensure clear cause-effect relationships between the thermo-mechanical load and the wear mechanisms. Currently there is no validated FE model taking into account the wear of cBN grains with real grain geometries in the single-grain scratching process depending on the cleavage planes of the cBN crystal. By simulating including cleavage planes, it is possible for the first time to predict the wear behavior of cBN crystals holistically. By adjusting the properties of the cBN crystals accordingly, the production of the cBN abrasive grains can then also be better understood and adapted to the corresponding load situations.

Thus, the aim of this work is to develop and validate a three-dimensional FE model for the wear of cBN grains during single grain engagement as a function of the cleavage planes. To validate the numerical model, empirical data from single-grain scribing studies are used.

2 State of the Art

The first works on the wear behavior of grinding wheels by MALKIN AND COOK [5] showed that there is a direct relationship between grinding force and grain wear due to the reduction in the grain protrusion in turn due to attrition. The thermo-mechanical load in the grinding process increased because of grinding wheel wear. The change in wear mechanisms over the service life of an electroplated cBN grinding wheel was investigated by SHI AND MALKIN [3]. For this purpose, the radial wear of the grinding wheel was determined quantitatively. They observed high initial wear that degressively decreased to a stationary wear condition. The initial wear was mainly caused by the breakout of the highest and weakly fixed grains in the bond. The stationary wear was dominated by grain fractures. MALKIN AND SHI [6] showed that for surface grinding and internal cylindrical grinding of 100Cr6 with electroplated cBN grinding wheels stationary grinding wheel wear was characterized by grain splintering. The attrition wear mechanism had only a minor influence on the tool life of the grinding wheel. UPADHYAYA AND MALKIN [4] also demonstrated experimentally that the wear of electroplated grinding wheels is characterized by the mechanisms of grain splintering, grain breakage and abrasion. UPADHYAYA AND MALKIN [4] showed that the crystal structure has an influence on the wear behavior of electroplated cBN grinding wheels to evaluate the influence of the crystal properties of cBN grains and the bond thickness on the grinding wheel wear. It became apparent that abrasion flattened the grain and increased the active grain density.

BERGS ET AL. [7] investigated the cBN fracture behavior by means of FEM simulations of individual cBN grains. They identified the wear mechanisms as a function of the mechanical stress on the grain as well as the orientation and shape of the grain. The investigation identified different wear mechanisms for cBN grains depending on the grain geometry. YIMING ET AL. [8] developed a FE simulation model for the wear of cBN in the single-grain scratching process. In the wear model used for cBN, crack initiation is detected according to the RANKINE criterion. The stress-strain behavior during the failure process was modeled using the critical strain energy release rate G_c according to Eq. (1). [8]

$$G_c = \frac{K_c^2}{E} \quad (1)$$

As a result of the simulations carried out with this model, the maximum tensile stresses at the rake faces of the cutting edges leading to grain wear were obtained. In the resulting wear behavior an alternation of blunting phenomena and self-sharpening effects were recorded. WANG ET AL. [9] developed a two-dimensional FE model to simulate cBN wear during grinding of Inconel 718. A hexagonal geometry was assumed for the grain. Using their wear model both macro- and microsplintering were represented in the simulation. Macrosplintering occurred mainly on the rake face of the grain as a consequence of strong crack propagation. The crack propagation necessary for macrosplintering was caused by high tensile loads. RAO ET AL. [10] developed a three-dimensional wear model for FEM simulations of pcBN wear. This model is based on the theory of cohesive elements. The simulation results showed that a stress concentration appears around the grain–filler bonding interface region and the grain vertex region when the grinding load is imposed. The stress-strain law based wear model developed by RAO ET AL. was also used by HUANG ET AL. [11] for the FE simulation of pcBN wear in the grinding process. In this model, a cuboidal grain geometry was used, which was divided into several VORONOI cells to represent the cBN crystals. They investigated the maximum infeed of the grain in order to achieve minimum wear and use the self-sharpening effect. In preliminary work for the paper presented here, BREDTHAUER ET AL. [12] developed a three-dimensional FE model to simulate the wear behavior of cBN for single-grain scribing of 100Cr6 steel. Real grain geometries were transferred to the simulation model. As a result of the simulations, grain wear due to abrasion, micro-splintering and macrosplintering were simulated. There were deviations in the expression of these wear phenomena compared to the results of experimental investigations. The deviations were, besides others, justified by the missing implementation of grid planes in the FEM model.

Numerous experimental as well as simulative studies have already been carried out on the wear behavior of grinding wheels. In most of the studies however, idealized grain models were used or the models were simplified. In addition, the simulations did not consider cleavage planes in the crystal structure of cBN and thus anisotropic behavior. Nevertheless, since cleavage planes have a significant influence on the wear behavior of cBN grains, the aim of this work is to develop a three-dimensional FE simulation model that represents the wear of cBN grains as a function of the cleavage planes.

3 Experimental Investigations

The single-grain scratch tests were carried out on the PROFIMAT MT 608 surface grinding machine from BLOHM JUNG. The experimental setup is shown in Fig. 1. The test setup installed on this machine comprised a scratch wheel on the tool side to which a screw-in sleeve was connected by means of a thread. The screw-in sleeve contained a grain holder onto which a steel base body was glued. The abrasive grain was electroplated onto the steel body. The abrasive grains used were cBN type ABN 900 grains from ELEMENT SIX for which an average grain diameter of $d_g = 251 \mu\text{m}$ was given by the manufacturer. The grain shape selected in this simulation was chosen at random. The grain size and shape is also used in the coating of electroplated cBN grinding wheels and is therefore representative for other grains of the ABN 900 specification. On the

workpiece side a cuboid workpiece made of hardened 100Cr6 steel with a hardness of 60 HRC was used. This workpiece was mounted on a piezoelectric dynamometer from KISTLER company. A measuring chain with measuring computer was connected to the force measuring platform so that the normal force F_n and the tangential force F_t were continuously recorded during the test (sampling rate 1 MHz). The test kinematics used was a circular path-bound single-grain engagement. For this purpose, a workpiece speed of $v_w = 0$ mm/min in tangential direction was selected and a sufficiently high axial grinding wheel speed $v_{s,axial}$ was set to produce a single engagement of the abrasive grain in the workpiece. The grain circle path radius was $r_s = 190$ mm, $a_e = 20 \mu\text{m}$ was selected for the infeed, and the grinding wheel peripheral speed at the grain was set to $v_s = 20$ m/s.

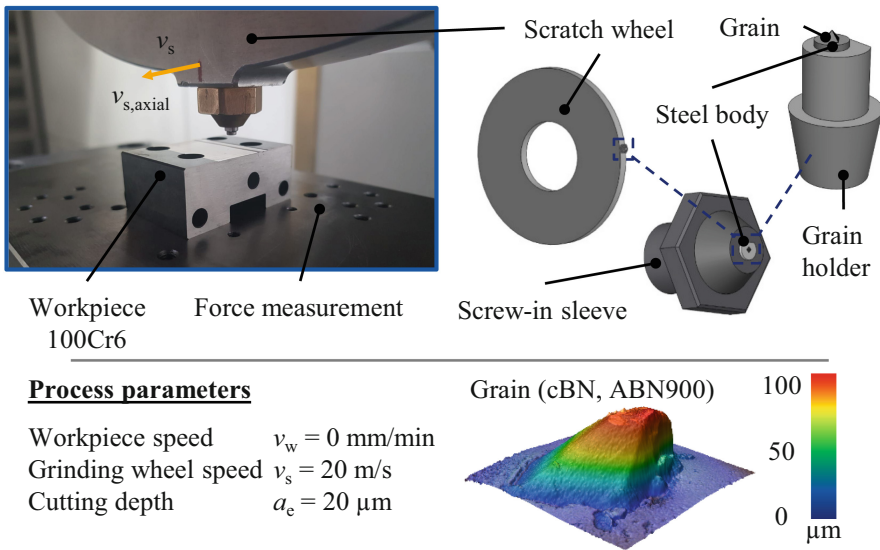


Fig. 1. Experimental setup, materials and process parameters

For the evaluation of the wear condition of the abrasive grains, a negative impression of the abrasive grain used was made before and after each validation test. The ACCUTRANS AB impression material from COLTENE was used for this purpose. These negative impressions were optically measured with the aid of the confocal laser scanning microscope VK-X-150 from KEYENCE and converted into three-dimensional grain topographies. Subsequently, the grain height difference Δh_g and the grain wear volume ΔV_g were determined by comparing the grain height h_g and the grain volume V_g in the initial and worn condition, as shown in Fig. 2.

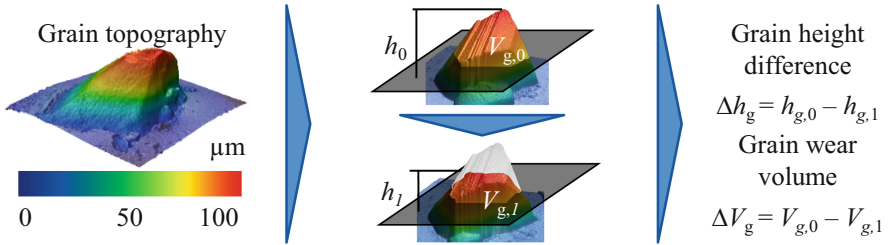


Fig. 2. Evaluation methodology of the grain wear

4 Development of a Simulation Model for the Wear Mechanisms of cBN Grains Considering the Cleavage Planes

4.1 Model Setup

Geometry and Discretization

The simulation model was built according to the boundary conditions of the single-grain scribing studies presented previously. The simulation model shown in Fig. 3 represents the contact between cBN grain and workpiece.

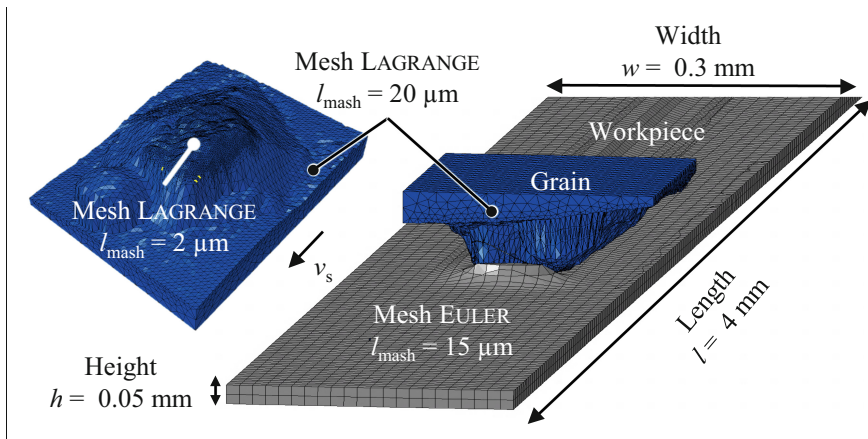


Fig. 3. Structure of the simulation model

Real grain geometries were used for the cBN grain. The grain topographies were converted into three-dimensional CAD files and imported into ABAQUS as deformable solids. The cBN grain was modeled as a LAGRANGE body with a mesh density of $l_{\text{Mesh}} = 2 \mu\text{m}$ at the grain-workpiece contact. In the non-contact area of the grain a more coarse mesh with $l_{\text{Mesh}} = 20 \mu\text{m}$ was chosen. The advantage of the LAGRANGE discretization approach was that the wear mechanisms were represented at high resolution by the failure of concrete elements.

For the workpiece a cuboid geometry was used which was created directly in ABAQUS. The workpiece had a length of $l = 4 \text{ mm}$, a width of $w = 0.3 \text{ mm}$ and a

height of $h = 0.05$ mm. The workpiece was modeled as an EULER body with a mesh length of $l_{\text{Mesh}} = 15 \mu\text{m}$. In the EULER approach, the FE mesh is stationary and the material can move within the mesh relative to it.

Kinematic of the Simulation Model

The kinematics of the simulation are shown in Fig. 4. They were identical to the real investigations. It was necessary to ensure compliance with the grinding wheel circumferential speed v_s , the grain circle path radius r_s and the cutting depth a_e from the validation tests. First, an auxiliary coordinate system was placed at a height of $r_s = 190$ mm above the cBN grain tip in the center of the contact arc, i.e. 189.98 mm above the global coordinate system. Thus, the axis of rotation of the cBN grain was defined. As the initial position of the cBN grain for the simulation of a single grain engagement, the cBN grain was rotated by $\alpha_R = 0.9^\circ$ around the center of rotation. Consequently, (to avoid) an initial contact of the cBN grain with the workpiece in the first time step was avoided. In total, a rotation of $\alpha_R = 1.66^\circ$ which corresponds to the contact arc length of cBN grain with the workpiece was simulated. For the rotational motion of the center of rotation, a velocity boundary condition was created with reference to the reference coordinate system. The angular velocity about the z' axis was defined to be $\omega = 105.263$ rad/s, which resulted in an orbital velocity at the grain tip of $v_s = 20$ m/s.

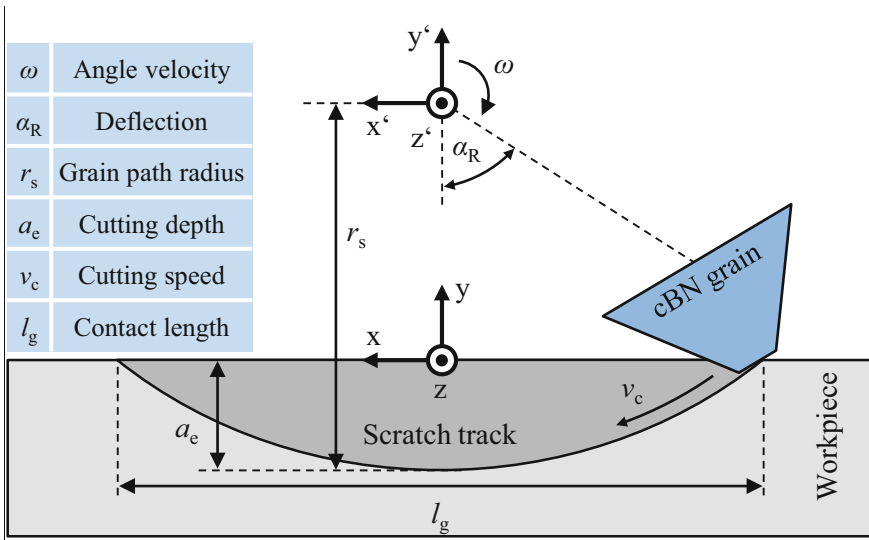


Fig. 4. Kinematic modelling of the engagement between the cBN grain and the workpiece

Material Model for 100Cr6 Workpiece

The material model of the workpiece was designed for applying a load to the cBN grain during the single-grain scratching process as realistic as possible. Since the validation tests were carried out with a workpiece made of hardened 100Cr6 steel (60 HRC), a material model had to be implemented for this material. The material parameters for 100Cr6 are given in Table 1 and are standard values extracted from ABAQUS.

Table 1. Material parameters for 100Cr6

Material parameter	Value	Unit
Young's modulus E	200,000	MPa
Poisson's ratio ν	0.3	–
Density ρ	$7.85 \text{ e}-9$	t/mm ³
Thermal conductivity λ	35.5	mW/(mmK)
Specific heat capacity c	$7.78 \text{ e}8$	mJ/(tK)
Melting temperature T_m	1,673.15	K

In addition to these physical material parameters, a constitutive material law was implemented to realistically simulate the plastic material behavior. For such processes, the empirical material model according to JOHNSON and COOK [13] is used in many research works. For this reason, the use of the constitutive material law according to JOHNSON and COOK was specified for the workpiece after Eq. 2,

$$\sigma = (A + B\varepsilon^n) \cdot (1 + C \cdot \ln(\frac{\dot{\varepsilon}}{\varepsilon_0})) \cdot (1 - [\frac{T - T_r}{T_m - T_r}]^m) \quad (2)$$

where ε represents the equivalent plastic strain; $\dot{\varepsilon}$ and ε_0 are the equivalent plastic strain rate and reference strain rate respectively; T_{melt} and T_r are melting temperature and transition temperature respectively. The empirical constants are as follows: A is the yield stress, B is the strain hardening constant, C is the strengthening coefficient of strain rate, n is the work-hardening exponent and m is the thermal-softening exponent. The parameters A , B , C , n and m used in this study are listed in Table 2. The parameters were selected based on those determined by BILICI [14] and MIKHAYLOV [15]. These were compared in the simulation and adjusted with the help of the validation by the empirical investigations. The parameters A , B , C and n were varied systematically and the optimum was chosen within the variations. The parameter C was adjusted the most in these investigations compared to MIKHAYLOV, because the parameter influences the strain rates, which are particularly high during grinding, the most.

Table 2. JOHNSON and COOK parameter 100Cr6 [BILI07], [MIKH15]

Material parameter	Chosen	BILICI	MIKHAYLOV
A	280 MPa	2,033 MPa	280 MPa
B	1,215 MPa	895 MPa	1,215 MPa
C	0.01	0.0095	0.031
m	1.0	1.03	1.0
n	0.4	0.3	0.43

The process forces with the material parameters according to MIKHAYLKOV were more similar to the process forces from the validation test. The material parameters for the JOHNSON and COOK model in further verification and comparison with the simulations were set to the parameters selected in Table 2 to represent the actual physical relationships as accurately as possible.

In addition to the material law, the friction between cBN grain and workpiece also has an influence on the process forces. In the simulations discussed previously, a COULOMB friction model was assumed according to Eq. 3

$$\tau_f = \begin{cases} \mu \cdot \sigma_n, \tau_f < \tau_{\max} \\ \tau_{\max}, \tau_f \geq \tau_{\max} \end{cases} \quad (3)$$

with a friction coefficient of $\mu = 0.4$, where τ is frictional stress, σ_n is normal stress and τ_{\max} is maximum frictional stress according to the VON- MISES equivalent stress. HABAK ET AL. [16] investigated the contact between cBN and hardened 100Cr6 steel. For a material hardness of 45 HRC and a cutting speed of $v_c = 2.5$ m/s, a friction coefficient of $\mu = 0.2$ was determined. Moreover, the effect that increasing the hardness and increasing the cutting speed v_c lead to a decrease in the coefficient of friction μ was found. Therefore, the simulation was repeated with friction coefficients from $\mu = 0.2$ to $\mu = 0.05$. Lowering the coefficient of friction μ resulted in an approximation of the ratio of the normal force F_n to the tangential force F_t from the validation experiments. Since further optimization of the model was necessary by adjusting the material parameters, a decision was made to use $\mu = 0.1$ as the friction coefficient for all further simulations, because for $\mu = 0.05$ the workpiece temperature was too low.

In addition to the constitutive material law, a damage model was implemented in the workpiece material model to allow for material failure. Hence, a more realistic material behavior was simulated. For this purpose, the damage model according to JOHNSON and COOK was chosen, which is given in Eq. 4 [18].

$$\varepsilon^f = \left[d_1 + d_2 \cdot \exp\left(d_3 \cdot \frac{\sigma_m}{\sigma_{v,M}}\right) \right] \cdot \left[1 + d_4 \cdot \ln\left(\frac{\dot{\varepsilon}}{\dot{\varepsilon}_0}\right) \right] \cdot \left[1 + d_5 \frac{T - T_r}{T_m - T_r} \right] \quad (4)$$

where ε^f is the equivalent elongation at break, $\sigma_{v,M}$ is the VON- MISES equivalent stress and $d_1 - d_5$ are material constants. The material constants of the JOHNSON and COOK damage model for 100Cr6 were taken from the work of RASIM [17].

Material Model for cBN Grain

Similarly to the material model for 100Cr6, in the material modeling of the cBN grain, physical properties, a damage model, as well as cleavage planes were implemented to represent the wear behavior of cBN grains. The physical parameters of the cBN specification used are given in Table 3 after MEI ET AL. [8]. The selection of the parameters was made on the basis of previous experience at the WZL of RWTH Aachen of the wear simulation of the identical grain specification in the work of Bergs et al. [7]. Therefore, no optimizations of the material parameters were carried out initially.

Furthermore, the Concrete Damaged Plasticity (CDP) damage model for quasi-brittle materials was implemented. In this damage model, the material behavior under tensile and compressive loading was considered separately. The basic parameters used in this

Table 3. Material parameters cBN grain after MEI ET AL. [8]

Material parameter	Value	Unit
Young's modulus E	710,000	MPa
Poisson's ratio ν	0.15	–
Density ρ	3.4 e-9	t/mm ³
Thermal conductivity λ	80.0	mW/(mmK)
Specific heat capacity c	4.3 e8	mJ/(tK)

work for the CDP model are given in Table 4. The dilatancy angle ψ gives the ratio of the plastic volume change rate to the plastic shear deformation rate [18]. Effectively, the dilatancy angle ψ influences the brittleness or ductility of the material behavior and was chosen to be $\psi = 10^\circ$ in order to achieve the brittle material behavior from the empirical investigations [19]. For the other basic parameters, the respective standard values were selected [20].

Table 4. CDP parameters cBN grain

Basic parameter	Formula character	Value
Dilatancy angle	ψ	10°
Eccentricity	ε_{CDP}	0.1
Uniaxial and biaxial compressive yield strength ratio	f_{b0}/f_{c0}	1.16
Ratio of second stress invariants under tension and compression	K_{CDP}	0.6667
Viscosity parameter	μ_{CDP}	0

Furthermore, a separate definition of the material behavior under tension and compression had to be made in the CDP model. Therefore, yield stress values and the corresponding inelastic strain after exceeding the linear elastic range had to be specified in each case. The tensile strength $R_m = 66$ GPa according to ZHANG ET AL. [21] was used as the limit value for exceeding the linear elastic range under tensile load. For the specification of the compressive strength $\sigma_{d,\text{max}}$, the investigations of LI ET AL. [22] were used, in which first-principles calculations were also performed to determine the stress-strain behavior of cBN. According to this, Eq. 5 applies before material failure as the relationship between the tensile stress σ_z and the compressive stress σ_d .

$$\sigma_d = \sigma_z \cdot \tan(68^\circ) \quad (5)$$

According to Eq. 5, a compressive strength of $\sigma_{d,\text{max}} = 163$ GPa was calculated for the tensile stress value $\sigma_z = R_m = 66$ GPa. Furthermore, the lowest possible elongation at break of $\varepsilon_{\text{ck}} = 10^{-7}$ was again assumed after exceeding the maximum stress in each case. The reason for this was to ensure rapid material failure after exceeding the linear elastic

range. Since the inelastic strain ε^{in} had to be specified in ABAQUS for the definition of the CDP model instead of the ultimate strain ε_{ck} , it was calculated using the values presented previously according to the work of QINGFU ET AL. [23] to be $\varepsilon^{\text{in}} = 0.001409$ for tensile loading and $\varepsilon^{\text{in}} = 0.002817$ for compressive loading. The damage parameter D was calculated according to the work of NAJAFGHOLIPOUR ET AL. [24] to be $D = 0.0152$ for tensile loading and $D = 0.0123$ for compressive loading.

If the simulation is executed without considering the cleavage planes in the cBN grain, the result shown in Fig. 5 is generated.

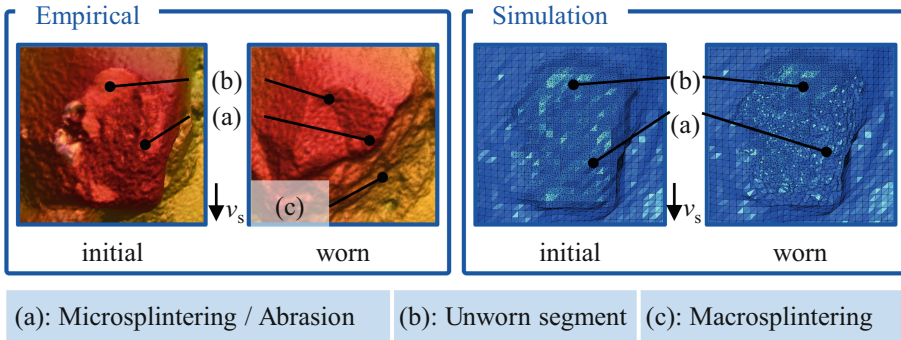


Fig. 5. Comparison of the wear mechanisms between the empirical investigations and the simulation not considering cleavage planes

When comparing the wear state at the end of the simulation with the wear state of cBN grain in the validation test, it was found that the part of the grain worn by abrasion and microsplintering was in both cases the area at the tip of the grain facing the workpiece in the scribing direction (a). In the area at the tip of the grain facing away from the workpiece no wear existed in either case (b). The simulated grain height difference due to wear was higher than the grain height difference in the validation test. The simulated grain wear volume was significantly lower than the grain wear volume in the validation test. The reason for this was the presence of macrosplinters in the validation test, which was not represented in the simulation (c). This can be attributed to the missing cleavage planes in the simulation, which can cause macrosplintering.

Implementation of Cleavage Planes

For the separation of a cBN grain fragment by macrosplintering the crack initiation and crack propagation at the cleavage plane had to be simulated. ABAQUS includes in the form of cohesive elements an element type designed for crack propagation at a known crack surface. Furthermore, cohesive elements are suitable for simulating brittle fracture and do not require an initial notch to implement crack initiation [25]. HUANG ET AL. [11] successfully used cohesive elements to simulate the fracture behavior of pcBN grains. With the help of the cohesive elements, different strength at the grain boundaries and within the grains was implemented. Due to these properties of the cohesive elements, the requirements for the modeling of the cBN cleavage planes for the implementation of macrosplinters in the simulation were given.

Since the cleavage plane is a part of the cBN crystal, the physical parameters of cBN were taken from Table 3 for the cohesive elements. The damage model used for the cohesive elements was the stress-crack opening law. The studies of ICHIDA were used to parameterize this damage model. In his research, fracture tests were performed on cBN grains. Based on the brittle fracture theory according to GRIFFITH, a fracture strength of $\sigma_z = 2,340$ MPa was determined for cBN [26]. The brittle fracture theory according to GRIFFITH describes the propagation of cracks in brittle bodies according to Eq. 6 [27].

$$\sigma_{ck} = \sqrt{\frac{E \cdot G_c}{\pi \cdot a}} \quad (6)$$

where σ_{ck} is the fracture stress, G_c the critical release rate of the strain energy and a the length of the crack. For the use of the fracture strength according to ICHIDA in the stress-crack opening law, the maximum nominal stress criterion was used as a criterion for damage initialization. With this criterion, the damage in a cohesive element is initialized as soon as one value of the normal stress and the two shear stresses reach the specified maximum. The ultimate strength of $\sigma_z = 2,340$ MPa was defined as the maximum value of the normal stress. For the two shear stresses, the tensile strength of $R_m = 66$ GPa according to ZHANG ET AL. [29] was used as the maximum value of the damage criterion. For the complete parameterization of the stress-crack opening law as a damage model for the cohesive elements of the cleavage plane, the critical release rate of the strain energy G_c also had to be specified. YIMING ET AL. calculated a critical strain energy release rate of $G_c = 0.084$ N/mm for cBN [14].

To investigate the influence of cleavage plane position and orientation the variations shown in Fig. 6 were examined. The first variation of the cleavage plane orientation was to incline the cleavage plane by an angle of $\alpha_1 = 5^\circ$ around the vector v_1 parallel to the intersection direction. The second variation consisted of tilting the cleavage plane by $\alpha_2 = 5^\circ$ about a vector v_2 orthogonal to the direction of intersection. Consequently, the first two variations were used to investigate a slight change in the cleavage plane orientation. The third variation consisted of a horizontal positioning of the cleavage plane with a distance of $h = 100$ μm from the bond bottom. The distance of the cleavage plane from the cBN grain tip in the initial condition of this variation was $h_{\text{tip}} = 46$ μm . As a fourth variation, the simulation was performed with the initial cleavage plane orientation according to the validation experiment, but with the cutting direction reversed.

5 Results and Discussion

The simulated wear process with cleavage planes for cBN grain is shown in Fig. 7 for the original orientation. For the initial state of the grain at time $t_0 = 0$ μs , the two grain parts and the cleavage plane are shown offset to clarify the modeling approach. The first initiation of a crack at the cleavage plane (a) occurred at time $t_1 = 33$ μs in the region of the grain-workpiece contact. The first difference in grain wear compared to the model without cleavage plane was recorded at time $t_2 = 50$ μs . At this time, micro splintering occurred due to the crack at the cleavage plane (b). At time $t_3 = 83$ μs , cracking occurred for the first time at the cleavage plane outside the contact area of the workpiece and cBN grain (c). In addition, at this time, advanced crack propagation occurred in the contact

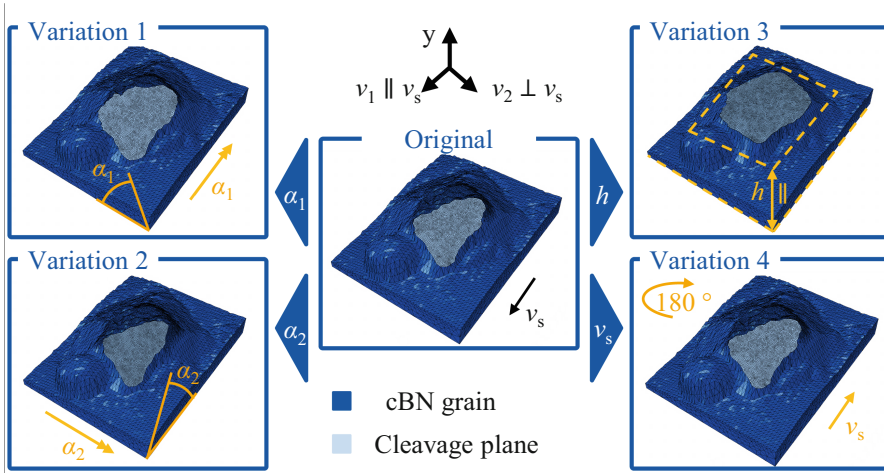


Fig. 6. Variation of cleavage plane orientation

area (d). After exceeding the deepest engagement point, a significant progress in crack propagation outside the grain-workpiece contact occurred in the upward movement of the cBN grain at time $t_4 = 156 \mu\text{s}$ (e). At the wear condition in the end of the simulation ($t_5 = 200 \mu\text{s}$), macrosplintering had resulted in separated grain fragments due to crack propagation at the cleavage plane (f).

In the simulation of the wear of cBN grain with cleavage plane, additional wear was caused by micro- and macrosplintering compared to the simulation without cleavage plane. A complete failure of the cleavage plane as in the validation test was not mapped. The potential reason for this is that the exact JOHNSON and COOK parameters of the workpiece material were not known and thus the process forces of the simulation did not match the process forces of the validation test. In addition, an exact positioning of the cleavage plane is not yet possible, so that deviations in results between reality and simulation can occur.

Results for the Variation of the Cleavage Planes

Since limited computational resources were available to perform the simulations with varied cleavage plane orientation, the longest simulated process time achieved for all variations was $t_{\text{end}} = 140 \mu\text{s}$. Therefore, the evaluation of the simulations was performed for this time. The comparison of the crack propagation at the varied cleavage planes at time $t_{\text{end}} = 140 \mu\text{s}$ is shown in Fig. 8.

This shows that the crack initiation for the variations with slightly inclined cleavage plane occurred at the same locations as in the original simulation. Furthermore, the volume change of the cleavage plane due to crack propagation at time $t_{\text{end}} = 140 \mu\text{s}$ was $\Delta V_1 = 8.12\%$ for Variation 1. Thus, there was a lower extent of crack propagation in Variation 1 than in the original simulation with $\Delta V_{\text{orig}} = 19.26\%$. For Variation 2, the crack propagation had a larger extent with $\Delta V_2 = 21.64\%$. For Variation 3 with the cleavage plane positioned horizontally, there was a crack initiation for the side of the grain facing the workpiece. The crack propagation had a very small extent in this

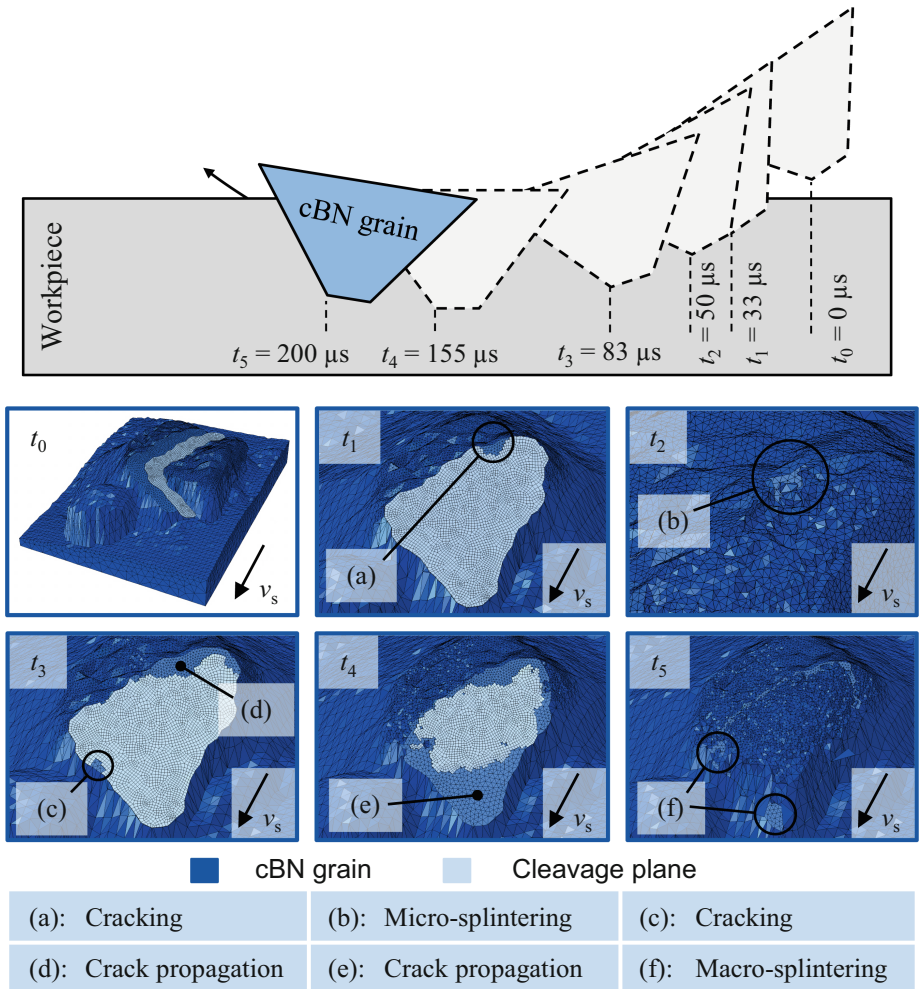


Fig. 7. Results for cBN wear mechanisms considering cleavage planes

simulation with $\Delta V_3 = 3.02\%$. The assumed reason for this was that due to the selected height of the cleavage plane, an initial distance of $h_{\text{tip}} = 46 \mu\text{m}$ of the cleavage plane to the point of application of the load to the grain existed. This distance was larger than in all other simulations. For Variation 4 with reversed cutting direction, there existed a crack starting from the grain tip with a significantly wider crack propagation than in the original simulation in the amount of $\Delta V_4 = 47.13\%$. Another difference in Variation 4 with reversed cutting direction compared to the original simulation was that no crack initiation occurred outside the contact area of the workpiece and cBN grain. Due to the reversed cutting direction, the cleavage plane in Variation 4 was initially inclined away from the workpiece. In the original situation, the cleavage plane was initially inclined towards the workpiece.

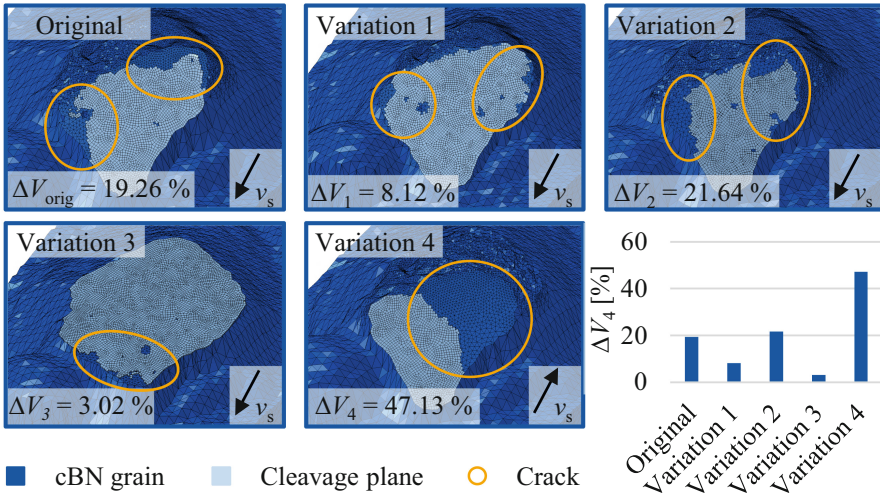


Fig. 8. Results for the crack formation depending on the cleavage plane orientation

From previously described observations, it was concluded that an orientation of the cleavage plane averted from the workpiece in the cutting direction leading to more severe crack propagation. The reason for this is that the fracture strength of $\sigma_z = 2340$ MPa calculated by ICHIDA was used as the damage criterion for the normal stress [26]. The tensile strength of cBN of $R_m = 66$ GPa calculated by ZHANG ET AL. was used as the damage criterion for the shear stresses [21]. In this way, the physical agreement of the model with GRIFFITH brittle fracture theory was ensured. It defines the propagation of cracks in brittle bodies based on the fracture stress normal to the fracture plane according to Eq. (6) [27]. As a consequence of this parameterization of the damage model, an orientation of the cleavage plane averted from the workpiece resulted in higher values for the normal stress σ_n compared to an orientation toward the workpiece. This resulted in a stronger crack propagation. As can be seen in the crack propagation in Variation 4 as well as in the strong increase in crack propagation in the original simulation in the upward movement of the cBN grain.

The second conclusion from the wear of the varied cleavage planes was that a greater distance of the cleavage plane to the point of application of the load on the cBN grain results in a lower crack propagation. The horizontal positioning of the cleavage plane in Variation 3 was further away from the grain tip than the original orientation. Although this is conducive to greater crack propagation, very little crack propagation was recorded in Variation 3. In addition to the inclination of the cleavage plane, the difference from the original simulation was the greater distance from the point of application of the load amounting to $h_{tip} = 46$ μm . Resulting in lower stresses at the cleavage plane and thus lower crack propagation.

In Variation 1 and Variation 2, minor differences were observed in the extent of crack propagation at slightly inclined cleavage planes compared to the original simulation. These differences were attributed to a combination of the slope of the crack planes and the resulting slight differences in the distance to the point of application of the load.

Figure 9 shows, for the simulations presented previously, the wear mechanisms that occurred in conjunction with crack propagation at the cleavage plane on the entire cBN grain at time $t_{\text{end}} = 140 \mu\text{s}$.

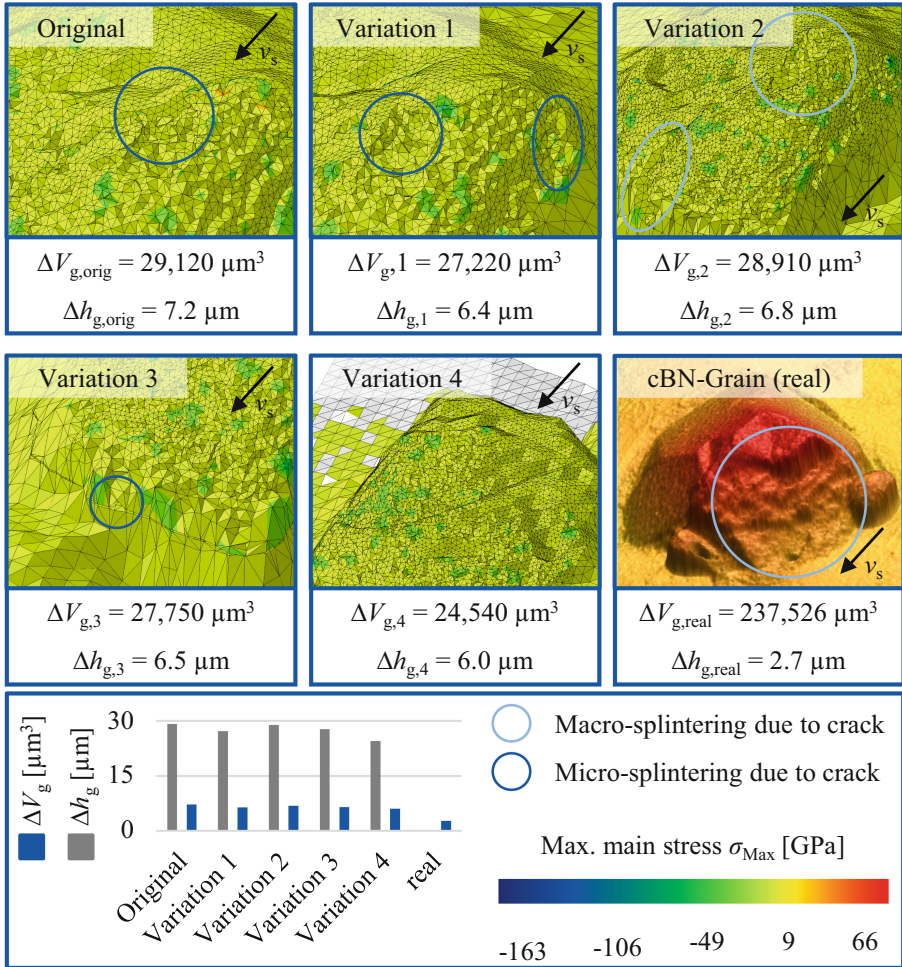


Fig. 9. Results for the cBN grain wear depending on the cleavage plane orientation

It was found that in the original simulation and Variations 1–3, micro- and macrosplintering occurred on the cBN grain due to the cracks at the cleavage plane. In Variation 4, no additional wear mechanisms were found on the cBN grain due to the integration of the cleavage plane although the largest crack propagation existed in this simulation with $\Delta V_4 = 47.13\%$. Variation 4 also had the lowest grain wear volume with $\Delta V_{g,4} = 24,540 \mu\text{m}^3$ as well as the lowest grain height difference with $\Delta h_{g,4} = 6.0 \mu\text{m}$. From these observations, it was concluded that an orientation of the cleavage plane averted

from the workpiece prevents the development of additional wear mechanisms on the cBN grain associated with crack propagation and, in this case, only complete material failure of the cleavage plane leads to macrosplinters. When the orientation of the cleavage plane is toward the workpiece, crack propagation causes micro- and macrosplinters on the grain. The assumed reason is that the elements adjacent to the cleavage plane are subjected to greater tensile loading when the cleavage plane faces the workpiece while the corresponding elements are mainly subjected to compressive loading when the cleavage plane faces away from the workpiece. The significantly higher compressive strength of cBN amounting to $\sigma_{d,max} = 163$ GPa compared to the tensile strength of $R_m = 66$ GPa thus causes the differences in the wear mechanisms.

The process forces with the varied cleavage plane orientations at time $t_{end} = 140 \mu s$ are shown in Fig. 10. The reference point of the results represents the deepest point of engagement of the grain in the workpiece in the simulation and real test. Since the course of the process forces over the engagement was comparable, the maximum scratch force was used as a comparative value. This shows that for Variations 1–3 with a maximum force deviation of $\Delta F = 10.7\%$ there were minor differences to the process forces in the original simulation. This was because the different cleavage plane orientations had a minor influence on the expression of the wear volume at the cBN grain. In Variation 4, the highest normal force was simulated with $F_n = 20.5$ N. This was due to the lower wear volume at the cBN grain resulting from macrosplintering not being represented in the simulation. Additionally, the geometric conditions of the cBN grain were different because of the reversed cutting direction. The larger deviation of the tangential force results from the deviating wear volume and height difference of the grain. Due to the lower wear in the simulation, the tangential forces increase accordingly.

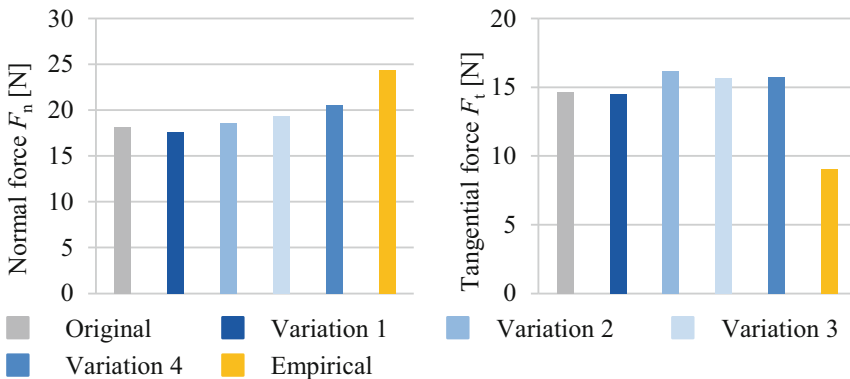


Fig. 10. Process forces depending on the varied cleavage plane orientations

6 Conclusion

In the present work, an FE simulation is set up that can determine the wear of cBN grains depending on the cleavage planes during single grain engagement. Real cBN grain geometries were used in the engagement with a workpiece made of 100Cr6 steel. Experimental single-grain scratch tests were performed to validate the simulation model. The main conclusions are summarized as follows:

- Development of FE simulation model for cBN grain wear during single-grain scratching based on CDP wear model with integration of cleavage planes by stress-crack opening law.
- Identification of cBN wear mechanisms abrasion, microsplintering and macrosplintering in close qualitative accordance to validation tests.
- Identification of cause-effect relationships between cleavage plane orientation and simulated cBN wear.
- Cleavage plane variation resulted in stronger crack propagation when the cleavage plane was oriented away from the workpiece and when the distance of the cleavage plane from the point of application of the load was smaller.
- In the simulation, slightly too low wear volumes were calculated together with too high grain height reduction. This results in deviations in the process forces compared to the test.

The results presented in this paper provide a very well approximated simulation model to represent the wear behavior of cBN grains as a function of cleavage planes. In order to be able to represent the wear behavior exactly, further optimization approaches must be conducted with regard to the material parameters. In addition, further simulation variations with regard to the process parameters used will follow in future investigations in order to investigate the influence of the parameters on the wear behavior. In this way, the real load condition on a grinding wheel (with regard to the engagement condition due to shadowing effects, etc.) can be modelled. This is because the engagement situation presented in this paper does not exist in a real grinding process. However, the engagement situation was necessary to validate the wear behavior in order to be able to reproduce real engagement situations in the next step. Then predictions on grinding wheel wear will also be possible.

References

1. Tönshoff, H.K., Peters, J., Inasaki, I., Paul, T.: Modelling and simulation of grinding processes. *CIRP Ann. – Manuf. Technol.* **41**(2), 107–114 (2004)
2. Davies, M.A., Ueda, T., M'Saoubi, R., Mullany, B., Cooke, A.L.: On the measurement of temperature in material removal processes. *CIRP Ann.* **56**(2), 581–604 (2007)
3. Shi, Z., Malkin, S.: An investigation of grinding with electroplated cBN wheels. *CIRP Ann. – Manuf. Technol.* **52**(1), 67–70 (2003)
4. Upadhyaya, R.P., Malkin, S.: Thermal aspects of grinding with electroplated cBN wheels. *Manuf. Sci. Eng. – Trans. ASME* **126**(1), 107–114 (2004)
5. Malkin, S., Cook, N.H.: The wear of grinding wheels: part 1—attritious wear. *J. Eng. Ind.* **93**(4), 1120–1128 (1971)

6. Malkin, S., Guo, C.: *Grinding Technology: Theory and Application of Machining with Abrasives*. Industrial Press Inc. (2008)
7. Bergs, T., Ohlert, M., Prinz, S., Barth, S.: Modeling of the fracture behavior of cBN grains during single grain dressing using FEM. *Proc. CIRP* **93**, 1514–1519 (2020)
8. Mei, Y., Yu, Z., Yang, Z.: Numerical investigation of the evolution of grit fracture and its impact on cutting performance in single grit grinding. *Int. J. Adv. Manuf. Technol.* **89**(9–12), 3271–3284 (2016). <https://doi.org/10.1007/s00170-016-9249-1>
9. Wang, J., Yu, T., Ding, W., Fu, Y., Bastawros, A.F.: Wear evolution and stress distribution of single CBN superabrasive grain in high-speed grinding. *Precis. Eng.* **54**, 70–80 (2018)
10. Rao, Z., Ding, W., Zhu, Y., Xu, J.: Numerical simulation analysis and experimental validation on wear/fracture mechanisms of polycrystalline cubic boron nitride superabrasives in high-speed grinding. *Ceram. Int.* **45**(3), 3377–3389 (2019)
11. Huang, X., Li, H., Rao, Z., Ding, W.: Fracture behavior and self-sharpening mechanisms of polycrystalline cubic boron nitride in grinding based on cohesive element method. *Chin. J. Aeronaut.* **32**(12), 2727–2742 (2019)
12. Bredthauer, M., Mattfeld, P., Barth, S., Bergs, T.: CBN-Kornverschleißmodellierung/Numerical modeling of CBN grain wear during single grain engagement – CBN-grain wear modelling. *Werkstattstech. Online* **111**(06), 414–418 (2021)
13. Johnson, G.R., Cook, W.H.: A constitutive model and data for metals subjected to large strains, high strain rates and high temperatures. In: *Proceedings of the 7th International Symposium on Ballistics*, vol. 21, pp. 541–547 (1983)
14. Bilici, M.A.: *An investigation on the ballistic behaviour of Alumina/Aluminum armor structures*. Dissertation. Ankara (2007)
15. Mikhaylov, A., Sydorova, E., Navka, I.: Determination of the working insert life in machining 100Cr6 hardened steel with cutting fluids. *Int. J. Mod. Manuf. Technol.* **2015**, 42–46 (2015)
16. Habak, M., Lebrun, J.L., Badie-Levet, D.: Effect of the microstructure on the tool/chip tribological contact in hard turning of 100Cr6 bearing steel. *Int. J. Mach. Mach. Mater.* **2009**(1/2), 120–138 (2009)
17. Rasim, M., Klocke, F.: *Modellierung der Wärmeentstehung im Schleifprozess in Abhängigkeit von der Schleifscheibentopographie*. Dissertation RWTH (2016)
18. Wosatko, A., Winnicki, A., Polak, M.A., Pamin, J.: Role of dilatancy angle in plasticity-based models of concrete. *Arch. Civ. Mech. Eng.* **19**(4), 1268–1283 (2019). <https://doi.org/10.1016/j.acme.2019.07.003>
19. Malm, R.: *Shear cracks in concrete structures subjected to in-plane stresses*. Dissertation. Stockholm (2006)
20. Silva, L.M.E., Christoforo, A.L., Carvalho, R.C.: Calibration of concrete damaged plasticity model parameters for shear walls. *Matéria (Rio de Janeiro)* **26**(1) (2021)
21. Zhang, Y., Sun, H., Chen, C.: Structural deformation, strength, and in-stability of cubic BN compared to diamond: a first-principles study. *Phys. Rev. B* **73**(14) (2006)
22. Li, B., Sun, H., Chen, C.: Large indentation strain-stiffening in nanot-winned cubic boron nitride. *Nat. Commun.* **5**, 4965 (2014)
23. Qingfu, L., Wei, G., Yihang, K.: Parameter calculation and verification of concrete plastic damage model of ABAQUS. In: *IOP Conference Series: Materials Science and Engineering*, vol. 794, no. 1, p. 12036 (2020)
24. Najafgholipour, M.A., Dehghan, S.M., Dooshabi, A., Niroomandi, A.: Finite element analysis of reinforced concrete beam-column connections with governing joint shear failure mode. *Latin Am. J. Solids Struct.* **14**(7), 1200–1225 (2017)
25. Dassault Systemes: *Abaqus 2016 Online Documentation*. <http://130.149.89.49:2080/v2016/>. Accessed 22 July 2022

26. Ichida, Y.: Mechanical properties and grinding performance of ul-trafine-crystalline cBN abrasive grains. *Diam. Relat. Mater.* **17**(7–10), 1791–1795 (2008)
27. Griffith, A.: The phenomena of rupture and flow in solids. *Philos. Trans. Roy. Soc. London* **1921**(221), 163–198 (1921)

Open Access This chapter is licensed under the terms of the Creative Commons Attribution 4.0 International License (<http://creativecommons.org/licenses/by/4.0/>), which permits use, sharing, adaptation, distribution and reproduction in any medium or format, as long as you give appropriate credit to the original author(s) and the source, provide a link to the Creative Commons license and indicate if changes were made.

The images or other third party material in this chapter are included in the chapter's Creative Commons license, unless indicated otherwise in a credit line to the material. If material is not included in the chapter's Creative Commons license and your intended use is not permitted by statutory regulation or exceeds the permitted use, you will need to obtain permission directly from the copyright holder.





Development of a Tool Temperature Simulation During Side Milling

Thorsten Helmig¹(✉), Hui Liu², Simon Winter¹, Thomas Bergs²,
and Reinhold Kneer¹

¹ Institute of Heat and Mass Transfer, RWTH Aachen University, Aachen, Germany
helmig@wsa.rwth-aachen.de

² Laboratory for Machine Tools and Production Engineering, RWTH Aachen University,
Aachen, Germany

Abstract. Current modeling approaches of cutting processes require on the one hand extensive numerical and analytical simulations and further an experienced user in the field of numerical simulations, which makes a large-scale application time-consuming to apply.

Therefore, the goal is to implement existing models into an established side-milling simulation program aiming for a computationally fast and user-friendly simulation approach capable of predicting transient tool temperatures along the cutting edge. Aim of this work is the development of the thermal model, which can later be implemented into existing programs. The model process involves the following two major steps: First, a geometric engagement simulation of the milling process with a parameterizable tool geometry is performed. These results are used to form a database linking the specific cutting force components with the heat flux components. Second, a three-dimensional transient heat conduction model of the cutter is established, applying the calculated heat flux components as boundary conditions in the simulation. Finally, first results of the performed simulation are presented and evaluated, in particular to validate the work flow and user accessibility. Future studies will then focus on further parameter analysis and experimental validation.

Keywords: Transient Thermal Modeling · Side-milling · Finite-Element-Method

1 Introduction

During milling, almost ninety percent of the used mechanical energy is converted into heat [1]. Part of this thermal energy is transferred from the cutting zone to the tool and the toolholder, resulting in three-dimensional temperature fields and gradients. In turn, thermal stresses arise inside the tool, which accelerate the thermo-mechanically induced tool wear on the one hand. On the other hand, the thermal distortion can lead to a displacement of the tool center point and thus to a reduction in machining accuracy. Therefore, understanding the heat partition in the cutting area and the development of tool temperature plays an important role not only in scientific research, but also in applied manufacturing processes.

© The Author(s) 2023

S. Ihlenfeldt (Ed.): ICTIMT 2023, LNPE, pp. 308–317, 2023.

https://doi.org/10.1007/978-3-031-34486-2_22

In milling, the estimation of the tool temperature by the given cutting has been investigated with comprehensive experiments in the last decades. Depending on the experimental approach, the investigations so far can be divided into local temperature measurements [2–6] and thermography-based temperature field measurements [7–9]. Local temperature measurement can be for example obtained by using a thermocouple or fiber optic cable connected to a pyrometer. To mount the sensor, a hole is usually drilled in the tool up to the measuring point by means of wire electro-discharge machining. A drawback of local temperature measurement is that it cannot provide information about temperature gradients, or the resulting temperature field. In contrast, Infrared Thermography yields spatially resolved temperature data, but only intermittent optical access of the tool surface is given due to the rotation of the milling tool and the evolving chips. Consequently, comprehensive temperature measurements during machining are challenging to acquire.

In order to reduce the amount of experimental effort and to support thermal analysis, modeling approaches come into focus. A popular analytical approach for orthogonal cutting processes is the use of superposition by Greens function to estimate the temperature field [6]. However, this approach is limited to comparable simple tool geometries and heat flux distributions. As an alternative, numerical methods can be used, as these can handle advanced (tool-) geometries and heat flux distributions along the tool surface and provide transient temperature fields as an output. In turn, the obtained temperature fields can be used in post-processing to estimate heat fluxes into the machine tool, ultimately leading to a shift in the tool center point (TCP). Hence, this work aims for the development of a novel numerical approach to estimate the transient temperature field of a milling tool by resolving the spatially varying and transient heat flux. The heat flux caused by the manufacturing process is a-priori calculated by a Finite-Element simulation and later used as input for the boundary condition in the thermal simulation. By using pre-calculated heat source terms, the simulation time of the process can be significantly reduced, allowing for faster and application-oriented studies.

2 Overview Workflow

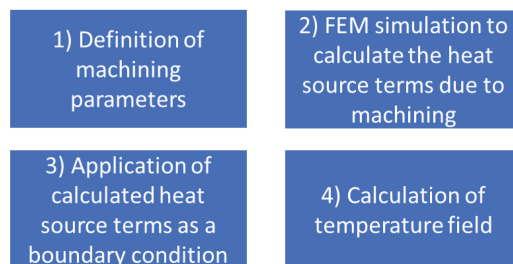


Fig. 1. Workflow to calculate a transient milling tool temperature field.

For an improved understanding of the overall procedure, Fig. 1 highlights the workflow.

In a first step the considered machining parameters are defined. The parameters are then used in a FEM simulation of the milling process to calculate the heat source terms. These are summarized in integral value and are later applied as a boundary condition in the thermal simulation of the tool. The heat source term is homogeneously distributed along the engaging cutting edge, which will be explained in the next section.

3 Tool Geometry, Mechanical and Thermal Modeling

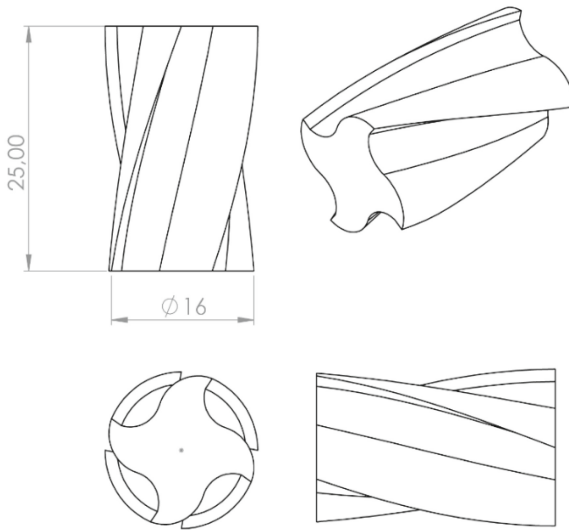


Fig. 2. Geometry of the modelled milling tool.

The considered tool for simulation is a solid carbide milling cutter from Sandvik Coromant, type 2P342–1600-CMA 1740. The geometry of the milling cutter is shown in Fig. 2. The flute helix angle of the tool is 38° . In a first step, the tool is not resolved in its entirety, but up to a height of 25 mm.

To estimate the heat flux into the tool, three-dimensional chip formation simulations of the milling process are performed. The simulation uses a Coupled Eulerian-Lagrangian (CEL) approach, where the workpiece is defined in the Eulerian domain and the tool in the Lagrangian domain. The tool is considered as a rigid body neglecting wear effects. The workpiece material under study is AISI 1045. The Johnson Cook material (JC) model is used to describe the thermo-viscoplastic behavior of the workpiece. The JC model consists of three multiplied terms that describe the influence of strain, strain rate and temperature:

$$\sigma_F = (A + B \cdot \varepsilon^n) \cdot \left(1 + C \cdot \ln\left(\frac{\dot{\varepsilon}}{\dot{\varepsilon}_0}\right)\right) \cdot \left(1 - \left(\frac{T - T_0}{T_m - T_0}\right)^m\right)$$

The model parameters for AISI 1045 are inversely calibrated in the previous work and used in this study, as shown in Table 1.

Table 1. Model parameters of the Johnson Cook material model for AISI 1045

A	B	C	m	n	T_m	T_0	$\dot{\epsilon}_0$
[MPa]	[MPa]	-	-	-	[°C]	[°C]	s^{-1}
541.5	460	0.004	0.05	1.047	1460	20	1

The simulations are performed in the commercial software ABAQUS version 2021. Figure 3 gives an overview of the simulation domain. The increase in internal energy of the tool at one revolution is used to estimate the heat source applied in the subsequent thermal analysis.

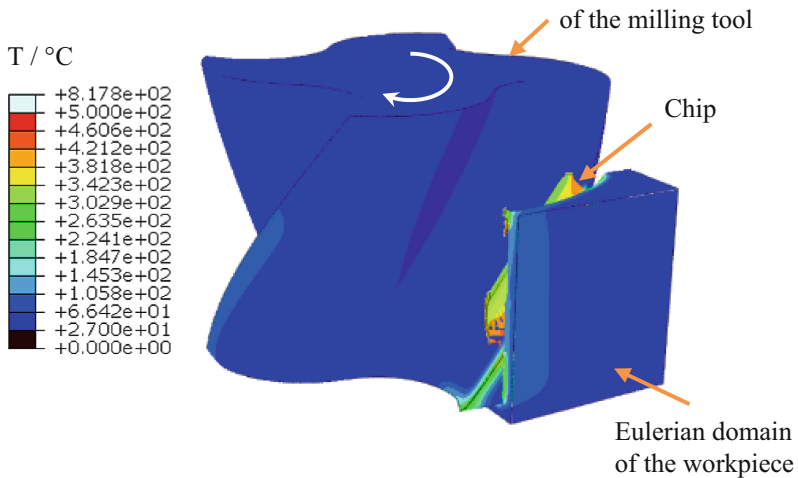


Fig. 3. Chip formation simulation of the milling process based on the coupled Eulerian Lagrangian method.

After the mechanical simulation, the thermal analysis is performed. To transfer the tool geometry into a thermal model, a Finite-Volume-Approach is chosen. The implementation is performed in a MatLab environment. The governing equation for a three-dimensional transient heat conduction problem with constant density ρ , heat capacity c_p and heat conductivity k reads:

$$\rho c_p \frac{\partial T}{\partial t} = k \frac{\partial^2 T}{\partial x^2} + k \frac{\partial^2 T}{\partial y^2} + k \frac{\partial^2 T}{\partial z^2} + \dot{q}'''(x, y, z, t)$$

Further, a heat source term \dot{q}''' is located on the right-hand side, to consider the heat flow into the tool during machining. The values of the thermophysical properties are shown in Table 2:

Table 2. Thermophysical properties of the tool.

Property	Value
Density	14800 kg/m ³
Heat Capacity	243 J/kg K
Heat Conductivity	81.78 W/mK

As outlined in the previous section, the workpiece and chip formation are not resolved in the thermal simulation of the milling tool. Instead, the machining of the workpiece and chip formation is resolved by the FEM approach. The results of the FEM approach are then used to calculate an integral heat source value (Table 3), which is then homogeneously distributed along the engaging cutting edge (Fig. 4).

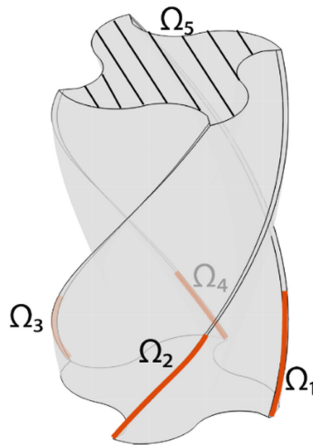


Fig. 4. Tool geometry with applied boundary conditions. For boundaries 1–4 a heat flux boundary is applied, while the tool top is set adiabatic. The sides of the tool and the bottom are set adiabatic but not particular highlighted here.

Along the boundary segment $\Omega_1 - \Omega_4$, the heat source term caused by the cutting process is applied up to a height of 7.5 mm. As the cutting tool is rotating during machining, the heat flux is not applied at all cutting edges simultaneously, but rather one cutting edge after another. An example sequence of one cutter revolution is shown in Fig. 5, highlighting that only one cutting edge engages at any timestep. Further, the applied heat source term is the same the for every cutter rotation. Due to the helix angle, the heat source is expected to move along the cutting edge during the engagement.

However, a spatially constant mean heat source is assumed in this work for two reasons: First, the focus is to establish and test the overall simulation workflow. Therefore, the model is built with the most essential parameters in order to eliminate possible sources of error in the development and ensure a stable model. In the future, the model is extended step by step to ensure a high stability for the later application in manufacturing environment. Next steps certainly include spatially varying heat source terms, convective heat transfer by cooling fluid. However, for now the heat source term is assumed to be constant along the engaging contact edge.

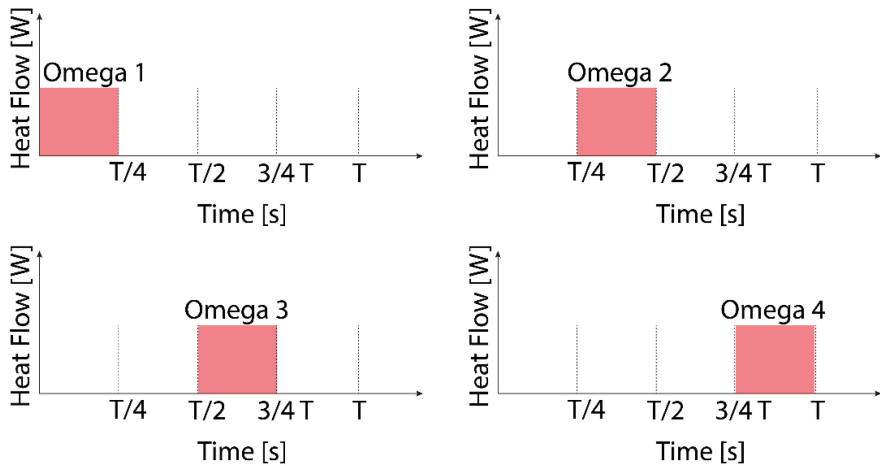


Fig. 5. Example of the applied heat source for the engaging cutting edges. The four cutting edges engage consecutively one after another.

Regarding further boundary conditions, the top of the tool is set adiabatic (Ω_5). Consequently, heat flux from the tool into the machine structure is not considered yet, but will be focused in future work. Due to the adiabatic boundary at the top, the tool temperature tends to be slightly overestimated. This will be particularly noticeable for longer simulation times. For future studies, the boundary Ω_5 will be enhanced to consider heat flow into the machine tool. The remaining faces at the side and the bottom of the tool are also set to an adiabatic boundary condition, however not particularly highlighted here. As the sides can be selected as an independent boundary, convective cooling due to the use of cooling lubricant or contact heat transfer at the chip-tool interface can be considered. Finally, the effect of tool wear is integrated implicitly in future studies. As for a worn tool surface an increase in generated heat is expected, the boundary heat source terms can be adjusted accordingly.

After establishing the model, three different test cases with varying feeds are investigated to analyze the impact on the temperature field. The varied parameters are shown in Table 3:

Table 3. Test Cases and corresponding cutting parameters

Test Case	Cutting Speed v_c [m/min]	Feed f [mm]	Cutting Width a_e [mm]	Cutting Depth a_p [mm]	Power W]
1	100	0.1	2.5	7.5	175.291
2	100	0.2	2.5	7.5	219.102
3	100	0.3	2.5	7.5	256.97

4 Results

Figure 6 shows local temperature trends from Test Case 1. The location of extracted temperature data is shown in the right sub-image. The measurement spot is located not directly at the cutting edge where the heat source term is applied, but a few cells below the surface. Further, the first ten revolutions of the cutting process are visualized.

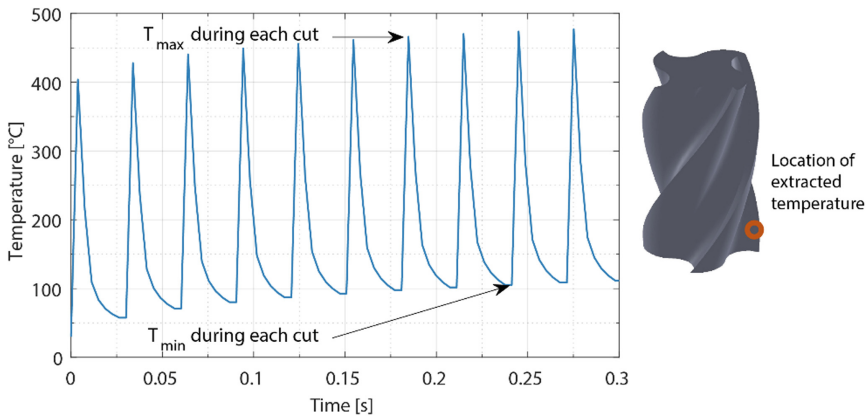


Fig. 6. Results of Test Case 1 during for the first 0.3s. The minimum and maximum temperature during each cut are highlighted.

In general, an oscillating behavior is observed. With a cutting speed of 100 m/min and a cutter radius of 8 mm, a cutting edge engages each 0.03 s, which corresponds well with the observed temperature oscillation. The engagement causes a fast increase in temperature, however followed by a rapid fall as the heat spreads into the tool. However, the temperature does not fall back to its initial value, but starts slightly higher as the next cut is already performed. In the long term, the entire tool will heat up. Of course, such temperature trends need an experimental validation, therefore a measurement setup with a high temporal resolution is required in order to resolve the occurring transient temperature trends. Previous studies applied a pyrometer to resolve such fast processes [10]. A similar approach is intended in the future, but requires comprehensive planning and layout of the experimental setup.

To get an overview of the temperature development during longer processing times, the maximum, minimum and mean temperature for each cut is calculated. The results are shown in Fig. 7, visualizing a fast increase in all depicted temperatures at the beginning. Afterwards, a transition into a linear trend for all three shown temperatures is observed. Further, due to the heat spreading and fast decrease in temperature, the mean is rather oriented towards the minimum than to the maximum value. The orientation of the mean value towards the minimum is maintained throughout the entire investigation time. The maximum temperatures approach a level of 600 °C after 5 s. In contrast, the time averaged values reveal about 350 °C, which is almost the half of the maximum temperature, indicating high thermal stresses inside the tool. As no convective cooling and heat flux into the machine structure is considered, the temperature level might be overestimated. However, the major aim of this work is the development and testing of the workflow. Future studies will adapt the boundary conditions and enhance thermal modeling.

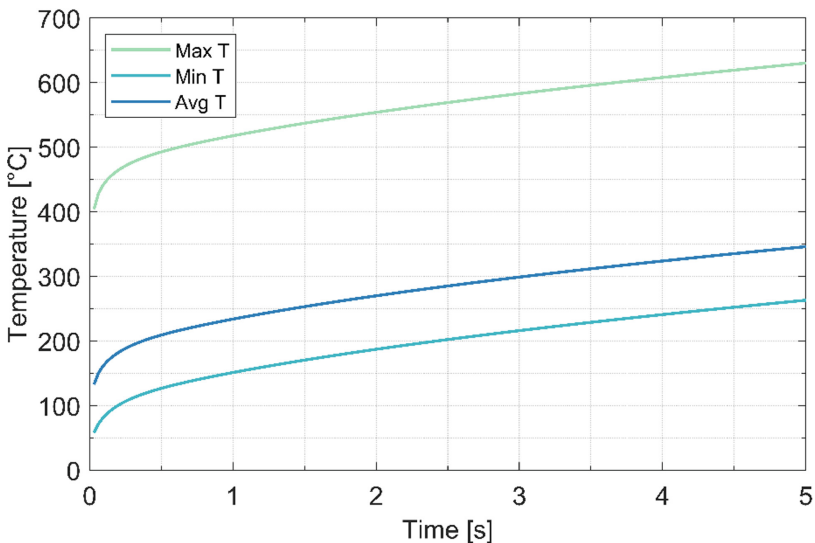


Fig. 7. Minimum, maximum and average temperature during the engagement of one particular cutting edge.

Finally, Fig. 8 investigates the impact of increasing feed rate on the maximum temperature. At the beginning, all three test cases show a similar temperature trend, which starts to deviate after 0.5 s. As expected for higher feed rates, the maximum tool temperature increases. For a feed rate of 3 mm, already after 2 s a maximum temperature of 600 °C is obtained, while for the minimal feed rate twice as much time is required to approach the same niveau. However, particular interesting is that the actual feed rate has no significant impact on the maximum temperature for short milling times. By adding cooling fluid to the process, the deviation from the trends might be shifted to later times.

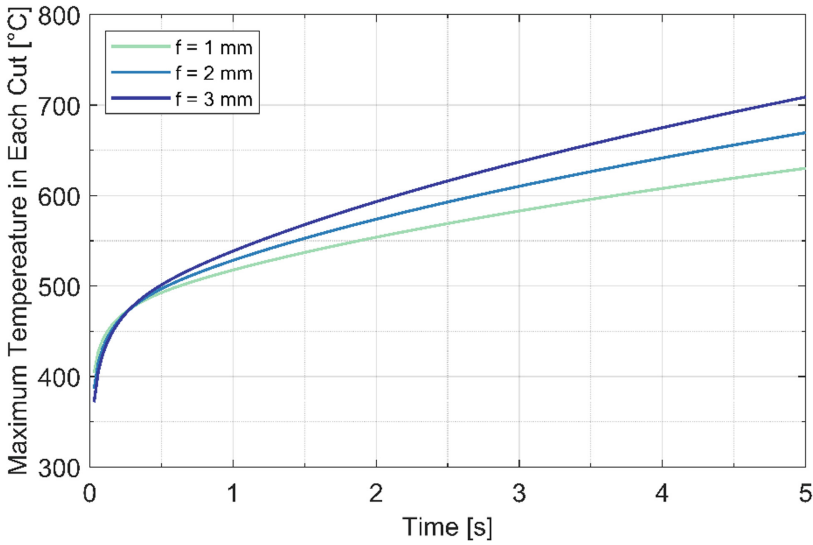


Fig. 8. Maximum tool temperature for three different feed rates.

5 Conclusion

A novel approach to estimate the transient temperature field of a side milling tool has been presented. In a first step, the heat sources are pre-calculated by a FEM simulation and used as a tabulated boundary condition for the later thermal simulation of the milling tool. The thermal model offers to consider transient and spatial varying heat sources during processing. Although time varying heat sources at each cutting edge are considered, the spatial trend is simplified in this work to a constant term. The model shows a physically reasonable results in predicting the transient tool temperature, in particular fast temperature changes at the cutting edge are quantified and can be used in future analysis to estimate thermal induced tool wear and stresses. However, experimental validation is required and will be focused in future research. Further, the thermal model will be enhanced to consider convective cooling by lubricants and contact heat transfer to the workpiece and chip. As significant temperature gradients inside the tool occur, temperature dependent thermophysical properties will also be included.

Acknowledgements. The authors would like to thank the German Research Foundation (DFG) for the funding the SFB/Transregio 96 collaborative research (Project ID 174223256-TRR 96) “Thermo-Energetische Gestaltung von Werkzeug-maschinen” subproject A02 and B02.

References

1. Taylor G.I., Quinney H.: The latent energy remaining in a metal after cold working. In: Proceedings of the Royal Society of London A: Mathematical, Physical and Engineering Sciences. vol. 143, no. 849, pp. 307–326 (1934)
2. Ueda, T., Hosokawa, A., Oda K., Yamada K.: Temperature on flank face of cutting tool in high speed milling. In: CIRP Annals – Manufacturing Technology. vol. 50, no. 1, pp. 37–40 (2001)
3. Sato, M., Tamura, N., Tanaka, H.: Temperature variation in the cutting tool in end milling. J. Manuf. Sci. Eng. **133**(2), 21 (2011)
4. Lin, S., Peng, F., Wen, J., Liu, Y., Yan, R.: An investigation of workpiece temperature variation in end milling considering flank rubbing effect. Int. J. Mach. Tools Manuf. **73**, 71–86 (2013)
5. Jiang, F., Liu, Z., Wan, Y., Shi, Z.: Analytical modeling and experimental investigation of tool and workpiece temperatures for interrupted cutting 1045 steel by inverse heat conduction method. J. Mater. Process. Technol. **213**(6), 887–894 (2013)
6. Karaguzel, U., Bakkal, M., Budak, E.: Modeling and measurement of cutting temperatures in milling. Procedia CIRP **46**, 173–176 (2016)
7. Sölter, J., Gulpak, M.: Heat partitioning in dry milling of steel. Ann. CIRP **61**(1), 87–90 (2012)
8. Lagarde, Q., Wagner, V.: Study of radial depth of cut influence on tool temperature and wear by infrared radiations camera measurements in intermittent cutting. In: Proceeding HSM Metz (2016)
9. Augspurger, T., Meurer, M., Liu, H.: Experimental study of the connection between process parameters, thermo-mechanical loads and surface integrity in machining Inconel 718. Procedia CIRP **87**, 59–64 (2020)
10. Augspurger, T., Bergs, T., Döbbeler, B.: Measurement and modeling of heat partitions and temperature fields in the workpiece for cutting Inconel 718, AISI 1045, Ti6Al4V, and AlMgSi0.5. J. Manuf. Sci. Eng. **141**(6), 061100 (2019)


Open Access This chapter is licensed under the terms of the Creative Commons Attribution 4.0 International License (<http://creativecommons.org/licenses/by/4.0/>), which permits use, sharing, adaptation, distribution and reproduction in any medium or format, as long as you give appropriate credit to the original author(s) and the source, provide a link to the Creative Commons license and indicate if changes were made.

The images or other third party material in this chapter are included in the chapter's Creative Commons license, unless indicated otherwise in a credit line to the material. If material is not included in the chapter's Creative Commons license and your intended use is not permitted by statutory regulation or exceeds the permitted use, you will need to obtain permission directly from the copyright holder.





Three-Dimensional Modeling of Thermomechanical Tool Loads During Milling Using the Coupled Eulerian-Lagrangian Formulation

Hui Liu¹ (✉) , Markus Meurer¹, and Thomas Bergs^{1,2}

¹ Laboratory for Machine Tools and Production Engineering (WZL) of RWTH Aachen University, Campus-Boulevard 30, 52074 Aachen, Germany

h.liu@wzl.rwth-aachen.de

² Fraunhofer Institute for Production Technology IPT, Steinbachstr. 17, 52074 Aachen, Germany

Abstract. Milling is a complex process where machining quality is influenced by tool geometry, chip flow, temperature, and wear. In recent years, the rapid development of computer technology has enabled the use of finite element simulation methods to study the relationship between the machining results and various process parameters. In this study, a three-dimensional thermal coupled Euler-Lagrange milling model is proposed. This approach provided unique advantages in terms of stability and computational speed. The simulation results showed a good agreement with the corresponding experimental cutting tests and provided further information on the heat source distribution characteristics, which form a basis for further theoretical investigations.

Keywords: Milling · Finite Element simulation · Coupled-Eulerian-Lagrangian

1 Introduction

Milling is an intermittent cutting process in which a tool, usually with multiple teeth, performs a circular cutting motion to produce a workpiece geometry. Due to the superposition of translational and rotational movements, the cutting edges traverse a trochoidal path, resulting in a variation of the uncut chip thickness thus changing the thermomechanical loads on the cutting tool. Thermo-mechanical state variables have a significant influence on machining results, for example various wear effects as well as the change in surface integrity of the workpiece [1]. Only detailed understanding of the process state variables enables effective process and tool design with correspondingly positive economic and ecological potentials.

The empirical study of process state variables has remained a major challenge to date. The complex dynamics of the milling process make direct process monitoring, especially temperature measurement, difficult. To solve this problem, model-based process analysis has become increasingly important. Process models are usually classified into analytical and numerical models. Analytical models, such as [2, 3], although easier to solve than

numerical models, are generally restricted to simple tool and workpiece geometries and are valid only for a limited range of state variables. In comparison, numerical methods are more flexible but require large computational resources. Nowadays, with the progress of computer hardware and the development of simulation programs, the 3D simulation of machining processes based on the finite element method (FEM) is possible. The advantage of the 3D numerical simulation of the milling process is not only the flexibility in setting the tool geometry and cutting conditions, but also the possibility to visualize all the state variables of the real cutting process, which can be considered as the realization of the digital twin [4–7].

1.1 State of the Art of FEM-Based Cutting Simulation

The FEM-based cutting simulations can be divided into Lagrangian and Coupled Eulerian Lagrangian (CEL) methods. The difference between the two methods lies in the definition of the mesh type for the workpiece. In the Lagrangian method, the mesh moves with the workpiece. This method has the advantage of accurately describing the material surface but is prone to mesh distortion due to the high strain rate of the material in the primary and secondary shear zones. The CEL approach, on the other hand, uses an Eulerian mesh for the workpiece material, and the mesh is fixed in space. With a sufficiently fine mesh, this approach can greatly improve the stability of the cutting simulation.

To date, the CEL method has been widely used for the simulation of a variety of cutting processes. Abdelhafeez et al. simulated the drilling of aluminum and titanium alloys using the CEL method. The simulated process forces were in good agreement with the experimental measurements [8]. Gao et al. Simulated the end milling of Al6061 aluminum alloy [9]. In this case, the cutting process was simplified to a linear motion. Their results showed that the simulation not only correctly predicted the cutting forces, but also accurately reproduced the chip morphology. The study by Persson et al. focused on burr formation during intermittent turning. They found that the burr heights determined by CEL simulations were in agreement with the experimental values [10]. The most recent CEL-based milling simulation study was published by Vovk et al. who simulated the peripheral milling of AISI4140 alloy [11]. Their results further confirmed that the numerical model can accurately predict cutting forces, and in addition they investigated the residual stresses and temperature variations of the workpiece in the simulation.

The results of milling and drilling simulations to date have shown that the CEL method can accurately predict cutting forces as well as chip formation processes. However, for all current studies, the tool was considered to be an adiabatic body. Neglecting the temperature change of the tool and the heat transfer between the tool and the workpiece material leads to the lack of accuracy of the thermal analysis in the milling process. To fill this research gap, a novel thermally coupled CEL approach for side milling is proposed in this paper. The advance of the model is the ability to predict the thermal load on the cutting tool, which is a prerequisite for subsequent models, such as tool wear models.

The process investigated in this work is side milling of AISI 1045 steel with carbide tools. Tool temperature, cutting force components and tool torque are measured and compared with the simulation results. In the following section, the experimental setup

as well as the tool and workpiece characteristics are first described. Section 3 outlines the setup of the thermal coupled CEL model for the milling process and the specific model parameters. Section 4 compares the simulation results with the experiments to evaluate the accuracy of the models. The final section summarizes the advantages and shortcomings of the proposed approach and provides guidance for the future development of the model.

2 Experimental Procedure

For model validation, milling experiments were performed on a CNC machine. In this section, the setup of the test rig and the specification of the sensors used are presented. Subsequently, the properties of the milling tool and the workpiece are described in detail.

2.1 Experimental Set-Up of Side Milling

The side milling experiments were performed on a Mazak VARIAXIS i-600 machining center. Figure 1 shows the experimental setup and sensor arrangement. The workpiece in the form of a 250 mm × 65 mm × 55 mm block was attached to a KISTLER 9255c dynamometer with four clamps. The dynamometer can measure the force components in the feed direction F_f and perpendicular to the feed direction F_{FN} up to 30 kN. During the process, the tool moved only in the X-direction and milled the front face of the workpiece. The door of the machine tool remained open during the experiment. A FLIR X6580sc thermal imaging camera is placed in front of the machine tool with the lenses perpendicular to the machining surface at the same height. The camera has been calibrated in the temperature range of 0 to 300 °C and is able to record the process at a resolution of 320 × 256 pixels with a frame rate of 670 Hz. Table 1 shows the investigated process parameters corresponding to the semi-finishing conditions commonly used in the industry. Each test was performed two times to ensure statistical repeatability. The measured transient temperature distribution of the tool as well as the measured process force components were used as validation variables for the simulation.

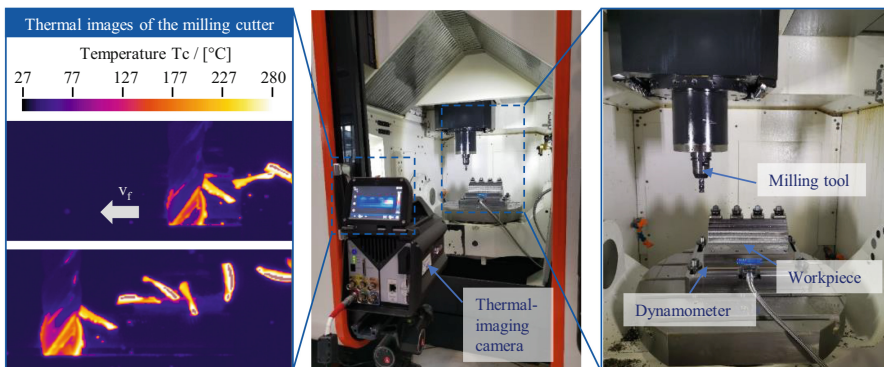


Fig. 1. Experimental setup for the validation of milling models.

Table 1. Process parameters for the cutting experiments.

Parameter	Symbol	Unit	Value
Cutting Speed	v_c	m/min	120, 150
Feed per tooth	f_z	mm	0.1, 0.2, 0.3
Width of cut	a_e	mm	2.5
Depth of cut	a_p	mm	7.5
Milling strategy	Down milling		

2.2 Workpiece Material and Cutting Tool

Machining experiments were performed with carbon steel AISI 1045, which has high strength and is widely used in industry for screws, bolts, shafts, and axles. The chemical composition of the workpiece material was measured by spark spectroscopy and is shown in Table 2.

Table 2. Chemical composition of the investigated AISI 1045.

Element	C	Si	Mn	P	S	Cr	Mo	Ni	Cu	Al
Mass fraction	0.469	0.145	0.686	0.025	0.026	0.337	0.036	0.087	0.056	0.029

The workpiece specimen was normalized at 860 °C, and its microstructure showed a homogeneous grain distribution, as shown in Fig. 2. The mechanical properties of the workpiece according to the material certificate are listed in Table 3.

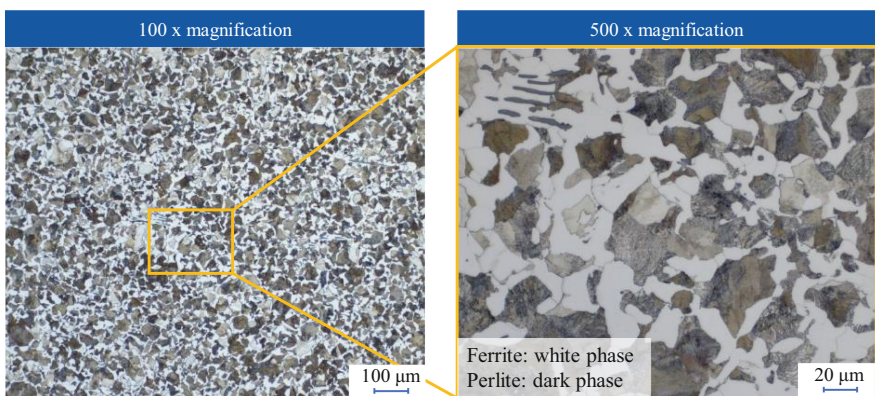

**Fig. 2.** Microstructure of AISI 1045 workpiece specimen.

Table 3. Chemical composition of the investigated AISI 1045.

Yield strength [N/mm ²]	Tensile strength [N/mm ²]	Elongation [A%]	Surface Hardness HB
392	695	23	200

The cutting tool used was a solid carbide end mill type CNMG 120404-SM from Sandvik Coromant without coating. The geometrical characteristics of the tool are summarized in Table 4.

Table 4. Technical data of the milling tool - 2P342-1600-CMA 1740.

Macro geometry	
Diameter of cutter – D / mm	16
Number of cutting edges – z / -	4
Flute helix angle – λ / °	38
Flute length – l / mm	34
Axial rake angle – γ_a / °	10.5
Radial rake angle – γ_r / °	10.5
Cutting edge radius – r_{β} / μm	10

3 Model Setup of Side Milling

In this paper, the Coupled Eulerian-Lagrangian (CEL) method is used to simulate the milling process. This method has the advantage that it can stably simulate the deformation of the solid with large strain rates and is therefore suitable for machining simulations. Figure 3 shows the model setup of the milling process and the partition of the Eulerian domain. The workpiece is defined by the volume fraction in the Eulerian domain and the tool is discretized into a Lagrange mesh. The height of the Eulerian domain is slightly larger than the depth of cut a_p . During the simulation, the tool performs only rotational movements and the workpiece the translational movement. The workpiece passes through the Eulerian mesh at feed velocity v_f . The workpiece section uses 5 μm hexahedral meshes to ensure the accuracy of the simulation.

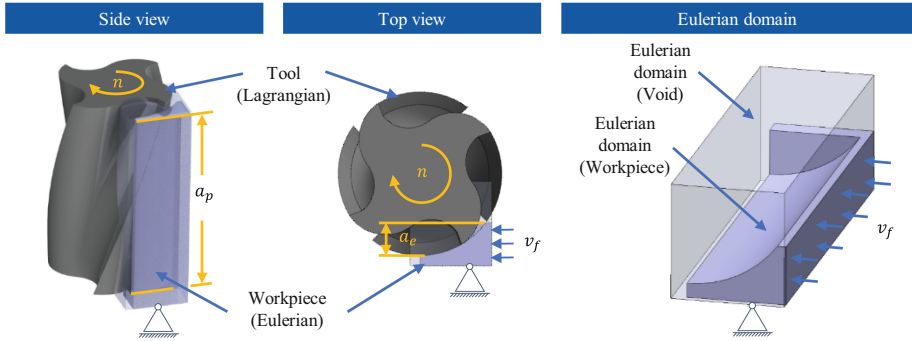


Fig. 3. Model setup of the CEL milling simulation.

The milling tool is considered as a rigid body, so that tool wear is neglected. Since the tool wear was measured after each cut during the tests and was very low, this assumption is valid. The friction between the tool and the workpiece is an important parameter since it determines the thermomechanical tool loads and the heat source distribution on the tool rake face. A temperature-dependent friction model developed by Puls [12] is implemented in the milling simulation, the mathematical expression is defined as follows:

$$\mu = \begin{cases} \mu_0, & T < T_f \\ \mu_0 \cdot \left[1 - \left(\frac{T - T_f}{T_m - T_f} \right)^{m_f} \right], & T \geq T_f \end{cases} \quad (1)$$

where T_f is the reference temperature and T_m is the melting temperature of AISI 1045. The model parameters for the contact between AISI 1045 and cemented carbide were experimentally calibrated in [12]. The plastic behavior of AISI 1045 was modeled as elasto-viscoplastic using Johnson-Cook material (JC) model [13]. The JC model characterizes material plasticity as a function of temperature, strain and strain rate and can be expressed as:

$$\sigma = (A + B \cdot \varepsilon^n) \cdot \left[1 + C \cdot \ln \left(\frac{\dot{\varepsilon}}{\dot{\varepsilon}_0} \right) \right] \cdot \left[1 - C \cdot \left(\frac{T - T_0}{T_m - T_0} \right)^m \right] \quad (2)$$

Table 5 summarizes the parameters of the material model and friction model used in this paper. Figure 4 shows the experimental results of the cutting forces for orthogonal cutting of the AISI 1045 used in this work compared to the results of the simulations using the CEL method. The simulated cutting forces agreed well with the experimental results, but the simulated thrust forces were underestimated. This is due to the inadequate description of the workpiece rebound after cutting by the material model. However, since the passive force is perpendicular to the cutting speed, it performs no mechanical work and thus has no contribution to the heat generation.

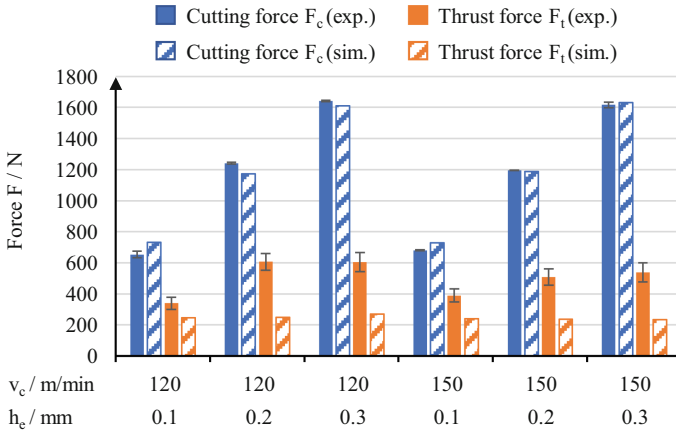


Fig. 4. Cutting force components of AISI 1045 from experiments and simulations for orthogonal cutting.

Table 5. Parameters of the material and friction models.

A [MPa]	B [MPa]	C-	m-	n-	μ_0 -	m_f -	T_f °C	T_m °C	T_0 °C	$\dot{\epsilon}_0$ s ⁻¹
541.5	460	0.04	1.047	0.05	0.7	0.35	600	1460	20	1

The simulations were performed with 48 cores on a high-performance computer with Intel Xeon Platinum 8160 processors “SkyLake” 2.1 GHz. The simulation time was on average 100 h for one revolution of the cutter. In the following section, the accuracy of the model is discussed by comparing the simulated and experimental cutting forces and tool temperatures.

4 Results and Discussion of Simulations and Experiments

In this section, simulated and experimental results are compared, and the accuracy of the simulations is thus evaluated. First, the active forces calculated from the cutting force components are compared, as shown in Fig. 5. The measurement results represent the transient force curve when the cutter is in stable engagement. The polar angle corresponds to the rotation angle of the milling cutter and the distance of the points from the origin indicates the force. Since the cutter has four flutes and only one flute was engaged at a time during the test, the polar force plots show a centrosymmetric petal-like distribution.

The experimentally measured forces are significantly smaller than the simulated forces. Furthermore, the measured force profile shows tool chatter, especially at the speed of $v_c = 120$ m/min. Tool chatter was not observed in the simulation because the simulation did not consider irregularities and disturbances in the actual machining process, such as thermal induced distortions, spindle runout and vibrations during machining. The deviation of the cutting forces is caused on the one hand by the underestimation of

the thrust forces, as shown in Fig. 4, and on the other hand by the “ploughing effect”¹. The smaller the uncut chip thickness, the greater the weight of the ploughing effect in the cutting process. In down milling, the uncut chip thickness gradually decreases from the maximum at the beginning of the engagement to the zero at the disengagement. The resulting cutting forces at the end of engagement act more on the cutting edge than on the rake face. This leads to a negative effective rake angle. Therefore, the use of material models determined from the orthogonal cutting for positive rake angles can lead to a large deviation in the milling simulation. One possible method to solve this deficit is to define different material models for the high and low uncut chip thickness.

The mechanical loads also have a direct effect on the temperature of the tool and the workpiece, since a large part of the mechanical work is converted into heat during the machining process. The simulated tool temperatures were compared with the experimental thermal images. CEL milling simulations are very time consuming and can only simulate one revolution of the cutter. To analyze the temperature development over a longer process duration, a hybrid simulation approach was applied, as shown in Fig. 6.

The CEL milling simulation provided the heat input into each flute at one revolution. This heat input was then used in a separate heat transfer model to simulate the long-term temperature development. The tool height for the temperature model is four times the depth of cut. Since the top surface is far from the heat source, it is set to an isothermal boundary condition with 27 °C. Except for the upper surface and the heat source, all surfaces are defined as adiabatic. The 3D heat transfer simulation is very fast compared to the cutting simulation. Therefore it is possible to simulate several seconds of the cutting process in a few minutes.

Figures 7 and 8 compare the simulated temperature field and the measured thermal image at different cutting conditions. The color indicates the temperature. To better resolve the temperature field, different scalar are used for experiment and simulation. The maximum temperature near the front cutting edges was measured and indicated in the figures. In general, the color of the temperature field shows a similar distribution between simulation and experiment. However, the absolute temperature from the simulation was overestimated. The difference in maximum temperature was about 100° at a feed per tooth of $f_z = 100$ mm and increased as the feed rises. The deviation can be attributed to the process forces. Due to the overestimation of the process forces, the heat generation in the cutting area in the simulation was higher than the actual value, resulting in a higher temperature. Moreover, the emissivity of the tool can lead to an additional deviation of the temperature measurement.

Figure 9 shows the simulated heat flow and the heat partition into the tool. The heat transferred into the tool was proportional to the cutting speed and the feed. The heat partition into the tool was 15.9% at $f_z = 0.1$ mm and to 17.8% at $f_z = 0.3$. The higher feed rate not only resulted in a higher heat input into the tool, but also in a higher heat partition. The reason for this is that at higher feed rates, more heat can be transferred into the tool due to the larger contact area between the tool and the chip. In contrast, the heat distribution in the tool was lower at higher cutting speeds. This is due to the fact that the higher cutting speed leads to faster heat removal by chips from the cutting area.

¹ Ploughing effect means that part of the material is pressed into the workpiece near the rounding of the cutting edge [14].

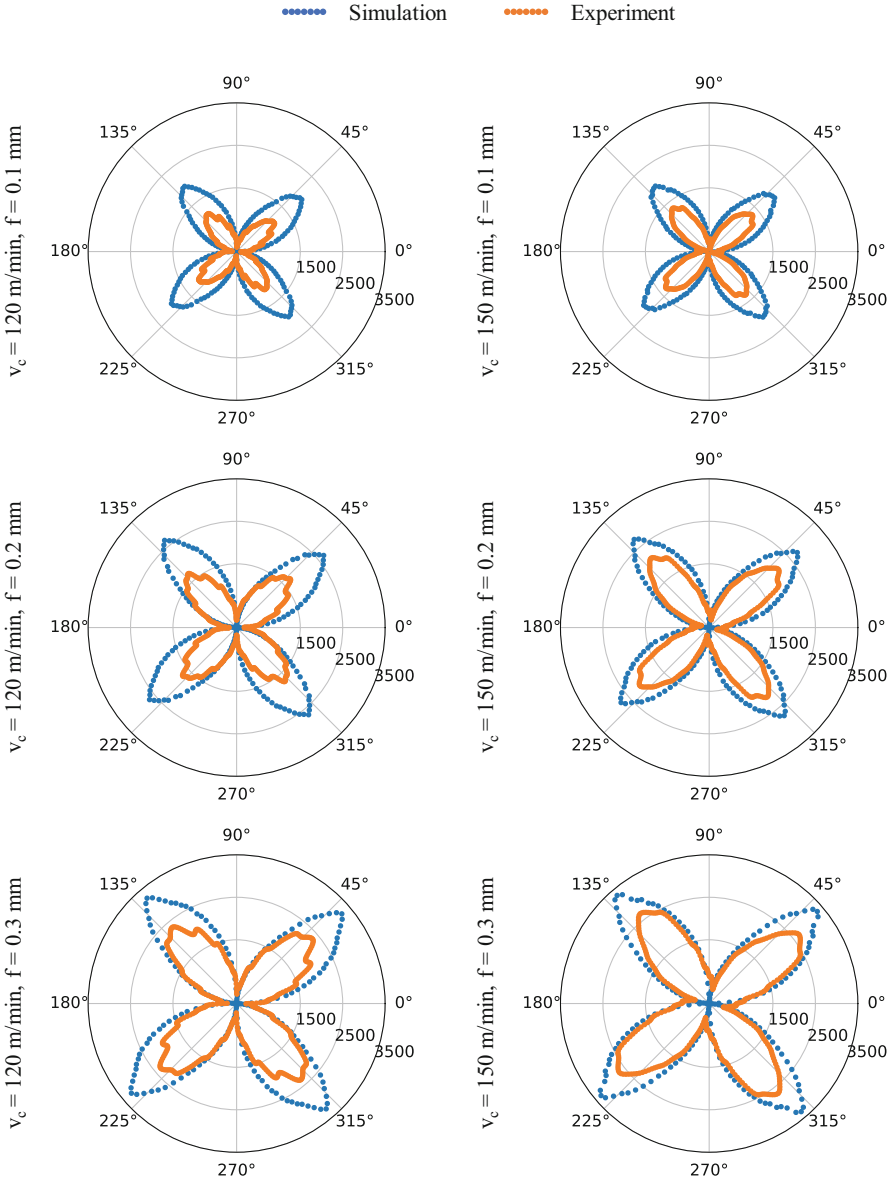


Fig. 5. Comparison of the measured and simulated active forces of the milling processes. The polar angle corresponds to the rotation angle of the milling cutter and the polar axis shows the magnitude of the forces F_a with the unit [N].

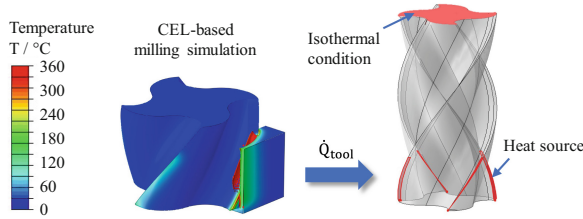


Fig. 6. Simulation approach for the analysis of tool temperature in long process times

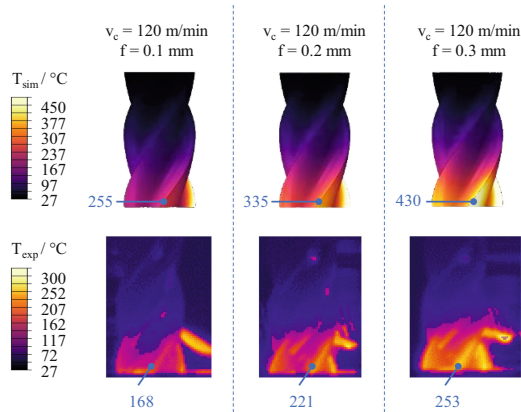


Fig. 7. Tool temperature from experiment and simulation at a cutting speed of $v_c = 120$ m/min and a process time of $t_c = 5$ s.

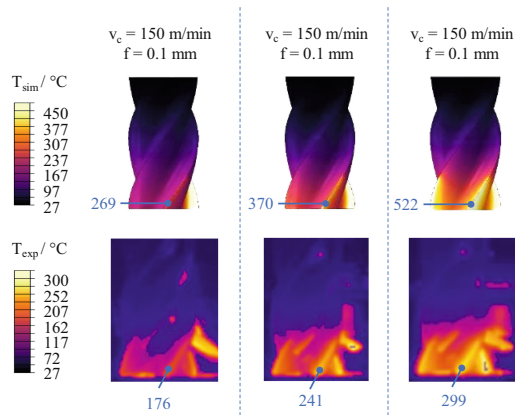


Fig. 8. Tool temperature from experiment and simulation at a cutting speed of $v_c = 150$ m/min and a process time of $t_c = 4$ s.

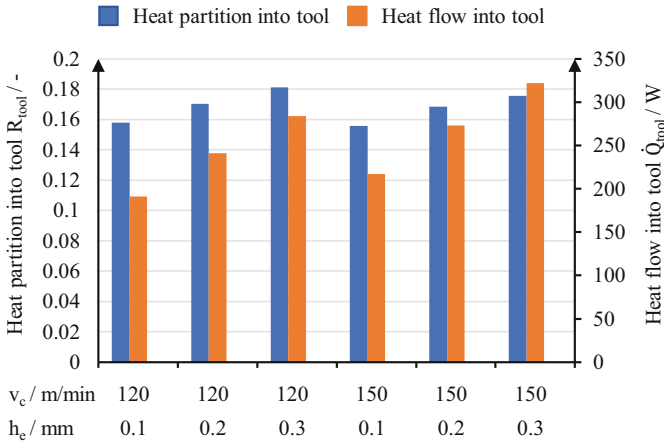


Fig. 9. Simulated heat partition and heat flow into the tool when milling AISI 1045.

5 Conclusion and Outlook

In this work, a new thermal coupled 3D FEM model based on the Coupled Eulerian Lagrangian (CEL) approach was proposed for the end milling process. The advantage of this model is the capability to analyze the temperature distribution in the tool. In particular, it allows direct determination of the heat partition into the tool under different cutting conditions. The model not only facilitates the thermal analysis of the cutting process, but also provides a theoretical basis for optimizing the process parameters under the aspect of thermal effects.

The comparison of the simulated results with experiments shows that the direct application of the material model determined for the orthogonal cutting to milling process leads to an underestimation of the process forces. One possible reason for this is the ploughing effect. When the uncut chip thickness decreases such that the ploughing effect dominates, the material model for large uncut chip thickness can no longer accurately represent the plastic properties of the workpiece. To address this issue, the use of different material models for large and small uncut chip thickness is proposed for the future work. To ensure the accuracy of the thermographic measurement, a reference measurement with a ratio pyrometer is required. This is because the ratio pyrometer measurement is not affected by the emissivity of the surface. Therefore, the emissivity can be calibrated by comparing the thermographic and pyrometer results.

Beside the process simulation, a hybrid simulation method for the fast calculation of the tool temperature is also presented. This simulation approach in combination with thermographic temperature measurements allows an efficient determination of the heat flow into the tool. Future research should focus on the validation of the model under different milling conditions. The general validity of the model needs to be further verified. Moreover, different tool geometries can be analyzed by simulations to determine the relationship between heat partition and tool design. This can not only save R&D costs, but also provide theoretical guidance for the tool optimization.

Acknowledgements. The authors would like to thank the German Research Foundation (DFG) for the funding the SFB/Transregio 96 collaborative research (Project ID 174223256-TRR 96) subproject A02. Furthermore, the authors gratefully acknowledge the computing time provided to them at the NHR Center NHR4CES at RWTH Aachen University (project number p0020236). This is funded by the Federal Ministry of Education and Research, and the state governments participating on the basis of the resolutions of the GWK for national high performance computing at universities (www.nhr-verein.de/unsere-partner).

References

1. Augspurger, T.: Thermal Analysis of the Milling Process, 1st edn. Apprimus Wissenschaftsverlag, Aachen (2018)
2. Sato, M., Tamura, N., Tanaka, H.: Temperature variation in the cutting tool in end milling. *J. Manuf. Sci. Eng.* **133** (2011). <https://doi.org/10.1115/1.4003615>
3. Stephenson, D.A., Ali, A.: Tool temperatures in interrupted metal cutting. *J. Eng. Ind.* **114**, 127–136 (1992). <https://doi.org/10.1115/1.2899765>
4. Zhu, Z., Xi, X., Xu, X., et al.: Digital twin-driven machining process for thin-walled part manufacturing. *J. Manuf. Syst.* **59**, 453–466 (2021). <https://doi.org/10.1016/j.jmsy.2021.03.015>
5. Bergs, T.: Internet of production - turning data into value. Fraunhofer-Gesellschaft (2020)
6. Bergs, T., Gierlings, S., Auerbach, T., et al.: The concept of digital twin and digital shadow in manufacturing. *Procedia CIRP* **101**, 81–84 (2021). <https://doi.org/10.1016/j.procir.2021.02.010>
7. Hänel, A., Seidel, A., Frieß, U., et al.: Digital twins for high-tech machining applications—a model-based analytics-ready approach. *JMMP* **5**, 80 (2021). <https://doi.org/10.3390/jmmp5030080>
8. Abdelhafeez, A.M., Soo, S.L., Aspinwall, D., et al.: A coupled Eulerian Lagrangian finite element model of drilling titanium and aluminium alloys. *SAE Int. J. Aerosp.* **9**, 198–207 (2016). <https://doi.org/10.4271/2016-01-2126>
9. Gao, Y., Ko, J.H., Lee, H.P.: 3D coupled Eulerian-Lagrangian finite element analysis of end milling. *Int. J. Adv. Manuf. Technol.* **98**(1–4), 849–857 (2018). <https://doi.org/10.1007/s00170-018-2284-3>
10. Persson, H., Agmell, M., Bushlya, V., et al.: Experimental and numerical investigation of burr formation in intermittent turning of AISI 4140. *Procedia CIRP* **58**, 37–42 (2017). <https://doi.org/10.1016/j.procir.2017.03.165>
11. Vovk, A., Sölter, J., Karpuschewski, B.: Finite element simulations of the material loads and residual stresses in milling utilizing the CEL method. *Procedia CIRP* **87**, 539–544 (2020). <https://doi.org/10.1016/j.procir.2020.03.005>
12. Puls, H., Klocke, F., Lung, D.: Experimental investigation on friction under metal cutting conditions. *Wear* **310**, 63–71 (2014). <https://doi.org/10.1016/j.wear.2013.12.020>
13. Johnson, G.R., Cook, W.H.: Fracture characteristics of three metals subjected to various strains, strain rates, temperatures and pressures. *Eng. Fract. Mech.* **21**, 31–48 (1985). [https://doi.org/10.1016/0013-7944\(85\)90052-9](https://doi.org/10.1016/0013-7944(85)90052-9)
14. Albrecht, P.: New developments in the theory of the metal-cutting process: part I. the ploughing process in metal cutting. *J. Eng. Ind.* **82**, 348–357 (1960). <https://doi.org/10.1115/1.3664242>

Open Access This chapter is licensed under the terms of the Creative Commons Attribution 4.0 International License (<http://creativecommons.org/licenses/by/4.0/>), which permits use, sharing, adaptation, distribution and reproduction in any medium or format, as long as you give appropriate credit to the original author(s) and the source, provide a link to the Creative Commons license and indicate if changes were made.

The images or other third party material in this chapter are included in the chapter's Creative Commons license, unless indicated otherwise in a credit line to the material. If material is not included in the chapter's Creative Commons license and your intended use is not permitted by statutory regulation or exceeds the permitted use, you will need to obtain permission directly from the copyright holder.



Model Verification



Definition of a Non-contact Induction Heating of a Cutting Tool as a Substitute for the Process Heat for the Verification of a Thermal Simulation Model

Lukáš Topinka¹(✉), Radomír Pruša², Rostislav Huzlík², and Joachim Regel¹

¹ Institute for Machine Tools and Production Processes (IWP), Chemnitz University of Technology, Chemnitz, Germany

lukas.topinka@mb.tu-chemnitz.de

² Institute of Production Machines, Systems and Robotics, Brno University of Technology, Brno, Czech Republic

Abstract. During metal machining, a large amount of heat is generated in the cutting zone, which has a negative impact on machining accuracy due to the thermal expansion of the materials. To reduce the temperature in the cutting zone, liquid coolants are used which increase the costs and can have a negative impact on the environment. This problem is being studied using Computational Fluid Dynamics (CFD) to better understand the behavior of the coolant flow in the cutting zone, which will allow optimization of the use of liquid coolants and the development of a correction method for thermal errors, resulting in more accurate machining with reduced resource and environmental footprints. However, due to the complexity of multiphase CFD simulations, the simulation model must be simplified as much as possible. This is particularly important for the process heat generation, as combining flow simulation of coolant flow around the rotating cutting tool with structural simulation of the milling process, including chip formation, would require excessive computational power. In following paper an alternative method of tool heating by electromagnetic induction is presented and the measurement dependencies required to determine the heat flux induced into the cutting tool are described. This can be further applied as a boundary condition for the numerical simulation as a verification method for the coupled Fluid-Structure Interaction FSI simulation model of the thermally induced deformations of the cutting tool and its holder.

Keywords: Thermal error · Cutting tool · Induction heating

1 Introduction

During a milling process, the tool engages the workpiece and removes material in the form of chips to achieve the final shape of the workpiece. This chip removal is caused by plastic deformation of the workpiece material due to high machining forces, which results in high frictional forces between the tool and the workpiece. This causes a large

amount of heat generated in the cutting zone. The generated heat is largely removed through the chips, but some of the heat is accumulated in the tool, causing its thermal deformation. This has a negative effect on the dimensional accuracy of the machined workpiece, and thereby reduces the efficiency of the machining itself.

Today, liquid cooling is a standard for a wide range of cutting processes. In addition to cooling the cutting zone itself, the use of a liquid coolant affects chip formation and friction between the cutting tool and the workpiece, thus changing heat transfer and reducing heat generation in the cutting zone [1, 2]. The use of cutting fluids not only increases the cost of a given machining process, but also reduces its environmental friendliness. However, simply reducing the amount of cutting fluid in the cutting zone can negatively affect the entire process and increase the dimensional variation of the workpiece due to thermal deformations.

In order to improve the efficiency of machining processes, the SFB/Transregio96 cooperative project has been set up, where the influence of different cooling strategies on the thermal behaviour of the cutting tool and thus its dimensional deviation is being investigated in subproject A01, mainly by means of numerical simulations. The aim of this subproject is not only to increase the efficiency of the use of cutting fluids and thus reducing both machining costs and environmental burden, but also to develop a correction method for thermal errors during the machining process itself and thus enable more accurate machining.

The simulation model is being developed within the framework of subproject A01 to simulate different cooling methods of cutting tools combines fluid (CFD), thermal and structural simulations within a Fluid Structure Interaction (FSI) coupling, as introduced in [3]. This simulation model has to be experimentally verified using real measured data to verify the accuracy of the simulated results.

The first stage is a fluid simulation of the coolant flow. Due to the complexity of fluid simulations in combination with vortex and turbulent flows around a rotating tool, the simulation model needs to be simplified as much as possible, i.e. only the components necessary to simulate the problem should be included, as described in [4]. After the functional fluid simulation, the thermal conditions need to be set to simulate the effectiveness of the different cooling strategies.

To verify thermal simulations, suitable boundary conditions must be defined that can be compared with the experimental measurements. These include stable and defined ambient conditions, which is why such investigations are often carried out in an isolated climate cell [5], as well as the accurate definition of the heat input in the machine structure like heating mats as a substitute for planar or punctual heat sources [6]. Since simulating the real cutting process including chip removal would be too time consuming and therefore inefficient, an alternative heating method must be developed that will supply a defined amount of heat to the tool while allowing the tool to rotate and not affecting other factors such as coolant flow. There are various ways of heating the cutting tool as a substitute for the heat from the cutting zone with the possibility of defining the heat flux into the cutting tool, e.g. heating rod, laser or induction heating. This article describes a method for heating the cutting tool by an electromagnetic induction and determining the heat input based on current and power measurements on the inductor and supported by an electromagnetic simulation.

2 Induction Heating and Design Boundary Conditions

Induction heating is described by Faraday's law of induction, which function is similar to that of a transformer. The primary winding is supplied with alternating current and emits an electromagnetic field. The heated object represents the secondary winding and receives the radiated magnetic field. According to the previously mentioned Faraday's law, a voltage is induced in the object and eddy currents are generated. Due to the eddy currents, Joule heat is released, i.e. the energy of electromagnetic radiation is converted into thermal energy. Heating by induction does not occur uniformly throughout the volume, but depends on the so-called penetration depth δ . The penetration depth is calculated according to the equation:

$$\delta = \sqrt{\frac{2}{\omega \cdot \mu \cdot \sigma}} \quad (1)$$

where ω is the angular velocity, μ is the magnetic permeability and σ is the specific electrical conductivity [7]. From the point of view of efficiency, the penetration depth is also important, since 99.6% of the total energy in the material is dissipated in three times the penetration depth [8]. For penetration depth, it is 86.5% of the energy [8]. In the case of magnetic simulations, it is necessary to keep this fact in mind and focus on that area.

Induction heating was found to be suitable for simulated heating of the cutting tool as it allows non-contact heating. This allows the cutting tool to rotate and be cooled by the liquid, so simplified boundary conditions can be used for the CFD simulation model. However, it is necessary to establish the basic criteria that the primary inductor coil should meet. The coil should have a sufficient inner diameter to ensure there is enough space between the coil and the tool so that the fluid flow around the tool is not affected by the position of the coil. On the other hand, a smaller coil diameter results in a better energy transfer to the tool and therefore a more effective tool heating. For this purpose, an inductor coil with an inner diameter of 56 mm was wound from a copper wire with a circular cross-section and a diameter of 1.8 mm. From the point of view of tool heating in machining, it is desirable that only a certain area is heated. The length of the primary coil must be as short as possible so that most of the heating power can be applied near the tip of the tool. Therefore, a coil with three wiring in two layers was designed, which enables the length of the coil to be reduced to only 8 mm, but also provides a small distance between the wires and thus a better flow of ambient air, helping in cooling the coil, as the coil was not internally cooled.

3 Determination of Heating Power

In the first step, a substitute tool model with a simplified shape was chosen instead of a further used end mill tool. The substitute was a cylinder with an outer diameter of 20 mm and a length of 105 mm, corresponding with the dimensions of the end mill tool. That simplifies the boundary conditions for the first version of an electromagnetic simulation model and avoids systematic errors in measurements and simulations due to the rotationally symmetrical shape of the test cylinder. The material of this test cylinder as well as of the further used end mill was HSS-E.

To provide the necessary conditions for the implementation and verification of the heating functionality, an experimental test stand was created, which is schematically shown in Fig. 1. The test stand can be divided into two sides - the power supply and the measurement section. The power supply section consists of a DC power supply for the frequency converter. At the end of the circuit the primary coil was constructed as described in the previous section. The frequency converter is based on a bistable oscillating circuit. The output sinusoidal signal is achieved by resonance between the capacitors and the primary inductor coil.

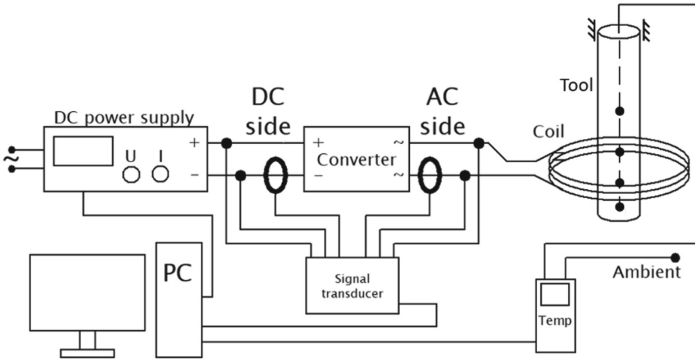


Fig. 1. Schematic arrangement of the measuring test stand

The measured electrical parameters were voltages and currents on DC and AC side. The determination of the electrical power on the DC side was easy and accurate. On the other hand, the determination of the power on the AC side was complicated. This was due to the limited accuracy of the high frequency current measurement. The converter was set to output at 40 kHz. Most current transducers have a given bandwidth, i.e. the waveform and magnitude are not problematic to determine. The calculation of electrical power results from the instantaneous voltage and current. For a valid power quantity, not only an exact amplitude value but also time accuracy, i.e. the phase shift between voltage and current, is required, as described in [9]. The selected power configurations on the DC side and the measured values on the AC side for this validation approach are given in Table 1. These power values were selected after a few probe measurements with the aim of not exceeding 100 °C, which was sufficient for the verification of the described methodology. For verification, it was not necessary to reach higher hundreds of degrees Celsius, as this could damage the plastic fixture used and thus reduce the reliability of the verification.

Table 1. Selection of power configuration and measured values test cylinder

$P_{DC}[W]$	$U_{DC}[V]$	$I_{DC}[A]$	$I_{pk-pk}[A]$	$f[kHz]$
6.5	3.91	1.67	22.4	39.47
8.2	4.26	1.93	25.5	39.39
10.1	4.59	2.21	28.6	39.34
12.2	4.94	2.47	31.4	39.29

3.1 Electromagnetic Simulation and Verification of Heating Power

In the second step, a 3D model of the induction coil and the heated object was created in the environment of ANSYS Maxwell® with the configuration based on the experimental test stand. This model simulates the electromagnetic field and resulting ohmic losses causing the heating of the object. The coil model has been simplified as the supply wires have not been considered. From a simulation point of view, this simplifies the creation of the mesh, since the possible error due to field asymmetry is negligible.

To be able to prove the correctness of the simulation model, the heated object in the first series of the simulations was a test cylinder. The basic shape of the cylinder enabled to verify the precision of the simulated results analytically. The dimensions and material of the test cylinder were chosen to correspond with further used end mill tool. The unknown electromagnetic properties, such as permeability, were defined based on the material steel_1010 from the ANSYS Maxwell® material library, which was the nearest to HSS-E from the available material data. This enabled to compare the transmitted energy for both test objects. The input boundary parameters were the amplitude of the measured current on the AC side and the measured frequency obtained on the previously described test stand (see Fig. 1).

Initial verification of the electromagnetic simulation was based on two main parameters – penetration depth δ , described in Sect. 2, and the calculated ohmic losses in the test object caused by eddy currents. For the basic test cylinder, these parameters could be analytically determined and thus compared with simulated results. For this verification, it was necessary to measure the total power delivered to the circuit and determine the heating power transmitted to the test object among other loss components. The total power measured on the DC side consists of following components:

- power dissipated by the frequency converter ΔP_C
- power dissipated by the supply cables ΔP_w
- ohmic losses of the main induction coil ΔP_J
- power transmitted by leakage magnetic fluxes to the surrounding environment and objects ΔP_o
- power transmitted to the body under test P .

All the listed power components could not be exactly identified or calculated. However, some of them could be neglected, as their percentage share is negligible compared to the other components. Since the efficiency of inverters is generally around 95% [10], the loss ΔP_C could be neglected. The DC supply cable was short with conductors of

sufficient cross section, therefore the losses ΔP_w could also be neglected. Due to the sufficient distance from all metallic objects and the large magnetic conductivity of the test object, the loss due to leakage magnetic fluxes ΔP_o was also negligible. On the other hand, the loss on the main induction coil ΔP_J cannot be neglected, because the coil also heats up during the measurements, which means a significant part of a total energy is transmitted into the heating energy of the coil. Based on the previous assumptions, the total power delivered to the test object P can be calculated according to the following equation:

$$P = U_{DC} \cdot I_{DC} - R \cdot I_{RMS}^2 \quad (2)$$

where R is the resistance value of the main induction coil, I_{RMS} is the effective current value on the AC side. When measuring the resistance of the induction coil, it was necessary to consider the increase in resistance due to the skin effect. For this reason, it was necessary to measure the magnitude using e.g. a milliohmmeter to adjust the measuring magnitude of the frequency at which the measurement will take place. According to Table 1, the supply frequency on the AC side was around 40 kHz. The resulting measured value was 20 mOhm. Furthermore, it was important to measure the resistance without the presence of the test object, otherwise the measured resistance would be increased by the iron losses occurring in this object. Table 2 shows the values obtained from the simulation of the electromagnetic field and the measurement and subsequent calculation for the test cylinder.

Table 2. Comparison of simulated and calculated ohmic losses for the test cylinder

Measurement			Simulation		Difference
$P_{DC}[W]$	$P_J[W]$	$P_M[W]$	$P_J[W]$	$P_S[W]$	$P_{M-S}[W]$
6.5	1.2	5.3	1.4	4.9	0.4
8.2	1.6	6.6	1.9	6.3	0.3
10.1	2.0	8.1	2.3	7.9	0.2
12.2	2.5	9.7	2.8	9.5	0.2

The result in Table 2 present that the power obtained from the measurement was higher than the simulated power. This confirms the fact, that the measured power included the neglected losses (ΔP_C , ΔP_w , ΔP_o) and thus resulted to slightly higher values of power dissipated into the test object. Furthermore, it can also be noticed that about 20% of the total power was dissipated in the main induction coil, causing its heating. Figure 2 shows an example of the solution for the power of 10,1 W on the DC side, specifically the representation of the ohmic losses in the test object. It is apparent that most power is transferred near to the coil position, where the electromagnetic field is strongest. Moreover, in the frontal cross-section it can be seen that the energy is mainly transferred only in the thin layer (penetration depth δ), which is confirming the information given before.

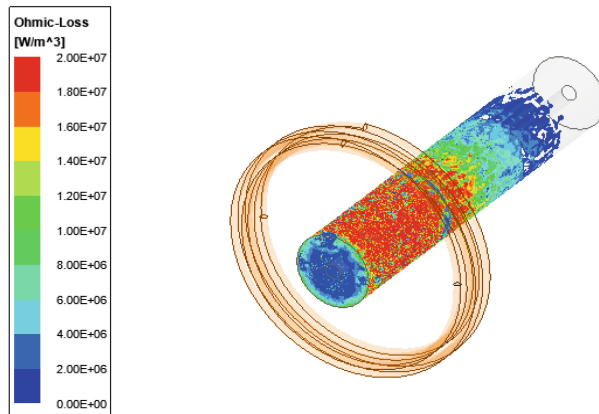


Fig. 2. Simulation results of ohmic loss in the test cylinder for DC power 10.1 W in ANSYS Maxwell®

3.2 Simulation of the Heating Power of an End Mill Tool

After the electromagnetic simulation of the basic test cylinder had been verified and its results were reliable, the model of the heated test cylinder could be replaced. The new heated object was a four-edged end mill, which was used for the investigations described in Sect. 1. The dimensions of the previously used test cylinder, corresponding to those of the end mill, allowed easy replacement, while keeping the coil position and the experimental setup the same, so that a comparison between both heated objects was possible. The experimental test stand with the end mill is shown in Fig. 3.

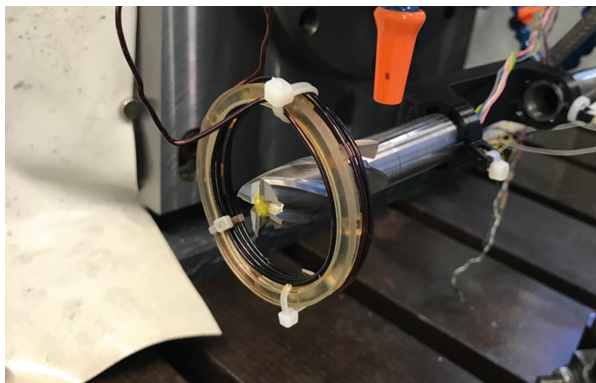


Fig. 3. Experimental setup on test stand with end mill tool

The same series of the previously described measurements was carried out on the test stand with the real end mill tool, made from the same material as the previous test cylinder, in order to obtain initial boundary conditions for the simulation. An example of simulated results in Fig. 4 shows similar distribution of the acting field, respectively

ohmic losses as in the previous simulation with the basic cylinder. This is caused by the electromagnetic field created around the main induction coil, which behaved similarly in both cases.

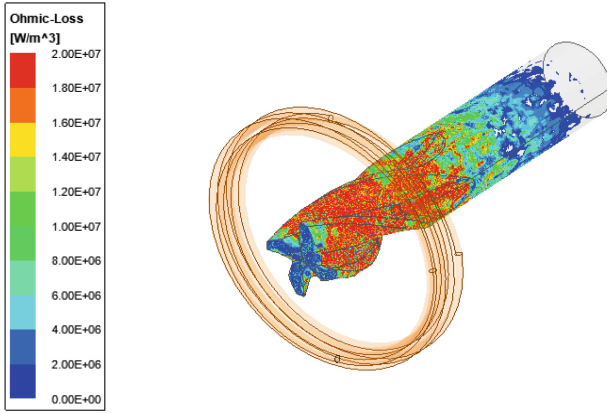


Fig. 4. Simulation results of ohmic loss in the end mill for DC power 10.1 W in ANSYS Maxwell®

The power dissipation into the end mill was also calculated based on the measured data and the Eq. (2). However, in comparison to the values obtained for the test cylinder, a slightly lower efficiency of heating purpose can be seen, as the power dissipated into the end mill tool was around 75–78% of the total power on the DC side, as shown in Table 3.

Table 3. Comparison of simulated and calculated ohmic losses for the end mill

Measurement			Simulation		Difference
$P_{DC}[W]$	$P_J[W]$	$P_M[W]$	$P_J[W]$	$P_S[W]$	$P_{M-S}[W]$
6.5	1.4	5.1	1.6	4.5	0.6
8.2	1.9	6.3	2.2	5.8	0.5
10.1	2.3	7.8	2.7	7.3	0.5
12.2	2.9	9.3	3.4	8.9	0.4

It should be noted that the resulting deviation of the results for both the test cylinder and the end mill tool may be caused not only by the simplified and thus slightly different shape and volume of the heated objects, but also by inaccuracies in the measurement process and due to the slightly simplified simulation models and boundary conditions. In the calculated differences P_{M-S} , the tendency can be seen that the difference decreases with increasing power configuration. However, the aim of this study was to find out whether it is possible to define the heating power as heat input into the simulation model

when using induction heating, and thus to use and further develop this methodology. The further goal is to tend rather to higher reached temperatures, and thus to use higher heating powers. There, the difference between experimental measurements and simulations is smaller and therefore the further investigation on finding the most influencing factor for these deviations was not carried out.

4 Thermal Simulation

The simulated ohmic losses from the previous electromagnetic simulation were exported as a 3D field based on Cartesian coordinates. This data file was further imported into a thermal simulation model as an input boundary condition for the simulated heating of the tested end mill. The comparison of these simulated thermal results and measured temperatures on the test stand (as described in Sect. 1) was the last step to prove the functionality of this methodology.

The thermal simulation model was created in the ANSYS CFX in a similar way as the FSI simulation model mentioned earlier in this article. Since the plastic fixture has only a few contact surfaces with the heated end mill, its presence in the simulation model would have minimal effect on the simulated temperatures but would increase the meshing requirements of the model and thus increase the calculation time. The same applies to the coil near the end mill tip, as it can slightly affect the flowing air, but not in such a way that it would influence the simulated temperatures. For this reason, both parts were neglected in the simulation model, which simplifies the conditions for meshing and allows faster and smoother convergence of the simulation model without significantly affecting the simulated results. Therefore, the thermal simulation model contained only a 3D model of tested end mill tool and a small ambient air area. The material parameters were defined according to the material properties of the HSS-E end mill on the test stand with a thermal conductivity of 27,4 W/mK and a specific heat capacity of 420 J/kgK.

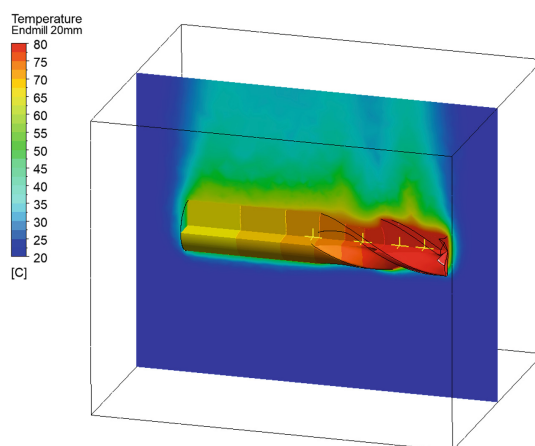


Fig. 5. Simulated temperature field of the end mill for set power of 10.1 W on the DC side in ANSYS CFX

Figure 5 shows an example of a resulting color map of the simulated temperature field of the end mill and ambient air from the steady-state simulation with marked positions of the read temperatures for power of 10,1 W on DC side.

The steady-state thermal simulations were carried out for the same series of power values as the electromagnetic simulations. In order to verify the results, the temperature profile on the tested end mill was measured during induction heating with four PT 100 sensors implemented into the tested tool. These sensors were placed into a small hole drilled along the rotational axis in the distances of 10, 20, 35 and 55 mm from the top face on the coil side. The position of the sensors along the axis of the tested object minimizes the possible influence of electromagnetic field as it acts just under the surface of the tool. The entire test setup was placed in a closed test stand, where the ambient temperature was measured so that the boundary conditions were stable and defined. The measurement time interval was 120 min. Although the measured time interval exceeds most milling operations, it was necessary to heat the tested tool fully to achieve a steady-state thermal condition for proper verification of the simulation model, since comparing only a few seconds of measured heating curve would not be sufficient for proper verification and would require transient simulation. The resulting steady-state temperatures could be compared with the simulated temperature values at positions corresponding to the position of the sensors during the experimental measurements. Since heating measurements can be affected by external conditions, such as changes in ambient temperature, all measurements were repeated three times. Subsequently, the *t*-distribution was used to calculate a confidence interval of the measured temperatures with a confidence level of 95%, based on the equation:

$$x_{CI} = \bar{x} \pm t \frac{s_x}{\sqrt{n}} \quad (3)$$

with the standard deviation of the number *n* of measured samples and the *t*-score for the selected confidence level. The calculated confidence intervals for each measured sample and applied heating power were used for comparison with the simulation results, as shown in Fig. 6.

The temperature results presented in Fig. 5 show a small deviation between the measured and simulated values. In the simulation, the temperature difference between the two sensor positions near the tool tip is slightly lower than the measured temperatures. However, the third and fourth sensor position already show a correct course. This deviation of the simulated results from the measured temperatures, respectively from the calculated confidence intervals, at the first two sensor positions may be caused by the smaller distance to the induction coil. At this area the intensity of the electromagnetic field is higher and thus the measured or simulation-based inaccuracies may also have a larger impact than at the other two sensor positions. However, despite these deviations, the simulated temperatures still achieve sufficient accuracy for further application of this methodology.

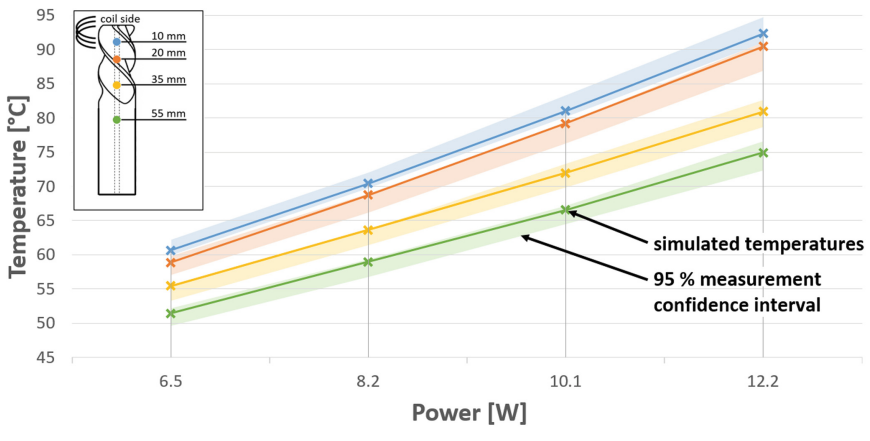


Fig. 6. Comparison of simulated temperatures with 95% confidence intervals from measured temperatures for selected power configuration

5 Summary

FSI-coupled simulations need to be verified experimentally. For this purpose, it is necessary to set a realistic and precisely defined heat input into the tool. This is not possible through a real machining process, since the simulation of the entire machining operation would be too complex. Induction heating has shown to be capable of heating a given test tool, and it is also possible to determine the induced energy through electromagnetic simulations supported by experimental measurements. By measuring the high-frequency waveform of the current flowing through the induction coil (in particular amplitude and frequency), the input values for the simulation in ANSYS Maxwell® were obtained. Simulation with the 3D models of the induction coil and the heated test tool was performed to determine the ohmic losses in the test tool, which are subsequently converted into heating power. This electromagnetic simulation was validated by measurements for a series of four different power levels. The subsequent comparison demonstrated that the measured power was higher than the simulated power. This proves the accuracy of the results, since the measured power includes P_{DC} losses that were neglected in the numerical simulation (ΔP_C , ΔP_w , ΔP_o).

The simulated ohmic losses in the test cylinder were further applied as a heat source in the thermal simulation created in ANSYS CFX. This simulation was set up to simulate the thermal heating process to prove the functionality of this methodology. A comparison of the simulated and 95% confidence intervals calculated from measured temperature values showed slight deviations, which may be caused by both the measurement inaccuracies and the simplifications of the simulation models. However, after taking into account multiple possible inaccuracies through the whole methodology, the final simulated temperatures reach approximately same values as the measured ones.

This paper proves the described methodology of the induction heating of the cutting tool and its simulation as sufficiently accurate and functional. Furthermore, a liquid cooling can be implemented into the methodology described in this paper as a last

step before the possibility of full verification of more complex FSI simulation model developed for the investigation of thermally induced displacement of the tool center point of the cutting tool under influence of a liquid coolant.

Acknowledgement. This work is funded by the German Research Foundation – Project-ID 174223256 – TRR 96. The authors are grateful for the provided support.

References

1. Helmig, T., Göttlich, T., Liu, H., Nguyen, N., Bergs, T., Kneer, R.: Numerical investigation on evolving chip geometry and its impact on convective heat transfer during orthogonal cutting processes. In: Proceedings of the 9th International Conference on Fluid Flow, Heat and Mass Transfer (FFHMT'22) (2022)
2. Liu, H., Peng, B., Meurer, M., Schraknepper, D., Bergs, T.: Three-dimensional multi-physical modelling of the influence of the cutting fluid on the chip formation process. *Procedia CIRP* **102**, 216–221 (2021)
3. Brier, S., Regel, J., Putz, M., Dix, M.: Unidirectional coupled finite element simulation of thermoelastic TCP-displacement through milling process caused heat load. *MM Sci.* **51**, 465–483 (2021)
4. Topinka, L., Bräunig, M., Regel, J., Putz, M., Dix, M.: Multi-phase simulation of the liquid coolant flow around rotating cutting tool. *MM Sci.* **5**, 5148–5153 (2021)
5. Glänzel, J.: Einzigartige Thermozone zur Untersuchung klimatischer Effekte auf Werkzeugmaschinen, *wt Werkstattstechnik online* **107**, 511–512 2017
6. Regel, J.: Bewertung konstruktiver und kompensatorischer Maßnahmen zur thermo-sensitiven Auslegung von Werkzeugmaschinenstrukturen, Dissertation (2018)
7. Lammeraner, J., Staff, M.: Eddy currents 232 (1964)
8. Hradilek, H., Laznicková, I., Kral, V.: Elektrotepelna premena 2011
9. Puyal, D., Bernal, C., Burdío, J.M., Acero, J., Millan, I.: Methods and procedures for accurate induction heating load measurement and characterization In: *IEEE Xplore*, pp. 805–810 (2007)
10. Park, C.Y.: Inverter efficiency analysis model based on solar power estimation using solar radiation 2020

Open Access This chapter is licensed under the terms of the Creative Commons Attribution 4.0 International License (<http://creativecommons.org/licenses/by/4.0/>), which permits use, sharing, adaptation, distribution and reproduction in any medium or format, as long as you give appropriate credit to the original author(s) and the source, provide a link to the Creative Commons license and indicate if changes were made.

The images or other third party material in this chapter are included in the chapter's Creative Commons license, unless indicated otherwise in a credit line to the material. If material is not included in the chapter's Creative Commons license and your intended use is not permitted by statutory regulation or exceeds the permitted use, you will need to obtain permission directly from the copyright holder.





Measuring Thermally Induced Tool Center Point Displacements on Milling Machines Using a Test Workpiece

Axel Fickert¹ , Hajo Wiemer¹ , Carola Gißke², and Lars Pentler¹ 

¹ Technische Universität Dresden, LWM, Helmholtzstr. 7a, 01067 Dresden, Germany
axel.fickert1@tu-dresden.de

² Digital Health, Technische Universität Dresden, Münchner Platz 3, 01087 Dresden, Germany

Abstract. The Collaborative Research Centre (CRC) “Transregio 96” focuses on the thermo-elastic behaviour of machine tools and the development of solutions, that aim at reducing thermally induced manufacturing errors. Various compensation and correction solutions were developed. To verify the efficiency of those solutions, a measuring technique involving a test work piece (TWP) and defined load cases were developed. The load cases are given in the form of NC-programs to create thermal loads on a machine tool by moving its feed axes on a pre-defined route, rotating the main spindle at pre-defined speeds or letting the machine tool rest for a pre-defined period of time. The TWP was used to capture the resulting thermally induced displacements of the tool center point (TCP).

In this publication the TWP and the two load cases are described. And the test procedure itself, as well as experimental data to validate the results are presented. The described approach has the potential to be a cost effective way for measuring thermally induced errors of machine tools. It allows for a simple and time saving experimental setup and is easy to apply on, and compare the results between multiple machine tools. Furthermore, the presented method of determining thermally induced displacements of a machine tool’s TCP will be compared to other commonly used direct or indirect measurement techniques, showing its benefits, drawbacks and limitations.

Keywords: measuring TCP errors · thermally induced TCP displacements · milling machine · tool center point · test work piece · thermal influence · milling

1 Introduction

Machine tools are exposed to thermal influences that can reduce the machining accuracy. The development phase and operational phase of milling machines require evaluating the accuracy of motion in order to guarantee high machining accuracy. Tactile measuring methods using linear displacement sensors (defined in DIN ISO 230-3), circular shape tests with double ball bars (defined in DIN ISO 230-4) or, less frequently, test work pieces (TWP) are current standards for this purpose. The TWPs according to VDI 2851, NAS 913, ISO 10791-7 and VDI/DGQ 3441 are used to determine reversal span, positioning

accuracy, interpolation properties, quadrant reversal, form and dimensional deviations based on standardized or recommended testing procedures. However, these TWP's do not allow for separating thermally induced geometrical errors of a machine tool from other error proportions [1]. Tactile measurements are not applicable during machining. Various test work pieces have been proposed [2–4], to measurement TCP displacements as a function of time. But recording the progressions of thermally induced motion errors and deviations of position over the course of a production shift remain unknown. Therefore, the Collaborative Research Centre “Transregio 96” (CRC) developed a compact TWP to measure thermally induced TCP errors during three axes milling operations over a time span of 6 h. This paper introduces the TWP and compares the TWP results to tactile measurements with linear displacement sensors according to DIN230-3.

2 Experimental Setup and Methods

Section 2 describes the developed TWP, the experimental setup, the procedure of validation measurements as well as data acquisition and processing.

2.1 Test Work Piece (TWP)

The imprint of TCP displacements into the TWP caused by the kinematic and static properties of the machine tool as well as the effects of process forces and wear had to be minimized. In addition, it was necessary to record the TCP displacements as a function of time until thermal steady state of the machine tool is reached.

The TWP has three reference surfaces corresponding to the X-, Y-, and Z-axis of the machine tool, which are machined at the beginning of an experiment. They represent the geometric initial state of the machine tool.

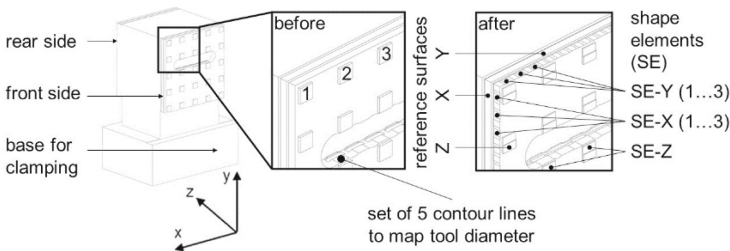


Fig. 1. Test work piece with ref. Surfaces and shape elements before and after measurements

To map the TCP position, shape elements, corresponding to the X-, Y-, and Z-axis of the machine tool, are machined. The distance between a shape element and its corresponding reference surface translate into TCP-displacements at specific times during the experiment (Fig. 1). In order to log a detailed TCP displacement progression, the TWP possesses 25 shape elements for each translational direction (X, Y and Z). When manufacturing these shape elements, tool wear can have a negative effect on the shape accuracy. Therefore, the actual diameter of the tool is recorded in the TWP five

times during the experiment by manufacturing counter lines 1 to 5 (Fig. 1). The rear side of the TWP is identical to that of the front side. Thus, two test trials can be recorded on the same part, e.g. running the machine tool once with and once without activated correction methods as introduced in [5–7].

2.2 Machine Tool DMU 80

The TWP tests were conducted on a 5-axis milling machine (DMG DMU 80 eVo linear). Only the three translational axes of the machine tool were active during the experiments. Machining was performed without compressed air or cooling lubricants. Machine-internal thermal correction methods (spindle length and translational axes) were deactivated during the experiments. The TWP was machined with an end mill for aluminium with the following set of cutting parameters (Table 1):

Table 1. Tool properties and cutting parameters.

Tool properties	Cutting parameters
Brand: Garant	cutting speed v_c : 450 m/min
Model: solid carbide end mill (DIN 6527)	depths of cut a_p : 0.2... 0.3 mm
Diameter: 12 mm; Number of teeth: 4	feed rate v_f : 400 mm/min

2.3 Test Setup

Two fixtures made of Fe65Ni35-Invar hold the measuring probes (MP). The test work piece was mounted on the machine tool table as shown in Fig. 2 and 3.

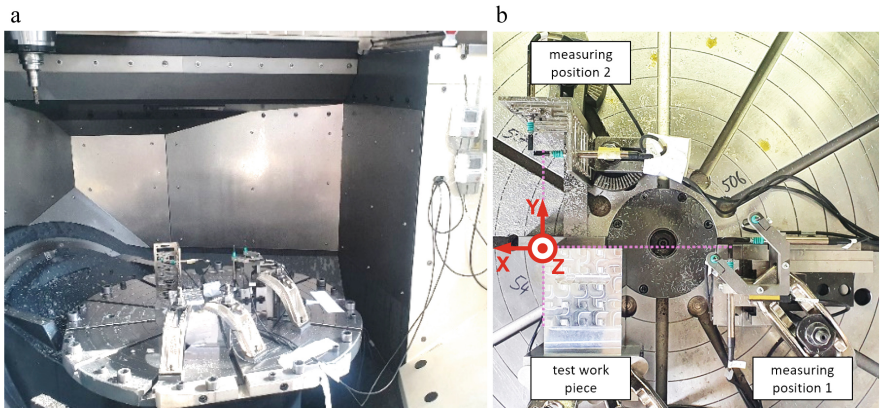


Fig. 2. Test setup on DMU80 machine tool: a) front view, b) top view.

Tactile Measurement

Once triggered by contact, the measuring probes recorded the TCP displacements every 200 ms. The dwell time during this measurement is one minute. During this time, each probe recorded approx. 300 values. Afterwards, the median value was calculated.

The sensors were aligned in such a way that point zero (middle of the measuring range) was in the same plane as the corresponding shape elements of the TWP. This clamping position minimizes thermally effective lengths, which would limit the comparison of the TCP displacements recorded on the TWP and the measuring probes. Furthermore, this reduces the linearity error and thereby increases the measuring accuracy of the measuring probes. The probes in z direction contact the bottom of the tool holder. The probes in X and Y direction contact the tool shaft. This avoids a tool change to switch to a mandrel for measuring purposes.

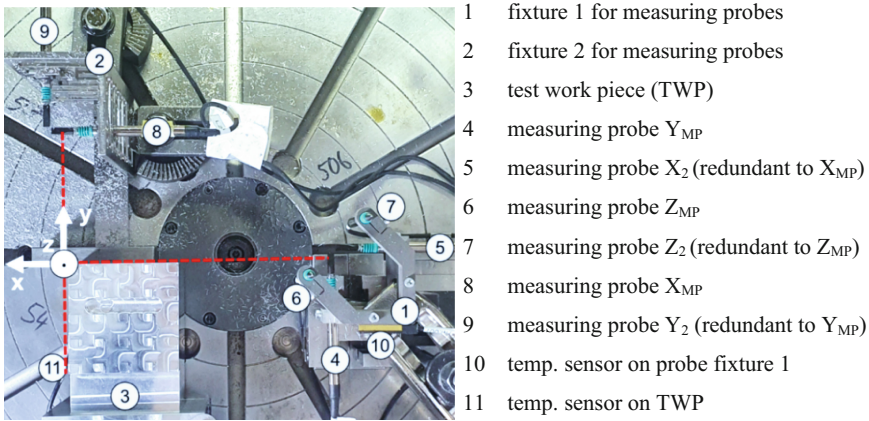


Fig. 3. Experiment setup on machine tool table: sensor positions and coordinate system.

Table 2 is an overview of the sensors used:

Table 2. Measured values, sensor features and measuring positions.

Measured values	Measurement method 1	Measurement method 2
TCP displacement values	Test work piece (TWP)	Measuring probe: TESA, GTL 21USB (electronic length gauge)
TCP error in X-direction	shape element X (1...25)	measuring probe X_{MP}
TCP error in Y-direction	shape element Y (1...25)	measuring probe Y_{MP}
TCP error in Z-direction	shape element Z (1...25)	measuring probe Z_{MP}
Temperature values	Platinum temperature sensors (IEC 60751:2008) by Testo	
TWP	Surface sensor, glued to the TWP (Model: 8692753)	

(continued)

Table 2. (continued)

Measured values	Measurement method 1	Measurement method 2
probe fixture 1	Surface sensor with magnet, attached to fixture 1(model: 8692753)	
Machine tool work space	Bar probe /w magnet, in workspace of machine (model: 8121418)	
Ambient temperature	Rod sensor with magnet, in front of machine (Model: 8121418)	
Data processing: Saveris Pt D - 1-channel temperature wireless sensor		

Table 3 shows the measurement uncertainties of the measuring equipment used:

Table 3. Manufacturer information on measurement uncertainties of the measuring equipment.

Measuring equipment	Uncertainty of measurement
coordinate measuring machine (CMM) [6]	$u_{\text{CMM}} = \pm 1,2 \mu\text{m}$
measuring probe, L (range) $\leq 0,5 \text{ mm}$ [8]	$u_{\text{MP}} = \pm 0,5 \mu\text{m} \pm 0,6 \mu\text{m/mm} * L \leq \pm 0,8 \mu\text{m}$
Combined measurement uncertainty (max.)	$u_{\text{comb}} = u_{\text{CMM}} + u_{\text{MP}} = \pm 2.0 \mu\text{m}$
Thermal sensors [9]	$u_{\text{T}} = \pm 0,1 \text{ }^\circ\text{C}$ (range: 0... 60 °C)

2.4 Test Execution

Two variations of the same experiment were performed, each with two trials, on consecutive days. For each trial, the machine tool was prepared in the afternoon of the previous day; the machine tool was set to the desired state (running or switched off) and the trial started on the next morning. The two experiments differ in the type of load case, that was applied, to simulate different machining scenarios.

Test Procedure

Each experiment starts with milling the TWP reference surfaces including the first tool wear groove. In a second step, the initial set of shape elements (Fig. 1) for translational errors in the x, y and z direction is machined. Third, the CNC moves tool to contact the probes for tactile measurement. In step four, the machine tool performs a motion sequence defined by load cases from industrial applications (see “artificial load cases”). Subsequently, the next set of shape elements is manufactured and tactile measurements are conducted. The procedure starts from step three is repeated for all 25 shape element sets.

Artificial Load Cases

Two artificial load cases were designed to induce thermal loads into the machine tool in order to simulate two different machining scenarios without actually machining. Thereby, the machine tool heats up or cools down, to create thermally induced positioning errors (Fig. 1 and Fig. 4).

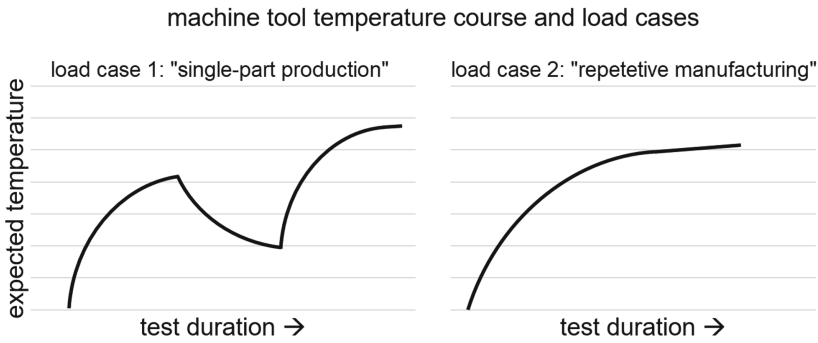


Fig. 4. Expected temperature changes of machine tool components under load case #1 and #2.

The machine tool performed axis movements and spindle rotations. Thermal loads result from friction and electrical losses of the feed drives during movement and acceleration of the feed axes and motor spindle. The measurement intervals were defined in such a way that short measurement intervals were used for periods with high temperature gradients and large measurement intervals for low temperature gradients. Table 4 shows the different measurement intervals, for the two artificial load cases that were investigated:

Table 4. Measuring intervals

Load case 1: “single part production”	Load case 2: “continuous manufacturing”
5 measurements every ~ 5 min, then	10 measurements every ~ 5 min, then
3 measurements every ~ 30 min, then	5 measurements every ~ 10 min, then
5 measurements every ~ 5 min, then	5 measurements every ~ 20 min, then
3 measurements every ~ 30 min, then	4 measurements every ~ 40 min
5 measurements every ~ 5 min, then	
3 measurements every ~ 30 min	

Load Case 1: “Single Part Production”

This load case simulates the production of individual components with intermediate idle times. The machine tool experiences alternating thermal loads and standstill, so that the temperature of the feed and spindle components rises and falls alternately. The machine

tool is switched off on the evening of the previous day and is at thermal equilibrium with the environment at the start of the experiment in the morning.

Load Case 2: “Continuous Manufacturing”

This load case simulates series production. The machine tool is subjected to a continuous, almost constant load with the exception of short dwell times during the tactile measurements. The temperature of the feed and spindle components rises continuously until the machine is in a steady state. In the following experiments, the machine tool was switched-on at the evening of the previous day (all feed axes in position control). Therefore, the machine tool was not in a state of thermal equilibrium with the environment at the beginning of the test. The planned motion sequence heats the machine including the feed axes and the main spindle. It simulates a representative machining process. The motion sequence consists of cyclic acceleration and braking processes of the feed axes and the main spindle. The TCP moves on spiral paths in the X-Y plane of the machine.

2.5 Experiment Evaluation

Removing material with the end mill tool imprints the TCP displacement directly on the TWP surface. A thermal compensation calculation of the TWP must be performed, to account for the thermally induced geometry changes during the trial. On the condition that the TWPs thermal expansion was compensated and that tool wear and its thermal expansion were negligible, the displacement obtained by measuring one specific TWP shape element is defined as the actual TCP displacement of the machine tool at the time of machining this specific shape element. The goal of the experiment was to compare two different measuring methods. Because tactile and TWP based TCP displacement measurements were conducted at a different location on the machine table and at different points in time, this entails uncertainties and difficulties in comparing the measurement data obtained by the two methods. Therefore, the measurement data were processed in the following way: First, a thermal compensation calculation was performed for all values and then an Offset was calculated to match the progressions of the two sets of data (TWP and MP). This procedure allows for comparing the progressions of the measured values of the two measuring methods.

Measurement of TWP on a Coordinate Measuring Machine

A coordinate measuring machine (CMM) is required to measure the geometry of the TWP. Wiemer et al. have shown that high-precision coordinate measuring machines provide a measurement uncertainty of about $\pm 0.6 \mu\text{m}$. Because two measurements are necessary to calculate the distance between reference surface and shape element, the maximum error can be up to $\pm 1.2 \mu\text{m}$ [6]. The evaluation is carried out by calculating the above-mentioned distances for all 25 sets of shape elements and the four groove widths (for tool wear determination). To reduce the influence of the surface roughness of the surfaces of the machined TWP, five measuring points per surface were to be measured and averaged.

Compensation of Thermal Expansion of TWP and Fixtures on Measurement Results

The aluminium TWP expands and shrinks with temperature changes ($23.1 * 10^{-6}/K$ at $20\text{ }^{\circ}\text{C}$ which requires a thermal correction of measured values.

Table 5 shows the expected linear expansion due to temperature change on the TWP:

Table 5. Calculated displacement of the TWP surfaces due to thermal expansion.

Displacement direction	X_{TWP}	Y_{TWP}	Z_{TWP} (face 1)	Z_{TWP} (face 2)
Thermally effective length in mm	42,5	117	85	42,5
Calculated thermally induced displacement in $\mu\text{m}/K$	1,02	2,81	2,04	1,02

The tactile probe fixture 1 was made out of Invar (thermal expansion negligible). But for technical reasons, it was mounted on a 100 mm high steel block. Therefore, the probe's measured displacements in the Z direction require thermal correction as well. The temperature at fixture 1 was recorded every minute. The temperature at fixture 1 was recorded every minute. Using the expansion coefficient of steel ($13.9 * 10^{-6}/K$ at $20\text{ }^{\circ}\text{C}$), the measured displacement values were corrected by a factor of $1.39\text{ }\mu\text{m}/K$. For comparison of tactile and TWP measurement, the offset for a given trial and direction was calculated from the difference in the median of two corresponding displacement variables (e.g. X_{TWP} and X_{MP}) for all measured values. Table 6 shows the calculated offset values:

Table 6. Differences in median values between TWP and MP (Offset values for MP values).

Load case, trail	Offset X_{MP}	Offset Y_{MP}	Offset Z_{MP}
Load case 1, trail 1	0,0 μm	-3,0 μm	-5,5 μm
Load case 1, trail 2	0,0 μm	-6,0 μm	-6,0 μm
Load case 2, trail 1	1,4 μm	-1,0 μm	-6,7 μm
Load case 2, trail 2	0,0 μm	-2,5 μm	-7,0 μm

3 Measured TCP Errors Due to Thermal Influences

3.1 Determined TCP Error Values

The results demonstrate that the progression of the recorded TCP displacements, determined by means of the TWP and the measuring probes, are consistent.

Load Case 1

Load case 1 showed increasing displacements during the (simulated) machining part of the load case in the first part of the experiment. Afterwards, during the transition to the cooling phase, the measured displacements decreased. During the second (simulated) machining part of the experiment, the displacements increased again due to the renewed increase in thermal load on the machine tool, as shown in Fig. 5.

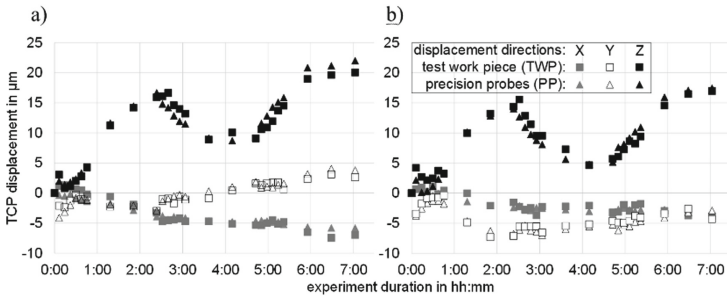


Fig. 5. Measured TCP displacements for load case 1: a) trial #1 and b) trial #2.

Load Case 2

The parameters for load case 2 were selected to ensure continuous heating of the machine tool and to reach a steady state towards the end of the experiment. The measured displacements increased during the experiment and approached a maximum, as shown in Fig. 6:

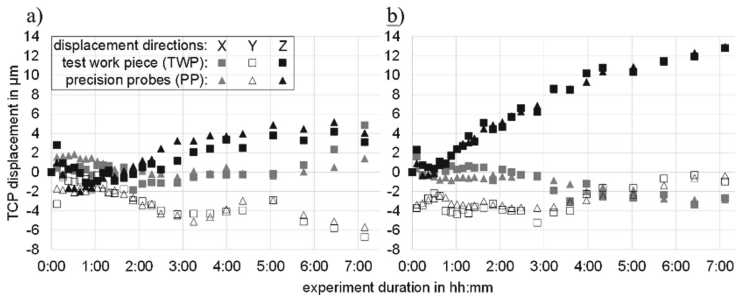


Fig. 6. Measured TCP displacements for load case 2: a) trial #1 and b) trial #2.

3.2 Comparison of the Deviation in the Determined TCP Error Values for TWP and Measuring Probe Measurements

The difference between the measured values with the TWP and the measuring probes was less than $\pm 2 \mu\text{m}$ (Fig. 7). The maximum total measurement uncertainty of the test setup

is $\pm 2 \mu\text{m}$. The red dashed lines indicate the upper and lower limits of measurement uncertainty. With the exception of a few outliers, all measured value differences fall within this range.

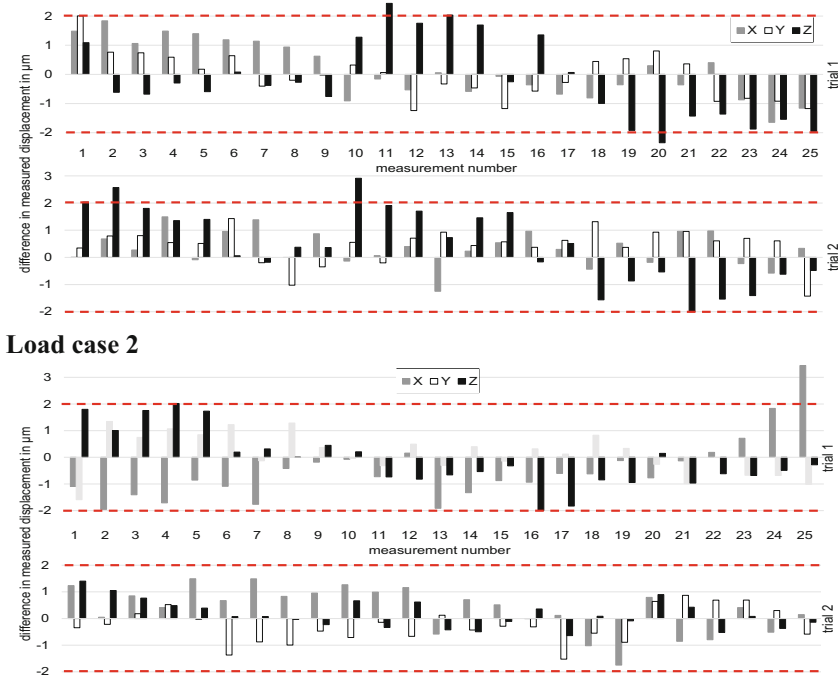


Fig. 7. Differences in TCP displacements measured with the TWP and with the measuring probes for the two load cases. The dotted line represents the maximum measurement uncertainty of the sensors.

4 Discussion

The experimental results show that the TWP is suitable for measuring thermally induced TCP displacements during milling with a high accuracy. During machining of the shape elements on the TWP, the machine tool's TCP displacement is transferred to the TWP by means of material removal. Therefore, it can be defined as a direct measurement of the machine tool's TCP. There are three factors, which can influence the accuracy of this direct measurement: the thermal expansion of the tool, of the TWP and tool wear. The radial tool wear was recorded several times during the test and the tool diameter change was below $0.5 \mu\text{m}$. The temperature and resulting shape change of the TWP during each trial was taken into account. Influences that could not be determined in a practicable way were the tool temperature itself and the actual TWP temperature field (temperature was measured on one side of the TWP only). In addition to the measurement

inaccuracies, specified by the manufacturers of the measuring equipment (Table 3), the following negative influences on the measurement accuracy caused by the test setup were identified:

- a) At the beginning of the measurement, the reference surfaces on the TWP are machined. This operation takes approx. 60 s. The end of this operation is the moment of the maximum heat flow into the TWP and the tool. The resulting thermal expansion leads to dimension deviations of the reference surfaces. Since, the reference surfaces serve as a reference for the measurement of the shape elements on a CMM, this phenomenon might cause a measurement uncertainty, which was not quantified.
- b) During the application of load case and machining of the shape elements, the motor spindle is running and heats up. During the measurement with the measuring probes, the motor spindle does not rotate and cools down. It is expected, that due to the deactivated thermal spindle length compensation, the spindle would begin to shorten. This effect was observed in the z direction displacement, measured by the probes. It reached up to 1.5 μm during the one-minute measuring period (Fig. 8).

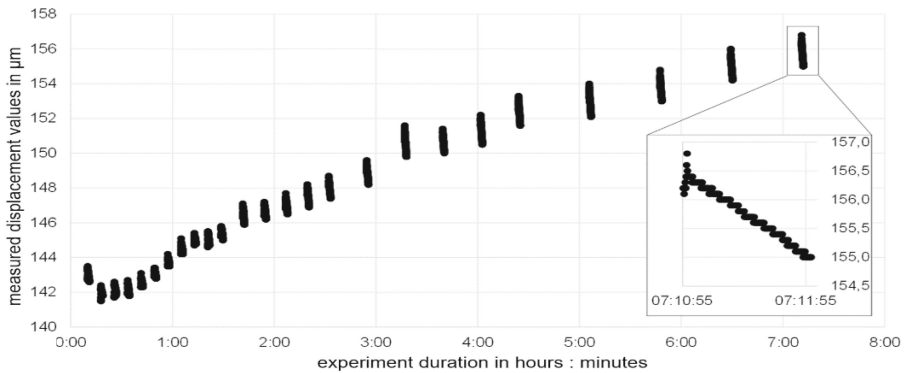


Fig. 8. The displacement of the measuring probe in the Z-direction as a function of time

Table 7 shows outliers and likely causes:

Table 7. Overview of identified outliers and presumption of cause.

outlier #	Load case, trial; component; measurement-#	cause
1	load case 2, trial 1; X; #25	a
2	load case 1, trial 1; Z; #11	b
3	load case 1, trial 1; Z; #20	b
4	load case 1, trial 2; Z; #2	b

5 Conclusion

Comparing the TCP positioning errors obtained by from the developed TWP with results from measuring probes showed deviations of only $\pm 2 \mu\text{m}$. Up to 25 TCP displacements (with 3 spatial components each) can be recorded with the TWP.

The preparation and post-processing as well as the execution of tests by means of the TWP require shorter set-up time than conventional probes. No other measuring equipment than temperature sensors are required. Even inexperienced machine operators can carry out measurements with the TWP. It is a user-friendly, time-efficient, and cost-effective alternative to conventional measuring methods. Since the TWP must be fixated on the machine table, the measurement of TCP displacements is limited to a plane at a distance of 85 mm above the machine table. The applicability of the TWP is limited to the measurement of translatory errors on 3-axis milling machines. The user needs access to a CMM to measure the shape elements on the TWP.

Since only low cost temperature sensors are used, there is no danger of damaging sensitive measuring equipment by chips and cooling lubricants. Therefore, a measurement can be carried out simultaneously to the machining of components.

The TWP was developed to validate the effectiveness of thermal compensation and correction methods on milling machines. The experiments confirmed its suitability for this application.

Acknowledgment. This research was funded by the German Research Foundation (DFG) – Project-ID 174223256 - TRR 96, which is gratefully acknowledged.

References

1. Springer, Berlin, Heidelberg: Ermittlung der Arbeitsgenauigkeit mit Prüfwerkstücken. In: *Werkzeugmaschinen 5*. VDI-Buch (2006)
2. Blaser, P., Hernandez-Becerro, P., Mayr, J., Wiessner, M., Wegener, K.: Thermal errors of a large 5-axis machine tool due to cutting fluid influences – evaluation with thermal test piece. In: *Proceedings of the 32nd ASPE Annual Meeting 2017* (2017)
3. Putz, M., Regel, J., Wenzel, A., Bräunig, M.: Thermal errors in milling: comparison of displacements of the machine tool, tool and workpiece. In: *Proceedings of 17th Conference on Modelling of Machining Operations* (2019)
4. Mareš, M., Horejš, O., Havlík, L.: Thermal error compensation of a 5-axis machine tool using indigenous temperature sensors and CNC integrated Python code validated with a machined test piece. *Precis. Eng.* **66**, 21–30 (2020)
5. Höfer, H., Wiemer, H.: Generation of motion sequences for thermal load of machine tools. *Prod. Eng. Res. Devel.* **11**(1), 75–83 (2016). <https://doi.org/10.1007/s11740-016-0708-1>
6. Neidhardt, L., Höfer, H., Wiemer, H.: Prüfwerkstück zum Nachweis von thermisch bedingten Verlagerungen an Fräsmaschinen—Konzept und erste Erfahrungen. *ZWF* **109**(11), 814–818 (2014)
7. Höfer, H., Wiemer, H.: Measurement of test pieces for thermal induced displacements on milling machines. In: *Proceedings of the Conference on Thermal Issues in Machine Tools, Dresden* (2018)

8. HAHN+KOLB Homepage. https://media.witglobal.net/stmedia/hahnkolb/documents/LANG_de/HK-39662321.pdf. Accessed 08 Sept 2022
9. Testo Homepage. <https://static-int.testo.com/media/1b/02/51ccb8bd5f9c/saveris-PROF-Bedienungsanleitung.pdf>. Accessed 08 Sept 2022

Open Access This chapter is licensed under the terms of the Creative Commons Attribution 4.0 International License (<http://creativecommons.org/licenses/by/4.0/>), which permits use, sharing, adaptation, distribution and reproduction in any medium or format, as long as you give appropriate credit to the original author(s) and the source, provide a link to the Creative Commons license and indicate if changes were made.

The images or other third party material in this chapter are included in the chapter's Creative Commons license, unless indicated otherwise in a credit line to the material. If material is not included in the chapter's Creative Commons license and your intended use is not permitted by statutory regulation or exceeds the permitted use, you will need to obtain permission directly from the copyright holder.



Author Index

A

Aguirre, Gorka 159
Aumann, Quirin 132

B

Bambach, Markus 41
Barth, Sebastian 289
Beitelschmidt, Michael 146
Benner, Peter 132
Bergs, Thomas 289, 308, 318
Bertaglia, Nico 28
Boos, Eugen 99
Brecher, Christian 28, 119
Bredthauer, Marc 289
Brezina, Jonas 203
Butz, Felix 240

C

Colinas-Armijo, Natalia 159

D

Dehn, Mathias 119
Denkena, Berend 192
Dix, Martin 28
Döpfer, Frank 240
Drossel, Welf-Guntram 179, 265

E

Engert, Michelle 278
Erben, Andreas 179

F

Fetzer, Christof 67
Fickert, Axel 168, 265, 345

G

Geist, Alexander 28, 179
Gißke, Carola 168, 345
Glänzel, Janine 28, 179
Gonzalez Degetau, Ana Maria 203

H

Heinze, Tassilo 219
Helmig, Thorsten 308
Herzog, Roland 28
Horejš, Otakar 54, 83
Huzlík, Rostislav 333

I

Ihlenfeldt, Steffen 67, 99, 179
Iñigo, Beñat 159
Iriño, Naruhiro 3

J

Jonath, Lucas 203

K

Kaftan, Petr 15
Karaoglu, Selim 203
Klemme, Heinrich 192
Kneer, Reinhold 308
Koch, Lukas 240
Koriath, Hans-Joachim 219
Kozlok, Tomáš 83
Krahn, Robert 67
Krüger, Gordana 240
Kuznetsov, Alexander Pavlovich 219

L

Lang, Sebastian 41
Liu, Hui 308, 318
López de Lacalle, Luis Norberto 159
Luderich, Jörg 203

M

Mäder, Thomas 179
Mareš, Martin 54, 83
Mattfeld, Patrick 289
Mayr, Josef 15, 41
Meier, Matthias 192
Meurer, Markus 318
Möhring, Hans-Christian 278
Mori, Masahiko 3
Müller, Jens 67

N

Naumann, Andreas 28
Naumann, Christian 28
Neus, Stephan 119
Nykodym, Pravoslav 54

O

Ota, Koji 3

P

Penter, Lars 345
Pruša, Radomír 333

R

Regel, Joachim 333
Rudolph, Holger 67

S

Saak, Jens 132
Sauerzapf, Stefan 146
Senf, Björn 179
Steiert, Christoph 99
Straka, Michal 83
Švéda, Jiří 83

T

Thiem, Xaver 67
Topinka, Lukáš 333

V

Vettermann, Julia 132
Voigt, Immanuel 179, 265

W

Wegener, Konrad 15, 41
Wenkler, Eric 99
Werkle, Kim Torben 278
Wiemer, Hajo 168, 265, 345
Winter, Simon 308
Wnendt, Eike 192

Z

Zimmermann, Nico 41
Zontar, Daniel 28